Developing metastable switchable materials towards scale-up production in continuous flow environment

Flandrin, Pierre-Baptiste

Award date:
2019

Awarding institution:
University of Bath

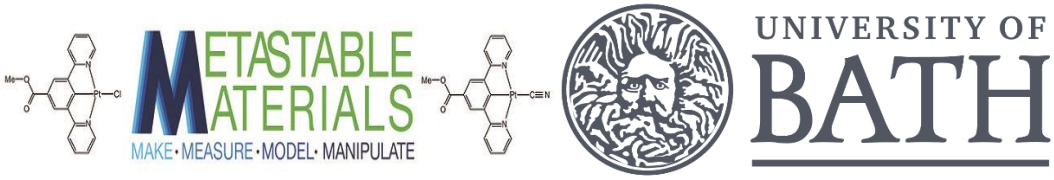

EPSRC
Engineering and Physical Sciences
Research Council

Developing metastable switchable materials towards scale-up production in continuous flow environment

Pierre-Baptiste Flandrin

A thesis submitted for the degree of Doctor of Philosophy

University of Bath

Department of Chemistry

Supervisor: Professor Chick Wilson, Professor Paul Raithby, Professor Harris Makatsoris and Doctor Karen Robertson

January 2019

Abstract

Metastable materials are characterised by a change in properties as a response to external stimuli such as heat, light, pressure, or changes in magnetic field. Such properties are of great interest for a range of industries, from sensors to data storage materials, due to their highly reversible switching properties. The molecular scale of those compounds is increasingly being considered as the answer to the miniaturisation of the components used in the construction of working devices, but process control of the synthesis of these compounds can be difficult to exact using batch production methods. The synthesis of several switchable compounds, notably of spin-crossover (SCO) materials, is investigated using different flow platforms; the Oscillatory Baffled Reactor (OBR) from the group of Professor Harris Makatsoris at Cranfield University, the Kinetically Regulated Automated Input Crystalliser (KRAIC) designed by Dr Karen Robertson at the University of Bath and a series of commercial Vapourtec Flow reactors.

It is found that by investigating a range of reactions and reactor parameters via design of experiments (DOE) principles, it is possible to create simulated models in order to predict and target particle size; the success of which has been confirmed by particle size analysis. Scale-up production of the materials presented herein has been achieved with actual control of the metastable properties of the materials using flow synthesis. Switching properties have been controlled and a particular correlation between method of production and switching ability has been observed. In addition, methods based on Computational Fluid Dynamics (CFD) are presented to combine data from CFD simulation experiments with practical experimental outcomes to have better insight of the reactors studied and improve metastable material production.

To my beloved grandmother, Granny.

Acknowledgments

First and foremost, I would like to thanks Professor Chick Wilson and Professor Paul Raithby for offering me a position in the Metastable Group at Bath and for all their overwhelming support during those years. It has been a wonderful experience and I loved to work with the group.

I would like to thanks particularly Dr Karen Robertson, for all her teaching on crystallisation and flow chemistry. I learn so much from you and my PhD would not have been possible without you. Thanks for proofreading my thesis draft and other project during my thesis.

Thank you to everyone at Cranfield University, Professor Harris Makatsoris, Samet Isaev and Ioannis Alissandratos for all the fantastic work we have done together during the past three years whether it was at Cranfield, Brunel University or outside academia.

A special thanks to Dr Ryan Skilton and Duncan Guthrie from Vapourtec for their help with the flow system and for giving me the opportunity to take part of the IMRET in Beijing in 2016.

A huge thanks to people I have worked with during my PhD, Dr Lauren Hatcher thanks for your help in analysing crystallographic data we obtained during my PhD. Dr Lucy Saunders for being always positive every day in our office and Alex Cousen my lab singing and music buddy. I would like to thank Dr Anuradha Pallipurath for her support and help during my thesis and for spectra analysis and teach me what to know about Raman and Spectroscopy. Dan Scott for all the experiments we carried out together at Bath and at Diamond Light Source, you will carry on the flow work at Bath. Dr Helena Shepherd for all her help and suggestion on Spin Crossover during my thesis. Dr Julien Schmitt thank you for your help on the DLS and for teaching me all the principle of DLS in depth. Dr Sunyhik Ahn and Professor Frank Marken for teaching me the basic of electrospray techniques.

Thanks to all the Chicklets past and present, Dr Lauren Agnew and Dr Anneke Klapwijk for the fun we had running the COBC and the KRAIC, Ruth Lunt for the random giggles times, Lois Wayment for the fun we add at Diamond Light Source, Dr William Gee, Dr Jane Knichal, Clare Stubbs and Pollyanna Payne, those three years would not have been as fun without you.

Thanks to the Bath French team, Dr Pascaline Patureau, Dr Martin Depardieu, Dr Anne-Frédérique Pecharman, Dr Fabienne Caggiano, Dr Rémi Castaing you made me have a little bit of France when I needed it.

A very special thanks goes to my parents Cathy and Jean-Vic, for their endless support during my whole thesis and for always looking after me.

Last but not least, I would like to thank Jacques of Guissény, and my aunts Jeannie, Bé, Cathou for their encouragement and support throughout those four years.

Table of Content

List of Figures

List of Tables

List of abbreviations

2BA	2-bromoaniline
2BA 3,4DNBA	2-bromoaniline 3,4-dinitrobenzoic acid
2BA-FJ-EtOH	2BA 3,4DNBA synthesis using an free jet
2BA-TP	2BA 3,4DNBA synthesis using T-piece and anti-solvent techniques
2CA 3,4DNBA	2-chloroanilinium 3,4-dinitrobenzoic acid
2CA-FJ-EtOH	2CA 3,4DNBA synthesis using an free jet
2CA-TP	2 CA 3,4DNBA synthesis using T-piece and anti-solvent techniques
2CLA	2-chloroanilinium
2IA	2-iodoaniline
2IA 3,4DNBA	2-iodoaniline 3,4-dinitrobznoic
2IA-Be-5m	2IA 3,4DNBA synthesis in bench flow 5 m tubing
2IA-FJ-EtOH	2IA 3,4DNBA synthesis using an free jet
2IA-K-st	2IA 3,4DNBA synthesis in the KRAIC
2IA-SFK-EtOH	2IA 3,4DNBA synthesis using segmented flow in the KRAIC
2IA-YT	2IA 3,4DNBA synthesis in y-tubing
2XA-IJ	2BA/2CA/2IA 3,4DNBA synthesis using an impinging jet
3,4DNBA	3,4-dinitrobenzoic acid
API	Active Pharmaceutical Ingredient
APS	Average Particle Size
AUC	Analytical Ultra Centrifugation
B	Batch experiment for PiC
BPR	Back pressure Regulator
BY	Batch experiments for YeC synthesis
C	CFD RTD Experiments for the OBR
CFD	Computational Fluid Dynamic
CFDK	CFD KRAIC simulation
Ch1	4-iodoanilinium 3,5-dinitrobenzoate
Ch2	4-iodoaniline 3,5-dinitrobenzoic acid solvate
Ch5	4-iodo-2-methylanilinium 3,5-dinitrobenzoat
COBC	Continuous Oscillatory Baffled Crystalliser
CSTR	Continuous Stirred Tank Reactor
DCS	Differential Centrifugation Sedimentation
DLS	Dynamic Light Scattering
DoE	Design of Experiment
DOEV	DOE for Vapourtec static mixer reactor
DSC	Differential Scanning Calorimetry

DTA	Differential Thermal Analysis
FEP	fluorinated ethylene propylene
FTIR	Fourier Transform InfraRed spectroscopy
FTY	Flow progressive mixer reactor experiments for YeC synthesis
FY	Flow initial experiments for YeC synthesis
GK	Gel Experiment KRAIC
GKV	Gel Experiment KRAIC with Vanillin
H	Velocity Ratio experiments for PiC synthesis with the OBR
HPLC	High Performance Liquid Chromatography
HS	High Spin
ID	Internal Diameter
IPA	Isopropanol
IR	Infra-Red
K	KRAIC Experiment for PiC
KRAIC	Kinetically Regulated Input Crystalliser
KRAIC-D	Kinetically Regulated Input Crystalliser Diamond
LS	Low Spin
MeOH	Methanol
MSMPR	Mixed Suspension Mixed Product Removal
MSZ/MSZW	Metastablle Zone/ Metastable Zone Width
NMR	Nuclear Magnetic Resonnance
OBR	Oscillatory Baffled Reactor
OD	Outer Diameter
PAT	process analytical technologies
PEEK	polyether ketone
PiC	$[Fe(Htrz)_2(trz)](BF_4)$
PiCKD	PiC experiment inside the KRAIC-D
PiCM	$[Fe(Htrz)_3](BF_4)_2{\cdot}H_2O$
PiCMB	PiCM synthesis in Batch
PiCMK	PiCM synthesis in the KRAIC
POM	Spin crossover PiCM synthesis OBR with piston system
POW	Spin crossover PiC synthesis OBR with piston system
PSD	Particle Size Distribution
PTFE	polytetrafluoroethylene
PXRD	Powder X-ray Diffraction
RBF	round bottom flask
RT	Residence Time
RTD	Residence Time Distribution
SA	Succinic Acid

SAK	Succinic Acid KRAIC Experiment
SCO	Spin Crossover
SEM	Scanning Electron Microscopy
SO	Spin crossover 1st PiC synthesis OBR
ST	Spin Transition
STC	Stirred Tank Reactor
TGA	Thermogravimetry Analysis
ThA	Ch1 synthesis with Acetonitrile
ThAW	Ch5 synthesis with Acetonitrile and Water as anti-solvent
ThE	Ch5 synthesis with Ethanol
ThEW	Ch5 synthesis with Ethanol and Water as anti-solvent
ThI	Ch1 synthesis with Isopropanol
ThIW	Ch1 synthesis with Isopropanol and Water as anti-solvent
ThM	Ch2 synthesis with Methanol
ThMW	Ch2 synthesis with Methanol and Water as anti-solvent
UBA	Urea Barbituric Acid
UBAK	Urea Barbituric Acid KRAIC Experiments
UV-Vis	Ultraviolet Visible
V	RTD Experiments for the OBR
Vb	Initial Vapourtec Experiment for PiC synthesis
VM	PiCM synthesis using Vapourtec R-series
Vta	Vapourtec PiC particle size targeting
YeC	$[FeL_2][BF_4]_2$ [L = 2,6-di(pyrazol-1-yl)pyridine]

General Introduction

Manufacturing smart materials with functional capabilities has been seen as a promising way to develop cost-efficient processes for specific applications. The possibility to tune properties of some nano/microscale materials such as Pt-pincers, spin crossover (SCO) or thermochromic compounds, in which switching between two electronic states can be achieved by different *stimuli* (temperature, pressure, shear rate, contact with other chemicals)[1–4] gives an opportunity to create new types of devices for industry such as building construction, vehicles, coloured materials, conductive materials and many more.[5–7] There are multiple advantages of using such materials, for instance colour switching displays with fast colour change between the phase transitions and also fast responsive sensors, providing flexibility for the production of such devices.[2] Even if the switching mechanisms are well known, e.g. for $[Fe(Htrz)_2(trz)](BF_4)$ a thermal induced spin crossover compound which will be presented in this thesis, finding an appropriate way of accessing these properties on an industrial scale is difficult.

The challenges in producing switchable materials are in scaling up the production to industrial scale whilst keeping the switching properties close to those presented at smaller scale. Some of the compounds studied in the Metastable Materials group at the University of Bath have been difficult to scale up in batch due to heat and mass transfer sensitivity and some properties can be altered as a result of differing particle size, for example in the spin crossover compound $[Fe(Htrz)_2(trz)](BF_4)$.

Detection of the changing properties of switchable compounds (SCO, thermochromics) are performed using different stimuli like temperature, pressure induced spin crossover, magnetic field and light[8–10]. But for those compounds, particle size is seen as an impact factor for switching properties;[11–14] smaller particles are often of particular interest e.g. in $[Fe(Htrz)_2(trz)](BF_4)$ whose nanoscale properties induce a lower temperature and faster transition when the particles get smaller. While, in batch, it is possible to control particle size *via* the reverse micelle technique for certain SCO compounds, using surfactant for that technique has been shown to change the switching behaviour of that material and this technique is not applicable at large scale without increasing the production cost due to surfactant use;[11] the successful production of small particles has not been shown in literature without using surfactant. For thermochromic materials, crystallisation techniques have be shown to deactivate the colour change and the reproducibility of these experiments while scaling up is an issue.[15] Therefore to overcome those issues, a new way of producing such materials is proposed. In this thesis flow chemistry and crystallisation have been studied in order to scale up and control switching properties of those materials.

The first objective is to successfully produce switchable materials using flow chemistry or crystallisation techniques. To this aim three reactors using different flow behaviour have been used, the Kinetically Regulated Automated Input Crystalliser (KRAIC)[3,16], the Oscillating Baffled Reactor (OBR)[17] and a Vapourtec flow synthesiser equipped with different mixing reactors. The second objective is to control particle size using those reactors, study the change in switching properties of those compounds produced in flow and compare them to batch synthesis, and investigate scale up capabilities.

Chapter I of the thesis will introduce switchable materials (SCO, thermochromics) and their applications, as well as flow technologies used in industry in order to produce fine chemicals around the world and their advantages compared to batch.

Chapter II will present the different methods and techniques, including background theory and apparatus used throughout this thesis.

Chapter III will be focused on the KRAIC and its use to synthesise different compounds in segmented flow. In this section the reactor will be introduced as a main crystalliser for pharmaceutical compounds in the Wilson group at the University of Bath and the optimisation of that reactor towards synthesis of smart switchable materials. Evaluation of mixing inside the segmented flow reactor will also be presented *via* computational fluid dynamics (CFD).

Chapter IV will present online *in situ* X-ray analysis at the Diamond Light Source synchrotron using a modified version of the KRAIC (KRAIC-D). Online Raman spectroscopy will be introduced in order to monitor the reaction steps of $[Fe(Htrz)_2(trz)](BF_4).6H_2O$.[4]

Chapter V presents the use of the Centillion® OBR reactor in order to produce $[Fe(Htrz)_2(trz)](BF_4).6H_2O$ and control its particle size using a surface response Design of Experiments (DOE) model. After the use of this model, an optimisation of the reactor properties and the particle size distribution will be discussed with residence time analysis and CFD simulation of the OBR.

Chapter VI introduces the use of the Vapourtec R-Series Flow Kit reactors (progressive mixer reactors, jets, static mixers, etc.) in order to produce a range of switchable materials (SCO, thermochromics). As in Chapter V, a DOE with a surface response model will be presented to control particle size of $[Fe(Htrz)_2(trz)](BF_4)$. A progressive mixer reactor will be introduced to produce a $[FeL_2][BF_4]_2$ [L = 2,6-di(pyrazol-1-yl)pyridine] SCO compound *via* anti-solvent flow crystallisation. The flow jet crystallisation technique will also be presented to produce a range of reversible thermochromic compounds.

Chapter VII will discuss the advantages of using each reactor for different purposes and will focus on the post-synthesis analysis of the compounds with different analysis techniques and post process incorporation of the switchable compound into devices.

The Appendix will contain supplementary data for each chapter. External supplementary information will be also given on a CD provided with this thesis presenting different mechanisms used for each reactor, along with CFD simulation videos.

Chapter I Introduction and literature review

I.1. Context of research

Materials are commonly classified into two categories: structural materials (e.g. for the construction of buildings, armour and vehicles) and functional materials (e.g. conductivity, transparency, colour and many more). Thanks to those functional materials, matter becomes adaptive and evolutionary, this has been a revolution for the XXIst century. The next step, smart materials, have been a significant new direction in this area over recent years. Smart materials, the subject of some of the work presented here, celebrate also the growing roles of biologically-inspired models in the conception of new products and devices.[18–21] In this context, biomimicry, micromachines (molecular or cellular), active or selective membranes and sensors can give the opportunity to explore varied applications in the medical or computing domain. More generally, smart materials impose themselves in diverse sectors, from buildings to sporting equipment, biomedicine, robotics and military sectors. [5–7,22]

A smart material is sensitive, adaptive and evolutionary. It is functional, allowing it to behave e.g. as a detector (signal detector), an actuator (perform an action on its environment) or as a processor (to process, compare or store information). This variety of material can spontaneously modify its physical properties, for example its shape,[23] its connectivity,[24] its viscoelasticity[25] or its colour,[26] in response to natural or induced excitations outside or inside the material. Examples of smart material property response to temperature variations, mechanical stresses and electric or magnetic fields have been reported. [18,27]

The Metastable Materials (M^4) group at the University of Bath was created to explore long-lived metastable states of complex compounds to control their desired functionality. Several compounds have been produced and have potential use in different sensor devices due to their properties changing during external stimuli.[1,2] These materials are currently produced on a milligram scale, the controllable production of these materials must be scaled-up in order to incorporate them into a large number of devices . These compounds have been shown to be difficult to scale up *via* usual batch production due to heat and mass transfer issues. The aim of this work was to explore a new way to scale up those materials using flow chemistry and crystallisation technologies while keeping the switching properties of the materials intact.

I.2. Spin crossover complexes

The first examples of spin crossover compounds (SCO) were Fe^{III} dithiocarbamate complexes reported by Cambi *et al.* in 1931.[28] The measurement of different magnetic susceptibility of the iron (III) complexes as a result of variation in temperature led to the first recognition of the temperature-dependent conversion of two spin states. These two states are called the low-spin (LS) and high-spin (HS) state.

Under certain constraints like temperature, pressure, light or magnetic field variations, change of spin states in SCO compounds can be induced. Metal complexes containing octahedrally coordinating iron (II) $3d^6$ ions have been of interest for decades due to their ability to reversibly transition from low-spin (LS) to high-spin (HS).[29] With an octahedral configuration, the 3d orbitals

of the iron (II) ion split into different subsets of energy levels, one subset of three orbitals collectively termed t_{2g} and a subset of two other orbitals called e_g (see Figure.I.1). The splitting between these orbitals is called the ligand field (Δ), the magnitude of which depends on the metal-ligand distance and the identity of the ligand (coordinating atom). During the change of spin state, the spin-pairing energy Π changes. When Π is larger than Δ the electrons can access the higher energy e_g orbitals thus the high-spin (HS) state is obtained. When Π is lower than Δ the d electrons will occupy the t_{2g} orbitals and then the lower set of orbitals is completely filled resulting in a low-spin (LS) state.

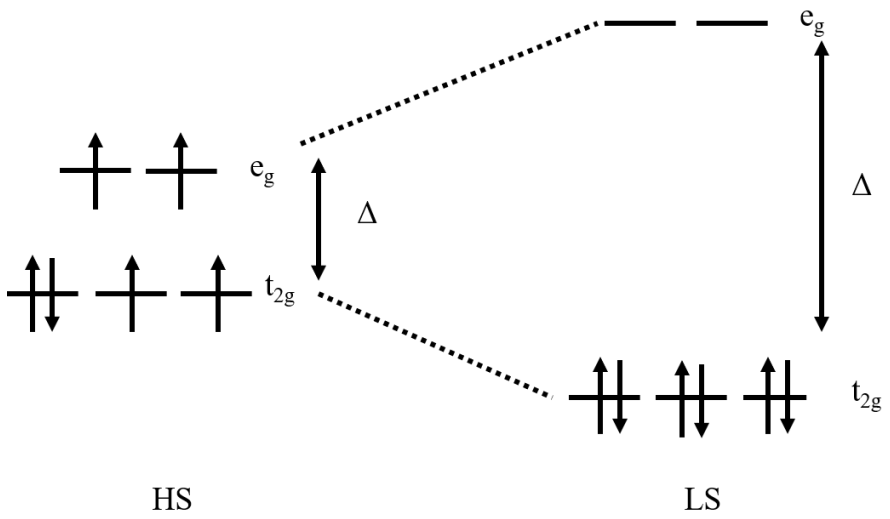

Figure.I.1 Electronic configurations during the two different spin states for iron(II) with the LS to HS spin transition indicating the change in Δ during the ST.

The spin transition phenomenon raised interest for different properties that could be used for switching devices and potential data storage capabilities.[5] The main interest for spin transition materials is the stability and the reversibility of the complexes with the possibility for a compound to have two metastable states; in addition, the external perturbation range can confer memory on some systems.[18]

After the initial Fe^{III} SCO complex discovery a lot of different complexes have been discovered, based on iron(II), iron(III) , cobalt(II), nickel(II) and manganese(III).[9,30,31] In this thesis $[Fe(Htrz)_2(trz)](BF_4)$, an iron(II) complex, will be used as an example to understand how particle size and morphology can be controlled and affect the spin crossover phenomenon.

I.2.1 Thermal spin crossover phenomenon

The spin crossover phenomenon can be induced *via* various stimuli. For example $[Fe(Htrz)_2(trz)](BF_4)$ possesses a spin transition that occurs when increasing the temperature of the material above 90 °C; the material turns white upon transition to the HS state from the pink LS state.[4,32,33] This change of spin state using temperature is the most commonly observed.[4] This change is driven by the entropy difference of the compounds in the LS state for low temperature and the HS state at high temperatures. The two-state equilibrium during the variation is expressed using the Gibbs free energy equation:

$$\Delta G = G_{HS} - G_{LS} = \Delta H - T\Delta S \qquad (1)$$

with ΔG the free Gibbs energy, ΔH the enthalpy and ΔS the entropy variations with:

$$\Delta H = H_{HS} - H_{LS} \quad (2)$$

and

$$\Delta S = S_{HS} - S_{LS} \quad (3)$$

While the variation of the enthalpy is related to the electronic configuration, the change in entropy values can also be attributed to the vibrational density of states, which changes due to the stretching of the Π distances with the coordination centre of the compound. During the spin transition (ST) the electronic entropy is higher in the HS than in the LS phase,[34] which is also linked to the fact that bond length is longer in the HS.[34] The temperature-induced spin crossover is then an entropy-driven phenomenon and the electronic states plays an important role in this transition.

I.2.2 Detection of spin crossover

In this thesis, the SCO compounds studied have thermally induced spin transitions. Depending on the stimulus (heat, magnetic field, pressure, light or chemical), iron(II) complexes display a change in the metal-ligand bond length.[33,35,36] This change is observed as a magnetic or optical property change. Different techniques can be used to describe and analyse spin state changes for those complexes.

One of the main measurements for studies of the potential use of spin crossover compounds for use in data storage applications, is the magnetic susceptibility change as a function of temperature $\chi(T)$.[30,37] One way of measuring this uses a superconducting quantum interference device magnetometer (SQUID). $\chi(T)$ is determined by the variation of the spin fraction γ_{HS} and γ_{LS} with:

$$\chi(T) = \gamma_{HS}\,\chi_{HS} + (1 - \gamma_{HS})\chi_{LS} \quad (4)$$

This can then be plotted as a function of temperature as shown in Figure.I.2 for $[Fe(Htrz)_2(trz)](BF_4)$.[4]

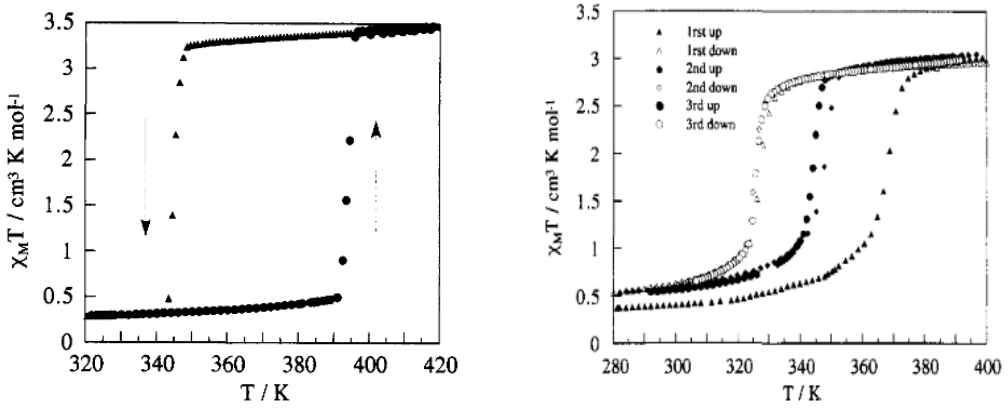

Figure.I.2 $\chi_M(T)$ versus temperature in the warming and cooling modes for $[Fe(Htrz)_2(trz)](BF_4)]$ $\chi_M(T)$ (left), and showing the change from LS to HS over several cycles (right). From Krober *et al.* 1994.[4]

Figure.I.2 shows the abruptness of the spin change during the several temperature cycles with the transition occurring from LS to HS at 385K in warming mode and HS to LS at 345K in the cooling

mode (Figure.I.2 left). The hysteresis loop of the sample over cycles on Figure.I.2 right shows that successive cycles can modify the shape of the hysteresis loop.[4]

Along with SQUID, Mossbauer Spectroscopy is also a standard method to analyse spin crossover compounds due to the nuclear resonance absorption of γ-radiation.[38] During the change from LS to HS states of the iron (II) complexes, the spin states can be detected by their spectral characteristics. The resonance taken from these analyses can be fitted with a least square model; molar fractions of LS and HS are proportional to the γ radiation emitted from each state. For instance, $[Fe(Htrz)_2(trz)](BF_4)$ displays a change in molar fraction at the temperature of spin transition (ST) close to that observed during SQUID experiments – 380 K for the LS→HS and 344K for HS →LS transitions (Figure.I.3).

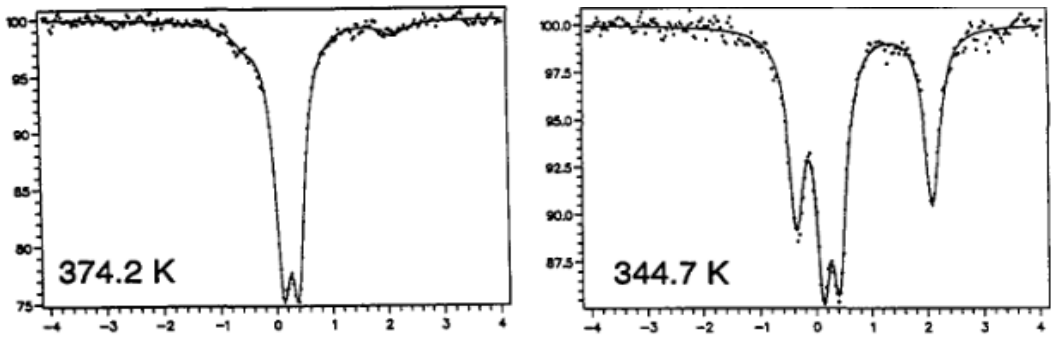

Figure.I.3 Mossbauer spectra for the temperature transition during heating(left) and cooling (right) for $[Fe(Htrz)_2(trz)](BF_4)$

Due to the enthalpy and entropy changes during the ST of SCO compounds, calorimetric measurements are useful tools to assess the LS to HS transition. This is done using differential scanning calorimetry (DSC) or differential thermal analysis (DTA); for example, Figure.I.4 shows the thermal events of $[Fe(Htrz)_2(trz)](BF_4)$ with a rate of 2.5 K/min during heating and cooling.

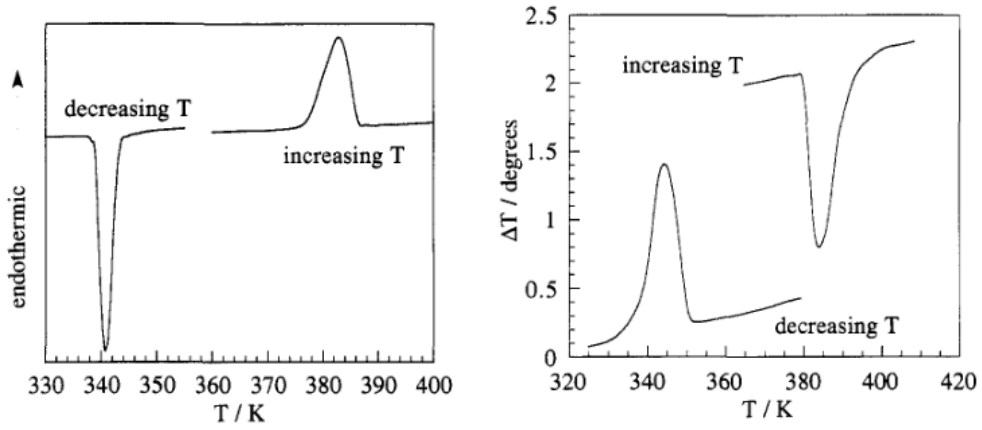

Figure.I.4 DSC (left) and DTA (right) showing the ST of $[Fe(Htrz)_2(trz)](BF_4)$.[4]

With the change of bond length of SCO compounds during the ST, and also the vibrational modes of LS and HS, infrared or Raman spectra have been used to study spin state behaviour. For $[Fe(Htrz)_2(trz)](BF_4)$ this has been studied[4,33] showing changes in the bonds (Figure.I.5). In this thesis this will also be studied in Chapter VII.

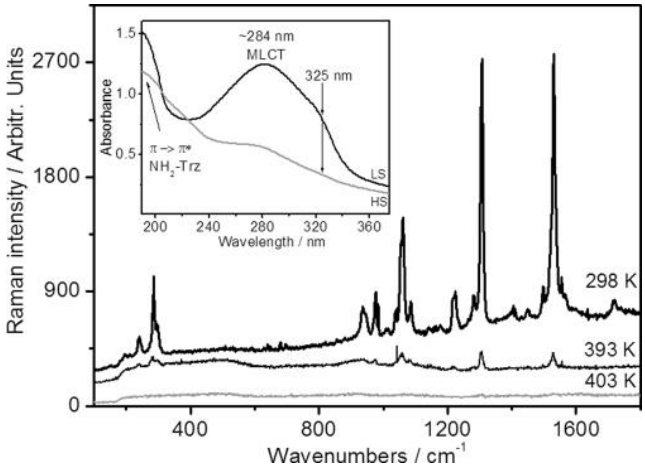

Figure.I.5 Raman spectra of gold coated $[Fe(Htrz)_2(trz)](BF_4)$ particles in the LS state at 298 K, and HS at 393 K and 403 K.[33]

X-ray structural studies can also analyse the thermal SCO transition. With the bond length increasing during the ST, the cell volumes of the compounds can change. Previous structure determinations *via* powder diffraction of the LS and HS states can identify the ST phenomenon and give more information on the compound itself. Several studies of the ST of $[Fe(Htrz)_2(trz)](BF_4)$ have been published showing a change in the cell volumes.[39] In Grosjean *et al*. the bond length and hence unit cell increased from LS to HS with a=17.3474(16) Å, b=7.3247(6) Å c=9.1907(9) Å (α 90° β 90° γ 90°) for the LS and a=17.4968(17) Å, b=7.7874(9) Å, c=9.5644(9) Å (α 90° β 90° γ 90°) for HS (Figure.I.6). Later in the present work, single crystal diffraction determinations are reported in Chapter IV and VII.

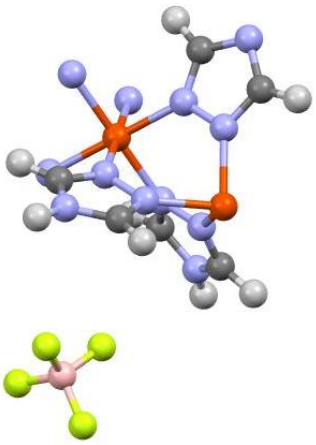

Figure.I.6 Structure obtained from powder data for the LS state of $[Fe(Htrz)_2(trz)](BF_4)$.[39]

During the ST, thermal SCO materials are always accompanied with a colour change (thermochromism).[20,40] This colour change can give a quick detection of the SCO ST changes with the colour at different temperatures and also allow determination of the HS fraction compared to the external perturbation. This also gives the possibility to obtain the electronic spectrum (through UV-vis spectroscopy) of the SCO at different temperatures.[27]

I.2.3 Applications of SCO compounds

Interest in SCO compounds for different applications has been increasing in the past decades. As introduced above, the change in colour and magnetic properties is an aspect of these compounds that could be used for smart switching devices. SCO compounds are potential candidates for data storage devices. Going further in the miniaturization of transistors have been slowed down by the limits of quantum mechanics. To bypass this problem spin-crossover compounds could be used as nano-scale units.

Making devices out of SCO compounds has already been achieved. Kahn *et al.*[12] succeed with a pink SCO compound switching to white during the LS-HS transition to make letters appear on particles trapped between two glass plates heated at different temperatures (Figure.I.7).

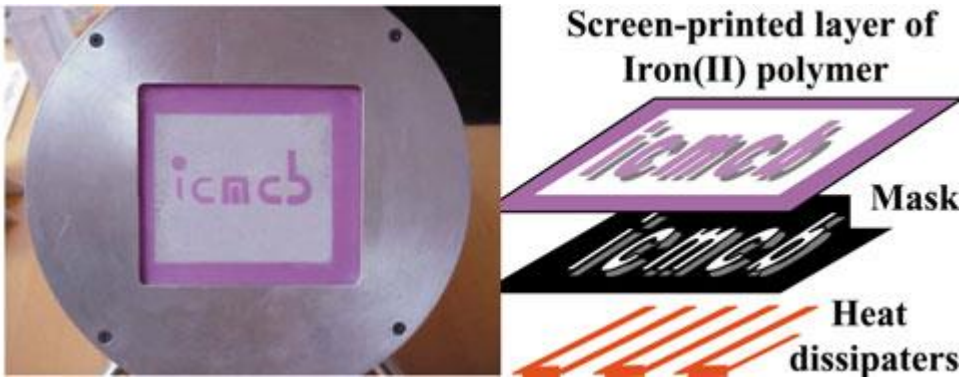

Figure.I.7 Example of devices using an SCO compound with a mask for the letters to be heated up forming the same pattern in the HS state. The pink particles are not heated due to the mask and stay in the LS state.[12]

Kahn *et al.*[12] showed that SCO compounds could be put onto a surface and be controlled easily for display devices and also that a wide surface of these materials can be used together. Due to the bi-stability of those thin film surfaces, the passage of binary data is enabled. It was also reported that ternary data are also possible with values "0","1" and "2" due to the compound structures.[12,18,41]

An important parameter for these compounds is particle size. The effect of nano-scale particles on the properties of a SCO compound were first studied by Létard *et al.*[41] for $[Fe(NH_2trz)_3]Br_2$ by obtaining 70 nm particles from the reverse micelle technique and in 2007 Coronado *et al.*[42] showed a similar approach for $[Fe(Htrz)_2(trz)](BF_4)$ using the reverse micelle method to control and produce nanoparticles. In those studies, they discovered that particle size has an effect on the magnetic properties; the reduction of size induced a modification of the hysteresis loop width and the abruptness of the transition.[31] In this thesis, the control of the particle size for $[Fe(Htrz)_2(trz)](BF_4)$ will be presented using flow chemistry platforms.

I.3. Thermochromics

SCO compounds change colour in response to temperature change, this is termed thermochromism, this property has potential applications in imaging or sensing materials and can occur in different materials types. For multi-component compounds which undergo a single-crystal to single-crystal thermochromic phase transitions, the colour can change due to a transfer of a proton between the two components, disrupting the electronic states of the individual components.

Several compounds which express proton transfer have been described in literature; 2-(2′,4′-dinitrobenzyl)pyridine has been known since 1925 and has a photoinduced proton transfer visible by IR and NMR.[43] Jones *et al.*[15,26] and Carletta et al.[44] showed 4-iodo-2-methylaniline:3,5-dinitrobenzoic acid co-crystal to have a thermochromic change when heating to 354 K, changing the colour of the compound from red to colourless(Figure.I.8).

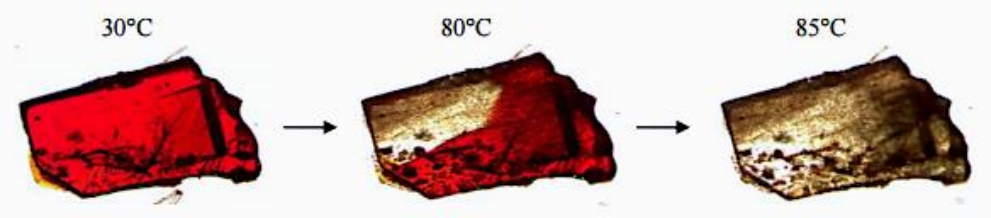

Figure.I.8 Thermochromism of the 4-iodo-2-methylaniline:3,5-dinitrobenzoic acid co-crystal.[15]

In this thesis a family of multi-component crystals based on the thermochromic co -crystal compound 4-iodo-2-methylaniline:3,5-dinitrobenzoic have been produced in different reactors. These compounds display proton transfer from the aniline to the hydroxyl group upon heating to 333.15 K.

I.4. Flow chemistry

In 1856 Henry Perkins (1838-1907) discovered the first synthetic dye by accidentally by oxidising allytoluidine ($C_{10}H_{12}N$), giving aniline purple also known as mauvein. Perkins decided to set-up a factory in 1857 to produce mauveine. This was the first large scale batch synthesis of fine chemical compounds and lead up to the democratisation of such installations in different fields.[45]

In contemporary chemistry, synthesising new molecules has been carried out using the same paradigm since the conception of batch chemistry, the design of a molecule for a targeted purpose, synthesis, characterisation and then larger scale production with scale-up of installation by changing the original batch synthesis design (Figure.I.9).

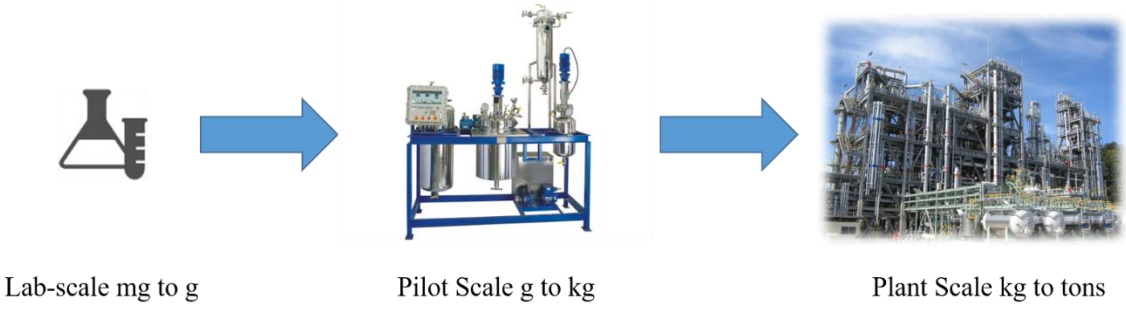

Figure.I.9 Usual batch processes representation for scaling up material production.

This type of industrialisation is used today in most chemical companies. But the evolution of mindset in the industry due to environmental issues, waste, size of equipment and demand led to a new way of doing chemistry. Flow chemistry has been studied as a potential way to produce compounds in a more compact, safer and environment friendly manner. This is a new approach to synthetic chemistry, using inexpensive glass or polymer reactors often called “Lab-on-a-Chip”[46,47] or lengths

of tubing put together to form reactors (Figure.I.10), often made of polytetrafluoroethylene (PTFE) or poly ether ethelyner ketone (PEEK).[48] Here instead of a stirring vessel, different mixing methods can be achieved in flow. Diffusion is the most common with a T-piece inlet where the two reagents are introduced, but turbulent mixing can be implemented inside the tubing *via* different changes of geometry inside the tubing such as static mixers, baffles or heart shaped diaphragm (Figure.I.11).[49] The residence time (RT) of the reagents inside the reactor is controlled by the volume of the reactor and the flow rate of the pumps. To achieve longer RT the reagent can be pumped more slowly or the length of tubing used increased. These tubes can be linked by different types of connectors and Back Pressure Regulators (BPR) can be used to control the pressure inside the reactor. Control of the reagents is made easy by these connectors which give the "plug and play" opportunity of such reactors. Several pumping systems are also available, e.g. peristaltic pumps, diaphragm pumps and HPLC (high performance liquid chromatography) pumps.[48]

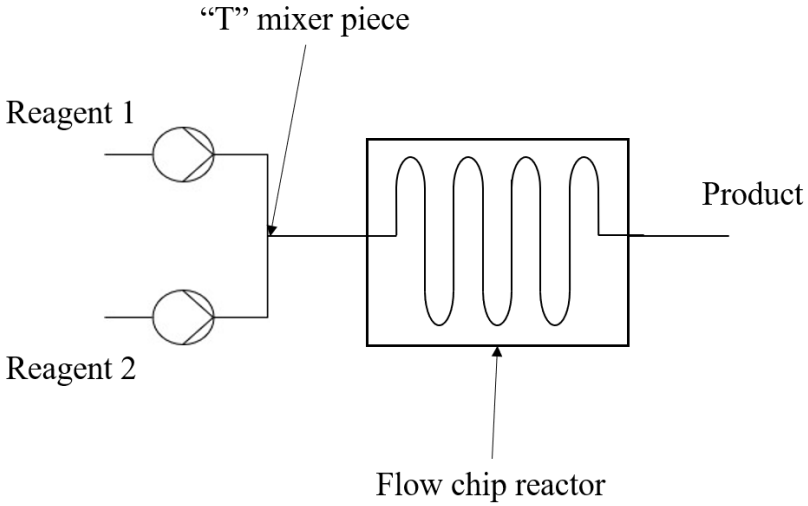

Figure.I.10 Schematic of a flow reactor involving a microchip, two pumps, and a recovery/filtration system.

In-line analysis and monitoring can be achieved using different probes for e.g. IR (infrared spectroscopy) or UV-Vis (Ultraviolet Visible). In this thesis, *in-situ* Raman and X-ray diffraction will be presented to monitor several reactions (in Chapter IV).

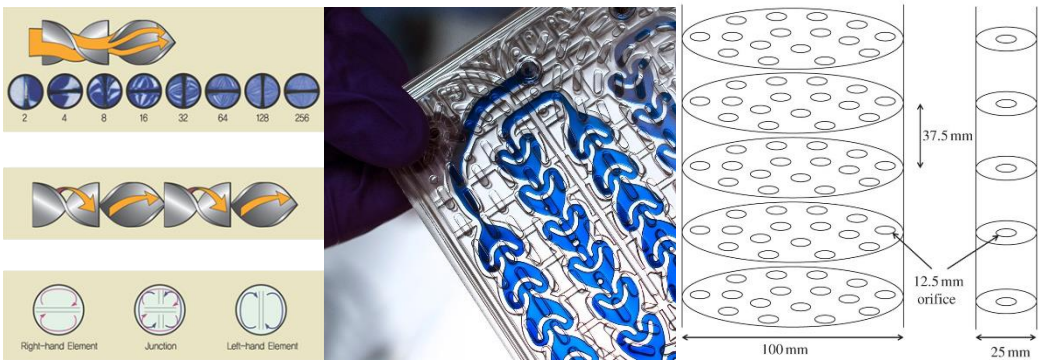

Figure.I.11 Static mixers schematic (left), Corning® reactor heart shaped mixers (centre) and the baffle tube reactor Rattlesnake® from Cambridge Reactor Design (right).

Today flow chemistry has grown into a distinct field from batch as a tool to produce different types of chemicals. One of the main uses for flow chemistry is for hydrogenation reactions, and this technique is often as a step towards the production of pharmaceutical compounds.[50,51] The use of

flow reactors in the past decades for hydrogenation have successfully shown their capabilities in improving safety, yield, selectivity and reduced purifications. The increased interest of pharmaceutical companies in flow technologies is still growing due to those potential benefits, but companies are still not convinced as flow reactors have difficulties in handling solids and the cost from transferring from batch to flow is high. Even with those problems present the pharmaceutical industry has chosen to go this way for some of their products and interest from other fields is also evident including use of flow in polymerisation or nanoparticle synthesis.[52–54]Advantages and disadvantages of flow are displayed in Table.I.1:.

Table.I.1: Table showing the advantages of flow chemistry systems and batch systems.

Advantages	Disadvantages
Large scale	High CAPEX (capital expenditure)
Better control	Solid precipitates
Reduced variation between process	Multi-steps reaction
Improved heat and mass transfer	Changing technology from batch to flow
Reduced space needed	Learning curve
Selectivity	Dedicated equipment
Hazardous reaction handling	
Exothermic reactions	
Reagent volume	
Green chemistry	
Optimisation	
Automation	

The small tubing used in flow chemistry has been seen to improve heat and mass transfer. Microreactors, for instance, show a large surface area to volume ratio compared to batch reactors like round bottom flasks (RBF), diminishing the diffusion distances. This surface area ratio is increased to 10 000 to 50 000 $m^2\,m^{-3}$ compared to the 100-1000 $m^2\,m^{-3}$ in conventional batch reactors (Figure.I.12). The heat transfer in these flow reactors is enhanced to an average of 10 kW $m^2\,m^{-3}$, higher than batch which are close to 2.5 kW $m^2\,m^{-3}$ on average.[55–57] This type of characteristic allows fast heating and cooling of reactions with isothermal conditions; coupled with precise residence time it can improve control over the synthesis.

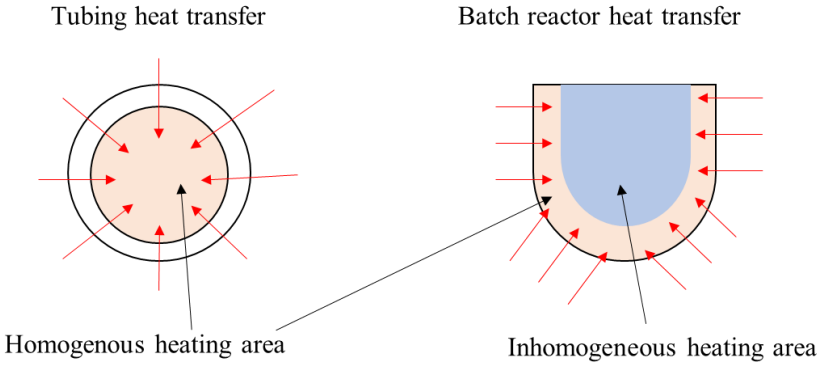

Figure.I.12 Heat transfer representation showing the advantages of flow chemistry using tubing.

With the enhanced heat transfer, mass transfer is also improved in flow reactors. The mixing times are reduced compared to conventional reactors and the diffusion inside them is very short, allowing the speed of the reaction to be increased.[55,57–59]

During synthesis of a compound, the chemical process can generate more than one reaction product from the same reaction. The product then can react again with one of the reagents and lead to unwanted side products. In flow environment the control over local conditions gives the opportunity to select a precise product over another with the enhanced mass and heat transfer control.[55,60] Due to this advantage, controlling or cooling down exothermic reactions is facilitated and any localized exotherms are dispersed safely; in the latter case hot spots are suppressed through excellent heat transfer due to the very high surface area.

In batch reactions, heat is removed from the reaction mixture at the surface of the reaction vessel. So even if the surface cools, the middle of the reactor could still contain a hot spot. In cases where it takes a long time for temperature to stabilize, this results in an uneven temperature distribution; for temperature sensitive reactions this is highly problematic and for exothermic reactions can be dangerous.[55] In addition, when the flask volume increases it is more difficult to remove heat; requiring larger cooling baths to be used as a heat sink which can be difficult at an industrial scale. To avoid this problem, chemists use slow addition of reagents to limit heat generated in exothermic reactions to be able to use standard equipment; this means that concentrations vary over time and the approach also slows the reaction. Flow reactors also reduce the amount of reagent required to gather the same amount of analytical data than required in bulk systems, which leads to reduction in cost of production.[60,61]

Process analytical technologies (PAT), such as Fourier Transform InfraRed spectroscopy (FTIR) and Raman spectroscopy process analysers, come also to hand in flow due to the ease of installation and being able to pinpoint certain parts of the reaction along the tubing of the reactor. Reactions can be monitored inline using infrared spectroscopy (IR) or Ultraviolet-Visible (UV-Vis) with a probe along the tubing. Online analysis can also be achieved by sampling a reaction product from the flow stream and using high performance liquid chromatography (HPLC) or mass spectrometry.[62–64] With the inline analysis automation having been improved for flow systems, information from the downstream process can be acquired (concentration variation, particle size, purity , temperature, *etc*) and used at the up-stream to remove any imperfection of the process with more precise pumps and temperature systems.[65]

These advantages can reduce significantly the space needed to achieve the same reaction than in batch, tubing can be compacted in smaller volumes for the same output, jacketing tubing for temperature control is also smaller than conventional batch reactors. This compactness has been raised by different companies in the last year. For instance, DARPA (Defense Advanced Research Projects Agency) have been developing a compact, portable pharmaceutical manufacturing system that can produce a variety of drugs on demand and can be deployed in the field faster than usual process, in research with Novartis and the MIT (Massachusetts Institute of Technology).[66]

Hazardous reaction products can also be produced in a safe, confined environment in flow. For example, the flow production of hypobromine has been successful for the company AFGA. In batch, to obtain hypobromine, liquid bromine is added to cold caustic potash at 0 °C. The solution has limited stability and the use of bromine is very hazardous, it is very toxic through inhalation, has high volatility, is very corrosive and the vapour is denser than air. The process is run at maximum 400 L scale due to the bromine supplier restriction. The company decided to use flow technologies to produce hypobromine using the same procedure but in flow synthesis which reduces the hazards of the reaction due to the confined environment which does not allow any bromine gas to escape. The advantages were also to use a smaller reactor at lab scale and flow reactors are easy to scale up to industrial scale while maintaining safety.[67,68]

Despite these advantages, flow chemistry has some drawbacks. One of these is solid precipitates or reagents; in general flow reactors are unable to handle solids or slurries used or created during reactions. Solids are also a problem for the back-pressure regulator (BPR) which contains small bore and mechanism or small connectors between parts of the systems. Pumps can also break due to solid entering the mechanism. In the next part of this introduction, flow crystallisation will be presented with solutions to these problems.[69]

With the advantages comes also a cost for the technology. First the equipment can be expensive due to the high-end materials used for tubing, connectors, BPR, pumps and operating system, including the provision of, for example, PAT to optimise exploitation of flow technologies. Companies are used to batch chemistry and changing infrastructure will be high cost in time, money and operator training. The research and development needed for a batch to flow investment could be expensive. But the combination of batch and flow could be an alternative to the all flow production in some cases for multi-step reactions.[70] Multi-step reactions are also difficult, certain reactions involving multiple reaction and separation steps in which some can involve solids or a column might need operations in batch between them reducing the effectiveness of flow reactors. To overcome this issue batch and flow can be used simultaneously to optimise a reaction.[65]

I.5. Flow crystallisation and solid management

To handle solids in flow several groups have developed different set-ups to produce different particles of different sizes in continuous systems. But to first understand solid creation inside those reactors, several concepts need to be discussed.

I.5.1 Supersaturation

In the crystallisation process, supersaturation is considered as one of the most important parameters to control. This parameter controls product quality and crystallisation process. Figure.I.13 shows an example solubility curve displaying the supersaturated and undersaturated state of the solution, as well as introducing the metastable zone (MSZ), the boundary where the crystal growth occurs.

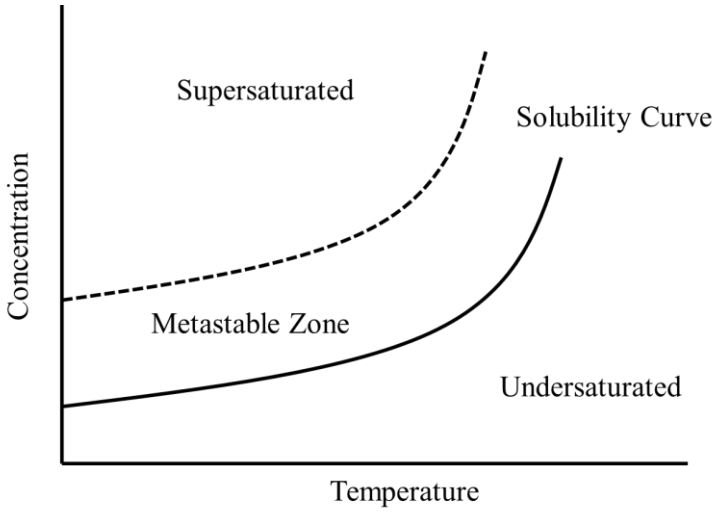

Figure.I.13 Example solubility curve displaying the three states of a solution. The solid line is the solubility curve, the dotted line is the metastable limit. [71]

Supersaturation is described as the driving force of nucleation and crystal growth;[71] in both flow and batch crystallisation supersaturation needs to be achieved. The initial solution at any given temperature is saturated where no more solids can be dissolved. When the solution is under equilibrium the solution is undersaturated the crystal will continue to dissolve until the solubility line reaches the supersaturated area. Above the undersaturated zone is the metastable region where the solution has a concentration beyond the saturated solubility level, but nucleation will only occur by a stimulus like cooling or seeding.[71] Beyond the metastable zone, there is a region of supersaturated solution (called the labile region) where uncontrolled nucleation and crystallisation can occur; this area will vary depending of process conditions (temperature, cooling rate, impurities, contact with surfaces).

I.5.2 Nucleation

Nucleation is the first stage of crystallisation, it is a physical process in which the formation of a nucleus is induced by condensation of one phase to another (vapour to liquid or liquid to solid). One of the most known examples is the condensation of water droplets from water vapour, or the formation of ice when water is freezing. [72]

This phenomenon is important in the field of crystallisation, allowing control over the particles formed and the determination of the resultant crystal structure of the material. In the current research on nucleation, two types (primary and secondary) are discussed.

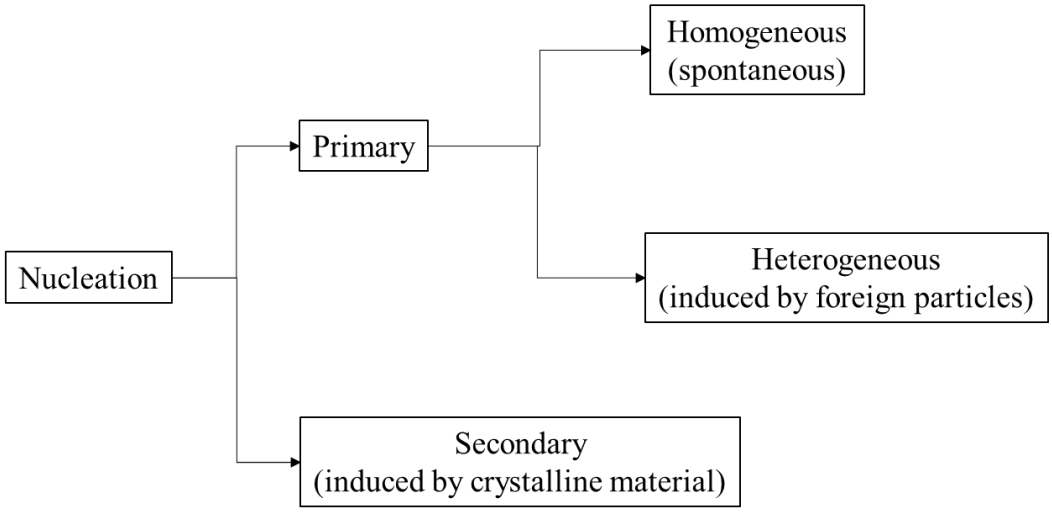

Figure.I.14 Schematic of the nucleation classification showing the secondary and primary nucleation.[71]

The primary nucleation as defined in Figure.I.14 can be distinguished as homogeneous or heterogeneous.[71] This depends on the presence or absence of a solid interface during the process. Homogenous nucleation is the nucleation of a solid due to supersaturation with the absence of a solid interface. To define this phenomenon, critical size of the nuclei is described as z_c and this depends on the free energy barrier, ΔG, of the system. This variation is described with the curve shown in Figure.I.15.

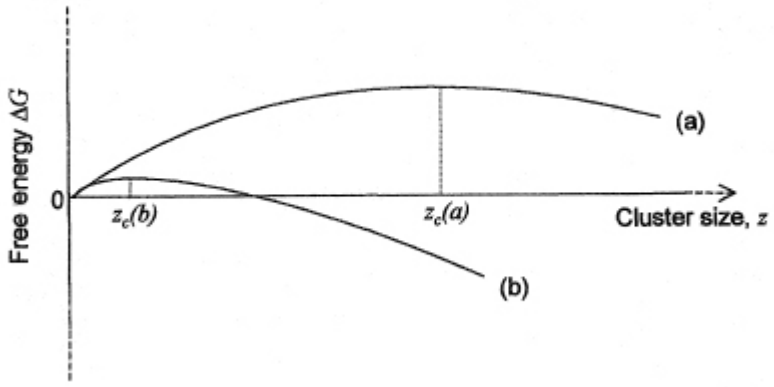

Figure.I.15 Change of free energy with cluster size and supersaturation with (a) low supersaturation and (b) high supersaturation. [71]

At the maximum of the curve is where further growth of the cluster induces a reduction of the free energy. When the size of the cluster is lower than this value the decrease of free energy can only be achieved by dissolution; these levels depend on the extent of supersaturation of the solution. Due to this parameter, homogeneous nucleation is less common than heterogeneous nucleation. In that case the heterogeneous nucleation will be induced by a foreign element in the solution like impurities or the wall of the tubing or vessel.

Secondary nucleation, on the other hand, is induced by contact nucleation with crystals of the solute and this phenomenon happens at lower supersaturation. When a dry crystal seed is present in the solute it can become a new centre for growth by the collision of bigger crystals with smaller ones.

I.5.3 Crystal morphology

During the crystallisation process crystal morphology is an important parameter to control. This aspect defines the external shape of a crystal and can have effect on the physical properties of a material and also can dictate the ease of processing.[73] For instance, during the filtration process the crystal shape can have undesirable effect as depicted in Figure.I.16.

Block crystals will be easier to filter than plate crystals due to the solvent being able to pass through them easily. On the other hand, having plate crystals can create an impenetrable layer preventing liquid from passing through, smaller particles such as micro or nano sized cluster can block pores of the filter and accumulate liquid. The shape and size of a crystal will also dictate its solubility and affect its ease of formulation into the end product.[74]

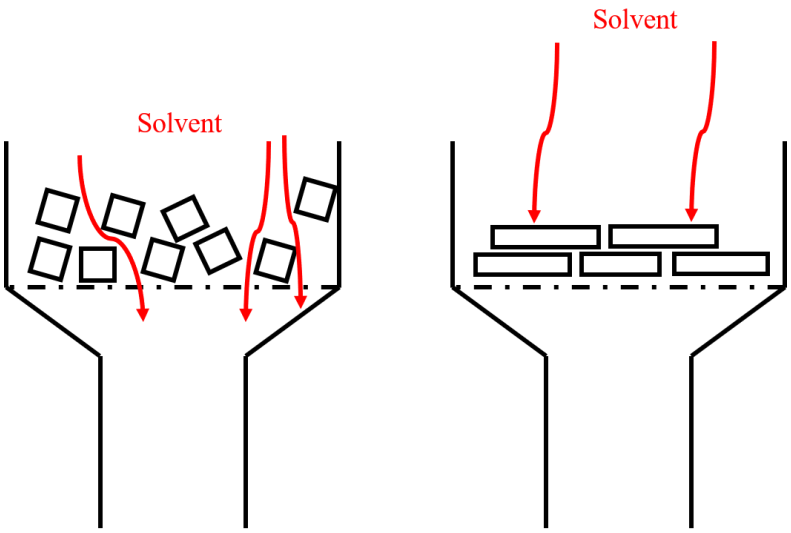

Figure.I.16 Scheme representing the effect of crystal morphology on filtration, on the left the crystal shape allows the solvent through, while on the right the crystals prevent this. Adapted from [71]

I.5.4 Crystallisation methods

I.5.4.i Evaporative Crystallisation

One of the main techniques used to crystallise materials is evaporative crystallisation. This way of obtaining crystals is often used for discovery purposes due to its experimental simplicity and compatibility with small volume process. In this method, the solution is initially undersaturated, due to evaporation of the solvent the concentration of the solution reaches the metastable zone (MSZ) and becomes supersaturated. At some point of the evaporation the solution reaches the boundary of the MSZ, moving into the labile supersaturated region, which induces nucleation and crystal growth (Figure.I.17).

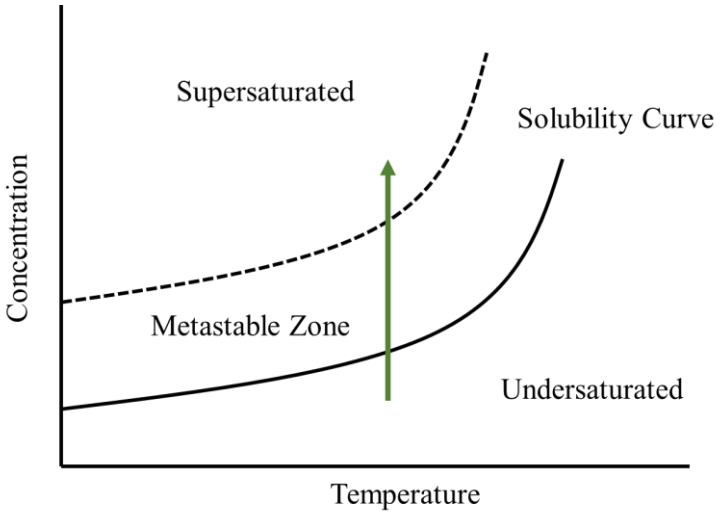

Figure.I.17 Solubility curve for evaporative crystallisation with the green arrow showing the change in concentration due to solvent evaporating.

I.5.4.ii Cooling Crystallisation

Cooling crystallisation uses the same principle as evaporative crystallisation except that this time the temperature is decreased (Figure.I.18). The solution that was unsaturated moves into the MSZ and then become supersaturated by reducing the temperature. The advantage of cooling crystallisation compared to an evaporative technique is that it is easier to control the temperature than the volatilisation of the solvent. Once the solution is in the supersaturated region it is possible to induce nucleation and subsequently remain within the MSZ (determined through solubility experiments) to promote crystal growth. Due to the ease in control over crystallisation, this technique is the most commonly used in industrial crystallisation.[75–77]

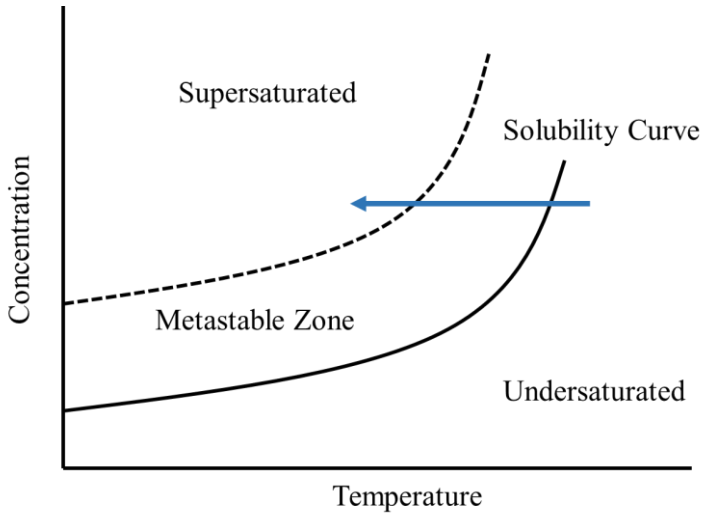

Figure.I.18 Solubility curve for cooling crystallisation with the blue arrow showing the decrease in temperature.

I.5.4.iii Anti-solvent crystallisation

Anti-solvent crystallisation changes an undersaturated solution to a supersaturated one by decreasing the solubility of the target *via* addition of a second solvent in which the solute is either insoluble or less soluble than the original solvent (Figure.I.19).[78,79]

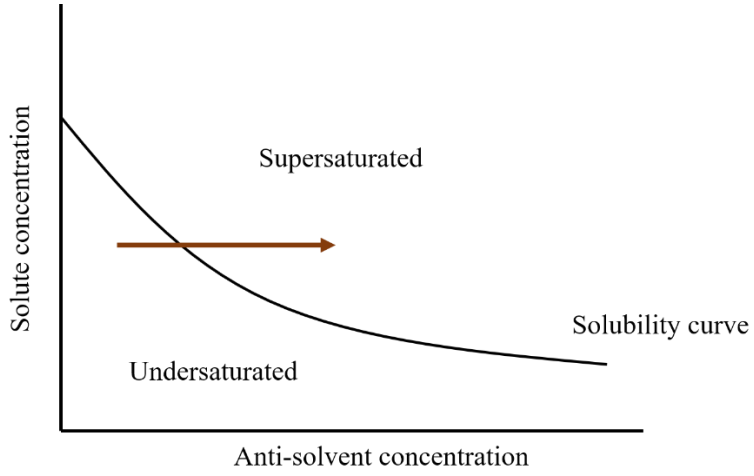

Figure.I.19 Solubility curve as a function of anti-solvent concentration.

I.5.4.iv Crystallisation induced by reaction

A reactive crystallisation is obtained by the interaction of two reagents which react in the solution state. This reaction creates a compound which is less soluble in the solvent used leading to crystallisation due to the obtention of a supersaturated solution. The crystallisation rate here depends on the kinetics of the reaction.

I.5.5 Polymorphism

Many crystalline compounds display polymorphism, where a compound can adopt more than one crystal structure. This phenomenon was first discovered in 1832 by Wohler and von Liebig[80] in the organic material benzamide. In the chemical industry, the presence of polymorphic structures can lead to materials with unstable properties at a given temperature, pressure or composition. Controlling the crystallisation process to access the more stable structure is therefore desirable in many cases.

The different properties displayed by polymorphs can have a lot of benefits in the pharmaceutical industry like solubility, but can also cause severe problems. For instance, in the HIV treatment Ritonavir®, one of the polymorphs of this compound, form I, was widely used. Then the presence of form II was discovered during the process of manufacturing the Ritonavir. This form had a reduced solubility compared to form I, which caused formulation problems. The enhanced stability of the form II also caused difficulties in reproducing the metastable form I polymorph in the production process. This resulted in a withdrawal of the Ritonavir product, causing severe problems for HIV sufferers.[81,82]

Due to problems such as these, the thermodynamic polymorph must be chosen with the optimal characteristics for the compound purpose. Polymorphs are all characteristic of their corresponding Gibbs free energies, and the thermodynamically stable polymorph will have the lowest free energy.[71,83] Some polymorphs are unstable with higher free energy (these are termed metastable) and with process conditions like temperature can transform to the thermodynamically stable polymorph.

The use of phase diagrams is then paramount to understand the effect of e.g. temperature on polymorphs. When the relative solubilities of the polymorphs are independent of temperature then the polymorphic system is said to be monotropic and when the relative solubilities are dependent on temperature it is termed enantiotropic[71] and the solubility curves intersect at the transition temperature (Figure.I.20). These parameters help to understand and target the polymorph wanted for a particular compound.

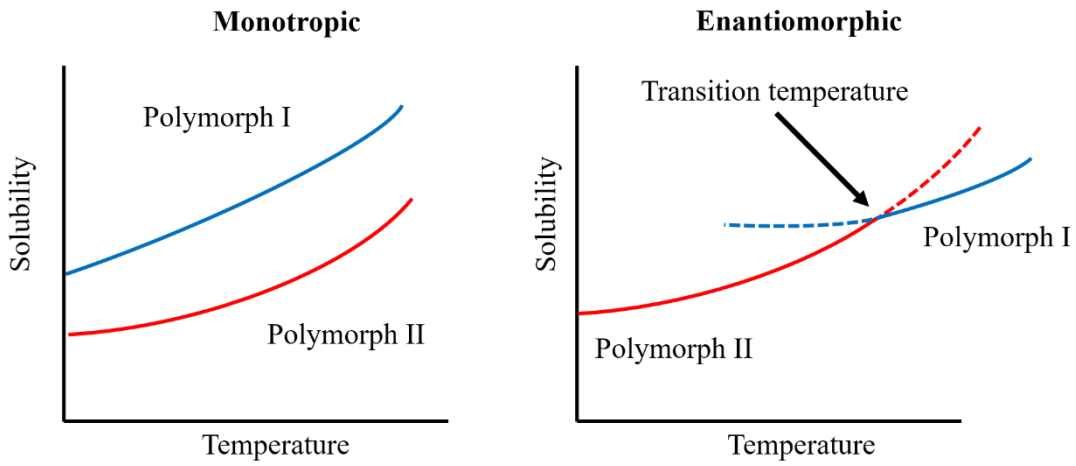

Figure.I.20 Monotropic and Enantiotropic systems solubility curve.

In this thesis, different polymorphs of the co-crystal urea: barbituric acid (UBA) will be studied using *in situ* diffraction in Chapter IV.

I.5.6 Co-crystals

To optimize compound properties in different industries to achieve different properties, co-crystallisation techniques are often used to produce multi-component compounds. This approach is used in the production of certain active pharmaceutical ingredient (API) compounds but also for other non-API products. [71,84,85]A target molecule (API or others) and a co-former molecule is used to create new crystal structure with enhanced physicochemical properties while keeping the original chemical properties. [86]

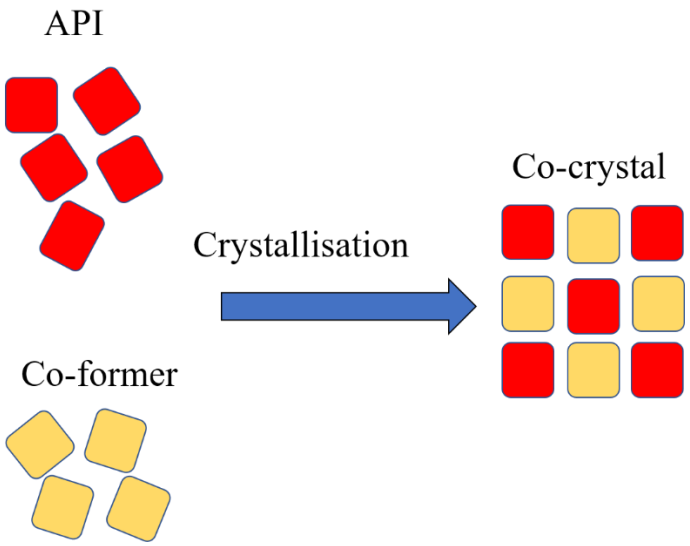

Figure.I.21 Schematic representation of co-crystallisation.

I.5.7 Industrial Crystallisation

To produce compounds at a larger scale when handling solids, different equipment can be used from batch crystallisation with large scale vessels to more specialised equipment. In recent decades a number of commercial flow systems have also been introduced to the market to give the capability to produce and handle solids forming for certain crystallisation or reactions at industrial scale.

The main way to the production of crystals is batch crystallisation, from lab scale with round bottomed flasks to larger scale with stirred tank reactors (STR). STRs for instance are sizeable batch vessels from 1 to 20000 litres.[75,87] with an impeller and often baffles to induce mixing during the process(Figure.I.22).

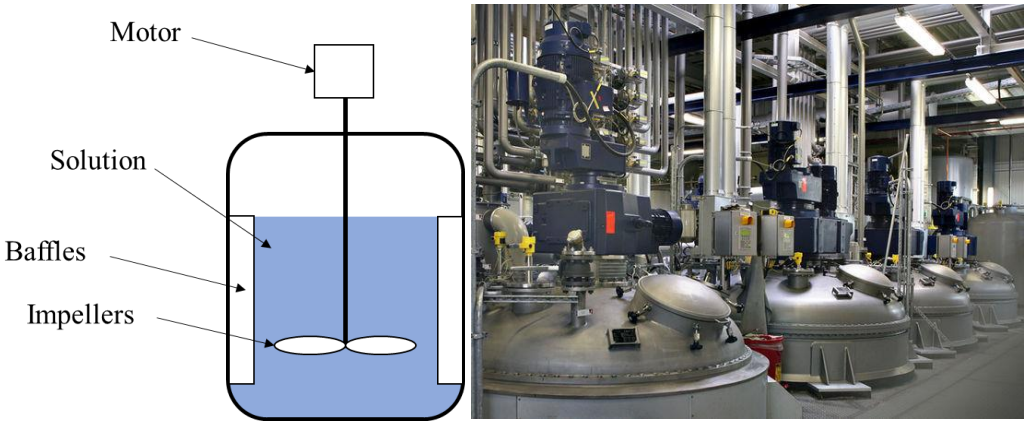

Figure.I.22 STR representation (left) and actual system (right).[88]

The problem of batch manufacturing at large scale, as previously stated, is heterogeneous processing conditions due to poor heat and mass transfer in such big reactors. As the scale increases control over these parameters diminishes resulting in batch-to-batch variability for the physical properties of the products, possibility of reduced product purity and may result in the crystallisation of undesired polymorphs. To address this problem, different flow platforms have been developed to give better control over the reaction at larger scale.

Today continuous processes for different types of chemistry and crystallisation have been invested in by a range of industries. Platforms like the mixed-suspension mixed-product removal (MSMPR) crystallisers are used where the feed solution is continuously fed in the vessel and the product obtained is withdrawn continuously. This device allows an equilibrium between the addition and the withdrawal of the feed and product which can then be controlled through the residence time *via* equilibration or pause period between operating cycles[89]. MSMPR systems have been used in different cases to produce crystalline products, the advantages of these reactors is the ease of converting the process from batch and the low cost and easier maintenance compared to other continuous systems. The drawback of these reactors is that a certain degree of supersaturation needs to be present for the process, resulting in a lower yield compared to batch process.[90] In Wong *et al.*[91] a single stage MSMPR with a recycle system for the initial liquid was used for cooling and anti-solvent crystallisations. with an increase in yield compare to a multistage MSMPR. In Wittering *et al*[86], for the urea-barbituric acid (UBA) co-crystal system, in a modified MSMPR, a periodic mixed suspension mixed product removal (PMSMPR) process was successfully implemented to produce preferentially the form I polymorph of this compound. This work showed the possibility of this type of reactor to isolate a certain polymorphic form of UBA and has promising applications for

polymorph isolations. This study demonstrated also an extensive use of PAT technologies to successfully control the crystallisation process of UBA.

In this thesis several types of reactor are used to achieve different chemical reactions and crystallisations. One is an oscillating baffled reactor (OBR), Centillion, designed by the Group of Professor Harris Makatsoris at Cranfield University that will be presented in detail in Chapter V [17] Baffled tube reactors have been widely used for continuous crystallisation, offering higher efficiency than MSMPR for the same volume used, can achieve plug flow behaviour with narrower residence time distribution and are easier to scale-up. For instance, the Continuous Oscillatory Baffled Crystalliser (COBC) from NiTech has been used at different scales for the production of API product. In Lawton *et al.* [92] a large scale 25 m long DN25 jacketed COBC was used to produce a proprietary API product from AstraZeneca showing a decrease in time for isolation of the API from 9 h and 40 min in batch to 12 min in the continuous crystallisation process in the COBC; the process was also easy to scale up. This work also showed the ease of controlling crystal size during the process by changing parameters of the reactor such as temperature profile; this was achieved with more ease than batch. In McLachlan *et al.* [93] the COBC was compared to a stirred tank reactor (STR) with added impurity to show that with the deliberately non-optimal initial conditions the COBC would give higher final product purities than STR, while also showing smaller particle size. The compound used was a technical grade of urea and the impurities added were biuret.

Other companies have also developed oscillatory flow reactor such as the Rattlesnake from Cambridge Reactor Design, giving an example of design variations for those reactors. Process of lactose in this reactor was successfully achieved by Siddique *et al.* and showed an improvement of 26% higher yield than in the usual batch process. The particle size distribution was also narrower than the batch process while being able to control it *via* the different parameters as in McLachlan *et al.*[94].

In the OBR, a series of baffles are equally spaced inside a tubing which is often jacketed for thermal control. A mechanism creates the oscillation of the fluid, for example through a syringe pump, linear motor or Scotch Yoke systems, while the baffle design also depends on the system, creating eddies between the baffles.[17,92,95,96] The net flow transports particles created during the process to the outlet of the system. Depending on the input parameters such as amplitude and frequency of oscillation, flow rate and baffle geometry, different turbulence intensities can be achieved in the reactor forming eddies inside each of the baffles (Figure.I.23).

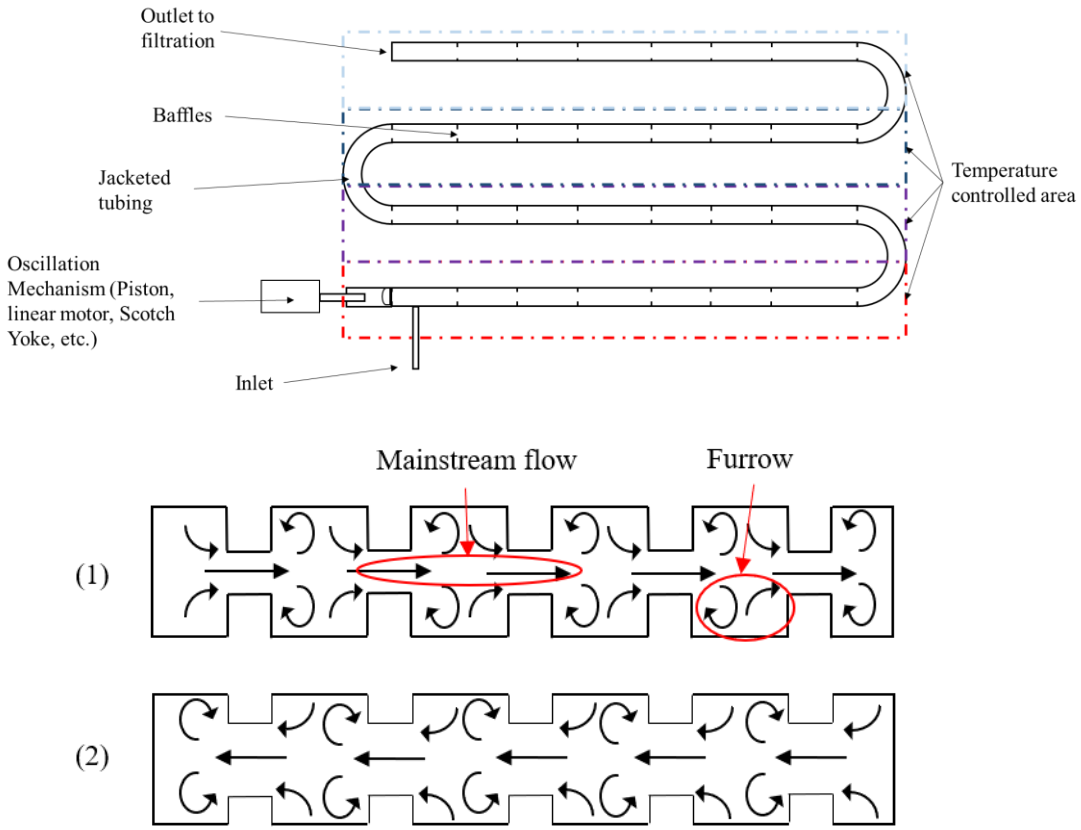

Figure.I.23 Representation of an OBR system and the turbulence inside a baffle tube reactor: (1) up stroke; (2) back stroke. (1) and (2) represent the change after one oscillation of the mechanism creating the flow movement.

In the case of an OBR continuous reactor plug flow can be achieved, where the fluid is mixed in the radial direction but not in the axial direction (the volume of fluid, V, does not disperse over time inside the tubing, Figure.I.24); this is important as it could lead to a highly reliable environment for nucleation and control over the process. In each of the baffles the interaction between the oscillating fluid and the baffles creates radial mixing repeatedly and gives uniform mixing in each inter-baffle area (Figure.I.23). Each baffle can be then considered as a small stirred tank reactor (STR). To achieve this plug flow behaviour residence time distribution (RTD) studies are necessary to obtain the parameters necessary. In Phan *et al.* [97,98] an equivalence model between the number of STR in series needed to achieve the same plug flow as an OBR has been studied. This study showed that more than 10 STR in series are needed to achieve the same narrow RTD curve as an OBR with certain parameters, showing that OBRs are more effective than a batch system showing equivalent performance, with benefits in terms of required space per volume of product.[99,100]

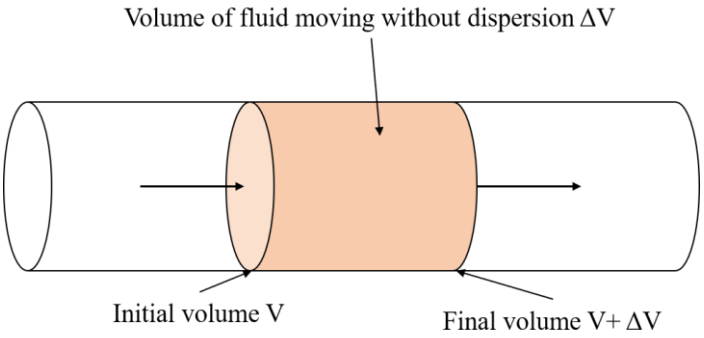

Figure.I.24 Representation of plug flow behaviour with no dispersion of the volume over time.

For such tubular crystallisers the disadvantages are an expensive and complex maintenance due to the number of parameters involved and the complexity of the equipment. Solids are also an issue due to fouling and blockages or encrustations in some connections or dead mixing zones. To palliate these problems segmented flow with multiphase flow has been used to remove the liquid-solid interface with the tubing. In Jiang *et al.*[101] crystallisation of L-asparagine monohydrate was successfully achieved using air-segmented flow where small slugs of solution are formed using hydrodynamic forces at a T-piece mixer. This showed that the crystals were not forming on the tubing and fouling was avoided inside the reactor; residence time was also reduced from an hour in batch to 2-5 min in the flow reactor, while particle size was also enhanced with a narrower particle size distribution (PSD). In this thesis a mesoscale segmented flow reactor, the Kinetically Regulated Automated Input Crystalliser (KRAIC), will be presented in Chapter III as a solution for solid handling, as there is no contact between the solution and the tubing that could induce unwanted nucleation or enable encrustation.

I.6. Computational Fluid Dynamics (CFD)

In industrial development, mixing analyses are mostly based on experimental data and empirical formulations. To analyse flow in mixing elements or reactors CFD (Computational Fluid Dynamics) is used as a tool to solve fluid problems. The development of solutions for fluid dynamic problems started in the early 1960s with different models to be solved such as the Riemann-based schemes for gas dynamics (Godunov *et al.*[102]), explicit methods for Navier-Stokes (MacCormack *at al.*[103]), complete airplane solution (Glowinsky *et al.*[104]), discontinuous finite element methods[105], *etc*. The evolution of those models was linked to the computational power needed to achieve a solution from the CDC6600 with 1 Megaflop in 1970 to the everyday laptop of 2.5 Gigaflops in 2011.[106,107]

The flows in gas or liquid are governed by partial differential equations (PDE) that represent the conservation of mass, momentum and energy. CFD works by replacing the PDE systems distinct to the case studied (multi-phase, turbulent, laminar, *etc*) by algebraic equations that can be solved by computers. CFD can give more information about the flow patterns that would be difficult and expensive to determine experimentally; CFD does not replace the experimental measurement but can significantly reduce the overall cost. CFD must also be done in parallel with experimental data because simulation is never 100 % reliable due to the input data which involve imprecision, the mathematical model can be inadequate and the results can be limited due to the available computing power. For instance, the reliability of CFD simulation is better for laminar flows, single phase flows and inert systems rather than turbulent, multi-phase or reactive flows.

To solve a problem in CFD, models and methods must be chosen in accordance to the situation (multi-phase, laminar, turbulence, *etc*.). Computer codes have been developed through the years to solve specific flow problems.

In CFD simulations a 3D model of the system (tube, reactor, plane, car, *etc*.) must first be created in order for the CFD software to apply numerical methods (called discretization) and make approximations in the governing equations in the region of the system studied. The software used can create a grid or mesh which is a collection of cells where the equations are applied and solved (Figure.I.25). In these simulations the conservation of matter, momentum and energy needs to be satisfied to model the fluid properties empirically. Assumptions are also made in order to reduce computational power needs, such as steady-state operation, incompressible fluids or two-dimensional models. Today a variety of software with commercial codes is available to make fluid studies; in this thesis the software Ansys Fluent® was used to solve different problems encountered in several flow reactors studied.

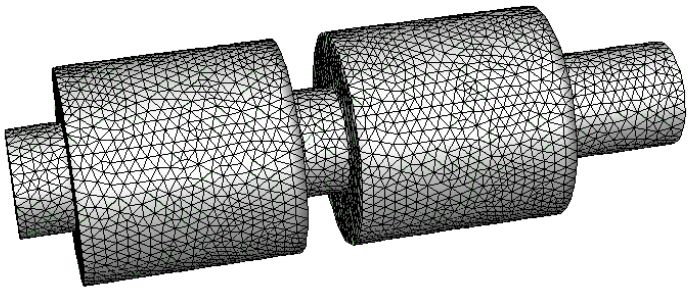

Figure.I.25 3D model of a baffle tube reactor processed into a grid mesh

In Tabor *et al.*,[108] the first calculation of a mixed tank reactor with a turbine impeller was reported, this led to more complex simulations as the computational power increased over the years and new fluid models were introduced. Predicting flow behaviour in flow systems can be useful to achieve new reactor designs, enhanced product development, troubleshooting or optimising of existing systems. In flow reactors different studies have tackled different problems. In Qian *et al.*[109] bi-phasic studies were done for segmented flow using Ansys® Fluent CFD simulations packages in order to see the impact of inlet flow rate on the size and formation of the slugs in the reactor; they described that slug size was dependent on the flow rate ratio at the inlet piece and also the fluid properties of the two phases such as viscosity, wetting angle or density. Kimuli *et al.*[110] showed simulation of a Meso-scale Oscillatory Baffled Crystalliser using STAR-CCM+ software to investigate axial dispersion and residence time distribution inside the reactor; parameters of the reactor were optimised and showed that amplitude needed to be below 1 mm and frequency around 6 Hz to achieve the narrowest RTD curve. The axial dispersion proved to be an important parameter to improve the mixing of the reactor obtained

Chapter II Methods and Instruments

II.1. Differential Scanning Calorimetry (DSC)

In this study Differential Scanning Calorimetry (DSC) was used to investigate thermal transition within materials and study their phase transitions. This technique is often used on organic materials (polymers, pharmaceutical, food) but also can be used, like in this case, on inorganic materials (alloys, liquid crystals). In the polymer industry, DSC is used as a purity control and to measure the degree of crystallinity or the degradation of the polymer. For pharmaceuticals, it is used to detect polymorphism or to check the stability of a protein. These checking methods are achieved through evaluating energetic events (exo- or endothermic) as a function of temperature.

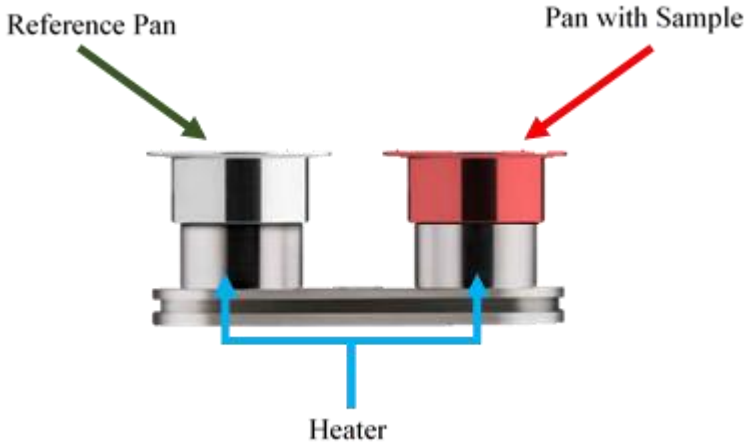

Figure.II.1 Sample holder representation of a DSC apparatus.

For inorganic materials, DSC can be used to study alloys, liquid crystals or chemical inorganic compounds, it can characterise phase transitions in smart materials. In the spin-crossover compound $Fe(Htrz)_2(trz)](BF_4)$, the Fe^{II} ions undergo a change in spin state which has a hysteretic behaviour that can be characterised by DSC. When it goes from low spin (LS) state to high spin (HS) state, this is shown for this compound by an endothermic peak upon heating for the first spin transition from LS to HS upon heating and an exothermic peak when cooling back from HS to LS to room temperature. DSC consists of measuring the quantity of energy required to heat a sample as a function of the temperature compared to a reference (or measuring the enthalpy or heat flux with respect to temperature). The device adjusts the quantity of energy given to a sample for it to have the same temperature as the reference and this change in supplied energy is displayed as thermal events in the DSC trace. [111,112]

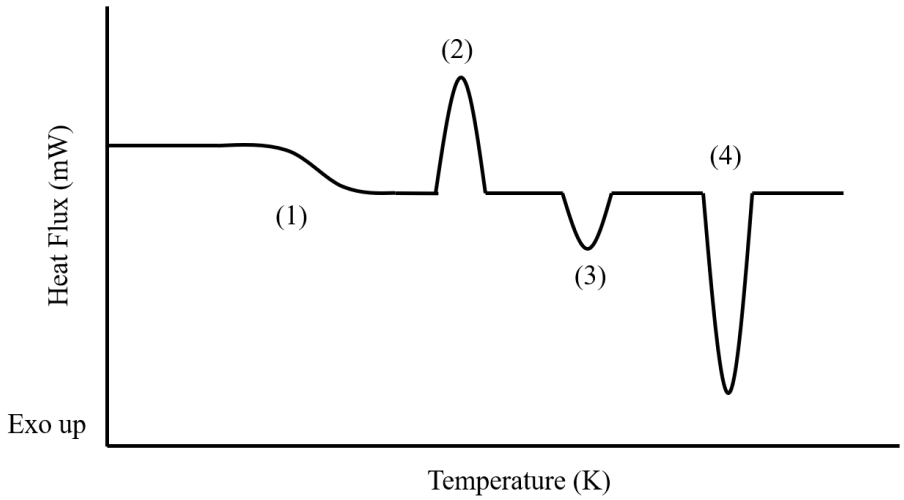

Figure.II.2 DSC graph showing example transitions observed within a material (1) glass transition, (2) recrystallisation, (3) phase transition, (4) melting/fusion.

Results are represented in form of a graphical trace showing the heat flux variation with temperature as in Figure.II.2. There are two distinct types of thermal event; exothermic when the sample releases heat during a transformation and endothermic where it absorbs heat. For example, during an exothermic process like crystallisation, less heat is necessary to increase the sample temperature with respect to the reference. Conversely, a sample with an endothermic transition, like from solid phase to liquid phase, will need more heat to maintain the same temperature as the reference because it absorbs energy.

For all DSC experiments that will be shown in this thesis, data have been obtained using a DSC Q20 from TA Instruments Cooling System 90 (Advantage for Qseries version 5.4.0 © 2001-2011 TA Instruments-Waters LLC.), operated with dry nitrogen purge gas flow of 18 cm^3 min^{-1}. Samples of 2-5 mg were placed in sealed Tzero aluminium pans and heated at the desired rate to the target temperature.

II.2. Thermogravimetric Analysis

Thermogravimetric Analysis (TGA) is a thermal analysis that measures the mass of a sample during variation of temperature. This technique is often used in the study of decomposition of certain materials or to detect a solvent loss in the material that can be linked to switching properties. For this measurement a precise balance is used. The sample of a few mg mass is placed in a crucible which is then placed on the balance arm which is within a furnace. TGA is often coupled with DSC to see if the mass loss is linked to an exotherm, endotherm or athermic phenomenon. Some TGA devices can also detect volatile components of the sample escaping upon heating by coupling the experiment with a mass spectrometer. For a TGA plot, the mass change is given as a function of temperature (Figure.II.3).[113]

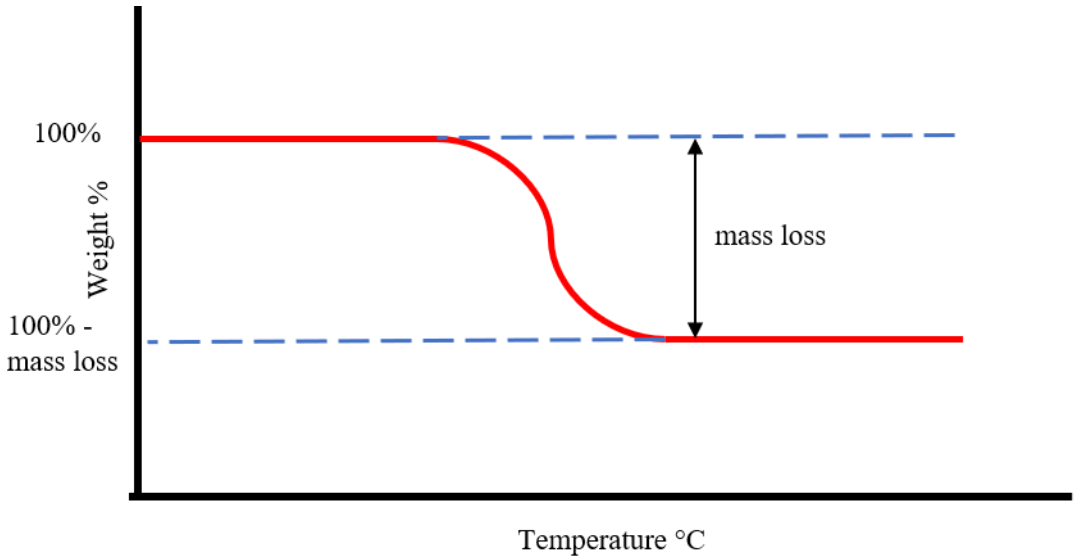

Figure.II.3 Schematic representation of a TGA graph with a loss of e.g. solvent.

In this thesis TGA was performed using 2-19 mg of sample in a Perkin Elmer TGA4000 under a nitrogen flow rate of 20 $mL.min^{-1}$ with the desired rate of heating. Simultaneously DTA (Differential Thermal Analysis) was carried out to measure the temperature difference between a sample and the reference. The DTA will detect exothermic or endothermic event upon heating between the sample and reference to investigate any change that may have occurred, similarly to DSC.

II.3. Powder X-ray Diffraction (PXRD)

PXRD is used to characterise the crystalline structure of materials; in this thesis, it is used, along with other characterisation techniques, to confirm the unit cell and hence structure of materials synthesised, notably the spin-crossover materials. PXRD is also able to detect any impurities that may be present as a result of a synthesis. At the heart of PXRD is the diffraction of X-rays by the crystalline lattice.

The production of X-rays is typically achieved when charged electrons are expelled from a heated tungsten filament and are accelerated under the effect of an electric field (~50 kV) to the anode (made of various materials depending on the targeted applications). The two metals often used for the anode are copper and molybdenum. Molybdenum sources give X-rays of shorter wavelength and are well suited to the study of small molecule materials. A copper source is often used for macromolecules or for powder analysis because the longer wavelength gives better separation of peaks in the diffraction pattern. In this thesis another source of X-rays will also be introduced, the tuneable wavelength radiation produced in the synchrotron, an introduction to which will be given in Chapter IV.

A crystal can be seen as a periodic repeat of three-dimensional elements (atoms or molecules); the regular repeating array is termed the lattice and the process of diffraction can be interpreted geometrically based on the Bragg construction (Figure.II.4). The angle θ (Bragg angle) is the incidence of parallel X-rays on the sets of parallel planes defined within the lattice; different sets of planes have different characteristic separations, the d-spacing, *d*. The difference of optical paths between two rays is represented by:

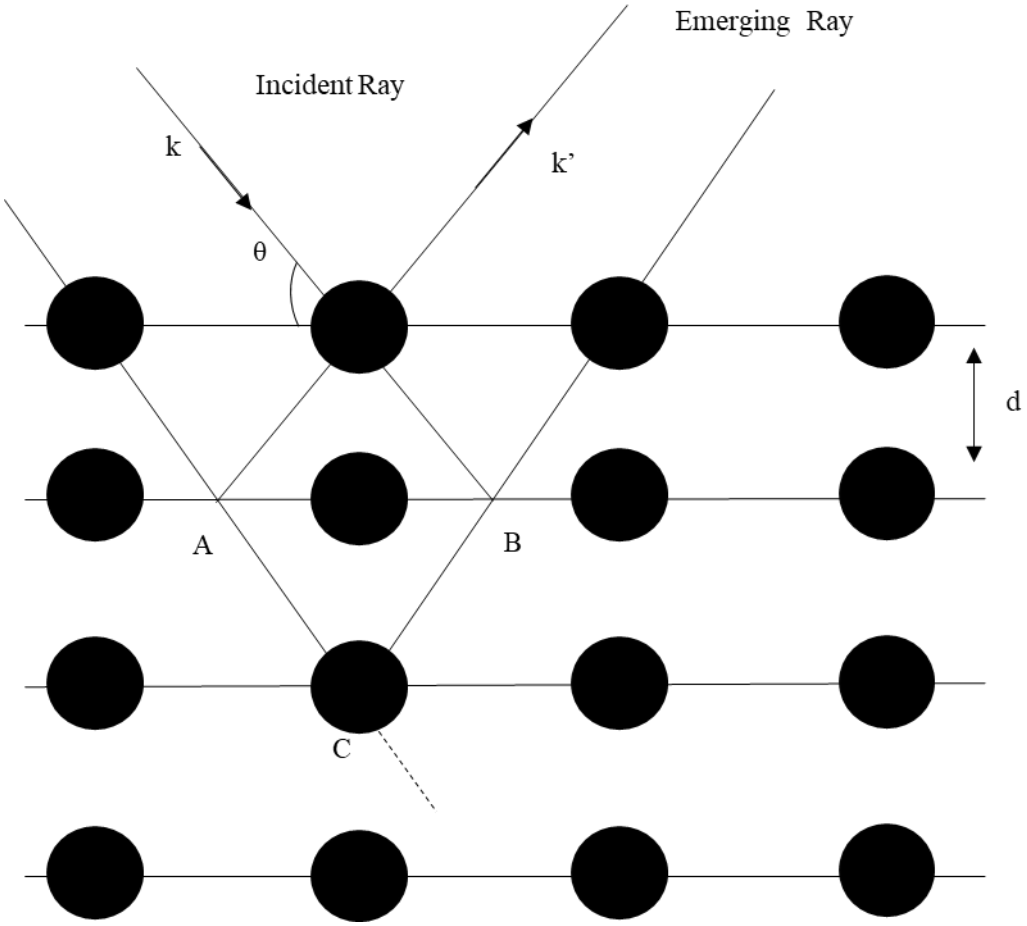

Figure.II.4 2D Scheme of X-ray diffraction geometry

$$AC + CB = 2dsin(\theta) \quad (5)$$

These two rays interfere in a constructive way when the difference in path length is equal to an integral number *n* of wavelengths. This gives the Bragg Law:

$$2dsin\theta = n\lambda \quad (6)$$

Where:

- θ is the angle of incidence of the X-ray
- *n* is an integer
- λ is the wavelength
- d is the spacing between atom layers

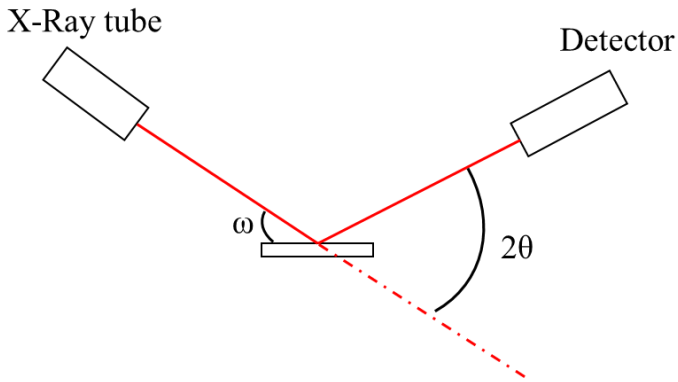

Figure.II.5 Scheme representing the X-ray being diffracted by the sample and then detected in a powder XRD experiment.

The incident angle ω is given by the orientation of the X-ray source and the sample. The angle at which diffraction from lattice planes separated by a certain *d*-spacing is given by Bragg's Law above. The 2θ angle is defined between the beam and the detector, the incident angle is half of the scattering angle 2θ. Each oriented crystallite of the sample produces a set of diffraction spots and the cone of diffraction is produced from the diffraction spots of all the crystallites within the sample (Figure.II.6). When a polycrystalline sample with randomly oriented crystallites is exposed to the X-ray beam, there is diffraction in all directions and a cone of diffraction is produced for each Bragg reflection (Figure.II.5).The combination of the peaks from differently oriented crystals/crystallites in a sample result in the production of 'rings' of diffraction rather than the individual 'spots' observed for single crystal XRD.

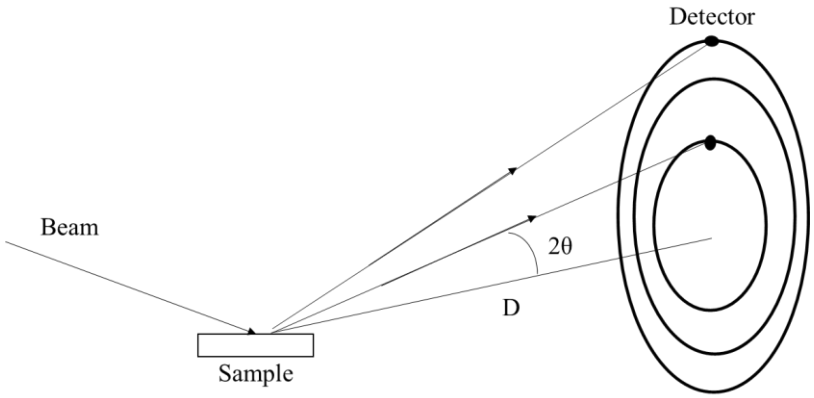

Figure.II.6 Cone formed by the sample during the diffraction process.

The PXRD pattern is produced from plotting the intensity against 2θ angle from a three-dimensional diffraction pattern to a one-dimensional pattern (Figure.II.7). The sample is fixed and the scanning in θ° is achieved by the movement of the X-ray source and flat-plate detector around the sample (Figure.II.7).

In experiments presented here, the samples are in the form of powders and are nanoscale materials up to macro scale at 100-300µm crystallite size, the use of powder diffraction is therefore appropriate for this application. A powder is comprised of microcrystals showing, ideally, an even representation of all crystalline orientations possible. Once the diffractogram is obtained it is possible to compare the intensity of observed peaks with known patterns. These can be obtained, for example, from the ICDD Powder Diffraction File (PDF)[114] or from previously determined crystal structures in a single-crystal database like the Cambridge Structural Database (CSD), from which structural information

can be converted to powder patterns or held in the P2D2 (Predicted Powder Diffraction Database).[115–117]

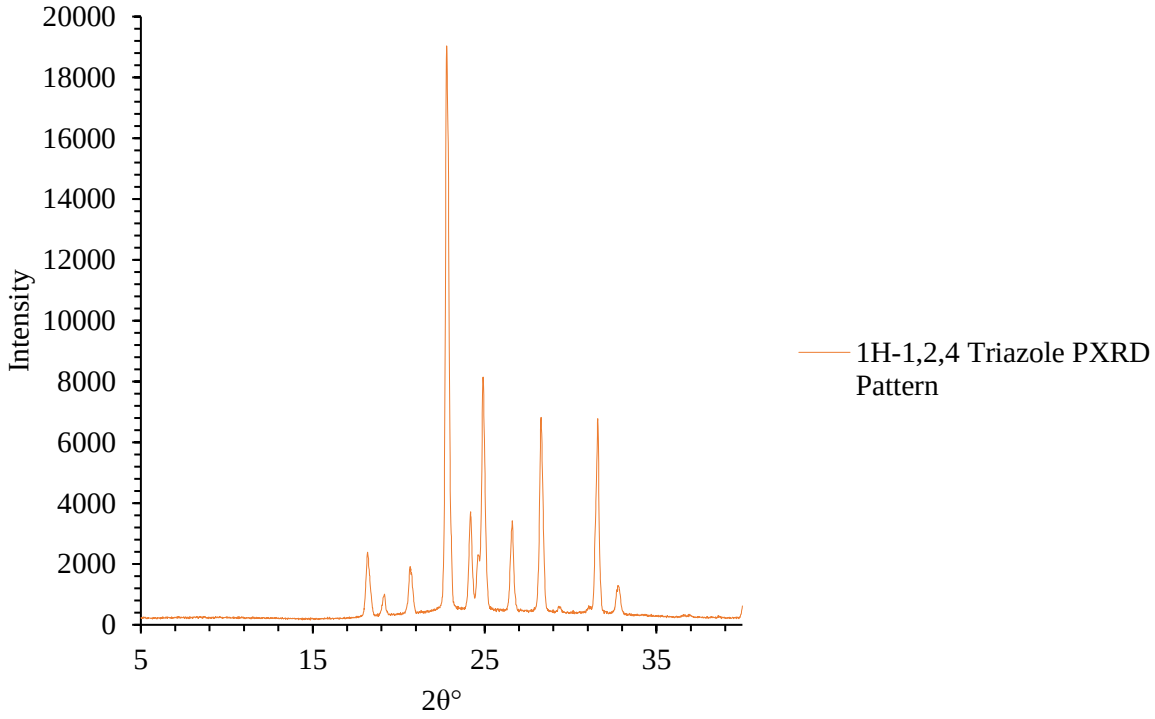

Figure.II.7 PXRD pattern of 1H-1,2,4 triazole.

For this thesis powder XRD analyses have been performed on a BRUKER D8-Advance diffractometer (Cu-K_α λ=1.54056 Å Radiation) with a 1-dimensional compound silicon strip detector SSD160, the samples were prepared on glass slides which are then placed on the sample holder for analysis. Samples were not ground before analysis as this may induce a phase change or otherwise detrimentally alter the phase under analysis. The data were collected *via* an area detector Pixium RF 4343 from Thales Group. The data obtained were post processed using Data Analysis Workbench (DAWN), Matlab®, and Total Pattern Analysis Solution (TOPAS,Bruker).

II.4. Scanning Electron Microscopy (SEM)

Scanning Electron Microscopy or SEM is based on the emission of electrons produced by a cathode and the detection of signal coming from the interaction of those electrons with the sample. Electrons irradiate the surface of the sample and penetrate deeply inside the material. The volume of material probed depends on the density and conductivity of the material under analysis and the energy of the incident electrons. In this volume of interaction, the electrons lose their energy by multiple collisions with the atoms of the materials generating the following secondary phenomena:

- Backscattered electrons
- Electron absorption
- Induced current
- Electric potential
- Locally rising temperature
- Network vibration

In Figure.II.8 is presented the radiation that can be emitted when the electron beam enters in contact with the sample. All those radiations can be used in order to analyse the object.

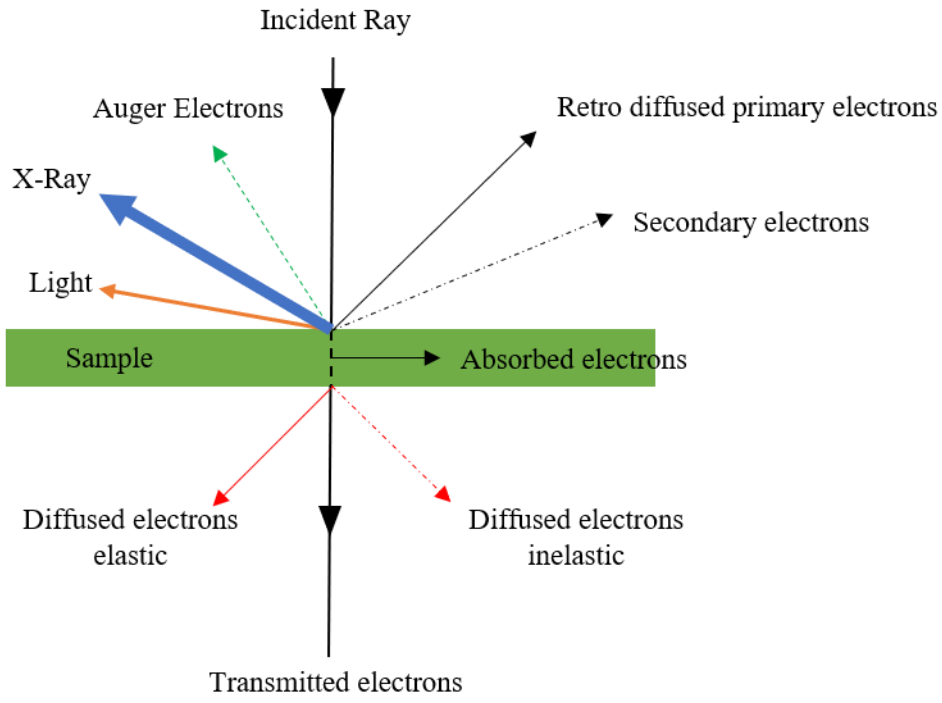

Figure.II.8 Radiation emission obtained from interaction of a sample with the electron beam during SEM analysis.

A SEM usually has three detectors: a secondary electron, a backscatter electron and an X-ray detector.

Secondary electrons are created by the incident electron passing close to an atom, and are ejected from the K-shell of the sample atoms. Each electron can create several secondary electrons. Because of their low energy, only secondary electrons emitted close to the surface (<10 nm) can escape the sample and be detected.[118,119] The change in topography of the sample will affect the amount of

secondary electrons detected as the edges will change the directions and number of the secondary electrons.[120]

Backscattered electrons are caused by the collision between an incident electron and an atom of the sample. The incident electrons are then dispersed in all directions without loss of energy (elastic scattering). Due to their high energy, the detected backscattered electrons can come from a deeper layer of the material than the secondary electrons emitted during analysis, thus they have a topography sensitivity lower than secondary electron emission. Because of their origin, the quantity of backscattered electrons varies depending on the atomic number of the sample.

When an electron from the K-shell of an atom is ejected by the incident beam, an outer shell electron will drop into the lower energy shell. The difference of energy between those two shells is emitted as an X-ray. Those X-rays have a characteristic energy distinct to the element that emitted them; these are analysed *via* their energy by energy dispersive X-ray (EDX) or by wavelength dispersive X-ray (WDX) to give information on the composition of the sample. They penetrate far in the interaction volume (around 1 μm^3).[121]

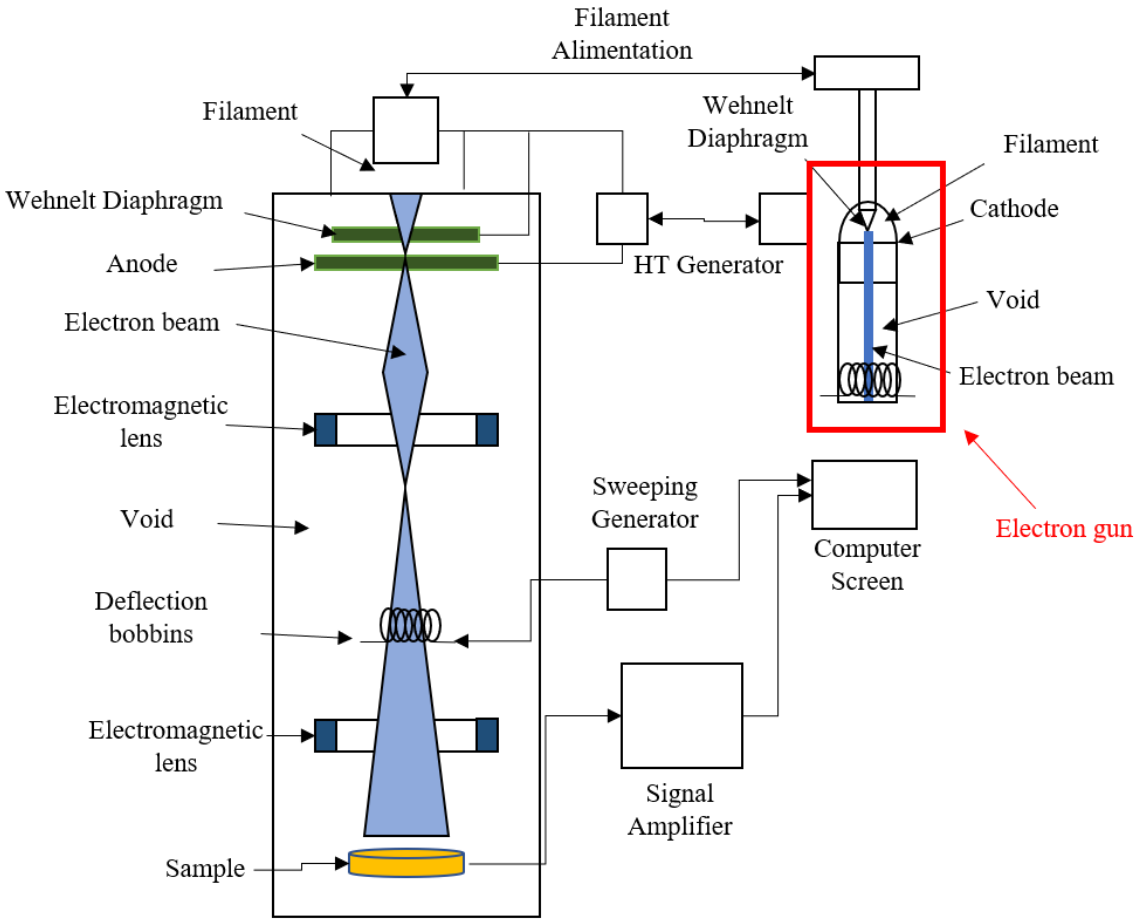

Figure.II.9 Schematic of an SEM. [120]

Figure.II.9 details the elements within a scanning electron microscope. The electron gun is used to produce the primary electrons. The cathode is a filament of tungsten in a V shape where the thermoelectrons are emitted *via* heating the filament at high temperatures.[120] It is heated to around 2700 K and has a lifespan from 40 to 120 hours. The filament is surrounded by a Wehnelt cylinder under which is the anode, with an aperture similar to the Wehnelt cylinder to allow passage of the

electron rays. The anode is grounded, the filament is at high voltage (1 kV to 30 kV); the potential of the Wehnelt is different from the filament at 200 Volts. The Wehnelt is used to tune the intensity of the electron beam and help focusing the image. The electrons are then accelerated by the anode. After this comes the electronic column which is constituted of three electromagnetic lenses. Those lenses are used to focus the primary beam into punctual spots. The important parameters to get a microscopic image are the brightness of the beam and the optical properties of the last focal lens (the objective). In this column are deflection bobbins to give the ability to sweep the sample.[118]

Detection of the secondary electrons is achieved with a detector using the Everhart and Thornley principle (1960)[122]. This detector uses a photo multiplier tube, the secondary electrons are attracted by the collector above 300 V and are accelerated towards the scintillator at 10 kV which absorbs the electron and emits photons. The photons arrive in the photomultiplier through a light guide and are then converted into electrons that are multiplied by successive dynodes and changed into an electric signal which are then transferred to a display screen. The backscattered electron detector is composed of silicon, this detector has two functioning modes: a composition mode which analyses the components of a sample during imaging and the topographic mode which measures the signal of the sample depth which gives its topography. The energy dispersive X-ray (EDX) detector consists of a silicon lithium drifted diode, each X-ray arriving at the diode provokes an impulse with a proportional intensity to the energy of this X-ray. The obtained spectrum is an histogram of the number of pulses as a function of their energy.[118] During the experiment the detector absorbs the X-rays and converts them into pulses using a preamplifier. The pulses are then amplified and send to a spectroscopic amplifier where the signal ratio is increased, then each pulse is measured individually using an analogue-digital converter. The pulses are then filtered to remove any noise to reach a good energy resolution and this analysis will give a spectrum corresponding to the sample studied.[121]

The SEM image is obtained point by point by moving the primary electron beam on the sample surface. The image is then constructed using the generated signal by the different detectors. The secondary electrons obtained are amplified *via* the photo multiplier and transferred to a display unit. The brightness of the image varies with the number of secondary electrons forming the SEM image. An example of the image obtained can be seen in Figure.II.10.

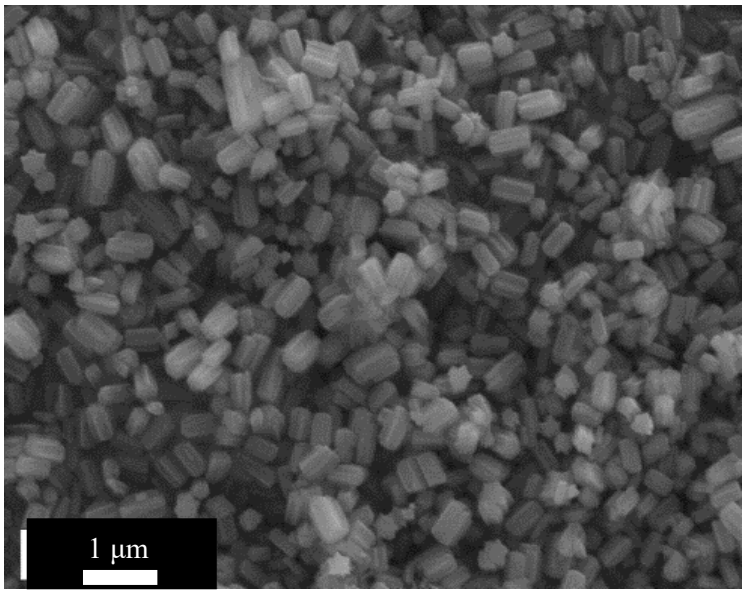

Figure.II.10 SEM picture of nanorods of SCO compound $[Fe(Htrz)_2(trz)](BF_4)$.

In this thesis several SEM apparatuses were used. A SEM JEOL SEM6480LV at the University of Bath, a Zeiss Supra 35VP at University of Brunel London and a JSM-6610LV at the Harwell Research Complex. The samples were coated beforehand using gold (Au) (which showed the best image resolution) with a Sputter Coater Quorum Q150T ES deposing a 4 nm to 10 nm coat on the samples. After coating the samples were placed in the SEM vacuum chamber to be analysed. For SEM-EDX analysis samples were not coated and the sample chamber was set to a low vacuum mode to avoid any interference.

II.5. Electron Diffraction

The diffraction of electrons (EDF) is a characterisation technique for surfaces in high vacuum. A tungsten cathode is used as an electron gun, the emitted electron is accelerated through a series of electrodes. The electrons projected on the surface of the bombarded sample surface are then diffracted. They pass through separators that slow and filter them, allowing those involved in elastic collisions with the sample to enter and blocking those resulting from inelastic electrons. The electrons are then projected on a fluorescent screen working as an anode and form the diffraction pattern that is observed. The sample must present a crystalline regularity and a high degree of order for the electrons to be diffracted and form a diffraction pattern.[123]

The electron diffraction apparatus is similar to SEM analysis (Figure.II.9) except that the electron beam is reflected by the target where the sample is placed. The electron beam is concentrated *via* a condenser lens and the projected diffraction pattern is displayed on a screen (Figure.II.11).

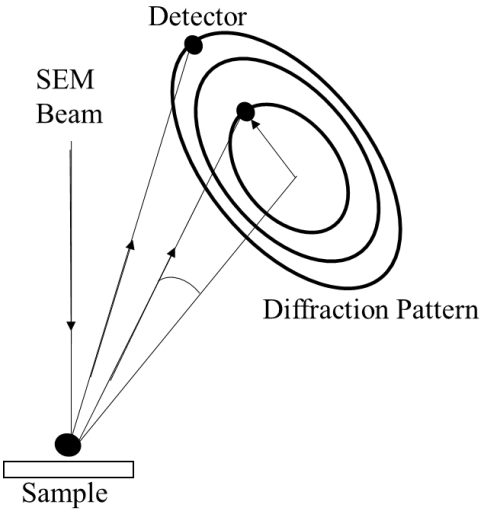

Figure.II.11 Representation of EDF apparatus.

The incident beam is scattered through a 2θ angle, when the electron beam passes through crystalline compounds a diffraction pattern can be observed (Figure.II.12) by diffraction of the different planes within the crystal structure of the target.[123]

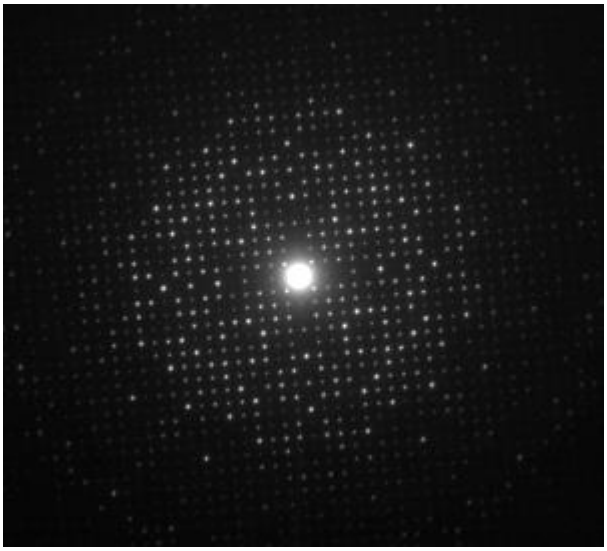

Figure.II.12 Typical electron diffraction pattern.[124]

EDF was performed on a Philips CM300 FEGTEM. Scans were 120×120 pixels with pixel steps of 7.5 nm. The scans were then processed using a Nanomegas Digistar connected to the SEM and using the ASTART software package.

II.6. Raman Spectroscopy

Raman spectroscopy is a type of vibrational spectroscopy which involves illuminating a sample with a monochromatic laser beam that interacts with the molecules and creates scattered light. This scattered light is different from the incident light due to interaction with vibrational modes within the sample, and is used to form a Raman spectrum (Figure.II.13).

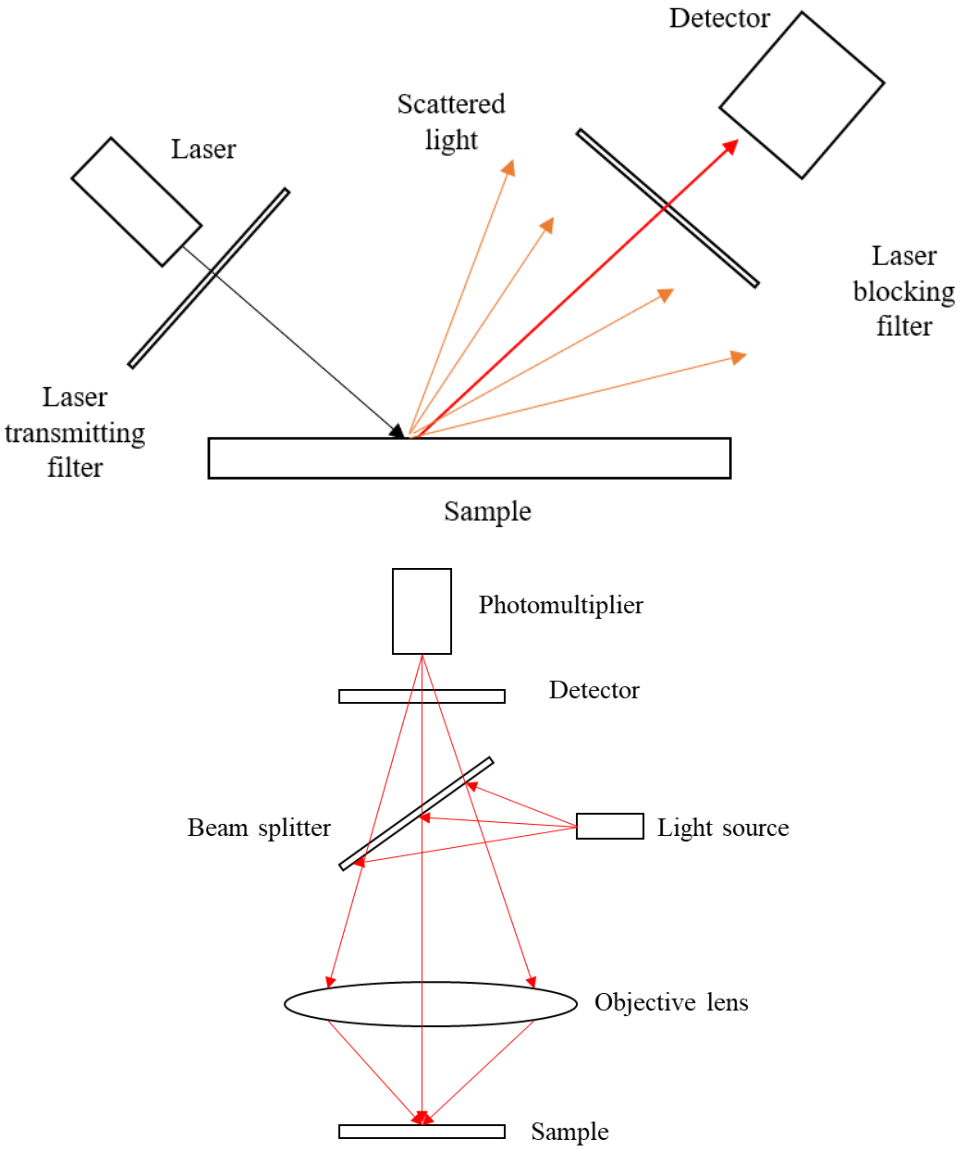

Figure.II.13 Raman spectroscopy scheme and confocal Raman probe system.

In this thesis a confocal Raman probe is used. Unlike conventional Raman apparatus the confocal microscope measures the light only from a small volume in the sample (Figure.II.13). The scattered light from the sample is then collected by the objective lens and passes through the detector. When the monochromatic radiation hits the sample, it is scattered in all directions and the main scattered radiation constitutes the Rayleigh scattering; a small fraction of this scattered radiation has a different frequency which constitutes the Raman scattering. The change in wavelength by the scattered radiations provides chemical and structural information. The shifted photons are of higher or lower energy following interaction with the vibrational state of the molecule. Raman spectroscopy is based on detecting changes in polarisablity of materials (during the vibrations).

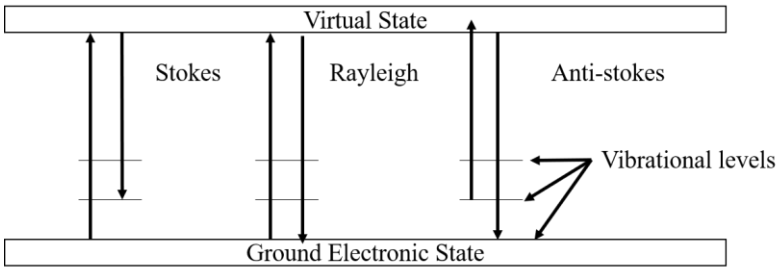

Figure.II.14 Representation of the difference between the Stokes and anti-Stokes radiation.

The Stokes radiation is at lower energy, longer wavelength than Rayleigh radiation and the anti-Stokes radiation is at greater energy. When the laser interacts with the molecule the energy increases and decreases in correspondence to interactions with the vibrational energy levels in the ground electronic state. The Raman shift is the measurement of Stokes and anti-Stokes lines due to the vibrational energy change of the molecule. The energy decreases or increases depending on the initial vibrational state in the ground electronic state of the molecule; if the molecule gains vibrational energy from the incident beam, this generates wavenumbers of the Stokes lines, while if the molecule loses vibrational energy this generates anti-Stokes lines; thus the Raman spectrum allows measurement of the vibrational energies of the molecule.[125,126] An example of a Raman spectrum is displayed in Figure.II.15.

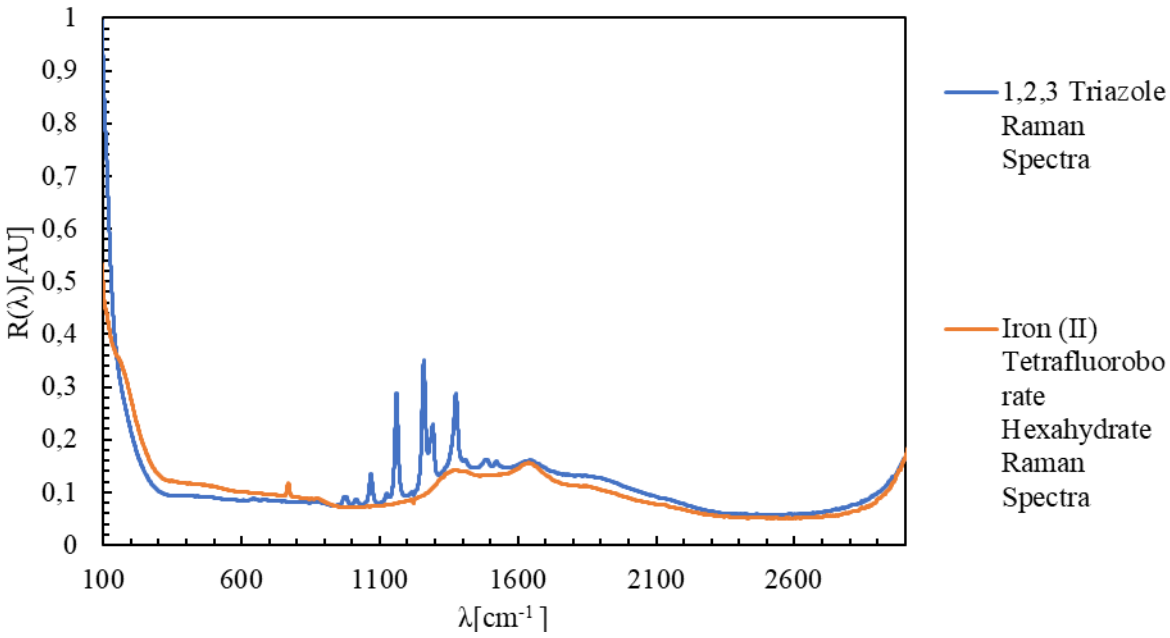

Figure.II.15 Raman spectra obtained of two different reagents, iron (II) tetrafluoroborate hexahydrate and 1,2,4H triazole.

In this thesis a Raman RXN1 System™ Probe spectrometer with a 785 nm laser MR probe filtered probehead with non-contact optic and NIR adapter from Kaiser Optical System, Inc was used. To process the spectrums iC Raman v4.1 software was used. Preparation of samples will be described in Chapters IV and VII

II.7. UV-Vis Spectroscopy

The absorption of visible and ultraviolet (UV) light is linked to the excitation of electrons from lower to higher energy levels. Light with the right amount of energy can therefore cause transitions from one level to another *via* absorption. The electrons are then excited from a full orbital at low energy, ground state, into an empty anti-bonding orbital at higher energy.[127,128] Each light wavelength is associated with a particular energy, if the energy is matched to these electronic transitions then the wavelength will be absorbed. To have an insight of the coloured behaviour of certain compounds, optical spectrometers measure the light absorption at different wavelength in the visible part of the spectrum. UV-vis spectrometers record the wavelengths at which the absorption occurs and the intensity of this absorption, this is done for each wavelength. The intensity of the light from the sample is measured and converted to the absorbance (A) using the Beer-Lambert law:

$$A = \log_{10} \frac{I_0}{I} \qquad (7)$$

Where I_0 is the intensity of the light passing through the sample, I the intensity wavelength measured.

The signal obtained *via* this technique is a spectrum representing the absorbance (A) versus the wavelength (Figure.II.16).

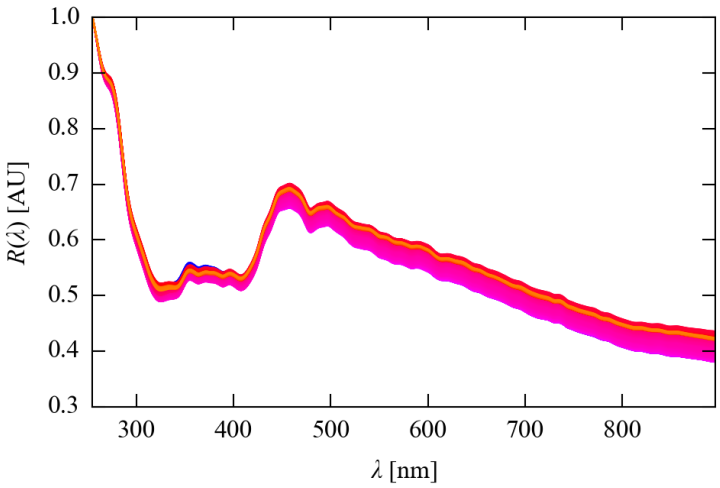

Figure.II.16 UV-Vis Reflectance spectra for $[Fe(Htrz)_2(trz)](BF_4)$.

Set-up of the UV-vis experiments used in this thesis will be described in Chapter VII.

II.8. Dynamic Light Scattering DLS

Particle size can be determined by the measurement of the aleatory variations of intensity of the light scattered by a suspension. Dynamic Light Scattering (DLS) is often used to analyse nanoparticle sizes like gold nanoparticles, proteins or submicronic particles.[129–131] When measured, the particles in suspension are affected by a thermally-induced movement called Brownian motion. This aleatory movement can be defined by the Stokes-Einstein relation:

$$D_h = \frac{k_B T}{3\pi\eta D_t} \quad (8)$$

Where:

- D_h is the hydrodynamic diameter of the particle (m)
- D_t is the transversal diffusion coefficient ($m^2.s^{-1}$)
- k_B the Boltzmann constant (k_B = ,380 648 52 × 10^{-23} J K^{-1})
- T the temperature (K)
- η the dynamic viscosity ($kg \cdot m^{-1} \cdot s^{-1}$)

In the cases studied, the DLS measurements were achieved with a Malvern Zetasizer Nano-S. The Stokes-Einstein equation is calculated to determine the particle size distribution (PSD) of the sample. It is important to note that temperature and viscosity are linked and interdependent, additionally D_h does not represent the size of the particle but an equivalent hydrodynamic sphere around the particle.[130,132] The hydrodynamic diameter of the particle is the diameter of the sphere that diffuses in the liquid at the same speed as the particle measured. This diameter will depend on the surface structure of the particle and if ions are present (Figure.II.17).

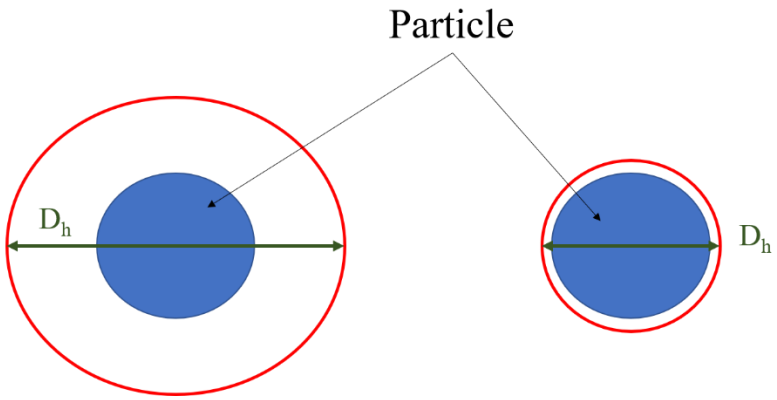

Figure.II.17 On the left a low ionic concentration is present extending the layer of ions around the particle reducing the diffusion speed and giving a larger apparent hydrodynamic diameter, on the right the higher ionic concentration will reduce the hydrodynamic diameter.

To analyse a sample, the monochromatic light of the source goes through the sample cuvette. The light scatters in all directions when entering in contact with the suspended particles (Figure.II.18). The intensity variation of the laser due to encountering the laser is recorded *via* a photon counting device (Figure.II.18). The fluctuation of this intensity is due to the Brownian motion of the particles and changes with time. Analysing the sample multiple times can reduce errors such as particles superposing each other which could be detected as a bigger cluster and give unwanted results.

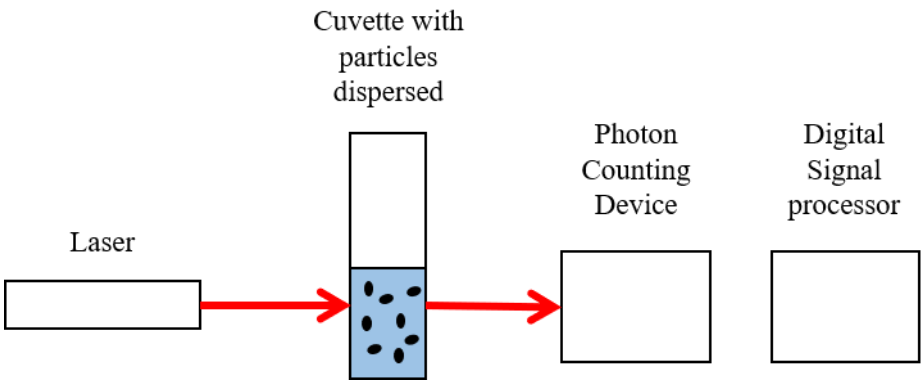

Figure.II.18 DLS cuvette representation.

The signal obtained is shown in Figure.II.19 and depends on the aleatory variations of the particle position.

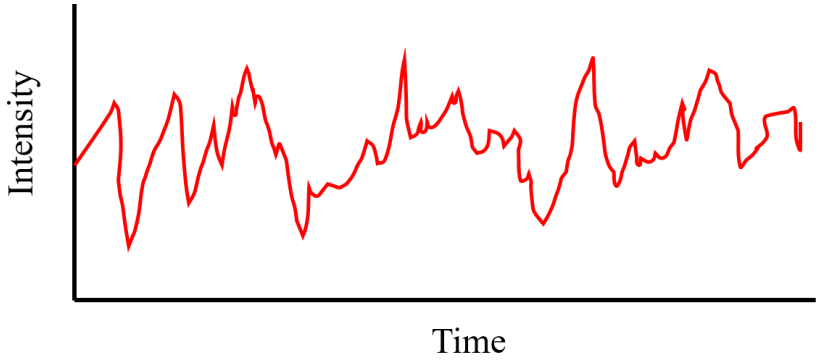

Figure.II.19 Intensity variation as a function of time obtained by the photon counting device.

The signal is then processed and a correlation function defined:

$$G(\tau) = \langle \frac{I(t) * I(t+\tau)}{I(t)^2} \rangle \quad (9)$$

Where G(τ) is the autocorrelation function of the scattering intensity with *I* the intensity, t the time and τ the delay time. G(τ) is then applied to the signal obtained on Figure.II.19 and graphs such as those in Figure.II.20 are obtained.

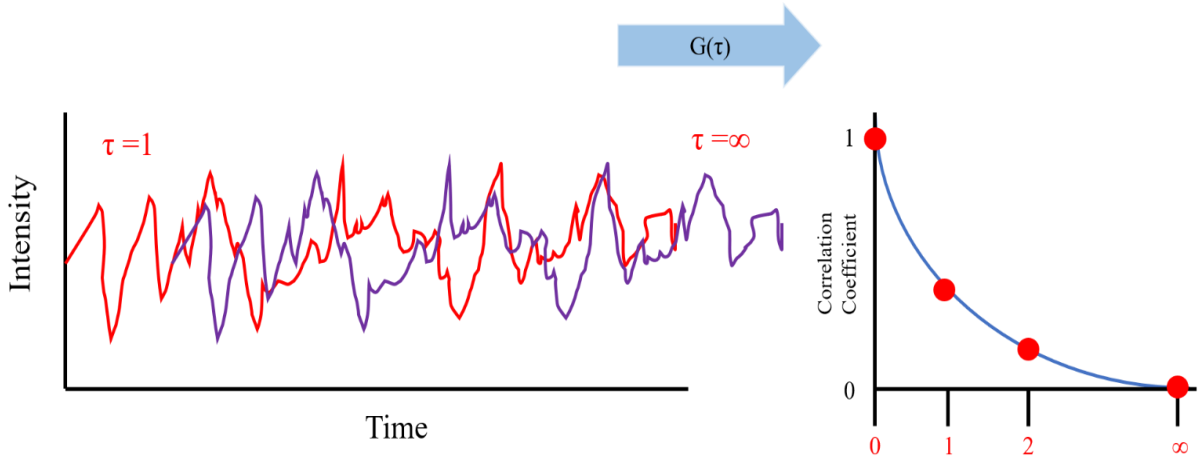

Figure.II.20 Application of the autocorrelation function on the intensity signal giving the correlation curve.

The correlation function can then be modelled following the equation:

$$G(\tau) = B + A\sum_{\tau=0}^{\infty} e^{-2q^2 D_t \tau} \quad (10)$$

Where B is the baseline at infinite time, A the amplitude, q the scattering vector defined by:

$$q = \frac{4\pi n_0}{\lambda}\sin\frac{\theta}{2} \quad (11)$$

With n_0 the dispersant refractive index λ the laser wavelength, θ the detection angle and D_t and τ the correlator delay time. The expression is then calculated and a curve can be obtained (Figure.II.21).

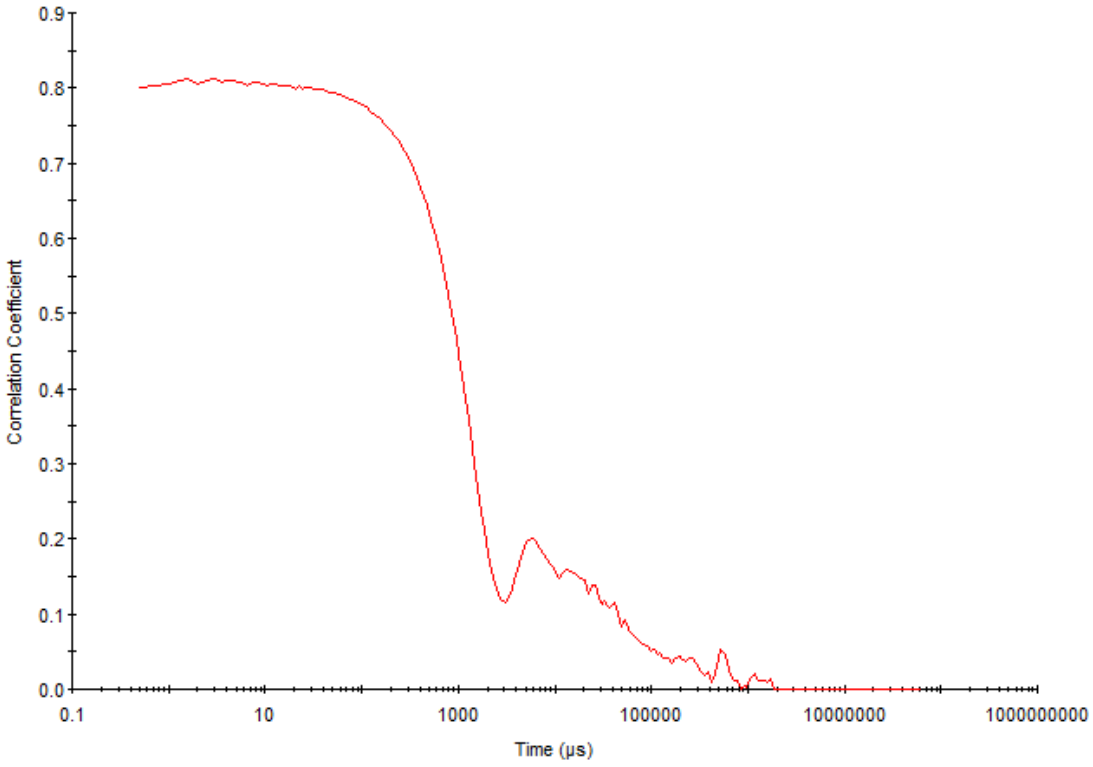

Figure.II.21 Correlation function obtained after refinement of the intensity signal obtained *via* DLS.

The correlation function in equation (10) contains the D_t diffusion coefficient that can be entered into the Stokes-Einstein equation (8). D_t is obtained by fitting the curve with the appropriate algorithm, here for general purpose non-negative least squares (NNLS). Cumulants analysis is used in this thesis to determine the particle size; this gives the Z-Average Diameter of the particle (Z_d).and the Polydispersity Index (Pdl). In each analysis the NNLS algorithm measures the intensity-weighted distribution obtained from the correlation function which then displays a size distribution of the intensity of the light scattered by particles on the y-axis *versus* size classes on the x-axis. The NNLS algorithm on the Zetasizer from Malvern uses 70 size classes.

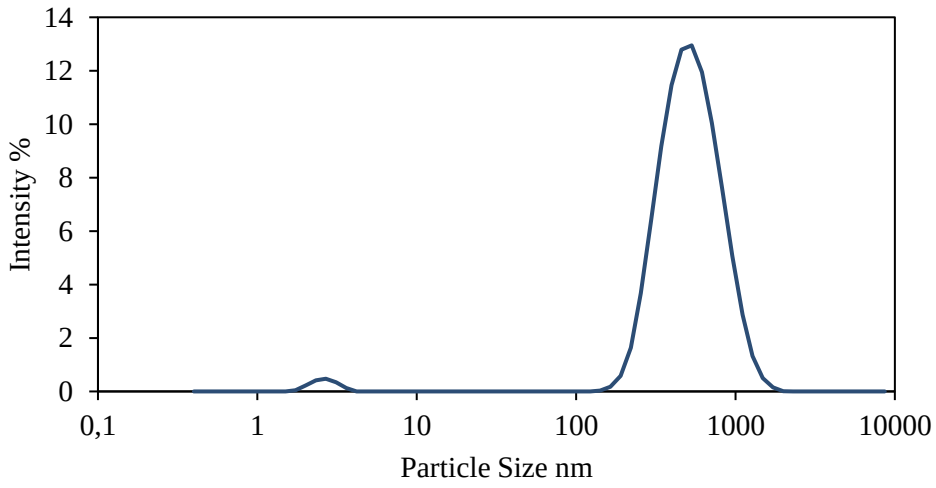

Figure.II.22 Particle size distribution of a nanorod sample of $[Fe(Htrz)_2(trz)](BF_4)$ obtained *via* DLS.

In this thesis samples were all prepared following the same procedure. Powder was diluted into water with a wt % of the sample between 0.01 wt % and 0.001 wt % to avoid any misleading signal from particles superimposing. The solution obtained was transferred into ZEN0040 disposable solvent resistant 40 µL cuvettes.

II.9. Analytical Ultracentrifugation and Differential Centrifugation Sedimentation

Analytical Ultracentrifugation (AUC) separates the constituents of variable mass and sizes contained in liquids, including molecules, cells and nanoparticles. Constituents contained within a sample are expected to either sink due to gravity or rise due to the Archimedes principle. But for a vast majority of experiments, another phenomenon intervenes that prevents these occurrences, the molecular agitation. This "force" does not have any particular direction, and at a microscopic scale the molecular agitation is more important than gravity and Archimedes principle to a point where they are negligible. When using centrifugation another force appears, the centrifugal force, which is a radial acceleration to the exterior of the rotation axis. For a given component, by choosing correctly the rotation speed, the acceleration obtained can be more important than the molecular agitation, which causes the sample to sediment to the bottom of the cuvette or rise to the surface. The acceleration *a*, is function of the radial speed and the distance from the rotation axis. It is given by the formula:

$$a = \omega^2 * r \qquad (12)$$

With:

ω: the radial speed (rad. s^{-1})

r: the distance to the rotation axis

Samples are prepared by suspending them in around 400 µL of a chosen solvent (usually water) with or without a percentage of thickeners (glycerol) in a cuvette which is then placed inside the holder as shown in Figure.II.23. While the sample a rotated to 10000 rpm, a laser is directed through the cells for spectroscopic analysis using ultraviolet light or infrared sensitive systems, giving information about the molecular mass, the form, the dimensions, the density or the interactions between species. The laser is placed above the rotor where the samples stand (Figure.II.24).[133]

Figure.II.23 Cells (left) and rotor (right) used for AUC.

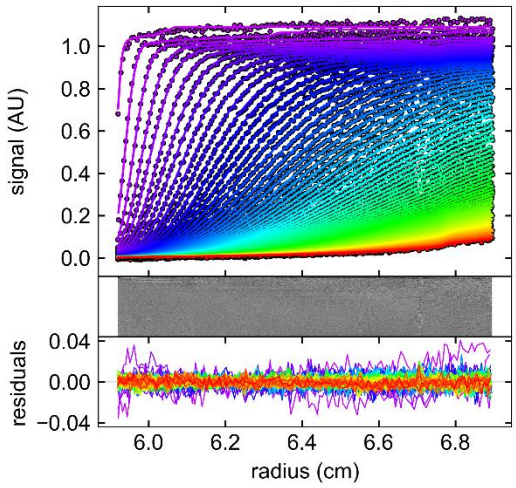

Figure.II.24 AUC data obtained for nanorods of $[Fe(Htrz)_2(trz)](BF_4)$.

While rotating, centrifugal forces are applied to the particles which sends them to the bottom of the cuvette. The laser going through the cuvette during the measurement records the centrifugal field which represents the distance of the particle from the axis of rotation and the square of the angular velocity. With this value the sedimentation rate and coefficient can be obtained based on the differences measured over time. The graph displayed in Figure.II.24 represents the signal obtained by the laser during the measurement showing the particles moving towards the bottom of the cuvette; the centrifugal field is measured *via* these results and then sedimentation rate and coefficient can be determined.

Another technique, Differential Centrifugation Sedimentation (DCS), was used in order to separate the different constituents using several cycles of centrifugation at an increasing acceleration. The DCS technique measures the sedimentation time of particles. The samples are loaded onto a disc, Figure.II.25, which is typically loaded with a density gradient solution with known viscosity and density. The particles will disperse and separate depending on the differences in size, density and shape. At a weak acceleration the heaviest elements of the sample will sediment and form a shell at the bottom of the tube. All other elements will stay in a liquid fraction called the supernatant. The supernatant and the material at the bottom of the cuvette is then recovered and analysed. Applying many cycles of centrifugation gives a more accurate size distribution of the sample. Progressively, the constituent is separated with the smallest ones separating last as their density is closest to that of the solvent. Turbidity detectors measure the time elapsed from the injection of the sample until the particles are detected. The equivalent hydrodynamic radius of the particle is then determined using Stokes law.[134–136]

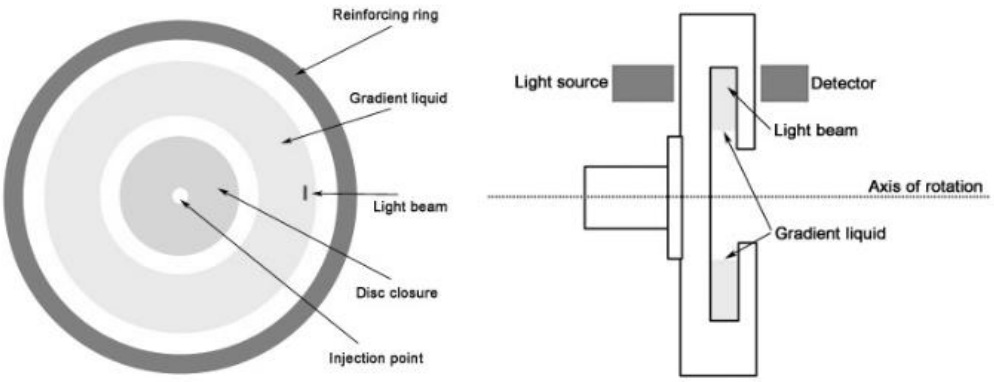

Figure.II.25 Disc scheme for DCS.[137]

II.10. Design of experiments (DOE)

Design of experiments (DOE) methodology was used in this thesis to control and optimise the process of different flow reactors. DOE has been used to determine the effect of certain parameters on a desired response (output). DOE in this case can detect and identify the different interactions between the parameters of a process. All possible combinations are studied with a certain number of experiments depending on how precise and feasible the process is. DOE can, with those combinations, facilitate understanding of the effect of reaction parameters on the particle sizes of a certain compound or development of an equation that can predict the output depending on the input parameters.

In our case the DOE methodology was used in order to establish a model for particle size control. For this purpose, a surface response model variant of DOE was implemented on two reactors and will be presented in Chapters V and VI. The background of this technique will be explained in this section. Coming from the work of Box and Wilson (1951),[138] the response surface methodology is widely used in engineering to optimise a parameter or response from a process.[139–141] Surface response gives the relation between a response variable, *y*, and several dependent variables, $x_1 \ldots x_n$, by adjusting a mathematical function in order to optimise *y*. The principle is to find the most optimised experimental conditions by undertaking a number of experiments depending on how precisely *y* needs to be optimised. At first a series of screening experiment are carried out to reduce the list of variables needed for the model depending on their importance. This helps to reduce the number of runs necessary for a full DOE and identify the important variables. If the response is far from optimised several changes to the process need to be carried out to have a near optimum response.

In the response surface model, it is necessary to obtain an approximation of a surface model in order to get the true response surface. The obtained observations give a certain idea of a surface from $y = s(x_1,\ldots,x_d)$ in this region (the studied parameters, such as particle size). It is then possible to use it to estimate the direction with the strongest descent of this surface (or weakest if the response needs to be increased or decreased). To model the surface, an interest region is obtained by using a regression polynomial model of 1st degree.

To build the empirical model of the surface response model, a linear regression model is used to obtain each coefficient to get a response. To obtain this coefficient the methods of least squares is used with the linear regression model to get to the response $y_1, y_2, \ldots, y_n$.(the parameter investigated in this thesis, for instance, is particle size). With each response obtained for each parameter a variable

x_{nm} (combination of variables) for the *n*th observation (or number of experiment) will be defined. The model can be written:[142]

$$y = X\beta + \varepsilon \tag{13}$$

With y defined as the response matrix obtained in a n * 1 vector, *X* is a n * p matrix representing each experiment's parameter level, β is the p * 1 vector representing the regression coefficient and ε the n * 1 vector for the errors that can be observed during the experiment (human or experimental). The matrix of the linear regression is described in Table.II.1.

Table.II.1 Linear regression data representing each experiment carried out (x) during the DOE with their response (y).

$y_{0,0}$	$x_{1,0}$	$x_{2,0}$	…	$x_{k,0}$
$y_{1,1}$	x_{11}	x_{12}	…	x_{1k}
$y_{2,1}$	x_{21}	x_{22}	…	x_{2k}
.	.	.	…	.
.	.	.	…	.
$y_{n,1}$	x_{n1}	x_{n2}	…	x_{nk}

In equation (13) *X* represents all the parameters combinations used in the *nth* experiment, and β the regression coefficient, these can be written as

$$X = \begin{pmatrix} 1 & x_{1,1} & \cdots & x_{1,k} \\ 1 & x_{2,1} & & x_{2,k} \\ \vdots & \vdots & \ddots & \vdots \\ 1 & x_{n,1} & \ldots & x_{n,k} \end{pmatrix} and\ \beta = \begin{pmatrix} \beta_1 \\ \beta_2 \\ \vdots \\ \beta_k \end{pmatrix} \tag{14}$$

When replacing *X* and β from (14) into (13) the response *y* can be obtained in (15):

$$y = \beta_0 + \sum_{n=1}^{d} \beta_n x_n + \sum_{n,m=1}^{d} \beta_{n,m} x_n x_m + \varepsilon, \tag{15}$$

with $\beta_{n,k} \in \mathbb{R}$ for every $n,m = 1,\ldots,k$.

The response *y* obtained is in the form of a polynomial of second order where each parameter can be replaced to optimize the process studied. Different equations such as (15) will be presented with actual coefficient values in order to target the response studied.

The choice of a design of experiments plan needs to answer two criteria, first the number of experiments required must be the smallest possible to minimise cost, and the estimation of the surface must be as precise as possible. Classic DOE usually uses factorial plans and central composition. Numerous other designs of experiments plans exist, each having advantages for different purposes, but in the case of particle size targeting no other method optimises an output when a variable is a function of a curve. The needs of the DOE must consider both the optimisation of the calculations and the results of the physical experiment. The surface response model used will be described in detail in the Oscillatory Baffled Reactor (OBR) reactor Chapter V.[139]

II.11. Materials

In Chapter III and IV Urea NH_2CONH_2 (BioReagent) Barbituric Acid $C_4H_4N_2O_3$ (99 %) and Succinic Acid $HOOCCH_2CH_2COOH$ (99 %) were purchased from Sigma-Aldrich® and used without further purification.

In chapter III, IV, V, VI and VII for the synthesis of PiC and PiCM, 1,2,4-H-triazole $C_2H_3N_3$ (98 %) and Iron(II) tetrafluoroborate hexahydrate $Fe(BF_4)_2 \cdot 6H_2O$ (97%) were purchased from Sigma-Aldrich® and used without further purification.

In chapter VI and VII the synthesis of YeC Iron(II) tetrafluoroborate hexahydrate $Fe(BF_4)_2 \cdot 6H_2O$ (97 %) was purchased from Sigma-Aldrich® and used without further purification. 2,6-di(pyrazol-1-yl)pyridine (2,6-bpp) was provided by Dr Laurence Kershaw-Cook from the Metastable Materials group.

In Chapter VI and VII, 4-iodoaniline (98 %), 3,5-dinitrobenzoicacid (99 %), 3,5-dinitrosalicyliacid (98 %), 4-iodo-2-methylaniline (97 %), 2-bromoaniline (98 %), 2-iodoaniline (98 %), 2-Chloroaniline (98 %) and 3,4-dinitrobenzoic acid were purchased from Sigma-Aldrich® and used without further purification.

In Chapter VII for electrospray polyacteonitrile $(C_3H_3N)_n$ average M_w 150,000 was purchased from Sigma-Aldrich® and used without further purification.

In this thesis PiC,PiCM and YeC synthesis were carried out at room temperature.

Chapter III A segmented flow reactor study

III.1. Introduction

Handling solids in flow has always been a challenge,[99,143] from premature nucleation due to contact with the tubing, continuous filtration, blockages or the need for special pumps that can work with solids. Some solutions like the COBC (Continuous Oscillatory Baffled Crystalliser) from NiTech [76,144,145] or CSTR (Continuous Stirred Tank Reactor)[84,87,99,146] are capable of crystallising many compounds from gram to tonne scale,[92] or at even smaller scale using mesoscale crystalliser tubular systems with static mixers[147,148] or segmented flow.[149,150] Gas-liquid or gas-liquid-liquid segmented systems are encountered in various reaction systems involving biphasic catalysis, such as hydrogenation [50,51] and carbonylation.[151,152] These systems require a large surface area interface between the phases to obtain good mass and heat transfer, with a controllable dispersion of the phases, to establish stable production.[150] An issue of gas-liquid segmented reactors is that the wetting of the wall is favoured by the solution (Figure.III.1) which can create unwanted crystallisation within the reactor.[143] In the last decade, innovative micro- and milli-scale multiphase reactors have been developed, giving high mass and heat transfer performances and opening up new ways of handling reactions and solids in flow. [153]

Presented in this chapter is an approach based on segmented flow using a mesoscale reactor, the Kinetically Regulated Automated Input Crystalliser, or KRAIC, designed by Dr Karen Robertson (University of Bath). Using two immiscible fluids (carrier fluid and solution), the tubing walls of the crystalliser are wetted by the carrier fluid resulting in the formation of discrete droplets of solution (‘slugs’) that avoid contact between the solution and the tubing (Figure.III.1). The only drawback of this technique is the need for separation of the two phases at the end of the crystalliser but a solution to this caveat is provided in this chapter.

The difference between segmentation behaviour in segmented flow with different liquids is due to the hydrophobicity/philicity. The contact angle between the two liquids will dictate how they will form the slugs and the shape of those slugs (Figure.III.2. In this work, segmentation by air, liquid (fluorinated fluid PFPE (Perfluoropolyether, Galden SV110 from Solvay) or both air and liquid is investigated.

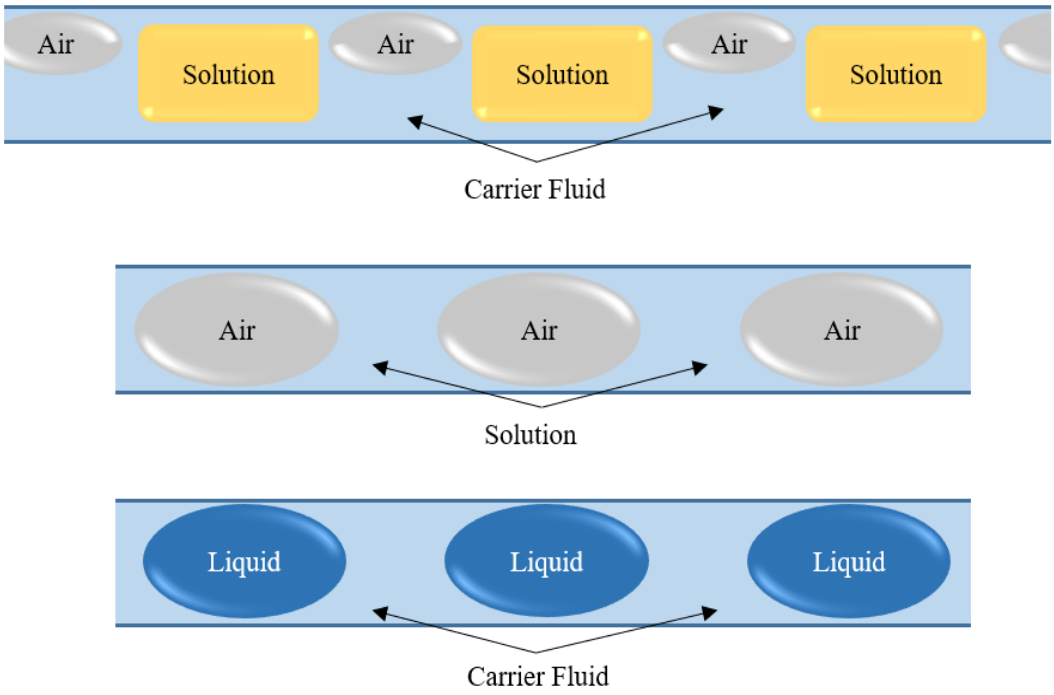

Figure.III.1 KRAIC wetting comparison between using liquid/air/liquid (top), air/liquid (centre) and liquid/liquid (bottom) segmentation

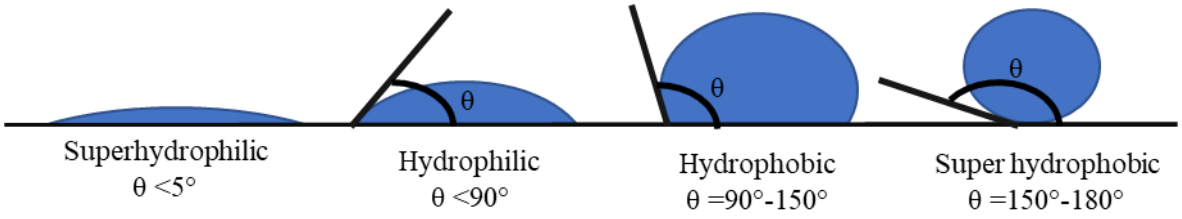

Figure.III.2 Representation of hydrophobic and hydrophilic droplets on a hydrophilic surface.

In the experiments reported in this chapter, the solid surface is replaced by a hydrophobic carrier fluid (PFPE) which wets the hydrophobic tubing surface in preference to the hydrophilic solution. In the case study the carrier fluid will remove the liquid-solid interface of the solution with the tubing wall, putting the experiment in the super hydrophobic region. As the carrier fluid has the same affinities as the fluoroethylene propylene (FEP) tubing, it tends to wet the wall creating a layer between the fluid and the walls. The liquid-liquid interface between the solution and the carrier fluid has a contact angle between 90° and 180°. This value varies depending on the solvent and carrier fluid used. The wetting, contact angle and surface tension are important variables in microchannel or mesochannel segmented flow as it will dictate the shape of the slugs (discrete droplets), which dictates the heat and mass transfer within the slug. The wetting conditions of the carrier fluid, solution and the wall can be described using Young's relation:

$$\gamma_{wg} - \gamma_{wa} = \gamma_{ga} \cos(\theta) \qquad (16)$$

Where γ_{wg} is the surface tension (in mN/m) between the wall (w) and carrier fluid (g), γ_{wa} the surface tension between the wall and the air (a), and γ_{ga} is the surface tension between carrier fluid

and air. θ is the contact angle (°). Fluoroethylene propylene (FEP) tubing is used as the reactor wall, in this case Galden has a surface tension of 14 nM/m and an hydrophobic contact angle of 110°, water has a surface tension of 72.80 nM/m[154] and an hydrophilic contact angle of 130° at room temperature on fluorinated surface [154]. This results in the Galden wetting the inner walls of the FEP tubing, creating a layer between the solution of water and the wall, avoiding any contacts. The value of contact angle of 130° will be used in Computational Fluid Dynamic (CFD) calculations in section III.4 below, in particular to model the slug formations.

Several versions of the KRAIC will be presented due to the modularity of the device and its adaption the different experimental requirements. As described elsewhere,[155–157] mixing inside the slugs is driven by the phase separation. The two immiscible fluids act as a wall to each other and the respective fluids are repelled in multiple directions, creating a bolus flow phenomenon (Figure.III.3). Each slug can be likened to a small batch reactor flowing along the tubing.

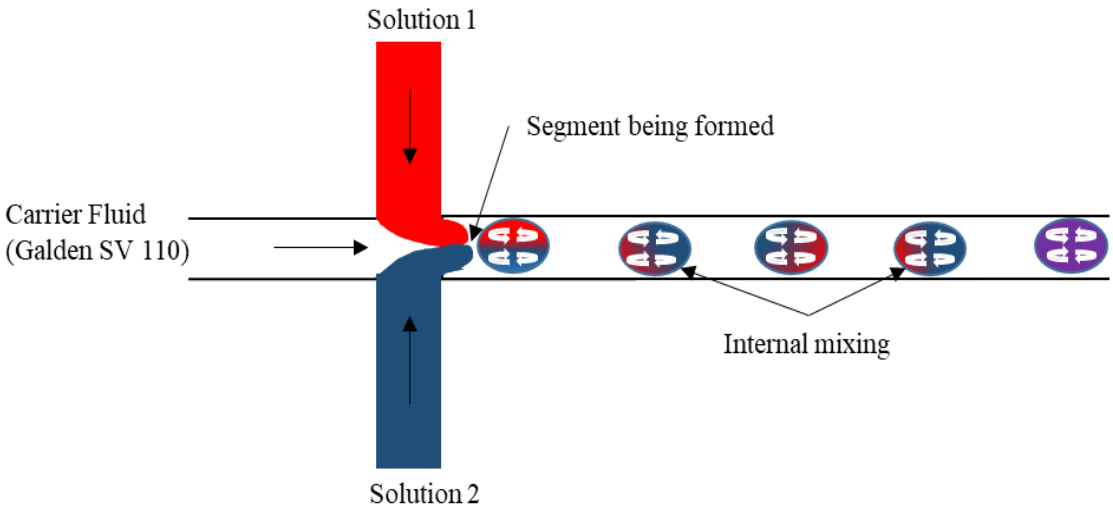

Figure.III.3 Representation of mixing happening inside the slugs, during the formation of the slugs mixing is induced at the cross piece, this mixing is then retained in each of the slugs *via* bolus flow, creating a homogeneous solution.

The bolus phenomenon is an eddy-like flow pattern which was first described by Prothero and Burton (1961). These microfluidic events, as illustrated in Figure.III.3, are often present in microcirculatory systems and this phenomenon widely describes the properties of blood flow and capillaries.[156,158,159] In a study by Prothero *et al.*,[158] the heat transfer between segmented flow and laminar flow in a small bore tubing was compared. It was found that the bolus phenomenon equilibrated the temperature inside a capillary much faster than laminar flow. As shown in Figure.III.3 the mixing behaviour is created at the inlet mixer where the phases are first introduced and is continued in the slugs *via* bolus phenomenon. In a laminar flow channel (single phase flow) the shear of the fluid with the walls leads to the formation of streamlines which increases mixing times due to high dispersion along the tubing, the laminar flow is preserved with the segment formation that occurs at low Reynolds number (*Re)*, in the KRAIC. This can be dealt with by employing static mixers or baffles in the flow reactor that can induce mixing faster and result in homogenous mixing.[93,148] In segmented flow, the slugs create a controlled environment that enables fast and homogenous mixing in each slug generated by the co- and counter-rotating vortices.[155]

Part of the work presented in this Chapter, on the synthesis of $[Fe(Htrz)_2(trz)](BF_4)$, is published in Robertson *et al*. 2017 and Robertson *et al.*2016.[16,160]

III.1.2 KRAIC set-up and operations

The KRAIC, displayed in Figure.III.4, is composed of feed vessels that are modular and can be changed depending on the reaction/crystallisation being undertaken. An Ismatec Gear pump REGLO-Z Series was used for the carrier fluid (fluorinated fluid PFPE Galden SV110 from Solvay) throughout these studies, whilst the solution pump was subject to change. The solution and carrier fluid pumps are connected to a cross mixer piece submerged into a mixer bath (providing heating or cooling). The tubing from the solution feed vessel to the mixer piece is jacketed and connected to a R3 Grant Circulating Bath to control the temperature. The cross-piece is then connected to a 15 m single extruded length of FEP (Fluorinated Ethylene Propylene) tubing, 3.2 mm ID; each 5 m section of the tubing is coiled inside individual aluminium DrySyn® cases that can be temperature controlled *via* hotplates.

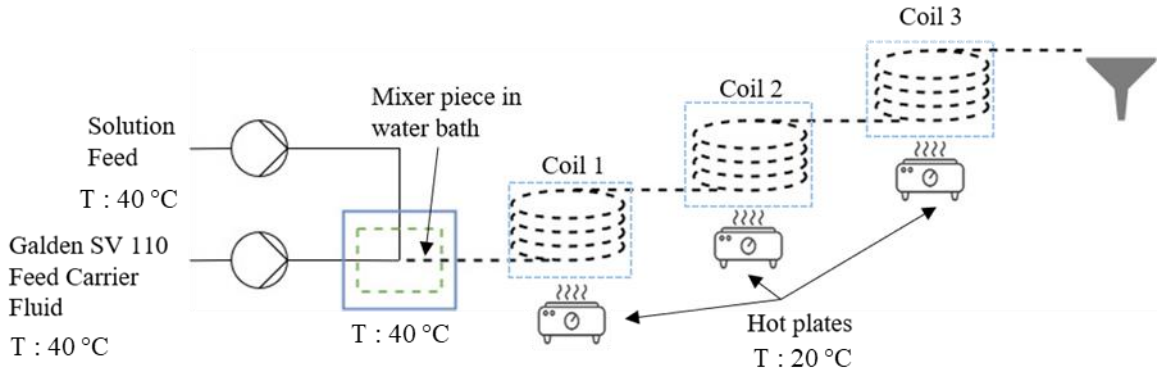

Figure.III.4 Schematic representation of the KRAIC reactor in first crystallisation configuration.

In this chapter the KRAIC is used to produce different materials; the first part will focus on the cooling crystallisations of succinic acid (SA) and urea-barbituric acid (UBA), from which different polymorphs have been detected. These two compounds each have several crystalline forms with different arrangements in the crystal lattice (polymorphs). Each of those polymorphs differ in terms of properties like stability and solubility.[76,161–163] The capability of the KRAIC to produce gels and coordination polymers will then be explored. The latter part of this chapter will focus on the development of a computational fluid dynamic model of the segmented flow environment of the KRAIC to better understand the mixing within the slugs.

III.2. Study of KRAIC capabilities

III.2.1 Crystallisation of Pharmaceutical Compounds

III.2.1.i Succinic Acid Crystallisation

Succinic acid (SA) is a widely used chemical as an excipient for pharmaceutical compounds or as a counter ion,[164,165] with 16000 to 30000 tonnes production each year.[166] This compound, a dicarboxylic acid, is a good model for morphology modification during crystallisation[85] and is often

used in industry as a co-former in crystallisation of APIs or different molecular systems.[167] This system was employed for the development of the KRAIC as the crystals grow fast and large, providing a good indication of any blocking hazards. Excluding the first experiment, the solution of SA was set with a concentration of 0.12 g/mL in water, the feed temperature was at 40 °C and the PFPE carrier fluid used was Galden® SV 70 (Table.III.1). The tubing from the solution feed vessel to the mixer piece is jacketed and actively temperature controlled at the same temperature as the feed vessel in order to avoid any crystallisation in the transfer tubes / pumps which could damage them or affect the crystallisation. The mixer piece used was a glass Y-piece with internal diameter (ID) of 3.1 mm displayed in Figure.III.5. Here, liquid-liquid (aqueous solution/carrier fluid) segmentation was used as a first development of the KRAIC.

Figure.III.5 Mixer Y piece

Table.III.1 Succinic acid crystallisation parameters for the KRAIC

Experiment	[SA] g/mL	Residence Time RT	Flow Rate Solution mL/min	Flow rate Galden® mL/min	Yield %
SAK 1	0.11	13 m 36s	17.9	17.9	7.6
SAK 2	0.12	13 m 39s	17.9	17.9	29.3
SAK 3	0.12	13 m 39s	17.9	17.9	21.7
SAK 4	0.12	13 m 30s	17.9	17.9	23.6
SAK 5	0.12	13 m 30s	17.9	17.9	18.2
SAK 6	0.12	11 min 6s	21.6	21.6	10.3
SAK 7	0.12	13 m 30s	17.9	17.9	22.4
SAK 8	0,12	7 min 25s	8.4	8.4	24.5

Experiment Temperature (°C)	Coil 1	Coil 2	Coil 3	Feed temperature	Jacketed tubing temperature	Temperature of Water Bath
SAK 1	34	26	24	50	50	30
SAK 2	30	24	22	40	40	30
SAK 3	30	24	22	40	40	40
SAK 4	30	24	22	40	40	40
SAK 5	30	24	22	40	40	40
SAK 6	30	24	22	40	40	40
SAK 7	30	24	22	40	40	40
SAK 8	30	24	22	40	40	40

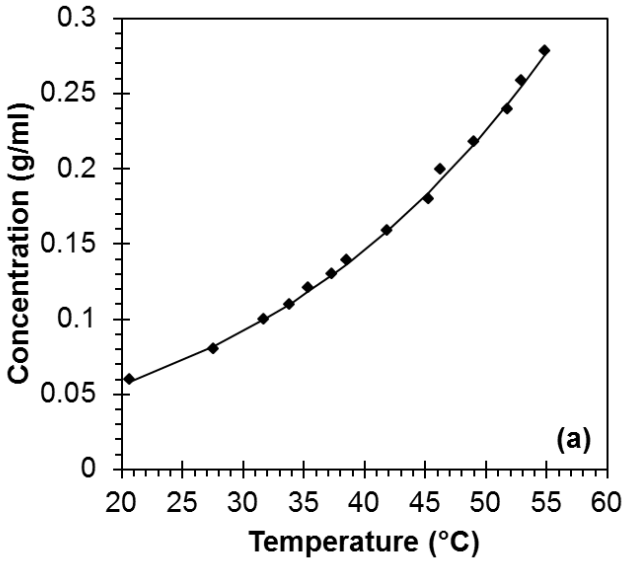

Figure.III.6 Succinic Acid Solubility Curve in water.[168]

The parameters were chosen from previous study of crystallisation of SA with the solubility curve shown (Figure.III.6). Prior to the experiment the system was primed with pure solvent and carrier fluid for two hours at 40 °C.

Trials SAK 1 to 7 were performed using a dual-head peristaltic pump whilst experiment 8 used gear pumps, used in all future experiments. The first experiment ran for 16 min without crystallisation being observed, it was then decided to reduce temperature of the feed vessel and jacketed tubing by 10 °C to 40 °C for the next set of experiments and the concentration of SA was increased to 0.12 g/mL. The temperature of the mixer piece and the tubing from the feed vessel to it was actively temperature controlled and the KRAIC coils used passive insulation to establish lower temperature regimes going from 30 °C for the first coil to 22 °C at the third coil (Table.III.1).

During experiment SAK2, crystals were first observed after 3 min 56 s at the end of the first coil at 456 cm and in each slug at 7 min of flow at the end of the 2nd coil at 853 cm. After 26 min the run was stopped due to fouling appearing at the mixer piece. The temperature of the mixer bath was therefore set to 40 °C for subsequent experiments to keep the SA in solution. The presence of carrier fluid in the filter funnel caused an impenetrable filter cake, preventing continuous online filtration. To avoid this problem in the future a recovery end piece was designed to recover the Galden continuously prior to filtration (Figure.III.7). The outlet of the 15 m tubing was then connected to a “duck bill” end piece with small holes on the bottom to recover the carrier fluid. The end piece is displayed in Figure.III.7, the carrier fluid, being denser and strongly preferentially wetting the walls, will trickle down the small pierced holes in the tubing and be recovered, the solution continues through the outlet and is immediately filtered through a standard vacuum filtration set-up.

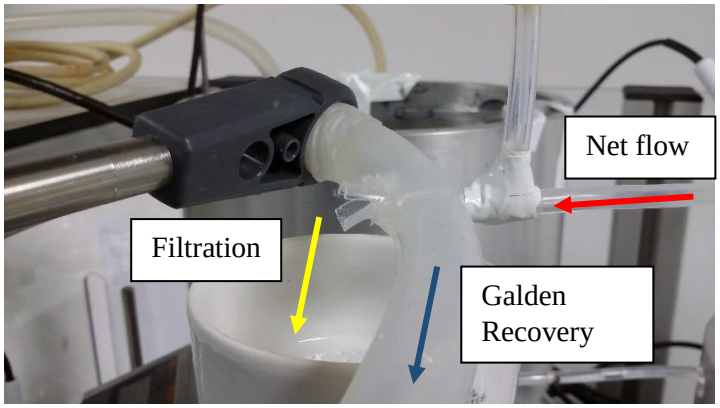

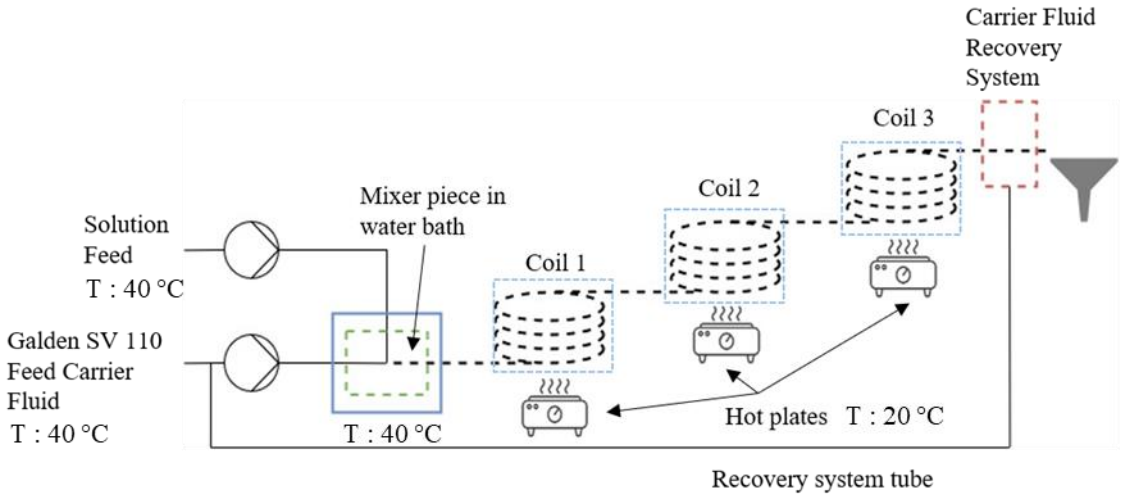

Figure.III.7 End-piece of the KRAIC and new set-up with carrier fluid recovery system.

For experiments SAK 3 and 4 crystals were observed at 8 min 22 s at the end of the second coil at 1051±5 cm. The experiment was stopped after 33 min of flow time due to crystals encrusting the outlet and preventing evacuation of crystals over time. In Figure.III.8, the crystals forming inside the KRAIC in the third coil in experiment SAK3 are shown.

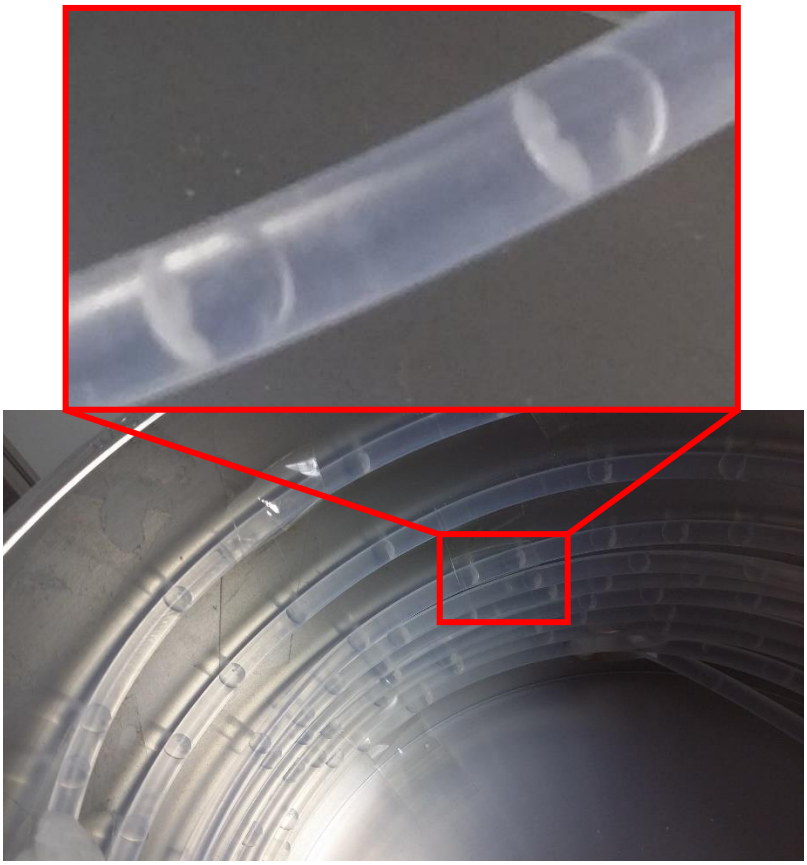

Figure.III.8 Crystals appearing in the KRAIC in the 3rd coil

Crystallisation runs with the same parameters using the same feed over time have proven to decrease the yield and affect the appearance of crystals along the KRAIC; this can be seen by comparing experiments SAK3, 4 and 5 where, in experiment SAK5, the feed solution was used a day after preparation. Using higher flow rates showed a reduction in yield and crystal appearance for experiment 6 using the same feed as experiments SAK3, 4 and 5 over a duration of 24 hours. This increased flow rate was chosen due to blockages happening in the last coil of the KRAIC and postponed the crystallisation to a later point in the tubing. The reduction in crystals observed could also be due to the solution being reused after a day and by re-heating it at 40 °C. During experiment SAK6 the crystals started to appear after 15 min in the third coil at 1422 cm. After one hour the crystal growth improved without changing the parameters and the crystals appeared at the top of the 2nd coil at 985 cm. This experiment ran for two hours with no fouling for the first time (previous experiments were stopped due to blockages). Following experiment SAK6, experiment SAK7 was carried out with 17.9 ml/min flow rate and a new feed solution, this experiment the crystallisation returned to its initial value for yield and position of observed crystals in the end of the first coil at 486 cm and with a crystal in each slug at 823 cm.

During the experiments, use of the peristaltic pump resulted in some pulsation along the flow which created inconsistent slug sizes. For experiment SAK8 a new design approach was used to solve this problem, gear pumps being used for the solution and carrier fluid. The residence time was reduced by 6 min to 7 min 25 s due to the minimum flow rate of 2.1 mL/min of the gear pump; the crystals were then observed in the 3rd coil due to the higher flow rate. However, the same filtration problem occurred with the Galden caking again the filter. This resulted from some of the crystals beginning to block the small pierced holes inside the end-piece, thus not allowing the Galden to pass through.

The resultant crystalline material from the above experiments was analysed by PXRD (Powder X-Ray Diffraction); both α- and β-polymorphs of SA were observed to be present. PXRD on the products obtained are displayed in Figure.III.9.

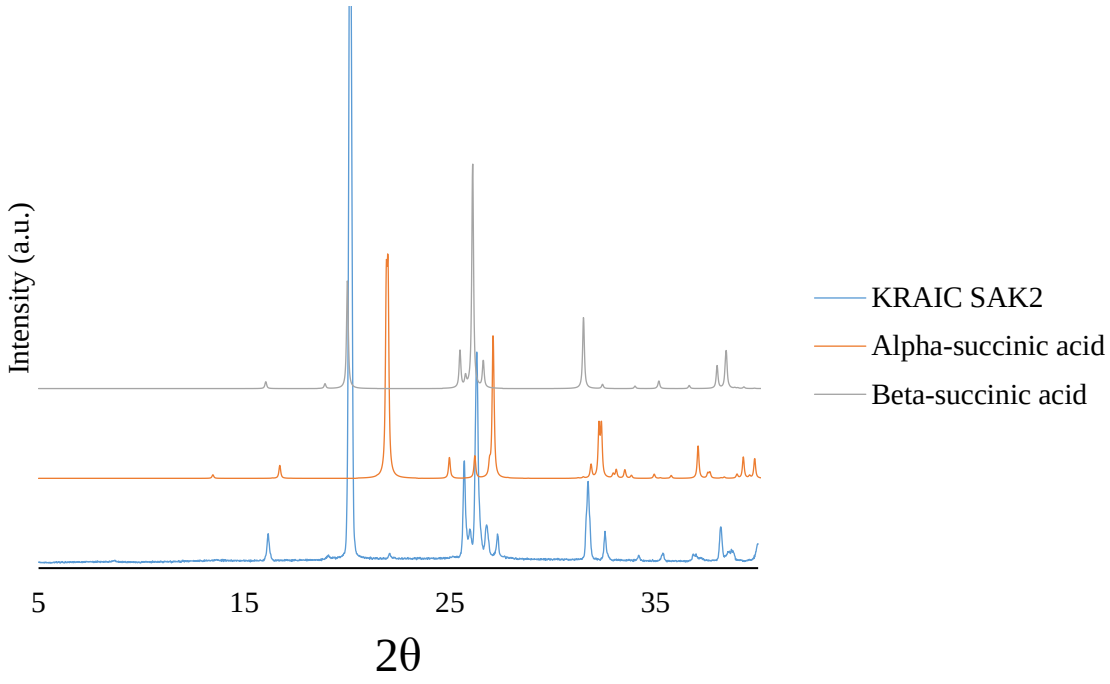

Figure.III.9 PXRD pattern for experiment SAK2 and simulated SA patterns showing both α- (SUCACB07) and β- (SUCACB12) polymorphs (patterns from each experiment show the same proportions of both polymorphs).

III.2.1.ii Neutral solvent implementation

Cooling crystallisation of SA experiments were used to improve the KRAIC crystallisation capabilities. The first improvement was to change the peristaltic pump – the pulsation created by use of this pump gave rise to different slug sizes along the system, also inducing perturbations inside the slugs. In experiment 8, gear pumps were used instead as they display low pulsations. The end piece was improved by cutting half of it at the end in a form of "duck bill" (Figure.III.10) which allows the slugs to fall without resulting in the carrier fluid dropping on the outside of the tubing due to surface wetting.

Figure.III.10 "Duck bill" end piece with recovery holes for the carrier fluid

The capabilities of the KRAIC to crystallise SA has been proven above, but the filtration was an issue due to the crystals caking with the Galden, making it impossible for the water to pass through. This was solved using an end piece with holes pierced prior to the end where the Galden falls into a recovery vessel or directly to the carrier feed vessel. The carrier fluid can flow through holes too small for the hydrophilic aqueous solution due to a combination of the contrasting wetting properties and surface tension of the carrier fluid and solution. The issue of adding a recovery system for the Galden was that the crystals could get trapped in the recesses caused by making the small holes in the end-piece. To avoid this problem a neutral solvent (same solvent as the solution without added solids) inlet was created at the top of the tubing Figure.III.11 to push the crystals into the Buchner vessel.

Results from these experiments are published in Robertson *et al.* [16]

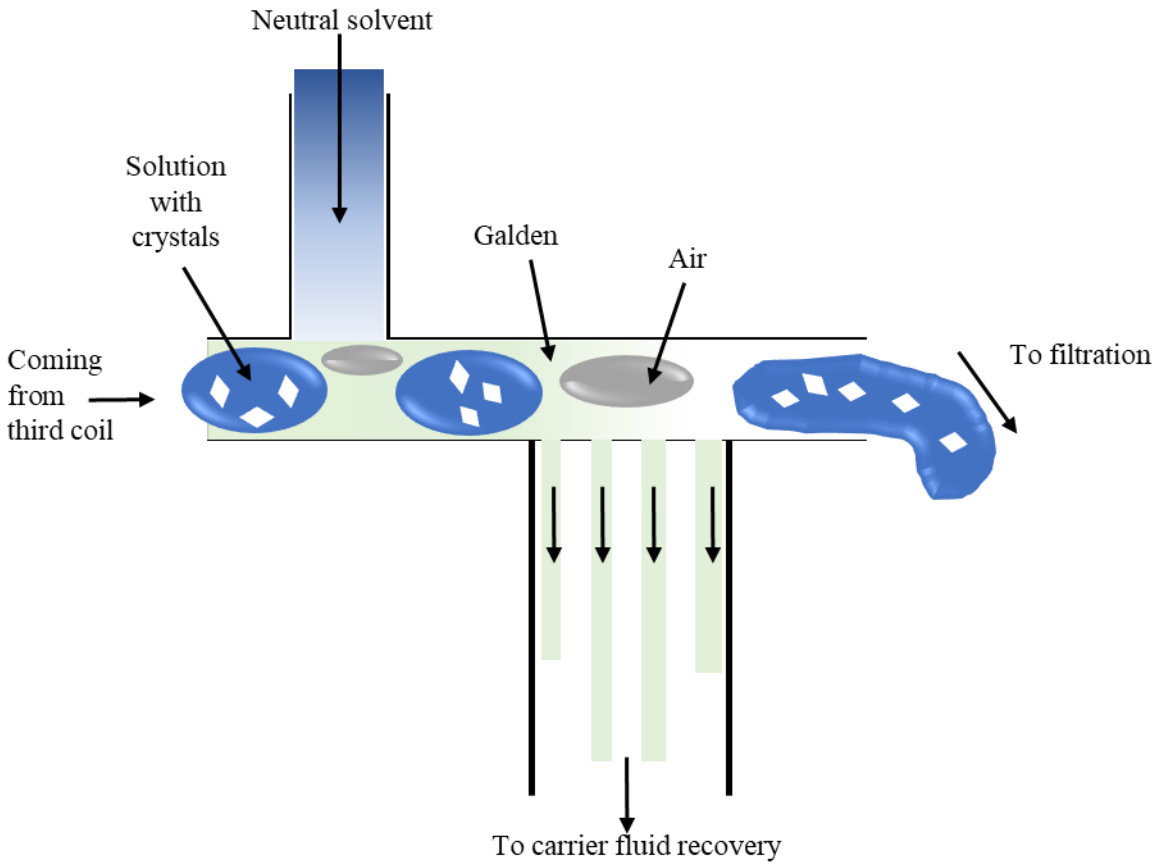

Figure.III.11 Schematic diagram of the final KRAIC end-piece design

During the SA crystallisation runs, the liquid-liquid segmentation slugs were often observed to merge, in part due to an elevation change and difference in density of the solution and carrier fluid. Use of non-aqueous solvents was also desirable for future applications and, at the internal diameter size used (3.2 mm), the surface tension of non-aqueous solvents was observed to be insufficient to result in discrete slugs. Therefore, three phase segmentation (liquid-liquid-gas with air) was used for future runs.

III.2.1.iii Urea Barbituric Acid Continuous crystallisation

Like succinic acid, the multi-component crystalline system urea-barbituric acid (UBA) was identified as a potential candidate for pharmaceutical crystallisation inside the KRAIC. This

compound is a co-crystal formed through hydrogen bonding of a co-former (urea) with the active pharmaceutical ingredient (API, barbituric acid). UBA displays three polymorphs, one of which (form III) has been shown to exhibit improved solubility of the API in water[86]; a further highly metastable polymorph (form II) exists but is elusive and its solubility has not been determined. Continuous crystallisation of UBA has been previously reported using periodic mixed suspension mixed product removal (PMSMPR)[86]. UBA presents three possible polymorphs and a hydrate which can be obtained with different crystallisation conditions. As the free energies of UBA form I and form III are close, a polymorphic change can occur during the crystal growth; the previously presented SA investigation showed the possibilities to obtain various polymorphic forms in the KRAIC and so UBA was also investigated in this platform. Parameters used for UBA runs are in correlation with the solubility curve of UBA in methanol Figure.III.12.[86]

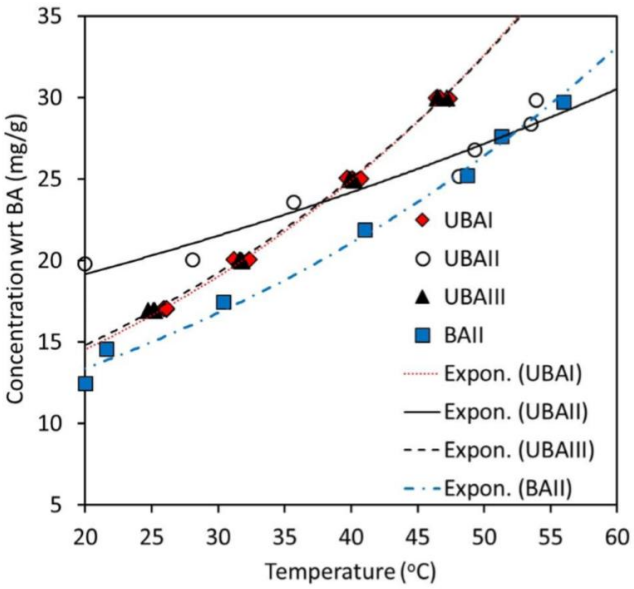

Figure.III.12 Solubility curve of UBA polymorphs Form I, II and III in Methanol.[86]

For these experiments the configuration of the KRAIC was changed to use air-liquid segmentation and the neutral solvent and carrier fluid recovery system as represented in Figure.III.13.

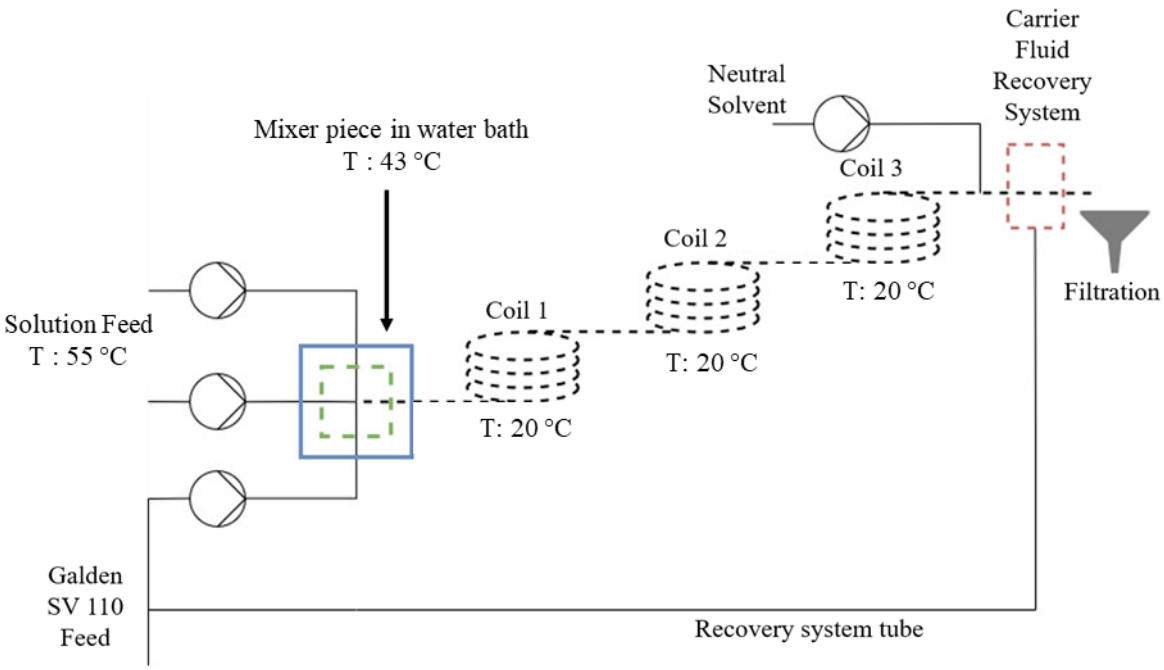

Figure.III.13 KRAIC configuration for UBA crystallisation.

Table.III.2 UBA Crystallisation Parameters for the KRAIC. † Residence time (RT)

Experiment	[Urea] (g/mL)	[Barbituric Acid] (g/mL)	RT†	Flow Rate Solution (mL/min)	Flow rate Galden (mL/min)	Flow rate air (mL/min)	Neutral Solvent (mL/min)
UBAK1	0.118	0.118	8 min 23s	8.4	4.2	4.2	4.2
UBAK2	0.118	0.118	8 min 41s	8.4	4.22	4.2	4.2
UBAK3	0.118	0.118	8 min 53s	8.4	4.2	4.2	4.2
UBAK4	0.118	0.118	8 min 45s	8.4	4.2	4.2	4.2

Table.III.3 Temperature readings of the KRAIC

Temperature Coil (°C)	1	2	3	Feed temperature (°C)	Temperature of Water Bath (°C)	Temperature of Jacketed tubing (°C)	Neutral Solvent Temperature (°C)
UBAK1	20	20	20	55	55	55	20
UBAK2	20	20	20	55	45	55	20
UBAK3	20	20	20	55	43	55	20
UBAK4	20	20	20	55	43	55	20

Table.III.4 Yield obtained for each experiment

Experiment	**1**	**2**	**3**	**4**
Yield %	35.6	41.3	46.3	47.1

The experimental parameters used for the UBA runs including pump and temperature are detailed in Table.III.2, Table.III.3 and Table.III.4In these experiments, the KRAIC configuration is different than in the SA runs previously presented – a neutral solvent was included into the end piece and gear pumps were employed for all fluids. As described above, neutral solvent is used before the carrier fluid recovery to help to push the crystals at the end of the reactor, due to the absence of carrier fluid in the last 2 cm of the KRAIC the crystals tend to stay in place and can cause blockages. The neutral solvent used throughout all experiments presented herein is the pure solvent used for the solution delivered from an ice bath.

With the new design of the KRAIC, crystallisation was successfully carried out in all experiments, with crystals appearing at 7 min 15 in the end of the second coil and in the start, middle, of the third coil (Figure.III.14) for experiments UBAK2 to 4, respectively. Experiment UBAK1 showed crystals at the end of the KRAIC; this was due to the high temp of the water bath at 55 °C which was then reduced to 45 °C to ensure crystallisation at an earlier point.

Figure.III.14 Crystals of UBA in the third coil of the KRAIC.

The crystals were filtered at the end of the third coil, the new end piece and neutral solvent helped the crystals flowing out and the Galden was easily recovered with the new end piece. It is noted that the orientation of the end piece is important, a horizontal position is preferable as tilting up of the end piece will prevent crystals getting out and create blockages at the end (Figure.III.15) of the tubing, while tilting down of the end piece prevent Galden recovery, if some carrier fluid goes into the filter the filtration can be disrupted.

Figure.III.15 UBA Crystals blockages at the KRAIC end piece

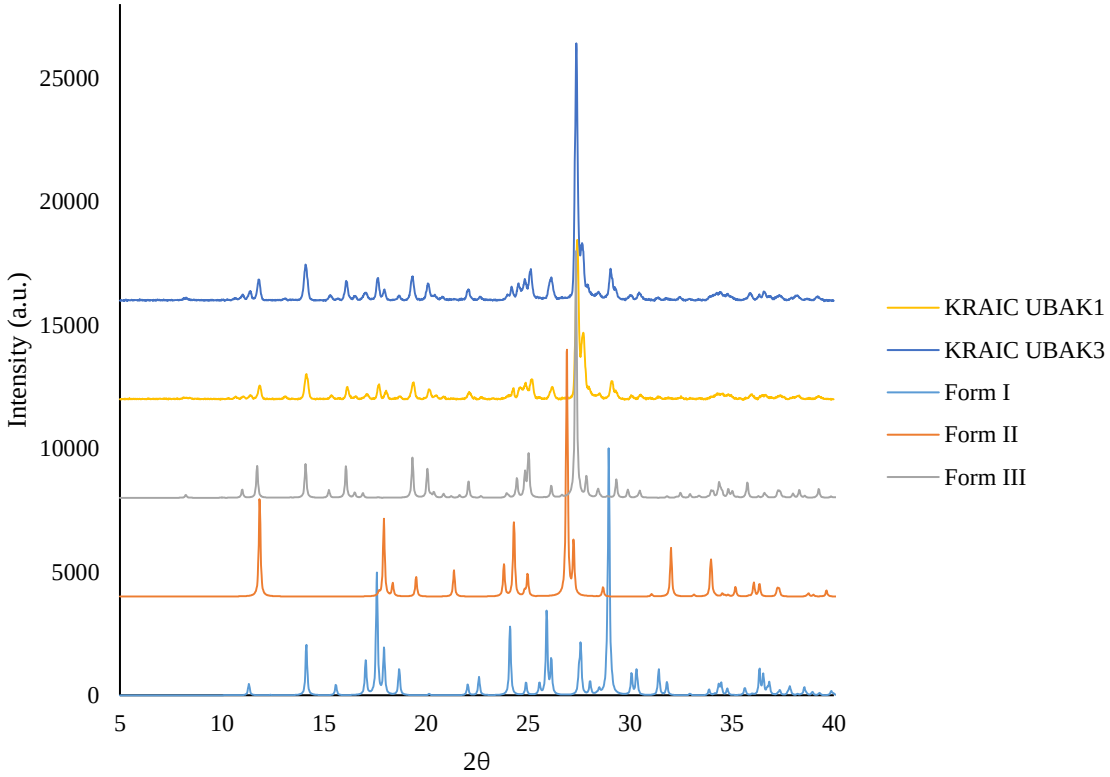

Figure.III.16 PXRD of UBA produced in the KRAIC with PXRD of simulated Form I (EFOZAB),II (EFOZAB01) and III (EFOZAB02)

Successful production of UBA in the KRAIC can be seen from the PXRD pattern of the samples; UBA form I and Form II were present as can be seen in Figure.III.16. This suggest that during the crystallization both polymorphs of UBA are formed. Using the new end piece showed improvement in the crystals formed and in carrier fluid recovery. The recycled Galden was able to be kept at a steady level during long runs which avoided the necessity of manual filling and reduced unnecessary waste. The filtration system also was better, no blockage was present during the experiment at the end piece. Liquid-liquid-air segmentation gives the possibility to have better slug management, the slug size was more homogeneous along the tubing. Using the gear pump also improved the slugs formation compared to use of the peristaltic pump due to the reduction in pulsation, the presence of which disrupts the flow at the mixer piece and created longer slugs. The combination of slugs due

to elevation of tubing between coils was also avoided with the presence of air slugs between each of them. Compared to PMSMPR UBA crystallisation studies by Powell *et al.*, [86] the yield of UBA recovered here was low, between 35.6 and 47.1% compared to the 66 to 92 % yield in the PMSMPR work. Both UBA I and III were present in the end product but not UBA II, in agreement with the PMSMPR studies, with form III being prevalent.

To assess the polymorphic evolution of UBA during the crystallisation, a method using a variation of the KRAIC at Diamond Light Source will be presented in Chapter IV.

III.2.1.iv Gelation in flow for potential hosting

One route of interest to the Metastable Materials (M4) project group is the possibility of using gels as responsive host materials. Being able to include a metastable compound inside a gel could be a way to trap a switching material without preventing its ability to switch; the functional switching is not impeded but some of its characteristics may change and the switching material may also be rendered chemically or physically more stable, for example. In some cases, the gel material can keep the ability of a metastable material to switch by creating vesicles with the metastable material hosted inside. This method is currently used for a wide range of guests such as phase change materials and living cell encapsulation [169,170]. Those materials can keep their properties while being in a gel; the advantage of this technique is that some stimuli can be enhanced or suppressed depending on the gel which could lead to selectivity among the stimuli. In collaboration with Dr Gareth Lloyd at Heriot Watt University the segmented flow KRAIC has been used to create large-scale gel slugs. This investigation was also used to show the ability of the re-configuration of the KRAIC to produce distinct shapes of gels by control of the slug characteristics through choice of flow parameters.

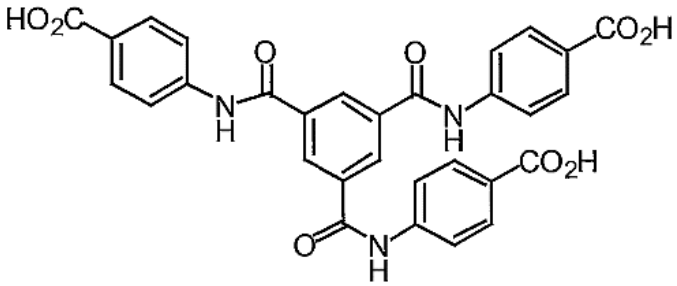

Figure.III.17 4-[[3,5-bis[(4- carboxyphenyl)carbamoyl] benzozoyl]amino]benzoate (BTA) gelator used for the gelation.

4-[[3,5-bis[(4-carboxyphenyl)carbamoyl]benzozoyl]amino]benzoate sodium salt (BTA, Figure.III.17) is a gelator which forms a gel with both a decrease in pH and relatively high temperatures. Glucono-delta-lactone (GdL) hydrolyses in solution with a reaction rate proportional to the temperature, by keeping this solution in an ice bath and an elevated temperature throughout the KRAIC the pH of the crystalliser can be changed over a length scale without the need for multiple injection points. Both 1 and 2 wt% gels were successfully synthesised in the KRAIC by combining the two flows of gelator and GdL and separating with the carrier fluid in a 1 mm ID PEEK (polyether ether ketone) cross-piece (net flow = 10.4 ml/min, R_T = 15 min 30 s). This cross-piece was used as the small bore resulted in highly uniform slugs and, due to the gelation being induced by a change of pH and temperature, the compound was not able to block the cross–piece (unlike in the crystallisation examples above). It was also easier to connect with the pumps used.

Table.III.5 Parameters used for the gelation inside the KRAIC

Experiments	[BTA] (g/ml)	[GDL] (g/mL)	RT	Flow Rate Solution (mL/min)	Flow rate Galden (mL/min)	wt% Gel
GK1	0.02	0.08	15 min 32 s	2.1	6.3	2
GK2	0.01	0.08	15 min 30 s	2.1	6.3	1
GK3	0.02	0.08	15 min 23 s	2.1	6.3	2

Table.III.6 Temperatures used for the gelation inside the KRAIC

	Temperature in Coil (°C)			Feed temperature	Temperature of Water Bath	Temperature of Jacketed tubing
	1	**2**	**3**			
GK1	70	45	45	40	40	0
GK2	70	50	45	40	40	0
GK3	90	65	55	40	40	0

For these experiments the coils were heated to 70 °C for coil 1 and 45 °C for coil 2 and 3. The increase of temperature at the beginning aims to induce the gelation (the first coil was put around a glass dish and coils 2 and 3 in stainless steel cylinders with controllable temperature), Figure.III.18. The feed vessels were cooled to 0 °C in an ice bath in order to avoid gelation before the segmentation could be established and jacketed tubing at 0 °C was used to transport the feed to the PEEK mixer piece, Figure.III.18.

Figure.III.18 Mixer piece modified to create segmented flow.

At the end of the final coil a separating funnel was put in place in order to recover the gel vesicles, filled with dilute HCl to stabilize the gelation process and keep the gelated slugs intact. Gentle mixing was achieved by employing a diffuse air inlet, thus ensuring stability of the gels and preventing cohesion. The carrier could be retrieved from the bottom of the flask in order to create a loop and avoid waste, Figure.III.19.

Figure.III.19 Recovering system of the Galden carrier fluid is at the bottom of the flask.

For experiments GK1, 2 and 3, the gel formation was successful and no issues were reported during the runs. The GK1 run showed good consistency and slug formed did not collapse, it was then decided to reduce the wt% of gel from 2 to 1 wt% to see if the slugs were still not collapsing. The gelated slugs were recovered and for both 1 wt% and 2 wt% had good consistency and were stable enough to be picked out of the feed vessel easily as shown in Figure.III.20. This technique would be beneficial to host materials in continuous system for scale-up of smart encapsulated switching elements.

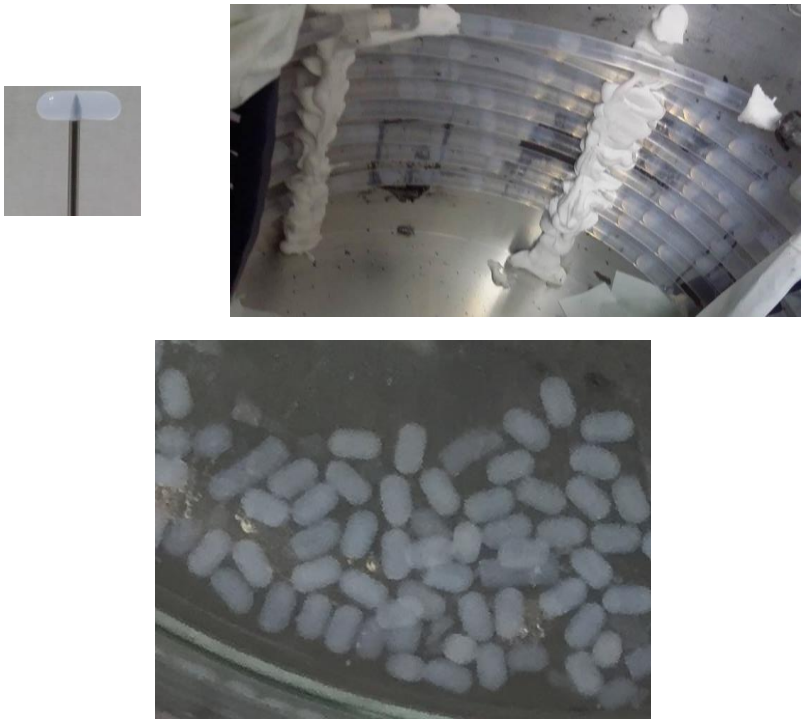

Figure.III.20 (top left) Gel lozenge obtained in the KRAIC from 1 wt% solution run, (top right) almost spherical gel capsules from 2 wt% solution run and (bottom) gelated slugs in a petri dish.

With the capability of the KRAIC to form gels proven, it was decided to use this technique as a potential solution to host crystals into a gel.

Vanillin was chosen as a target system which could crystallise under similar experimental conditions and duration as the previously achieved gelation [77,171]. The temperatures were accordingly reduced in the second and third coil to induce the crystallization inside the gels (as shown in Table.III.7) and Table.III.8 without deteriorating the gels.

Table.III.7 Concentration of BTA, GdL,vanillin and flow parameters used for simultaneous gelation and vanillin crystallisation in the KRAIC

Experiment	[BTA] (g/mL)	[GdL] (g/mL)	RT	Flow Rate Solution (mL/min)	Flow rate Galden (mL/min)	Gel (wt%)	[Vanilin] in GdL (g/mL)
GKV1	0.02	0.08	15 min 32s	2.1	6.3	2	0.005
GKV2	0.01	0.08	15 min 30s	2.1	6.3	1	0.005

Table.III.8 Concentration of Vanillin used inside the GDL

Temperature Coil (°C)	1	2	3	Feed temperature	Temperature of Water Bath	Temperature of Jacketed tubing
GKV1,2	70	30	20	40	40	40

The initial experiment with the same concentration of GdL, BTA and vanillin were first carried out in batch, Table.III.5. Vanillin was incorporated into the BTA solution. The solution was put into an ice bath at 0 °C and then heated up at 70°C to induce the gelation. In those batch experiments the gel was less firm than the one obtained from the KRAIC described previously and the colour of the gels changed to a yellow tint. This phenomenon could be due to the environment of the gelation which is not confined in small slugs. The KRAIC runs were carried out with those parameters, the gel colour still changed from the colourless gels shown above to an orange/yellow tint as can be seen on Figure.III.21. This colouration is stronger with 2 wt% of gel which could indicate that the vanillin is reacting with the BTA gelator molecules. Under pure gelation runs the BTA can be recovered by denaturing the gels in a basic solution and then using isopropanol, IPA, (in which GdL is soluble), to precipitate out the BTA. However, during recovery from a run with vanillin the precipitate was orange in colour unlike the white BTA powder and the yield recovered was very low compared to the amount recovered from the gel without vanillin. NMR analysis of the vanillin and gel obtained in the KRAIC GKV1 is shown in the Appendix (**Figure A3.2 and 3**).

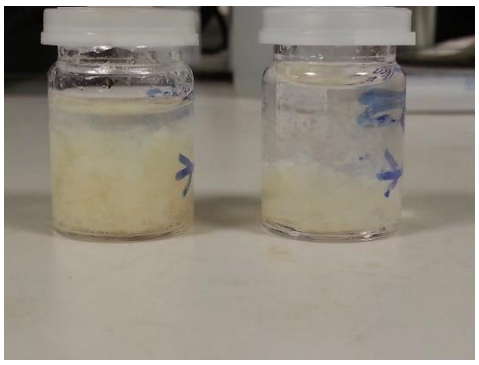

Figure.III.21 Colour of gels with vanillin produced in batch (left) and in the KRAIC (right) at 1 wt%.

Optical microscopy could not clearly identify crystals within the formed gels (Figure.III.22). In some pictures distinct contained regions can be seen among the gels which may be crystals or may be due to imperfections within the gel. The confirmation of the presence of crystals in the gel was not possible due to the trace amounts of candidates present.

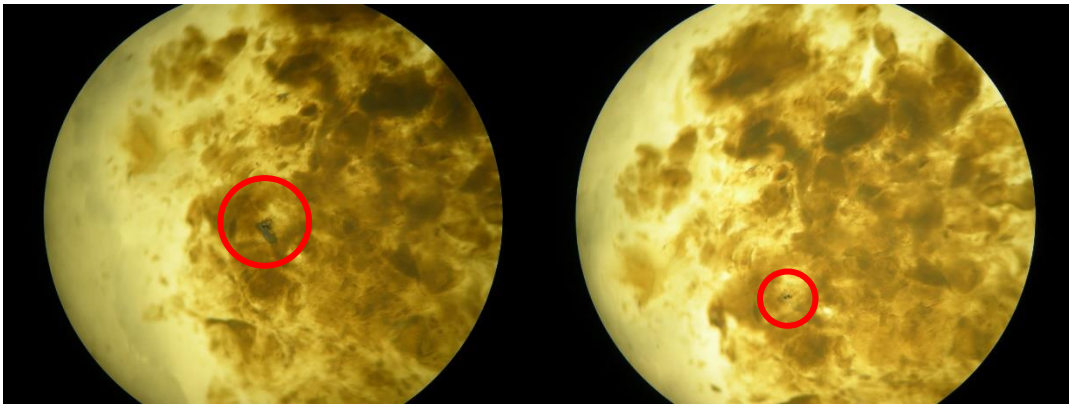

Figure.III.22 Potential vanillin crystal inside gel vesicle

III.2.1.v Conclusion

From crystallisation to gelation the KRAIC has shown its capabilities to produce different types of compounds. Gelation in flow has been of interest in the last decade due to the easier possibility to scale-up the production of certain microgels in the bio-industry.[172,173] In the case observed the control and consistency of the gel slug was easily controlled with the flow rate and temperature. Usually gel production involves extruders or batch synthesis which can lead to consistency problems with slight parameter variations.[173] Using flow synthesis has been shown to induce new properties and the discovery of new hydrogels[174]. The use of segmented flow for gelation has been reported but at a microfluidic scale for the synthesis of microgel droplets. In Chang *et al.*[175] yeastosomes have been produced using a microfluidic chip to form slugs where the gelation of microgels occurred, forming a hydrogel-cell. Vitor *et al.* also describe a droplet microfluidic system for gelation of hydrogel to create hosts for *in vivo* cells for better incorporation in patient bodies. These techniques could potentially lead to new way of encapsulating pharmaceutical compounds for better delivery to the patient or as responsive hosts for switching compounds.

The polymorphic crystallisation aspect of UBA will be further discussed in Chapter IV for *in situ* analysis with another KRAIC configuration, the KRAIC-D. The gel formation inside the KRAIC was first investigated for the encapsulation of crystals but in the next part the gelation will be explored for the synthesis of a spin cross-over compound.

III.3. A controlled synthesis of spin cross-over compounds in segmented flow

In the M4 group switchable materials are of substantial interest, and one such material types is the class of spin-crossover compounds (SCOs). Here is studied the synthesis of $[Fe(Htrz)_2(trz)](BF_4)$ (Htrz = 1,2,4-triazole) and $[Fe(Htrz)_3](BF_4)_2 \cdot 6H_2O$ in the KRAIC. This material is a coordination polymer where the Fe^{II} ion undergoes a spin transition when increasing the temperature. This compound was the first reported to have a change in magnetism and thermal hysteresis at the nano-scale.[13,32]

The material is produced by a precipitation reaction in water from combination of aqueous solutions of $FeBF_4 \cdot 6H_2O$ and 1,2,4-H-triazole ($C_2H_3N_3$). By replacing methanol as the solvent, the related complex $[Fe(Htrz)_3](BF_4)_2 \cdot 6H_2O$ can be synthesised. This latter complex has also been studied in the KRAIC as, above a critical concentration, it can produce a gel.[27] This could potentially be used to created gel slugs like those shown in section III.2.1.iv. For clarification, in this chapter the low spin state (as synthesised) of the SCO material $[Fe(Htrz)_2(trz)](BF_4)$ (Htrz = 1,2,4-triazole) will be referred as Pink Compound or PiC due to the compound colour.

III.3.1 Batch Synthesis of $[Fe(Htrz)_2(trz)](BF_4)$

To assess the precipitation reaction in the KRAIC, batch syntheses with different concentrations of reagents and mixing intensities were investigated (stirred and non-stirred). Each experiment was performed in a 10 ml vial by slowly pouring each reagent into the vial simultaneously and either leaving the vials static during reaction or stirring inside the vial with a magnetic bottom stirrer bar. During the synthesis the colour of the solution was observed to change from colourless to cloudy white and then taking a pink colour which is retained by the powder obtained; this was also reported in Krober et al.[4]. The induction time is here termed by the first appearance of the initial colourless precipitate, the change to pink corresponds to what has been termed the onset of growth.

Table.III.9 Batch parameters used with different concentration of reagent for the synthesis of $[Fe(Htrz)_2(trz)](BF_4)$ (Htrz = 1,2,4-triazole)

	Stirring rate (rpm)	$Fe(BF_4)_2$ $6H_2O$ solution		Htrz solution		Induction time (min)	Onset of growth (min)	Yield from $[Fe(BF_4)_2]$ (%)
		Mass (g)	Volume (ml)	Mass (g)	Volume (ml)			
B1	0	0.165	2	0.173	2	18:20	41:21	45.2
B2	250	0.165	2	0.173	2	15:12	33:43	46.1
B3	0	0.040	2.5	0.040	5	20:25	36:36	20.3
B4	250	0.040	2.5	0.040	5	14:35	31:15	22.3
B5	250	0.124	2	0.125	4	10:45	27:39	15.7
B6	0	0.050	5	0.049	10	41:23	65:14	42.6
B7	0	0.050	2	0.049	6	29:38	53:11	51.6
B8	0	0.055	1	0.084	1	22:05	56:06	32.5
B9	250	0.055	1	0.084	1	18:09	48:48	33.2

As can be seen in Table.III.9, using different concentrations and static or stirred solutions affects the induction time and onset of growth of PiC. The induction time varies between 15 and 41 min, it seems that the compound formation strongly depends on the concentration although the presence of stirring plays a role also. For instance, in experiment 6 the induction time is very long at 41 min while by increasing the concentration by 60 % for iron and 40 % for Trz for experiment 7 both induction time and onset of growth are reduced by 11 min, showing the importance of concentration on induction time and onset of growth. The yield is also increased by 9 % between experiments B6 and 7. Stirring experiments B1,2 and 3,4 reduce the induction time and onset of growth by 3-6 min depending on the experimental parameters, the concentration in particular. When the concentration is high and mixing is present more reagent enters in contact faster which leads to lower induction time than found when no mixing is present. The mixing has no statistical effect on the yield. Using flow synthesis for this compound could help to have a more controlled environment for the reaction which would give more control over the onset of growth of PiC

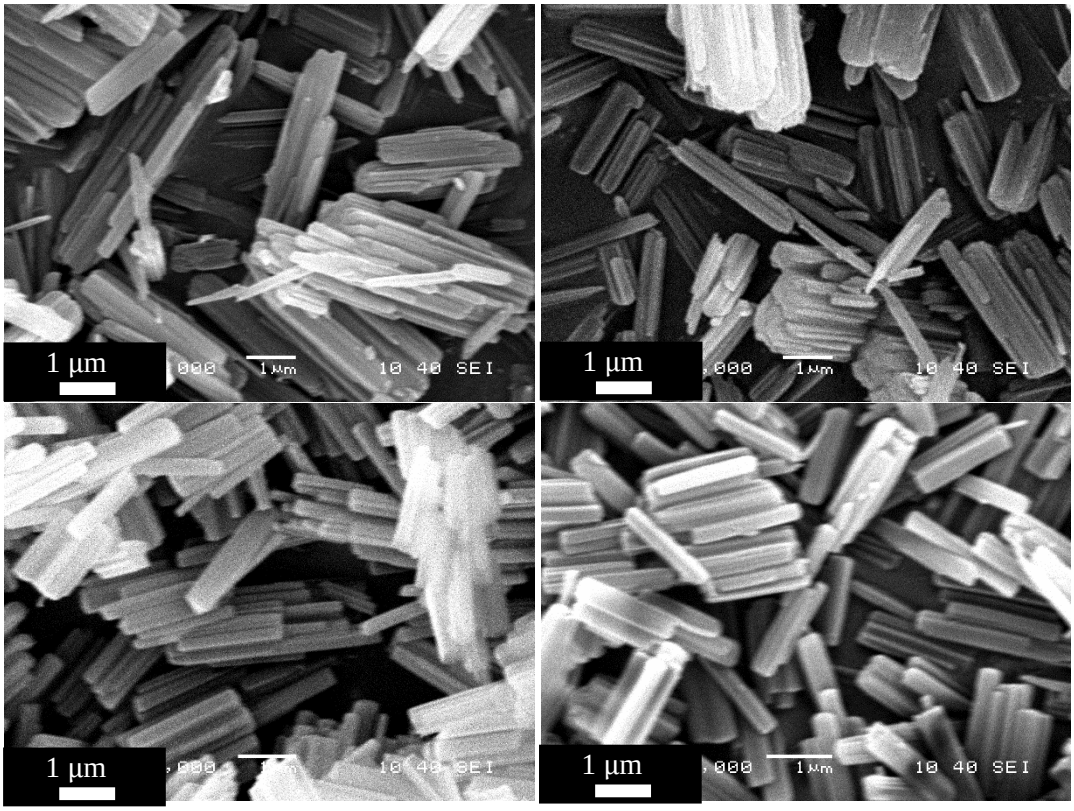

Figure.III.23 SEM of product from experiments B1, 2 (top left and right), 3 and 4 (bottom left and right) for PiC synthesis in batch

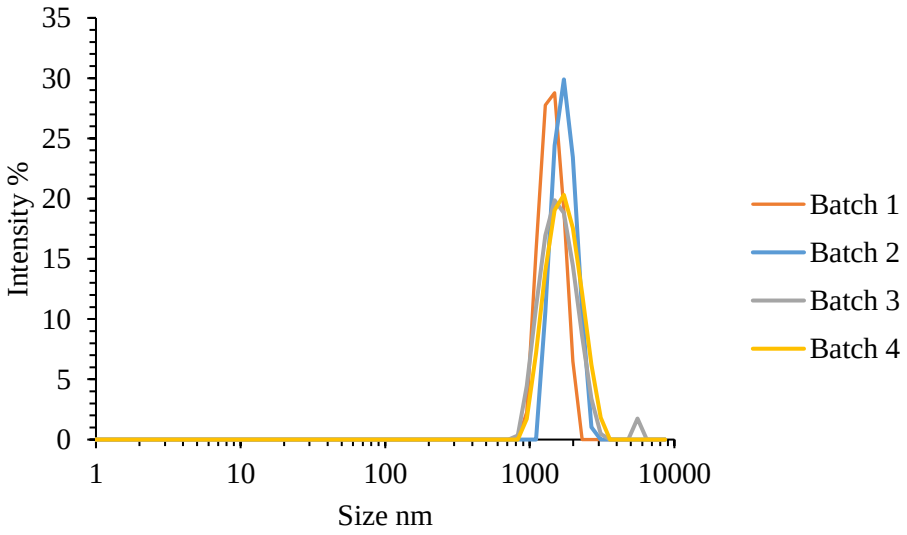

Figure.III.24 DLS results from experiments B1, 2, 3 and 4 for PiC synthesis in batch.

As can be seen from Figure.III.23 and Figure.III.24, the rod-like shaped particles reported in the literature are obtained through this preparation; the rod shape is usually obtained using reverse micelle technique in batch.[11]

SEM analysis of several experiments confirms the rod-like shaped crystals are present here as described in previous literature [13,40] with sizes between 1000 and 1200 nm and agglomerations which can exceed 5 μm. DLS analysis confirms this behaviour with particles ranging from 800 nm to 3000 nm (Figure.III.24) for each batch synthesis, suggesting a low control over particle size in batch environment. The DLS results suggest there is limited impact of the mixing on the particle size distribution, other than an increase in size of ~100 nm when stirring is present, which suggests a faster growth of the material due to stirring. The concentration reduction from the comparison of experiments 1 to 4 did not show any pattern in particle size change. As the induction time and onset of growth are quite high in batch, the particles have more time to react further thus grow large particles; using flow synthesis could avoid this problem.

PXRD confirmed the desired compound was obtained during these experiments, Figure.III.25.

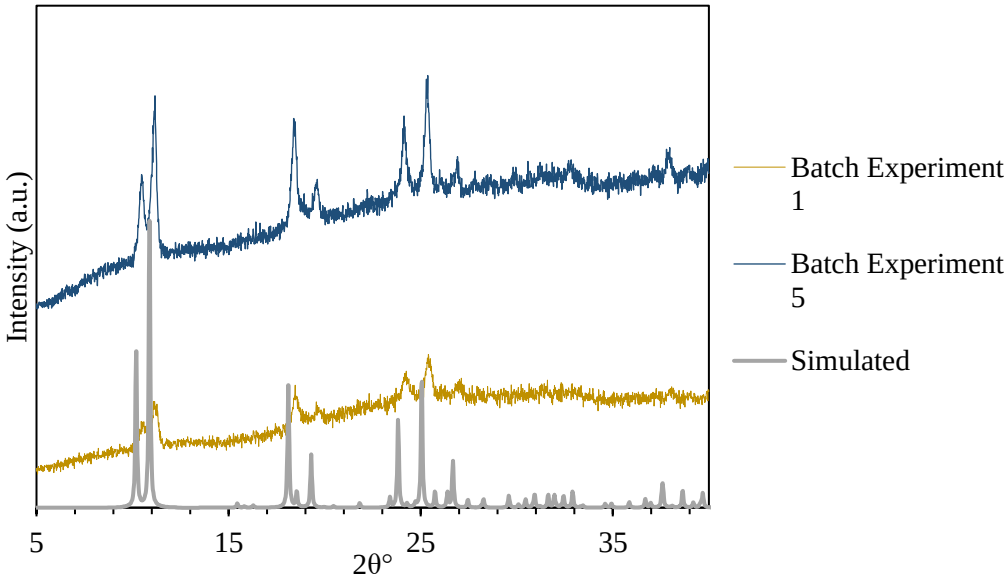

Figure.III.25 PXRD of SCO compound obtained in batch for experiments B1 and 5 (for full comparison see Appendix (**Figure A3.1**).

These investigations of the batch synthesis of $[Fe(Htrz)_2(trz)](BF_4)$ provided important information in designing the subsequent flow experiments. Looking to improve control over particle size and shape will be one of the main focus in flow reactors to see if this affects the switching properties of the SCO material. The compound also displays an unknown intermediary white phase during the reaction which could potentially be the high spin state (HS) state of the material or a reaction intermediate; the KRAIC studies discussed below also form preliminary studies for *in situ* analysis of this phase reported in Chapter IV. The parameters in Table.III.9 will be used as the main comparison with other reactors presented in this thesis.

III.3.2 Synthesis of $[Fe(Htrz)_2(trz)](BF_4)$ with the KRAIC

As shown above, the synthesis of $[Fe(Htrz)_2(trz)](BF_4)$ in batch gave the expected rod particles but instead of the nanoscale expected, micro-sized particles were obtained. Here the KRAIC is used to synthesise the PiC with the concentration range as used in batch. The KRAIC set-up used is displayed in Figure.III.26.

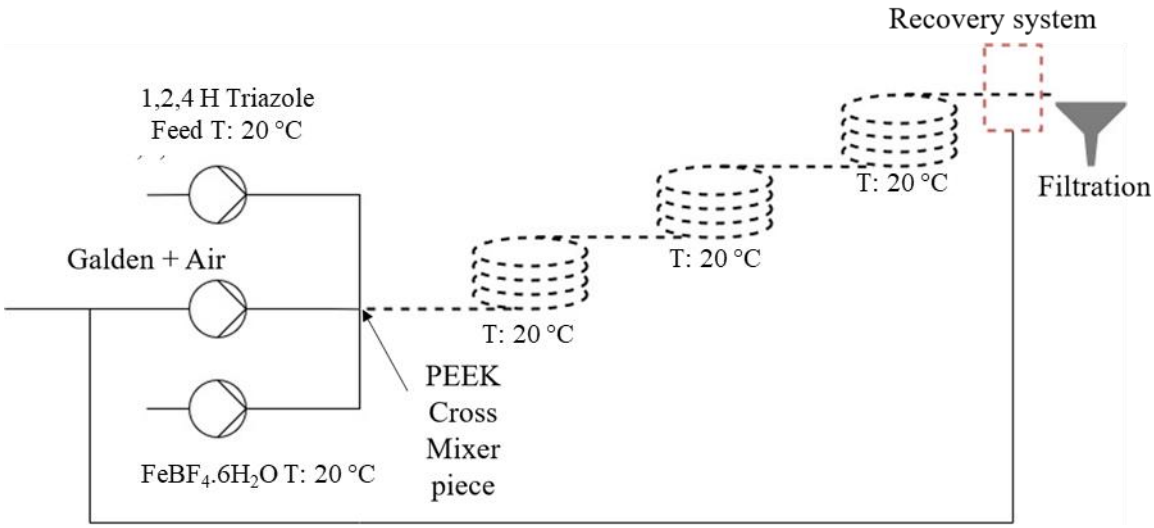

Figure.III.26 Scheme of the KRAIC configuration for $[Fe(Htrz)_2(trz)](BF_4)$ synthesis.

The configuration of the KRAIC used in these experiments is similar to that used in the UBA crystallisation except that the neutral solvent is not used as the small particles produced here are not expected to block the reactor. The mixer piece is also different as we are combining two reagents similar to the gelation studies above. The mixer piece used was a PEEK cross piece of 1 mm ID as shown on Figure.III.27. The whole experiment is performed at room temperature.

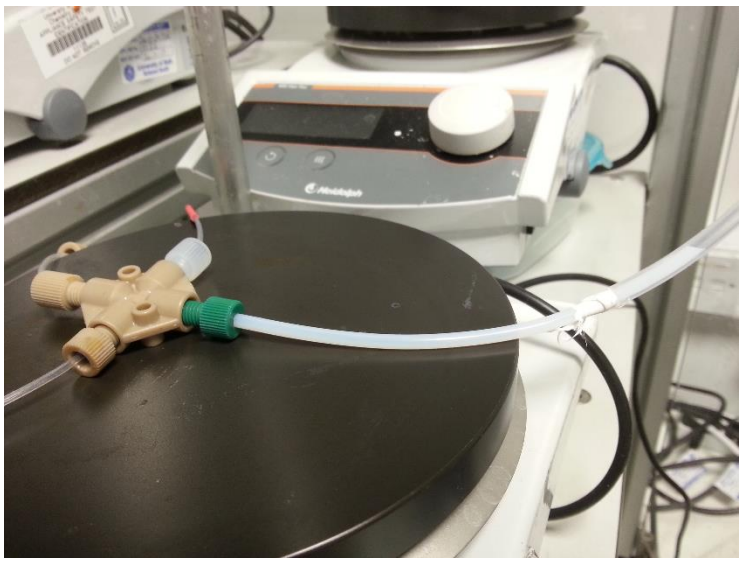

Figure.III.27 Mixer piece used for the synthesis of $[Fe(Htrz)_2(trz)](BF_4)$ in the KRAIC.

The experimental parameters used for $[Fe(Htrz)_2(trz)](BF_4)$ synthesis in the KRAIC are displayed in Table.III.10 and Table.III.12. In all experiments the flow rate of each reagent was 2.1 mL/min.

Table.III.10 KRAIC synthesis parameters for $[Fe(Htrz)_2(trz)](BF_4)$ ‡ + indicates recovery issues resulted in a lower yield recovery than actual

Batch Synthesis correspondence		$[Fe(BF_4)_2 6H_2O]$ (g/mL)	[HTrz] (g/mL)	Galden/Air Flow Rate (mL/min)	Solution Flow rate (mL/min)	Yield from $[Fe(BF_4)_2 6H_2O]$(%)
B1	**K1**	0.0827	0.0866	6.3	4.2	21.3+
B3	**K3**	0.0162	0.008	6.3	4.2	N/A
B5	**K5**	0.0624	0.0312	6.3	4.2	15.2+
B6	**K6**	0.0101	0.0049	6.3	4.2	N/A
B7	**K7**	0.0253	0.0082	6.3	4.2	19.6+
B8	**K8**	0.055	0.084	6.3	4.2	12.3+

Table.III.11 Stochiometric ratio of $Fe(BF_4)_2$ 6H2O /HTrz

	$[Fe(BF_4)_2 6H_2O]$ (mmol/mL)	[HTrz] (mmol/mL)	Stochiometric Ratio $Fe(BF_4)_2$ 6H2O /HTrz
K1	0.25	1.25	1/5
K3	0.05	0.12	2/5
K5	0.18	0.45	2/5
K6	0.03	0.07	3/7
K7	0.07	0.12	5/8
K8	0.16	1.22	1/7

Table.III.12 $[Fe(Htrz)_2(trz)](BF_4)$ synthesis in the KRAIC induction and onset of growth observations.

	Induction time (min)				Onset of growth			
	initial		final		KRAIC (initial) with distance cm ±5 cm		KRAIC (final) with distance cm ±5 cm	
	(min)	(cm)	min	cm	min	cm	min	cm
K1	11:20	842	9:11	871	21:23	1210	9:05	1089
K3	16:43	1224	13:05	1230	N/A	N/A	N/A	N/A
K5	9:53	688	7:12	620	15:36	870	8:40	953
K6	19:12	1452	15:42	1406	N/A	N/A	N/A	N/A
K7	16:04	1196	13:03	1218	23:53	1311	N/A	N/A
K8	12:33	865	8:35	750	20:45	1174	10:29	1220

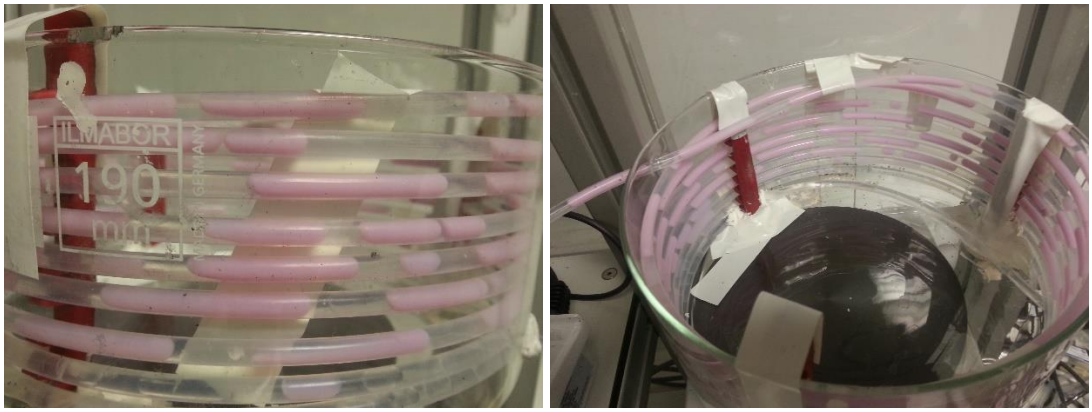

Figure.III.28 Slugs of SCO compound formed in the KRAIC for experiment K5.

Depending on the experiment carried out, different induction and onset of growth times have been measured as well as the distance from the mixer piece of first appearance of product. Displayed in Table.III.10 and Table.III.12 are the results from different experiments using the same concentrations as those previously studied in batch. N/A value indicates that no onset of growth was observed. Despite the same flow rate parameters being used, after several repeat experiments (in experiment 8 in particular) the slug size increases in size as displayed Figure.III.28; this could be due to inconsistent air delivery through a dual purpose air/Galden pump disrupting the flow. From these experiments, it can be seen that the concentration has an important effect on where the compound starts to appear. At high concentration for both reagents the compound appears in the first coil (experiment K5, Figure.III.28); the white cloudy phase appears at 688 cm of the KRAIC first coil and is pink at 953 cm which is mid-1st coil. When using a lower mid-range concentration, as in experiments K1 and 8, the appearance is more gradual with induction times of 11:20 min and 12 min 33 s at 842 cm and 865 cm, respectively, starting to appear before the end of the first coil and then having a pink conversion at the beginning of the third coil at 21 min 23 s and 20 min 45 s for 1210 and 1174 cm distances. At low concentration of reagents, the compound only starts to appear in the initial white cloudy phase in the beginning in the first coil (K3,7) or at the end of the KRAIC (K6). In those cases the reaction does not begin the onset of growth phase before the end of the reactor, suggesting it needs more time to form $[Fe(Htrz)_2(trz)](BF_4)$ completely.

Compared to batch, the induction times and onset of growth are faster, 3-15 min reduction for the induction time and 18- 46 min for the onset of growth of the experiments carried out as displayed in Table.III.13. This reduction shows the advantages of carrying out the synthesis within slugs formed in a confined environment. This is presumably due to the better mass transfer inside each slug of the KRAIC in comparison to the stirred vials. Materials from these runs were recovered using a 0.45 μm pore cellulose filter.

Table.III.13 Time reduction for PiC synthesis using the KRAIC compared to batch

	Batch		KRAIC		Reduction of time	
Experiment	**Induction time min**	**Onset of growth**	**Induction time final**	**Onset of growth final**	**Induction Time**	**Onset of growth**
B/K1	18:20	41:21	09:11	09:05	9:09	32:16
B/K3	20:25	36:36	13:05	12:23	7:20	24:13
B/K5	10:45	27:39	07:12	08:40	3:33	18:59
B/K6	41:23	65:14	15:42	19:24	26:19	46:10
B/K7	29:38	53:11	13:03	17:14	16:35	35:57
B/K8	22:05	56:06	08:35	10:29	14:30	45:37

During the runs no blockages or sedimentation were observed, however a small portion of the Galden was not recovered and thus was captured in the Buchner vessel. The fluoro polymer was not able to pass through the 0.45 µm pores and due to its density, it prevented access of the lower density product solution to the filter, making the filtration difficult for some runs.

The flow experiments showed lower yields than batch experiments even at high concentration. In Table.III.10 the + sign indicates that the yield is possibly higher than the estimated value quoted due to these recovery issues.

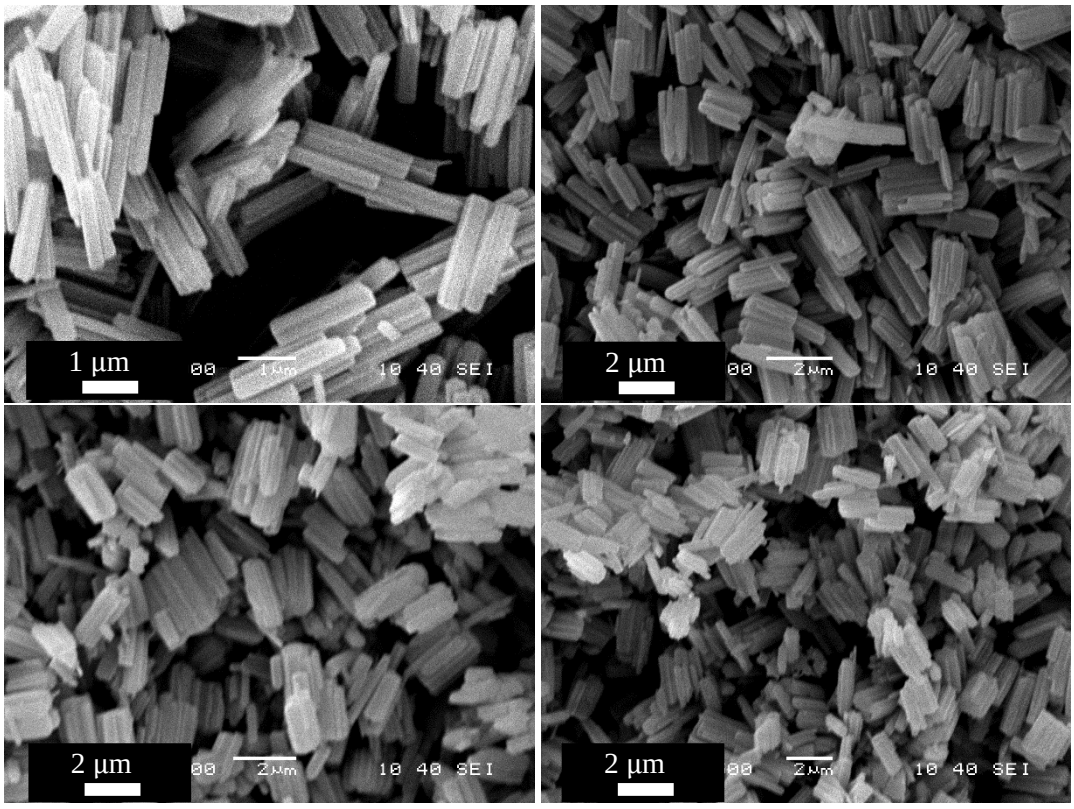

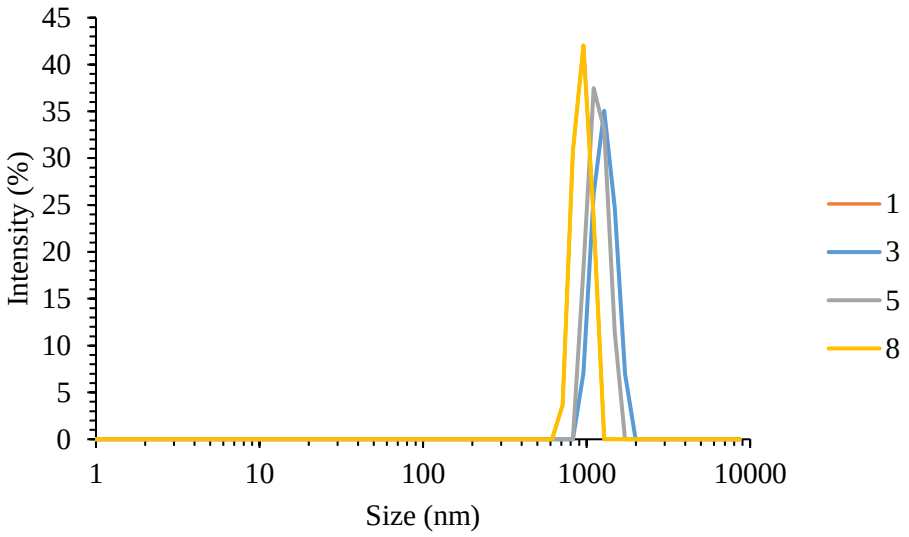

Figure.III.29 SEM of experiments K1, 3, 5 and 8 (top) with corresponding particle size distribution (PSD) from DLS (bottom).

Figure.III.29 shows the SEM of products from experiments K1,3,5 and 8 with the corresponding DLS PSD. The rod-like shaped particles are still present, like in batch produced samples. The PSD is narrower compared to that obtained in batch with particles ranging from 600 nm to 1900 nm. This shows the capability of the KRAIC to obtain smaller particles depending on the configuration used. PXRD analysis confirms that $[Fe(Htrz)_2(trz)](BF_4)$ was again obtained here (Figure.III.29).

III.3.3 Synthesis of $[Fe(Htrz)_3](BF_4)_2{\cdot}H_2O$ in Methanol

It was shown above that it was possible to achieve gelation inside the KRAIC. The combination of $Fe(BF_4)$ and Trz in methanol (as opposed to aqueous solution) has been shown to result in a different complex from the $[Fe(Htrz)_2(trz)](BF_4)$ discussed so far in this chapter, $[Fe(Htrz)_3](BF_4)_2{\cdot}H_2O$ (PiCM).[4] The reaction in Krober *et al.* 1994 uses the same experimental parameters as those used to obtain $[Fe(Htrz)_2(trz)](BF_4)$ (except the substitution of methanol for water), although the compound obtained at the end is $[Fe(Htrz)_3](BF_4)_2{\cdot}H_2O$ and a violet/dark purple colour instead of pink. In Mahfoud *et al.* 2012[27] it is mentioned that using high concentration of reagent to produce $[Fe(Htrz)_3](BF_4)_2{\cdot}H_2O$ can lead to a gel formation which has the same switching properties as the PiC itself. After the success of the gelation within the KRAIC, previously reported in this chapter, it was therefore decided to undertake high concentration runs of $[Fe(Htrz)_3](BF_4)_2{\cdot}H_2O$ synthesis inside the KRAIC. The parameters used are displayed in Table.III.14 and Table.III.16.

Table.III.14 Parameters for synthesis of PiCM in batch

No.	Concentration $[Fe(BF_4)_2\,6H_2O]$ (g/mL)	Concentration [HTrz] (g/mL)
PiCMB1	0.1	0.1
PiCMB2	0.15	0.15
PiCMB3	0.2	0.2

Table.III.15 Stochiometric ratio of [$Fe(BF_4)_2$ $6H_2O$] /[HTrz]

No.	[$Fe(BF_4)_2$ $6H_2O$] mmol/mL	[HTrz] mmol/mL	Stochiometric Ratio [$Fe(BF_4)_2$ $6H_2O$] /[HTrz]
PiCMB1	0.30	1.45	1/5
PiCMB2	0.44	2.17	1/5
PiCMB3	0.59	2.90	1/5

Table.III.16 Parameters for synthesis of PiCM in the KRAIC

No.	Concentration [$Fe(BF_4)_2$ $6H_2O$] (g/mL)	Concentration [HTrz] (g/mL)	Galden Flow Rate (mL/min)	Air Flow Rate (mL/min)	Trz and Iron Flow rate (mL/ min)
PiCMK1	0.1	0.1	2.1	2.1	2.1
PiCMK2	0.15	0.15	2.1	2.1	2.1
PiCMK3	0.2	0.2	2.1	2.1	2.1

Table.III.17 Transition of reaction from white to pink for PiCM synthesis in the KRAIC and in batch

		Time (s)	Distance (cm)
Flow	**PiCMK1**	33	46
	PiCMK2	27	40
	PiCMK3	19	32
Batch	**PiCMB1**	39	N/A
	PiCMB2	31	N/A
	PiCMB3	26	N/A

The parameters in Table.III.14,Table.III.16 and Table.III.17 were also initially tested in batch and the viscosity increased until forming a pink paste for PiCMK1,2 and3. This was then tried in the KRAIC due to the possibility to create viscous slug and perhaps obtain a consistency high enough to have a gel at high concentration allowing the mixing inside the slugs to induce gel formation.

During the experiments the viscosity of the solution changed in the KRAIC, as found in batch, and the pink onset of growth appeared in the first coil after 25 cm inside the KRAIC. This is very fast compared to PiC production in water. The mixing phenomenon inside the slugs could not be seen as the viscosity inhibited the bolus flow; this was observed through the concentration gradient not changing inside the slugs. Compared to PiC, the colour change for PiCM formation was fast, the initial white phase disappeared faster than the water produces PiC compound and the appearance of pink was faster. Using the KRAIC also decreases the time needed for the pink phase to appear compared to batch. The increase of concentration also decreased this time in both batch and in the KRAIC. For instance, for PiCMK1 and PiCBK1 using the KRAIC reduced the time by 6 sec while increasing the concentration between PiCMK1 and 2 decreased the distance by 14 cm (and 14 sec) (Table.III.17). It was reported that in batch without mixing PiCM would form a gel[27] but in the KRAIC a paste was obtained; the non-presence of a gel could be due to the mixing bolus flow present inside the slugs which may inhibit the gel formation in this case.

Figure.III.30 PiCM on the filter, PiCM is produced in methanol, as can be seen the viscosity is higher than PiC production.

It was expected that at the end of the KRAIC the solution might form gels like those produced in Mahfoud *et al.*[27] but in this case, the slugs containing PiCM collapsed into a viscous purple paste as seen on Figure.III.30 for PiCMK3. SEM analysis (Figure.III.31) shows a large change in the physical structure of the particles obtained with respect to the $[Fe(Htrz)_2(trz)](BF_4)$ phase obtained in water. The rod-like shapes observed for PiC are completely absent from the samples, instead large blocks were obtained with a pore like surface.

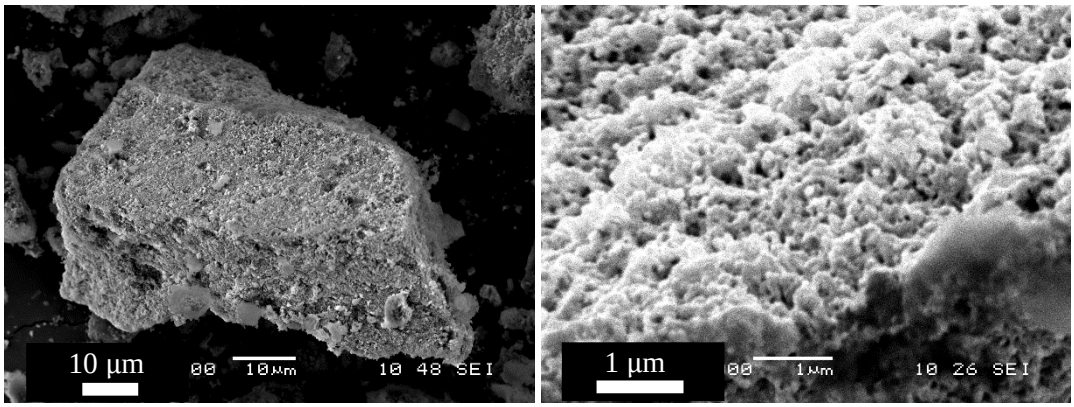

Figure.III.31 SEM of the gels obtained in batch and in the KRAIC for PiCMK 3.

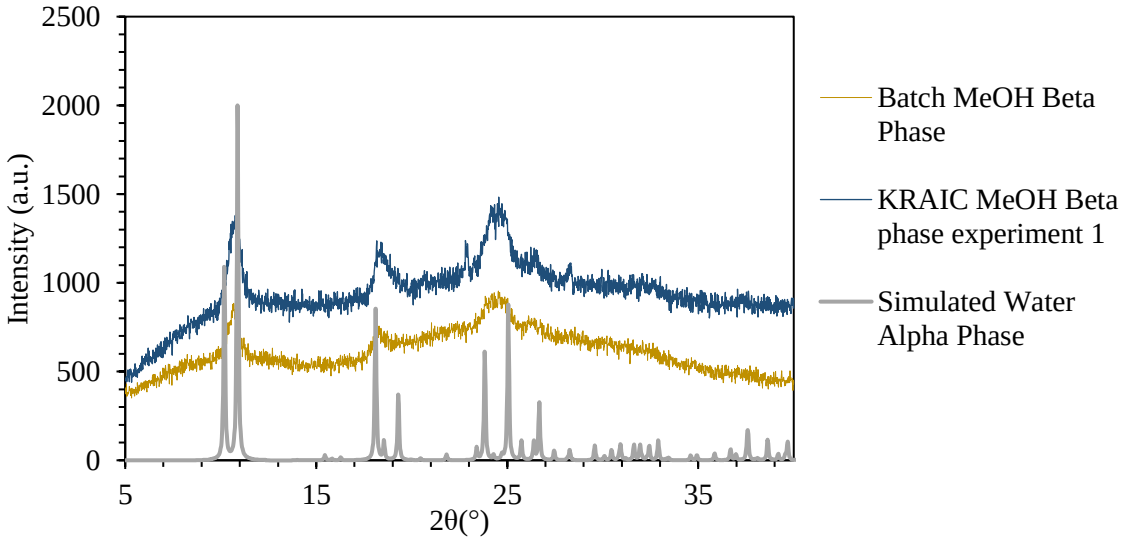

Figure.III.32 Comparison of PXRD analysis from $[Fe(Htrz)_3](BF_4)_2.H_2O$ produced in the KRAIC, batch and simulated.

While it was difficult to compare the PXRD with that from PiC produced in water; it is also reported in Krober et al. 1994 that washing the PiCM with methanol induced a change to the alpha phase. Although very broad, there seems to be some match of the observed peaks with those from the phase obtained in water as shown on Figure.III.32

III.3.4 Conclusion

In this chapter, the KRAIC has been deployed successfully in different configurations to produce crystals, with the crystallisation of SA and UBA; gels, with BTA and GdL; and for the synthesis of the nano-scale compounds $[Fe(Htrz)_2(trz)](BF_4)$ and $[Fe(Htrz)_3](BF_4)_2.H_2O$. The crystallisation of SA and UBA gave good insight in how to improve the KRAIC design to have better continuous crystallisation control. Studying those two crystallisations allowed the KRAIC design to be improved over time and gave better understanding on the slug formations and control. It was discovered that using segmented flow with a carrier fluid could avoid the contact of the solution with a solid interface which could lead to unwanted crystallisation. The air-liquid-liquid segmentation also improved the homogeneity of slug size and avoided the elevation problem with the slugs merging together. With the recovery system implemented for the carrier fluid the KRAIC was able to run continuously without the need to fill the Galden vessel during the experiments. The crystallisation analysis results showed that several polymorphs are present during the crystallisation of those compounds therefore an *in situ* analysis, presented in Chapter IV, will be used to understand the crystallisation process of those APIs.

The synthesis of $[Fe(Htrz)_2(trz)](BF_4)$ (PiC) and $[Fe(Htrz)_3](BF_4)_2.H_2O$ (PiCM) was successfully conducted. Compared to batch production of PiC using segmented flow showed a narrower particle size distribution from DLS, also the induction and onset of growth of the particle were significantly reduced due to the intensity and homogeneity of mixing inside the slugs. This environment is favouring narrower PSD than batch production as observed in Figure.III.24 and Figure.III.29. The use of the KRAIC for PiC showed with ease the change from colourless to white cloudy phase and then pink, this particularity of the transparent tubing could be used for several *in situ* analysis like Raman spectroscopy or *in situ* X-ray diffraction that will be investigated in the next chapter.

The gel synthesis using BTA and GdL showed the possibility to obtain gel slugs that kept their form overtime after production. This technique could be used for encapsulating materials for different purposes from pharmaceutical delivery to switchable devices. Unfortunately, the encapsulation of vanillin was not successful due to unwanted reaction between the reaction components. Further investigation would be needed in that area with other gelators. For PiCM, it was seen that the gel was not obtained in batch or in flow using the KRAIC but a paste was obtained with a change of viscosity during the synthesis. As it was reported in Mahfoud *et al.*[27] that a gel was possible to be obtained, production of this paste might be due to the internal mixing inside the slugs which prevents the formation of the gel. Compared to the conditions that led to improved gel formation in the BTA and GdL experiments, increasing the concentration for the PiCM synthesis might induce the gelation but at the KRAIC scale more reactant would be needed to achieve higher concentrations than previously used (Table.III.16).

III.4. Segmented Flow analysis with CFD

In the present work, a range of different CFD (computational fluid dynamics) simulations have been employed aimed at increasing the efficiency of mixing inside various. flow reactors. In industry, simulation software packages are used to achieve better design and help in the manufacturing of products. This prediction of product behaviour and low-cost testing of innovative concepts and optimisation of designs early in the design and engineering process. It also provides the capability to validate and better understand the implications of design choices before manufacturing. For instance, in Gupta *et al.* two-dimensional, axisymmetric CFD simulations of slug formations were modelled in a small 0.5 mm diameter tube with the VOF (Volume of Fluid) and level-set methods

and different slugs size and shape were obtained depending on the initial parameters like flow rate. This study showed that the initial velocity of the slugs inside the tube controlled their shape and velocity vector inside the slug (bolus flow).[176] In Baten *et al.,* mass transfer inside slug flow was simulated, where the volumetric mass transfer coefficient was calculated and showed that this one was affected by different parameters of the flow such as slug velocity, length of the slug, length of the liquid film between the two phases and the tubing diameter.[177] These types of study show the importance of using CFD to better understand and optimize flow systems.

Analyses were made using the Ansys *Fluent* Software with different UDFs (user defined functions), giving insight into flow behaviour in an initial set of reactor geometries. For segmented flow, a Y-piece mixer inlet and internal diameters the same as those found in the KRAIC were simulated. The choice of the y-piece was to allow comparison to literature results already pursued[176,178,179] and to keep the CFD model simple to avoid high computational needs. The different resultant slug sizes and mixing behaviour within the slugs are presented herein. In these simulations bi-segmentation will be modelled using only water and Galden as fluids.

A 3D model of the Y-piece was created in Autodesk Inventor, whilst a model of the KRAIC and CFD calculations were set-up and performed using Ansys Fluent. The Ansys Fluent CFD package was used to perform the numerical simulations. To define the interface between the carrier fluid and the solution slugs, the multiphase VOF model was used on the different junctions. This model has been applied in various applications that can be found in the Ansys Fluent Theory Guide.[180] The governing equations of the VOF formulations are as follows:

Equation of continuity:

$$\frac{\partial \rho}{\partial t} + \nabla \cdot (\rho \vec{v}) = 0 \tag{17}$$

Equation of momentum conservations:[181]

$$\frac{\partial (\rho \vec{v})}{\partial t} + \nabla \cdot (\rho \vec{v} \vec{v}) = -\nabla p + \nabla \cdot [\mu (\nabla \vec{v} + \nabla \vec{v}^T)] + \rho \vec{g} + \vec{F} \tag{18}$$

With v the velocity vector, ρ the density, μ the dynamic viscosity of the fluid. The pressure is denoted by p and $\vec{F}$ is the surface tension force, t is the time, g the net acceleration and T the temperature.

Volume fraction α equation is then defined as follows:

$$\frac{\partial \alpha}{\partial t} + \vec{v} \cdot \nabla \alpha = 0 \tag{19}$$

Because the pressure along the tube is small the fluid is considered as incompressible. The VOF model has been described by solving continuity equations for volume fraction with a number of phases.[182] The two phases are immiscible reflecting the immiscibility of the carrier fluid (Galden SV70) and the solution. The volume fractions of the component phases L and C are related in equation (20), which defines the density in each cell:

$$\rho = \alpha_L \rho_L + \alpha_C \rho_C, \qquad \mu = \alpha_L \mu_L + \mu_C \alpha_C \tag{20}$$

If the volume fraction, α, of one is tracked, the volume fraction of the other liquid can be computed by 1-α. Simulating the behavior of the flow in VOF calculations is challenging because the equation of motion, equation (18), is dependent on the volume fractions of all phases through ρ and μ. One limitation of the model is that in cases where large velocity differences exist between the phases, the accuracy of the computed data can be affected. Depending on the problem definition, additional scalar equations may be required. One aspect of VOF simulations is that they are computationally expensive.

Table.III.18 Flow parameters used in the CFD simulation for the total flow rate at the outlet

No.	Flow rate (ml/min)	Total Flow rate (m/s)	Inlet 1 Water flow rate (m/s)	Inlet 2 Galden flow rate (m/s)
CFDK1	1	0.020	0.01	0.01
CFDK 2	2	0.041	0.0205	0.0205
CFDK 3	4	0.082	0.041	0.041
CFDK 4	6	0.124	0.062	0.062
CFDK 5	10	0.207	0.1035	0.1035
CFDK 6	20	0.414	0.207	0.207
CFDK 7	50	1.036	0.518	0.518
CFDK 8	2	0.041	0.013	0.027
CFDK 9	2	0.041	0.027	0.013

The corresponding flow parameters for the CFD experiments are displayed in Table.III.18. Each simulation ran 10000 steps of 1 ms with 20 iterations each time step to perform convergence of the model and to avoid reaching the 250 VOF courant number limit.[109] Experiments 3 to 6 span the flow rates used within the KRAIC when operated with a Y-piece mixer.

The flow inside the KRAIC is essentially laminar in the way the slugs are moving inside the tube and go from the inlet to the outlet. Inside the slugs, on the other hand, the bolus flow described previously is considered as turbulent. In the software the transient model is then used to model that turbulence whilst keeping the plug flow behavior of the slugs. The transient model is used due to the presence of a change of magnitude and direction of flow with time inside the slugs. In Ansys Fluent Steady State (SS) or Transient Flow (TF) can be chosen, but in this case, SS would not take account of the time dependent variables (magnitude and direction) that is needed here.[183] Here the surface tension force dominates over the gravitational effect due to the small size of the system studied, while the wall adhesion is also an important parameter in the formation of the slugs and defines the contact angle between the carrier fluid and the wall. In Ansys Fluent, the CSF (Continuum Surface Force) model proposed in Brackbill *et al.*[184] is used to simulate the surface tension between all the interfaces. This model is needed to define the contact angle between the phases and the wall (tube) during the simulation.

The 3D model of the Y piece was implemented into ANSYS *Fluent* and the mesh was created with 44248 nodes and 200372 elements. Simulations were conducted on a Stone© computer with 8 Gb RAM and an i7-4790 CPU. All 4 cores were used during the simulation. The other options selected in *Fluent* were as follows: the PRESTO! (pressure staggering option) scheme for the pressure interpolation, the PISO (pressure-implicit with splitting of operators) scheme for the pressure–velocity coupling, second-order up-wind differencing scheme for the momentum equation, the geometric reconstruction scheme for the interface interpolation, implicit body force treatment for the body force formulation, and Courant number 0.25 for the volume fraction calculation.

For the Galden-water surface contact, an angle of 160° was considered the closest to reality due to the high hydrophobicity of the fluoropolymer of both the carrier fluid (Galden SV70) and FEP tubing.

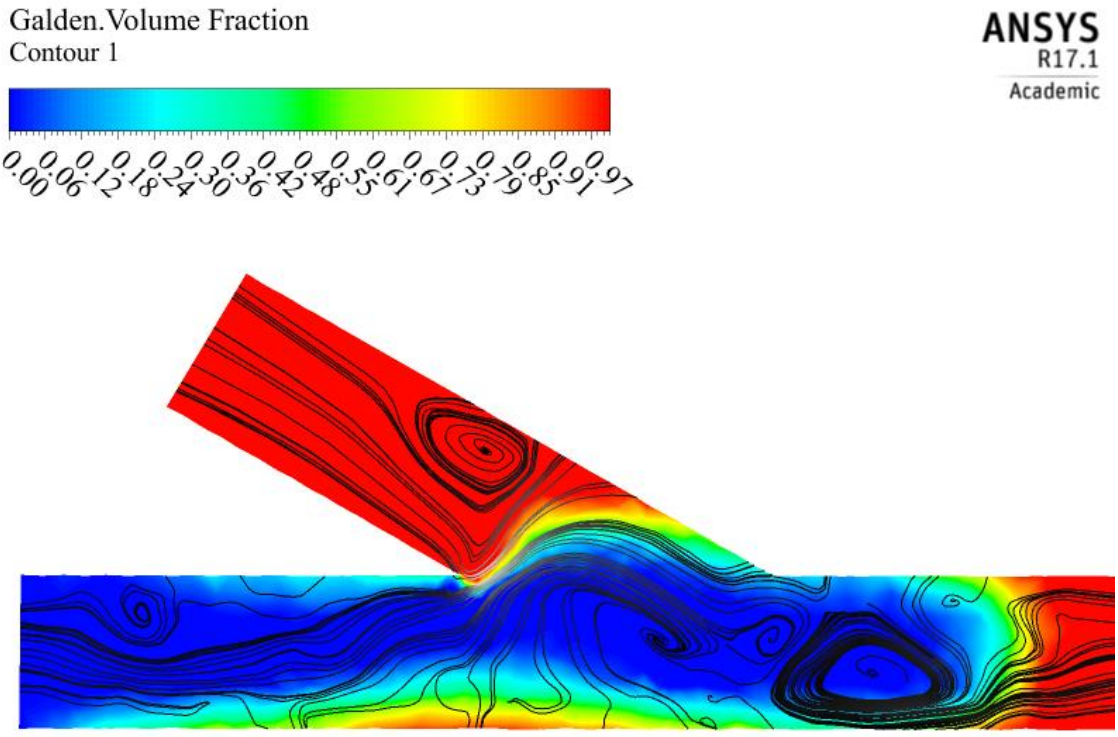

Figure.III.33 Inlet formation of the slugs with the flow streamline: red is Galden, blue is water. Carried out for CFDK 1 with total net flow rate of 1 mL/min.

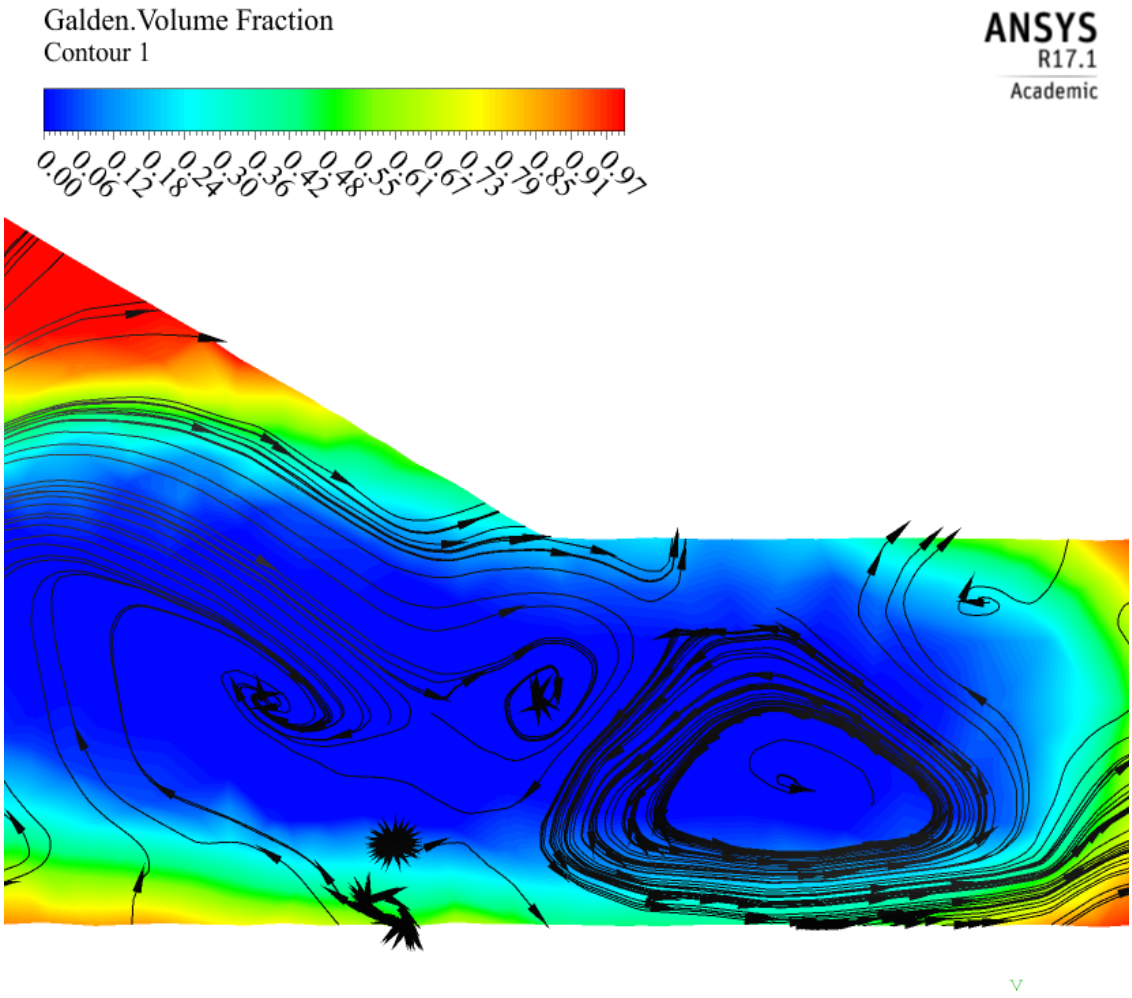

Figure.III.34 Formations of eddies close to the inlet indicating the formation of the bolus flow in each segment for CFDK 1 with 1 mL/min.

The first main information to get out of the simulation is the formation of the slugs at the Y piece. As the two phases are immiscible and the Galden wets the wall of the tubing, the water is rebounded at the Galden inlet both from the stream of Galden and the opposing wall, as shown in Figure.III.33 and Figure.III.34. The streamlines show eddies being formed at the interface between both fluids.

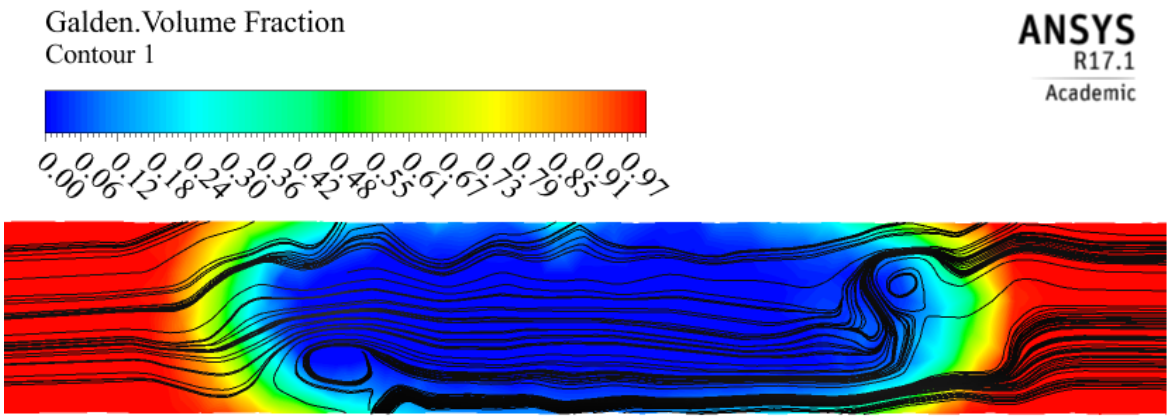

Figure.III.35 First slug showing the streamline forming the bolus flow at the corner of the slug for CFDK 11 with total net flow rate of 1 mL/min at a distance of 0.8 cm from the mixer piece.

This behaviour of eddies continues throughout the reactor due to the inertial forces of the induced total net flow rate of the carrier fluid behind the solution slugs and the boundary between the phases). In Figure.III.35 mixing eddies are observed within the slug at both ends; every simulated slug has eddies forming as can be seen in Figure.III.36.

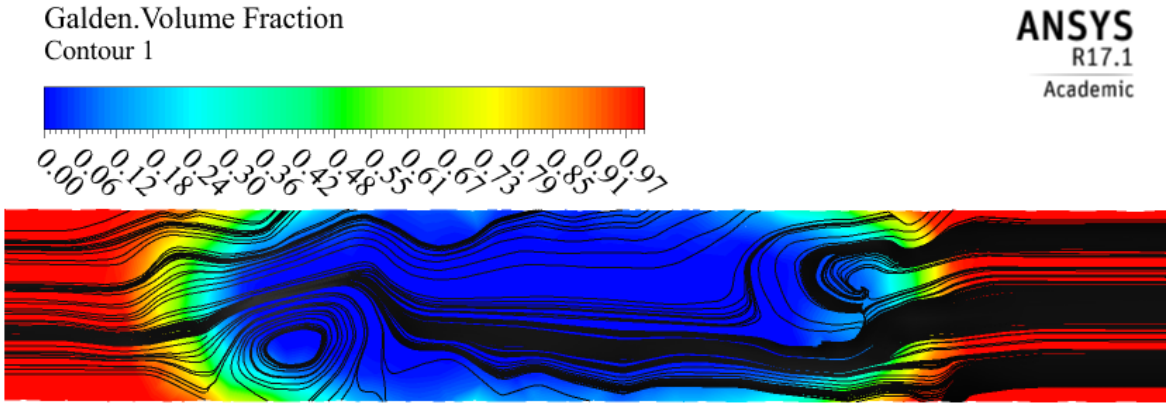

Figure.III.36 Second slug showing the streamline forming for the CFDK 1 for a total net flow rate of 1 mL/min at a distance of 3.1 cm from the mixer piece.

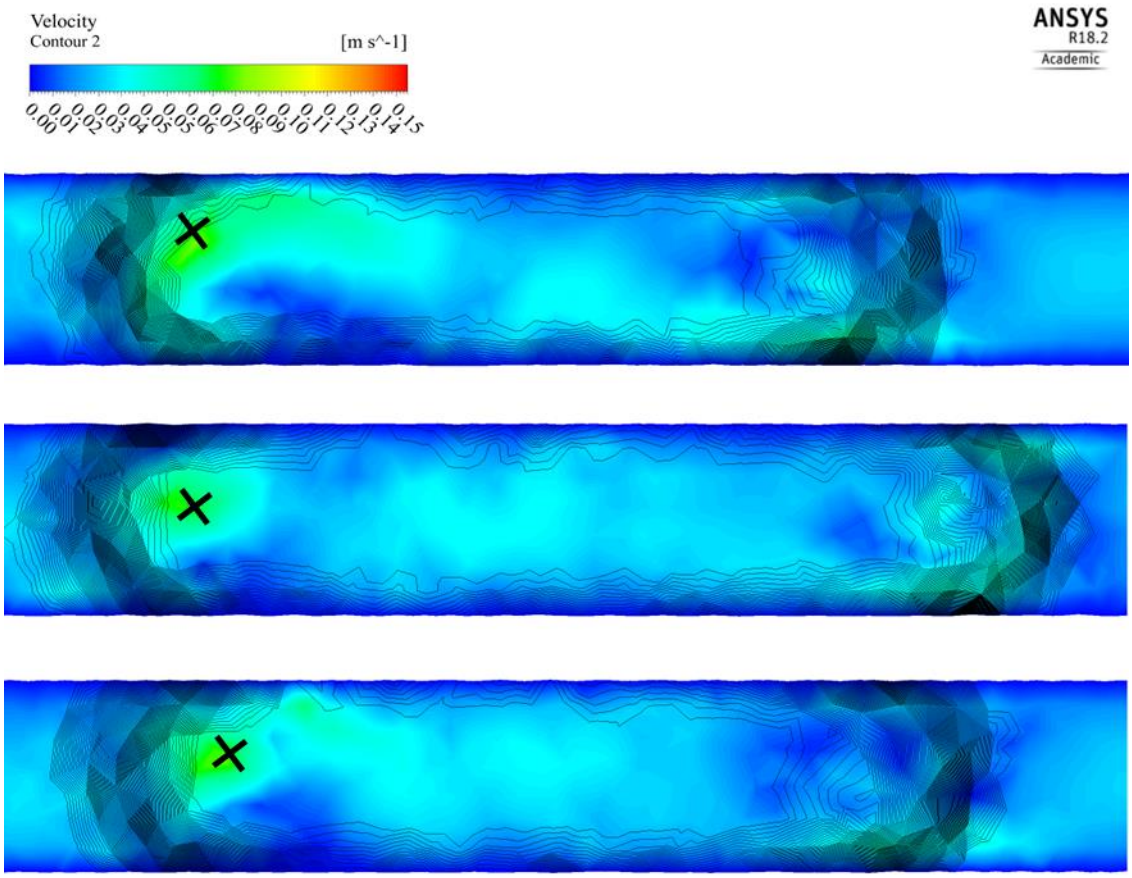

Figure.III.37 Mixing velocity in different slugs for CFD K 1 – the separation of both phases is represented in black, inside the slugs is water and outside the Galden carrier fluid. Between first (top) slugs and second (middle) slugs a 0.5 s time period is present, while between second and third (bottom) this is 0.55 s.

As can be seen from Figure.III.37, where the velocity contours are displayed overlaying the phase boundaries, the velocity is more turbulent inside the slugs than outside, complementing the results of the streamline experiments above. The velocity vectors for the continuous phase are more laminar going in the direction of the flow from the mixer piece to the outlet. Comparing experiment 1 and 4 for instance, inside the slugs at different inlet flow rates, the maximum velocity varies between 0.0739 m/s (CFDK 1, min 0.0223 m/s) to 0.158 m/s (CFDK 4, min 0.0105 m/s) but the continuous phase does not exceed the total flow rate. Changing the flow rate changes the top velocity reached by the eddies, for CFDK 1 the top velocity is 0.0768 m/s in the first slug and for CFDK 2 the top velocity in the first slug is 0.1053 m/s. For CFDK 1 from first slugs to third the maximum velocities stay close to the same value (1st 0.0768 m/s, 2nd 0.0792 m/s and 3rd 0.0772 m/s), this could potentially show that the homogeneity of the mixing is kept in each of the slugs with the bolus flow. For CFDK 2 the same behaviour is observed, with 1st slug maximum velocity at 0.1053 m/s, 2nd 0.1026 m/s and 3rd 0.01075 m/s. Other velocity differences are displayed in Table.III.19 and were obtained by Ansys CFX post process software to determine the highest velocity in the area of the slugs; in Figure.III.37 the point of highest velocity is displayed as a cross on the slugs.

Table.III.19 Velocities inside the slugs for different inlet flow rate. * No slug formation presents in these cases due to the high flow rate forming annular flow.

Exp	Total Flow rate m/s	Ratio of water:Galden flow rate	Highest velocity inside the slug m/s	% increase in velocity inside slug (m/s)	Comment	Slug length (cm)
CFDK 1	0.020	1:1	0.0739	270		1.2
CFDK 2	0.041	1:1	0.1053	157		0.9
CFDK 3	0.082	1:1	0.1152	40		0.7
CFDK 4	0.124	1:1	0.15878	28		0.5
CFDK 5	0.207	1:1	0.2349	13		/*
CFDK 6	0.414	1:1	0.401	-3	Annular flow	/*
CFDK 7	1.036	1:1	1.021	-1	Annular flow	/*
CFDK 8	0.041	1 :2	0.1012	147	measurement on the water slug	0.7
CFDK 9	0.041	2 :1	0.1076	162	measurement on the water slug	0.9

The different flow rates used show that using a higher net flow rate increases the velocity inside the slugs. However, the relative velocity increases, with respect to that of the continuous phase, is significantly higher for slow flow rates (270 and 157% increase in CFDK 1 and 2) than for higher flow rates (40 and 27 % for CFDK 3 and 4).

In Figure.III.38 and Figure.III.39 are displayed the slug patterns formed for the different experiments as well as the fluid velocities for each experiment. It can be seen that increasing the flow rate increases the velocity inside the slugs, this is important when intense mixing is required, but with too high a flow rate the slugs start to become disrupted (CFDK 4) or even produce annular flow (experiments CFDK 5 and CFDK 6).[176,185,186] Comparing to the velocity aspect it seems that longer slugs (achieved here at lower flow rates) induce lower velocity and therefore low mixing intensity and more gentle mixing. The smaller slugs have more intense mixing compared to the total net flow rate.

As can be seen from Table.III.19, changing the ratio of Galden and water from 1:1 to 1:2 changes the slug size. When the ratio of water is higher more water slugs are present as in CFDK 9, and the opposite is found when the Galden flow rate is higher for CFDK 8. For the same total flow rate CFDK 2 and CFDK 9 have a close slug size, but more slugs are present and closer together in CFDK 9. This would mean that the net flow rate of water at 0.0205 m/s for CFDK 2 is close enough to the flow rate of CFDK 9 at 0.027 m/s to obtain the same slug size and also the lower flow rate for Galden has an effect on the distance between the slugs due to the lower flow rate. The maximum velocity of CFDK 8 and 9 inside the slug, at 0.1012 m/s and 0.1076 m/s, is close to that of CFDK 2 at 0.1053 m/s; having more slugs on the other hand could improve the output of the reactor for the same reaction.

The size of the slugs varies with the flow rate, when increasing the flow rate more slugs are formed of smaller sizes. For CFDK 1 the slugs are at 1.2 cm and for higher flow rate in CFDK 3 the slugs are at 0.7 cm. This would be due to the higher flow rate at both inlets starting to form slugs faster as the fluids encounter with higher intensity. At a break point like for CFDK 4 (Figure.III.38) a form of jetting starts to appear that forms slugs 2 cm after the inlet, for certain experiment like crystallisation some encrustation could appear on the tubing due to this phenomenon.

As can be seen in Figure.III.39 the flow rate of each fluid has, as expected, an impact on the slug size formed as well as the velocity as shown on Figure.III.40. This type of behaviour has been reported in Qian & Lawal 2006 for a t-piece segmented flow where changing the inlet flow rate or ratio affects the size of the slugs. Increasing the flow rate decreases the slug size until it disrupts the flow and lowering flow rate increases the slug size. Also, as observed on Figure.III.38, having different ratio affects the distance between slugs, when one flow rate is higher than the other, the solution with higher flow rate engulfs the other solution until forming droplets.109 For the velocity on the other hand, only the rear edge seems to be mixing over time. In several case studies of CFD simulation looking at velocity in slugs, the flow pattern inside the slugs is symmetrical along the horizontal axis and homogeneous.187 However, in Kashid et al. cyclohexane-water system was used to form the slugs and a different model (SS) was used which could lead to differences between the model employed here and those models previously reported. Bringer at al. describe experimentally this mixing behaviour by using a dye inside water to form the slugs and look at the mixing pattern, showing that smaller slugs have a more efficient mixing and in the bigger slugs a flipping phenomenon was observed where both coloured and non-coloured solution moved from one side to another of the slug without mixing.188,189 In the next Chapter using a similar platform it was observed for the production of PiC that some particles were mainly observed at the rear of the slug, this phenomenon was similar to that calculated here. Controlling the flow rate at the inlet for segmented flow led to control over the mixing intensity inside each of the slugs. The important part is to find the optimal ratio between velocity and slug size. Between 1 and 10 mL/min, it is possible to get slugs of different sizes and different velocities. For 20 and 50 ml/min, the slugs are completely disrupted which was to be expected as the surface tension in the defined environment (3.2 mm ID tubing) is not great enough to overcome the degree of immiscibility and speed of combination to create slugs. For the different KRAIC experiments the flow rate used was between 2 and 10 mL/min depending on the crystallising system. Usually with smaller slug sizes the velocity seems faster inside due to the space available to disperse the eddies; in a more confined space the flow has less space between the frontal and rear edges of the slug (location of the fast eddies) to disperse and lose velocity while in bigger slugs there is more space to lose this induced velocity.

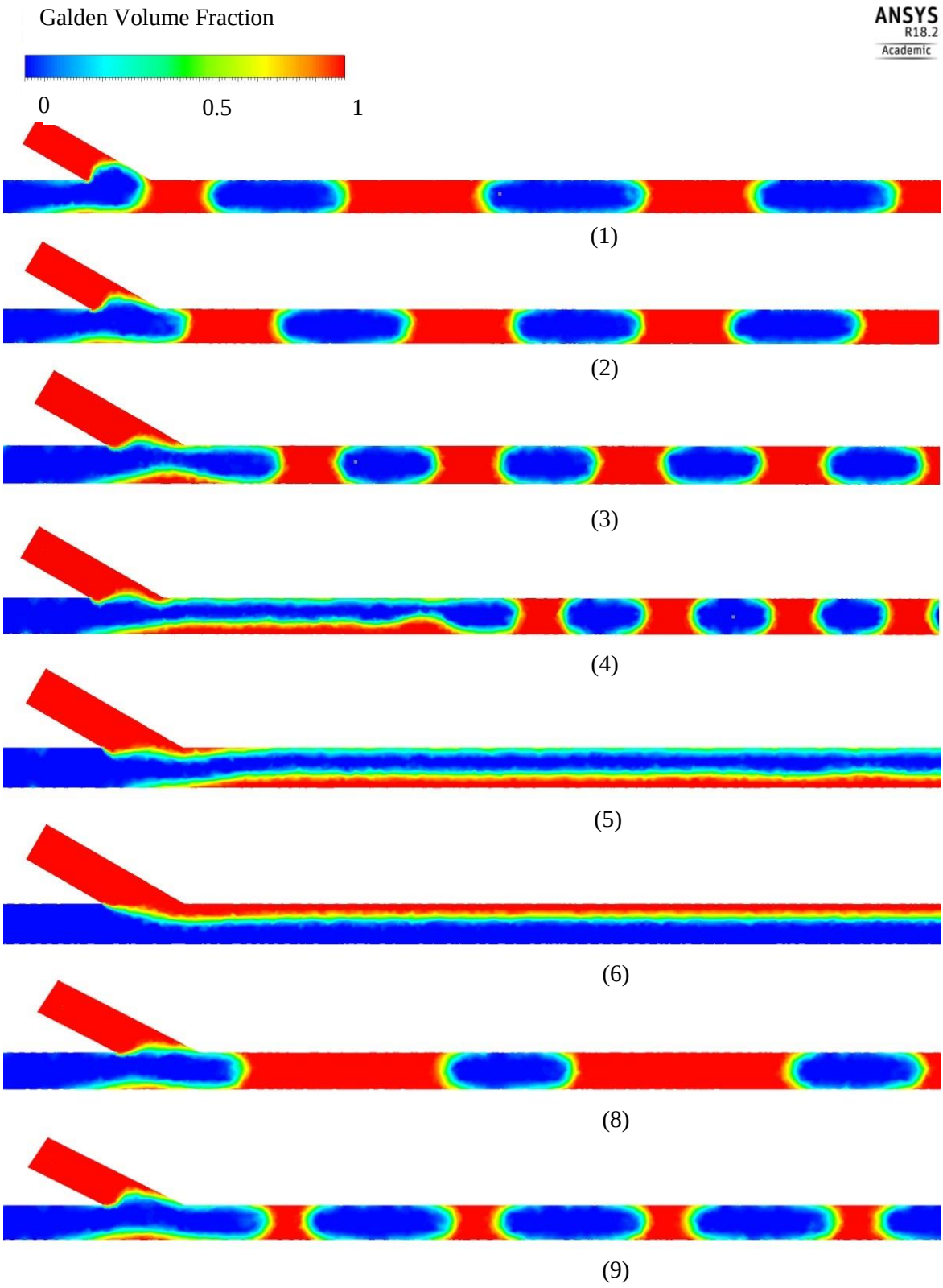

Figure.III.38 . Different flow rate formation of slugs from experiment CFDK 1 to 8. 7 is not shown due to its similar behaviour to 6 with no slug formation.

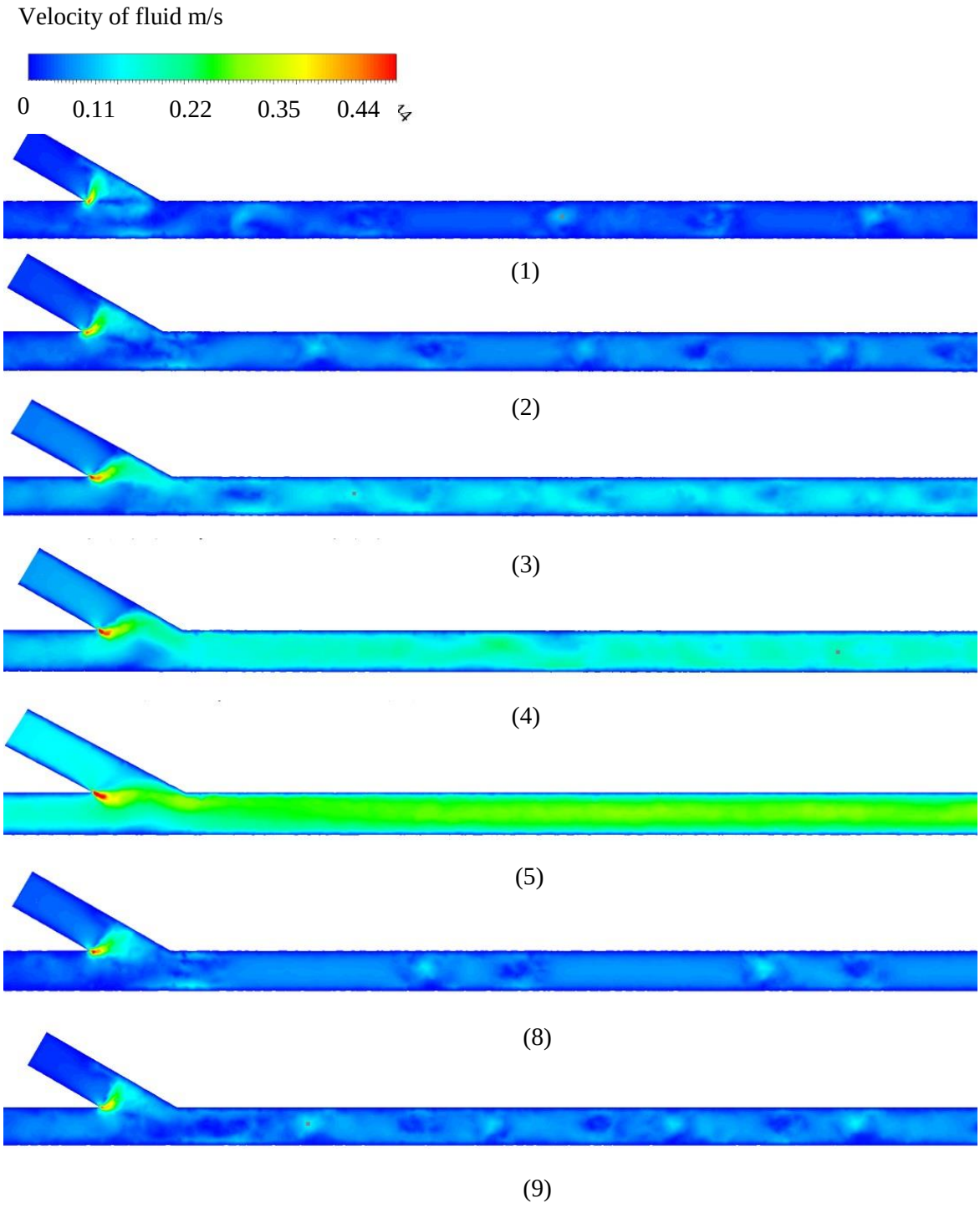

Figure.III.39 Difference of velocity inside the slugs with different flow rate. Number refers to Figure.III.19.

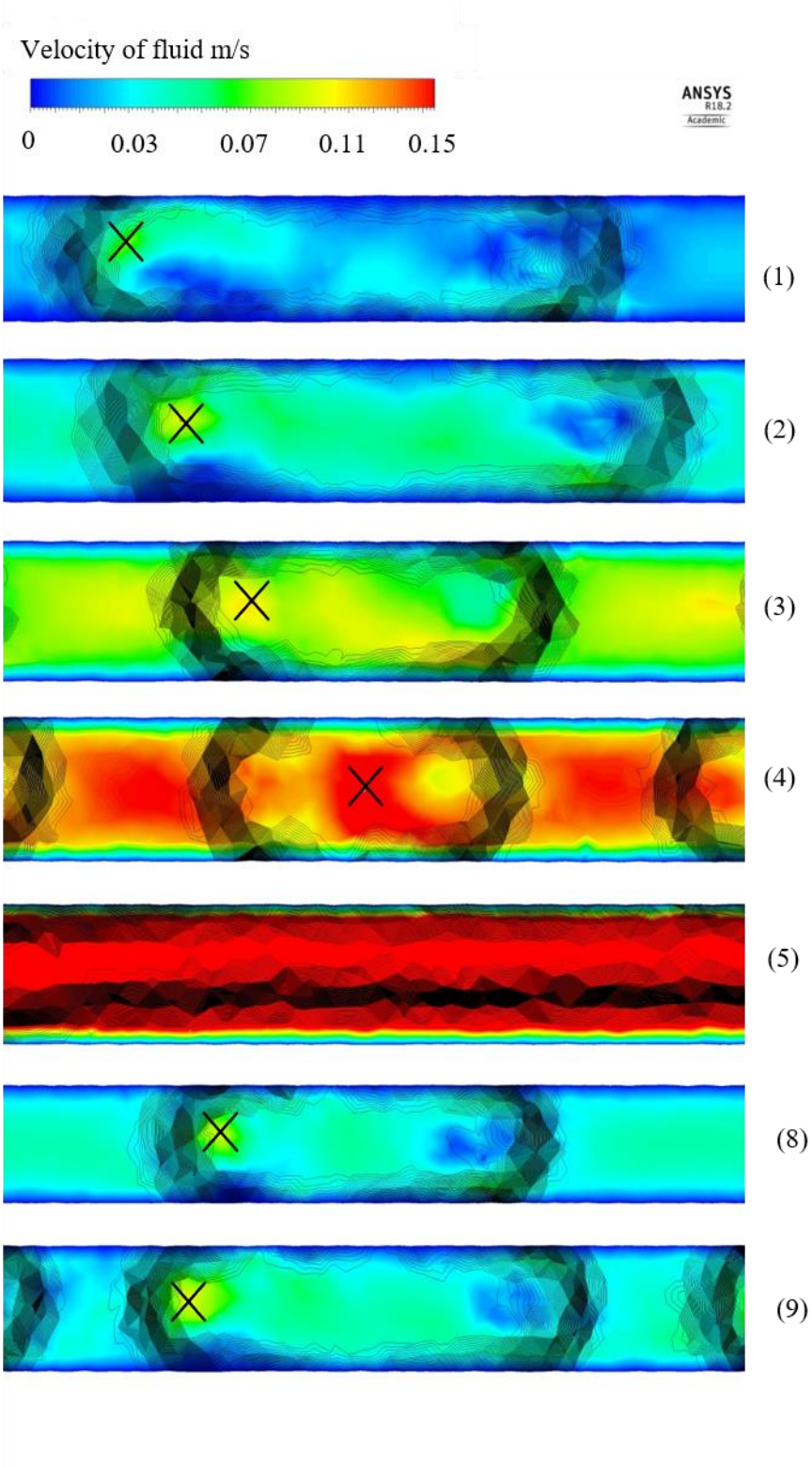

Figure.III.40 Velocity inside the slugs for CFD K 1 to 5 and 8,9 after 8 s of flow at 3.5 cm. The cross represents the highest velocity point.

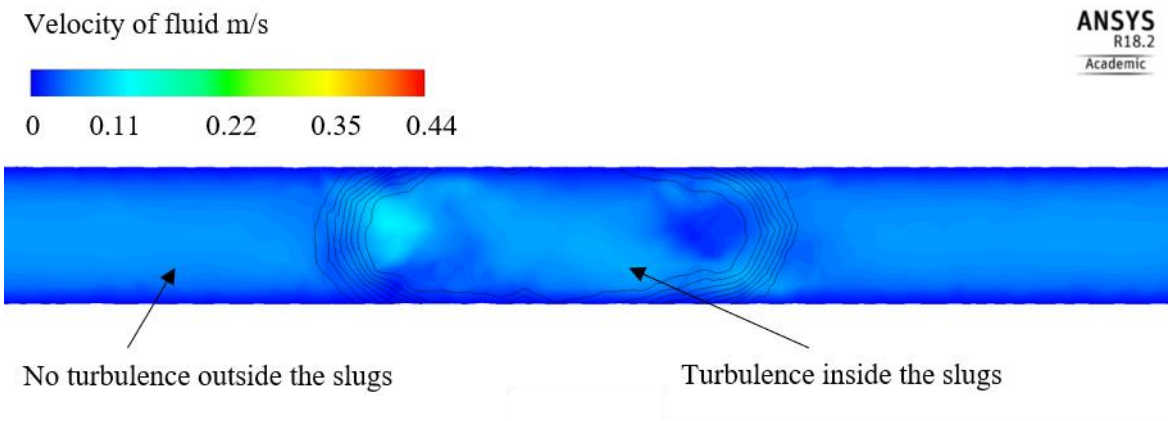

Figure.III.41 Slugs showing the difference inside and outside the water slug for CFDK 8.

In Figure.III.41, the difference inside and outside the slugs is shown for CFDK 8 which shows the bolus flow creating a distortion of the velocity field inside the slugs. Comparing this inner velocity field to that outside of the slugs, it can be seen that the latter has a more laminar expression. These correlations can be used to predict the slug behaviour depending on the conditions of operation during an experiment and those simulations could be applied to both heat and mass transfer simulations.

The CFD modelling was computer intensive with each experiment taking several days to be fully converged and simulated. Even if the CFD model was not able to compute a 3-phase (air-liquid-liquid) or 4–phase (air-liquid-liquid-solid) flow to improve accuracy in relation to the KRAIC, Ansys Fluent was able to give information about the bolus flow phenomenon and how to optimise it for future applications. The 3-phase flow was tried without success due to insufficient computational power and software limitations (exceeding a VOF Courant number of 250).

To convey a better appreciation of the slugs forming at the inlet and flowing through the tubing a movie is available in the supplementary information (**CDCh3-1**) data showing the CFD simulation of experiment 3 (which has the highest relevance to the experimental example of SA crystallisation discussed above (Table.III.1), in terms of slug size and the same Y-piece configuration).

The experiments on CFD showed the importance of the flow rate parameters at the mixer piece and also that segmented flow is difficult to control. Undertaking prior priming of the reactor to control the size and mixing inside the slugs is paramount to a successful run in the KRAIC. In the CFD model other impacts could be studied but would require more computational power, e.g. the effect of the pressure build-up due to the volume of the 15 m tubing after the mixer piece or different solution viscosity interactions with the Galden.

III.5. Conclusion

The KRAIC segmented flow device is capable of producing a wide range of materials, from pharmaceutical compounds to metal complexes with switching properties. For the crystallisation of pharmaceutical compounds, segmented flow has been shown to be a suitable technique to control nucleation in a controlled environment, here the slugs. The advantage of segmented flow is the ability to have a visual confirmation of the crystal in the slug making it easy to measure onset of growth; it also prevents back mixing of old and new material together.

The crystallisation of pharmaceutical compounds of SA and UBA showed that different polymorphs appeared during the process for UBA and will lead to further investigation in Chapter IV. This is one of the advantages of using tubing for *in situ* analysis and monitor transient events along the tubing, where a particular step of the crystallisation or reaction can be pinpointed to be analysed. These crystallisations offered the opportunity to improve the KRAIC and test different equipment; for example, the switch from peristaltic to gear pump substantially improved the flow behaviour along the KRAIC and kept the slug size constant. In the next Chapter discussion of the KRAIC-D will introduce other pump systems used to form segmented flow. The recovery system was able to continuously maintain the level of Galden along all experiments and avoided any loss. To improve this aspect the hole made in the end piece could be replaced by a membrane with small pores like fluorinated meshes or laser drilled holes directly in the tubing. The filtration was also an issue during those experiments – a continuous solution to filter any products must be found to avoid moving the end piece during the experiment, a carousel was originally designed but the dimensions were too high for the end piece; a belt could be the solution for such a system.

Of central interest in this thesis is the production of switchable materials. The KRAIC was successfully used in order to synthesise nanoparticles of the spin-crossover compounds $[Fe(Htrz)_2(trz)](BF_4)$ (PiC) and $[Fe(Htrz)_3](BF_4)_2{\cdot}H_2O$ (PiCM). It was shown that using a segmented flow environment to produce this material can give a reduction in size of the resultant crystalline rods. For PiC the induction and onset of growth times were significantly reduced and showed the advantages of using segmented flow to accelerate the reaction through the internal mixing in the slugs of the KRAIC. The particle size distribution was also narrower compared to its batch counterpart. For PiCM on the other hand the expected gel formation in the KRAIC (using the BTA/GdL mix) was not successful. The switching properties of the material produced during those runs will be discussed in Chapter VII with the comparison to other flow platform production. The observation of the different colour phases during the synthesis also was of interest and will be developed in Chapter IV.

CFD modelling was able to simulate the bolus flow to see how it was formed for different flow parameters. The inlet flow rate was shown to be important during the slug formation and inner mixing of the slugs and was affecting size and inner velocity of the slugs. Optimising the net flow rate with CFD would be a way to control the mixing intensity inside each slug depending on which reaction or crystallisation is carried out inside the KRAIC.

The next chapter goes further in-depth into the detection of different phases or polymorphs using *in situ* XRD and Raman using the segmented flow reactors KRAIC and KRAIC-D.

Chapter IV *In situ* analysis using segmented flow

IV.1. Introduction

With the growth of flow technologies in recent years to carry out chemical reactions or crystallisations, they present analytical challenges that differ from those in batch reactions. The main difference in flow environment is that the chemical reaction or crystallisation is continually initiated during the entire period of the run because of the new starting material being injected into the reactor. In a flow reactor the same material is obtained over a several runs due to consistency and repeatability of the experiment. However, for a lot of reactions a change in reactor parameters (flow rates, temperature, concentration of reagents) can change the residence time and reaction conditions of the system, and lead to significant improvement in the product quality. Flow crystallisation and chemistry can therefore benefit from improvement in online analysis to assess product purity over time. [94,187]. The advantage of using flow in this context is the possibility to monitor different steps of the process at specifics point of the reaction/crystallisation by monitoring a specific point of the flow reactor, compared to batch where the analysis is done where initial and final product coexists which could lead to false analysis. The drawback of such flow installation is to work out the best point at which to study the reaction; this needs flow rate, reaction kinetics, background removal and concentration study beforehand. The background that needs to be removed in the analysis can change due to tubing composition or if multiple phases are present. A number of analytical technologies including Fourier-Transform Infrared (FTIR), UV-Vis and Raman spectroscopy, Nuclear Magnetic Resonance (NMR), mass spectrometry, concentration/supersaturation measurement, particle counts, direct nucleation control (DNC) and high-performance liquid chromatography (HPLC) have been used in flow to monitor reactions.[63,187–191]

During a flow experiment, the analysis is ideally done directly using an in-line probe, removing the sampling step. However this requires compatibility between the Process Analytical Technology (PAT) system and the flow reactor. [192,193]

Described in this chapter is the *in situ* analysis of different compounds produced in flow using X-ray synchrotron radiation and using a Raman probe. The focus will be on the analysis of several compounds previously studied in Chapter III, in a modified Kinetically Regulated Automated Input Crystalliser (KRAIC) specially designed for integration onto the high-resolution powder X-Ray diffraction beamline at Diamond light source (I11). The analysis presented also includes *in situ* Raman spectroscopy of $[Fe(Htrz)_2(trz)](BF_4)\cdot H_2O$ (Htrz = 1,2,4-triazole) (PiC) inside a modified KRAIC reactor. The first two compounds that will be presented are the pharmaceutical-related compound, urea barbituric acid (UBA) and PiC. As reported in Chapter III, after crystallisation within the KRAIC, a mixture of polymorphs of UBA was observed. It is possible that the presence and possible progression of these polymorphs could be detected during crystallisation by high resolution powder X-ray diffraction (PXRD) at different point of the process using segmented flow to ensure there is no back mixing and a true representation of the crystallisation process is presented along the length of the crystalliser. The spin cross-over compound PiC ($[Fe(Htrz)_2(trz)](BF_4).H_2O$ (Htrz = 1,2,4-triazole)) was also studied using the KRAIC-D. In the previous chapter it was reported that a white intermediate phase appeared during the experiments in batch and in flow; this phase could be an intermediate during the reaction or a high spin state white form appearing during the synthesis, whose appearance may be detected by *in situ* synchrotron XRD. For PiC, flow Raman analysis was also carried out using the KRAIC to analyse the different phases (pink final and intermediate white) during the reaction.

IV.2. *In situ* analysis using segmented flow at Diamond Light Source

IV.2.1 *In situ* Synchrotron Radiation

The KRAIC-D was designed to be implemented on a beamline at Diamond Light Source to study *in situ* X-ray diffraction in flow. In this type of particle accelerator, electrons are accelerated to 3 GeV energy and circulated at high speed in a ring of 561.6 m circumference to produce synchrotron radiation (Figure.IV.1). This radiation is then used to observe matter with different applications: biological molecules (crystallography of proteins), molecular and materials structure (including pharmaceuticals and solid-state chemistry), nanostructure and polymers (diffraction), electronic components (diffraction, spectroscopy), archaeology (often via lithography), medical imaging and many more. These studies are rooted in knowledge of the material structure at the molecular and atomic level. [194,195]

With the development of synchrotrons over several decades, the technique has improved in terms of equipment. The electron gun, running at a high voltage through a heated cathode, produces pulses of free electrons which are gathered in packets and injected into the LINAC, LINear ACcelerator, which accelerates them into the booster (Figure.IV.2). Electrons form the booster are then accelerated to their full energy (3 GeV for Diamond), and injected into the storage ring, where their energy and velocity is maintained by aa serious of magnets and RF power supplies. By bending the electrons in magnets around the ring, they are accelerated and emit synchrotron radiation. This radiation is then sent to the beam line where the experiment can be carried out. In this Chapter experiment were carried out at beamline Instrument 11 (I11) for high resolution powder diffraction.

Figure.IV.1 Diamond Light Source Complex. [196]

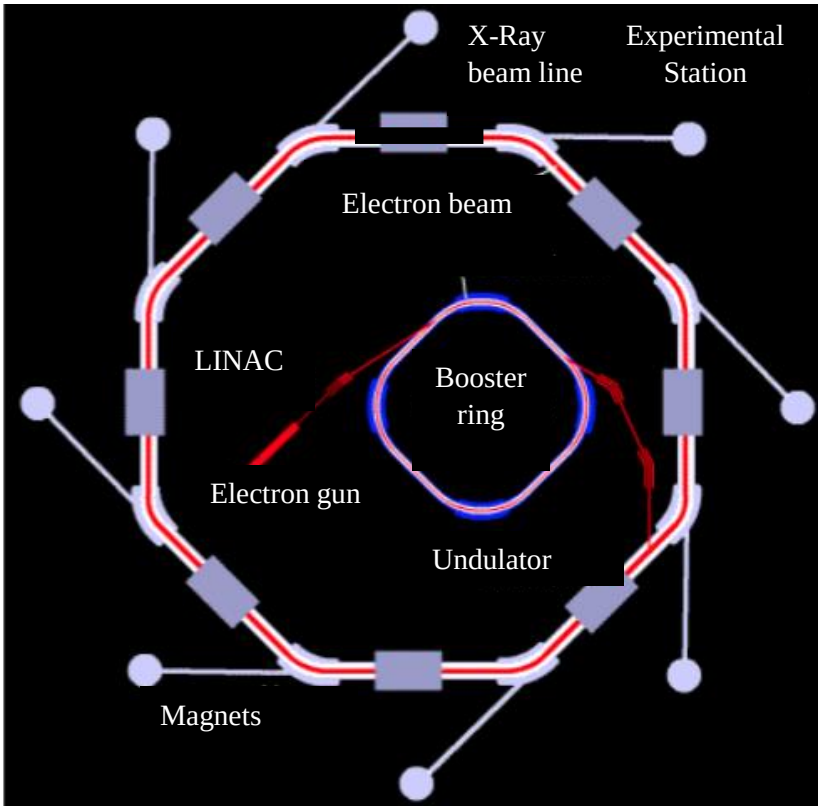

Figure.IV.2 Generating synchrotron radiation electrons are generated in an electron gun then accelerated *via* the booster ring and then stored in the outer ring to be used at different beam lines for analysis.[196]

IV.3. The KRAIC-D at Diamond Light Source

To investigate the potential use of the synchrotron beam for characterisation for *in situ* analysis, a variation of the KRAIC segmented flow reactor was designed. As previously presented, the KRAIC is composed of three coils of FEP (fluorinated ethylene propylene) tubing. The slugs are formed using a range of different mixer piece geometries connected to the coil tubing. Using a liquid-segmented flow environment could give further opportunities for online analysis during the flow. In each slug the solids are in good mixing condition and are well suspended with good homogeneity and no back mixing which can improve *in situ* analysis. This also means that each point in the reactor corresponds to a point in crystallisation / reaction time which means that the observations of certain events such as onset of growth, intermediate phases during the synthesis are easier. Thanks to the carrier fluid used, the solution to be crystallised does not enter in contact with the wall or any solid interface. This type of flow can avoid any unwanted crystallisation but also can lead to a different crystallisation mechanism.

The experiment involves observing those mechanism changes in each of the isolated slugs during flow in real-time using *in situ* X-ray diffraction. The KRAIC-D (Figure.IV.3) has been designed with five X-ray transparent windows along the length of the crystalliser. The windows themselves are made of polyimide Kapton® tubing, this material has been used to facilitate the X-ray penetration and minimise background scattering from the windows. Kapton® is a useful material for X-ray windows as it is resistant to high flux densities of X-ray beam, has low X-ray absorption and low diffraction in the keV energy range.[197–199]

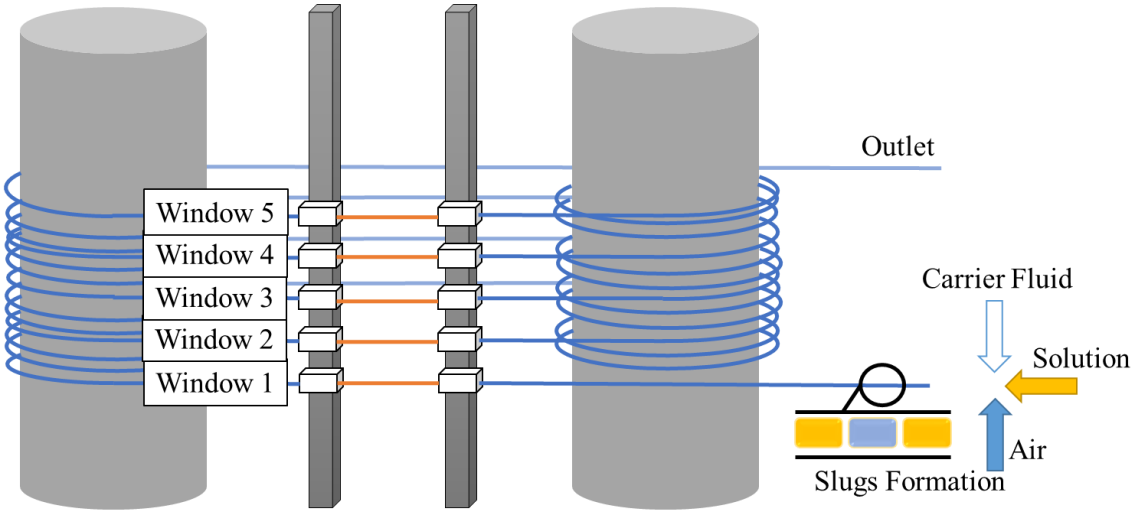

Figure.IV.3 KRAIC-D scheme showing the Kapton® windows in orange and the slug formation at the inlet using tri-segmented flow with air, solution and carrier fluid.

The Kapton® tubing, a polyimide, is not hydrophobic and would result in disruption of the segmented flow during the experiment as the segmented flow goes though the FEP tubing to Kapton® and then back to FEP. To avoid this problem the Kapton® tubing was surface treated using a plasma cleaner to improve the adhesion of the tubing for subsequent coating with Aquapel®. This is a glass treatment for rain repelling properties, it consists of fluorinated compounds (fluoroalkyl silane (FAS)) that creates a chemical bond to the surface and make the tubing more hydrophobic.[200] The internal diameter (ID) of the Kapton® tubing is the same as the FEP tubing to avoid any flow disruption when changing type of tubing. To connect the two tubing types, machined PTFE cylinder blocks were created to have a perfect connection with no change of diameter that could cause disruption of the slugs.

A scheme of the KRAIC-D is displayed in Figure.IV.3 with a picture of the actual system in Figure.IV.4. The characteristics of the system are displayed in Table.IV.1

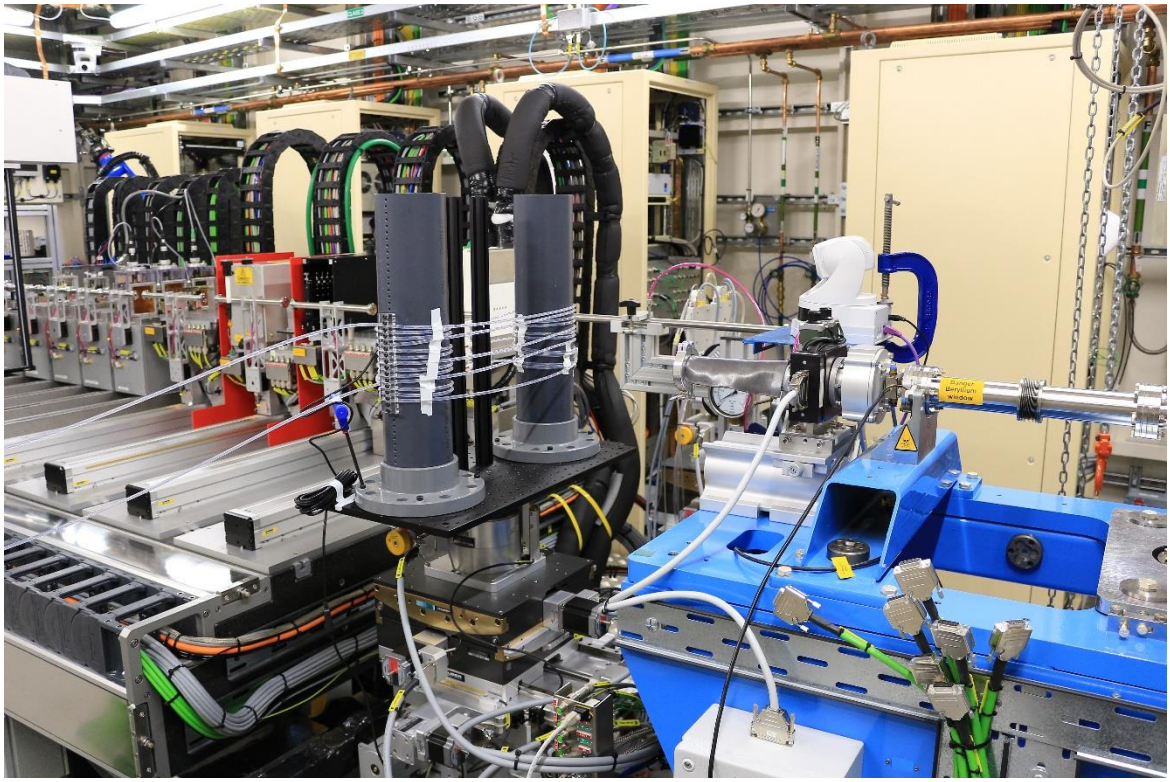

Figure.IV.4 KRAIC-D installed on the beam line (I11) platform at Diamond Light Source.

Table.IV.1 KRAIC-D tubing distances of each point of interest

Location	Crystalliser length (m)
Water bath	0
Outlet to water bath	0.05
Top of inlet to KRAIC-D	1.06
Window 1	1.20
Window 2	3.787
Window 3	6.40
Window 4	9.04
Window 5	11.72
Outlet	14.03

The whole system was then installed in different configurations for UBA and PiC, to study the different particularities of the compounds. The KRAIC-D experiment was carried out in experimental hutch (EH2) at Instrument I11 at Diamond (I11, high resolution powder XRD) using the large goniometer stage available there, for alignment of the 7 cm long X-ray transparent windows with the synchrotron beam, Figure.IV.5

The distances between the windows are measured precisely using a ceria standard on the centre of the middle window (Figure.IV.5). This standard is used to calibrate the distance between the detector and the centre of the windows which are all aligned by measuring the ceria diffraction pattern. The data were collected in 100 ms pulses using a 400 x 400 μm^2 collimated X-ray beam controlled *via* the shutter, on an area detector (Pixium RF 4343 Thales Group). The data obtained were post

processed using Data Analysis Workbench (DAWN), Matlab®, and Total Pattern Analysis Solution (TOPAS, Bruker).

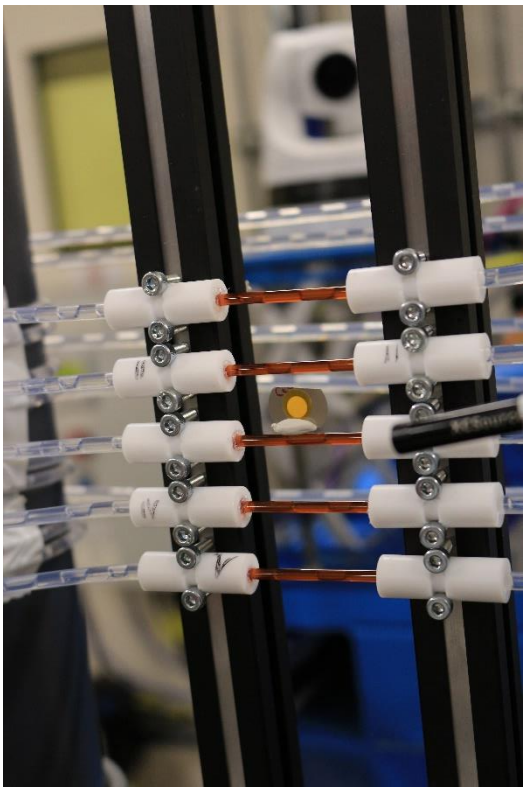

Figure.IV.5 Kapton® Windows of the KRAIC-D with ceria sample on Window 3.

In this chapter, various Urea Barbituric Acid (UBA) polymorphs are studied; it has been seen that in the KRAIC, several polymorphs of those compounds are present during the crystallisation, as analysed *via* offline powder X-ray diffraction (PXRD). PiC synthesis is also studied as the reaction transition from intermediate white phase to final pink phase could be a high spin state form or an unknown form that appears during the reaction. If this is a crystalline state, the synchrotron experiment could identify any phase change. In batch PiC synthesis, the time available for evaluation of each colour transition is limited and so it would be more difficult to assess compared to flow where the length along the crystalliser is equal to the crystallisation time. It is difficult to quench the reaction in batch to analyse one phase but using the plug flow approach quenching can be avoided.

IV.3.2 Pharmaceuticals compound polymorphs studied on KRAIC-D

In Chapter III it was shown that using the KRAIC different polymorphs of urea barbituric acid (UBA) were observed in the crystallisation product. Understanding and controlling those changes would be beneficial for the potential pharmaceutic application of compounds such as UBA, offering better understanding and control during the production.[76,85,86,193] In this section is described the crystallisation of UBA in the KRAIC-D and how the polymorphic content was detected using the *in situ* PXRD on I11.

IV.3.2.i Urea Barbituric Acid

UBA was the first compound to be evaluated using beam line I11 and the KRAIC-D combined. It was reported in Wittering *et al.*[201] that two of the polymorphs are close in energy and it is difficult

to detect the relationship between these during crystallisation with offline PXRD. The set-up used is similar to the KRAIC UBA runs from Chapter III (Figure.III.13), Figure.IV.6. Three Ismatec gear pumps are used for the air, carrier fluid and neutral solvent and, a Vapourtec SF-10 peristaltic pump was used for the solution; this pump displays low pulsation with respect to standard peristaltic pumps reducing variability in slug sizes whilst maintaining compatibility with the crystallising solution. The mixer piece where the slugs are created is submerged into a water bath to control its temperature. The flow parameters used for the runs are displayed on Table.IV.2 urea and barbituric acid were dissolved in methanol with a concentration of 0.118 g/mL for each component. The priming fluid and feed vessels are heated and the solution is transferred to the rest of the reactor using the SF-10 peristaltic pump with jacketed tubing. The feed vessels and the jacketed tubing were set to 60 °C and the mixer piece was placed in a water bath at 43 °C, the change of temperature from the feed vessel to the KRAIC-D induced the nucleation and crystal growth.

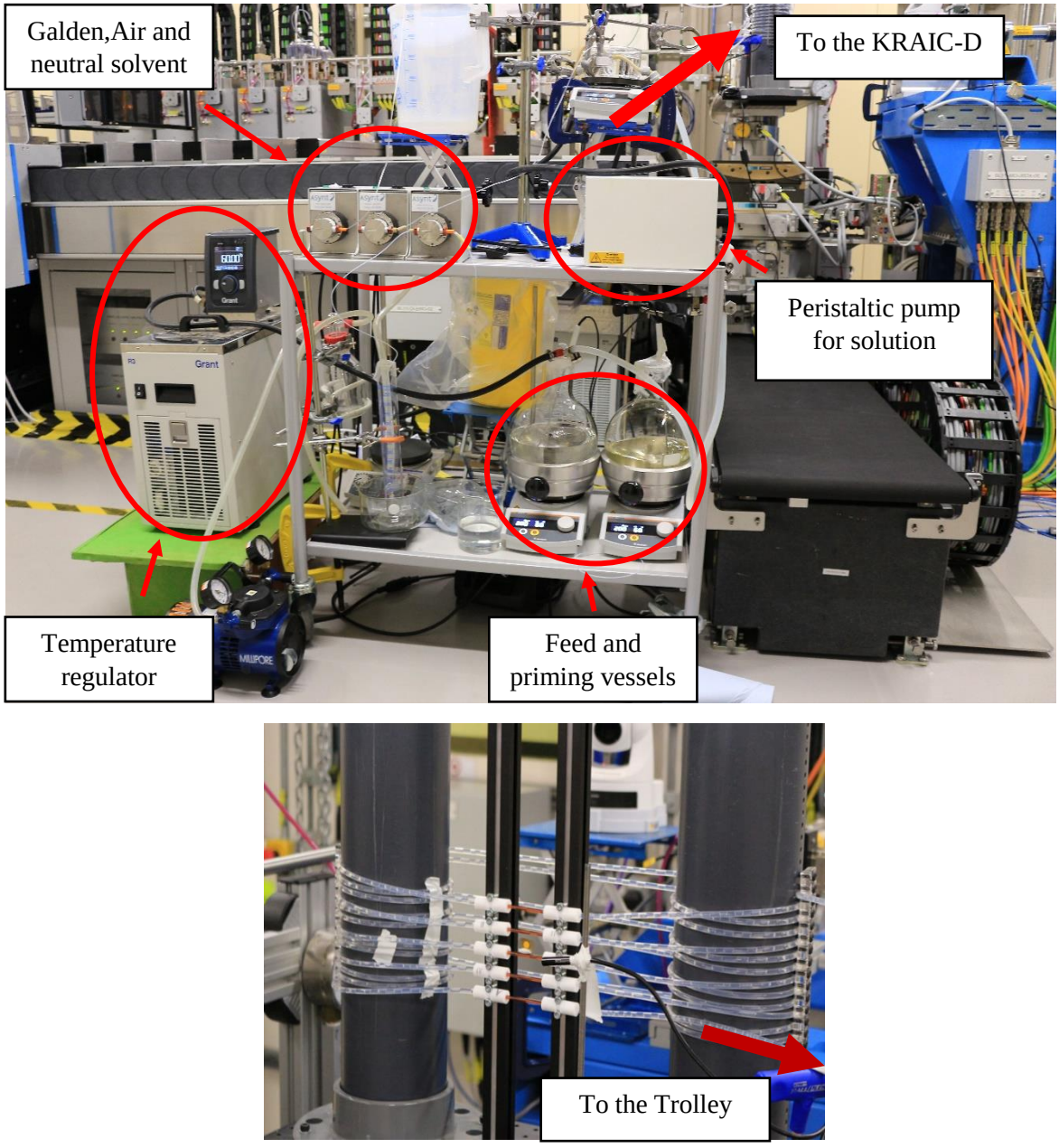

Figure.IV.6 Full set-up of the KRAIC-D at I11 Diamond Light Source

Table.IV.2 Parameters used for the KRAIC-D UBA runs and window number of exposures (each set = 100 x 100 ms).

	Ismatec gear pump			Vapourtec SF-10	Total without N.S.
	Carrier fluid	**Air**	**Neutral solvent**	**Solution**	
Flow Rate (ml/min)	4.18	4.18	12.5	4	12.36
	W1	W2	W3	W4	W5
Number of exposure sets	4	17	14	7	1

First the background signal of the Kapton® tubing with air and Galden was acquired to allow this to be removed from the obtained experimental signal for UBA. During the experiment four sets of 100 x 100 ms exposures were obtained from each single window (1-5; Figure.IV.5). During data processing, the background previously measured was removed from each signal obtained on these windows. The detected diffraction data were then filtered to remove any data sets which did not contain diffraction spots above the background threshold. After these steps the signals obtained were added together to obtain a combined 2D diffraction image which was then integrated to obtain the 1D plot intensity versus 2θ. The area under the curve of this 1D plot gives the integrated intensity from the scattering power correlated to the crystal growth. During experiments it was found that the Aquapel ® coating on the Kapton® tubing was damaged with too long exposures, which leads to slug disruption. This was observed for exposures exceeding 100 x 100 ms at a single point.

In Chapter III it was shown that using the KRAIC to crystallise UBA, different polymorphs were obtained in the end product (Figure.IV.6). On Figure.IV.7is displayed the XRD of the UBA compound obtained in the KRAIC showing the presence of polymorphs I and III. To have a better understanding of this behaviour during the crystallisation this crystallisation has been carried out in the KRAIC-D. The use of *in situ* PXRD showed (Figure.IV.6) that a polymorphic transition from form III to form I occurred over the crystalliser length under the parameters chosen. Data processing was carried out by PhD students Lois Wayment from the University of Bath and Mark Levenstein from the University of Leeds. The data processing took account of the differences in wavelength between the Bruker D8 Advance Diffractometer used at the University of Bath with a monochromatic Cu-K_α (λ = 1.54056 Å) and the synchrotron radiation used on I11 with a wavelength 0.8224 Å; Figure.IV.7 has all data normalised to λ = 1.54056 Å.

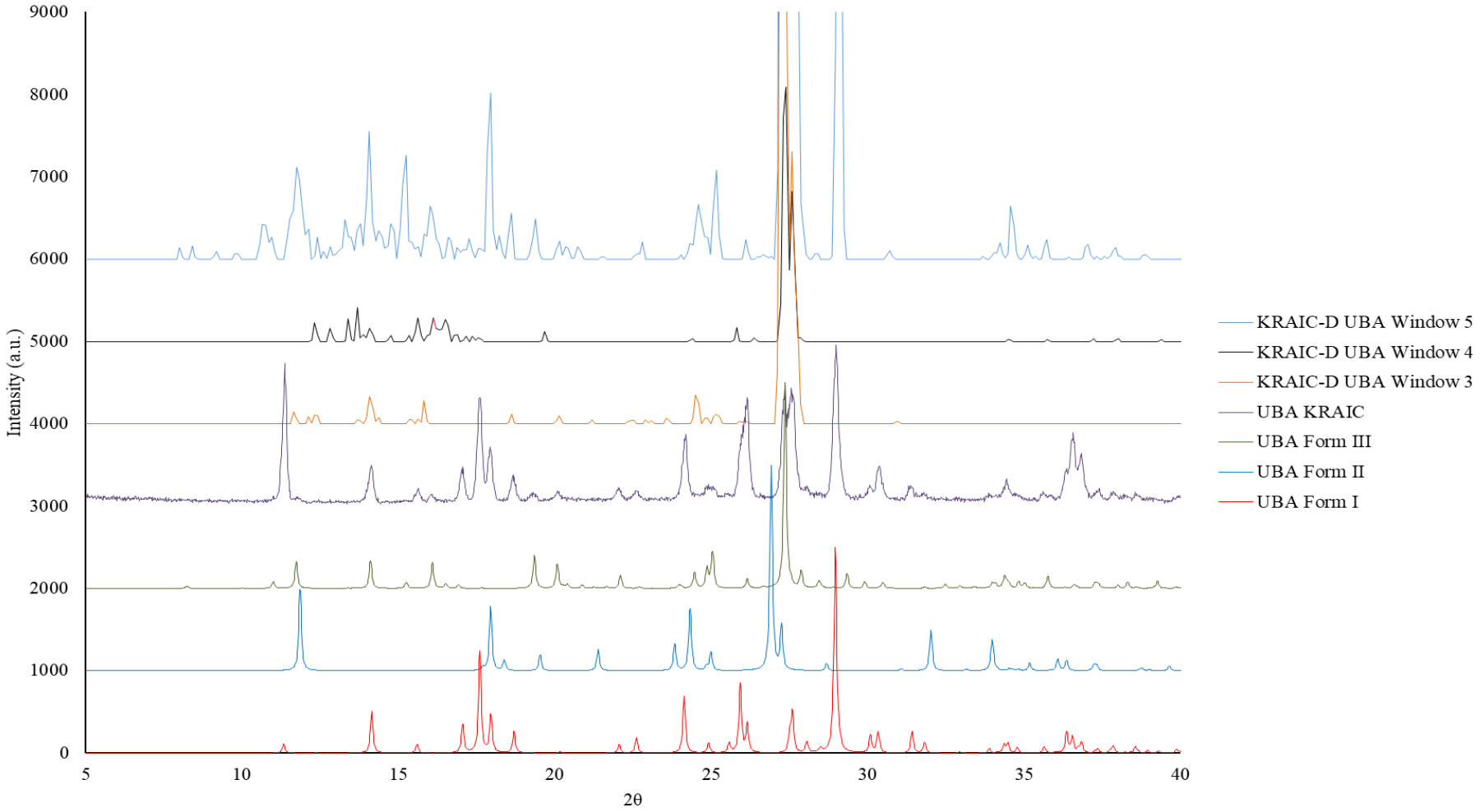

Figure.IV.7 UBA XRD comparison obtained previously in KRAIC, during beam time at I11 and with simulated Form I, II and III patterns

During the experiment, only the last three windows were analysed, with little to no crystallisation being present in the 1st and 2nd windows. As can be seen on Figure.IV.7 the presence of different polymorphs has been confirmed at different points inside the KRAIC. In the 3rd window, with a crystallisation time of 4 min 10 s, peaks are present that correspond to UBA form I and III polymorphs, with III being predominant. In window 4 with crystallisation at 5 min 47 s, the signal has a lot of noise which could be due to difficulties in selecting the background threshold. In the last window, window 5, with a crystallisation time of 7 min 50 s, both UBA form I and III are still present but the proportion of UBA form I is becoming greater than that observed in windows 3 and 4. In particular the peak at 15.5° which is only present in UBA Form I has a much higher intensity compared to the other windows. With the diffraction patterns of the three windows studied it is seen that UBA Form III is the dominant one in windows 3 and 4, UBA I on the other hand becomes more prominent in the final window (window 5). This can lead to the conclusion that even if both polymorphs are present, under these conditions Form III is less stable than Form I and with time Form III will undergo a phase transition to the more stable Form I.

One of the limiting factors of this crystallisation study was the run time which was limited to 45 minutes due to the PTFE unions blocking as shown in Figure.IV.8.

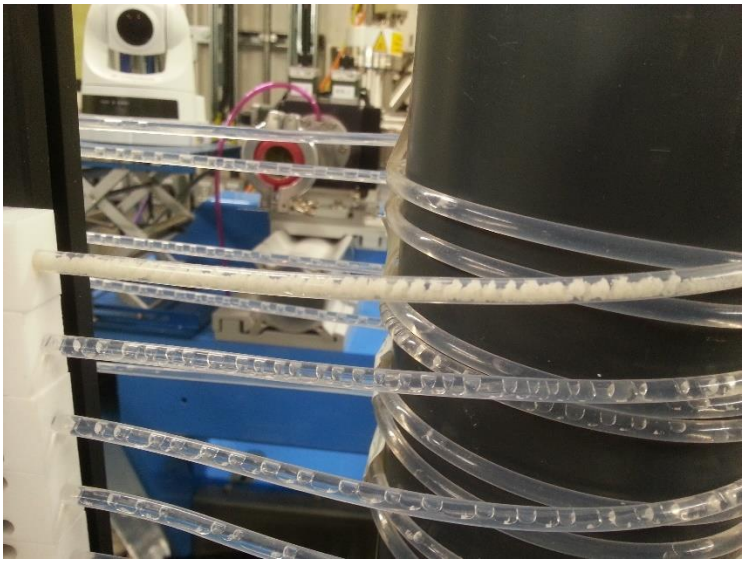

Figure.IV.8 Crystallisation blockage inside the KRAIC-D for UBA in Methanol prior to Window 5.

IV.3.3 Conclusion

The KRAIC-D has proven to be a suitable platform to evaluate the crystallisation mechanism *in situ* and non-invasively as exemplified by the study of UBA. It was possible to detect the relative proportion of different polymorphs at each window of the system giving the possibility to monitor the polymorphic transformation. As observed in the end products from crystallisation within the KRAIC and mixed-suspension, mixed-product removal (MSMPR),[86] the presence of both Form I and III was detected in the final Window (5) of the KRAIC-D. The diffraction pattern in the first windows analysed (3 and 4) had a mix between Form I and Form III (predominantly Form III) but form I is then becoming more prominent in window 5. This is in accordance with offline PXRD

results obtained from UBA crystallisation in the KRAIC and confirms that the offline preparation for PXRD has not instilled a polymorphic change.

The main challenge experienced in deploying the KRAIC-D is the blockages occurring after around 45 min in each UBA run in some of the windows. This was the case for the last two in particular where some unwanted crystallisation was happening due to a change of tubing in the windows creating small protrusions of a solid interface into the otherwise protected solution droplets; this could induce nucleation which created blockages. The Aquapel® coating worked as intended not disrupting the slugs but after several experiments is was seen that the wetting was getting worse due to the beam damaging the coating.

With the possibility to detect change in polymorphism during the crystallisation of UBA demonstrated, the KRAIC-D was considered to be suitable to analyse in more depth the SCO compound $[Fe(Htrz)_2(trz)](BF_4)\cdot H_2O$ (PiC). This is a nanoparticle system which would not present the challenge of the blockages experienced in UBA crystallisation. *In situ* PXRD monitoring of PiC would be of interest as the change in colour during the synthesis could be reaction intermediates which have not been studied in depth, this will be discussed in the next section.

IV.3.4 *In situ* X-ray analysis of $[Fe(Htrz)_2(trz)](BF_4).H_2O$

It has been described in Chapter III that during synthesis in the KRAIC and in batch synthesis of PiC a transition to a white phase was evident at different induction times depending on the conditions. This white intermediate phase is often reported during the synthesis but has not been studied in literature as an intermediate during the synthesis.[4,13,33,202]

For this study the KRAIC-D was modified. For the UBA runs described above, blockages were observed due to imperfect connections at the unions between the Kapton® and FEP tubing. The segmented flow was disrupted at these points causing the solution to come into contact with the walls of the crystalliser enabling nucleation and rapid growth leading to blockages. In the case of the reactive precipitation of nanoparticles of PiC, wall nucleation and blockages are not a concern within the KRAIC-D. However, the change in mixing conditions will cause a change in the expected progression of the PiC reaction as shown by the mixing studies presented in Chapter III. To avoid this the unions were removed and the Kapton® tubing windows connected directly to the FEP tubing by flaming the FEP, softening the edges of the tubing and inserting the windows inside it. Inserting the Kapton® tubing this way avoids the small gap that could happen in the previous PTFE window unions between the FEP tubing and the Kapton® which led to disruptions in the segmented flow. The new set-up is displayed in Figure.IV.9.

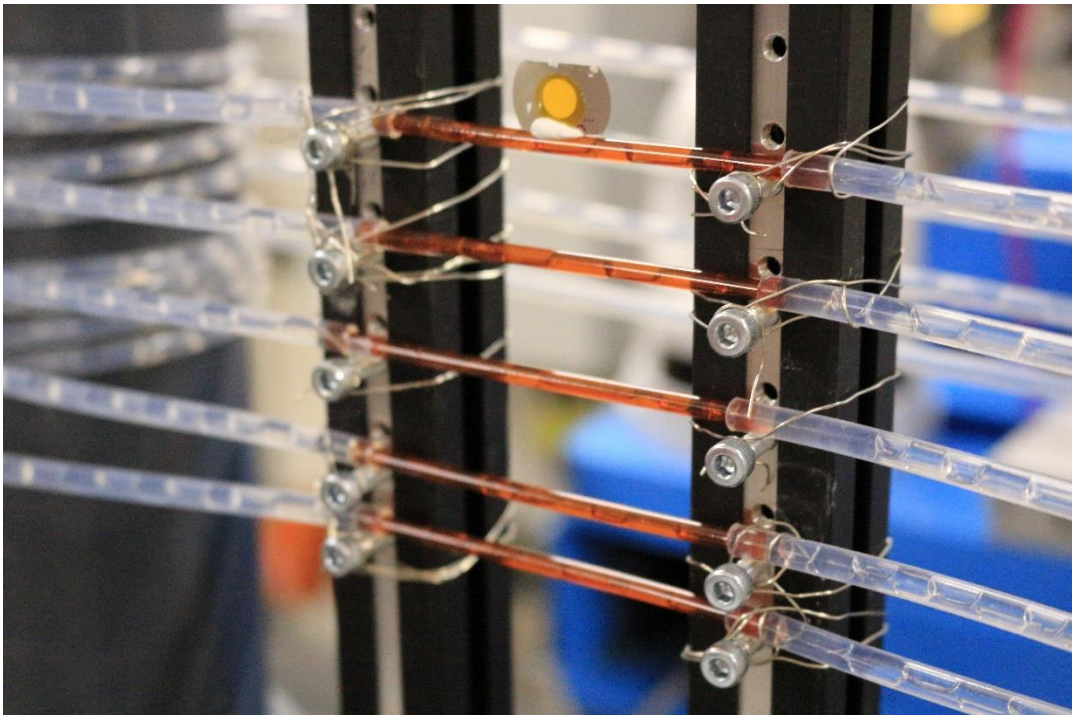

Figure.IV.9 KRAIC-D Kapton® windows after modifications for PiC synthesis.

The mixer piece was also changed to have mixing of the reagents delivering equal volumes of each reagent in each slug to see a uniform colour gradient along the length of the crystalliser. The new mixer section is a combination of a cross and Y piece to create both the slugs and consistency in reagent ratio in each slug.

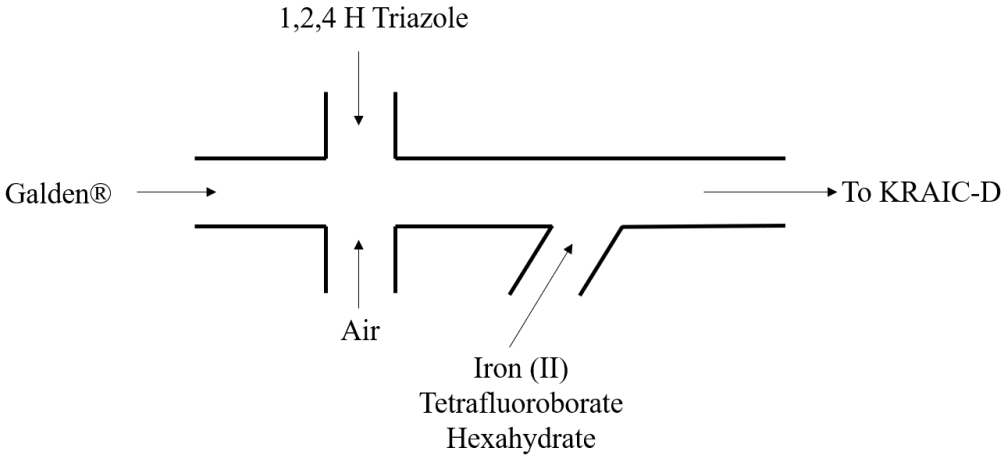

Figure.IV.10 Mixer arrangement for PiC synthesis in the KRAIC-D.

IV.3.4.ii Control of Onset of Growth inside the KRAIC-D

Prior to beamtime experiments, tests were carried out on the KRAIC-D in order to define residence time (RT) inside the system for different pump flow rates. The time taken for the flow to reach each window was also recorded to know precisely when the solution will be present in front of the beam.

The first test was carried out with water as the solution to check residence time and wetting due to the change from PTFE unions and direct tubing assembly by flaming technique. The results of each residence time and time to windows is displayed in Table.IV.3.

Table.IV.3 Flow rate, residence time and windows time for the flamed windows set-up of the KRAIC-D.

Flow rate	$Fe(BF_4)_2$ $6H_2O$ (mL/min)	1,2,4 H Triazole (mL/min)	Galden flow rate (mL/min)	Air inc/flow rate (mL/min)	Total (mL/min)
Slow	0.8	0.8	2.1	4.2	7.9
Medium	1.6	1.6	2.1	4.2	9.5
Fast	2.4	2.4	2.1	4.2	11.1

Times for slug arrival at windows (min:sec), for medium and slow flow rate repeats

Flow rates	W1	W2	W3	W4	W5	RT
Medium	01:30	04:50	08:07	11:24	14:43	17:44
Medium	01:34	05:02	08:25	11:47	15:09	18:24
Slow	01:52	06:22	10:43	14:59	19:11	22:18
Slow	01:52	06:01	10:07	14:10	18:13	21:51
Slow	01:50	05:58	10:07	14:07	18:11	21:51

It was noted that stopping the air (gear) pump in order to obtain a marker to follow the residence time in a fully primed crystalliser results in the flow reversing towards the air pump. Avoiding this was achieved by stopping the solution pump instead.

For the trials with PiC, the same flow rates have been used for the medium flow rate experiment (Galden 2.1 ml/min, Air 4.179 ml/min and two solution pumps 1.6 mL/min each). The first PiC KRAIC-D run was carried out with concentration of $Fe(BF_4)_2 \cdot 6H_2O$ and 1,2,4 H triazole at 0.08 g/mL and 0.10 g/mL respectively. RT and windows timing are shown on Table.IV.5. For Trial 2 the concentration of $Fe(BF_4)_2 \cdot 6H_2O$ was changed to 0.05 g/mL to change the appearance of the intermediate white phase to a later window to allow all reaction steps to be analysed.

Table.IV.4 Trials experiment for Beam Time, showing times of arrival of slugs in the various Windows (min:sec). PiC slugs represent the first slugs with product coming out of the reactor.

First Trials Concentration of $Fe(BF_4)_2 \cdot 6H_2O$	Flow rate	W1	W2	W3	W4	W5	RT	PiC Slugs at Outlet	Induction time
0.08 g/mL	**Trial 1 Medium**	01:36	05:06	08:42	11:24	15:41	18:49	20:05	4:53
0.07g/mL	**Trial 2 Medium**	01:40	05:02	08:20	11:40	15:03	18:17	19:47	7:12
0.05 g/mL	**Trial 2 Medium**	1:40	5:12	8:28	11:53	15:24	18:57	20:29	10:44

From Table.IV.4 the RTs are close between the trials and the time when the final phase arrives at the outlet varies only by 24 s. For the 0.08 g/mL concentration of $Fe(BF_4)_2 \cdot 6H_2O$ the induction time where the colour changes between the colourless to the intermediate white phase was observed at 4 min 53 s before the 2nd window. For 0.07 g/mL of $Fe(BF_4)_2 \cdot 6H_2O$ the induction time is increased to 7 min 12 s with the intermediate phase appearing before the 3rd window. After this run the concentration of $Fe(BF_4)_2 \cdot 6H_2O$ was reduced to 0.05 g/mL, with that concentration the intermediate phase appeared before window 3 at 10 min 44 s. For the phase investigation, this concentration would be well suited to ensure the intermediate phase is observed through the windows. This preparation work showed the importance of the concentration chosen in order to get the desired phase of the PiC synthesis at the desired window to be analysed using the synchrotron beam.

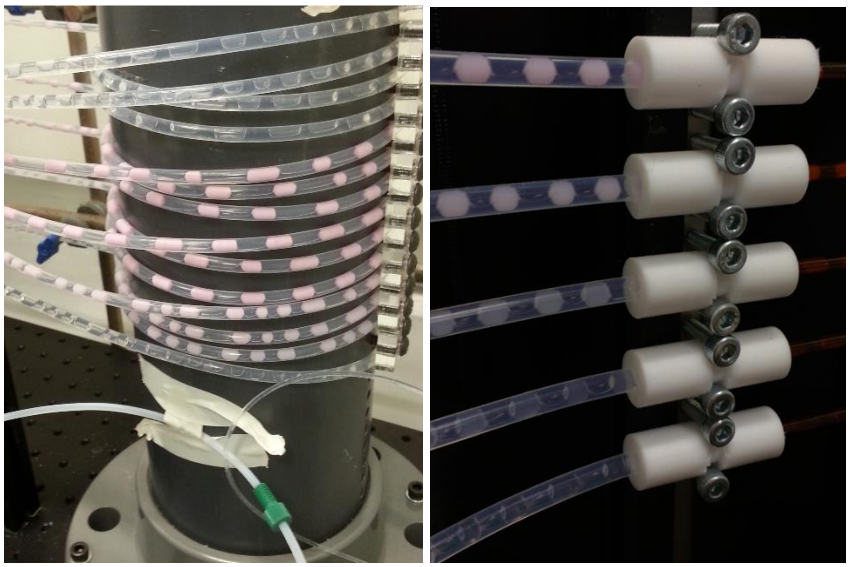

Figure.IV.11 KRAIC-D PiC experiments for $Fe(BF_4)_2 \cdot 6H_2O$ concentrations of 0.08 g/mL (left) and 0.07 g/mL (right) showing the difference of phases and colour intensity of the solution at medium flow rate.

IV.3.4.iii PiC Beamtime experiments

For each run using the KRAIC-D on I11 the residence time was measured in the middle of each window. All times measured are reported in Table.IV.5.

Table.IV.5 Residence time and windows timing (min:sec) for each run performed with active beam. 'medium', 'slow' and 'fast' flow rate parameters are described in Table.IV.3. All experiments are done with a concentration of 0.10 g/mL for 1,2,4-H triazole.

Concentration $Fe(BF4)_2 \cdot 6H_2O$ (g/mL)	Flow rate	Experiment number	W1	W2	W3	W4	W5	RT	Pink Slugs at Outlet
0.07	**Med**	**PiCKD 1**	**01:40**	**05:02**	**08:20**	**11:40**	**15:03**	**18:17**	**19:47**
0.08	**Med**	**PiCKD 2**	**01:42**	**05:10**	**08:15**	**11:32**	**15:03**	**18:17**	**19:35**
0.08	**Med**	**PiCKD 3**	**01:38**	**05:00**	**08:18**	**11:31**	**14:42**	**17:42**	**19:38**
0.08	**Slow**	**PiCKD 4**	**01:54**	**05:50**	**09:39**	**13:26**	**17:17**	**20:41**	**22:45**
0.08	**Fast**	**PiCKD 5**	**01:16**	**03:56**	**06:31**	**09:05**	**11:39**	**14:07**	**15:10**
0.10	**Med**	**PiCKD 6**	**01:30**	**04:35**	**07:39**	**10:40**	**13:43**	**16:40**	**18:09**
0.08	**Fast**	**PiCKD 7**	**01:18**	**03:52**	**06:32**	**09:06**	**11:44**	**14:07**	**15:01**

Table.IV.6 Stochiometric Ratio $[Fe(BF_4)_2\ 6H_2O]$ /[HTrz] for PiCKD experiments

Experiment number	$[Fe(BF_4)_2\ 6H_2O]$ (mmol/mL)	[HTrz] (mmol/mL)	Stochiometric Ratio $[Fe(BF_4)_2\ 6H_2O]$ /[HTrz]
PiCKD 1	0.21	1.45	1/7
PiCKD 2	0.24	1.45	1/6
PiCKD 3	0.24	1.45	1/6
PiCKD 4	0.24	1.45	1/6
PiCKD 5	0.24	1.45	1/6
PiCKD 6	0.30	1.45	1/5
PiCKD 7	0.24	1.45	1/6

For these experiments the X-ray exposure time for a single frame was 100 ms, but each set of exposures was reduced from 100 in the UBA experiments to 50 exposures of 100 ms for PiC, to reduce the impact of the X-ray beam on the coating of the Kapton® windows. The number of exposure sets are displayed on Table.IV.7; a distance of 0.5 mm was travelled between each exposure set. On PiCKD 1, the concentration of $Fe(BF_4)_2 \cdot 6H_2O$ was 0.07 g/mL. At 8 min 20 s a colourless opaque solution was observed 2-3 cm before the second window. After several minutes the top (5^{th}) window showed wetting issues in the middle. This is not due to the exposure of the window to the X-ray beam; the first window was exposed for the same period of time and did not have the same wetting issue. Instead, it could be due to damaging the coating while manipulating or changing the Kapton® tubing between the test and the actual beamtime.

For PiCKD 2, the concentration of $Fe(BF_4)_2 \cdot 6H_2O$ was changed to 0.08 g/mL. It appears for this run that each slug has a higher concentration of particles at the back of the slug with respect to the direction of the flow. This could be due to the effect of the mixing on the nano particles in the slug, related to the mixing studies in Chapter III; further investigation on particle motion will be discussed in Chapter VII. This concentration gradient could lead to an inhomogeneous particle size distribution during the recovery. The computational fluid dynamic (CFD) study carried out for segmented flow in Chapter III showed asymmetry in the liquid flow field of particles at different parts of the slug; the rear side of the slug had the highest velocity with the front of the slug second and the middle significantly lower in velocity. This shows the importance of carrying out CFD study for flow experiments, and including particles in those CFD studies. The behaviour of PiC particles in liquids will be further studied in Chapter VII where DCS and AUC was used to measure particle behaviour in liquids.

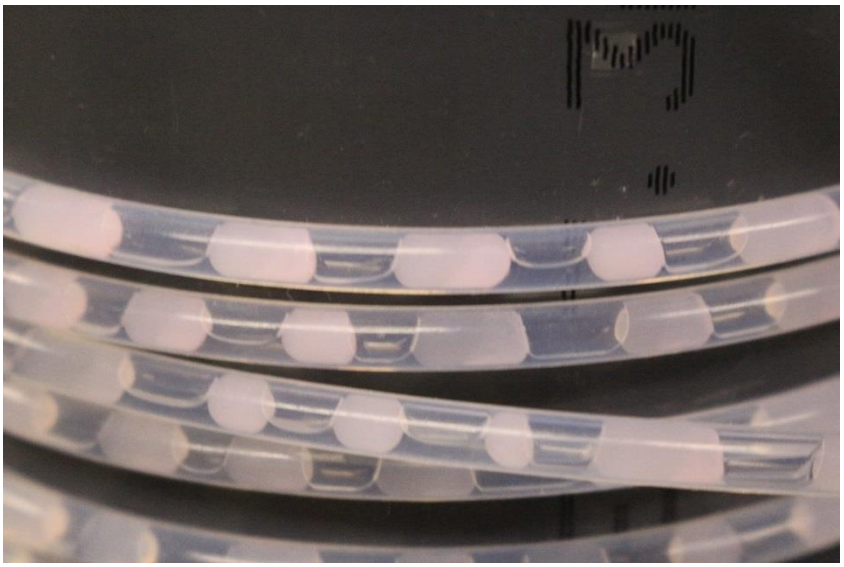

Figure.IV.12 $[Fe(Htrz)_2(trz)](BF_4)$ slugs inside the KRAIC-D showing a change in colouration in some parts of the slugs.

After this run, fouling was observed on the Y-piece, this is presumably due to some of the reagent staying inside the Y-piece due to a dead zone inside the geometry or adhesion to the polypropylene surface. The resultant change of wetting on the mixer gives alternating slugs of the two reagents, not mixing the two aqueous solutions. For the following experiments the Y-piece was changed to PP T-piece which resulted in better consistency of segmentation.

During PiCKD 4 to 5 the concentration of $Fe(BF_4)_2 \cdot 6H_2O$ was 0.08 g/mL and slight fouling was observed at the T-piece. PiCKD 4 was carried out with slow flow rate and PiCKD 5 with fast flow rate. For PiCKD 5 the onset of growth was in its final pink phase before 5^{th} window and in the

intermediate phase before the 4th window. The change in time observed for the onset of growth is mostly due to the change in flow rates and was chosen to see if detection was possible for the first windows with a low number of particles.

For PiCKD 6 the concentration of $Fe(BF_4)_2 \cdot 6H_2O$ was changed to 0.10 g/mL. During collection of the data it was noticed that the remaining 1,2,4-H triazole solution was twice the volume of $Fe(BF_4)_2$ $6H_2O$ solution due to pumping issues. This would explain the differences between the slugs in terms of crystallisation where the intermediate and final phase of the reaction were not present at the same point in the KRAIC-D and also that in some regions of the KRAIC-D some slugs were longer than others. Both of these events were present in the previous PiCKD 5 run, but not as pronounced as in run 6. After stopping PiCKD 6, the volume of the two solutions were 80.5 mL for $Fe(BF_4)_2 \cdot 6H_2O$ and 168 mL for 1,2,4 H-Triazole. The pumps were then cleaned and after calibration the flow rates of the pumps were found to be accurate once more. For the following runs the pumps were cleaned with IPA after each experiment. After the cleaning, PiCKD 7 was commenced with a concentration of iron (II) tetrafluoroborate of 0.08 g/mL. The progression of crystallisation returned to those found during the first trials done prior to beamtime with an intensely mixed system.

For beamtime runs scanning electron microscopy (SEM) and dynamic light scattering (DLS) were carried out offline to check the particle size and shape of the final product material.

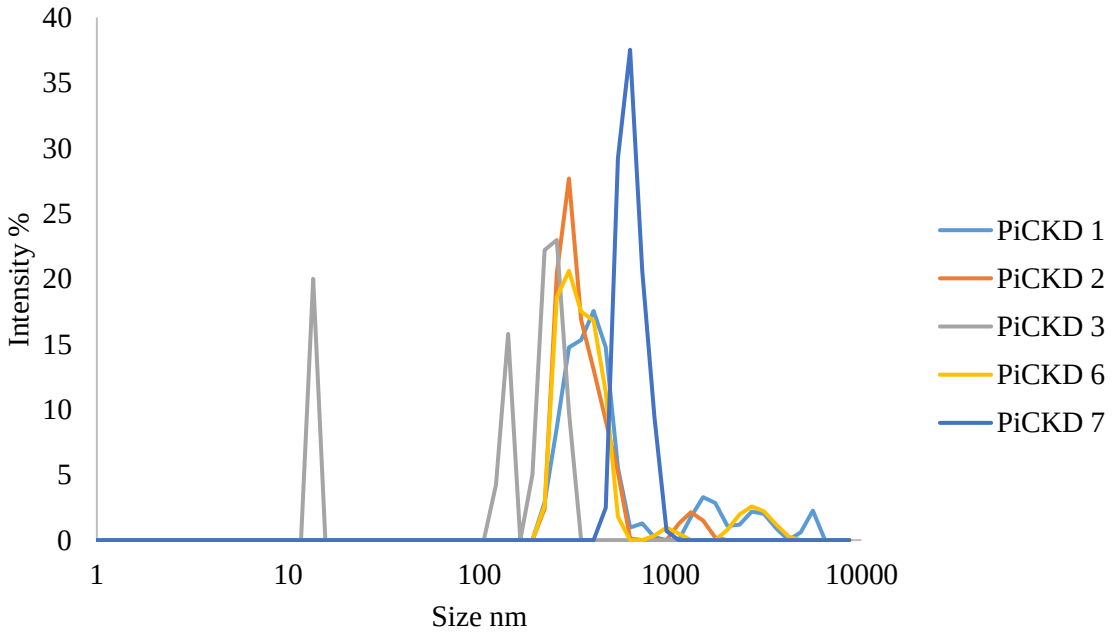

Figure.IV.13 DLS analysis of product from beamtime runs PiCKD 1, 2, 5, 6 and 7 in the KRAIC-D on I11.

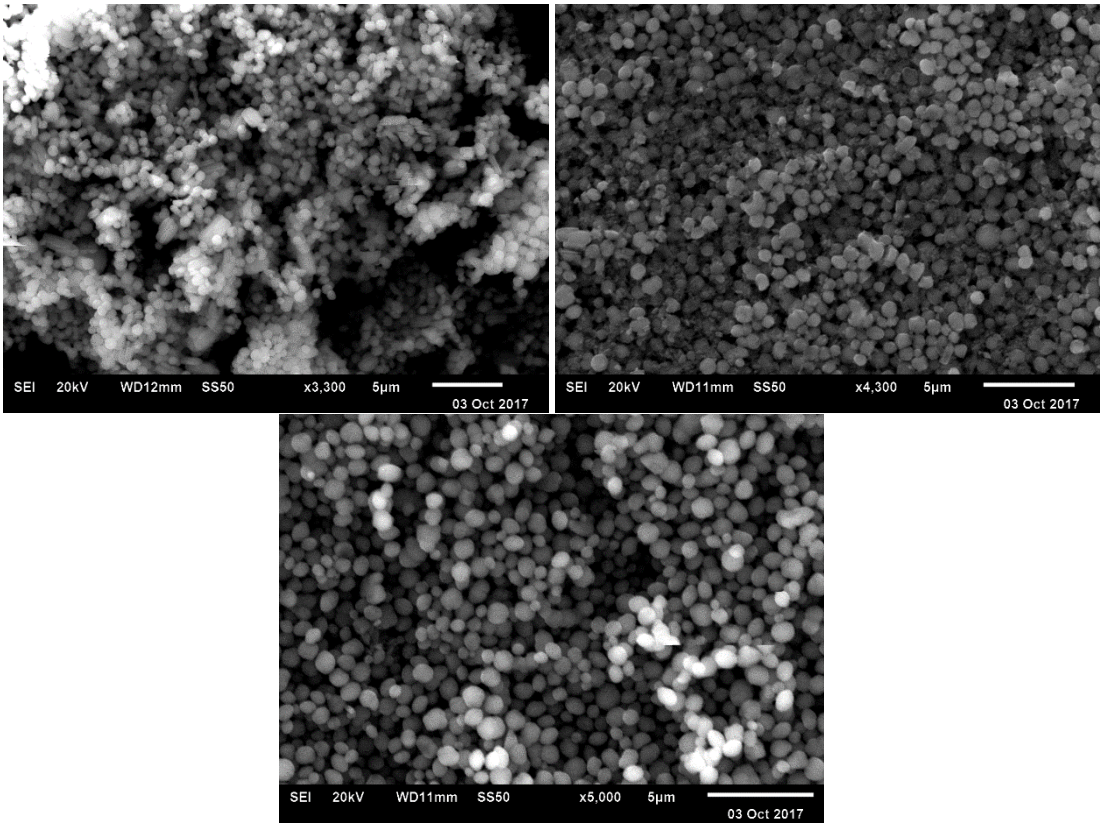

Figure.IV.14 SEM of beamtime runs PiCKD 5, 6 and 7 carried out in the KRAIC-D.

As can be seen in Figure.IV.13 and Figure.IV.14, the particles obtained were different from those previously obtained in the KRAIC run in Chapter III. Here spherical particles are obtained and not rod-shaped crystals; the concentration of reagents was higher than the experiments presented in Chapter III so this shape change is expected. Offline PXRD has confirmed that PiC is the obtained product (Figure.IV.15) The DLS plot (Figure.IV.13) shows a range of particle sizes generally ranging from 150 nm to 1000 nm across the runs. From the SEM images, PiCKD 5 and 6 show particles ranging around 150 to 400 nm, PiCKD 7 shows bigger average particles sizes (around 400 to 600 nm). The size difference between the three runs could be due to the change in flow rate, PiCKD 5 and 6 are at 1.6 mL/min and run 7 at 2.4 mL/min for the solutions. A fast flow rate will induce a faster mixing rate and intensity inside each slugs (as seen in CFD simulation in Chapter III) which leads to particles being able to react more in the same time frame and creating larger particles.

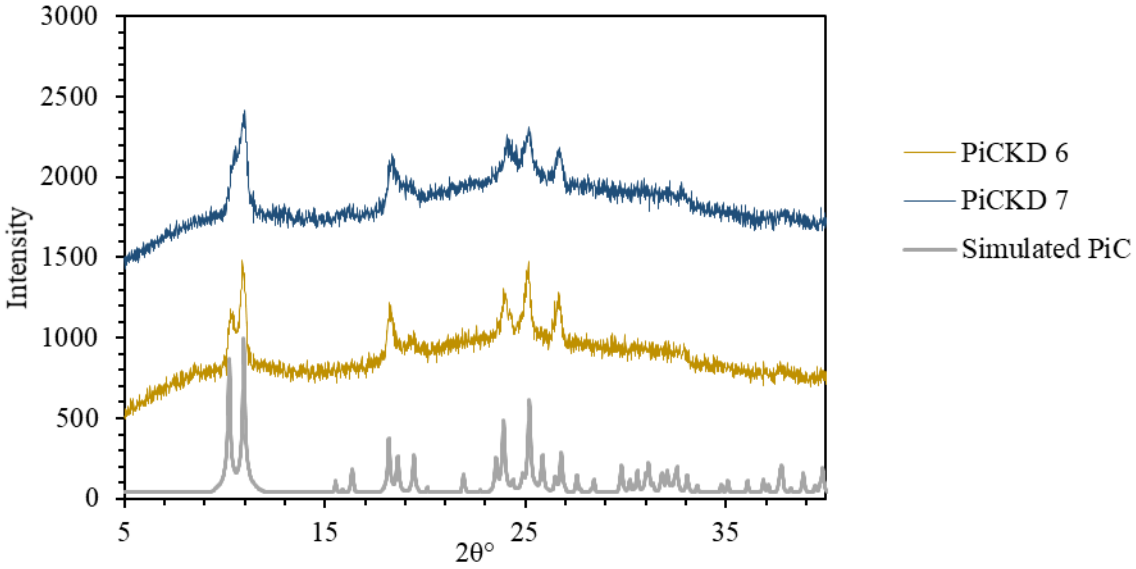

Figure.IV.15 PXRD of PiC from PiCKD 6 and 7 (window 5) fro product from the KRAIC-D/I11 beamtime, compared to simulated powder pattern from Grosjean *et al.* [14]

Batch trials at the same concentrations have been carried out for PiCKD 5, 6 and 7 and the same particle shape and sizes are observed (Figure.IV.16). It is possible that the high concentration affects the growth of the compound inside each slug, the reaction happening so fast that the crystals do not have the time to grow in their usual rod form. Further work using SEM and electron diffraction to study the shape behaviour of $[Fe(Htrz)_2(trz)](BF_4)\cdot H_2O$ will be discussed in Chapter VII.

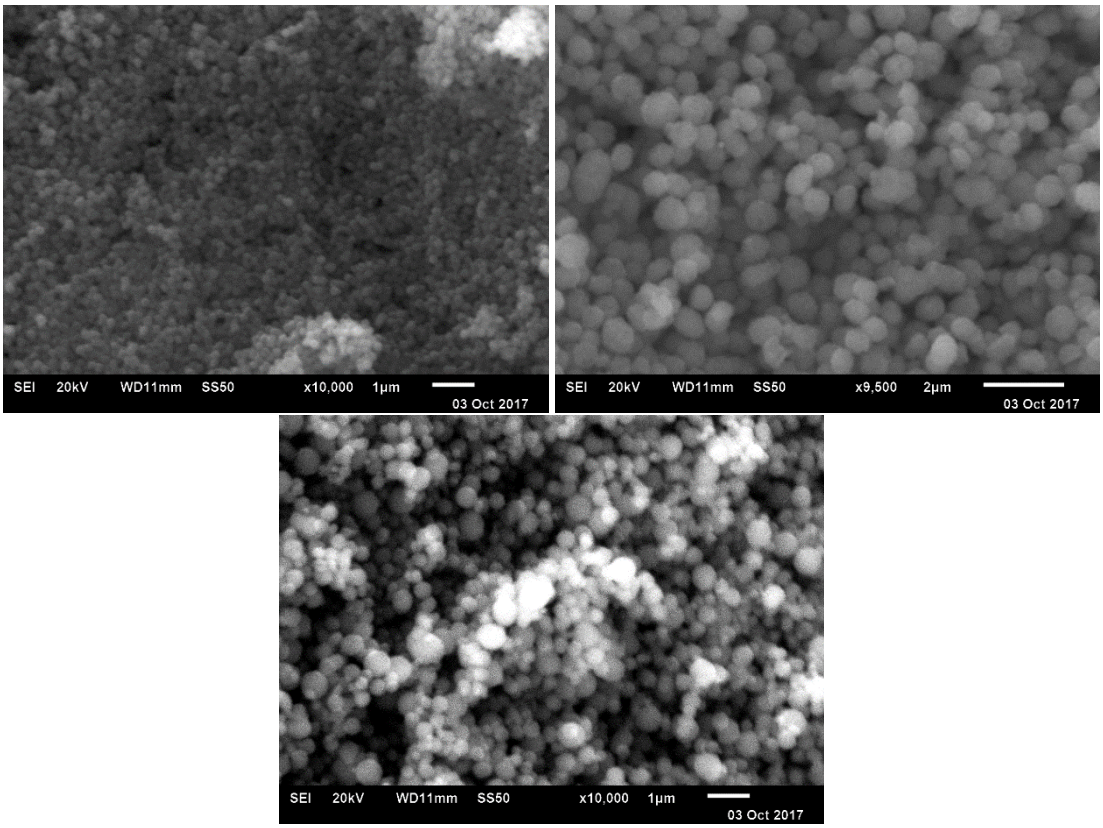

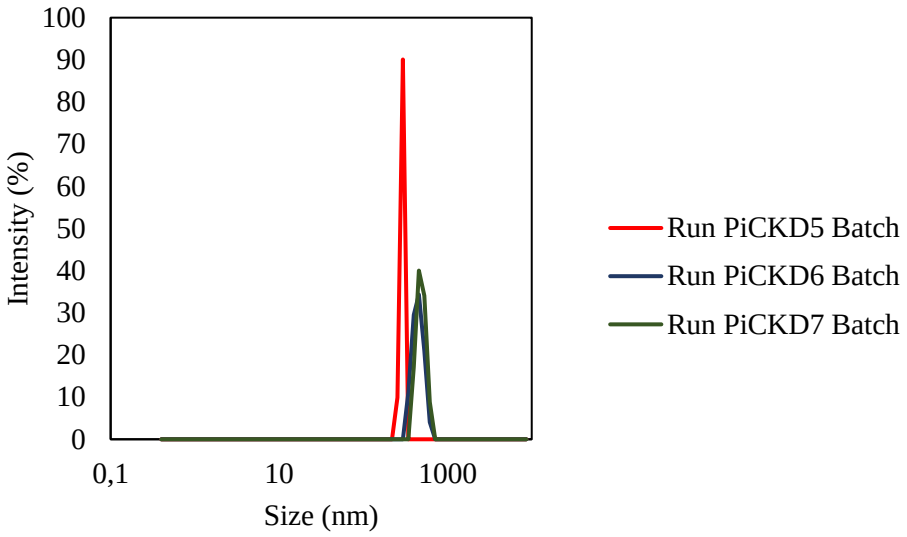

Figure.IV.16 (top) SEM of products from batch experiments using PiCKD 5, 6 and 7 concentrations and (bottom) DLS results obtained.

DLS and SEM analysis of PiC particles produced in batch synthesis give similar results with the spherical material appearing and a particle size ranging from 150 to 700 nm depending on the sample (see supplementary info **CDCh3-2**).

Unfortunately the *in situ* KRAIC-D diffraction patterns of $[Fe(Htrz)_2(trz)](BF_4)\cdot H_2O$ (Htrz = 1,2,4-triazole) were difficult to analyse. Some broad events were present but did not allow the phase to be identified. During the experiment each window was analysed two times with four scans for each analysis going from the bottom window, window 1, to the last window, window 5. This gave several diffraction patterns (Figure II.17); the plots in this Figure can be related to the relevant diffraction patterns shown in Table.IV.7. The 2D patterns shown in Figure II.18 emphasise the lack of sharp crystalline diffraction in these experiments.

Table.IV.7 Position and Run for each diffraction pattern obtained.

Data Number	PiCKD	Window
20357-60	1	5
20340-43	1	5
20396-400	2	2
20419-22	3	4
20443-6	4	3
20585-9	7	5

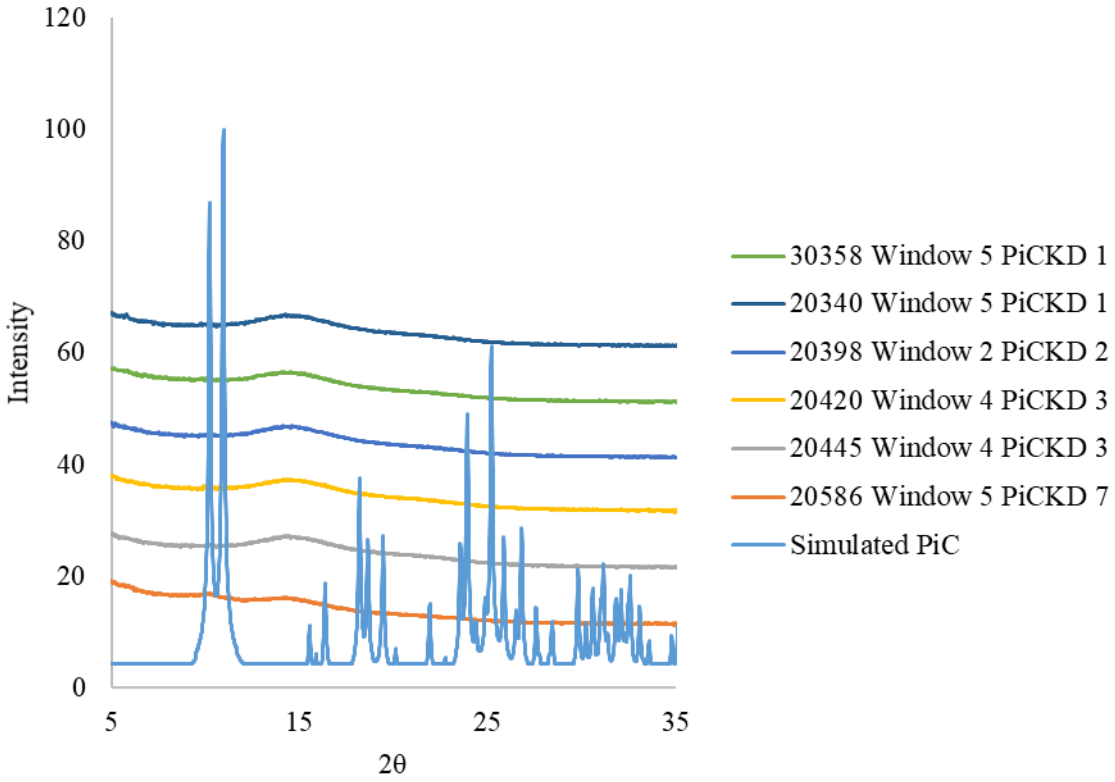

Figure.IV.17 Diffraction patterns obtained during KRAIC-D run compared to simulated PiC pattern.

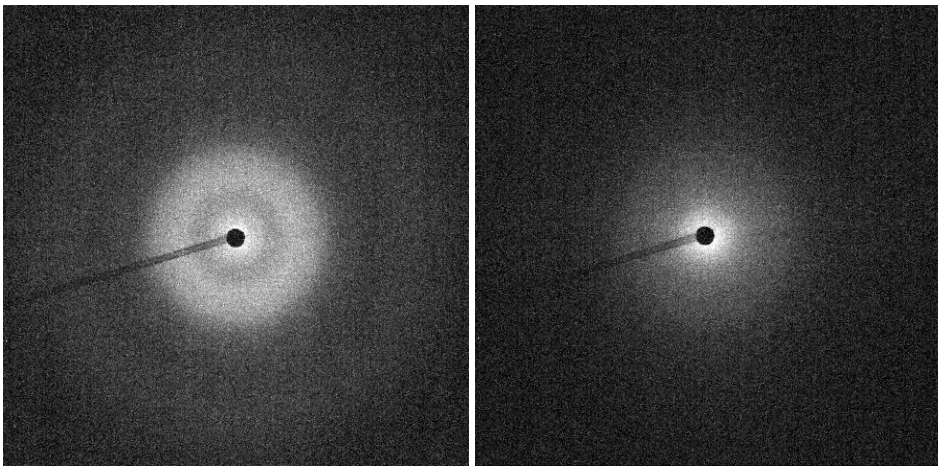

Figure.IV.18 2D Diffraction pattern obtained for 20586(left) and 20358 (right).

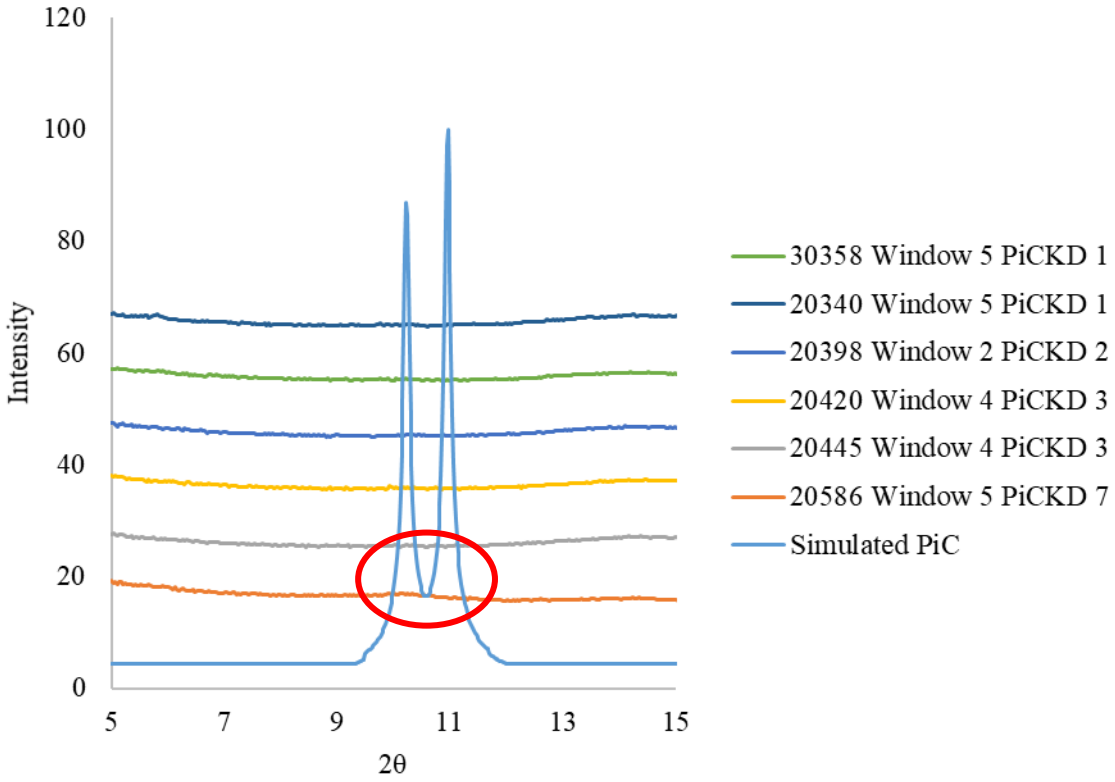

Figure.IV.19 PXRD patterns obtained during KRAIC-D run compared to simulated PiC pattern from 5 to 15°.

On Table.IV.7 is displayed the position parameters of the beam alignment for each of the signals obtained. Figure.IV.17 and Figure.IV.19 show at different scale the XRD data obtained for several experiments, patterns are displayed only where a potential similar (if broad) peak has been observed. It was difficult even after background removal to see convincing signals from the experiments. It appears that the most promising region is between 10-11° where a hump could correspond to the 10.5° and 11.2° peak of $[Fe(Htrz)_2(trz)](BF_4)\cdot H_2O$, seen in windows 2, 4 and 5. On other windows for different experiments no significant signal is apparent. This could be due to the nanoscale of the material or that it is not crystalline enough for the beam at this timescale. More beamtime experiments would be needed to get better results, and other analysis such as *in situ* Raman will be presented later in this Chapter.

IV.3.5 Beam damage on Kapton® Tubing

During the experiments it has been seen that the Kapton® tubing for the windows started to lose its hydrophobic properties meaning that the Aquapel® was removed during the flow. After some investigation it was discovered that the beam of the synchrotron was destroying the Aquapel® which is at the surface of the tubing and creating small hydrophilic areas disrupting the flow inside each window after a certain amount of exposure time.

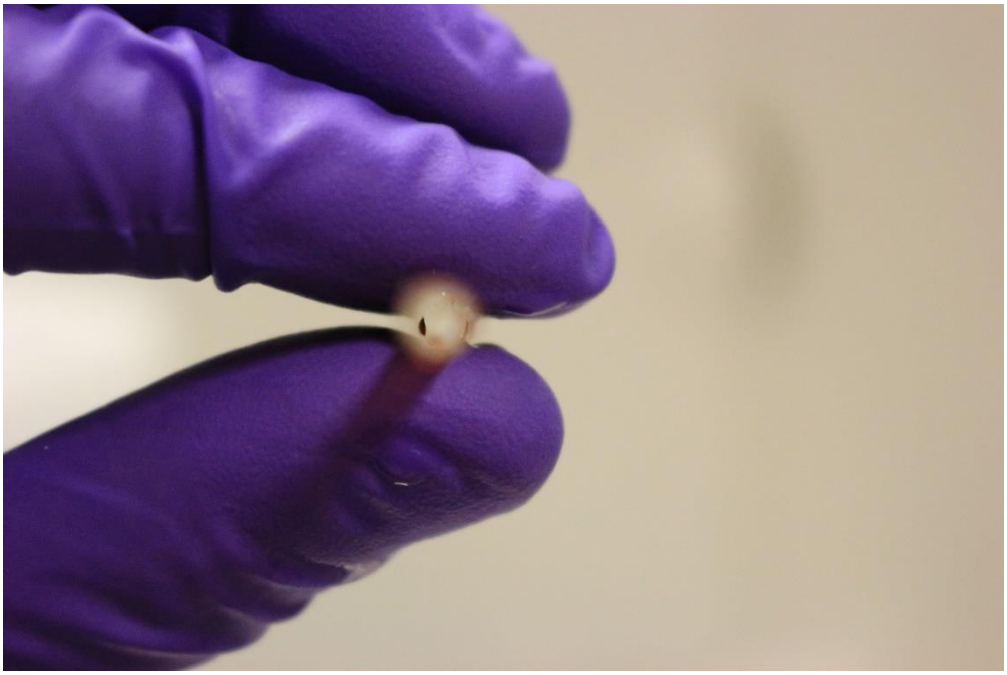

Figure.IV.20 Tubing wetting after beam time experiment, the black spot is a water droplet stuck onto the damaged portion of the tubing.

As can be seen in Figure.IV.20 the tubing shows a change in wetting properties at a specific point. To assess this some water was poured through the tubing showing that some droplets were staying on the inside of the tubing on the less hydrophobic area where the Aquapel® was removed. To check the damage SEM was carried out on the Kapton® tubing (Figure.IV.21). This shows the Kapton® tubing recovered from the 1st window used for the first UBA beam time experiment under SEM and the damage caused by the synchrotron beam Spectral analysis with Energy Dispersive X-ray (EDX) was done to see if the Aquapel®, which is fluorine based, was still present in the damaged areas. The spectra, Figure.IV.21, show that fluorine is still present in both places but the surface is also deeper as can be seen on the SEM Figure.IV.22. Less fluorine is thus present, and could cause flow disruptions which could mean that the coating has been removed during the exposure. As Galden, a fluorinated fluid, was flowed through the tubing some fluorine might have adhered to the surface in those "holes" during the experiments. The depth of those marks is around 1-5 µm (calculated approximately from Figure.IV.22. The silicon present on the tubing could be due to the reference or the silicone rubber used to fix the Kapton® tubing on the unions. Aquapel® : $C_{16}H_{19}F_{17}O_3Si$, Galden® : $C_{50}F_{102}O_{16}$ and Kapton® : $C_{22}H_{10}N_2O_5$

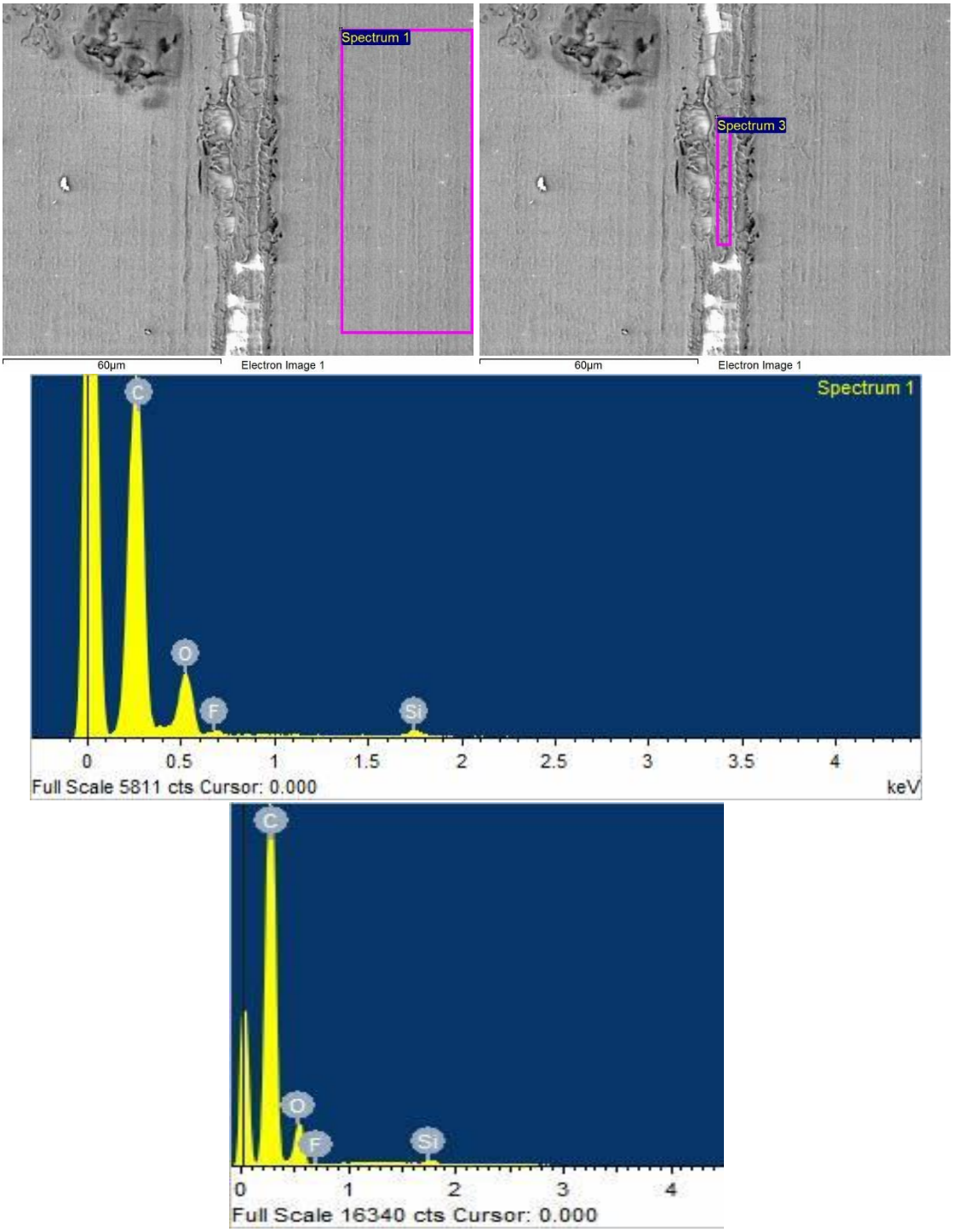

Figure.IV.21 SEM of Kapton® tubing showing the damage done by the beam. The EDX spectral analysis of different tubing points is also displayed.

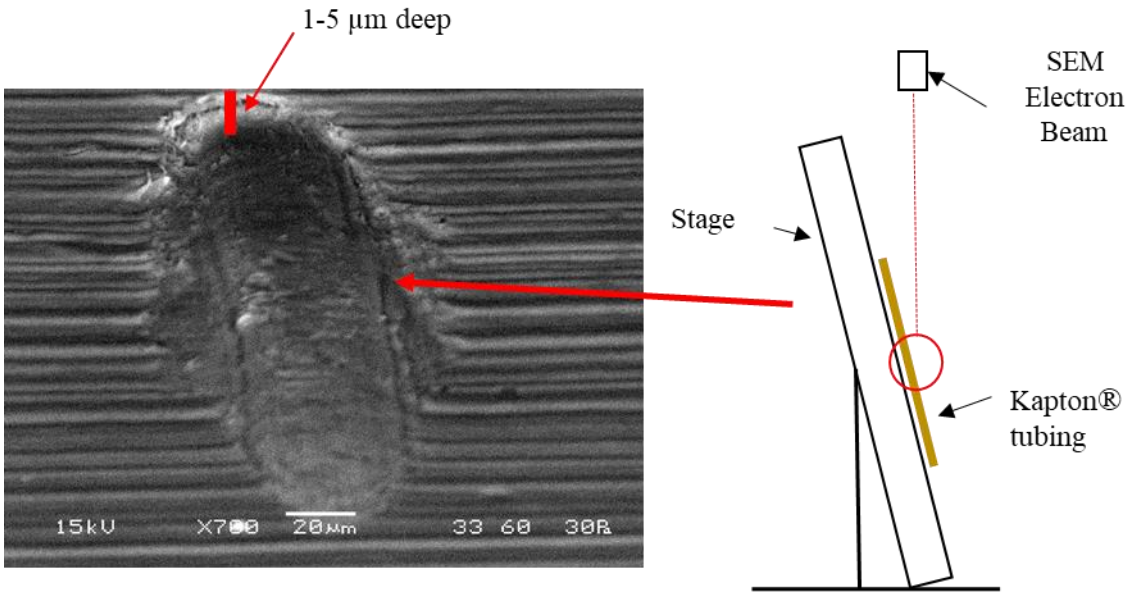

Figure.IV.22 SEM of damage on Kapton® tubing with stage rotated at 80° to give a horizontal view of the tubing.

This problem is difficult to avoid due to the Kapton® tubing being hydrophilic, it needs to be coated with Aquapel® or another compound to avoid slug disruption during the experiments.

IV.3.6 *In situ* Raman analysis of $[Fe(Htrz)_2(trz)](BF_4)\cdot H_2O$ synthesis using the KRAIC-R

IV.3.6.i Introduction and set-up

As stated previously, it is suspected that during the reaction for the synthesis of PiC there is a change of spin states or an intermediate that could present the same colouration as the high spin (HS) state, this change appears as a change in solution colour during the synthesis. It has been reported by Guillaume *et al.* and Tobon *et al.* that the Raman spectrum of the compound changes when the Fe centres cross the low spin (LS) to HS transition, due to external vibrations involving the metal-ligand or ligand-metal-ligand bending vibrations.[33,35,203] It is also noted that the Raman signal diminishes in the HS state of PiC. Investigating this in flow was possible using a confocal Raman probe from Kaiser Optical Systems with the KRAIC and segmented flow. As shown above, employing the KRAIC-D at Diamond Light Source, it was not possible to observe a convincing diffraction pattern from the nanoparticles obtained at different points of the crystalliser *via* the Kapton® windows. Using Raman as a different technique to analyse the change during the reaction might thus be able to give more information on the synthesis process for $[Fe(Htrz)_2(trz)](BF_4)\cdot H_2O$.

The confocal probe itself was set up at different points of the KRAIC probing different points of the reaction (Figure.IV.23 below). A custom optical box was placed at different parts of the KRAIC, one at the end of the flow stream before the outlet (1443 ± 5 cm) and one after the first coil (486±5 cm). Preliminary experiments were done in order to observe the white intermediate phase at the box after the first coil and final pink coloured product at the outlet. Table.IV.8 shows the flow parameters used to obtain an appropriate gradient of reaction between the Raman probe points. The experiment was done with the concentration and flow rate parameters from the previous Diamond experiment PiCKD 1 (Table.IV.8) which had shown to display the unknown intermediate white phase at 5 m of crystalliser length (Raman probe point 1).

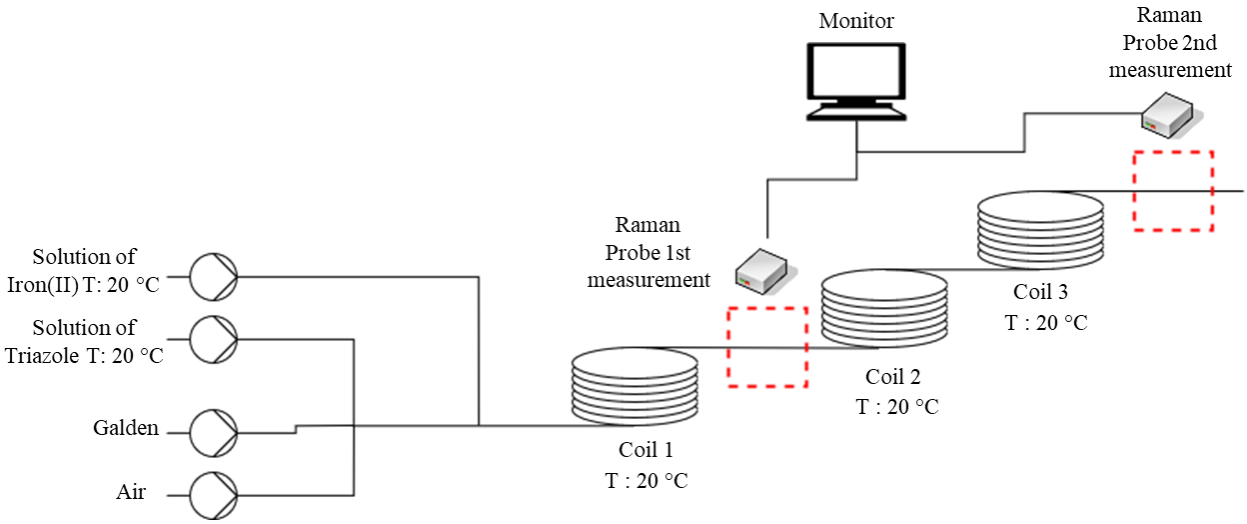

Figure.IV.23 Set-up of the *in situ* Raman analysis using the KRAIC ("KRAIC-R").

Table.IV.8 Parameters used for the KRAIC Raman combination during the synthesis ofPiC

	$Fe(BF_4)_2$ $6H_2O$ (mL/min)	**1,2,4,H Triazole (mL/min)**	**Galden flow rate (ml/min)**	**Air flow rate (mL/min)**	**Total flow rate (mL/min)**	**Concentration $Fe(BF_4)_2$ $6H_2O$ (g/100mL)**	**Concentration 1,2,4,H Triazole(g/100mL)**
Flow rate	1.6	1.6	2.1	4.2	9.5	7	10.79

IV.3.6.ii Results and discussions

Because segmented flow is employed, the Raman probe will detect signals from the FEP tubing, air, Galden and the solution. A background spectrum was therefore first taken to indicate the spectra for the variables other than the sample solution. On Figure.IV.24 is shown the background for the FEP tubing with air and the thin film of Galden surrounding the slug. Each time a slug of Galden goes in front of the probe the fluorescence rises, giving information on which phase within the slug flow the data represent.

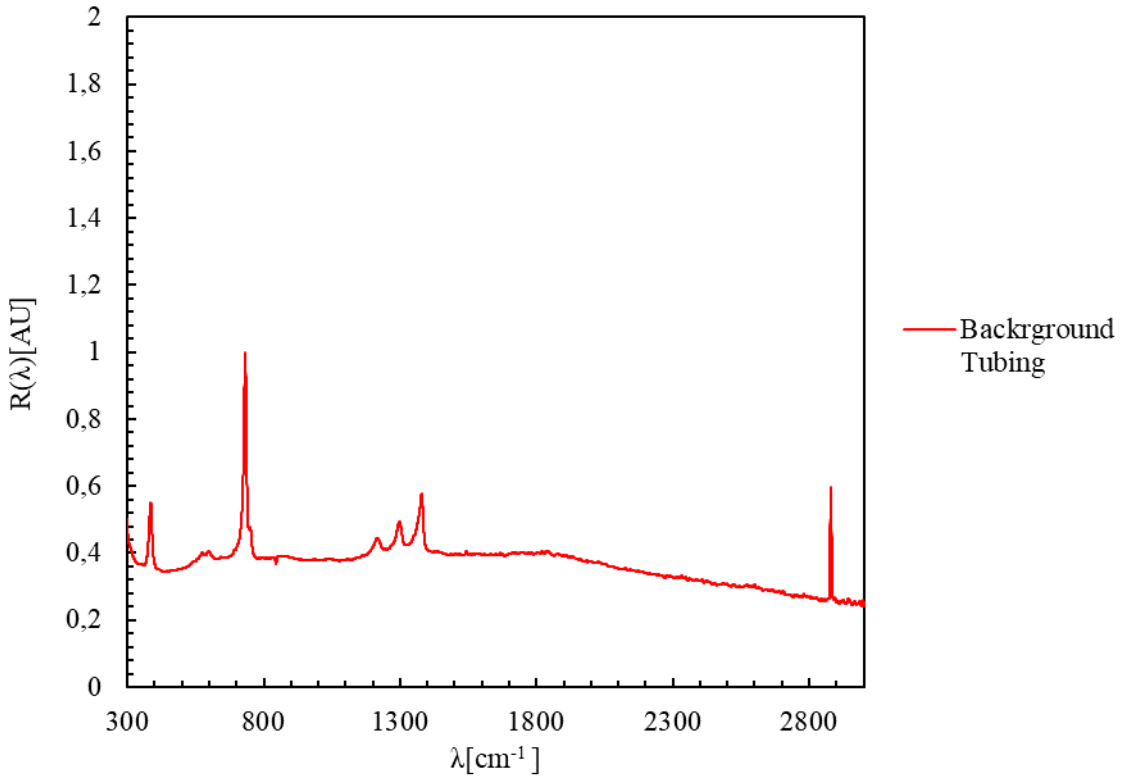

Figure.IV.24 Background Raman spectrum for fluorinated ethylene propylene (FEP) tubing

The Kaiser® confocal Raman probe used was set at 500 ms acquisition and with four accumulations for all experiments. All data were recorded every 15 sec. During the experiments different Raman spectra can be seen at the outlet and after the first coil. Beforehand reagent spectra were taken (Figure II.25) in order to see if unreacted starting materials were still present at different points in the KRAIC.

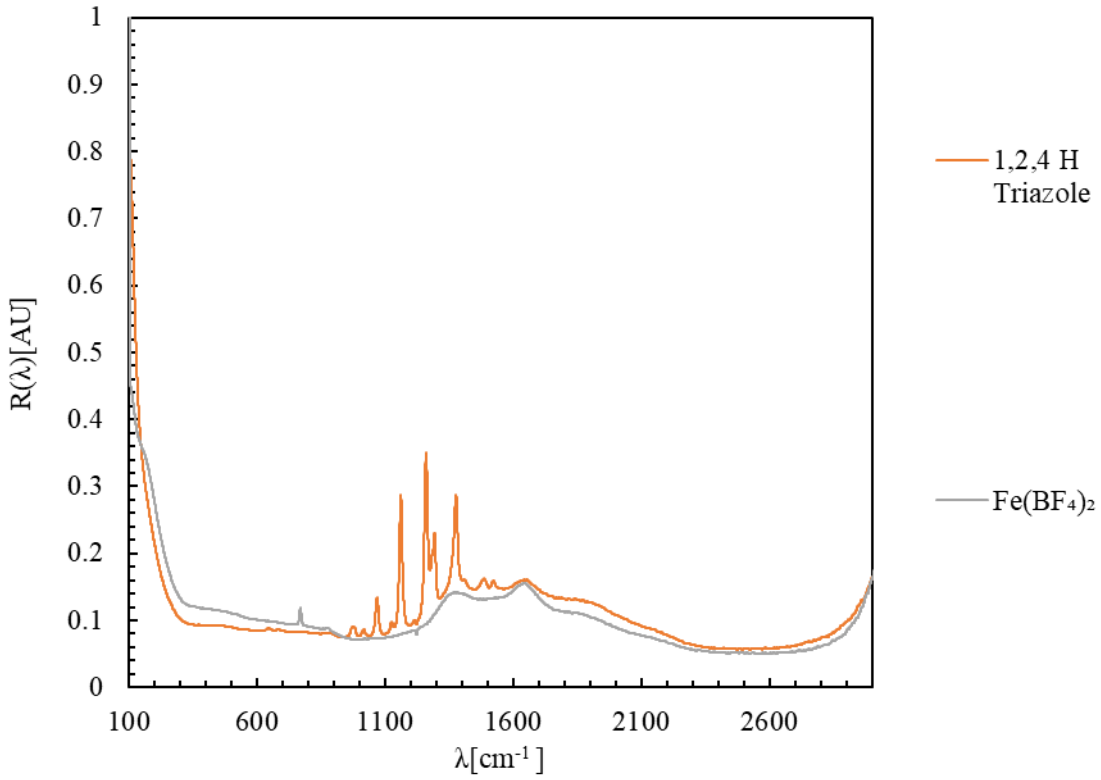

Figure.IV.25 1,2,4-H triazole and iron (II) tetrafluoroborate hexahydrate Raman spectra.

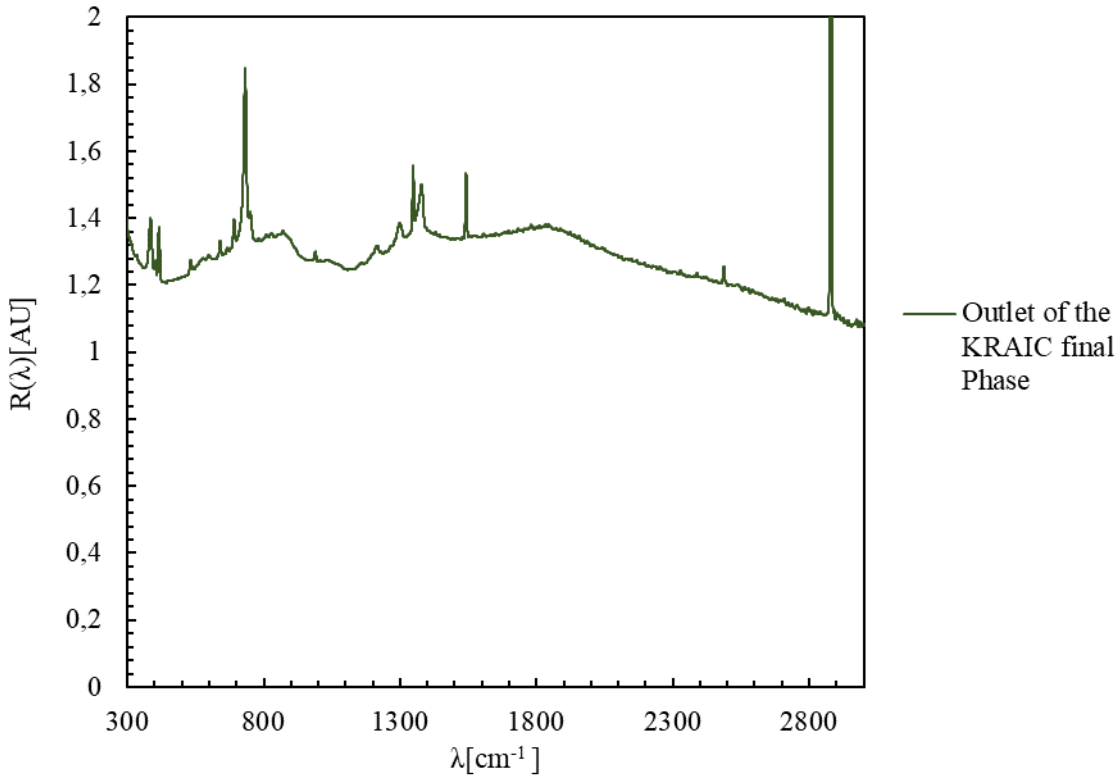

Figure.IV.26 Raman spectrum of PiC from the outlet of the KRAIC.

Figure.IV.26 shows the spectrum of the final pink phase at the end of the KRAIC, while Figure.IV.27 shows the white intermediate phase spectrum. These show some differences which will be discussed.

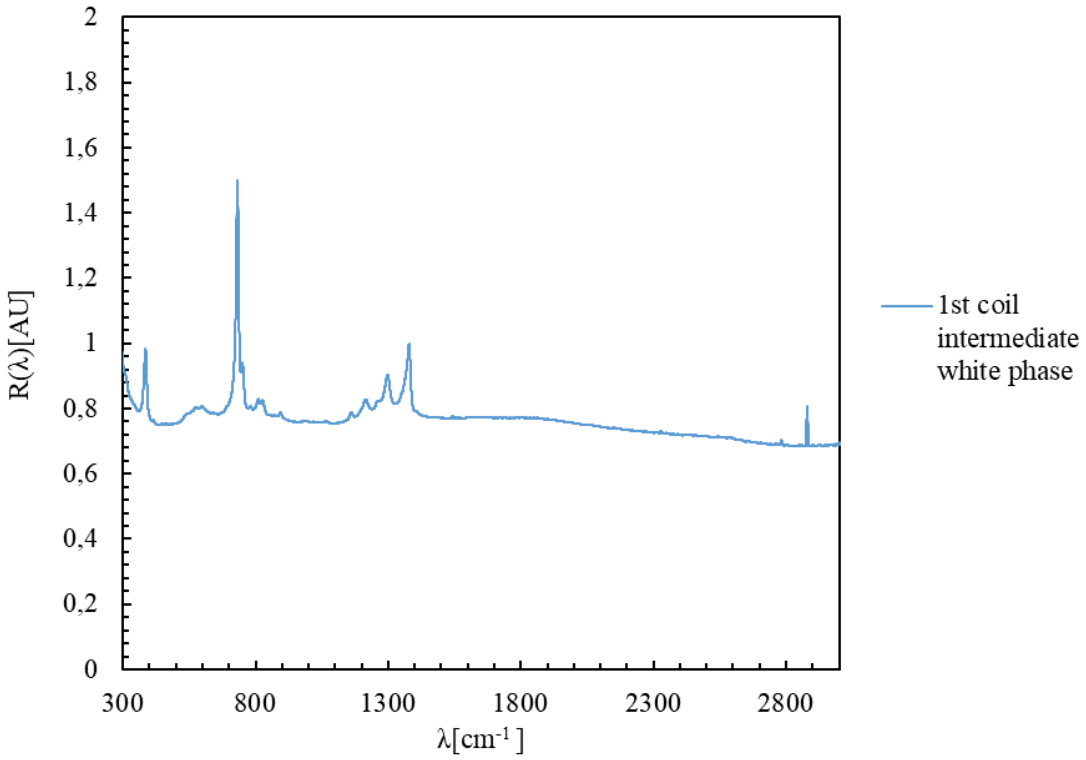

Figure.IV.27 Raman spectrum of the "white" initial phase obtained during the synthesis of PiC inside the KRAIC.

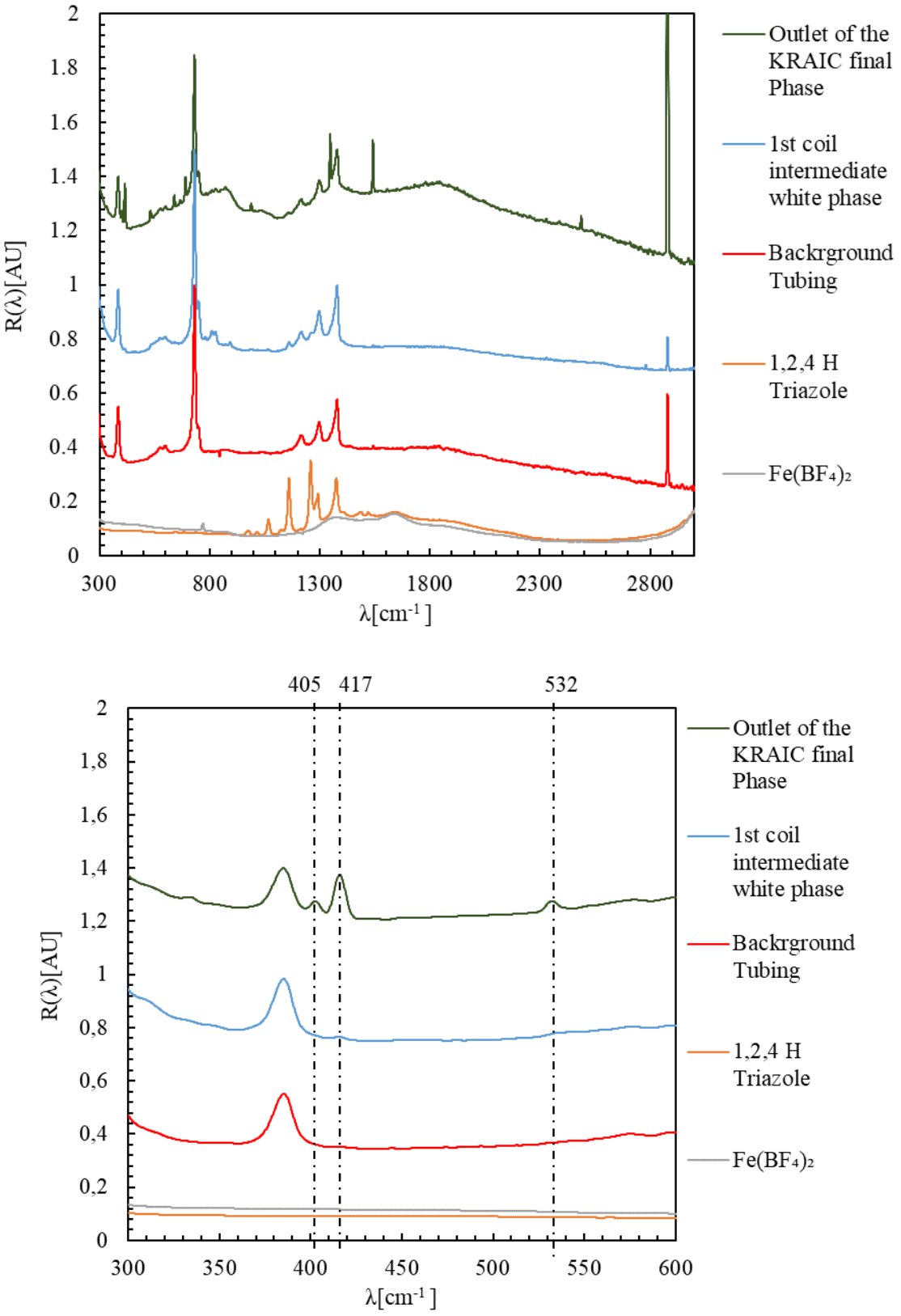

Figure.IV.28 Raman spectra comparison between 1,2,4 H triazole , iron (II) tetrafluoroborate hexahydrate , final and intermediate phase of $[Fe(Htrz)_2(trz)](BF_4)\cdot H_2O$ (PiC). (top) full pattern, (bottom), expanded 300-600 cm^{-1} wavenumber region. Peak differences at vertical lines 405, 417 and 532 cm^{-1}.

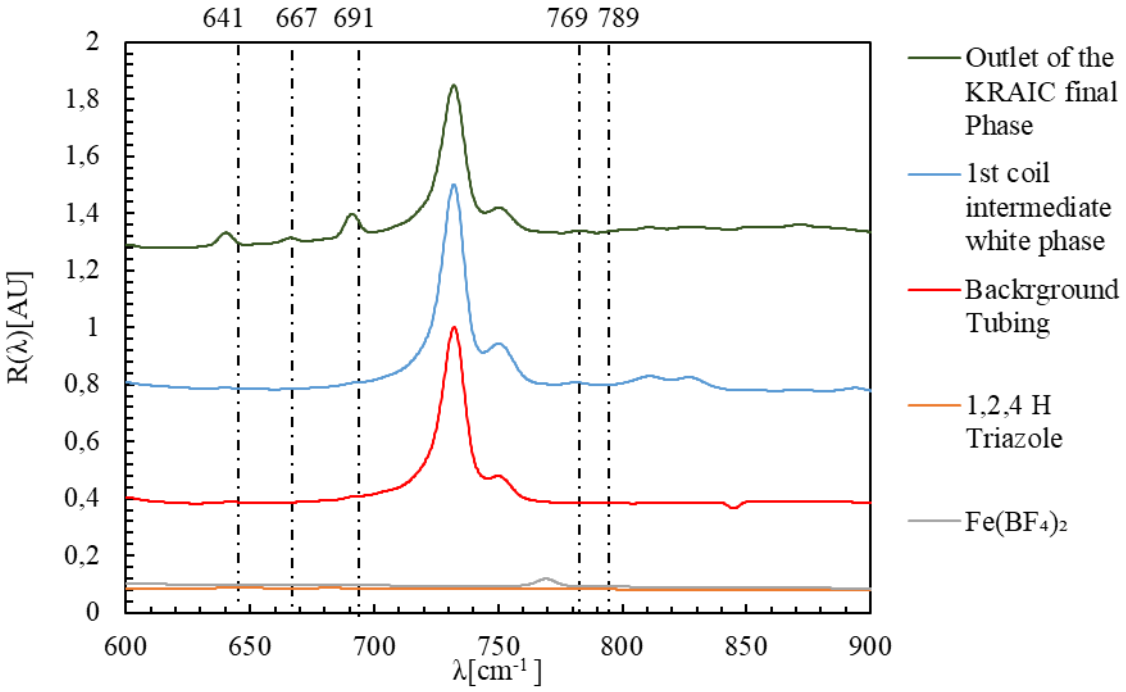

Figure.IV.29 Raman spectra comparison between 1,2,4 H triazole , iron (II) tetrafluoroborate hexahydrate , final and intermediate phases of $[Fe(Htrz)_2(trz)](BF_4)\cdot H_2O$ 600 to 900 cm^{-1} wavenumber. Peak differences at vertical lines 641, 667, 691, 769 and 789 cm^{-1}.

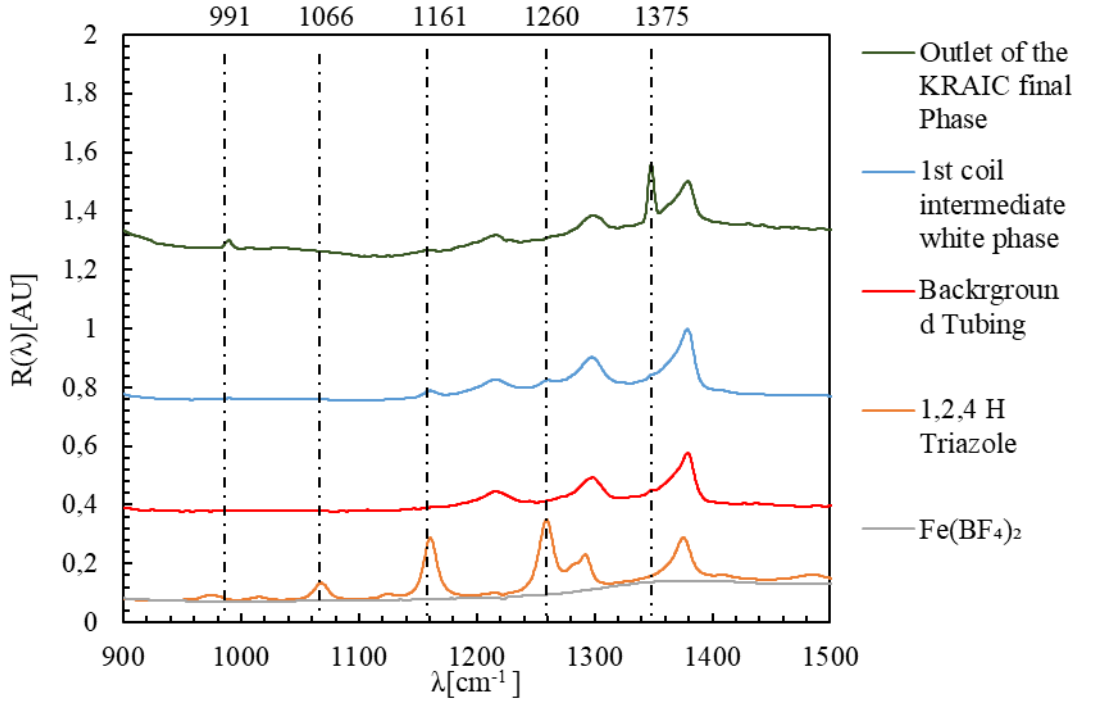

Figure.IV.30 Raman spectra comparison between 1,2,4 H triazole , iron (II) tetrafluoroborate hexahydrate, final and intermediate phase of $[Fe(Htrz)_2(trz)](BF_4)\cdot H_2O$ 900 to 1500 cm^{-1} wavenumber. Peak differences at vertical lines 991, 1066, 1161, 1260, 1375 cm^{-1}.

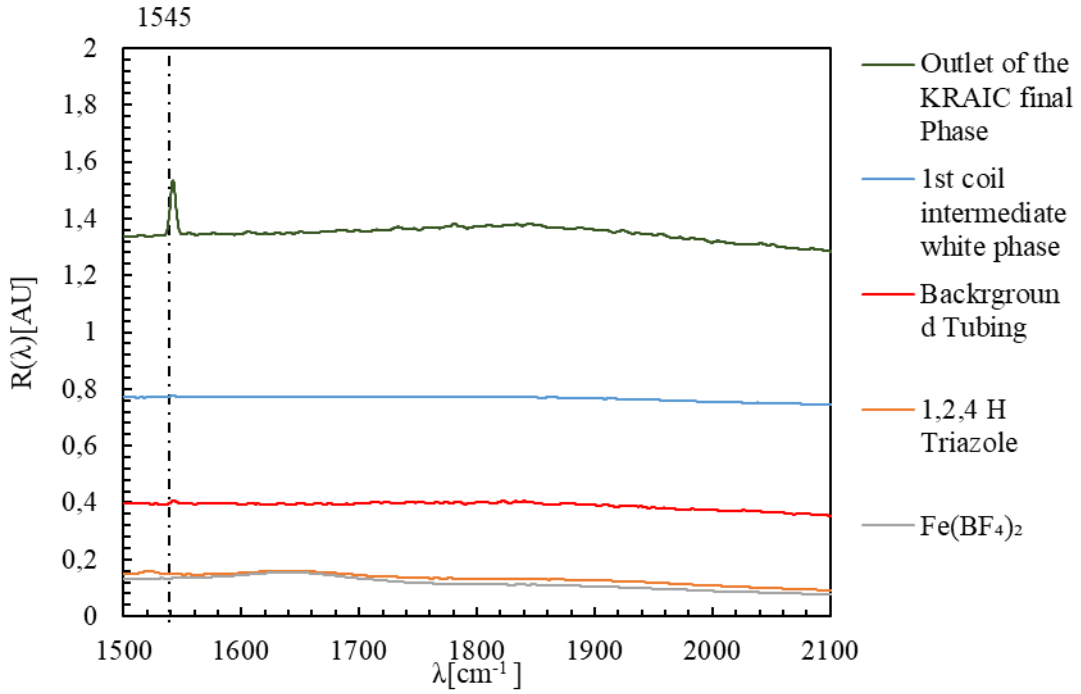

Figure.IV.31 Raman spectra comparison between 1, 2,4 H triazole, iron (II) tetrafluoroborate hexahydrate, final and intermediate phases of $[Fe(Htrz)_2(trz)](BF_4)\cdot H_2O$ 1500 to 2100 cm^{-1} wavenumber. Peak differences at vertical lines at 1545 cm^{-1}.

Figure.IV.26 to Figure.IV.31 show the differences in Raman spectra for the various detection points of the PiC reaction within the KRAIC at different values of wavelength. It is observed that several 1,2,4-H-triazole and iron (II) tetrafluoroborate hexahydrate peaks are still present in the intermediate and final phase but some new ones appear in the different synthesis steps of PiC; the Raman peaks that change over time are highlighted.

Table.IV.9shows the Raman peaks that change during the reaction. The peak at 770 cm^{-1} corresponds to the B-F bond present in iron (II) tetrafluoroborate hexahydrate, during the reaction in the white intermediate phase this peak shift to 789 cm^{-1} which suggests a bond lengthening of B-F due to the interaction with the N bond from 1,2,4-H-triazole. A peak appears at 1375 cm^{-1} due to the stretching and ring vibrations of the triazole ring during the reaction with B-F bonds. [33,40,203] In Guillaume *et al.* 2014; and Tobon *et al.* 2012 it is reported that a vibration of the Htrz molecule at 1530 cm^{-1} occurs involving C-N bond stretching in the LS state; in the present cases C=N vibrations (within the triazole ring) are present in the final phase solution at 1545 and 1375 cm^{-1} which suggests the LS state of the solution at the end of the KRAIC.[33,35] The HS and LS state markers are expected according to Guillaume *et al.* 2014 at 105,150 and 182 cm^{-1} for HS and 200, 213, 287 and 300 cm^{-1} for LS, unfortunately those are not present or not visible during the synthesis of the compound even for the LS state at the end of the KRAIC. In the region below 600 cm^{-1} only C-N-C deformations in secondary amines are seen at 405 and 417 cm^{-1} in the final and intermediate phase of the solution. It is also reported that during the LS to HS change the Raman spectra start to decay in intensity but it is not the case for the white intermediate phase that appears during the synthesis. In the literature the powder studied was analysed with a conventional Raman spectrometer which would give a better signal during Raman analysis compared to the *in situ* flow experiments.[33,35]

Table.IV.9 Raman spectra bond interaction value appearing in different phases

Raman Wavelength (cm^{-1})	Bond interaction	Solution properties
405	C-N-C deformation in secondary amines	Final phase
417	C-N-C deformation in secondary amines	Intermediate and final phase
532	NH out-of-plane bending	Final phase
641		Final phase
667	Ring torsion	Final phase
691		Final phase
769	B-F bond	Iron (II) Tetrafluoroborate Hexahydrate
789	B-F bond lengthening	Iron (II) Tetrafluoroborate Hexahydrate and Intermediate phase
991	Ring bending mode	Final phase
1066	CH bending mode	1,2,4 Triazole
1161	Ring breathing mode	1,2,4 Triazole and Intermediate White Phase
1375	C=C and C=N vibrations	Present in 1,2,4 Triazole reagent
1545	C=C and C=N vibrations	Final phase

It is clear that during the synthesis of $[Fe(Htrz)_2(trz)](BF_4)\cdot H_2O$ Raman analysis detects a change in bonding during the synthesis of PiC due to the interaction of the metal and ligand. In depth analysis of the Raman peaks and comparison to previously reported Raman spectra of the HS and LS state of $[Fe(Htrz)_2(trz)](BF_4)\cdot H_2O$ confirms that the initial colourless phase formed is not the HS state of PiC. There will be further discussion in Chapter VII on the Raman analysis of the dried powder of this compound and also the product from batch synthesis. This study will compare the properties of both syntheses and may be useful to get more information on the assembly mechanism of PiC. If the Raman spectrum can be compared to the powder patterns, it would be possible to identify each reaction steps to the LS and HS of PiC in the powder form to see if the colour change observed is a result of a spin transition of the material during synthesis.

IV.4. Conclusion

In situ analyses have been successfully integrated into a segmented flow environment and have indicated intermediary stages to the final product obtained for the co-crystal system UBA and spin-crossover coordination polymer PiC. The UBA crystallisation KRAIC-D experiments at Diamond beam line I11 showed that different polymorphs were present during the flow experiment. Observing the polymorphic transformation of UBA in methanol during the crystallisation identified a transition from form III to form I polymorph. The transparent nature of the KRAIC-D enables visualisation of crystal appearances, enhancing the potential for useful data collection.

During the synthesis of the $[Fe(Htrz)_2(trz)](BF_4)\cdot H_2O$ spin crossover compound in the KRAIC-D, the X-ray data collection was difficult to process but some signals between 10° and 11° 2θ were seen in some diffraction patterns. It was difficult to tell if improved patterns might be detected using the synchrotron beam without further investigation and modification of the KRAIC-D.

On the other hand, Raman analysis gave more promising results with the detection of two distinct phases during the synthesis inside the KRAIC, the initial colourless and previously unreported phase and the final LS state. These findings confirm the presence of an intermediate during the synthesis of PiC; it was believed that the intermediate phase appearing was the high spin state of the SCO PiC compound present in solution but the Raman showed a completely different spectrum which precludes this hypothesis. In Chapter VII investigation of the batch synthesis of PiC with concurrent reflectance UV-Vis and Raman studies will be discussed and variable temperature Raman spectra of the dry powder of $[Fe(Htrz)_2(trz)](BF_4)\cdot H_2O$ will be studied.

In the next chapter study and optimization of an Oscillated Baffled Reactor (OBR) will be presented to target particle size of $[Fe(Htrz)_2(trz)](BF_4)\cdot H_2O$.

Chapter V Oscillated Baffled Reactor study for the synthesis of $[Fe(Htrz)_2(trz)](BF_4)$

V.1. Introduction

The requirements of modern synthetic chemistry are currently undergoing a transformation from traditional batch processes to continuous flow processes. Flow chemistry techniques have grown rapidly in recent years.[204] Oscillatory flow reactors (OFRs) are a type of continuous reactors which offer uniform mixing and plug flow conditions by changing the operating parameters amplitude, frequency and residence time.[205] The parameters are involved in the creation of eddies in each inter-baffle spacing by oscillation of the fluid inside the reactor through baffles. Each inter-baffle spacing acts as small batch reactor where reagent can be mixed (Figure.V.1).[96,206,207] The advantage of this design of Oscillatory Baffled Reactors (OBR) is to achieve plug flow behaviour under a turbulent flow. Plug flow was previously limited to CSTRs (cascade stirred tank reactors) in series at high turbulent flow. In Chapter III the Kinetically Regulated Automated Input Crystalliser (KRAIC) was presented as a solution to achieve plug flow while keeping turbulent flow at the same time inside each slug. In CSTRs, to achieve plug flow an infinite number of them is needed which is impossible – the alternative is to use a compact tubular baffled reactor.[205,208] These reactors need to work under a turbulent regime in order to mix, that is why oscillation is superimposed on the net flow creating eddies in each baffle. This produces a mixing environment while keeping plug flow behaviour inside the reactor; the fluid is mixed in the radial direction but not in the axial direction (the volume of fluid, V, does not disperse overtime inside the tubing(Chapter I section V)).[100,146,209]

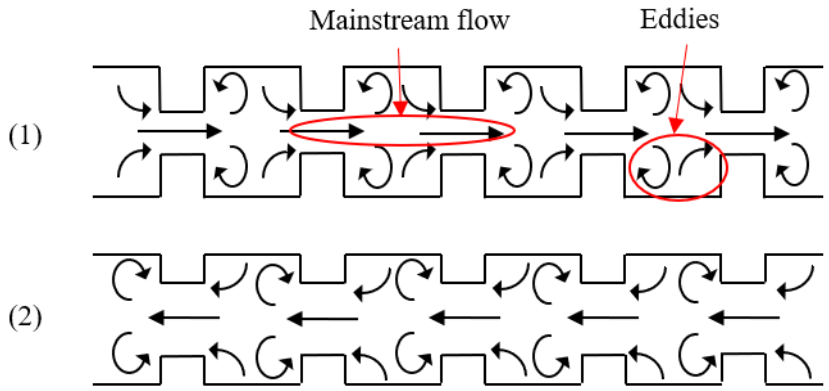

Figure.V.1 Turbulence inside an OBR (1) up stroke (2) back stroke (1) and (2) represent the change after one oscillation of the mechanism creating the flow movement

The advantages of OBRs are the ability to have shorter reaction time due to the mixing along the fluid passage and the ability to handle solids due to the constant momentum of particles with the fluid oscillation from one baffle to another with the radial mixing during the flow.

Despite tremendous developments in nanotechnology and chemistry, there are still numerous challenges in smart nanomaterials development. These challenges include targeting particle size and shape, optimal and adaptive particle size control, model-based predictive methods and developing

safe and sustainable nanofabrication platforms.[210] In this section, a novel method to synthesise a spin crossover (SCO) compound, $[Fe(Htrz)_2(trz)](BF_4).H_2O$ (PiC), at nanoscale using the combination of continuous manufacturing and predictive modelling to overcome these challenges is presented.

Experimental work were carried out with Samet Isaev PhD student in Professor Harris Makatsoris Group at Cranfield University using different design of the Centillion®.[211–214]

V.2. Preliminary experiments

The patented reactor called the Centillion® is a Oscillatory Baffled Reactor (OBR) formed of modular discs as shown on Figure.V.4.[211–214] Each disc is provided with half a cell baffle with an 8 mm internal diameter and a 4 mm baffle constriction orifice between them. Cells are 12 mm in length with 2 mm between them. The solution feed is connected above the first baffle of one channel then each disc of the OBR has seven channels in total which can be connected in series *via* external tubes, enabling a reactor length seven times that of the length of the reactor body,.Figure.V.3.

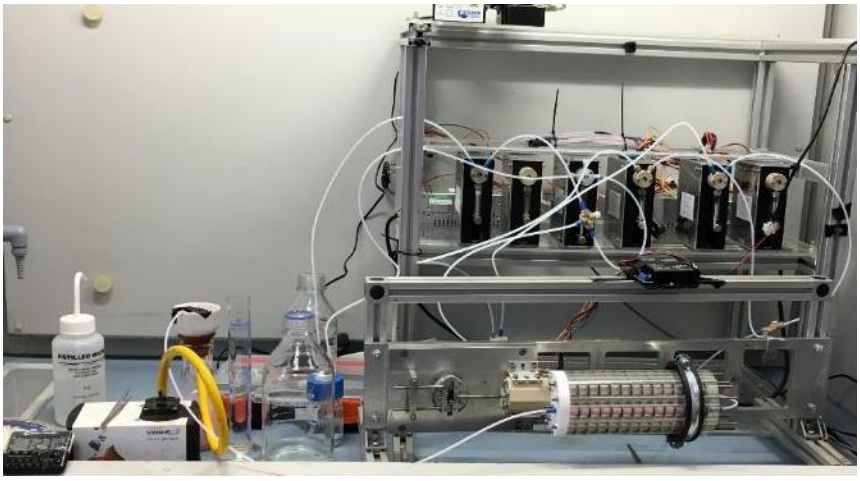

Figure.V.2 Oscillatory Baffled Reactor (OBR) Centillion® Platform

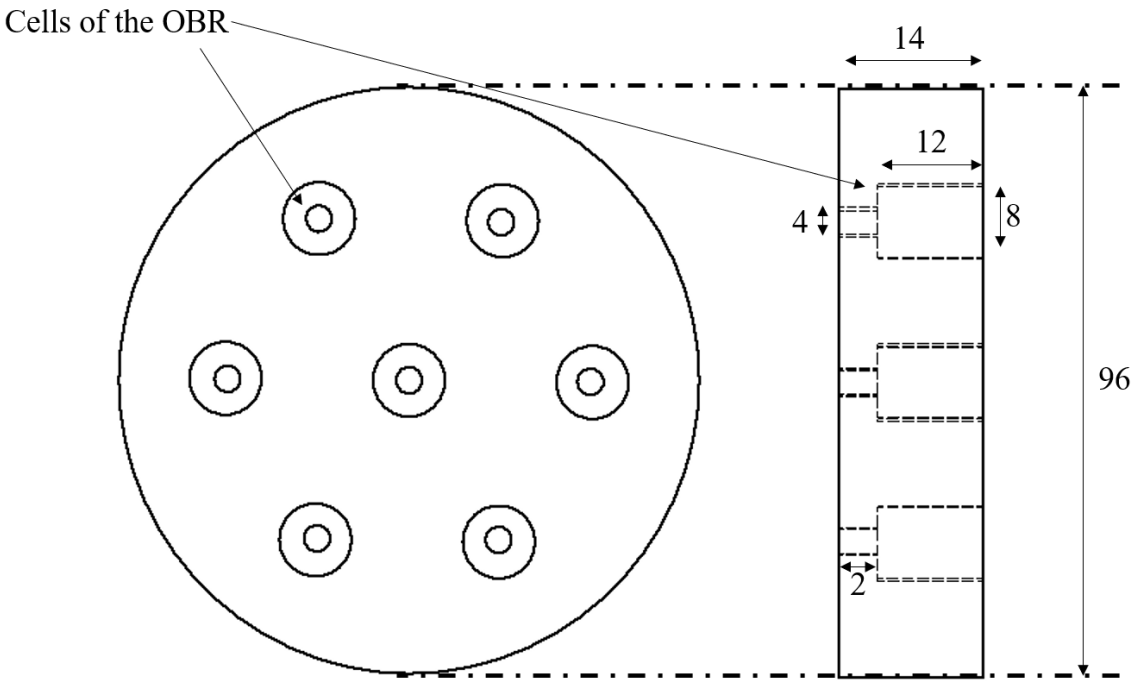

Figure.V.3 Centillion® disc representation, measures are given in mm.[211–214]

The inlet of the reactor is connected to four TriContinent C-Series precision OEM syringe pumps which control the flow rate *via* LabView programming designed by the Makatsoris Group for Continuous Processes Engineering at Cranfield University. The oscillation mechanism presented here has been modified three times with different solutions to create mixing conditions inside the reactor, which are presented in the different introduction parts of this chapter. For the first solution the oscillations were created *via* a fifth syringe pump filled with air, the second was a piston that created the oscillation and in the third, used for the majority of the trials, a rotating disc with a plunger was used to create the oscillation. The differences in oscillation mechanism have been tested to find the most suitable design for the reactor and future experiments, as the reactor is still in development and in improving testing some mechanical parts have been changed during the experimental process.

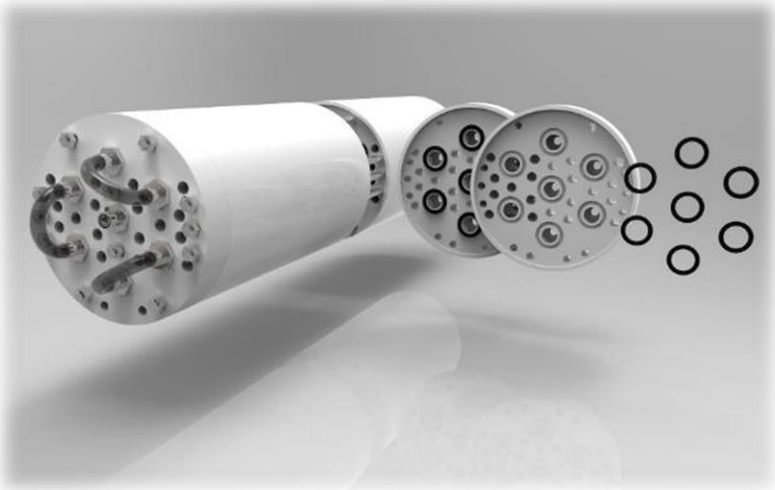

Figure.V.4 3D representation of the Centillion® discs created by PhD student John Alysandratos from the Makatsoris group.[211–214]

Understanding the flow behaviour in baffled tube reactors like the OBR, Centillion®, or the COBC from Nitech® it is important in order to optimise this type of reactor. The oscillations generate Reynolds turbulence inside each baffle creating a mixing environment. Trying to improve the mixing is a must for any researcher designing a flow reactor in order to have the best mixing parameters to achieve better synthesis control. Such reactors can be positioned vertically or horizontally and used with single or multiphase flow. For the chemical engineer it is necessary to have better knowledge of the fluid dynamics of the reactor to increase the predictability of the reactor design and improve the efficiency of the process.

During the process the amplitude and the frequency of the oscillation control the mixing of the fluid inside the baffles. The governing equations defined by Harvey *et al* are: [96]

$$Re_0 = \frac{2\pi f x_0 \rho d}{\mu} \tag{21}$$

$$St = \frac{d}{4\pi x_0} \tag{22}$$

$$Re_n = \frac{\rho v d}{\mu} \tag{23}$$

Where Re_0 is the oscillatory Reynolds number, Re_n is the net Reynolds number, ν is the fluid velocity, ρ is the fluid density, μ is the fluid viscosity, f is the frequency of oscillation, x_0 is the amplitude centre-to-peak of the oscillation, *St* is the Strouhal number and d is the tube diameter.

Re_0 is controlled by the oscillation frequency and amplitude and describes the intensity of the mixing, while St is the ratio between tube diameter and the amplitude of oscillation and the effective propagation of eddies.[215]

Another parameter, the velocity ratio, ψ, can be defined as: [96]

$$\psi = \frac{Re_0}{Re_n} = \frac{2\pi f x_0}{v} \quad (24)$$

Where Re_n is the Reynolds number of the fluid which describe how the fluid behaves in the reactor; values of Re_n under 2000 represent laminar flow, above this the flow is said to be turbulent. For this equation having the velocity ratio between 2 and 6 is best for oscillatory flow which is the optimum condition to achieve plug flow in OBRs.[97,216] Those parameters will be particularly used in the optimisation of the reactor for the Design of Experiment (DOE) and the plug flow achievement inside the reactor discussed in part V.4 of this Chapter.

V.2.2 Oscillation of the reaction mixture

The first synthesis of the target SCO material using the Centillion® to induce oscillation of the reaction mixture was done by using the syringe pump and was designed by the Makatsoris Group. This gave an initial understanding of the flow oscillation phenomenon and how to improve the reactor to target and control particle size. The synthesis of the SCO compound, PiC, was achieved following the procedure set out in Krober *et al*.[4] Two solutions of iron(II) tetrafluoroborate hexahydrate, $Fe(BF_4)_2.6H_2O$, and 1,2,4-H triazole (Trz) in water were used as feed and a cross-piece was positioned before the entrance of the first baffle. This cross piece was used to have both solutions encounter together and to induce the oscillation *via* the third central inlet. The Centillion® experimentation scheme is displayed in Figure.V.5 showing the different parts of the system; various oscillation mechanisms are discussed in the following sections.

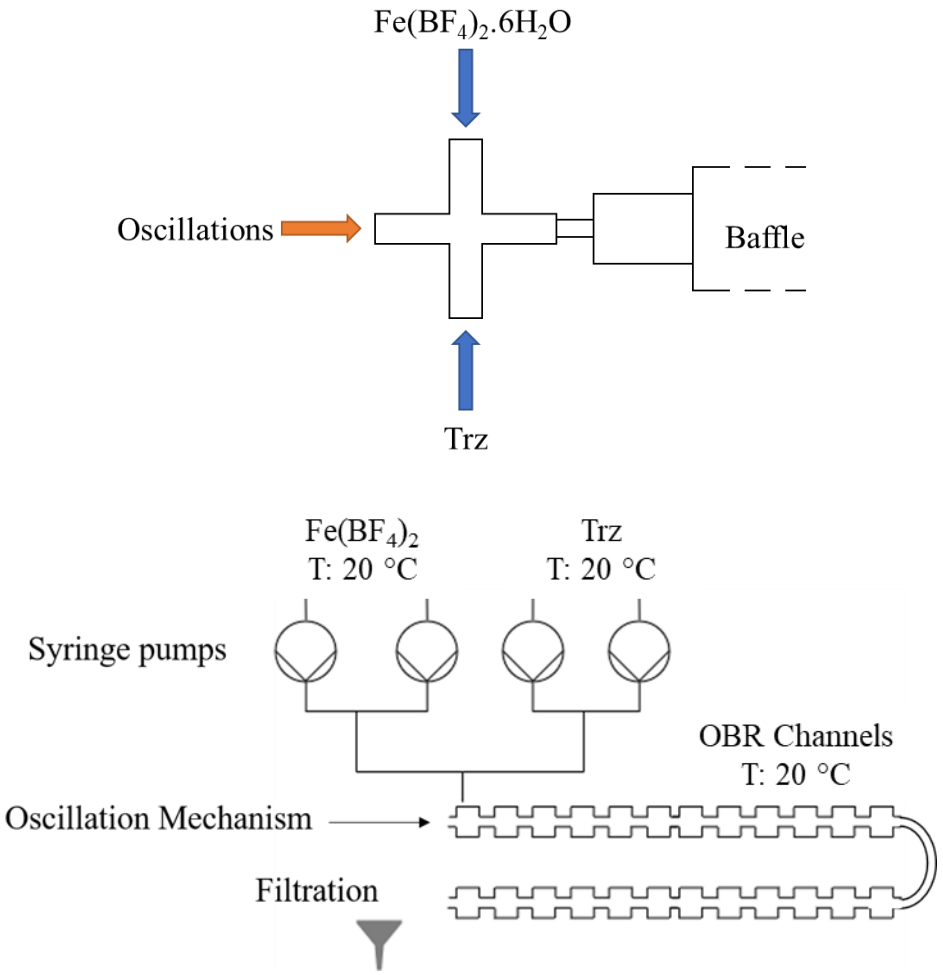

Figure.V.5 Cross-piece schematic representation and OBR experimental set-up scheme.

Experimental parameters for this system are shown in Table.V.1 with CI denoting concentration of $Fe(BF_4)_2.6H_2O$ and CT denoting concentration of Trz. In this configuration two syringe pumps were used to have a dual pump mode giving a continuous flow of reagent.

Table.V.1 Parameters used for the first oscillation set-up (syringe) of the Centillion®

Experiment Syringe OBR (SO)	Freq (Hz)	Amp (mm)	Total Flow rate (mL/min)	CI (g/100 mL)	CT (g/100 mL)	Number of channels	Yield % from $Fe(BF_4)_2$	Onset of growth (min)
SO 1	2.01	3	2.3	5.25	8.39	2	13.3	39
SO 2	1.58	3.5	1.5	8.3	8.67	2	10.8	45
SO 3	1	2.5	9	5.25	8.67	2	5.3	20
SO 4	2	4	4.5	8.3	8.67	2	8.7	30
SO 5	2	4	4.5	8.3	8.67	4	7.4	25
SO 6	1	2.5	2.5	8.3	8.67	2	12.6	36

Table.V.2 Stochiometric Ratio [$Fe(BF_4)_2$ $6H_2O$] /[HTrz] for SO experiments

Experiment Syringe OBR (SO)	CI (g/100 mL)	CT (g/100 mL)	[$Fe(BF_4)_2$ $6H_2O$] (mmol/mL)	[HTrz] (mmol/mL)	Stochiometric Ratio [$Fe(BF_4)_2$ $6H_2O$] /[HTrz]
SO 1	5.25	8.39	15.55	121.48	1/8
SO 2	8.3	8.67	24.59	125.53	1/5
SO 3	5.25	8.67	15.55	125.53	1/8
SO 4	8.3	8.67	24.59	125.53	1/5
SO 5	8.3	8.67	24.59	125.53	1/5
SO 6	8.3	8.67	24.59	125.53	1/5

During the experiments it was observed that the flow parameters had an important impact on the onset of growth of the PiC product. For example, with trial SO 1 a cloudy pink solution appeared at 39 minutes run-time, whereas for trial SO 3 a pink solution appeared after 20 min. Adding two more channels to the system gives the possibility for the reaction mixture to spend more time in the reactor; using this configuration the apparition of cloudy solution has been reduced by 5 min from 30 min to 25 min, appearing in the 5th cells of the second channel at 10.8 cm (22.3 cm from inlet to 5^{th} baffle of second channel). The change in onset of growth time was not investigated deeply for those first tests, as the main goal for those initial experiments was to assure the possibility to produce PiC inside the reactor. It has also been observed that some of the compound remained inside some of the reactor joints which for use of the reactor in long time runs would be a problem. This will be discussed in this section with respect to the change in oscillation system, but could explain the reduction in yield on run SO 5 from that in run SO 4.

To compare particle size of the product from these tests, scanning electron microscopy (SEM) was used. Images from three different experiments are shown in Figure.V.6. As can be seen, using the OBR to produce PiC with a range of frequency, amplitude and flow rates, gives different particle sizes and size distribution, although rod shaped particles are still observed as described in literature.[11,13]

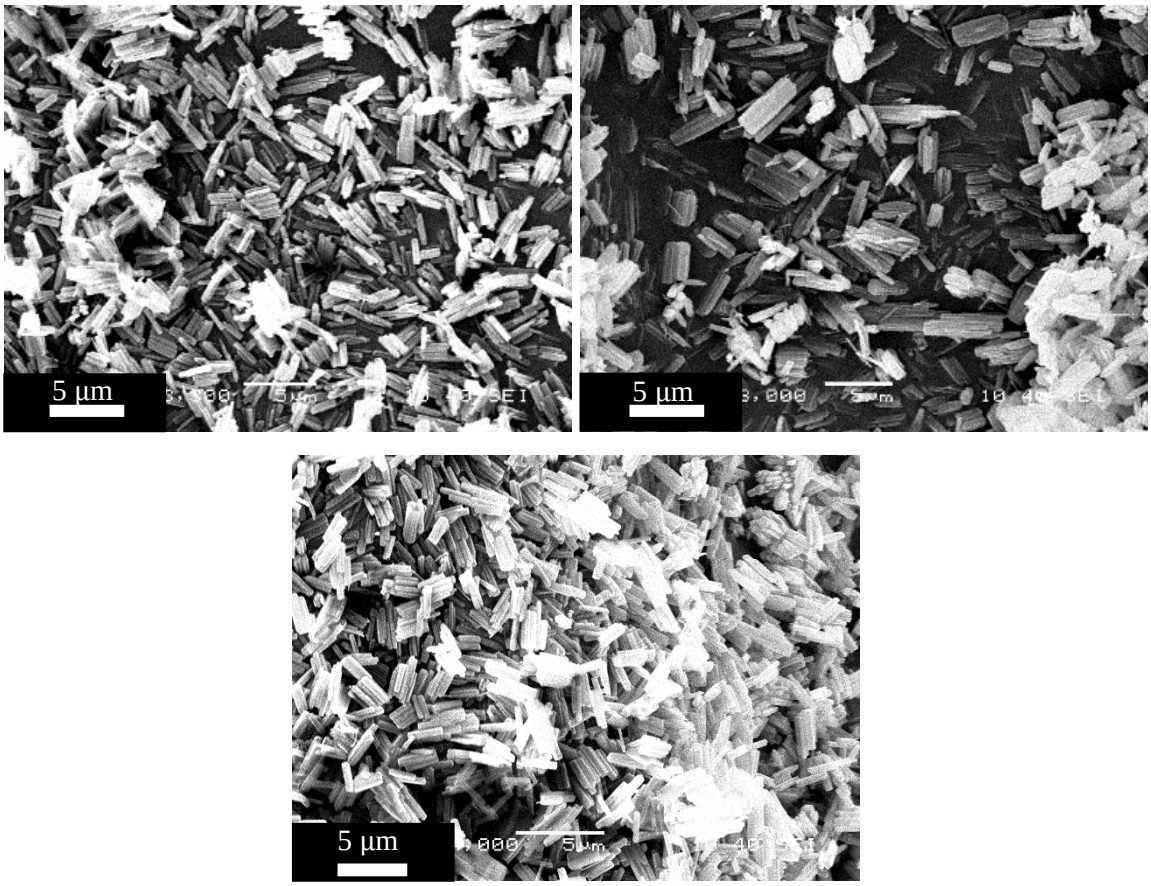

Figure.V.6 Comparison between PiC particles from batch (top left), experiment SO 2 (top right) and experiment SO 5 (bottom).

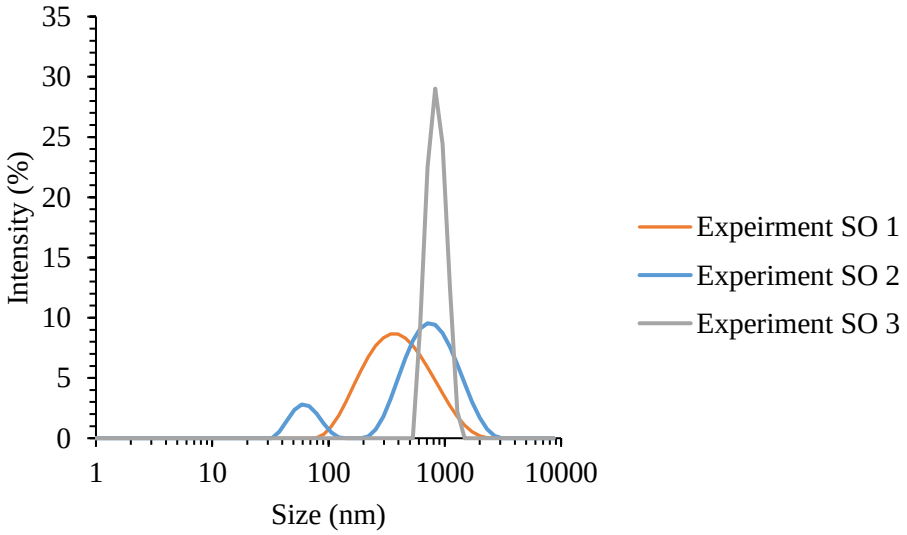

Figure.V.7 Dynamic Light Scattering (DLS) results for experiments SO 1,2 and 3.

From batch crystallisation as described in Chapter III (B1 to B8), crystal sizes range from 1 µm to 3 µm where obtained, while in the OBR these range from 400 nm to 3 µm with similar crystal shapes as seen on SEM (Figure.V.6). The Dynamic Light Scattering (DLS) analysis of the experiments showed the presence of crystals between 100 nm to 1000 nm, which could indicate the possibility to have smaller particle size with the right parameters with the OBR. The population is also broader for experiment SO 1 and SO 2 than the batch synthesis, which suggests an inability to target the particle size with some parameters. In terms of yields, the flow rate seems to have an impact; at high flow rate the yield is 5.3 % for 9 mL/min (SO 3) and upon decreasing to 4.5 then 2.3 mL/min for experiment SO 1 the yield increases up to 13.3 %. This suggest that the mixing is an important factor inside the reactor, increasing the interaction between the two reagents. Compared to the product from the KRAIC smaller particle size can be obtained but the variation of particle size and yield with different parameters for the OBR is difficult to assess with this limited number of experiments. Hence, a Design of Experiment (DOE) study will be presented in section V.3 below. The different particle size behaviours for the same concentration of reactants shows the importance of mixing differences between a flow reactor and batch.

These experiments were a first step to target the particle size of PiC in the OBR. The syringe system to induce oscillation in the OBR showed its limit during the experimentation, for instance using the cross-piece showed to result in back mixing with the reaction occurring inside the tubing leading to the pump used for oscillation. Despite the liquid filled tube leading from the air-filled syringe pump, air was also present due to this design where cavitation occurred at high frequency oscillations. The investigation of parameters to assess the importance of the frequency, amplitude, flow rate and reagent concentration will be discussed in section V.3. The synthesis of the desired compound PiC has been confirmed *via* PXRD (Figure.V.8). [14]

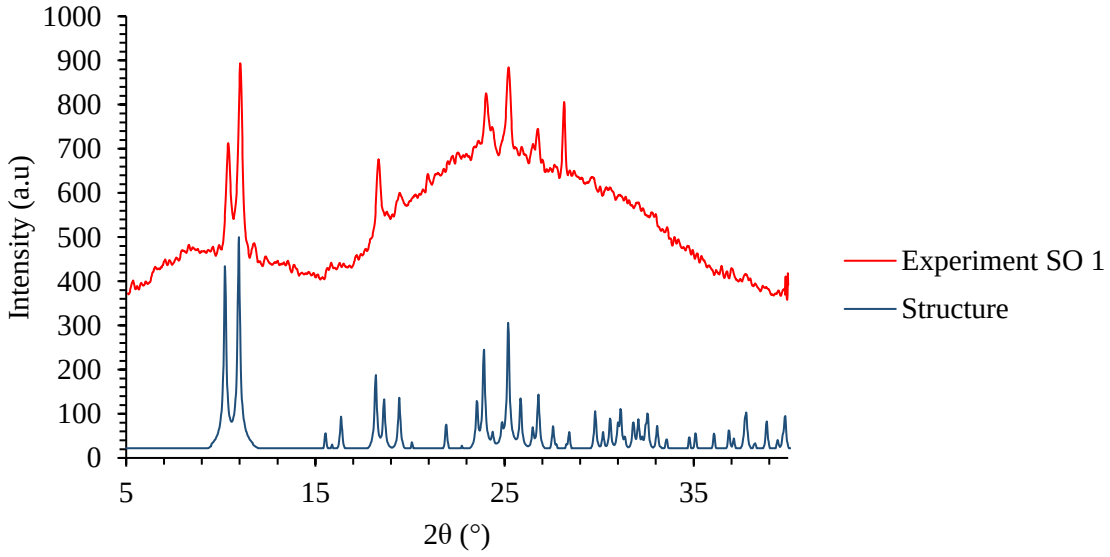

Figure.V.8 PXRD Data from product of OBR Synthesis of PiC for experiment SO 1 compared to simulated data.[39]

V.2.3 Oscillation *via* Piston

The OBR design was then changed to a different mechanism of oscillation developed by the Makatsoris Group [211–214] and the reagents were injected inside the reactor at the top of the first cell in the first channel to avoid any contamination of previously reacted compound. These changes were to answer the issue encountered in section V.2.2. For the second set of trials a piston was used for the oscillation and controlled *via* LabView (Figure.V.9). The feed system was kept the same with the syringe pump for the reagents and injecting the solutions through the top of the first baffle. Here the same concentration for both reagents was used, but different parameters were implemented. In addition to aqueous trials, methanol was also used as solvent to investigate the other phase that it is possible to obtain from complexation of $Fe(BF_4)$ and Trz, $[Fe(Htrz)_3](BF_4)_2 \cdot H_2O$ (PiCM) reported in Krober *et al.*[4]

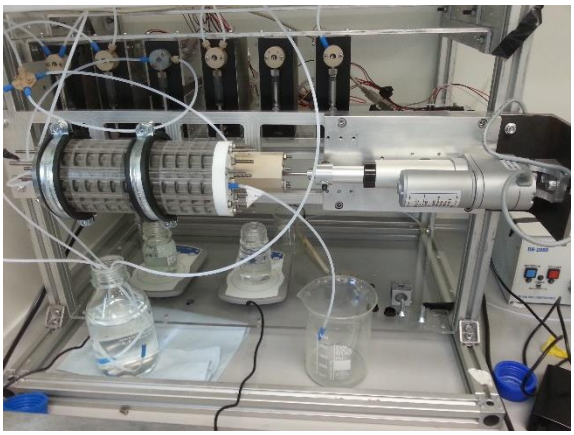

Figure.V.9 Piston for the oscillation mechanism attached to the Centillion®.

Table.V.3 OBR Flow Parameters for piston mechanism

N°	Freq (Hz)	Amp (mm)	Residence Time (min)	CI (g/100 mL)	CT (g/100 mL)	Number of channels	Solvent	Yield % from $Fe(BF_4)_2$
POM1	2	2	14	8.3	8.67	2	Methanol	62.1
POM2	4	2	14	8.3	8.67	2	Methanol	53.2
POM3	4	4	14	8.3	8.67	2	Methanol	71.7
POM4	2	4	14	8.3	8.67	2	Methanol	65.9

N°	Freq (Hz)	Amp (mm)	Residence Time (min)	CI (g/100 mL)	CT (g/100 mL)	Number of channels	Solvent	Yield % from $Fe(BF_4)_2$
POW1	2	2	14	8.3	8.67	2	Water	12.3
POW2	1	2	10	8.3	8.67	2	Water	14.6
POW3	0.5	4	15	8.3	8.67	2	Water	11.1

Table.V.4 Stochiometric Ratio $[Fe(BF_4)_2\ 6H_2O]$ /[HTrz] for POM and POW experiments

CI (g/100 mL)	CT (g/100 mL)	$[Fe(BF_4)_2\ 6H_2O]$ (mmol/mL)	[HTrz] (mmol/mL)	Stochiometric Ratio $[Fe(BF_4)_2\ 6H_2O]$ /[HTrz]
8.3	8.67	24.58894979	125.5302822	1/5

For the reactions detailed above in Table.V.3, SEM analysis of the products was undertaken in order to compare particle size and shape of PiC with the different parameters and solvent. As seen in Figure.V.10 it is clear that changing solvent has a huge impact on particle shape; the rods are not present at all in PiCM samples. The colour is also changed, with the product dark purple rather than pink, as also observed in the PiCM synthesis in the KRAIC in Chapter III.

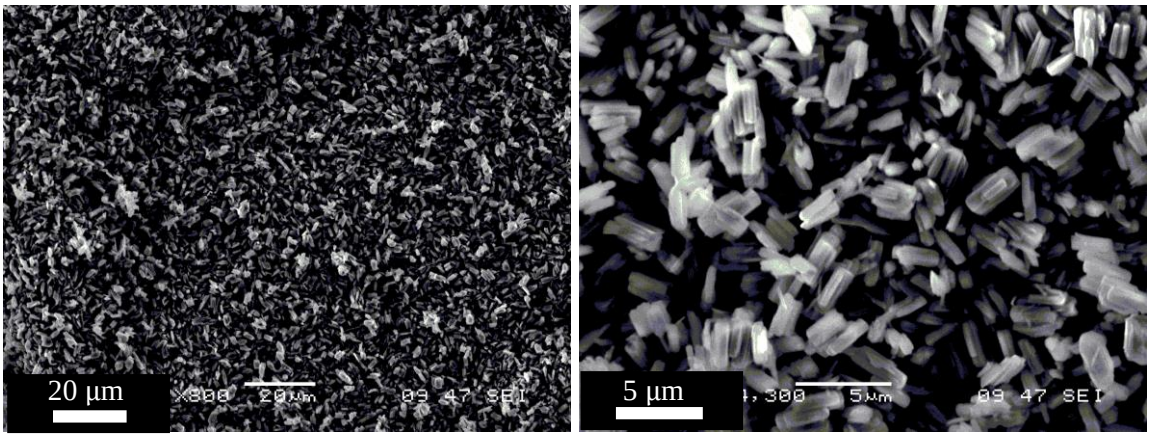

Figure.V.10 PiC particles produced inside the OBR with water as solvent:2 Hz Frequency, 2 mm Amplitude, 14 min residence time (POW1).

PiC synthesis with the piston system did not show a change in particle size and shape under SEM compared to the syringe pump. The same rod shaped like material was observed over the samples, with sizes ranging between 1000 nm to 1200 nm.

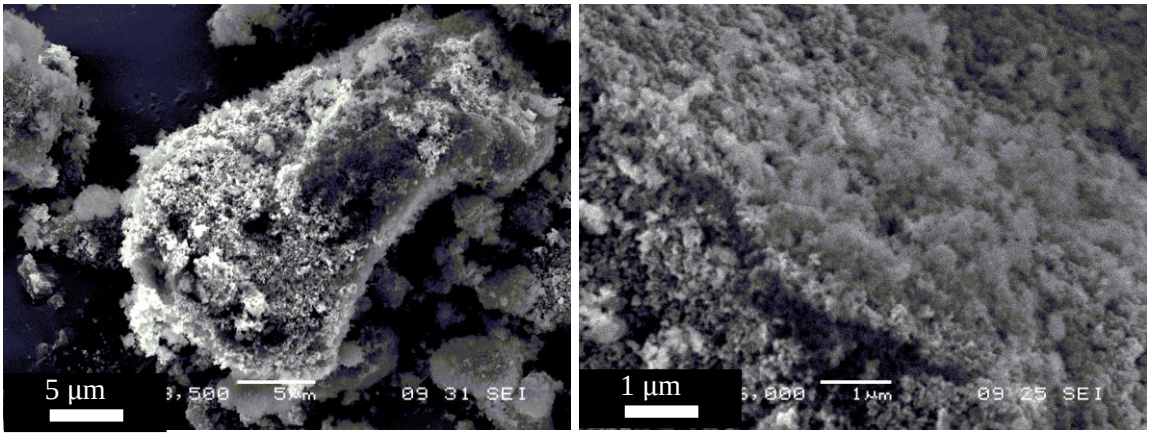

Figure.V.11 PiCM particles produced inside the OBR with methanol as solvent: 2 Hz Frequency, 2 mm Amplitude, 14 min residence time (POM1).

Figure.V.12 (left) PiC produced in water with colour change from pink to white. (right) PiCM produced in methanol with colour change from violet to orange.

On Figure.V.12 is shown the change of colour of the material. Each compound was heated up to 95 °C using a hot plate. PiC produced in water shows the change reported in literature, at the spin transition the compound changes from pink to white and then goes back to pink when cooling down. For PiCM the same colour changing behaviour is observed but instead of a white transition, an orange colour appeared, and when cooling down to room temperature PiCM went back to violet. This orange colour could be due to oxidation of the unreacted Fe^{2+} ions during the synthesis or filtration as, in Faulmann *et al.*, it is reported that the violet PiCM goes white at high spin state.[113]

The PiCM compound produced in methanol was previously reported in Krober *et al.* As shown in Figure.V.11 and Figure.V.12 the difference between PiC and PiCM is presented clearly in terms of particle shape. [4] On Figure.V.11 the same rod shaped materials observed before are present for POW 1 to 3 using water as solvent, but when using methanol for the same flow parameters and concentrations (experiment POM1 and POW1 shown in Figure.V.10 and Figure.V.11), sizeable aggregates which display a very different and indeterminate crystal habit are formed. After those experiments, comparisons with the products from batch were made for the PiCM with methanol and (Figure.V.13, to be compared with Figure.V.11).

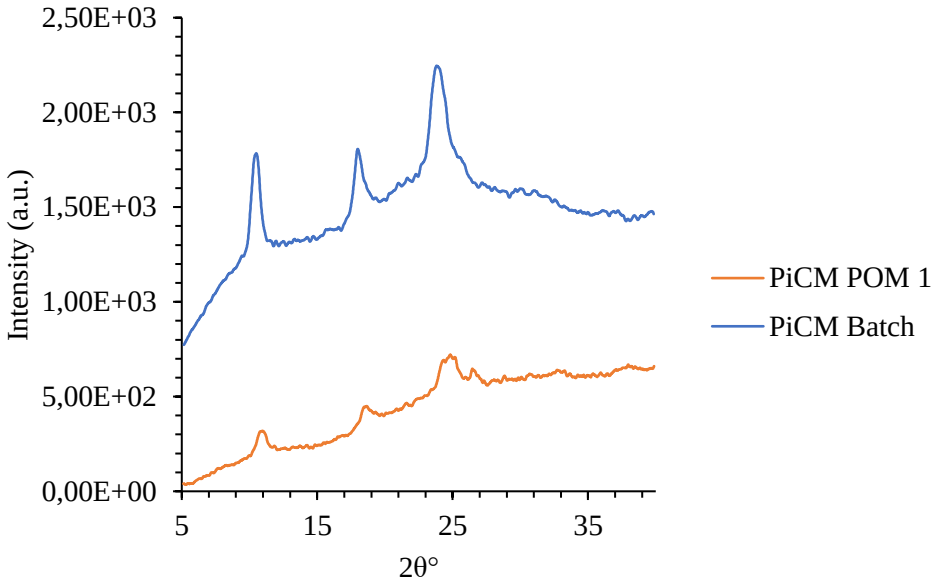

Figure.V.13 PXRD of POM 1 and batch synthesis of PiCM

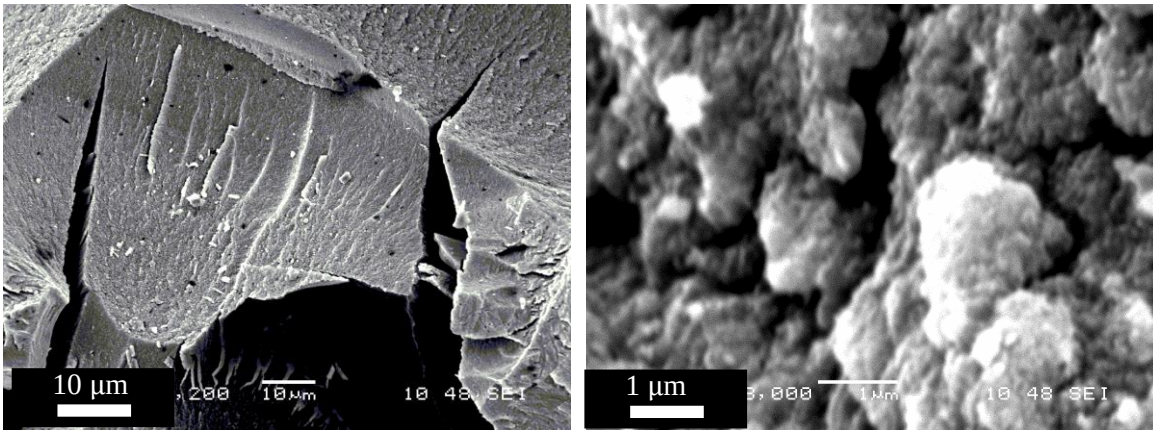

Figure.V.14 SEM images of products of batch synthesis of PiCM

During the synthesis of PiCM, a difference in colour change of the solution was observed and the reaction appears to be faster than using water, as observed in the KRAIC in Chapter III. The solution is also more viscous, and sedimentation occurs until the bottom of the cells is filled with compound as shown in Figure.V.15.

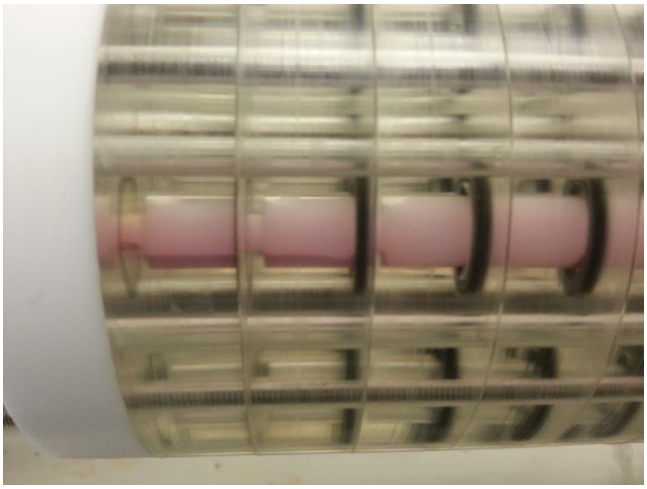

Figure.V.15 Sedimentation occurring inside the Centillion® during PiCM synthesis.

It has been concluded from the methanol trials after some repetition of the experiment that using water as solvent was more suitable to control and observe a change in particle size for that compound. Like PiCM production in the KRAIC, the viscosity of the solution increased and produced this sedimentation in the inter-baffle spacings. Therefore, for all subsequent experiments water was used as solvent.

In these experiments, the piston used for the oscillation proved to be a more efficient way to create oscillation while avoiding back mixing of the reagents at the initial mixer-piece. On the other hand, the range of oscillation that could be achieved was lower due to the length of the piston and its precision.

V.3. Targeting particle size of PiC

V.3.1 Set-up for OBR design of experiment

For the DOE experiments and improvement of the reactor the set-up, a revised platform design of the Centillion® presented in Figure.V.16. [211–214] The new oscillation mechanism consists of a scotch yoke system. This alternative oscillation mechanism was employed here to combat the problems encountered by previous oscillation mechanisms described in this chapter. The scotch yoke mechanism is shown in Figure.V.16, a video is given in the supplementary info **CDCh5-1** showing the mechanism in action. This system consists of transforming a rotation into a translation movement. A motor rotates the pin which is attached to a sliding roller which is then attached to the piston which creates the translation movement and induce the oscillation of the OBR.

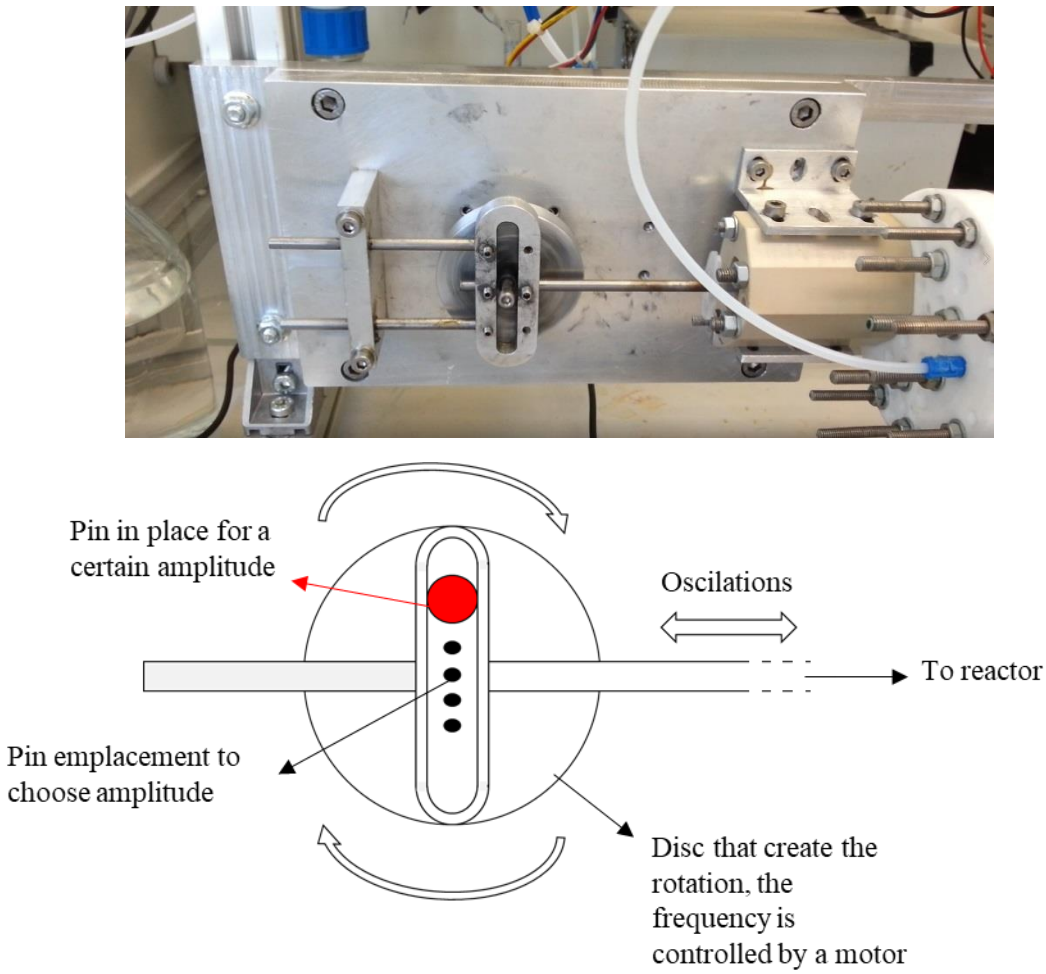

Figure.V.16 Scotch Yoke system used for generating oscillation in the Centillion®.

Conditions for the DOE experiments were chosen by inputting the preliminary experiment concentrations for the synthesis of PiC carried out previously. Parameters were input to MiniTab which then calculated the concentration, frequency, amplitude and residence time to use for the design of experiment response surface model.

V.3.2 Design of experiments for PiC particle target

Fundamental understanding of chemical materials and accurate predictive models are of critical importance to the manufacturing of desired particle size and properties of nanomaterials. In the previous section several designs and parameter choices for the OBR were tried, with the results showing the importance of choosing the right synthesis environment. Towards this target, improvement in nanofabrication techniques are not enough in themselves, but reliable and repeatable experimental design is critically important to move from guessing which parameter has more impact than others, to predict an actual model to control nanomaterials particle size and shape. A design of experiments approach (DOE) was performed to minimise the number of experiments required to achieve simultaneous identification of all factors that influence the outcome of the reaction and to develop an accurate predictive model after the set of experiments. Particle size on PiC has been investigated as a function of five process factors. The names of factors, with their variation levels are shown in Table.V.6. A central composite model has been used to develop an experimental matrix from the initial experiments presented in section V.2, V.2.2 and V.2.3 and estimate a first- and

second order terms to create a targeting equation. The design matrix by the central composite method with experimental parameters is shown in Table.V.5 (V.3.4). The factors and their levels have been selected from the combination of previous studies on PiC synthesis and considering the range of process limitations.

V.3.3 Screening parameters affecting particle size

Preliminary screening experiments were conducted to understand the influence of chemical and process variables such as the concentrations of reactants, the mixing conditions and the residence time of the reaction. Effects of five different factors on PiC nanoparticle size distribution and particle shape were investigated by conduction of 32 screening experiments. All experiments were performed in the OBR within different operating parameters and different concentrations of aqueous solutions. For each experiment three residence times (RTs) have been recovered and measured *via* DLS and the 3rd RT was used for the DOE and considered as the achievement of the steady state.

The morphologies and sizes of the synthesised samples were systematically investigated by SEM and DLS. DLS and SEM analysis of the samples revealed that the OBR is able to synthesis SCO compounds PiC in a wide range of nanoparticle sizes including narrow particle size distribution and a variety of particle morphologies.

The ability to control particle size, shape and distribution of the PiC nanoparticles crucially relies on operating conditions, residence time under plug flow conditions and concentrations of reagents. A full discussion on nanoparticle shape will be given in Chapter VII.

Particle size was determined with dynamic light scattering (DLS) with Zetasizer Nano S from Malvern and SEM pictures obtained with a JEOL SEM6480LV to create the screening parameters. For the particle size analysis of PiC, the samples were dispersed in water, at a temperature of 20 °C, and viscosity of 1.002 mPa.s and refractive index 1.023 were inputted in Malvern Zetasizer software.[5,27]

V.3.4 Design of Experiment for average particle size distribution results

The design of experiment was carried out and each experiment was analysed using SEM and DLS to check particle size and shape. Results from the experiments are displayed in Table.V.8.

Table.V.5 High and Low limits of each parameters for the PiC synthesis inside the OBR.

Factor	Name	Levels	
		Low	High
X_1	Frequency (Hz)	1	4
X_2	Amplitude (mm)	2	4
X_3	Residence Time (min)	8	20
X_4	$[Fe(BF_4)_2]$ (g/100mL)	3.374	8.32
X_5	[1,2,4-H Triazole] (g/100mL)	3.374	8.32

Table.V.6 Parameter screens given by Minitab after implementing the Low and High levels of each parameters.

Experiment Number	Frequency (Hz)	Amplitude (mm)	Residence time (min)	CI (g/100mL)	CT (g/100mL)
1	2.25	3	14	5.8	5.8
2	2.25	5	14	5.8	5.8
3	2.25	2	14	5.8	5.8
4	2.25	3	26	5.8	5.8
5	2.25	3	14	5.8	5.8
6	5.75	3	14	5.8	5.8
7	1.25	3	14	5.8	5.8
8	2.25	3	14	5.8	5.8
9	2.25	3	14	5.8	5.8
10	2.25	3	14	5.8	5.8
11	2.25	3	14	5.8	5.8
12	2.25	3	2	5.8	5.8
13	2.25	3	14	5.8	0.9
14	2.25	3	14	5.8	10.8
15	2.25	3	14	0.9	5.8
16	2.25	3	14	10.8	5.8
17	4	2	20	8.3	3.4
18	4	4	8	8.3	3.4
19	0.5	4	20	8.3	3.4
20	0.5	2	8	8.3	3.4
21	0.5	4	8	8.3	8.3
22	0.5	2	20	8.3	8.3
23	4	4	20	8.3	8.3
24	4	2	8	8.3	8.3
25	4	2	20	3.4	8.3
26	4	4	8	3.4	8.3
27	0.5	4	20	3.4	8.3
28	0.5	2	8	3.4	8.3
29	0.5	2	20	3.4	3.4
30	0.5	4	8	3.4	3.4
31	4	4	20	3.4	3.4
32	4	2	8	3.4	3.4

Table.V.7 Stochiometric Ratio [$Fe(BF_4)_2$ 6H2O] /[HTrz] for OBR DOE

Experiment Number	CI mmol/100mL	CT mmol/100mL	Stochiometric Ratio [$Fe(BF_4)_2$ $6H_2O$] /[HTrz]
1	17.3	84.7	1/5
2	17.3	84.7	1/5
3	17.3	84.7	1/5
4	17.3	84.7	1/5
5	17.3	84.7	1/5
6	17.3	84.7	1/5
7	17.3	84.7	1/5
8	17.3	84.7	1/5
9	17.3	84.7	1/5
10	17.3	84.7	1/5
11	17.3	84.7	1/5
12	17.3	84.7	1/5
13	17.3	13.0	1 1/3
14	17.3	156.3	1/10
15	2.7	84.7	3/100
16	32.0	84.7	4/10
17	24.6	48.9	1/2
18	24.6	48.9	1/2
19	24.6	48.9	1/2
20	24.6	48.9	1/2
21	24.6	120.5	2/10
22	24.6	120.5	2/10
23	24.6	120.5	2/10
24	24.6	120.5	2/10
25	10.0	120.5	1/10
26	10.0	120.5	1/10
27	10.0	120.5	1/10
28	10.0	120.5	1/10
29	10.0	48.9	2/10
30	10.0	48.9	2/10
31	10.0	48.9	2/10
32	10.0	48.9	2/10

Table.V.8 Experiments carried out on the Centillion® with average particle size of PiC obtained.

Experiment Number	Frequency (Hz)	Amplitude (mm)	Residence time (min)	CI (g/100mL)	CT (g/100mL)	Average Particle Size (nm)
1	2.25	3	14	5.847	5.847	161.8
2	2.25	5	14	5.847	5.847	496.7
3	2.25	2	14	5.847	5.847	182.7
4	2.25	3	26	5.847	5.847	429.0
5	2.25	3	14	5.847	5.847	179.0
6	5.75	3	14	5.847	5.847	166.0
7	1.25	3	14	5.847	5.847	95.8
8	2.25	3	14	5.847	5.847	165.5
9	2.25	3	14	5.847	5.847	108.2
10	2.25	3	14	5.847	5.847	140.2
11	2.25	3	14	5.847	5.847	121.5
12	2.25	3	2	5.847	5.847	823.9
13	2.25	3	14	5.847	0.901	153.9
14	2.25	3	14	5.847	10.793	236.5
15	2.25	3	14	0.901	5.847	106.2
16	2.25	3	14	10.793	5.847	1211.4
17	4	2	20	8.32	3.374	743.3
18	4	4	8	8.32	3.374	859.5
19	0.5	4	20	8.32	3.374	1120.1
20	0.5	2	8	8.32	3.374	189.8
21	0.5	4	8	8.32	8.32	264.6
22	0.5	2	20	8.32	8.32	1611.0
23	4	4	20	8.32	8.32	561.8
24	4	2	8	8.32	8.32	574.5
25	4	2	20	3.374	8.32	141.2
26	4	4	8	3.374	8.32	1029.4
27	0.5	4	20	3.374	8.32	787.7
28	0.5	2	8	3.374	8.32	1273.4
29	0.5	2	20	3.374	3.374	575.1
30	0.5	4	8	3.374	3.374	441.8
31	4	4	20	3.374	3.374	858.6
32	4	2	8	3.374	3.374	183.7

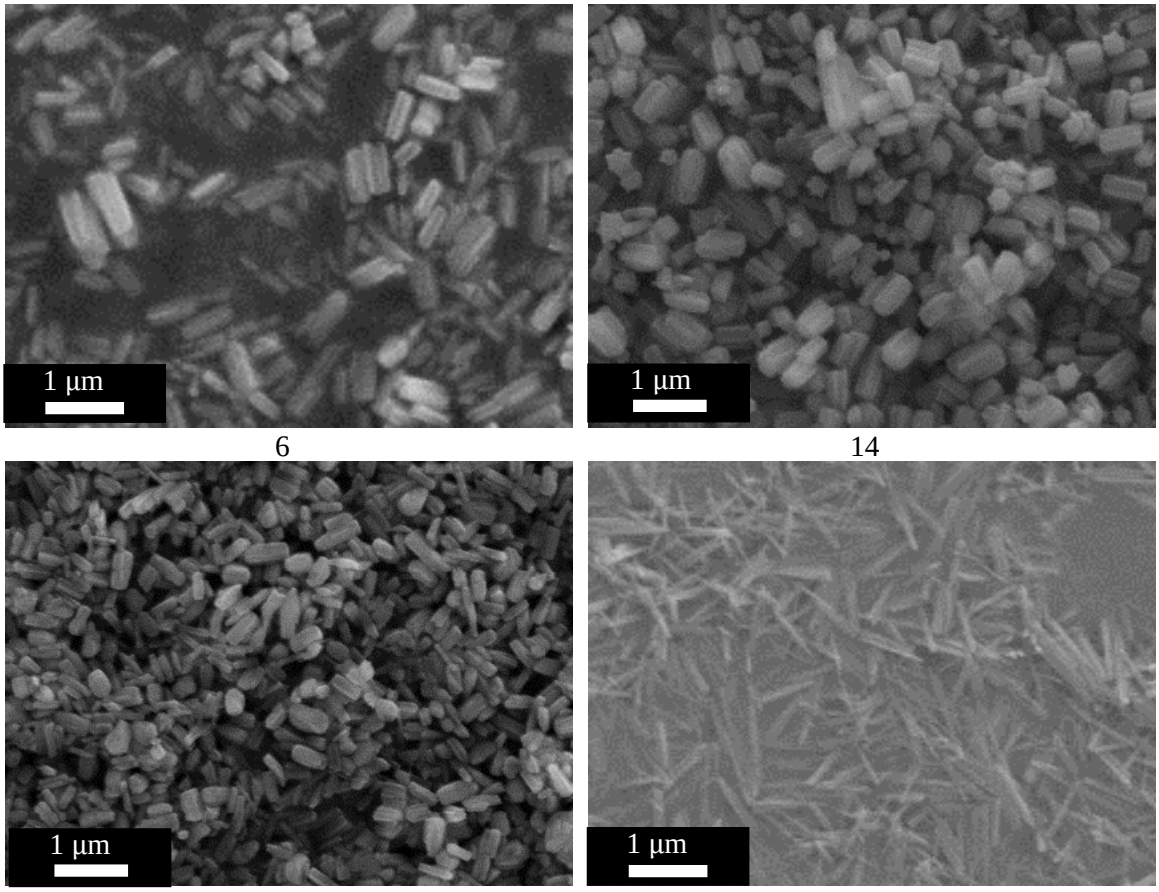

6 14

23 32

Figure.V.17 SEM of experiments DOE 6, 14, 23 and 32.

As shown on Figure.V.17 the SEM images from four different experiments (DOE 6, 14, 23 and 32) show a wide variety of particle size distribution. This shows the importance of the parameters used in this reactor. Having a better understanding of the effect of frequency, amplitude, residence time, concentration of $Fe(BF_4)_2\ 6H_2O$ and concentration of Trz on particle size is important, and for this purpose the DOE surface response model was used in order to target and control particle size.

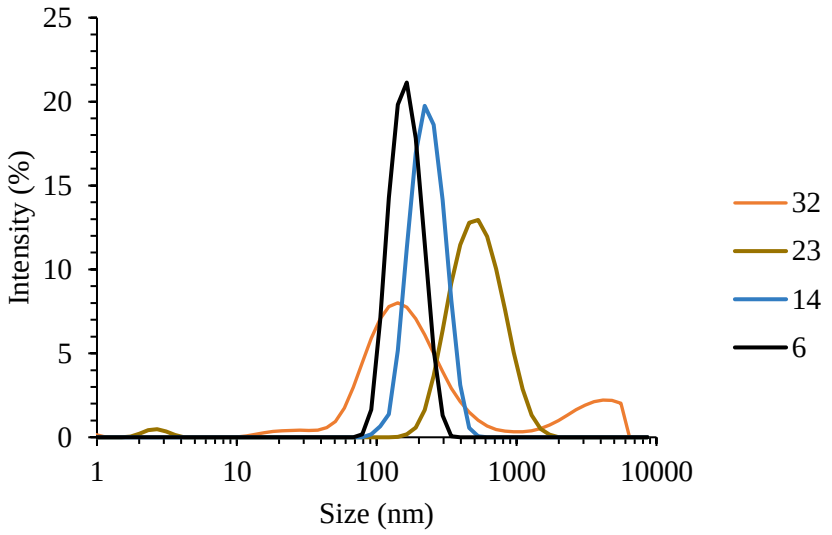

Figure.V.18 DLS results for DOE 6, 14, 23 and 32.

Figure.V.18 shows the DLS particle size analysis of the corresponding experiments of Figure.V.17. The DLS shows a corresponding PSD to the SEM pictures with peaks for DOE 6 at 164 nm, DOE 14 at 456 nm, DOE 23 at 531 nm and DOE 32 at 164 nm, for the largest population detected. Compared to the SEM (Figure.V.17) the DLS concords with the particle size observed by Moulet *et al.*. [11] For DOE 23 the DLS gives a PSD with a peak at 458 nm and the SEM shows clearly particles ranging between 400-500 nm. For DOE 6 on the other hand some particles are not detected, on the SEM sizeable rods are seen of dimension 2.5 µm but these are not apparent from the DLS analysis. This appears to be the case for several experiments where the DLS results do not show a representative PSD compared to the SEM. It is noted that the particle size of PiC ranges from 100 nm to 2.5 µm, but it has been reported that sub-100 nm particles can be obtained using the reverse micelle technique which suggests that using surfactant during the reaction gives the possibility to get smaller particles. [11]

With these results a DOE equation mapping was created with Minitab and is discussed in the next section.

V.3.4.ii Effect of the frequency on the particle size

Frequency of fluid oscillation is one of the main variables which highly affects the particle size and shape. A low frequency resulted in smaller nanoparticle sizes (200 – 400 nm). A high frequency also resulted in low nanoparticle sizes (200 nm), as shown in Figure.V.19. From this, 4-5 Hz would be the optimum frequency in order to produce smaller nanoparticles below 300 nm. Different nanoparticle morphologies such as spherical, star shaped and rods can be produced with different combinations of other variables in low and high frequencies, as produced with the KRAIC and KRAIC-D in Chapters III and IV. Mixing intensity depends on frequency, increased frequency provides higher Oscillatory Reynolds (Re_o) number, consequently the power of the mixing increases with high frequency. This frequency behaviour will be investigated in section V.5 of this chapter *via* Computational Fluid Dynamic (CFD) studies of the OBR.

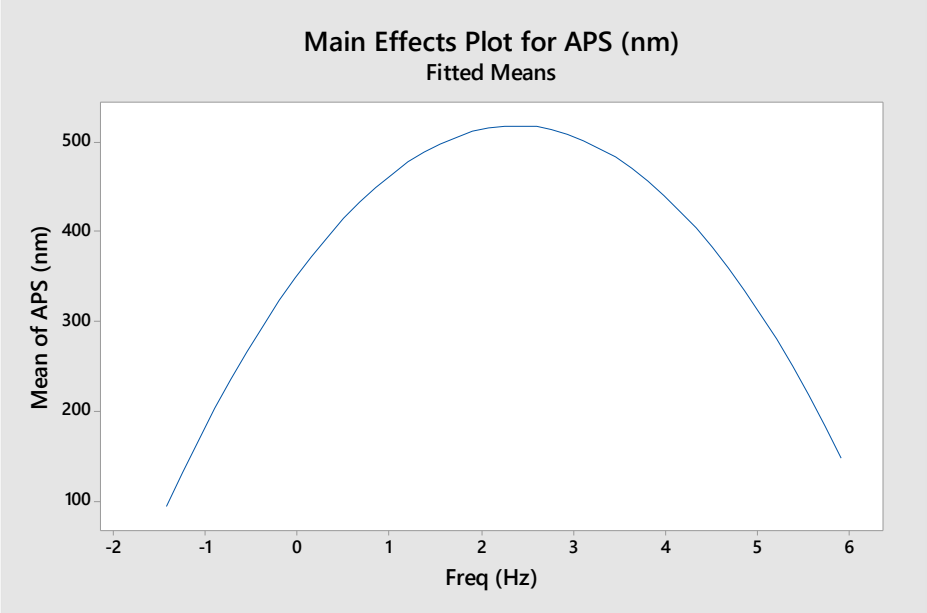

Figure.V.19 Main effects of frequency on particle size of PiC produced inside the OBR.

V.3.4.iii Effect of the Amplitude on the Particle Size

The effect of the amplitude of the OBR system on the particle size of PiC was investigated between 1-5 mm. Lower amplitudes (1-2.25 mm) produced larger nanoparticles (400-800 nm). Smaller nanoparticles (100-200 nm) were achieved within mid-range amplitudes (2.25-3.5 mm). Above 3.5 mm, increased amplitude resulted in larger nanoparticles as shown in Figure.V.20. Amplitude has similar influence as frequency in terms of mixing intensity, higher amplitude means higher Re_o.

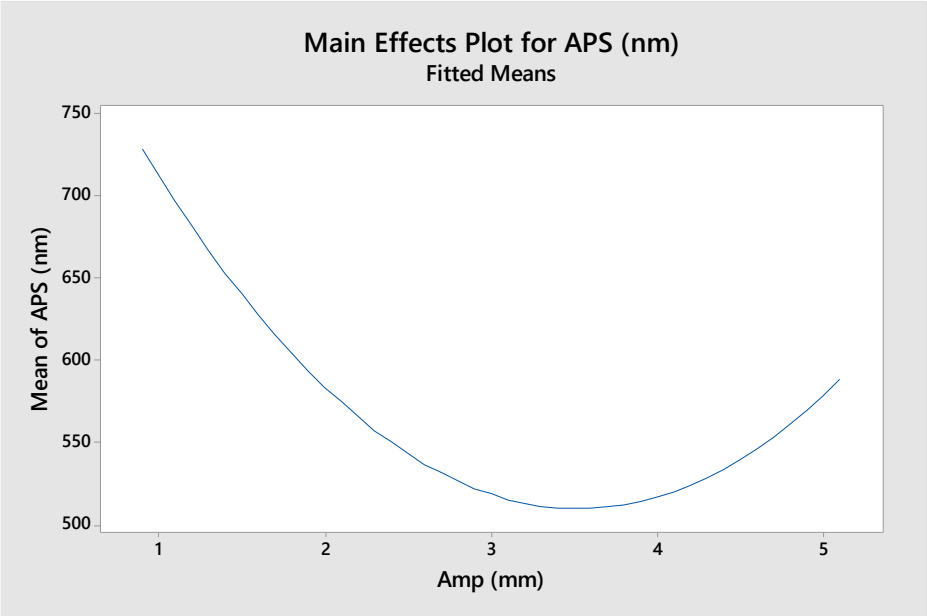

Figure.V.20 Main effects of amplitude on particle size of PiC produced in the OBR.

V.3.4.iv Effect of the Residence Time on the Particle Size

Residence time (RT) effect had similar trend as for amplitude. 20-25 minutes was the optimum residence time to synthesise the smallest PiC nanoparticle compounds (100 nm). Faster (4-15 min) residence times resulted in nanoparticle sizes between 400-500 nm. Longer residence times (between 15-20 min) resulted in smaller nanoparticles (between 100-500 nm).

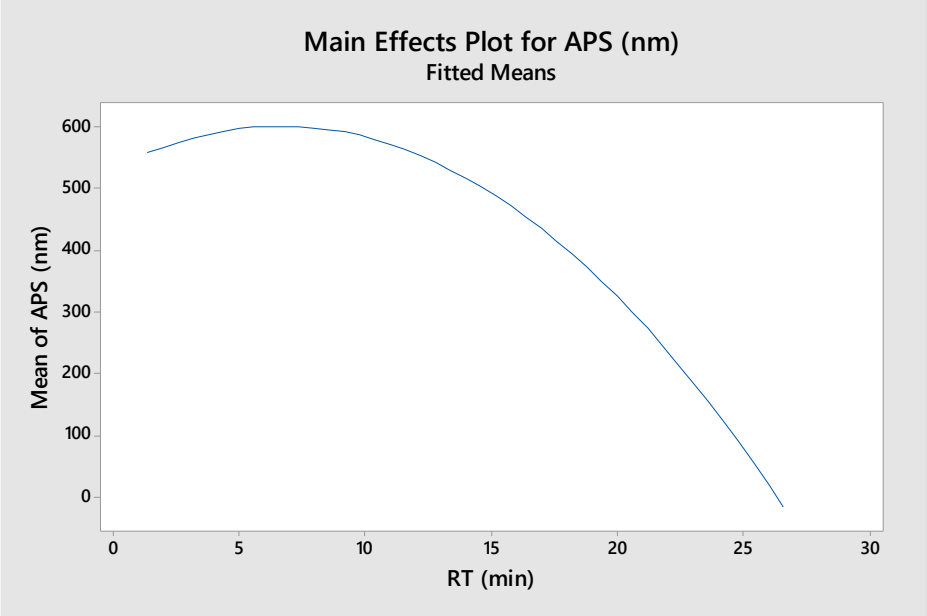

Figure.V.21 Effect of residence time (RT) on particle size of PiC produced in the OBR.

V.3.4.v Effect of the iron (II) tetrafluoroborate hexahydrate $Fe(BF_4)_2$ $6H_2O$ and 1,2,4 triazole (Trz) Concentration on the particle size

The concentration of $Fe(BF_4)_2 \cdot 6H_2O$ and (Trz) was used between 2 and 10 g/100mL to investigate its effect on the particle size. With 6 g/mL $Fe(BF_4)_2 \cdot 6H_2O$ concentration the smallest nanoparticles were achieved (520 nm). An increase beyond 10 g/mL resulted in larger nanoparticles (600-900 nm). Concentration below 4 g/mL also increase the size of the particle size to (600-900 nm).

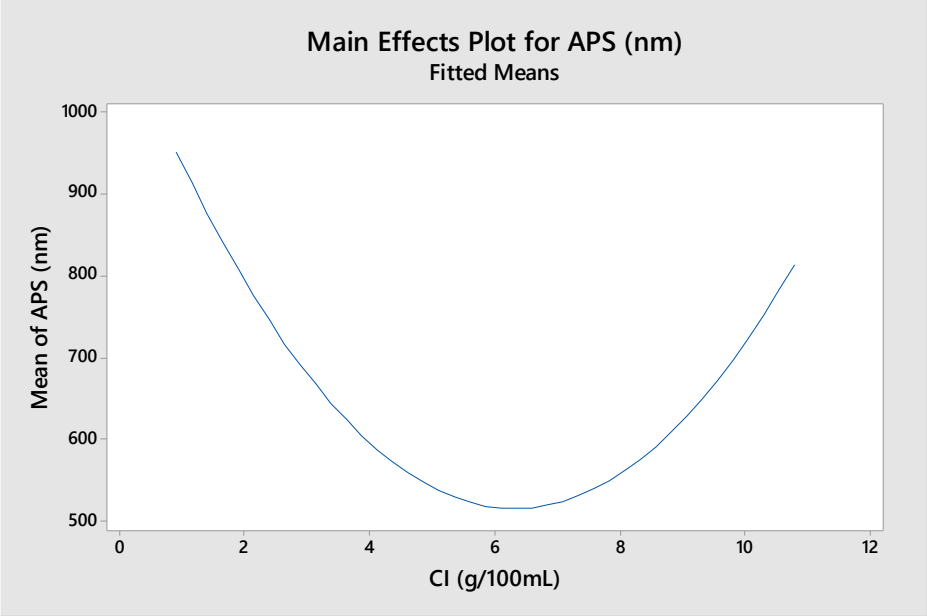

Figure.V.22 Main effects of concentration of $Fe(BF_4)_2$ $6H_2O$ (CI) on particle size of PiC produced in the OBR.

The effect of the concentration of 1,2,4-H-triazole was interesting, with a reverse correlation between particle size and concentration of the 1,2,4 H-triazole and $Fe(BF_4)_2$ $6H_2O$. An increase in the concentration of the triazole resulted in smaller nanoparticles as shown in Figure.V.23 but the range of particle size stayed between 400 nm and 540 nm.

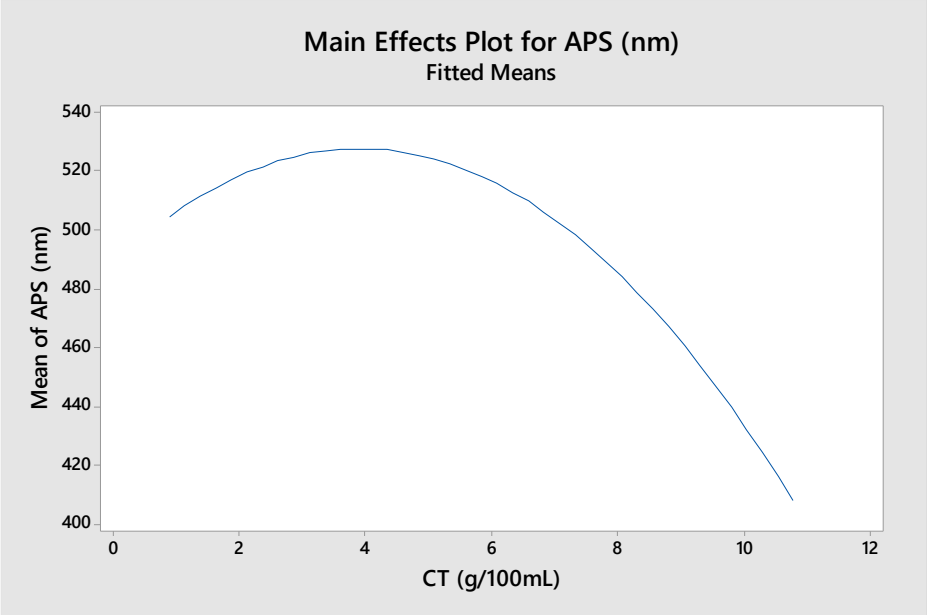

Figure.V.23 Main effect of 1,2,4 H triazole (CT) concentration on particle size of PiC produced in the OBR.

The behaviour (Figure.V.23) of particle size changing with the concentration was previously reported in Zhao *et al*, where SEM results are reported for PiC and the shape and size of particles is correlated with the concentrations of both reagent but was difficult to control. [217] However the reverse micelle technique has been shown to control particle size with concentration, temperature and time by Moulet *et al*.[218], but the use of surfactant could potentially affect switching properties.

With the main effect of each parameters studied in part V.3.4.ii, **Error! Reference source not found.**V.3.4.iii and V.3.4.iv it is seen that the model was not capable of processing some values. For the frequency, Figure.V.19, negative values are present which is not realistic, the model should consider values under 0 to be removed. Compared to the amplitude, Figure.V.20, the frequency has an opposing effect on the particle size, which together contradicts an expected trend, at high frequency and small amplitude the mixing should be more intense and the reagents should react faster but for small amplitude (1 mm , 2 mm) particles between 550 and 750 nm (183 nm for DOE 32) are obtained while for high frequency (5 – 6 Hz) the particle size is between 300 to 100 nm (496 nm for DOE 2). For the overall effect of RT on the APS,Figure.V.21, it is seen that at longer RT smaller particle sizes are obtained which is not the case as can be seen for DOE 17 and 19 with 20 min RT and 743 nm and 1120 nm average particle size. It is also noted that the particles have more time to grow inside the reactor with longer residence which should lead to bigger particle size than small ones. However other parameters should be taken into account such as baffle spacing, but also considering a factor by itself while ignoring the others is not representative of the model, looking at the overall trend is necessary to have a better view of the results than factors by factors.

Comparing the average particle size in relation to the concentration of each reagent, CI and CT, Figure.V.22 and Figure.V.23, it is also difficult to assess a trend. It is expected that, for higher concentrations of CI (above 8 g/100mL), particles above 600 nm should be present looking at Figure.V.22 but DOE 20 and 21 have average particle size of 189 and 264 nm with CI of 3.375 g/mL and 8.32 g/mL. From the overall particle size effect plot in Figure x, a concentration of 0.901 g/100mL CI would be expected to produce an APS of 950 nm but DOE 15 displays an average particle size of 106 nm. Low concentration of CT is expected to lead to particles averaging around 500 nm, Figure x, but DOE 13 show particles of 153 nm for 0.901 g/mL of CT.

With the assumptions stated above, the next section will focus on the model equation itself while introducing the variance which will show the confidence in the DOE to target particle size.

V.3.5 DOE Equation Mapping for PiC targeting

The surface response method (SRM) constructs a polynomial approximation of the limit state function based on the results obtained by DOE. This method is used to build and optimise a model. SRM is a mathematical procedure for the analysis of problems, in this case the particle size targeting optimisation.

In this study, the effect of the input parameters frequency (Freq), amplitude (Amp), residence time (RT), concentration of $Fe(BF_4)_2 \cdot 6H_2O$ (CI) and concentration of $C_2H_3N_3$ (CT) on particle size targeting of PiC is discussed.

The SRM approach will be expressed by a response surface as a second order polynomial regression (Section II.10) equation like the following:

$$ASP = a_o + \sum a_i x_i + \sum a_{ii} x_{ii}^2 + \sum a_{ij} x_i x_j + e_r \qquad (25)$$

The polynomial regression equation is described in the methods section Chapter II.

Using the data presented in the sections above and the regression model in Minitab has determined the statistical significance of each factor in terms of average particle size (nm) (Table.V.9). The selection confidence level of 95% was chosen for the P values to be above 0.05. The analysis reveals

that some parameters need to be optimized in the model – the average particle size has a total variance of R^2 = 63.75 %. If R^2 is closer to 100 %, the accuracy of the predicted model is better.

Adj SS is the adjusted sum of squares that quantifies the variation in the response data in each term. Adj MS is the adjusted mean squares which measures how much the variation of a term affects the model. DF is the degree of freedom which is the amount of information in the data obtained. F-value shows if the terms is associated to the response model, it is the ratio of two variances and can assess their equality and test the significance of the regression model. Data have been investigated by means of normal probability plot. Residual normal probability plot for APS is shown in Figure.V.24. Even with a large residual, the normal probability plot is close to the straight line. These results show that errors are positioned normally and scattering has not been observed for the APS.

Following the Table.V.9, residence time (RT), concentration of $Fe(BF_4)_2{\cdot}6H_2O$ (CI), Frequency x concentration $C_2H_3N_3$ (Freq x CT), residence time (RT) x concentration $Fe(BF_4)_2{\cdot}6H_2O$ (RT x CI) and residence time x concentration $C_2H_3N_3$ have the most significant influence on the APS. However, other parameters including frequency have a high P-value compared to other factors, and the interaction between Freq x Amp suggests that the particle size is not as affected by the combination of those two parameters. From this model the response surface equation can be obtained for APS and is given below: (The equation has been factorised for more visibility and the full version will be given in the appendix (**A5, Equation A5.1**).

$$\begin{aligned} PSD = 225 + a(187 - 29.5a - 17.3b - 13c - 12.8e + 44.4d) \\ + b(31.8b - 28 + 8.5e - 19.2c - 28.1d) \\ + c(14.9c - 183) + d(273 - 2.5d - 17.c) + e(19 \\ - 1.56e + 12.98c - 12.03d) \end{aligned} \quad (26)$$

A = Freq, b = Amp, c = CI, d = CT, e = RT

With this expression surface equations can be obtained for a combination of two parameters, Figure.V.25 presents the 2D contour plots of the APS versus five input parameters (CI, CT, RT, Amp, Freq) Regions with different colours describe the interaction of the input parameters and their impact on the APS.

Table.V.9 Regression coefficients and model of Average Particle Size (APS)

Source	DF	Adj SS	Adj MS	F-Value	P-Value
Model	20	3434286	171714	0.97	0.545
Linear	5	523092	104618	0.59	0.709
Freq	1	3023	3023	0.02	0.899
Amp	1	26880	26880	0.15	0.705
RT	1	450578	450578	2.54	0.139
CI	1	28583	28583	0.16	0.696
CT	1	14028	14028	0.08	0.784
Square	5	527644	105529	0.59	0.705
Freq*Freq	1	135396	135396	0.76	0.401
Amp*Amp	1	29719	29719	0.17	0.69
RT*RT	1	92555	92555	0.52	0.485
CI*CI	1	243069	243069	1.37	0.267
CT*CT	1	7090	7090	0.04	0.845
2-Way Interaction	10	2378220	237822	1.34	0.318
Freq*Amp	1	14742	14742	0.08	0.779
Freq*RT	1	287326	287326	1.62	0.23
Freq*CI	1	50907	50907	0.29	0.603
Freq*CT	1	590969	590969	3.33	0.095
Amp*RT	1	41501	41501	0.23	0.638
Amp*CI	1	36028	36028	0.2	0.661
Amp*CT	1	77444	77444	0.44	0.523
RT*CI	1	593342	593342	3.34	0.095
RT*CT	1	509937	509937	2.87	0.118
CI*CT	1	176024	176024	0.99	0.341
Error	11	1953095	177554		
Lack-of-Fit	6	1263700	210617	1.53	0.329
Pure Error	5	689395	137879		
Total	31	5387381			

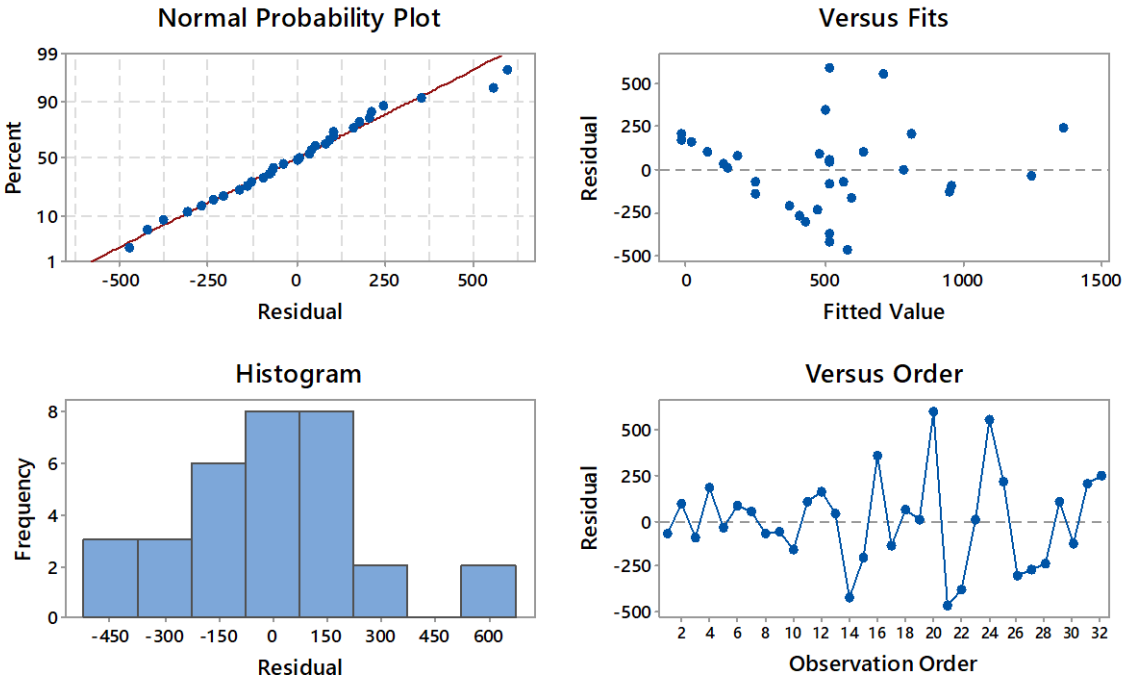

Figure.V.24 Residual normal probability plots for Average Particle Size (APS)

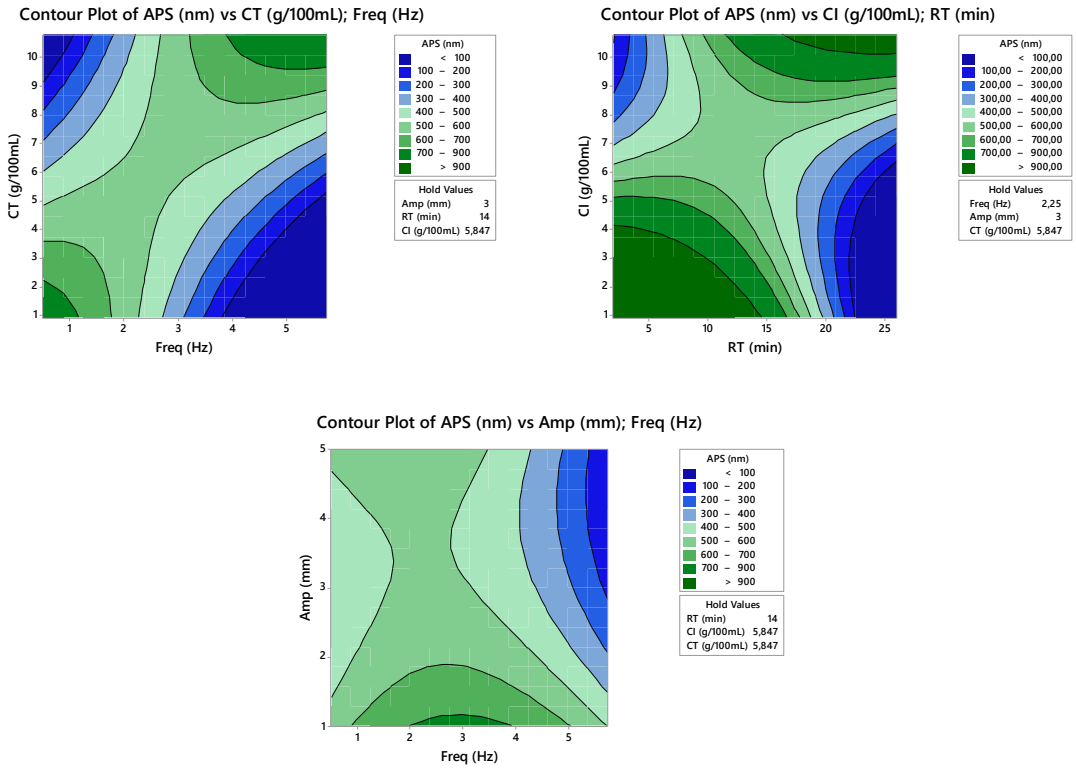

Figure.V.25 2D contour plots of Average Particle Size (APS) versus input parameters based on DOE surface response model equations.

Examining the 2D plots of CT and Freq, as they increase together the APS increases as well. However, when one of the parameters stays the same and the other increases the APS increases then reduces. The graph Amp x Freq shows the APS is not much affected and stays at values around

400 nm unless the frequency is considerably increased to near the limit of the system. Specifically, the interaction graphs present that the concentration of both reagents have an effective role in the particle size control. The results show the impact of the residence time (RT) on the APS compared to CI, at low RT and low CI the particle size is above 1000 nm, when keeping low value of CI and increasing the RT the APS diminishes to 100 nm for CT value of 5.847 g/100mL.

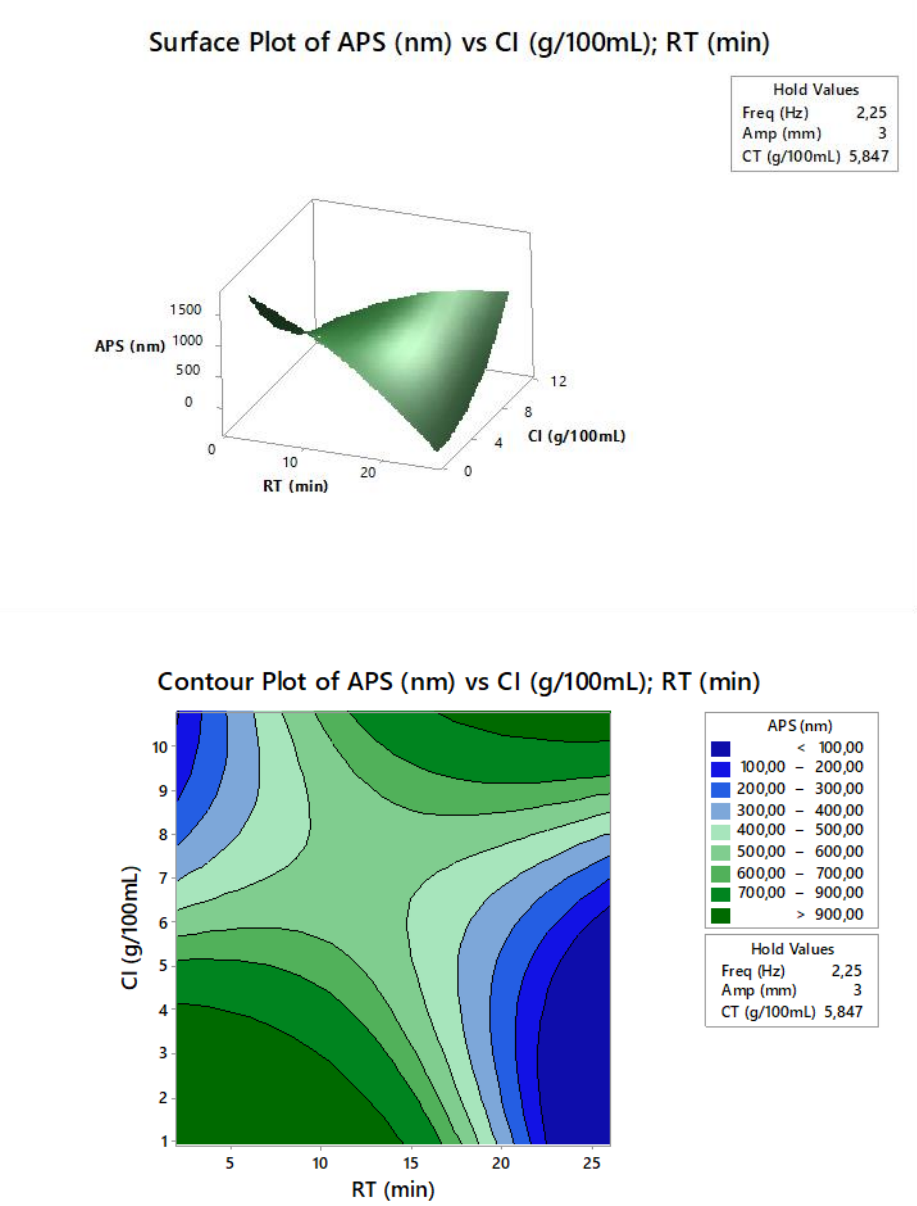

Figure.V.26 3D Surface plot of RT versus CI for APS with the corresponding 2D plot

Figure.V.26 shows a 3D surface of the APS versus the residence time and CI. In cases where the RT is shorter than 5 minutes and CI is low, the APS increases drastically for a CT of 5.847 g/100 mL. However for high RT at 20 min with a CI below 4 g/100mL, the APS starts to reduce and even goes below zero which means no product can be found for those concentrations at some point. The model shows that the APS is adversely affected when the concentration of one of the reagents is increased or decreased. It is seen as well from Figure.V.25 that increasing CT and CI contributes to a decrease in the APS. This is in accordance with the findings of Chapter III, where the KRAIC was able to produce small, 100 nm, particles with high concentration, CI and CT at 10.793 g/mL as displayed on the 2D plot for the OBR DOE on Figure.V.27

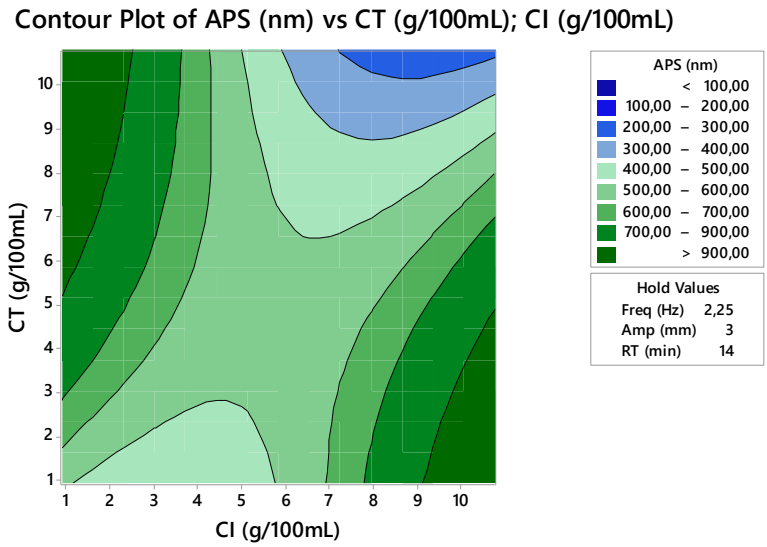

Figure.V.27 CT and CI 2D plot showing the small size of PiC obtained at high concentration.

The 2D plots show that the majority of parameter values return particles with a calculated APS between 400 and 600 nm, corresponding to the highehst surface area in those graphs. As previously stated a lot of experiments on SEM and DLS show an APS oscillating between 400 nm and 600 nm for middle range concentration and parameters. This has been confirmed in sections V.3.2, V.3.3, where most of the experiments oscillate between those values. This suggests that the OBR system is most suitable for particles ranging from 400 to 600 nm APS. The advantage of using the OBR for this purpose is to avoid using surfactants as used in the reverse micelle technique.[218] To investigate the targeting capabilities of the OBR the response surface model will be used to obtain specific particle size of PiC in part V.3.6. The theoretical model of the OBR with the surface response equation shows also that to get small particles, the parameters required include extremely high concentration of reagents, high frequency, low RT or high amplitude and the OBR would have physical limits to target smaller particles below 300 nm.

The graphics presented above are useful to determine and to optimize the process. The equation generated to create those surfaces is used in the next section V.3.6 to target PiC particles of a specified particle size. Other surfaces and 2D plots will be given in the appendix (**A5, Figure A5.1 to 3**).

V.3.6 Surface response model application to targeting

Using the equation (26) previously defined with the regression surface response, input parameters were optimized to target particle size. Parameters from the algorithm are subject to limitation, the reactor being not suitable for some parameters. For instance, amplitudes below 1 mm are not achievable nor are frequencies below 0.5 Hz. The precision cannot be below 1 decimal (0.1 Hz or 0.1 mm). The residence time is controlled with the flow rate of the four pumps which is in this case more precise; these parameters can be precise up to 0.01 ml/min.

Two of the most important aspects of the model to ascertain are the capability of targeting particles and the consistency of those results over several residence times inside the reactor.

A range of experiments were carried out to target particle sizes from 100 nm to 1000 nm. Each of those experiments parameters are shown in Table.V.10 and have been created *via* the Minitab model previously presented.

Table.V.10 Targeting PiC from 100 nm to 1000 mm with particle size results from three residence times.

	Freq	Amp	RT	CI	CT	APS obtained (nm)		
Target	**(Hz)**	**(mm)**	**(min)**	**(g/100mL)**	**(g/100mL)**	**RT 1**	**RT 2**	**RT 3**
1000 nm	4.0	2.0	2.3	0.9	2.4	458.7	255.0	141.7
900 nm	3.0	2.0	2.3	0.9	2.4	458.7	825.0	122.4
800 nm	5.0	2.0	2.2	0.9	2.0	458.7	342.0	458.7
700 nm	5.0	2.0	2.1	0.9	1.7	458.7	255.0	255.0
600 nm	3.1	3.0	14.0	5.7	10.8	220.2	615.1	615.1
500 nm	3.0	5.0	2.0	2.6	0.9	712.4	1483.9	712.4
400 nm	5.7	3.5	26.0	10.8	0.9	458.7	396.1	615.1
300 nm	5.1	2.0	7.5	10.8	3.2	396.1	712.4	531.2
200 nm	1.0	5.0	4.0	10.8	0.9	458.7	458.7	190.1
100 nm	3.5	2.0	25.2	10.8	10.7	531.2	295.7	531.2

Table.V.10 shows the average particle sizes resulting from each experiment after three RT (corresponding SEM images shown in Figure.V.28). For 200 nm and 600 nm the particle size corresponds to the targeting of the model for the third residence time. The resultant average particle size corresponds to the targeted size within 10 %. For 800 and 1000 nm targeted runs, the divergence of obtained particle sizes *vs* calculated shows discrepancies of 90 and 85 %. Some results like the RT 2 for 500 nm at 1483 nm could be due to aggregates or dust inside the DLS cuvette or solution (those were still present after repeating the measurement). It was also often observed through the Malvern Zetasizer analysis that the samples had a fast sedimenting behaviour which could give some inaccurate particle size measurements such as calculating larger particles than those present; this issue will be addressed in Chapter VII using Analytical Ultra Centrifugation (AUC). For a targeted range of 400 nm to 600 nm the DLS results show a close range of particles between 700 and 500 nm, in this area of targeted APS the experimentally obtained results are generally close to those targeted. To explain the change of particle size compared to the target, the difference in residence time and concentration of reagent have a significant importance.

For 100 nm target the residence time is 25.2 min and the reagent concentrations 10.793 and 10.71 g/100mL. In that case particles have a lot more time to grow and with those concentrations sedimentation can occur easily; this small APS target may be reached for instance with round baffles instead of sharp baffles to avoid the problem of dead zone. For the 700 nm to 1000 nm targeted APS the opposite measures should be taken – RT and concentration should be increased whilst retaining the same Iron/Trz concentration ratio. As stated before, the confidence of the model from Minitab is 63.75 % from DLS results.

However, DLS does not discern between length and width of particles, this is of particular consequence for rod-shaped particles like those analysed here. The rod length or cross-section is analysed as the hydrodynamic diameter of the particle, the equivalent sphere, around it as displayed in Figure.V.29. In Figure.V.28 the SEM images show that, for big particles (700 to 1000 nm), the particle size is in the targeted range for 700 nm with some aggregates, while on the other hand for 1000 nm needle shape particles around 1500 and 2000 nm are found which does not correspond to the DLS-detected particle ranging from 141 nm to 458 nm. For 100 nm targeting, particles ranging from 100 nm to 180 nm are seen in the SEM which suggest the targeting may in fact work for these small particle sizes. This target was also achieved at high concentration of reagent close to those used for the KRAIC and KRAIC-D in Chapter III and IV which displayed spherical particles in that size range. For the 700 nm target APS, the SEM image shows particles around 1000 nm.

This epitomises the inherent DLS problem in describing the size of non-spherical particles. As explained in the Methods Section in Chapter II.8, this technique is sensitive to particle properties such as aspect ratio, density and scattering intensity and those properties will affect the hydrodynamic diameter measurement from the DLS. Therefore, the use of SEM to check particle size is necessary even if the size under microscopy techniques will depend on parameters such as edge or contrast of the particle. However, in these cases, the SEM showed that the targeting was not obtained except for the 100 nm particle target, which displayed spherical particles in that range. For the 500 nm target, particles are around 1000 to 1500 nm sizes with rod shape like particles and for the 1000 nm target, the particles aspect are needles with particles ranging between 1100 nm and 2000 nm which suggests that the model needs improvement with more experimental data.

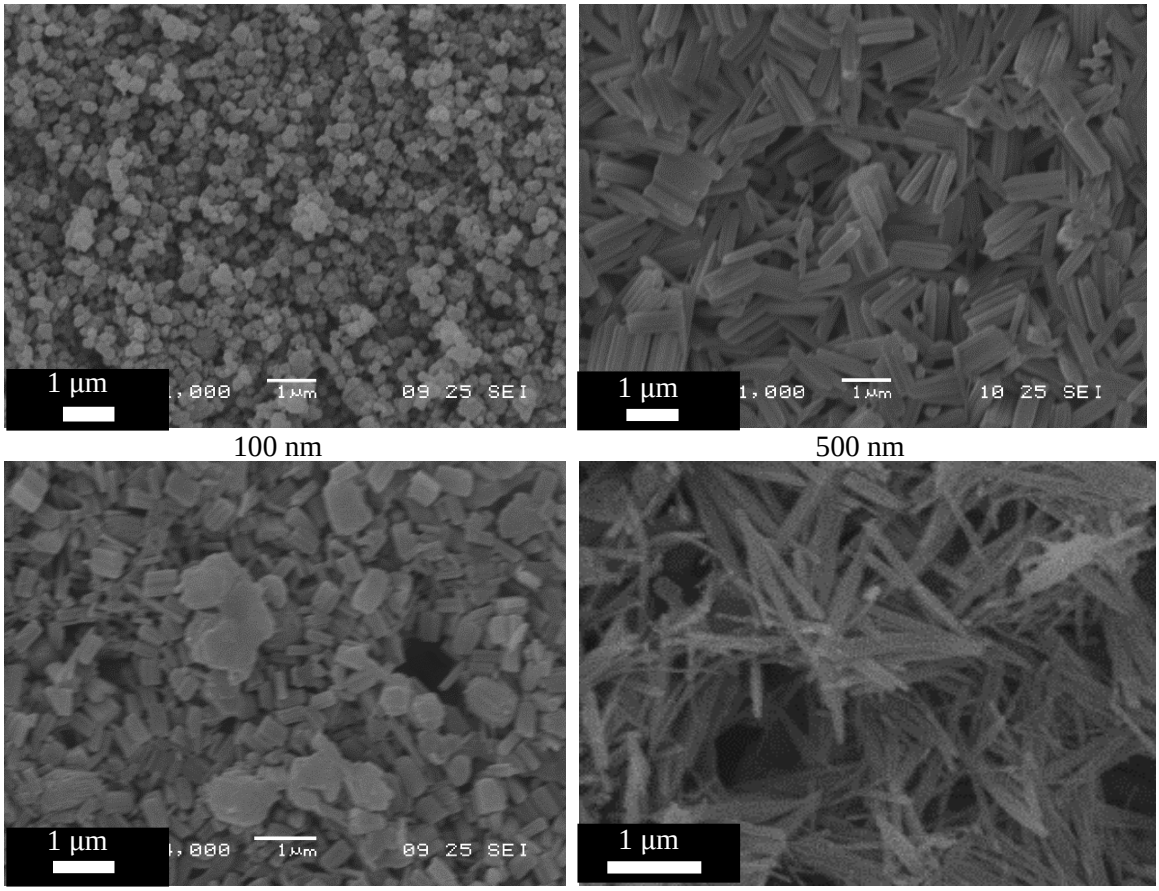

Figure.V.28 SEM of 100 nm, 500 nm, 700 nm and 1000 nm target particle size for PiC produced with the OBR.

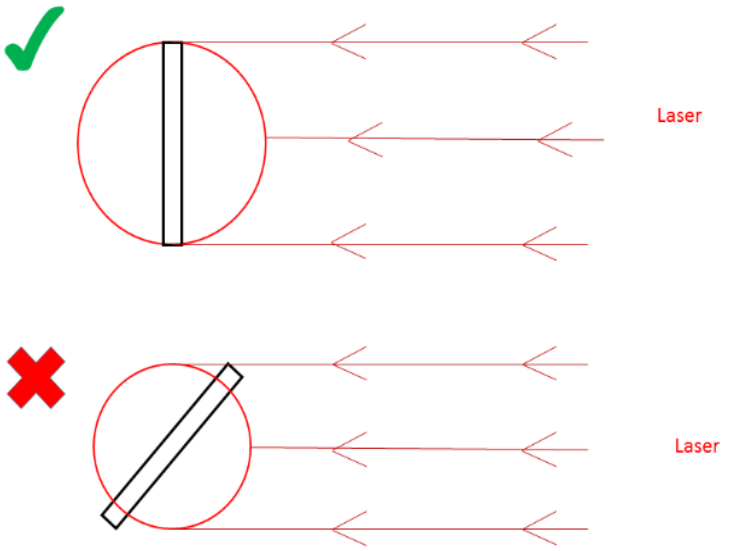

Figure.V.29 Scheme of the effect of particle orientation on DLS analysis around a rod shaped like particle.

The DOE and the targeting showed the importance of each parameter on the particle size for PiC. The model needs improvement due to the variance of 63.75 %, and this can be achieved through optimization of the measurement system, a coupling system between DLS and SEM but also an optimization of the reactor design. Other SEM image analysis methods could be used such as ImageJ®, which with a proper black/white threshold could potentially lead to better particle size distribution of the sample. Adding a more viscous solvent such as ethylene glycol in the DLS cuvette could also help slowing down the sedimentation rate of the particle, this is also addressed *via* AUC analysis in Chapter VII.

V.3.7 Study of steady state for PiC production

To see consistency and steady state of the process, longer experiment runs are needed. At the beginning three residence times were evaluated for all given sets of parameters. Results in Table.V.11 show that consistency of particle size is not necessarily achieved within 16 RT in a run with the following parameter values: 2.25 Hz Frequency, 3 mm amplitude, 14 min RT , 5.847 g/100 mL CI and 10.793 g/100mL CT; these correspond to the DOE 14th experiment described above. With an increase in residence time the average particle size initially increases in size until stabilizing towards a certain value.

Table.V.11 APS consistency measurements for 16 residence times using DOE 14 parameters for PiC synthesis inside the OBR.

Residence Time (min)	APS from DLS(nm)
RT 1	549.7
RT 2	605.8
RT 3	609.8
RT 4	831.5
RT 5	662.1
RT 6	1581.7
RT 7	869.8
RT 8	624.2
RT 9	661.2
RT 10	791.0
RT 11	546.8
RT 12	928.5
RT 13	466.8
RT 14	388.9
RT 15	410.4
RT 16	412.44

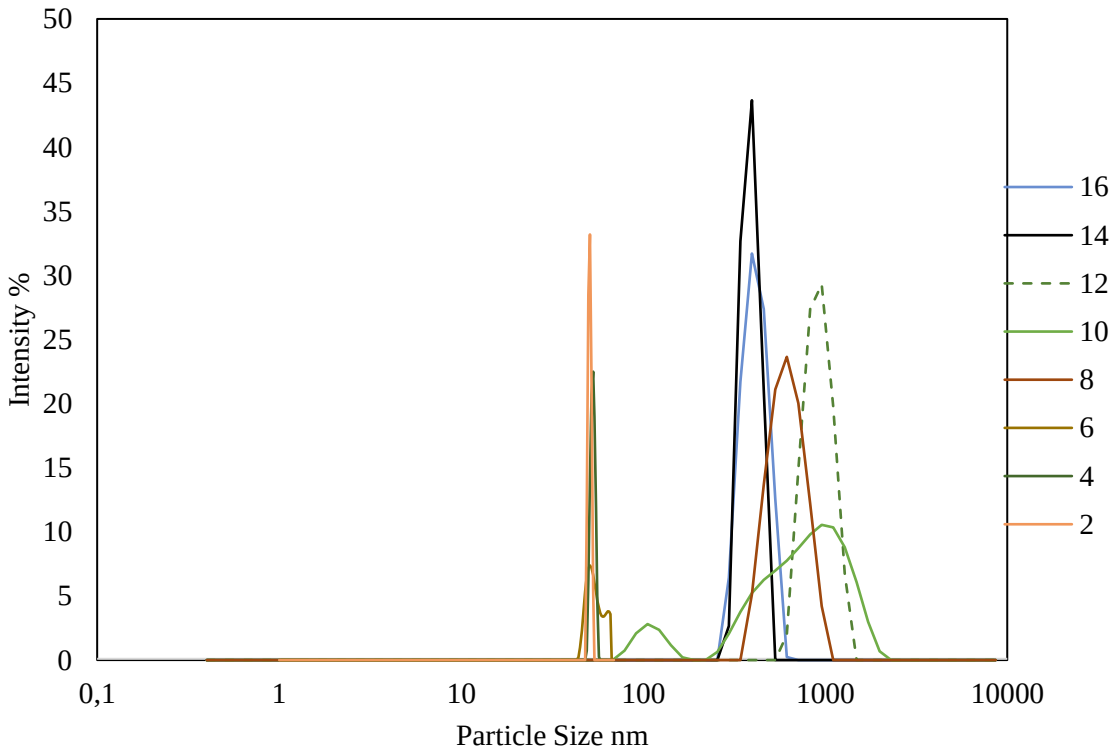

Figure.V.30 DLS results for the 16 RT consistency run using the parameters for DOE 14 for PiC synthesis in the OBR. For clarity only every second RT is displayed.

The results shown in Table.V.11 and Figure.V.30 above show the APS stabilises at around 410 nm. The results have been verified by SEM microscopy every second RT, Figure.V.31. Analysis of all RT is given in Appendix (**A5, Figure A5.4**).

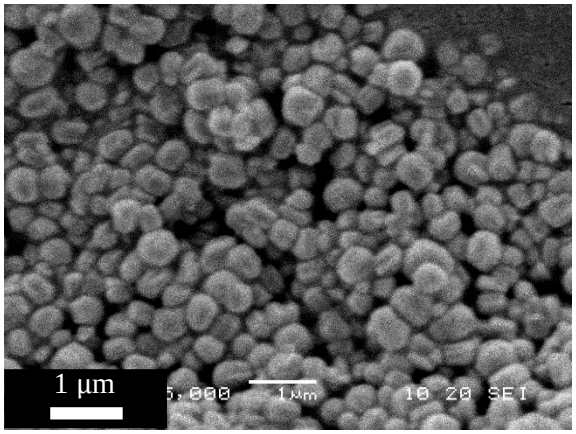

2

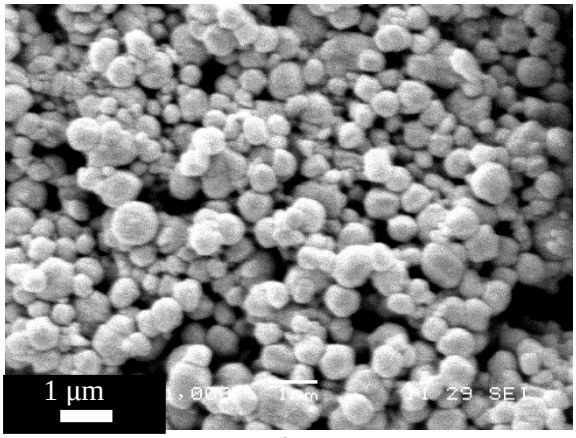

4

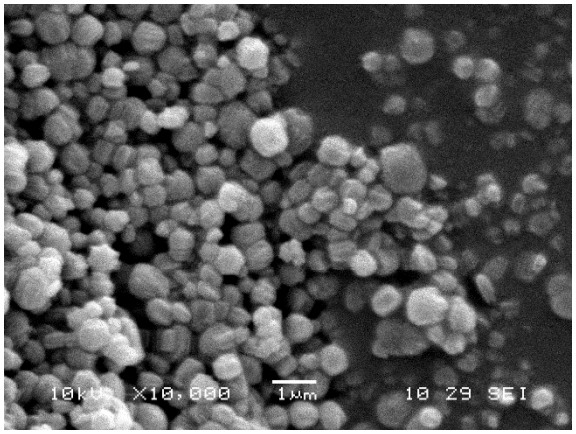

6

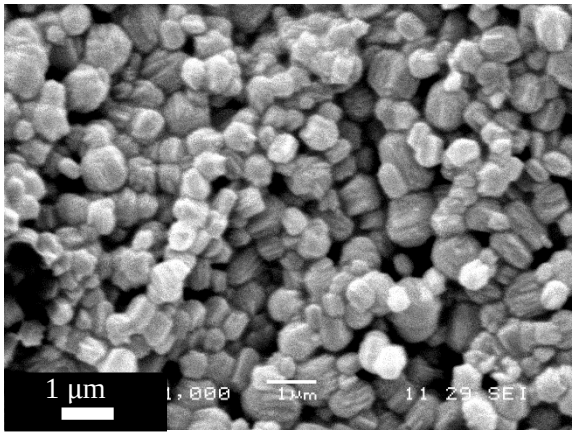

8

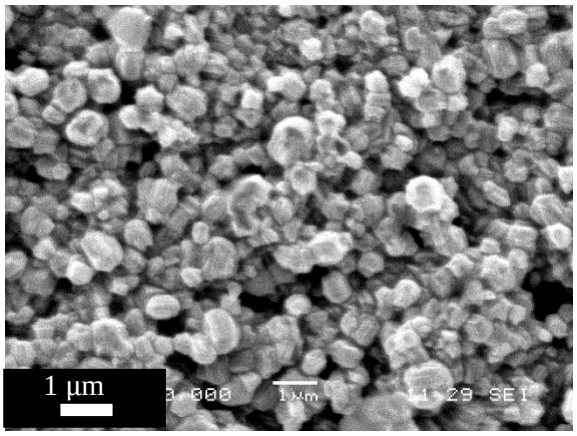

10

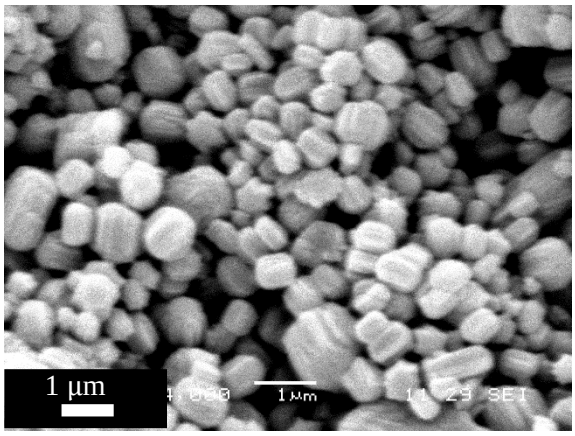

12

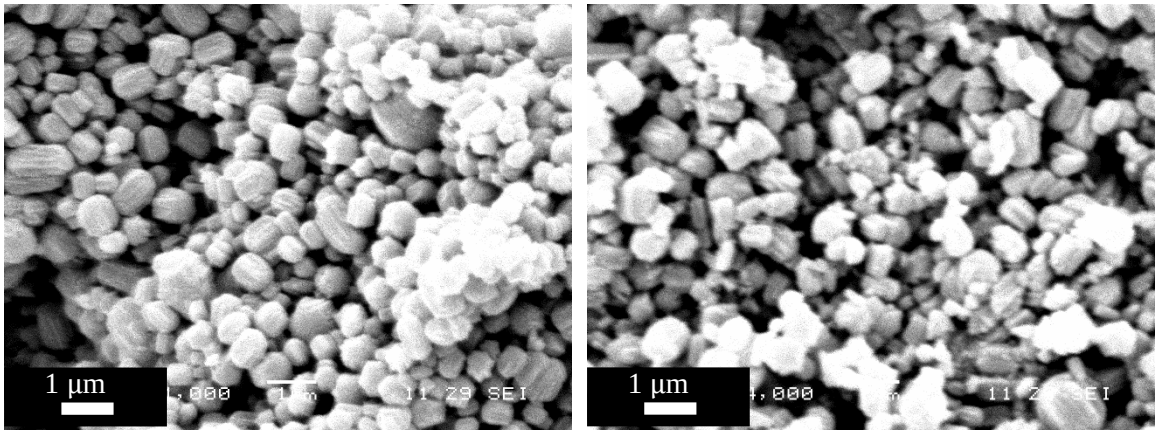

14 16

Figure.V.31 SEM for the 16 RT consistency run using the parameters for DOE 14 for PiC synthesis in the OBR. Displayed are RT 2, 4, 6, 8, 10, 14, 12, 16.

Table.V.11 shows that, after the 13th RT, where DLS results indicate that the particles are clos eto the 400 nm target, the particle size obtained was consistent. Before the 13th RT, the particle size varied between 500 nm and 1500 nm with some consistency plateau at the beginning as displayed on Figure.V.32. between RT 1 and 5 and between RT 8 and 11.

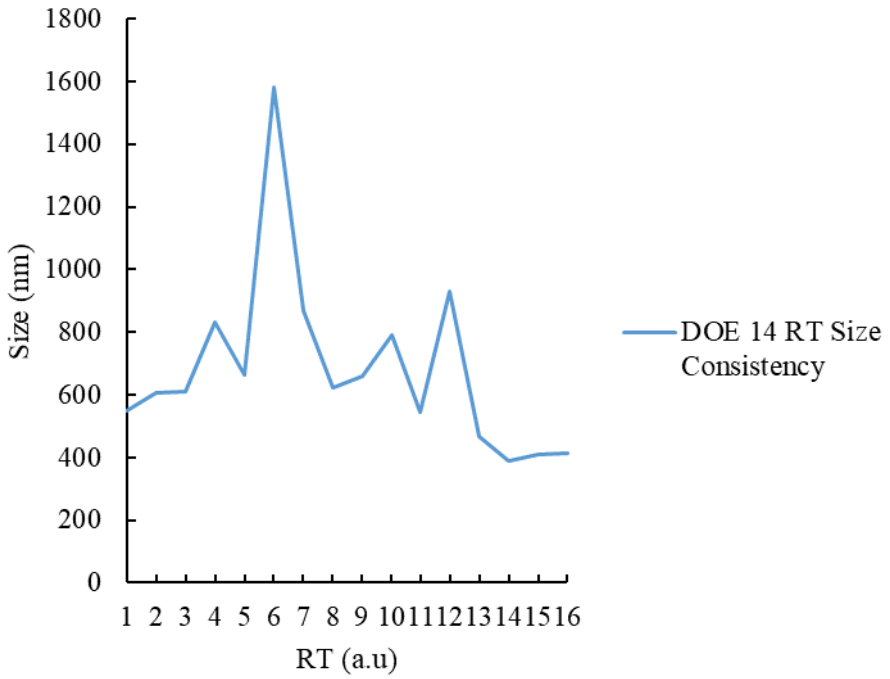

Figure.V.32 16 RT particle size variation inside the OBR obtained *via* DLS, for DOE 14 parameters.

The sub-optimal reactor geometry is still evidenced by the level of sedimentation observed at the end of the 16 RT run (Figure.V.33). This reactor geometry was designed for emulsion generation and so, despite the low density of the nanoparticles, sedimentation has occurred. That the APS of the effluent of the reactor remains steady despite increasing sedimentation, suggests that, under these

parameters and above a critical particle size, the sedimenting particles cannot re-suspend and so do not influence the continuing particle production.

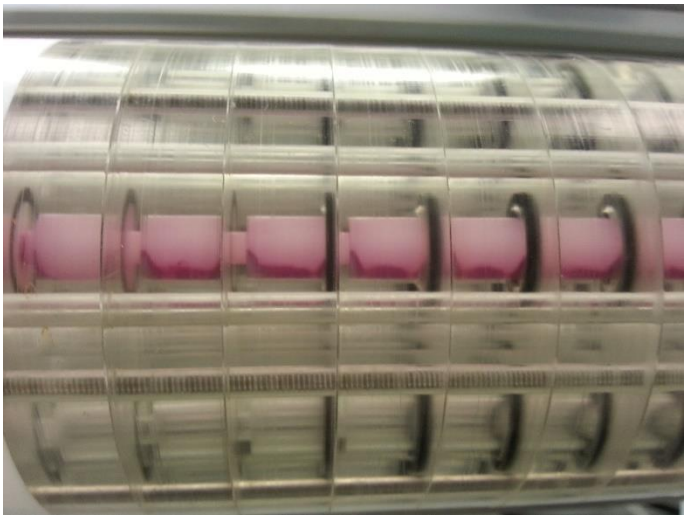

Figure.V.33 Sedimentation in the OBR at RT 16 showing the sedimentation of PiC occurring between baffles.

Table.V.12 Repeatability of experiment DOE 14 in the OBR for PiC synthesis

	Experiment DLS APS size (nm)		
Residence time	1	2	3
RT1	510.5	432.7	400.6
RT2	456.3	456.7	476.87
RT3	461.9	531.2	536.3

Consistency checking over multiple experiments was also carried out for the same set of parameters as used for the 16 RT run: 2.25 Hz frequency 2 mm amplitude 14 min residence time (DOE 14). Table.V.12 shows the repeatability of the experiment over three RTs, each one shows an APS between 400 nm and 536 nm. This corresponds well to the targeting for those parameters, 458 nm, and shows the consistency through experiments.

DOE experiments 7, 5, 20 and 30 have also been repeated to see if particle size and shape were the same as those found in the original DOE results. These have been reproduced three times at different intervals and dates to confirm consistency. Figure.V.34 shows the SEM images of the results of those experiments (images from the second and third SEM repeat experiments are given in supplementary information **CDCh5-5**. It is shown that DLS (Figure.V.35) and SEM results correlate with the results previously obtained during the DOE. Shapes of particles are also reproducible over several experiments. It should be noted that the experiments were performed with a spacing of several days between experiments to ensure there is minimal systematic error.

DOE Repeat

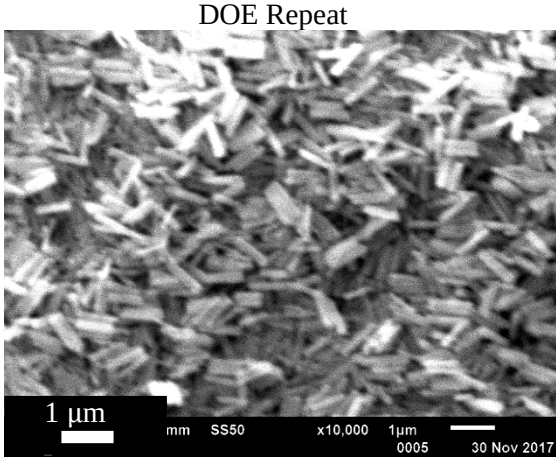

Original DOE

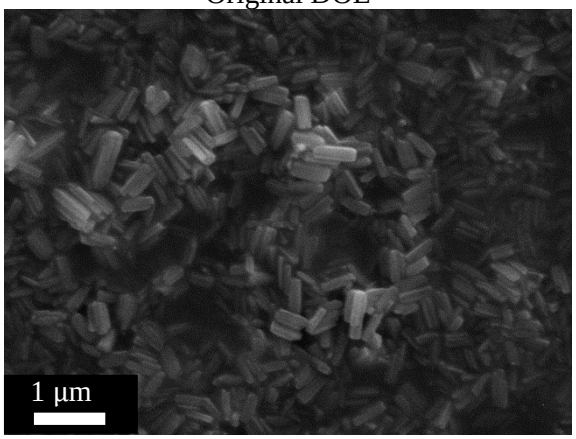

5

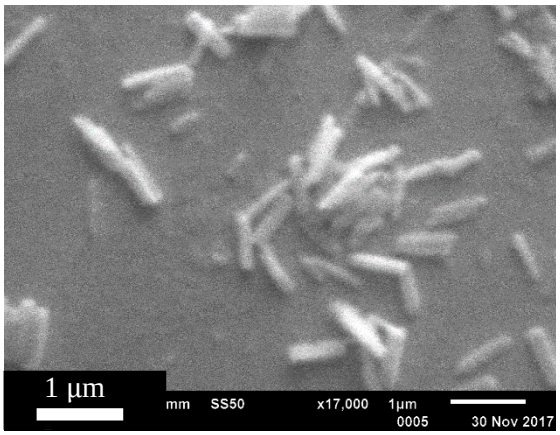

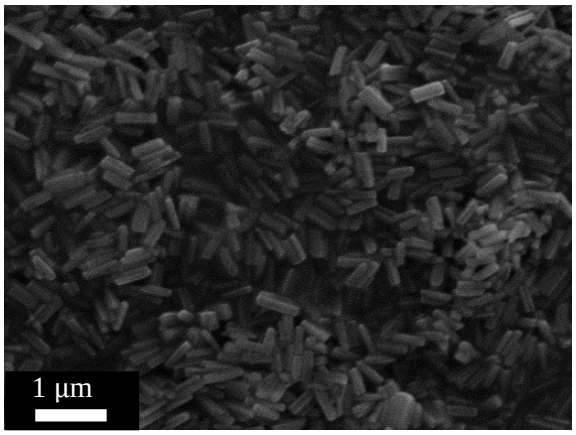

7

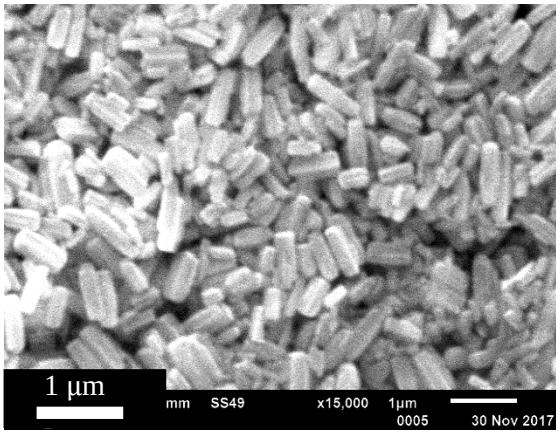

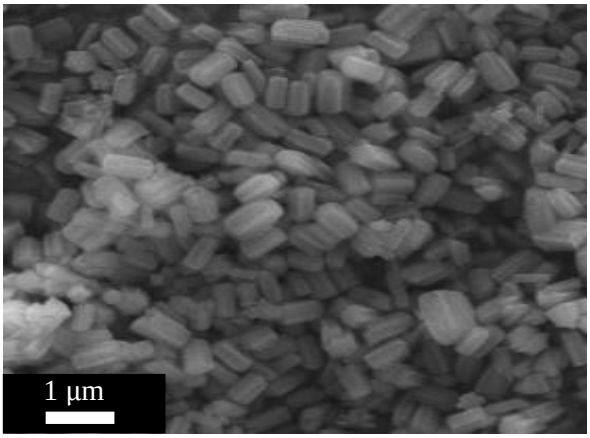

14

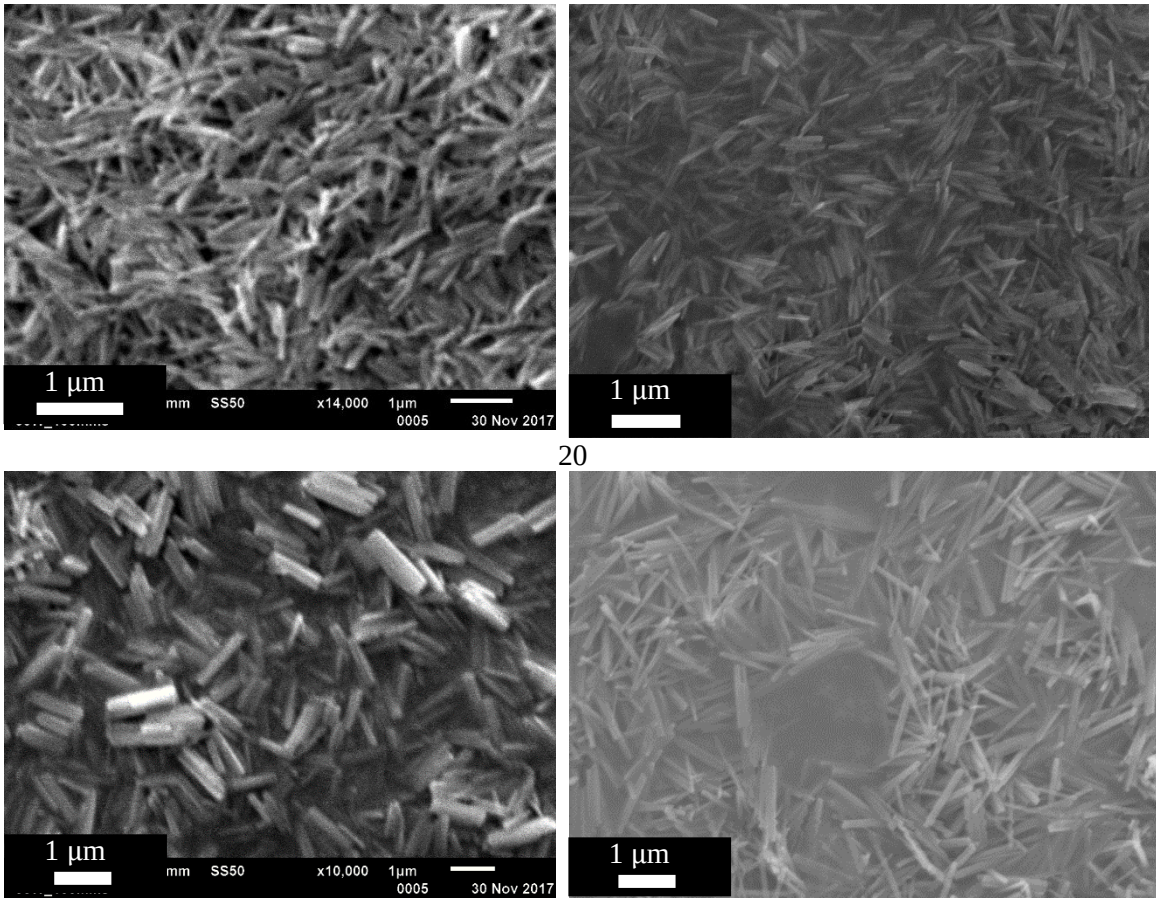

Figure.V.34 SEM images of PiC repeat experiments for DOE 5, 7, 14, 20, 30 experiments.

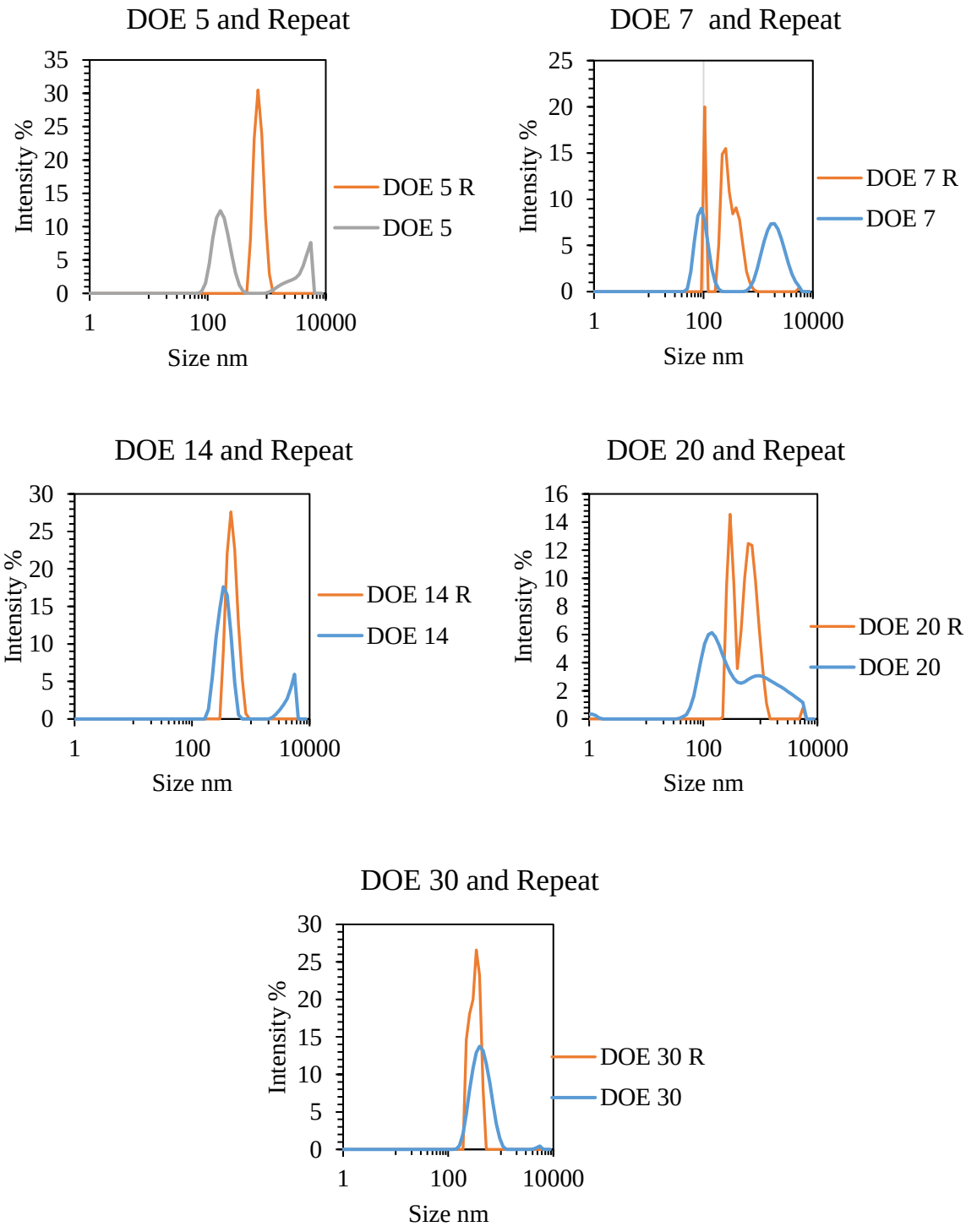

Figure.V.35 DLS results from repeated DOE experiments in the OBR.

As can be seen from Figure.V.35, the SEM confirms the repeatability of some runs in terms of both the particle size and shape (DOE 5, 7 and 20). For DOE 14 and 30 the SEM shows similar sizes but the shape of the particle differs, the shape aspect will be further investigated in Chapter VII. However, the DLS results show some discrepancies to the SEM results (for DOE 5,7 and 20). On the other hand, DOE 30 and DOE 14 show close results with an additional signal above 3000 nm observed for DOE 14; this is likely an artefact due to sedimentation, as it is known from SEM that the particles are within a range of 400-500 nm. In DOE 5, the peak at 729 nm is close to that from

the particles seen on the SEM picture which are around 700-800 nm. There is also the possibility of a wide range of particles of different size giving different particle size for DOE 5, it is unclear if some particles are hidden behind others or if aggregates are counted in the analysis. A number of the DLS experiments displayed a large sedimentation occurring after several measurements of the same cuvette which is why measuring clean sample in a new cuvette was done for the measurements.

Compared to the previous crystallisation methods it is seen that SEM indicates close agreement between original experiments and repeated set. For DLS, it is seen that depending on the particle shape the Zetasizer results do not always agree with those from SEM. For instance for spherical particles obtained at high concentration, SEM and DLS concorded giving particle size around 100-150 nm as shown in the previous experiment. When particle shape is rods with a star section (herein described as 'stars') like for DOE 14 experiment, the DLS is capable to have a close hydrodynamic diameter around the particle giving particle size close to the SEM. On the other hand, general rod shaped particles have been difficult to measure *via* DLS due to this inaccurate hydrodynamic diameter.

For confirmation of the accuracy of these results, other light scattering techniques like Analytical Ultra Centrifugation (AUC) or Differential Centrifugation Sedimentation (DCS) will be presented in Chapter VII. In the next section optimization of the reactor was carried out using RTD curve analysis.

V.4. Residence Time Distribution (RTD) Analysis for the OBR

The experimental work of this section was led by PhD student Samet Isaev at Cranfield. Further detail on the RTD results can be found in the PhD thesis of Samet Isaev: "Advanced flow technologies for the controlled, continuous manufacture of nanoscale materials" (expected submission May 2019)

In an ideal plug flow and batch reactor, all the particles spend exactly same amount of time in the reactor. In the work presented in this Section, a number of residence-time distribution measurements were conducted in the OBR to investigate the characteristics of the mixing for various oscillation and net flow conditions. To measure this data an inline UV-Vis spectrometer is used in order to measure an injected tracer inside the reactor. The tracer was injected *via* a 6th syringe pump connected to a T-piece stopcock before the first detection point.

The experimental set-up with the Scotch Yoke oscillation system for the RTD in the OBR is shown in Figure.V.36. The RTD and UV-Vis measurements were determined experimentally by injecting a known amount of the tracer (0.1 mL blue food colouring agent) at the inlet of the reactor in a short time as possible (0.1 mL/s). At the exit of the reactor, the corresponding concentration of the tracer was measured using QE-Pro Absorbance Spectrometer in transmittance mode equipped with a SMA-Z-flow cell with 10 scans, 100 ms integration time, resulting in one spectrum every second. (scan range between 220 nm and 930 nm). The absorbance measurement was recorded until the concentration reached zero.

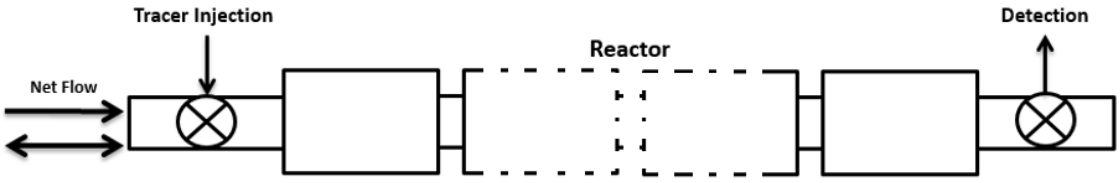

Figure.V.36 Set-up for the injection of a water-based tracer inside the OBR Centillion®.

In several cases the velocity ratio (ψ) has been studied to define plug flow behaviour inside baffle tube reactors and values of this ratio have defined the satisfaction of those conditions. Those studies recommended a range for the velocity ratio between 2 and 6 (for OBRs) which measure the degree of plug flow which can then be determined using the tank in series model. [94,96,98,205] For this purpose normalised RTD curves are needed.

To get the normalized RTD curve and the equivalent of tank in series model for the OBR which describes the fluid as flowing inside a series of continuous stirred tank reactors (CSTRs), the results obtained from the spectrometer are converted into dimensionless forms in order to quantify them statistically. RTD curve are normalized to be able to compare different types of reactor of different sizes directly. For this purpose, the following equations are used:

First the dimensionless time Θ is defined as:[98]

$$\Theta = \frac{t_i}{\tau} \tag{27}$$

Where t_i is the initial time and τ is defined as:

$$\tau = \frac{\sum_i t_i C_i \Delta t_i}{\sum_i C_i \Delta t_i} \tag{28}$$

Where C_i is the tracer concentration at t_i (in the case study this will be the absorbance detected by the spectrometer) and Δt_i the interval between measurement.

The distribution curve obtained from the results is:

$$E(\Theta) = \tau E(t) = \tau \frac{C_i}{\sum_i C_i \Delta t_i} \tag{29}$$

To determine the equivalent number of stirred tank reactors, it is described elsewhere that for an OBR to be operating near plug flow it needs to be as close as possible to 10 stirred tank reactors in series[97,216]. For this the variance σ is defined, which measures how far the set of values obtained are from the average: [98]

$$\sigma(\Theta)^2 = \frac{\sigma(t)^2}{\tau^2} = \frac{\sum_i (t_i - \tau)^2 E(t) \Delta t_i}{\tau^2} \tag{30}$$

Then the exit age distribution E, which describe how much time certain fluid elements have spent inside the system for N tanks, is defined as:

$$E(t) = \frac{C(t)}{\int_0^\infty C(t) dt} = \frac{t^{N-1}}{(N-1)!\,\tau_i^N} e^{-t/\tau_i} \tag{31}$$

Here τ_i represents the mean residence time for the i[th] tank, this value is defined as:

$$\tau = \frac{\int_0^\infty tC(t)dt}{\int_0^\infty C(t)dt} = N\tau_i \quad (32)$$

The dimensionless form for Θ is then described as:

$$\Theta = \frac{t}{\tau} = \frac{t}{N\tau_i} \quad (33)$$

And then:

$$E(\Theta) = \tau E(t) = \frac{N(N\Theta)^{N-1}}{(N-1)!} e^{-N\Theta} \quad (34)$$

This gives the number of tanks (N) as:

$$\sigma(\Theta)^2 = \frac{\sigma(t)^2}{\tau^2} = \int_0^\infty (\Theta - 1)^2 E(\Theta) d\Theta = \frac{1}{N} \quad (35)$$

$$N = \frac{1}{\sigma(\Theta)^2} \quad (36)$$

With the DOE results (section V.3 above) and the equation presented above, a set of experiments was pursued. Table.V.13 details the initial experiments, the tracer concentration was calculated from the absorbance of 467 nm. In order to gain maximum information of the range of mixing conditions possible within the OBR, literature procedures were followed where the velocity ratios from 2 to 6 were retained as was a Re_o of *ca.* 100.[96,206] Table.V.14 shows each experiment and the equivalent Stirred Tank number to each experiment obtained using the equation (35) and (36). Detailed results of the RTD curves will be given in Appendix (Supplementary information **CDCh5-7**).

Table.V.13 Experiment parameters to measure Residence Time Distribution.

	Amplitude (mm)	Frequency (Hz)	Net flow (ml/min)	Residence time (min)	Re_n	Re_o	Strouhal Number	Velocity Ratio	Number of equivalent tanks in series (N)
V1	2	1	9	1.7	26.822	112.95	0.318	4.211	7.06
V2	2	1	11.16	1.36	20.044	112.95	0.318	5.635	5.8
V3	2	0.125	9	1.7	26.822	14.119	0.318	0.526	2.39
V4	2	0.1	11.16	1.36	20.044	5.64	0.318	0.281	1.81
V5	3	0.55	11.16	1.36	20.044	93.188	0.212	4.65	5.69
V6	3	2.5	19.8	0.93	59.6	423.58	0.212	7.1	6.47
V7	3	2	19.8	0.93	59.6	338.86	0.212	5.68	3.58
V8	2	3	19.8	0.93	59.6	338.86	0.318	5.68	7.4

The RTD curves (Figure.V.37) are approaching a narrow distribution, which could lead to better plug flow behaviour inside the reactor. Other RTD curves for experiments V1 to V8 will be displayed in the supplementary information **CDCh5-7** and show similar behaviour with a narrow distribution. With those optimal parameters from Table.V.13, achieving plug flow behaviour as shown in the RTD curves Figure.V.37 was possible. These parameters were then applied with different concentrations of CI and CT to investigate the effect on particle size (experiments H1-8 below).

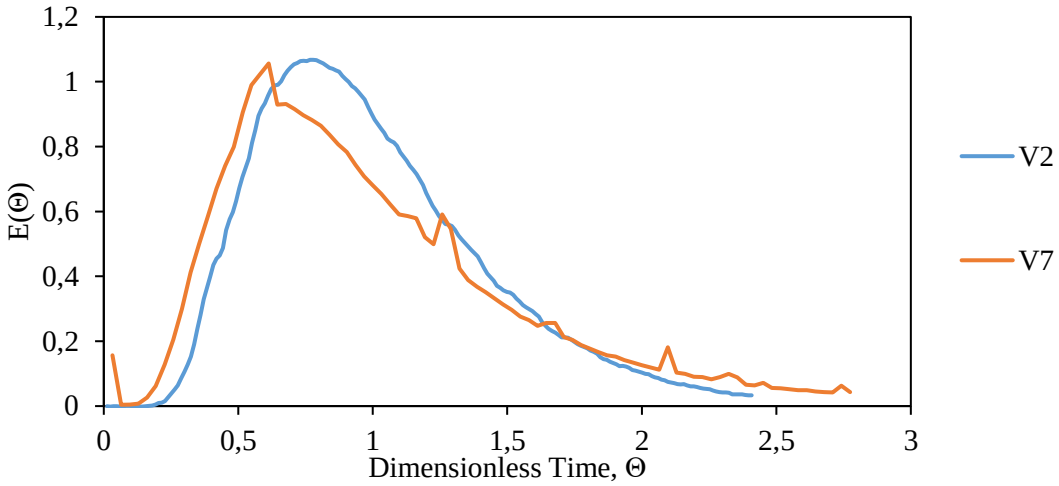

Figure.V.37 RTD graph for tracer experiments V1 and V8 in the OBR.

These experiments used different concentrations that have been used in the KRAIC-D (PiCKD 1 to 5) in Chapter IV to obtain spherical particle during beam time, as well as concentrations used previously in the OBR (DOE 7, DOE 20, DOE 30) which present different particle shapes and sizes. The relevant parameters are shown in Table.V.14 and Table.V.15 with the oscillatory Reynolds Number, Strouhal Number, Reynolds Number and Velocity Ratio (V.1).

Table.V.14 Parameters for the OBR used for experiments H1 to H8 with corresponding concentration.

Experiment Number	CI (g/100mL)	CT (g/100mL)	Amplitude (mm)	Frequency (Hz)	Flow Rate (ml/min)	Number of Channels	Residence Time (s)
H1	5.847	8.53	2	1	9	2	108
H2	10.793	10.793	2	1	9	2	108
H3	8	10.793	2	1	9	2	108
H4	7	10.793	2	1	9	2	108
H5	5.847	10.793	2	1	9	2	108
H6 (DOE 7)	5.847	5.847	2	3	19.8	4	98
H7 (DOE 20)	8.32	3.374	2	3	19.8	4	98
H8 (DOE 30)	3.374	3.374	2	3	19.8	4	98

Table.V.15 Corresponding Velocity Ratio, Reynolds number and oscillatory Reynolds number for Table.V.14 Parameters with corresponding DLS results

Experiment Number	Strouhal Number	Reynolds Number	Oscillatory Reynolds Number	Velocity Ratio
H1	0.318	23.8	100.249	4.21
H2	0.318	23.8	100.249	4.21
H3	0.318	23.8	100.249	4.21
H4	0.318	23.8	100.249	4.21
H5	0.318	23.8	100.249	4.21
H6 (DOE 7)	0.318	52.9	300.74	5.68
H7 (DOE 20)	0.318	52.9	300.74	5.68
H8 (DOE 30)	0.318	52.9	300.74	5.68

Each of those experiments have been carried out on the OBR and repeated three times to check consistency, the repeats are given in supplementary information **CDCh5-5** and show results close to those obtained in first set with variations of ±50 nm. The DLS and SEM results are displayed in Figure.V.38 and Figure.V.39.

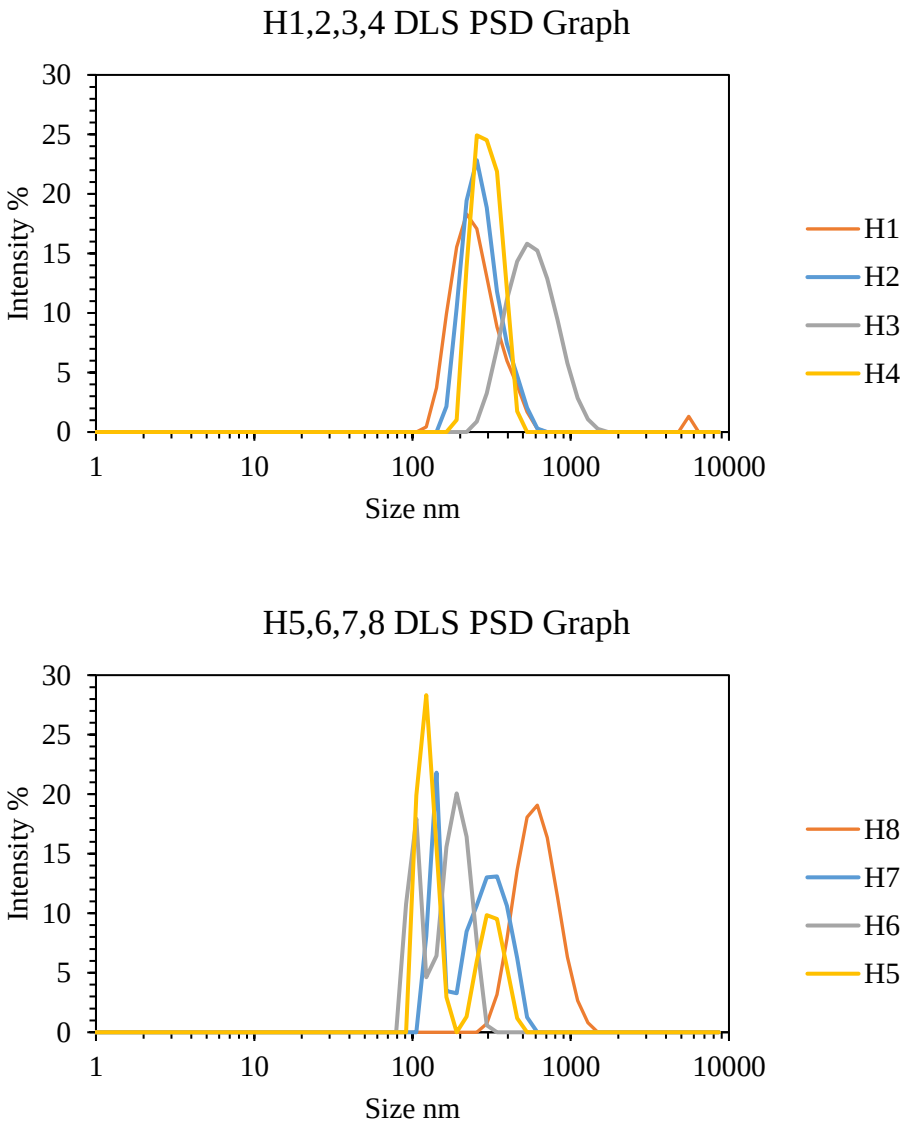

Figure.V.38 DLS PSD results from H1 to H8 experiments.

Figure.V.38 shows the particle size distribution of H1 to H8 experiments, from which it is seen that the particle size varies between 100 nm and 1000 nm.

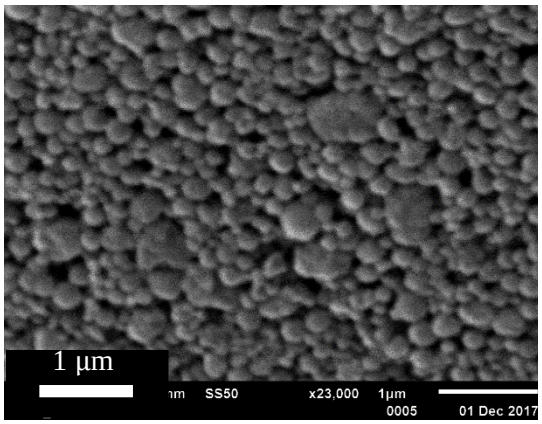

H1

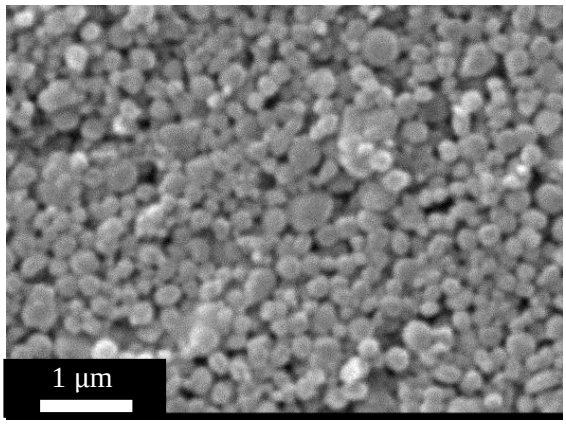

H2

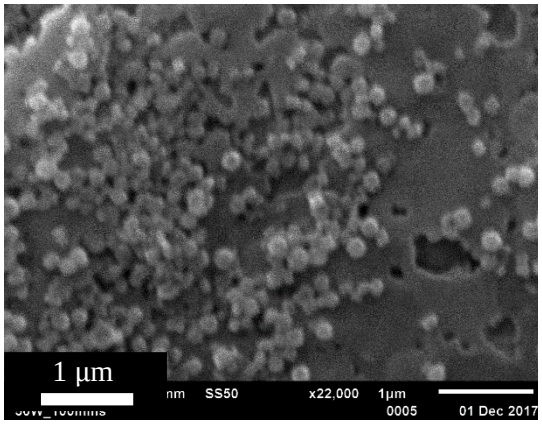

H3

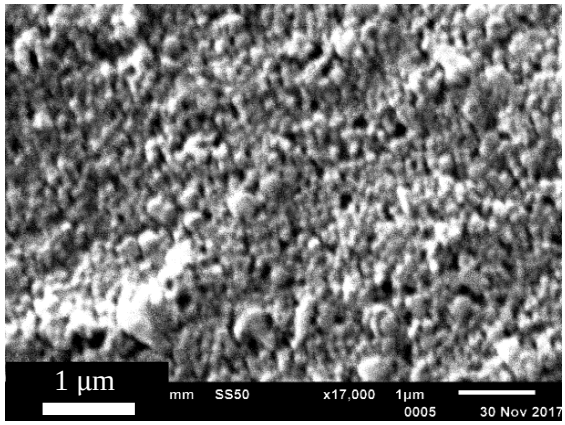

H4

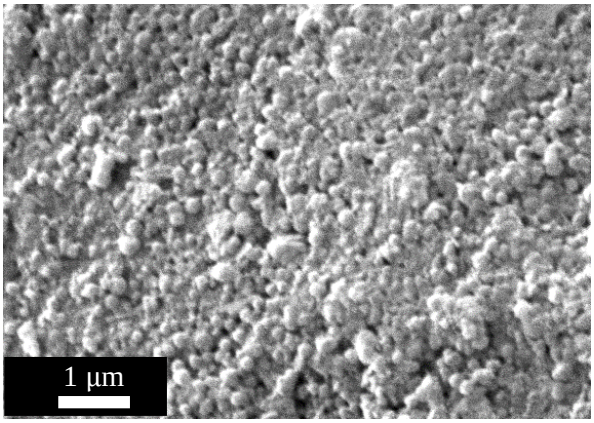

H5

Figure.V.39 SEM Picture of H1, 2, 3, 4 and 5.

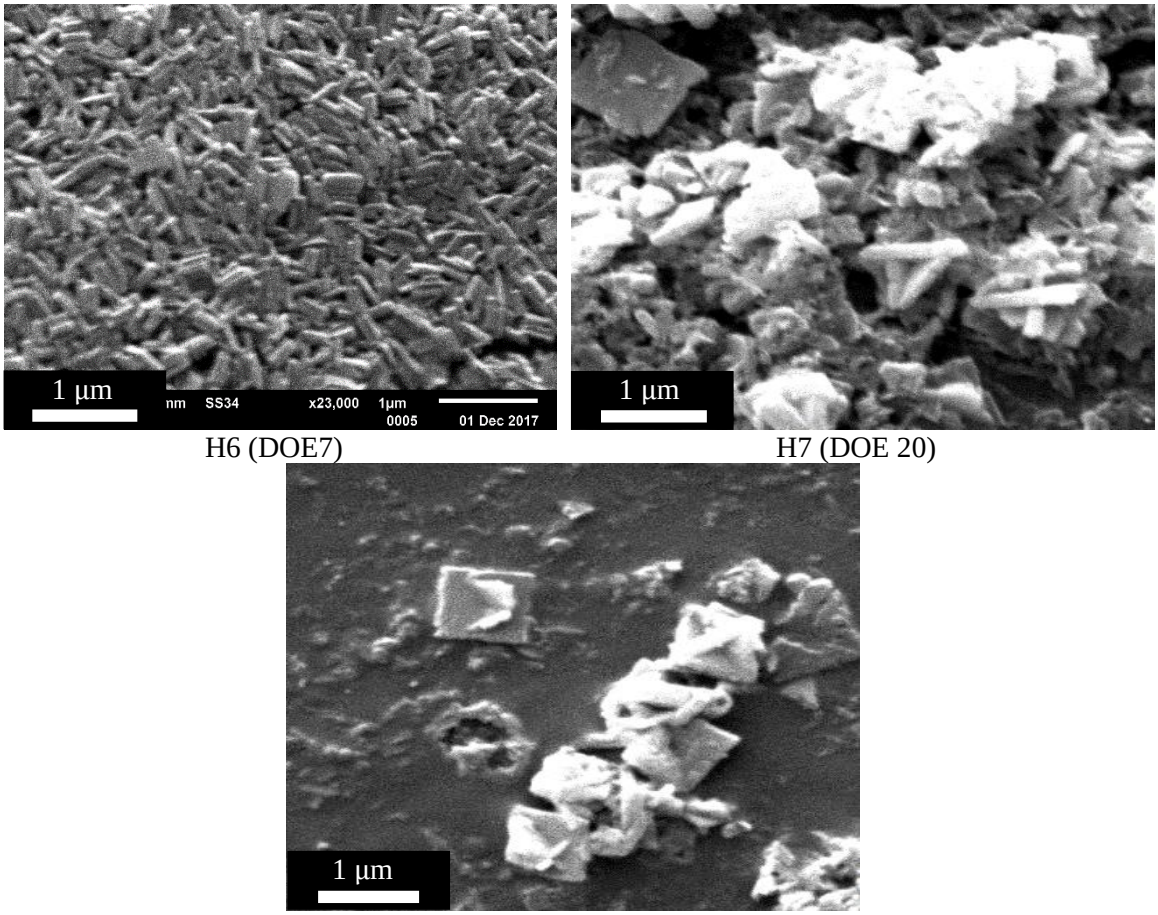

H6 (DOE7) H7 (DOE 20)

H8 (DOE 30)

Figure.V.40 SEM pictures of H6 (DOE 7), H7 (DOE 20) and H8 (DOE 30).

H1 to H8 have been carried out on four channels to increase the residence time and be able to obtain enough material at the end of the reactor to be analysed as is was seen that two channels were not enough to obtain enough material for SEM and DLS even at high concentration. It was also easier to recover several residence times as some RT are as low as 24 s for two channels which is not enough time to change filter. The issue of increasing the number of channels is that the RTD might be affected, even with the tank in series model some discrepancies might appear. H1 to H8 had fast reaction times as confirmed through visual observation. From SEM analysis it was observed that the particle size and shape changed depending on the parameters used. Experiments H2 and H3 produced spherical particles and H1, H4 and H5 produced spherical particles which in some places aggregated into bigger blocks. If concentrations of DOE 5, 7 and 30 are used completely different particle shapes are obtained due to the new flow parameters implemented in these experiments; the higher flow rate and the plug flow behaviour obtained with the RTD curve optimisation. H6 (DOE 7) showed the expected rod-shaped particles but in H7 (DOE 20) and H8 (DOE 30) many of the particles were square plate crystals, which has not been previously observed, it was supposed that it was one of the reagents that did not react but from the SEM none of starting materials present square shaped behaviour. On the DLS graph the particle size agreed with the SEM images with particle size between 200 and 250 nm with spherical particles of H1 to H5. For the experiments comparable to DOE concentrations, H6 has been comparable with particle size close to the SEM while obtaining rods around 200 nm. But for H7 and H8 it is difficult to analyse the APS using the Zetasizer due to the different particle size and shape as shown on the SEM pictures and the square shaped behaviour that they have. For H7 and H8 square shaped particles have been obtained with some rods over them

which might suggested that some reagent did not get enough time to react together which suggests the use of more channels. A too high concentration of one of the reagents could also explain this event where the starting materials are crystallising without reacting.

The OBR has shown the capability of repeating experiments with the same output for H1 to H8. Using the flow parameters known to achieve plug flow behaviour for the concentrations in DOE 7, 20 and 30, the resultant particle size and shape of PiC have been altered. To achieve the same RT as the previous experiments presented in section V.3, adding more channels would be necessary therefore increasing the volume of the reactor and also the reagent amount which would be a next step for scale-up for the production of this compound. The needle-like shape obtained for DOE 20 and 30 in the original experiments are also replaced by square shaped particles. This shows that more data is needed with plug flow behaviour to have a proper control over particle size and shape and to optimize the reactor.

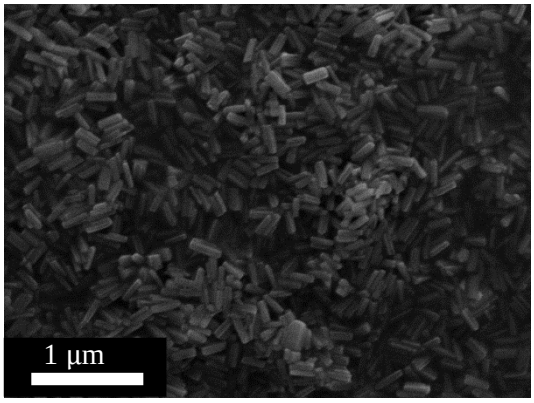

DOE 7 Original

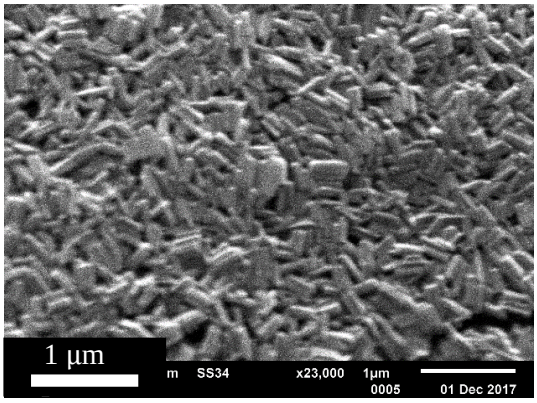

DOE 7

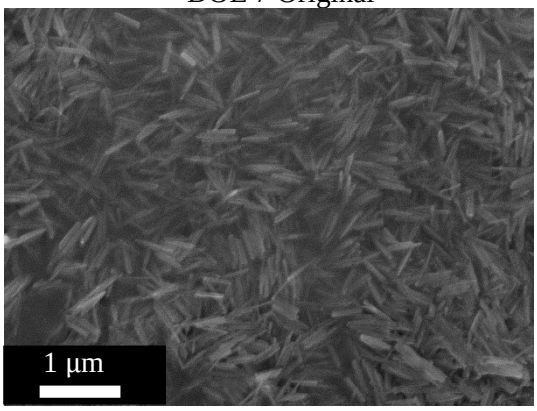

DOE 20 Original

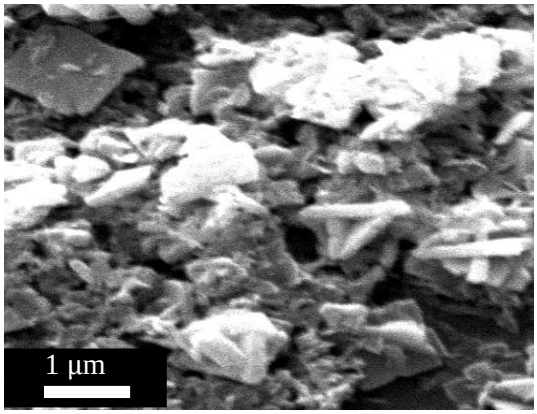

DOE 20

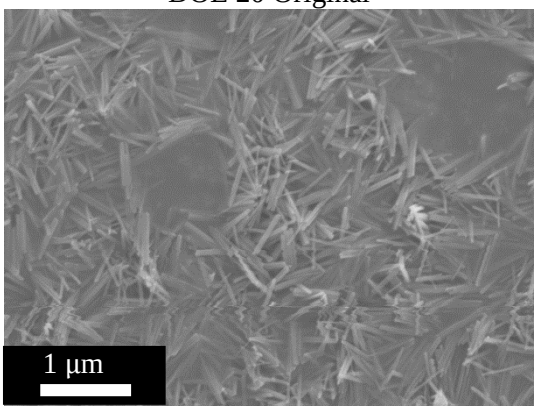

DOE 30 Original

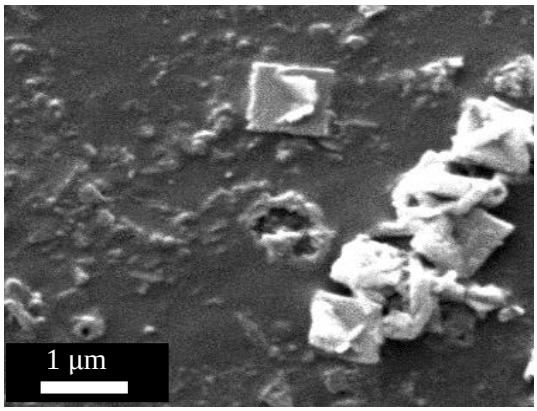

DOE 30

Figure.V.41 Comparison of DOE 5 H6,7 H7 and 30 H8 with plug flow parameters to their original counterparts.

The impact of the concentration is important in those cases, this dependency to concentration will be further discussed in Chapter VII. Using the new set of parameters with optimised plug flow showed that a higher volume for the reactor would be needed to produce PiC continuously with the optimised parameters.

V.4.2 Synthesis of PiC with Stabilisers in the OBR

As reported in Moulet *et al.* and Letard *et al.*, a variety of synthesis techniques have been explored to produce different particle sizes or phases of PiC. Here is described the effect on particle size of PiC synthesised inside the OBR with the use of surfactant.[5,218] In Moulet *et al* the reverse micelle

technique was used to produce PiC and showed good results in batch at small scale with particle sizes ranging from 75 to 1000 nm while being able to control the particle size *via* temperature control but with longer production time exceeding overnight to 24 hours.[218]. Here the surfactant stabilising technique is applied to the flow synthesis set-up with a range of surfactants (benzoic acid (BA), poly(vinyl acetate (PVA), polyethylene glycol (PEG), sodium dodecyl sulfate (SDS)) and expedited timescales with respect to those employed by Moulet *et al*. These techniques have been used in literature and showed good results in controlling particle size of nanomaterials in those reported cases. [218–220] The set-up used for this experiment was the Scotch and Yoke system from section V.3 for the oscillation with two channels. Experiment parameters were set to 2.25 Hz frequency, 3 mm amplitude, 14 min residence time, 5.794 g/100 mL CI and 10.794 g/100mL CT, as for the DOE 14 experiment carried out previously. Surfactants were added to the 1,2,4 H triazole feed vessel as the stabilizers showed to react with the $Fe(BF_4)_2$ solution creating a cloudy white precipitate.

Figure.V.42 shows the effect of adding stabilizer to PiC synthesis in the OBR. Reactions were performed using a total of 0.02 g/100mL of stabilizer in the reagent Trz. For PiC synthesis with BA, PEG and SDS, the particles obtained showed similar size to those when surfactant is not used, at 400 nm to 600 nm. The shape on the other hand has been affected; while the particles from PEG and SDS show similar shape they do not show the star cross-section shaped material fond with BA and DOE 14 without surfactant, but using stabilizer seems to smooth the edges of the rods for PEG and SDS. PVA on the other hand produces bigger particles and almost needle-like shape at 6 µm, this could be an interaction between both reagents and the PVA; it is reported that borate (the counter ion used for he Fe^{II} source) has a cross-linking effect on PVA.[221] DLS was attempted but the samples obtained were not suitable for measurement as the Zetasizer was not capable to identify the hydrodynamic diameter of the particles with the surfactants. This route to produce the materials was not pursued due to its drastic change of material properties and also the difficulty for DLS analysis; this part of discovery was outside the scope of the project and was not pursued in detail but could be a potential candidate for improving particle size control of PiC. In Chapter VII the PEG sample has been studied under DSC and it is shown that the spin transition was drastically affected by the surfactant.

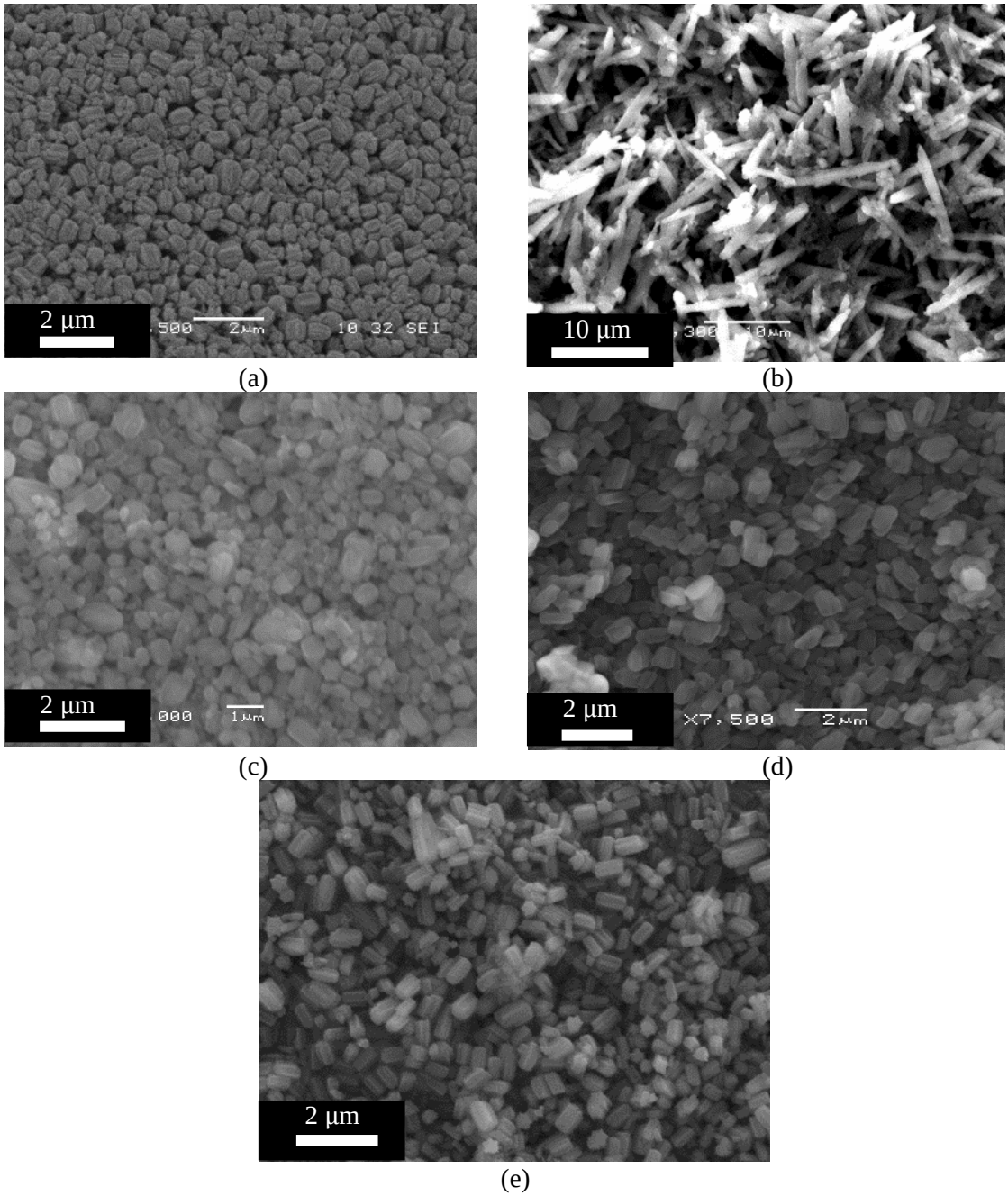

(a) (b)

(c) (d)

(e)

Figure.V.42 Effect of stabilizer on PiC particles produced in OBR. BA (a), PVA (b), PEG (c), SDS (d) and without stabilizer DOE 14 (e) .

V.5. Optimization study with a computational fluid dynamic approach for an OBR

V.5.1 Introduction

Computational Fluid Dynamic (CFD) calculations following particle trajectory, residence time and velocity throughout the reactor were undertaken to understand the mixing environment of a bi-phasic system in the OBR. With the same parameters used in the lab, experiments characteristic of the OBR

reactor with the focus on determining mixing intensity and residence time distribution were carried out. As is the case in the actual OBR, the baffles were stationary and the fluid oscillating.

The CFD package used was Ansys Fluent 17 2016. Meshes were created using Fluent and the 3D model with Autodesk Inventor. In Fluent, the velocity at the inlet had to be precise and the oscillation defined with a user defined function (UDF).[93,222] For continuous flow, the mean flow velocity was specified using the UDF function using the equation:

$$v(t) = v_0 + 2\pi f x_0 \sin(2\pi f t) \quad (37)$$

With v_0 the velocity in m.s^{-1}, f the frequency in Hz, x_0 the amplitude in m and t the time. For the simulation the solver was pressure based, velocity formulation was absolute, the system was considered transient, and gravity was on. The boundary conditions set *via* a UDF function for the unsteady flow velocity with oscillation and a pressure outlet was set at the end of the flow boundary outlet. The simple scheme was used as solution methods with the first order implicit. A monitor was implemented in order to obtain the residence time distribution.[94]

A tracer was defined to create a mixture and be able to measure the residence time. The tracer was then injected with the same parameters as the lab experiment and the UDF was changed according the input parameters used in the lab. A discrete phase was also implemented in order to control particle tracking within the system. The diameter of the nanoparticles is unknown and was estimated to be close to that of a similar nanoscale coordination polymer, 1 µm. A courant number C_o has been respected for turbulent flow inside the reactor and to confirm convergence of the model on Ansys Fluent.[223] The UDF function is defined as follows:

Table.V.16 User Define Function UDF used in Ansys Fluent to simulate the oscillation

User Defined Function of Oscillation inside the OBR

```
/************************************************************************
unsteadfffy.c
UDF for specifying a transient velocity profile boundary condition
************************************************************************/

#include "udf.h"

DEFINE_PROFILE(unsteady_velocity, thread, position)
{
face_t f;
real t = CURRENT_TIME;

begin_f_loop(f, thread)
{
       F_PROFILE(f, thread, position) = 0.0008 + 0.008*2.2242*sin(2.2242*t);
}
end_f_loop(f, thread)
}
```

V.5.2 Velocity and mixing simulation of the OBR

Investigating the mixing intensity and formation of eddies inside an OBR can be challenging without specialised equipment in the lab. Having a better understanding of the reactor behaviour can help optimise the design and production output. OBR mixing conditions have been studied in the literature in order to optimise those reactors.[93,223] It has been shown that it is possible to see the

mixing by injection of a tracer during the flow and that, depending on the parameters, the eddies generated change with the oscillatory Reynolds number. In this section, CFD simulations have been carried out with the UDF function previously introduced to model the eddies inside the reactor.

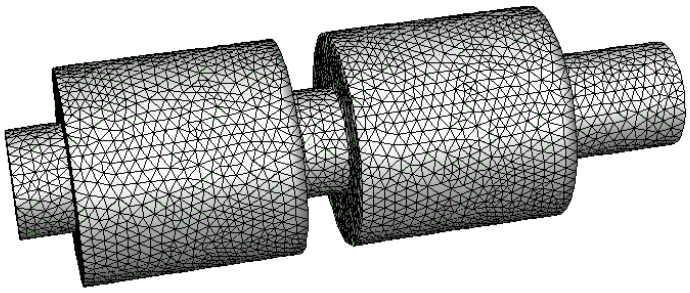

Figure.V.43 Meshing of OBR 2 baffle model.

The model of the reactor has been reduced to only one channel for this type of experiment, as it is not possible to exceed 512000 elements in the mesh on Ansys Fluent, and the computational cost for that kind of reactor is extensive. Meshing was done in Ansys Fluent, a part of this meshing is shown in Figure.V.43 and includes 71293 mesh elements. All simulations are done on a 3D model to detect any possible chaotic behaviour like that described by Manninen *et al.*.[93]

For these simulations, the Large Eddy Simulation (LES) model was used with Smagorinsky-Lilly Subgrid-Scale Model. LES is a technique for simulating turbulent flows. In the cases of turbulences Kolmogorov's theory is applied which implies that the large eddies are dependent on the reactor geometry and transfer the energy from them to smaller eddies during the flow. [224] Adding this theory allows Fluent to solve the calculation for large eddies and then with a subgrid-scale model (SGS model) solve smaller eddies.[225]

The Navier-Stokes equations are first solved for the large eddies while the smallest eddies are modelled following the results. This uses a filter width to define the portion of the flow which need to be modelled.[180] This is defined in terms of the filtering kernel: *G*

$$\overline{u_i}(\vec{x}) = \int G\,(\vec{x} - \overrightarrow{\xi})u(\overrightarrow{\xi})d\overrightarrow{\xi} \tag{38}$$

With *x* and ξ the external and internal coordinates of the system.[226]

which results in:

$$u_i = \overline{u_i} + u_i' \tag{39}$$

where $\overline{u_i}$ is the resolvable scale part and u_i' is the subgrid-scale part of the system. In the case of incompressible flows, with "*i*" the column and "*j*" the row of the vectors, the filtered equations derived from the incompressible Navier-Stokes equations (40) are:

$$\frac{\partial u_i}{\partial t} + u_j \frac{\partial u_i}{\partial x_j} = -\frac{1}{\rho}\frac{\partial \rho}{\partial x_i} + \frac{\partial \rho}{\partial x_j}(\mu \frac{\partial u_i}{\partial x_j}) \tag{40}$$

Where ρ is the density of the fluid and μ its viscosity.

From equation number (38) u_i can be replaced and (41) is obtained:

$$\frac{\partial \overline{u_i}}{\partial t} + \overline{u_j}\frac{\partial \overline{u_i}}{\partial x_j} = -\frac{1}{\rho}\frac{\partial \overline{\rho}}{\partial x_i} + \frac{\partial}{\partial x_j}\left(\mu\frac{\partial \overline{u_i}}{\partial x_j}\right) + \frac{1}{\rho}\frac{\partial \tau_{ij}}{\partial x_j} \quad (41)$$

The extra term $1/\rho\frac{\partial \tau_{ij}}{\partial x_j}$ arises from the non-linear advection terms, due to the subgrid-scale stress with the molecular viscosity.[227] The subgrid-scale stress is then defined by:

$$\tau_{ij} = \overline{u}_i\overline{u}_j - \overline{u_i u_j} \quad (42)$$

The stress resulting is unknown and needs to be determine *via* modelling. For this purpose Ansys Fluent uses the Boussinesq Hypothesis which describes the momentum transfer due to turbulent eddies in the system[228], computing the stress *via*:

$$\tau_{ij} - \frac{1}{3}\tau_{kk}\delta_{ij} = -2\mu_t\overline{S}_{ij} \quad (43)$$

Where μ_t is the viscosity of the subgrid-scale, $\overline{S}_{ij}$ is the rate-of-strain given by:

$$\overline{S}_{ij} = \frac{1}{2}\left(\frac{\partial \overline{u_i}}{\partial x_j} + \frac{\partial \overline{u_j}}{\partial x_i}\right) \quad (44)$$

The term τ_{ij} can be defined as two terms, with isotropic and deviatoric parts:

$$\tau_{ij} = \underbrace{\tau_{ij} - \frac{1}{3}\tau_{kk}\delta_{ij}}_{deviatoric\ part} + \underbrace{\frac{1}{3}\tau_{kk}\delta_{ij}\overline{u_i u_j}}_{isotropic\ part} \quad (45)$$

With those two parts defined, the deviatoric part can be determined *via* the Smagorinsky Model, by:[229]

$$\tau_{ij} - \frac{1}{3}\tau_{kk}\delta_{ij} = -2(C_s\Delta)^2|\overline{S}|S_{ij} \quad (46)$$

The isotropic term on the other hand is not modelled and is instead added to the static pressure.[180]

Here for the OBR simulations, the Smagorinsky-Lilly model is used and the eddy viscosity is modelled *via*:

$$\mu_t = \rho(C_s\Delta)^2|\overline{S}| \quad (47)$$

the local grid scale Δ is define by:

$$\Delta = (Volume)^{\frac{1}{3}} \quad (48)$$

With

$$\overline{S} = \sqrt{2S_{ij}S_{ij}} \quad (49)$$

And *Cs*, the Smagorinsky constant, has value that varies with the application. Lilly describes that a value for the constant of 0.1 gives the best results for different type of flow.[180]

With these equations, the software can model the behaviour of the turbulent fluid with the eddies *via* the UDF function.

The first investigation carried out here was the mixing behaviour of the reactor. Here UDFs were created for each DOE experiments employing the experimental parameters. Amplitude, frequency and flow rate were interpreted by the UDF function into the software.

Figure.V.44 displays the streamline and velocity contours of several experiments from the DOE to the Velocity Ratio Experiments during the forward stroke of the mechanism. This set of experiments was chosen because they show three different mixing behaviours: H1 to H8 displays better plug flow behaviour, DOE 14 showed the longest run achieved in the OBR with consistent particle size and no oscillation to show the importance of the oscillation inside such type of reactor.

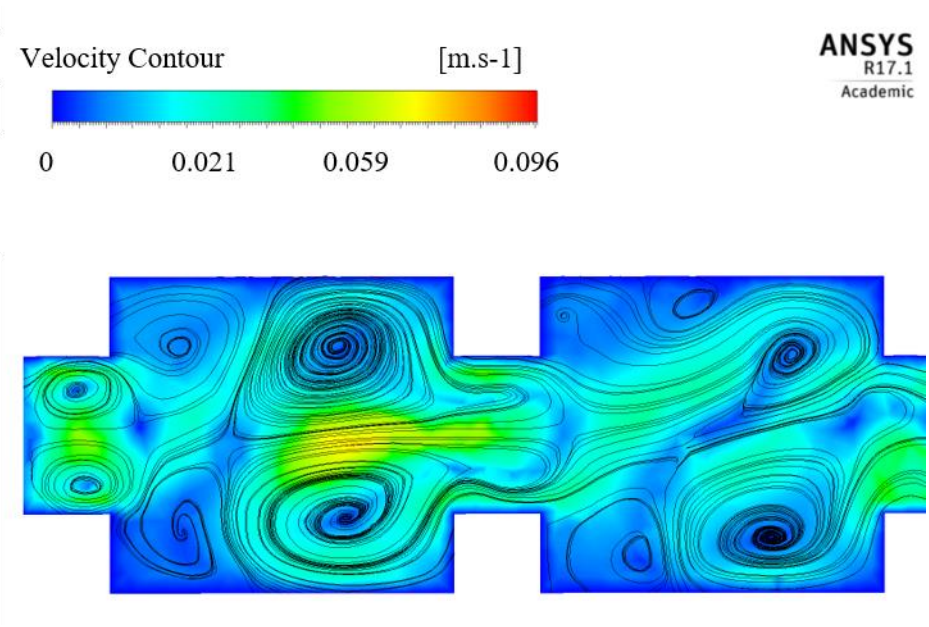
Velocity Contour
[m.s-1]
ANSYS
R17.1
Academic
0
0.021
0.059
0.096

(a)

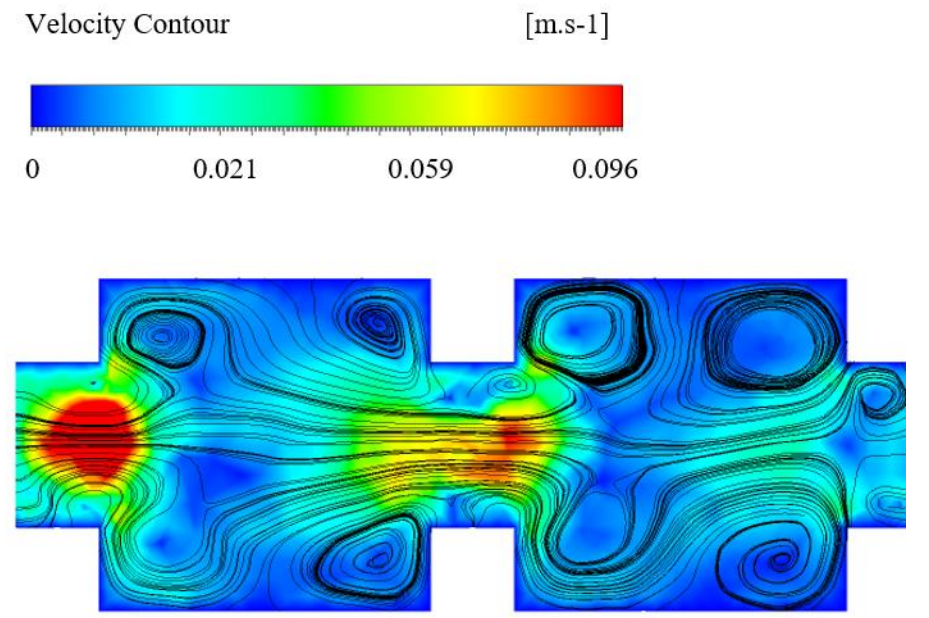
Velocity Contour
[m.s-1]
0
0.021
0.059
0.096

(b)

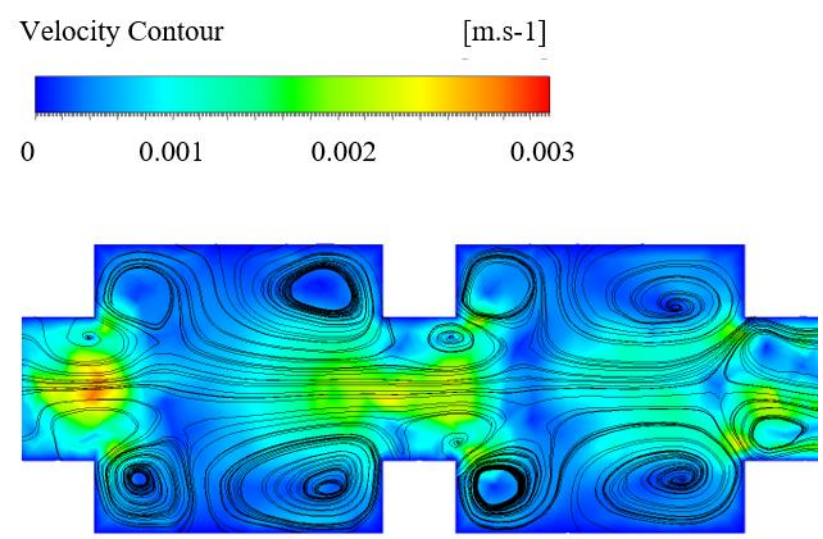

(c)

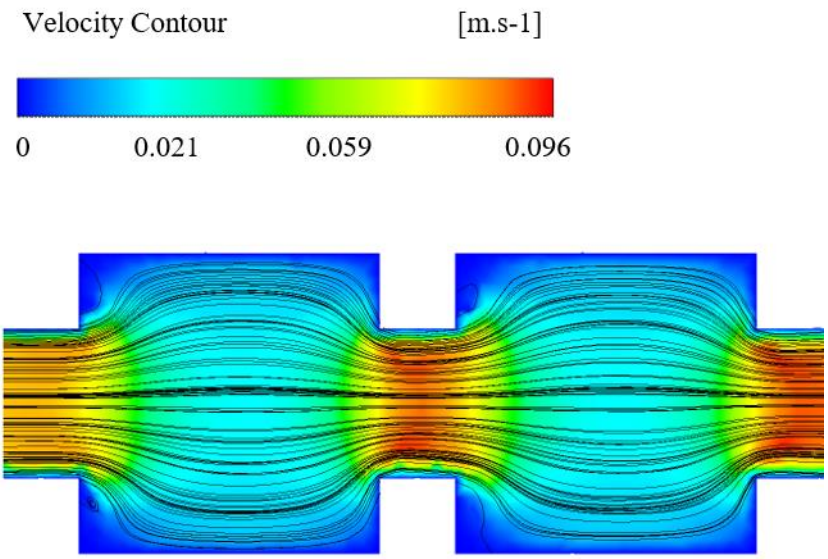

(d)

Figure.V.44 Representation of streamline with different flow parameters: (a) 2 mm, 1 Hz, 54s RT H1 to H5; (b) 3 mm, 2 Hz, 24s RT H6 to H8; (c) DOE 14, 2.25 Hz, 3mm, 14 min RT; (d) no oscillation 8 min RT.

From the flow patterns in Figure.V.44 it is seen that depending on the parameters employed streamline patterns change drastically for the same reactor geometry. On the streamline (a) significant eddies are present at the right of the baffle. It was experimentally derived (as discussed above in section V.3) that this parameter had the most ideal velocity ratio and was equivalent to 7.48 STRs, corresponding to the most optimal mixing behaviour inside the OBR achieved here. For (b) and (c) eddies are still present but smaller in each corner of the baffle. On (c) some dead zone appears at the bottom of the baffle and could create the sedimentation observed experimentally with long run experiments with these same parameters (section V.3); both of those experiments use DOE 14

parameters. The flow pattern (d) shows the importance of the oscillation, without them the OBR acts like a normal open bore tubing with exaggerated laminar flow.

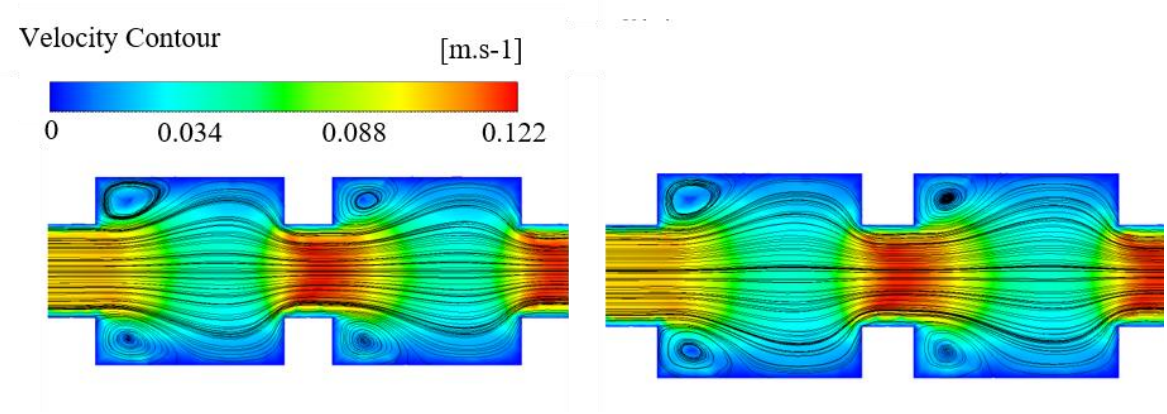

Figure.V.45 Comparison between DOE 17 and 18.

Figure.V.45 shows the difference between DOE 17 and DOE 18 experiments; for DOE17 the parameters are 4 Hz Frequency, 2 mm Amplitude and 20 min RT; for DOE 18 4 Hz Frequency, 4 mm amplitude and 8 min RT time. In both cases the eddies are closely similar. It is seen that having drastic changes in amplitude and residence time inside the reactor has a low impact on the mixing eddies. This is where CFD is useful to determine which parameters are right for each reaction.

Table.V.17 Streamline analysis *via* CFD and SEM obtained in experimental synthesis of PiC.

Streamline CFD with parameters	SEM of experimental synthesis of PiC
No Oscillations 8 min RT, 8.32 g/100 mL CI and CT 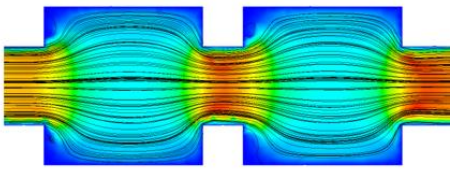	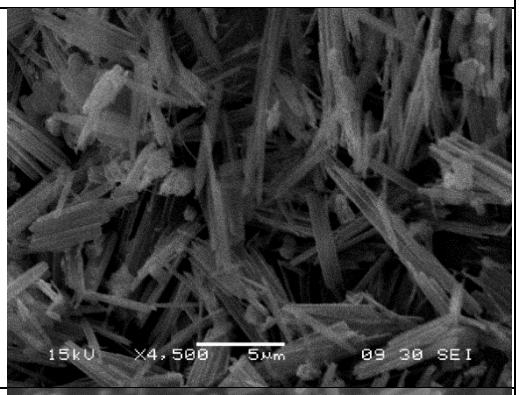
DOE 21, 0.5 Hz Frequency, 4 mm amplitude, 8 min RT , 8.32 g/100 mL CI and CT 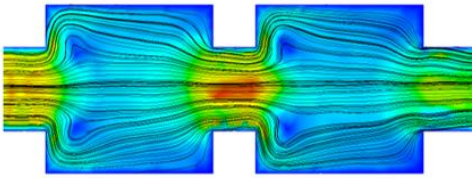	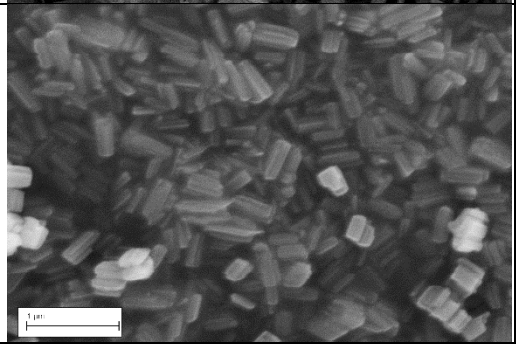

DOE 24, 4 Hz Frequency, 2 mm amplitude, 20 min RT, 8.32 g/100 mL CI and CT 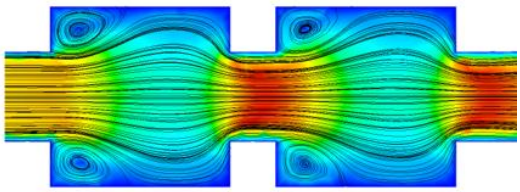	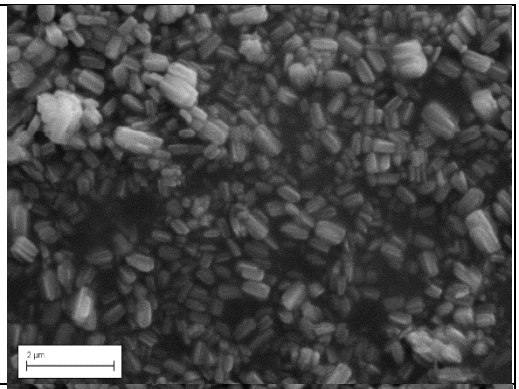
DOE 9, 2.25 Hz Frequency, 3 mm amplitude, 14 min RT, 5.847 g/100mL CI and CT 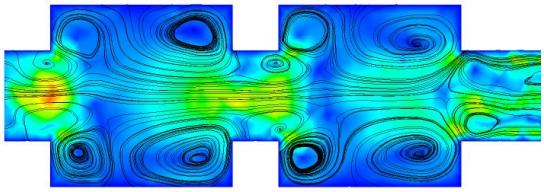	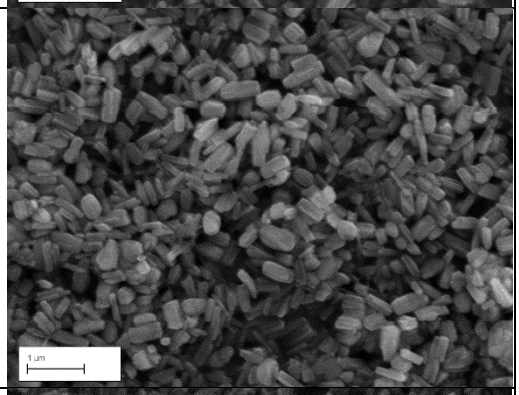
DOE 4, 2.25 Hz Frequency, 3 mm amplitude, 26 min RT, 5.847 g/100mL CI and CT 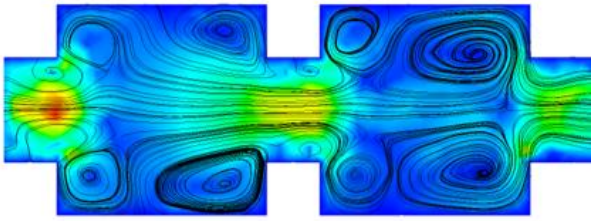	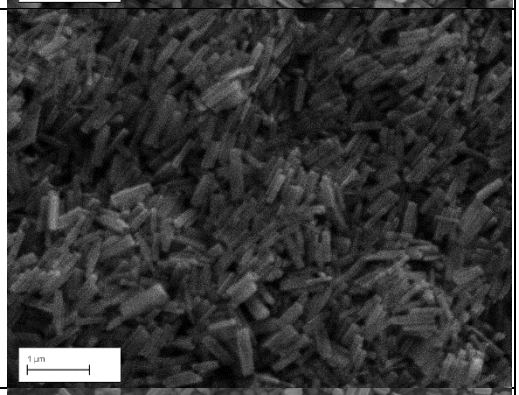
DOE 14, 2.25 Hz Frequency, 3 mm amplitude, 14 min RT, 5.847 g/100mL CI and 10.793 g/100mL CT 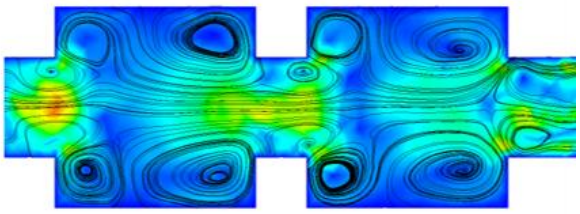	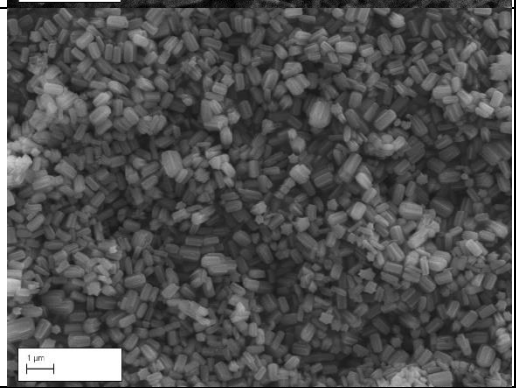

Table.V.17 shows different streamline simulations with their parameters and corresponding SEM of the PiC synthesis products achieved with the OBR. When no oscillation is present needle shaped particles are obtained for PiC for a concentration of 8.32 g/100 mL for both reagents. When adding for the same concentration-controlled mixing (DOE 21 and 24), rod shaped particles are obtained with more control and the needles disappeared. From the streamline of DOE 21 and 24 it can be seen that eddies start to appear when increasing the frequency from 0.5 Hz to 4 Hz and decreasing the amplitude from 4 to 2 mm (inter-baffle spacing of 2 mm) and the residence time also increase

from 8 (1.92 mL/min) to 20 min (0.78 mL/min). From the SEM of DOE 21 to 24 particle size and shape starts to become more homogenous, presumably due to the improved mixing conditions, as can be seen from the streamline of the CFD showing improved formation of eddies inside the baffles, but no size and shape differences are observed. Particles range from 400 to 600 nm which suggests, like stated in section V.3, an important dependence of particles with concentration of reagents.

For DOE 4 and 14 the oscillation parameters are the same but the RT is decreased from 26 (0.6 mL/min) to 14 min (1.1 mL/min). DOE 4 displays on the SEM rod shaped particles for a concentration for both reagents of 5.847 g/100 mL. DOE 14 shows star shaped particles for CT concentration 10.793 g/100mL and 5.847 g/100mL for CI. In this case streamline eddies are present on both CFD with similar patterns in each experiment due to the same oscillation parameters. In DOE 9, the flow parameters were the same as for DOE 14 but the concentration of triazole was doubled in DOE 14 with respect to DOE 9. The particle size and shape are similar which indicates that the mixing parameters are also important to control particles obtained for PiC (Figure.V.46).

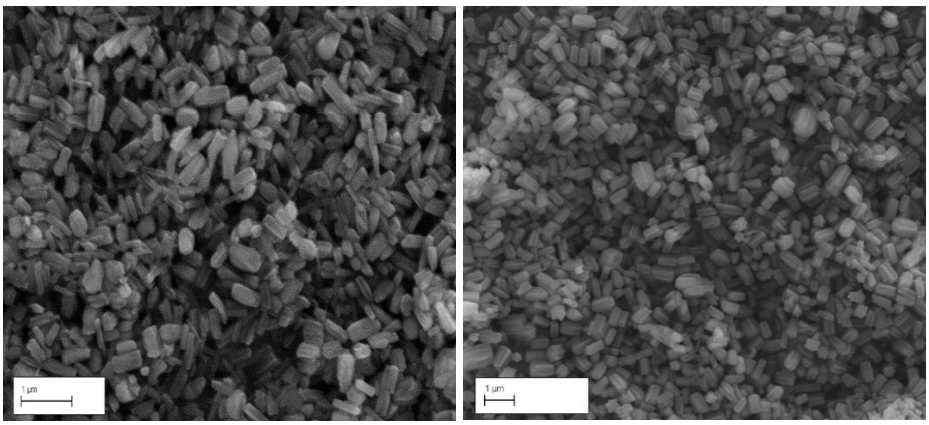

Figure.V.46 SEM images for DOE 9 (left): 2.25 Hz Frequency, 3 mm amplitude, 14 min RT, CI and CT 5.847 g/100 mL, and DOE 14 (right): 2.25 Hz Frequency, 3 mm amplitude, 14 min RT, CI 5.847 g/100 mL and CT 10.793 g/100mL

Compared to DOE 4 and 14 the mixing is minimally present (from the streamline Table.V.17) in some part of the baffles like for DOE 21 and 24, and could conceivably result in some dead zones inside the reactor where the two reagents are not mixing as well as other parts. This could lead to a sub-optimal particle size distribution, this is where particle tracking enters into consideration and will be introduced in section V.5.5. The difference of morphology will be addressed in Chapter VI.

To have a better appreciation of the flow dynamics vectors inside the OBR a video is given in **CDCh5-3** for H1 parameters, while other streamlines for different DOE parameters are given in Appendix **A5, Table A5.3**.

V.5.3 Tracer experiments for residence time monitoring

Complementary computational experiments to the experimental results previously presented on the RTD curve have been intensively studied to optimize the reactor. In this section is presented a method to model those graphs with Ansys Fluent.

The tracer can be treated as a continuous fluid by solving the transport equation (50) for the tracer species. Usually two methods for solving tracer experiments are used: the Species transport model and the User defined scalar (UDS) transport model.

In this case the species transport model is used. The tracer is modelled as a species. The properties of the tracer and the background liquid, here water, will be identical as the tracer is water based and the concentration of the tracer will not have a significant effect on the flow field. The fluid flow equations are first solved with a steady state approach. Then the species equation is solved as an unsteady simulation. The area-weighted-average concentration is measured at the outlet of the reactor to obtain the RTD curve.

The pulse method is used here, on Ansys Fluent the tracer is injected at t = 0 by putting the mass fraction of the tracer to 1 for 0.1 s. Then the fraction is put back to 0 and the simulation is launched for as long as needed, from 1 to 26 minutes of flow.

To simulate an injected tracer the same parameters are used to simulate the oscillation, but the species transport is added to the model. This modelling is used to differentiate between the two species, here water and the tracer. For those experiments the tracer is considered as water-based, like that used for real time experiments.[93,223]

For this purpose, Ansys *Fluent* uses the Species Transport Module which can simulate the incorporation of a water-based substance in the flow model. This is achieved through the solution of conservation equations for species where *Fluent* predicts the local mass fraction of each species, Y_i of species *i*. The conservation-diffusion equation is given as follows:

$$\frac{\partial}{\partial t}(\rho Y_i) + \nabla \cdot (\rho \vec{v} Y_i) = -\nabla \cdot \vec{J_i} \tag{50}$$

Where ρ is the density, v the velocity, Ji the diffusion flux of species defined as:

$$J_i = -\left(\rho D_{i,m} + \frac{\mu_t}{Sc_t}\right)\nabla Y_i \tag{51}$$

where Sc_t is the turbulent Schmidt number, μt is the turbulent viscosity and D_t is the turbulent diffusivity).

V.5.4 Result for tracer injection

For those simulations the area-weighted average concentration is measured after the outlet of the second baffle. The length of tubing after the second baffle was increased and the measurement was set 4 mm after the second baffle to avoid the disappearance of the tracer due to the Neumann boundary condition.[110,230] Here only two baffles are used to reduce the computational need for those experiments.

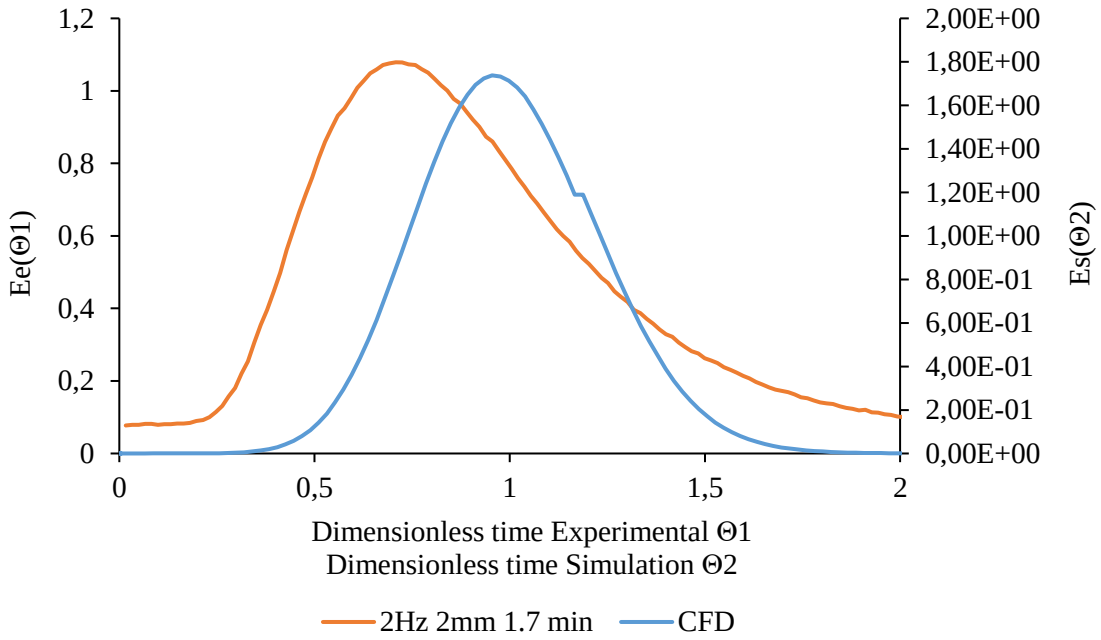

Figure.V.47 The difference between CFD and lab experiment V1 RTD curve.

Figure.V.47 is the comparison between CFD and lab experiment RTD curve and the model shows a close similarity with the experiment conducted. The RTD curve for the CFD is narrower due to the fact that the conditions on Fluent are supposed perfect whereas for the lab experiment the curve is wider resulting from more dead zones not simulated in the model.[53,94,206,231]

To compare different RTD distributions several experiments from the DOE and plug flow behaviour parameters have been used. On Figure.V.48 is displayed the RTD curve of three different parameters obtained *via* CFD showing the comparison between a non-optimized experiment (DOE 14) and two optimized plug flow behaviour parameters.

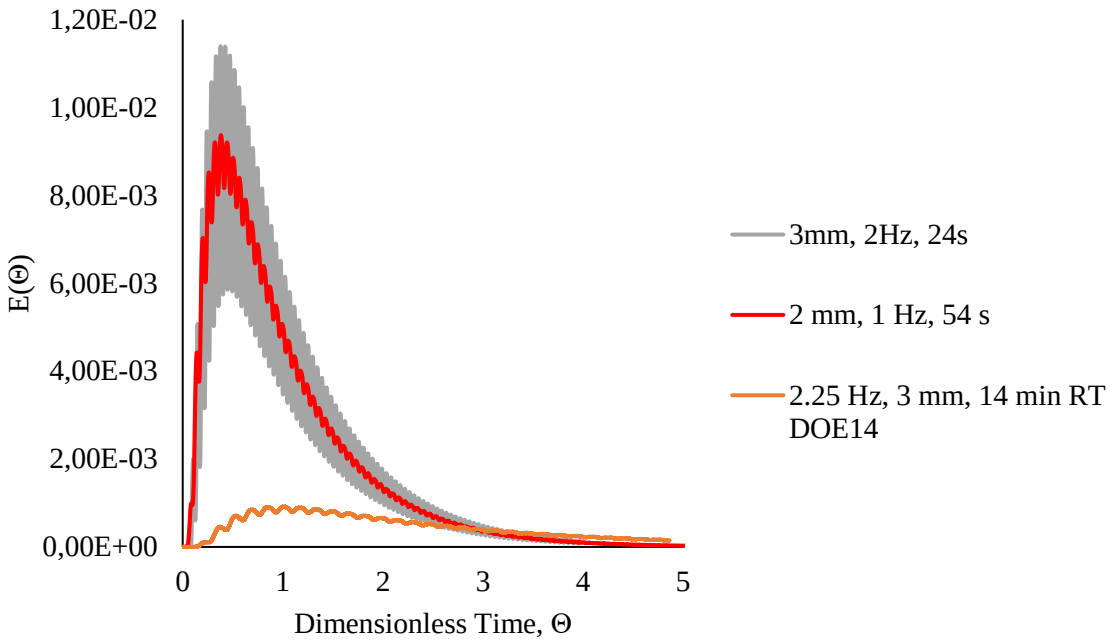

Figure.V.48 RTD curve simulated on Ansys Fluent for different parameters.

The results shown on Figure.V.48 correlate with those from Gonzalez *et al.* using the same type of baffle geometry as this OBR. On the graph variations in E(Θ) in each line is due to the oscillation of flow, each change in tracer concentration measured at the outlet is detected every iteration which causes the software to falsely report a reduction of concentration during the flow, creating the wave-like behaviour on the graph. [223]

Table.V.18 Parameters used to compare CFD and Experimental Data

Corresponding Experimental	CFD Experiment	Amplitude (mm)	Frequency (Hz)	Net flow (ml/min)	Number of equivalent tanks in series	CFD Fit Data to experimental
V1	**C1**	2	1	9	7.06	Slight offset
V2	**C2**	2	1	11.16	5.8	Fits
V3	**C3**	2	0.125	9	2.39	Fits
V4	**C4**	2	0.1	11.16	1.81	Slight offset
V5	**C5**	3	0.55	11.16	5.69	Slight offset
V6	**C6**	3	2.5	19.8	6.47	Fits
V7	**C7**	3	2	19.8	3.58	Fits
V8	**C8**	2	3	19.8	7.4	Fits

The results displayed in Figure.V.48 show that for the sets of parameters 3 mm, 2Hz, 24 s and 2 mm, 1Hz, 54 s, the reactor shows plug flow behaviour but with the DOE 14 parameters the reactor loses this behaviour. The reactor simulated under CFD achieves the same flow behaviour results as the experiments carried out in the lab. Table.V.18 details the parameters used and shows if the modelling on Ansys of the RTD curve fits the experimental data. It is seen that in some cases the experimental data is shifted compare to the simulation. As can be seen from Figure.V.49 and Figure.V.50 the experimental data is shifted to the right but the overall RTD curve behaviour is similar to the simulation. Figure.V.51 shows on the other hand a good fit between experimental and simulated data of the RTD curve. From these results, we can see that the CFD model is accurate, showing its potential to study RTD curves, comparing to experimental data, although there is still some improvement to do to improve both model and experiment. The offset of the axes on Figure.V.49 suggests that the 3D model injection point of the tracer is closer to the end of the baffles than in the experiment The injection point of the tracer in the experimental and simulated data are not at the same place. The experimental injection point is just after the pumps with a 5 cm length, 1 mm ID connecting tube to the reactor. In the simulated data the injection point is at the side of the reactor immediately before the first baffle due to complication occurring during modelling of the full system. The simulation represents only two baffles which could remove some parameters such as pressure outlet due to the volume of the filled reactor. Sedimentation in the OBR was also observed and these phenomena has not been input into the simulation which could create these offsets in RTD curves.

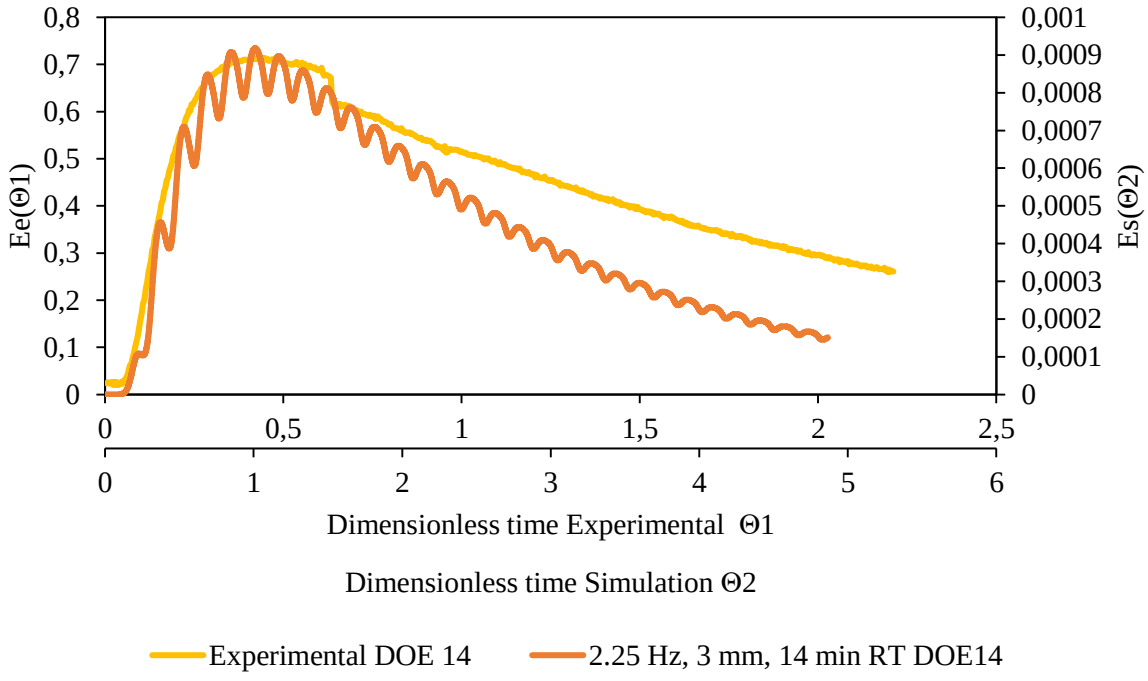

Figure.V.49 RTD simulation compared to experimental for experiment DOE 14.

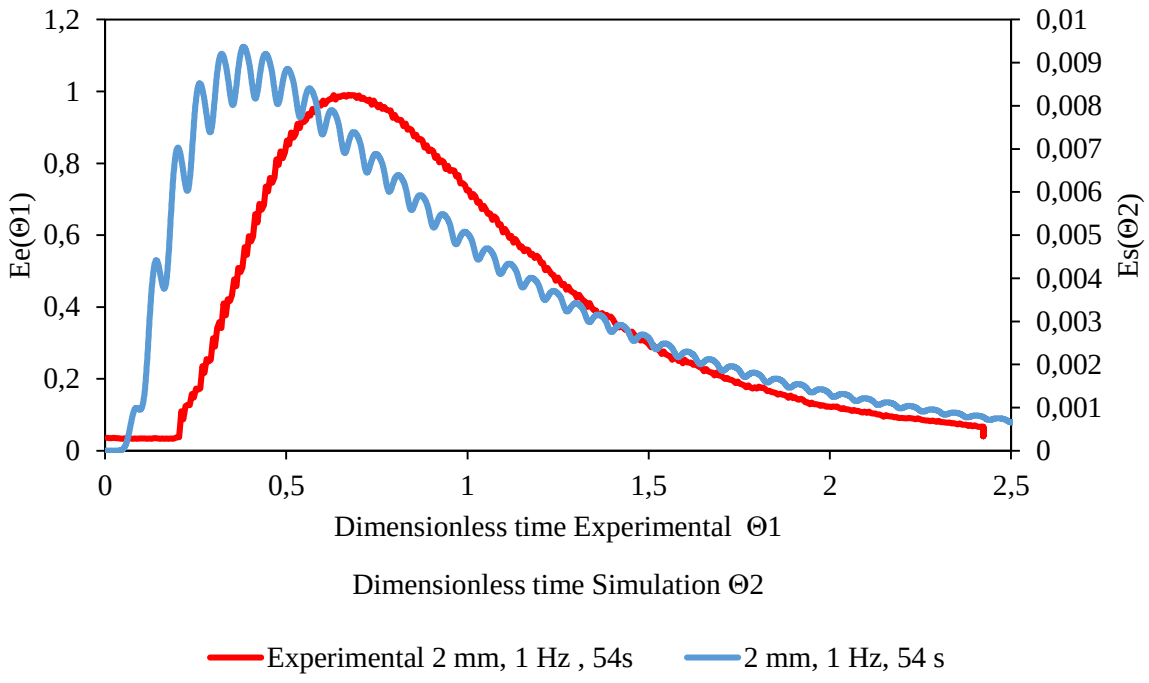

Figure.V.50 RTD simulation compared to experimental for experiments with parameters 2 mm, 1 Hz , 54 s (H1 to H5).

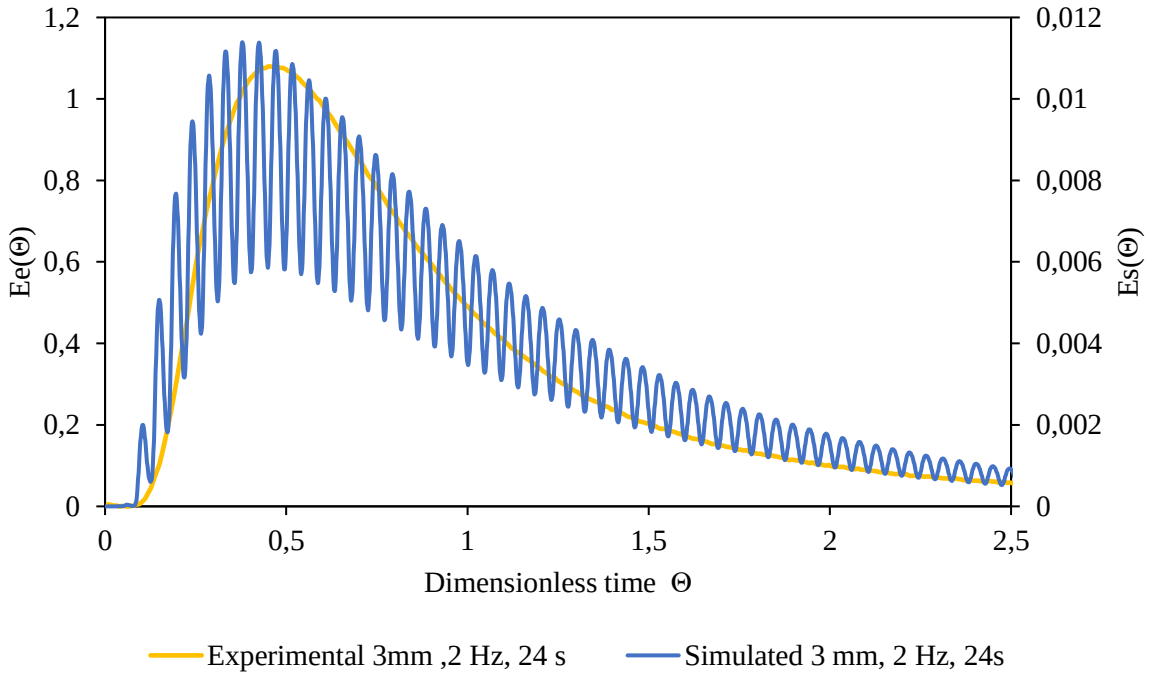

Figure.V.51 RTD simulation compared to experimental for experiments with parameters 3 mm, 2 Hz, 24 s (H6 to H8).

Using this technique to improve the plug flow behaviour showed that it is possible to predict beforehand the plug flow behaviour of the OBR with CFD simulation while knowing that it is possible to add particle tracking to those models to check for dead zones where particles may get trapped. Achieving plug flow behaviour in a reactor is challenging but having a tool capable of modelling oscillation parameters and tracer RTD curve is an advantage to reduce time and cost. The comparison of experimental behaviour to simulated data model will be used in the future to improve the OBR design for different type of reactions.

V.5.5 Particle Tracking

In section V.5.2 some streamline simulations showed potential dead zones inside the OBR for certain parameters. Here is discussed the potential use of particle tracking to detect such dead zones inside the OBR using the injection of a discrete phase with Ansys Fluent.

For this purpose, the Dense Discrete Phase Model (DPM) is used. On Ansys Fluent the main equation to simulate the motions of particles is the particle force balance equation. The software predicts the trajectory of a discrete phase with the equation:

$$\frac{d\overrightarrow{u_p}}{dt} = \frac{\vec{u} - \overrightarrow{u_p}}{\tau_r} + \frac{\vec{g}(\rho_p - \rho)}{\rho_p} + \vec{F} \tag{52}$$

Where $\vec{F}$ is an acceleration term of the domain, $\frac{\vec{u}-\overrightarrow{u_p}}{\tau_r}$ is the drag force per unit particle mass and:

$$\tau_r = \frac{\rho_p d_p^2}{18\mu} \frac{24}{C_d Re} \tag{53}$$

Where τ_r is the particle relaxation time, $\vec{u}$ the fluid velocity, $\overrightarrow{u_p}$ the particle velocity, μ is the viscosity of the fluid, ρ is the fluid density, ρ_p the density of the tracked particle and d_p is the particle diameter. Re is the relative Reynolds number of the stream:

$$Re = \frac{\rho d_p |\vec{u} - \overrightarrow{u_p}|}{\mu} \tag{54}$$

In the case studied sub-micron particles are produced by the use of the Brownian Force and the Stokes Cunningham drag law. The Brownian forces are modelled using a Gaussian white noise *via* the spectral intensity $S_{n,ij}$:

$$S_{n,ij} = S_0 \delta_{ij} \tag{55}$$

where δ_{ij} is the Kronecker delta function, and S_0 is given by:

$$S_0 = \frac{216 v k_b T}{\pi^2 \rho d_p^2 \left(\frac{\rho_p}{\rho}\right)^2 C_c} \quad (56)$$

T is the temperature of the fluid, *v* is the kinematic viscosity, C_c is the Cunningham correction, and k_b the Boltzman constant. For the Stokes Cunningham drag law the force is defined as:

$$F_D = \frac{18\mu}{d_p^2 \rho_p C_c} \quad (57)$$

Where C_c is the correction to Stoke's drag law defined and computed *via*:

$$C_c = 1 + \frac{2\lambda}{d_p}(1.257 + 0.4e^{-(\frac{1.1 d_p}{2\lambda})} \quad (58)$$

Where d_p the particle diameter, λ the mean free path, μ the viscosity and ρ_p the density.

For this model the Large Eddies Simulation is used with the energy equation on and the discrete phase implemented. The same procedure as the vector simulation has been input and the operation was run with a time step of 1 ms and for about 10 s of flow, so 10000 iterations. Convergence is obtained, and the Courant number is in the specifications of the Fluent Manual (0<Co<40). For the oscillation the same UDF function was used as in the previous section V.5.2.

As can be seen on Figure.V.52, in non-ideal conditions (such as Figure.V.52(b), with 0.5 Hz frequency, 2 mm amplitude, 20 min residence time) the particles moving through the OBR stay inside the first inter-baffle spacing after 40 seconds of flow, in the real experiment this results in a wider particle size distribution with larger particles. This result is because the reactor does not behave as a plug flow reactor and due to the particles having more time to grow inside the reactor. Under more ideal conditions (such as Figure.V.52 (a), DOE 14, with 2.25 Hz frequency, 3 mm amplitude, 14 min residence time), the particles seem to progress through the OBR at a more uniform rate resulting in a better particle size distribution, confirmed by SEM (Figure.V.53) and DLS. The APS is 450 nm for DOE 14, but there is a wide range of particle size for other settings such as in DOE 22. In DOE 22 the residence time of 20 min gives to the particle more time to settle into a bottom baffle and the short amplitude, 2 mm, stroke and the low frequency, 0.5 Hz, create a suitable environment for growing particles and creating aggregates. CFD gives a good opportunity to optimize the reactor shape and parameters to control particle size. Here the use of two baffle modelling helped significantly to avoid long simulations and Ansys Fluent crashing.

On Figure.V.54 is displayed a particle track performed for 111 particles with the parameters used in the velocity ratio experiment H1 previously presented. Particles size were considered as a sphere of 400 nm with a density of 0.49 Kg/L (calculated from CIF file from Grosjean *et al.* structure using Mercury[39])

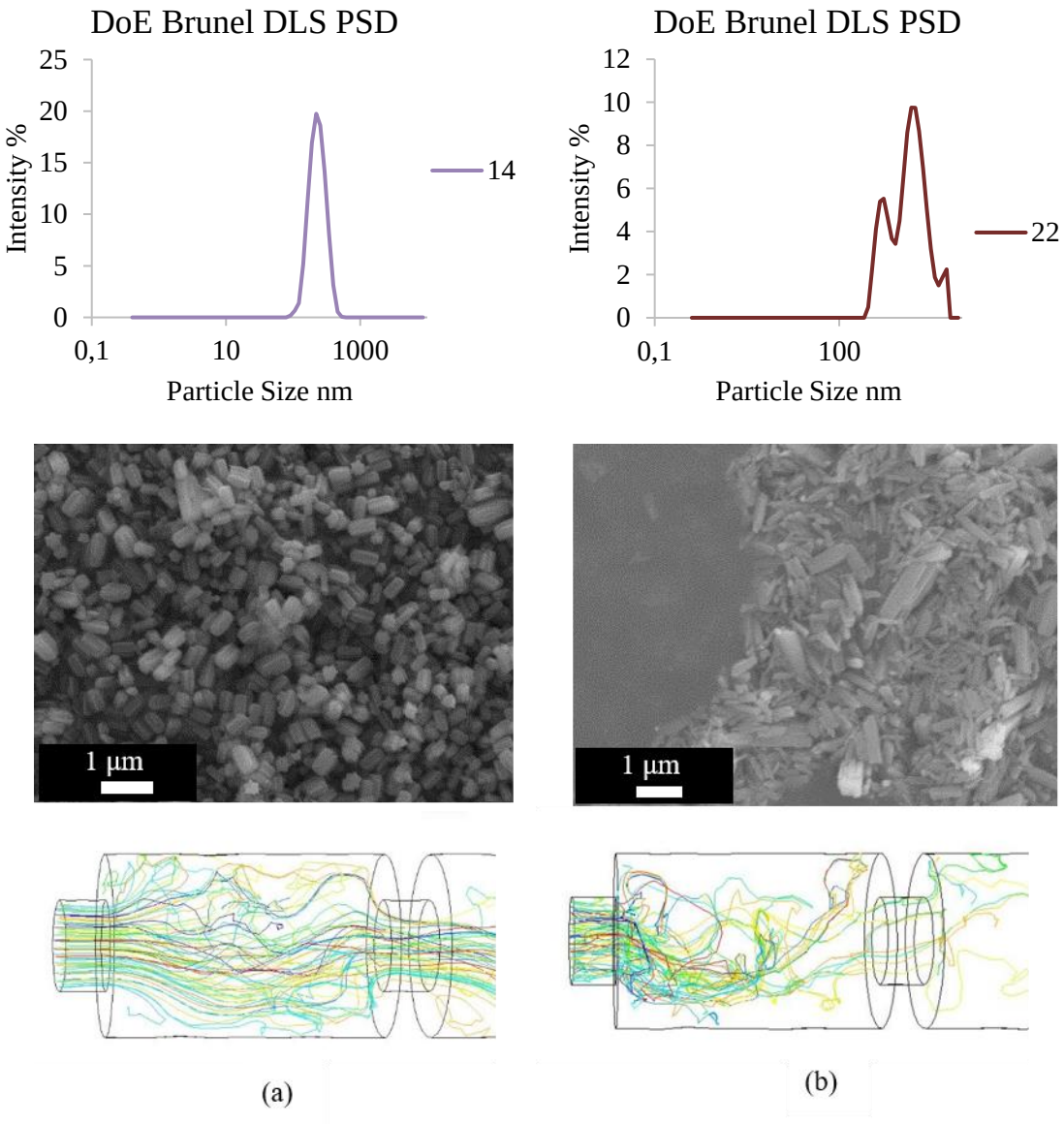

Figure.V.52 Particle tracking from Ansys Fluent with corresponding SEM image and DLS graph for experiments carried out in the Centillion®. Same concentrations of reagents were used with parameters for the oscillation of DOE 14 (left) and DOE 22 (right).

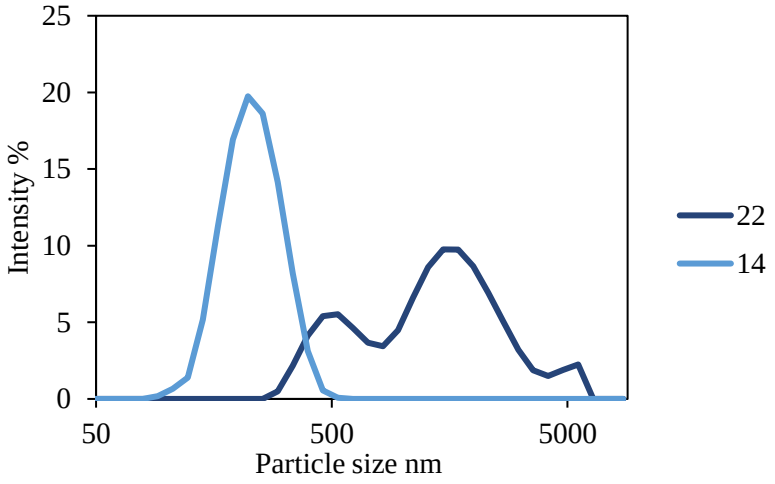

Figure.V.53 DLS of DOE 14 and DOE 22 experiment confirming the SEM results.

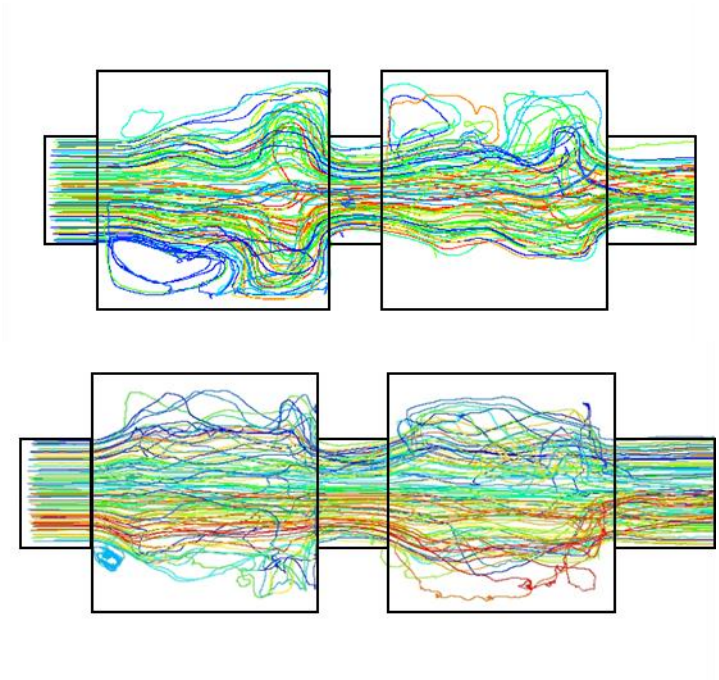

Figure.V.54 Particle tracking of H1. Each colour represents a particle ID. The pictures correspond to different view angles with a 90° rotation.

Compared to Figure.V.52 the particles clearly proceed without significant deviation from one baffle to another and even beyond with the same flow parameters as before. H1 experiment was shown to exhibit good plug flow behaviour on RTD curves and also resulted in small, homogenous, particle size production of PiC.

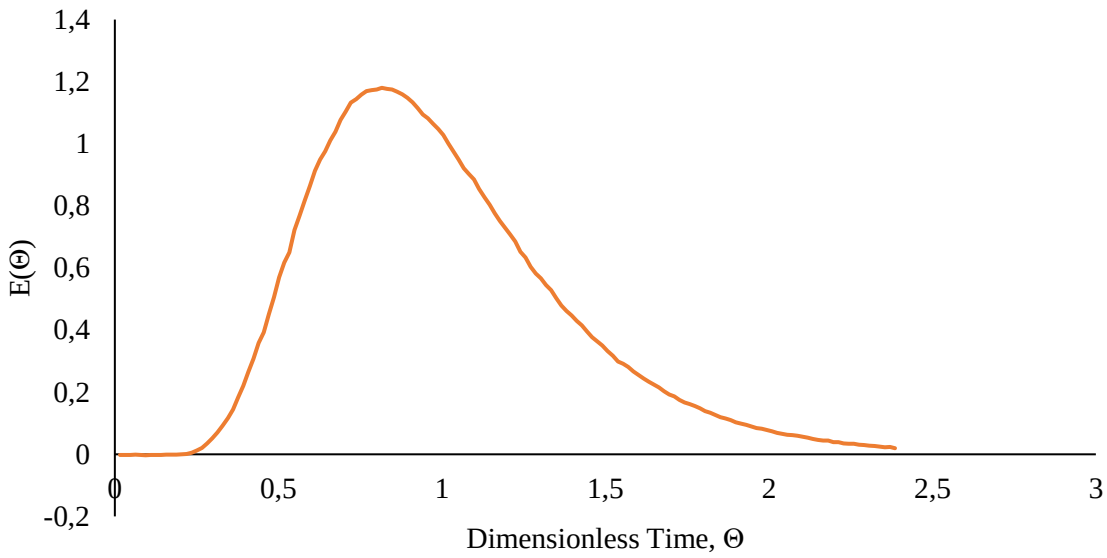

Figure.V.55 RTD curve for experiment H1, with parameters 2 mm Amplitude, 1 Hz Frequency, 54 s RT, obtained experimentally.

With those parameters the OBR was capable to produce fast and continuously SCO PiC particles with a good particle size distribution as reported in Figure.V.38 for different concentrations of reagents. The downside of those parameters is the flow rate which require larger scale of reagent to achieve long production time; adding several channels together would increase the residence time and a larger volume of particles would be produced.

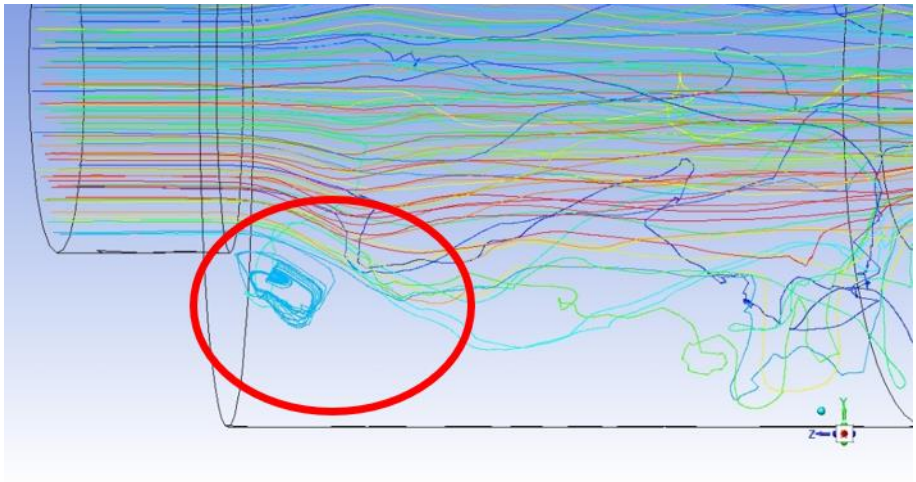

Figure.V.56 Dead zone appearing in the OBR for parameters 2 mm Amplitude, 1 Hz Frequency, and 54 s RT.

With the particle tracking it is still seen that particles are trapped in some areas. On Figure.V.56 is displayed one of the particles that stays in the first inter-baffle spacing for a long time despite the otherwise plug flow behaviour within the reactor. This would lead to sedimentation with crystallisation or precipitation like that observed in Figure.V.33 for a long duration run where some particles due to

the dead zone were staying inside the baffle and aggregating with each other, creating a layer of particles at the bottom of the channel baffles. This sedimentation happened in two cases, one was for the long experiment run over several RT (>14) or when synthesising PiCM in methanol where the viscosity of the solution changed. Additionally, an increase in particle size was observed (DOE 22) corresponding to the trapped particle reacting again with fresh reaction solution and creating bigger crystals such as those seen in Figure.V.52. It is reported in Reis *et al.* that baffle geometry and dimension have a significant impact in reducing dead zones. For instance, the COBC from NiTech has rounder shaped baffles and those may avoid dead zones, for PiC this would avoid particle sedimentation or getting trapped in some points of the reactor. [208]

V.6. Conclusion

In this chapter the Centillion® OBR[17] has been introduced and used to synthesise $[Fe(Htrz)_2(trz)](BF_4)$ H_2O with control over particle size. It has been revealed that particle size can be controlled using different parameters such as frequency, amplitude, flow rate and concentration of reagent. At first the reactor had some changes in design to find the most suitable for the reaction needs, and then a DOE was implemented in order to target particle size. It has been seen that the reactor can target a middle range particle size of 100 nm to 1000 nm. Compared to other studies, the particle size and shape were shown to be importantly dependent on the concentration as also observed with the PiC synthesis in the KRAIC. [13,218]

The optimization of the average particle size (APS) with different variations of the input parameters was essential to provide conditions under which the reaction would proceed in less time and with less reagent waste by being able to select the product wanted. After several investigations, optimal parameters have been found for the reactor to continuously produce PiC. It has been shown that targeting particle size with this reactor was possible while care must be taken while analysing the data from DLS, confirming the results with SEM. The DOE model has helped to have a better understanding of the reactor and how to optimize it by studying flow behaviour *via* RTD analysis. Consistency and repeatability of experiments has been confirmed over time with different parameters, this shows that the OBR is a platform suitable for production of small particles continuously. The problem of longer runs was sedimentation which can be caused by dead zones inside each baffle due to geometry, those have been confirmed also with CFD and this needs to be assessed for future OBR designs. It was shown in Section V.5.5 that dead zones were present inside the reactor at the bottom edges of the cells which could cause sedimentation. In Chapter VII study will be also done on the particle density and behaviour in fluids using Analytical Ultra Centrifugation (AUC). Switching properties of the material produced have been tested and the study will be presented in Chapter VII.

Using CFD as a tool to actively process flow information to optimize the reactor has been proven. The RTD study showed that the DOE parameters were far from plug flow behaviour and thus led to velocity ratio analysis being undertaken. The velocity ratio was optimized to get as close as 10 continuous stirred tank reactor (CSTR) in series as reported Ni *et al.* which led to a better plug flow behaviour of the reactor and improved the RTD of the reactor by optimising the parameters. [216] The CFD also confirmed the improvement of the RTD curve by simulating the same parameters as the experimental, this showed that CFD could be trusted to further improve the OBR production of PiC. A full DOE would be necessary with the new parameters to target these improved particles in the presented OBR but it should be noted

that another DOE campaign would be needed upon scaling-up from lab to pilot scale. The comparison between the streamlines on the CFD and the SEM obtained for PiC showed the importance of controlled mixing behaviour inside the OBR, as particle size and homogeneity changed depending on the parameters used during experimentation.

Chapter VI Spin-crossover and thermochromics synthesis with Vapourtec R-Series flow Kit

VI.1. Vapourtec R-Series Flow Reactor

In order to scale up production of a material, a lab scale reactor must first be designed. Some companies develop reactors from lab scale to industrial scale in order to have a gradient of reactor development. Vapourtec is one of those companies, producing systems compatible with milli-scale to litre-scale reactors without changing the pumping or heating unit. Having access to modular and easily reconfigurable reactors for scaling-up material is one of the challenges of flow chemistry. In this section is described the work on a Vapourtec R-series Flow Unit equipped with different types of reactor for different flow solutions to produce metastable materials.

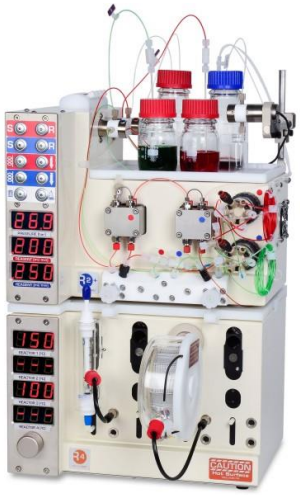

Figure.VI.1 Vapourtec R-Series Flow Kit.

Figure.VI.1 shows the Vapourtec R-series Flow Kit reactor with the flow system attached. The system is equipped with two HPLC pumps with a chamber of 10 mL capable to deliver a flow rate from 0.01mL/min to 10 mL/min. A manifold control the pressure after the pump and is used to prime the pump with the reaction / crystallisation solvent. The heating system is composed of four chambers that dock the heating reactors as shown in Figure.VI.2. The reactor has been widely used in the literature for different reaction types from RAFT polymerisation[52,232] to green chemistry [233] and gas liquid reactions.[61] In this section, the use of several reactor types for the production of different material will be presented.

Figure.VI.2 Docked heated reactor coil for Vapourtec R-series.

The first reactor presented here is a simple 1 mm open bore tubing reactor with a volume of 10.2 mL; this reactor was used for the synthesis of the SCO compound $[Fe(Htrz)_2(trz)](BF_4)$ (PiC)[4] with different solvents as investigated for the Oscillated Baffle Reactor (OBR) in Chapter V and the Kinetically Regulated Automated Input Crystalliser (KRAIC) in Chapter IV. This small reactor was used to show the capability of the Vapourtec Flow Kit to produce nanoscale materials.

Table.VI.1 presents the large bore tubing with static mixer inserts used to produce PiC in a similar design of experiment (DOE) approach as the OBR presented in Chapter III, targeting particle size with the same algorithm. Static mixers in reactors are widely used in industry to mix two phases or more efficiently, they come in different size and shape, from helicoidal to rods changing angle periodically like SMX static mixers.[234] In this case study helicoidal static mixers were used. Static mixers provide blending and dispersion of the mixtures injected inside the reactor by redirecting the flow dynamics and patterns that are present in normal tubing (Figure.VI.3). The advantages range from better heat transfer and temperature uniformity to residence time improvement as shown in Figure.VI.4, where the difference in residence time distribution between non-static mixers reactor and larger scale reactor is shown.

The dispersion model in static mixer reactors has been widely studied in literature[147,234] showing the improvement of mixing inside different size of tubing and shape of static mixers. The two static mixer reactors used in this study use 3.2 mm and 5.6 mm bore tubing with the Kenics® type inserts with a total volume of 65 mL and 142 mL. In addition to the experimental results obtained from use of these reactors, study of the fluid behaviour inside those reactors *via* computational fluid dynamics (CFD) using Ansys Fluent will be presented.

The third type of reactor presented here is a progressive mixer tube-in-tube reactor. The system was used in [235] as a solution to make gradient copolymer where the monomer is continuously injected into the flow stream in order to get an uniform polymer chain at the end of the production. In the case studied here, the SCO compound $[FeL_2][BF_4]_2$ [L = 2,6-di(pyrazol-1-yl)pyridine] (YeC) [20] is synthesised using an anti-solvent technique inside the reactor. There are laser drilled holes along the length of inner tube of the reactor of 50 µm diameter enabling progressive mixing of the solutions, Figure.VI.5.

The principle of the tube-in-tube reactor is also displayed in Figure.VI.5; the anti-solvent is flowed from the outer tube into the inner tube where the solute is precipitated, and the precipitation occurs inside the inner tube, the solids are transported to the outlet. The whole investigation for the synthesis of YeC compound will be discussed in part VI.3, and the advantages of using that type of reactor shown.

Table.VI.1 The four reactors used with the Vapourtec R-series for the production of different materials.

	Type of reactor	Volume (ml)	Material investigated in the reactors
	Open bore 1 mm ID	10.42	$[Fe(Htrz)_2(trz)](BF_4)$ (PiC) $[Fe(Htrz)_3](BF_4)_2{\cdot}H_2O$ (PiCM)
	Static mixer 5.6 mm ID	142	$[Fe(Htrz)_2(trz)](BF_4)$ (PiC)
	Static mixer 3.2 mm ID	65	$[Fe(Htrz)_2(trz)](BF_4)$ (PiC)
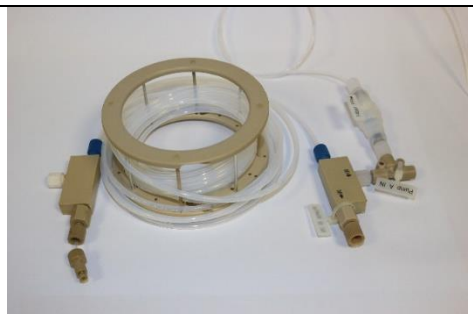	Progressive Mixer	26.2	$[FeL_2][BF_4]_2$ [L = 2,6-di(pyrazol-1-yl)pyridine] (YeC)

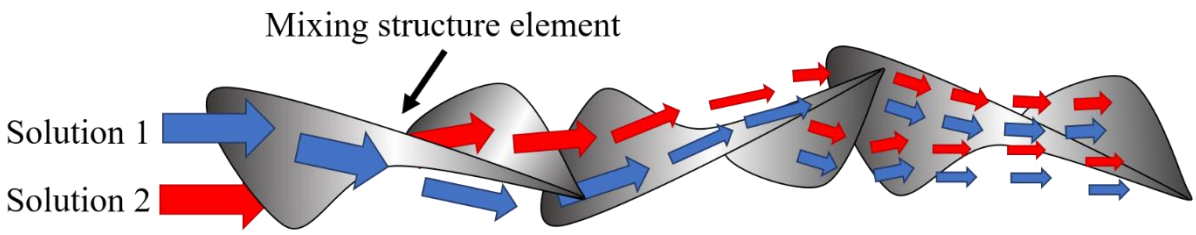

Figure.VI.3 Static mixers structure with mixing effect.

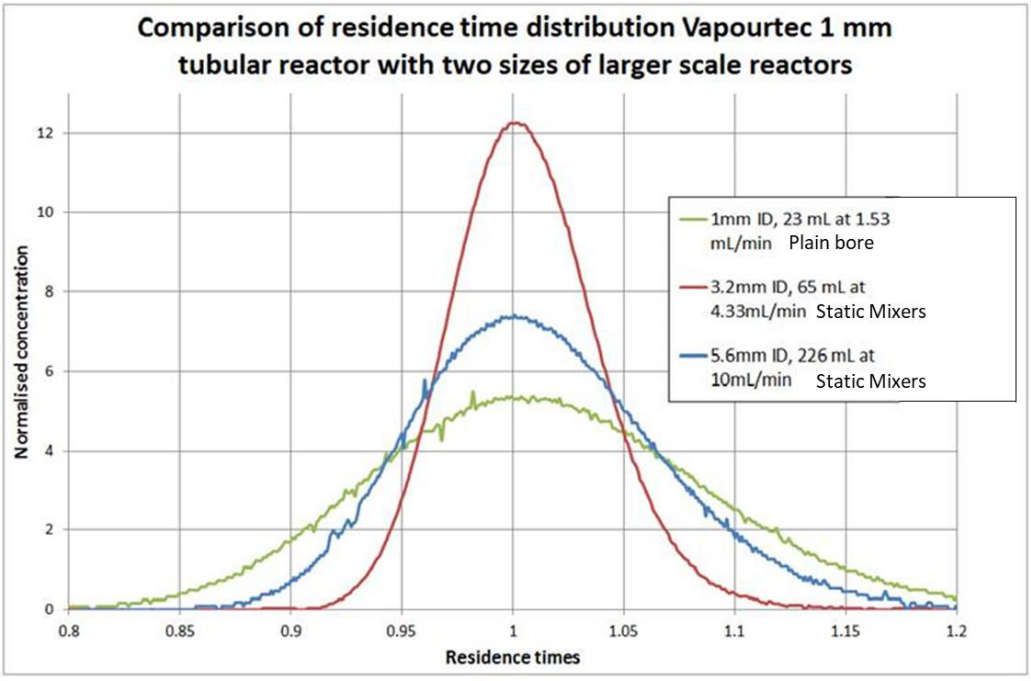

Figure.VI.4 Static mixer reactor and bigger scale reactor residence time comparison (courtesy of Vapourtec, UK). In green is the 1 mm ID open bore tubing in blue the 5.6 mm bore tubing with static mixers and in red the 3.2 mm bore tubing with static mixer.

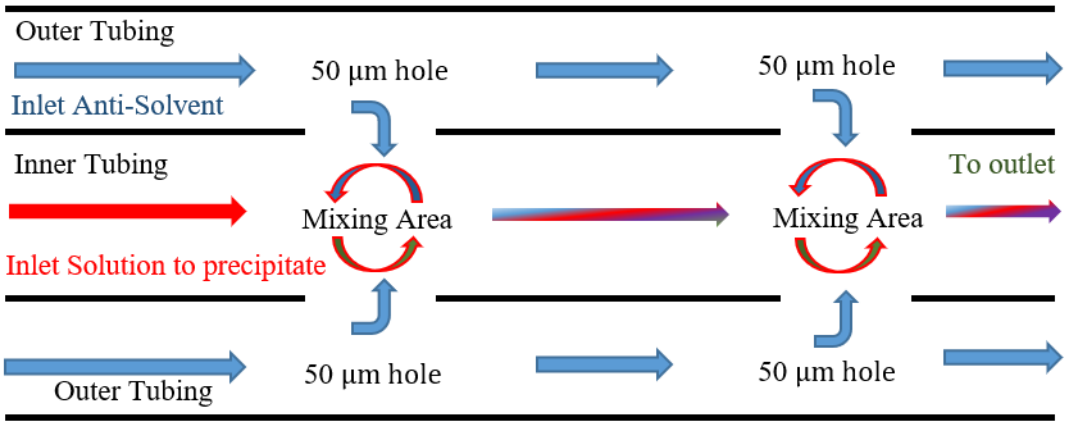

Figure.VI.5 Scheme of the tube-in-tube reactor

VI.2. Synthesis of Fe(Htrz)2(trz)](BF4)

As previously noted in studies with the OBR, presented in Chapter V, the control of production of PiC is difficult without using the reverse micelle technique.[218] Unfortunately, the reverse micelle technique is difficult to scale. A methodology to control the particle size of PiC using an OBR was presented in Chapter V. Here this methodology is applied to open tubular and static-type static mixer insert reactors.

VI.2.1 Synthesis of PiC in simple bore tubing

For synthesis of PiC in 1 mm bore tubing, feed solutions of 8.67g of 1H-1,2,4-triazole in 100 mL of water and 8.3 g of iron(II) tetrafluoroborate hexahydrate in 100 mL water were prepared (concentrations are the same as those investigated for batch synthesis: Chapter III, experiments B1 to B8). Parameters for each experiment are displayed in Table.VI.2. Pumps were set to 1 mL/min for each solution – a total of 2 ml/min inside the reactors. The residence time was equal to 16 min for a 1 mm bore tubing for a length of 10.19 m.

Table.VI.2 Parameters for the synthesis of PiC inside 1 mm bore tubing

No.	Batch Synthesis corresponding	Concentration of $[Fe(BF_4)_2]$ g/mL	Concentration HTrz g/mL	Flow rate mL/min	Yield % from $Fe(BF_4)_2$ in 1 mm bore tubing	Yield % from $Fe(BF_4)_2$ in Batch
Vb1	**B1**	0.0827	0.0866	2	63.3	45.2
Vb2	**B3**	0.0162	0.008	2	42.6	20.3
Vb3	**B5**	0.0624	0.0312	2	35.1	15.7
Vb4	**B6**	0.0101	0.0049	2	58.4	42.6
Vb5	**B7**	0.0253	0.0082	2	45.2	51.6
Vb6	**B8**	0.055	0.084	2	49.7	32.5

Figure.VI.6 . Synthesis of PiC in the open bore 1 mm Vapourtec R4 reactor. Left: initial PiC production, right: steady state production of PiC for experiment Vb6.

For experiment Vb1, after 23 min runtime (for reference, RT is 16 min), a pink hue appeared uniformly throughout the tubing, indicating the appearance of PiC. As observed in experiments in the KRAIC and OBR, the transparent to cloudy white and finally pink colour change was also observed for all experiments. Here the presence of a pink hue throughout the tubing showed the presence of particles getting stuck into the static mixer compared to other reactors like the KRAIC or OBR where the change in colour was progressive along the length rather than in run time. The product was recovered by filtering at the end of the reactor and the yield was recovered at 79 %. The compound was then analysed by scanning electron microscopy (SEM) and dynamic light scattering (DLS) to compare particle size and shape with that produced in other reactors (Figure.VI.7).

As can be seen in Figure.VI.7 the experiment Vb1 gave different particle morphologies, rods, from the star shaped rods obtained for experiments Vb2-Vb4. Compared to experiments B1 to B8 carried out in Chapter III the particle size is lower as observed through DLS analysis. For instance, Vb1 in the 1 mm bore tubing gives a particle size distribution (PSD) ranging from 396 to 1100 nm while the batch experiments produced a range from 826 nm to 2203 nm. The same behaviour of size reduction, with respect to corresponding batch experiments(B1-8), is also present for experiments Vb2, 3 and 4 with 4 presenting a broader particle size range (141-1989 nm). The shape of the particles for Vb2 to Vb4 is similar to those observed in the KRAIC (PiCK1 to PiCK8) and OBR (SO 1 to 6) (Figure.VI.8).[13,218] The yield is also increased in comparison to batch as displayed on Table.VI.2. It was observed that the particles get stuck in some of the pipe links and start to accumulate which can cause blockage during long runs, greater than 3 residence times (47 min), and an increase of the pressure inside the system. This would be avoided by using bigger tubing to avoid aggregation of particles over time.

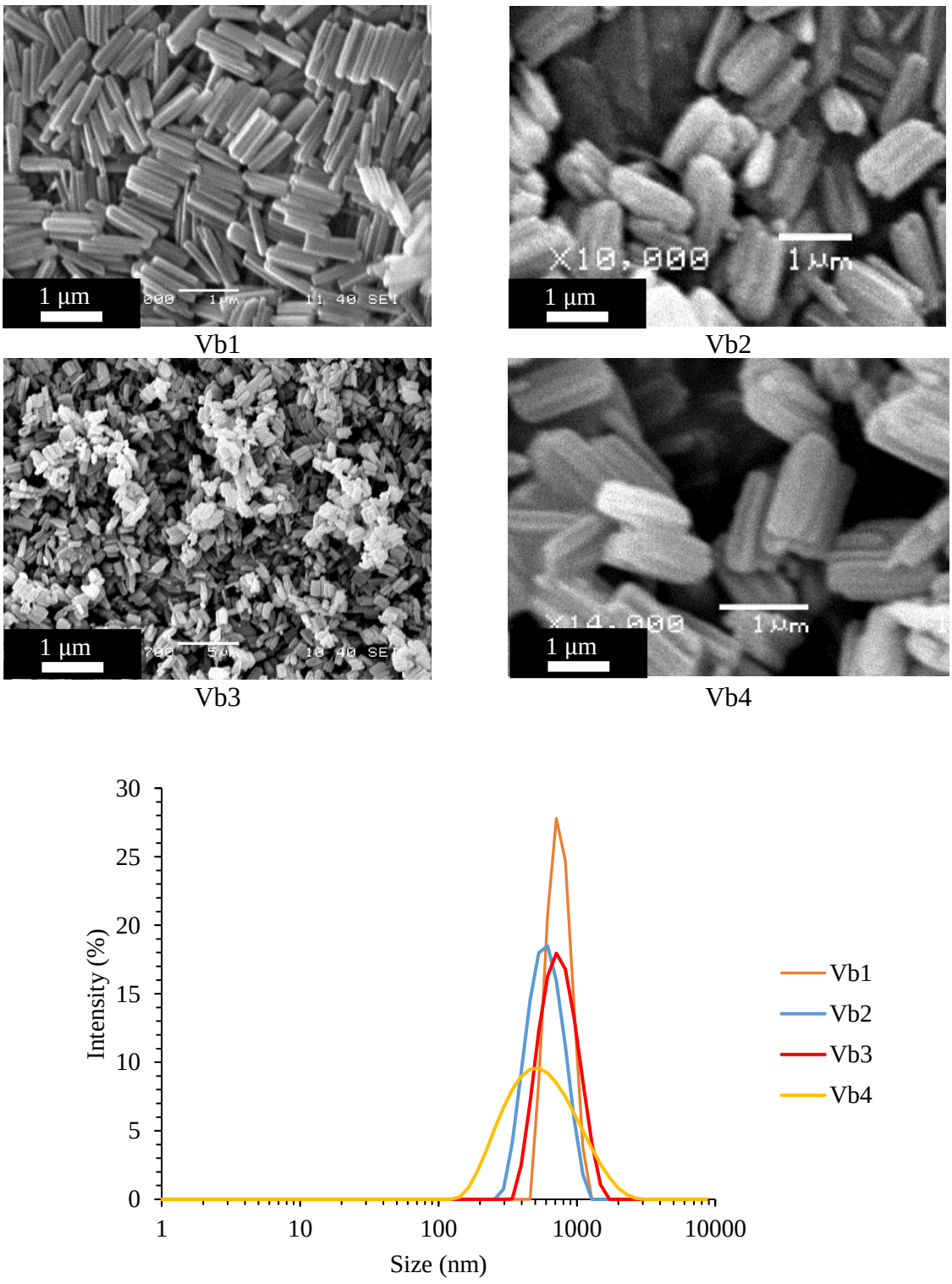

Figure.VI.7 SEM images of PiC synthesised for experiment Vb1-4 with corresponding particle size distribution from DLS (bottom)

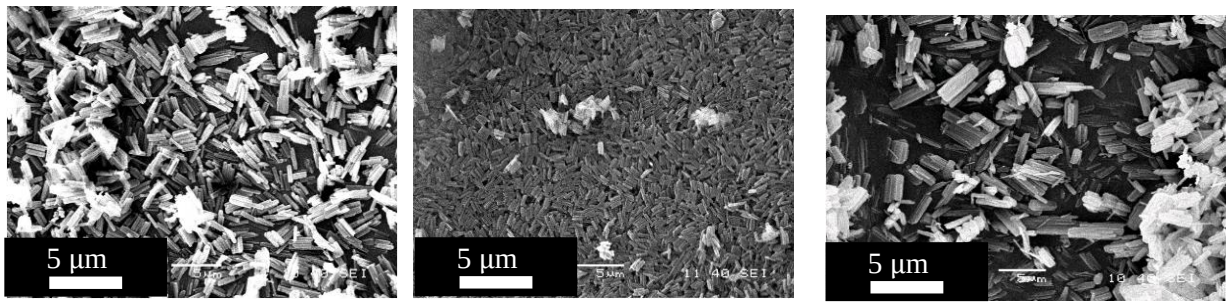

Figure.VI.8 SEM images of PiC synthesised on (left). B4, (centre) Vapourtec experiment Vb4 and (right) OBR SO 2 carried out with the same concentration.

In the 1 mm bore tubing reactor, the compound $[Fe(Htrz)_2(trz)](BF_4)$ was successfully synthesised (confirmed by PXRD A6, Figure A6.1).In the next section a design of experiment (DOE) approach will be presented as a solution to control particle size.

VI.2.2 PiC Particle size control using static mixer reactor

To control the particle size of PiC, a similar approach was taken as that followed for PiC synthesis in the OBR, but this time only three categorical factors have been used and one fix factor, concentration of iron(II) tetrafluoroborate hexahydrate $Fe(BF_4)_2.H_2O$ (CI), concentration of 1H-1,2,4 Triazole (CT), total flow rate of the two pumps (Fl) and a fix factor which is given for the size of the reactor (S=0 for 3.2 mm bore (65 mL) reactor with static mixer inserts and S=1 for the 5.6 mm bore (142 mL) reactor with static mixer inserts). Here, compared to the OBR where the mixing was induced by an oscillation mechanism, the mixing is directly linked to the flow rate due to the static mixer insert which creates intermixing depending on the static mixer shape and flow rate. In total 40 experiments (20 for S=0 and 20 for S = 1) have been carried out with each one employing different parameters. The concentration range was as used in the OBR, 0.532 g/100 mL to 12.532 g/100ml. The set-up of the experiment is described in Figure.VI.9.

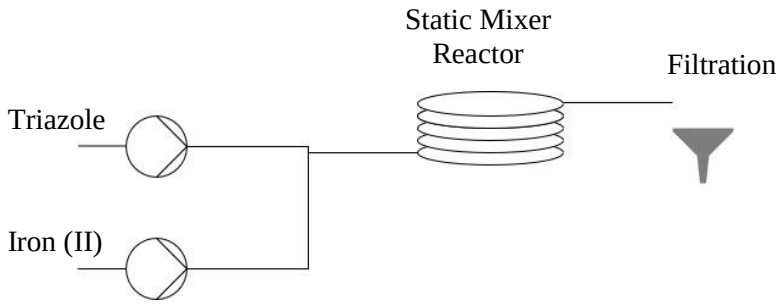

Figure.VI.9 Scheme of the Vapourtec Flow Kit DOE set-up

The particle size of Fe(Htrz)2(trz)](BF4) was monitored *via* DLS. The DLS results are displayed inTable.VI.3.

Table.VI.3 Average particle size obtained *via* DLS of Fe(Htrz)2(trz)](BF4)

Run Order	CI (g/100 mL)	CT (g/100mL)	Fl (mL/min)	S Size	Average Particle Size (APS) (nm)
DOEV 1	2	2	2	0	629.5
DOEV 2	6	6	6	0	478.2
DOEV 3	10	10	2	0	398.5
DOEV 4	10	2	10	0	500.8
DOEV 5	6	6	6	0	587.1
DOEV 6	2	10	10	0	841.8
DOEV 7	2	10	2	0	1178
DOEV 8	6	6	6	0	461.5
DOEV 9	10	2	2	0	834.3
DOEV 10	2	2	10	0	369.1
DOEV 11	10	10	10	0	260.1
DOEV 12	6	6	6	0	347
DOEV 13	6	6	6	0	553.6
DOEV 14	6	6	6	0	377.1
DOEV 15	6	12.532	6	0	468
DOEV 16	6	6	0.532	0	1198
DOEV 17	6	6	12.532	0	474.1
DOEV 18	12.532	6	6	0	495.6
DOEV 19	6	0.532	6	0	764
DOEV 20	0.532	6	6	0	911.3
DOEV 21	2	2	2	1	788.9
DOEV 22	2	10	10	1	695.6
DOEV 23	6	6	6	1	335.7
DOEV 24	6	6	6	1	639.9
DOEV 25	10	2	10	1	514.6
DOEV 26	10	10	2	1	427.9
DOEV 27	2	10	2	1	1015
DOEV 28	6	6	6	1	551.4
DOEV 29	10	2	2	1	586.8
DOEV 30	2	2	10	1	421.5
DOEV 31	10	10	10	1	175.2
DOEV 32	6	6	6	1	552.2
DOEV 33	6	6	12.532	1	636.1
DOEV 34	12.532	6	6	1	461.2
DOEV 35	6	12.532	6	1	316.7
DOEV 36	6	6	6	1	639.6
DOEV 37	6	6	6	1	577.6
DOEV 38	6	6	0.532	1	1616

DOEV 39	0.532	6	6	1	798.2
DOEV 40	6	0.532	6	1	769.6

Table.VI.4 Stochiometric Ratio $[Fe(BF_4)_2\ 6H_2O]$ /[HTrz] for Vapourtec Static mixer DOE

Run Order	CI mmol/100mL	CT mmol/100mL	Stochiometric Ratio $[Fe(BF_4)_2\ 6H_2O]$ /[HTrz]
DOEV 1	5.9	29.0	2/10
DOEV 2	17.8	86.9	2/10
DOEV 3	29.6	144.8	2/10
DOEV 4	29.6	29.0	1
DOEV 5	17.8	86.9	2/10
DOEV 6	5.9	144.8	4/100
DOEV 7	5.9	144.8	4/100
DOEV 8	17.8	86.9	2/10
DOEV 9	29.6	29.0	1
DOEV 10	5.9	29.0	2/10
DOEV 11	29.6	144.8	2/10
DOEV 12	17.8	86.9	2/10
DOEV 13	17.8	86.9	2/10
DOEV 14	17.8	86.9	2/10
DOEV 15	17.8	181.4	1/10
DOEV 16	17.8	86.9	2/10
DOEV 17	17.8	86.9	2/10
DOEV 18	37.1	86.9	4/10
DOEV 19	17.8	7.7	2 3/10
DOEV 20	1.6	86.9	2/100
DOEV 21	5.9	29.0	2/10
DOEV 22	5.9	144.8	4/100
DOEV 23	17.8	86.9	2/10
DOEV 24	17.8	86.9	2/10
DOEV 25	29.6	29.0	1
DOEV 26	29.6	144.8	2/10
DOEV 27	5.9	144.8	4/100
DOEV 28	17.8	86.9	2/10
DOEV 29	29.6	29.0	1
DOEV 30	5.9	29.0	2/10
DOEV 31	29.6	144.8	2/10
DOEV 32	17.8	86.9	2/10
DOEV 33	17.8	86.9	2/10

DOEV 34	37.1	86.9	4/10
DOEV 35	17.8	181.4	1/10
DOEV 36	17.8	86.9	2/10
DOEV 37	17.8	86.9	2/10
DOEV 38	17.8	86.9	2/10
DOEV 39	1.6	86.9	2/100
DOEV 40	17.8	7.7	2 3/10

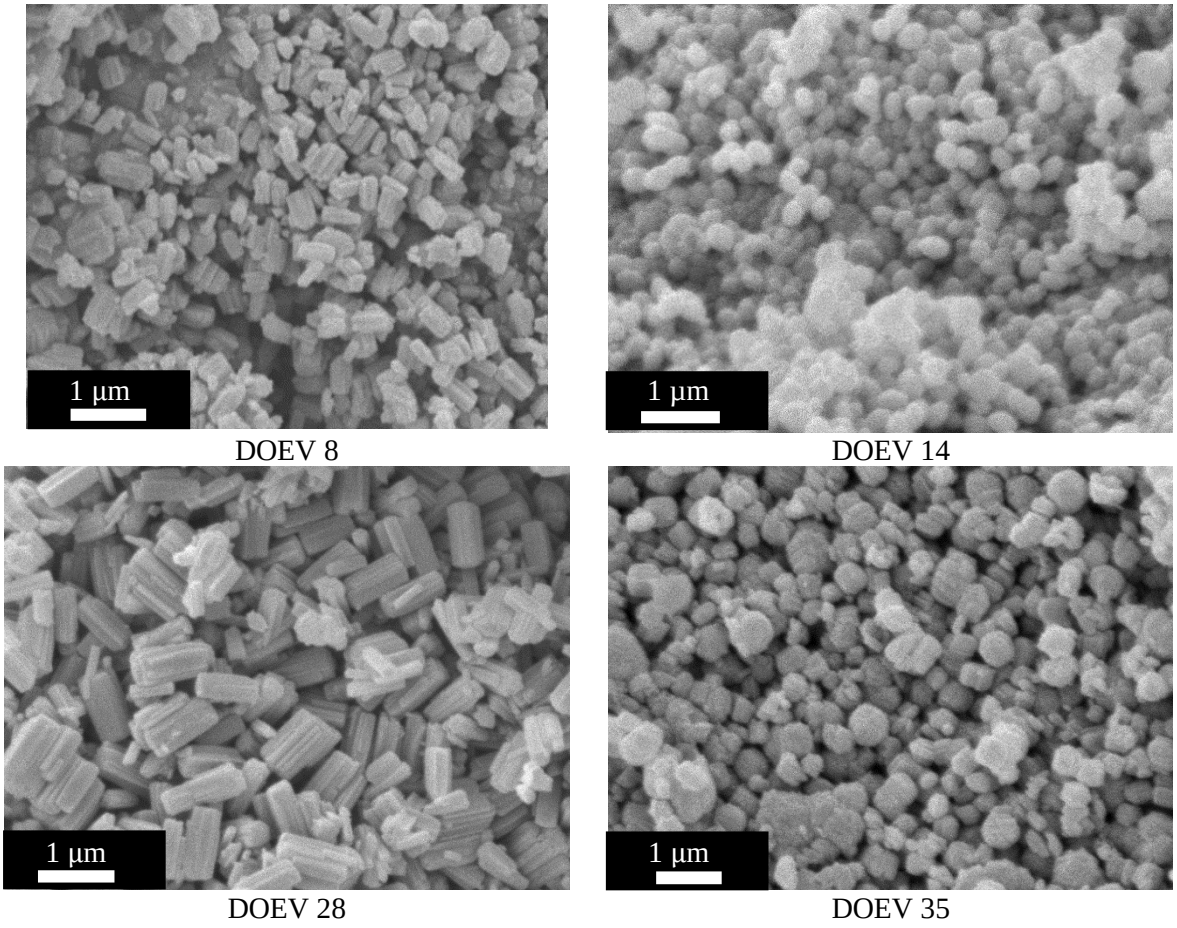

Figure.VI.10 SEM of products from PiC experiments 8,14,28,35 (other SEM pictures will be given as supplementary information in **CDCh6-2**).

In Figure.VI.10 the SEM images show different particle sizes and shapes for different parameters. The particle sizes observed in the above experiments are small (100-600 nm) and rarely exceed the micron level, which is in contrast to observations of PiC synthesis in the OBR in which larger particles were typically produced (400-1200 nm) for the DOE. The DLS results of the corresponding experiments of Figure.VI.10 are shown in Figure.VI.11.

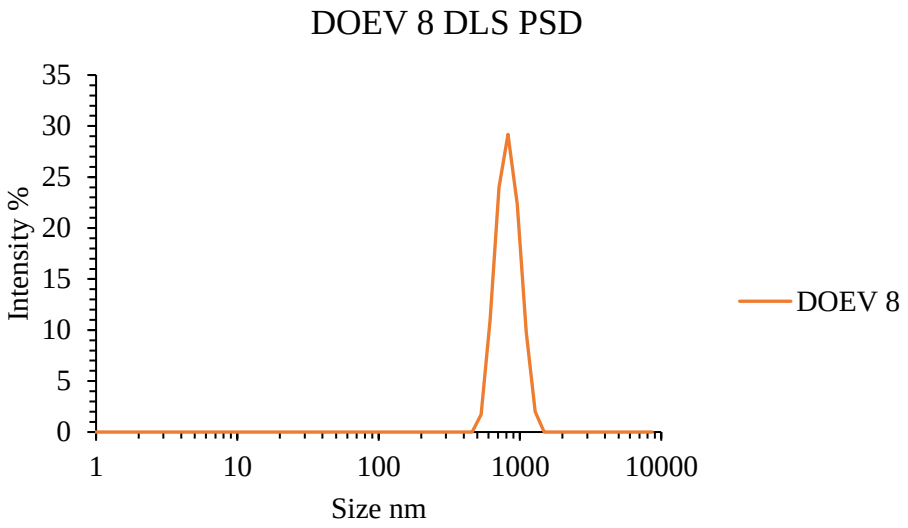
DOEV 8 DLS PSD
35
30
25
20
15
10
5
0
Intensity %
1
10
100
1000
10000
Size nm
DOEV 8

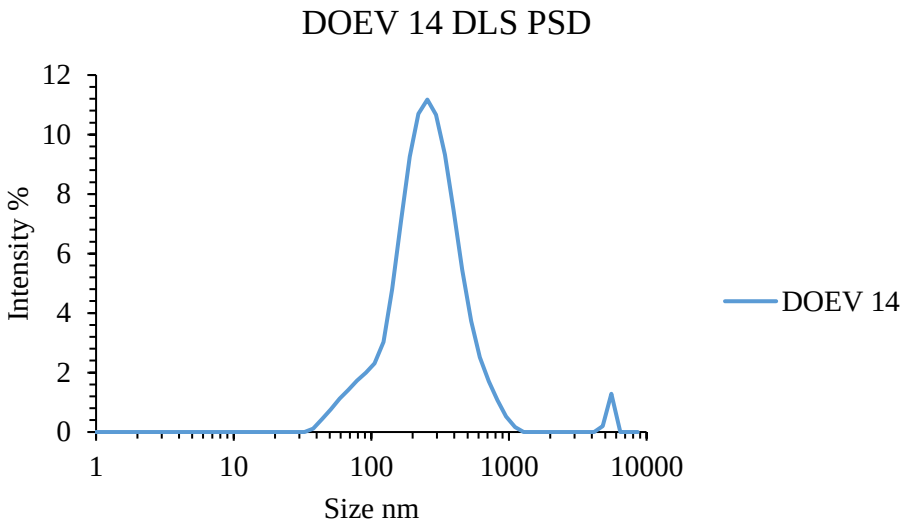
DOEV 14 DLS PSD
12
10
8
6
4
2
0
Intensity %
1
10
100
1000
10000
Size nm
DOEV 14

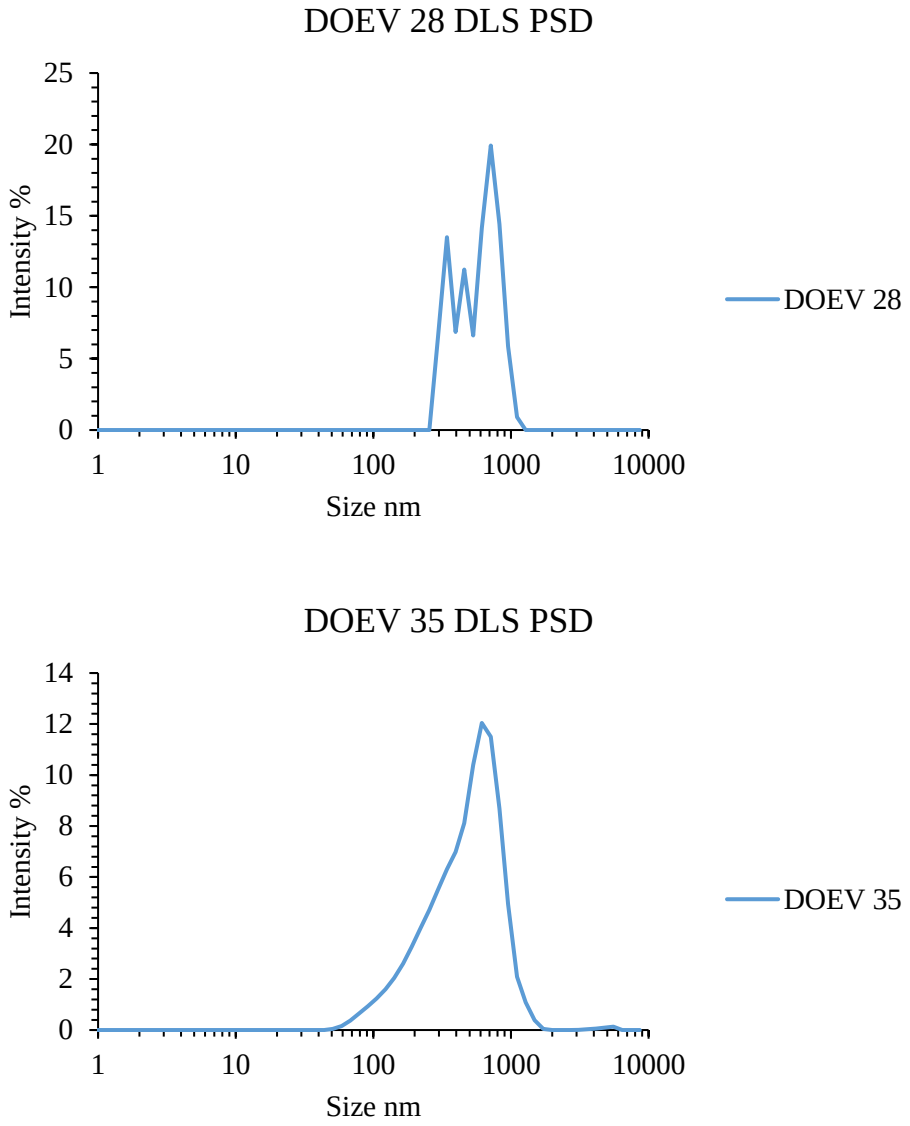

Figure.VI.11 DLS results of corresponding experiments DOEV 8, 14, 28 and 35.

From the DLS graphs it can be seen that the particle size distribution is closely related to the SEM images displayed in Figure.VI.10. For DOE 8 and 14 a concentration of 8 g/100 mL has been used for both reagents and a flow rate of 6 mL/min. The DLS and SEM results from DOEV 8 show particles from 500 nm to 1100 nm. DLS results from DOEV 14 show particles from 100 nm to 1000 nm whilst SEM images show some aggregates, giving the 500 nm average particle size, but the SEM shows also a large number of particles in the 100-300 nm range, which is close to the DLS results. It is noted that, as it is a DOE model, some experiments with the same parameters are repeated in order to calibrate the surface response model equation. DOEV 8 and 14 experiments are a good example of the need for these repeats; the experiments have the same parameters but different output in particle size and shape with rod-like particles for DOEV8 and spherical-like particles for DOEV14. In other trials for the different size of reactor with the same parameters the average particle size varies between 330 to 600 nm which creates a better approximation of the APS for a certain parameter. DOEV 28 on the other hand has the

same parameters but is carried out on the 5.6 mm bore static mixer reactor and gives rod-like particle shape more like DOEV 8. In the 5.6 mm reactor DOE 35 has an increase in CT which induces spherically shaped material which has been seen in other reactors (KRAIC-D and OBR) with high concentration runs. It is to be noted that for this model set-up the static mixer reactor has a better correspondence of the DLS and SEM outcomes compared to the results obtained from reaction in the OBR, which will be significant in the particle size targeting described in the next section. A contributing factor to this improvement could be the optimized design of the reactor, with industrial static mixer 3D printed design, while the OBR was a prototype reactor with some geometry flaws.

VI.2.3 DOE Equation mapping for PiC size targeting

As explained in Chapter V Minitab creates an equation mapping of the DOE experiment in the form:

$$APS = a_o + \sum a_i x_i + \sum a_{ii} x_{ii}^2 + \sum a_{ij} x_i x_j + e_r \quad (59)$$

The select confidence P was chosen to be above 0.05 %. The average particle size variance of R2=71.23% is closer to 1 and hence better than that in the OBR which may be due to the better correspondence between the SEM and the DLS compared to the OBR DOE. This improves confidence in the resultant model.

The residual probability plot for the average particle size is shown in Figure.VI.12 from Table.IV.4. Here the impact factor was 5%, meaning that if a P-value is below 0.05, the impact is important; above that value the parameter becomes less significant. In this case the flow rate and the concentration of iron have a significant impact on the particle size with a P-value of 0.001, this agrees with the results of the DOE in the OBR where the concentration had an important impact on the particle size, although here the total flow rate also has a high significance. The size of the reactor and concentration of Triazole has a P-value higher than 0.05 which indicates there is minimal consequence in altering these parameters in comparison to changing the flow rate or CI. During the experiments it has been seen that sedimentation of the particles occurs in the static mixer reactors with high concentration runs. This phenomenon was also observed during high concentration runs in the OBR, using higher flow rate has been a solution to that matter in the static mixer reactor, the issue is the high volume of reagent that the reactor will use for a single experiment. The residuals plot shows random variation around the normality line (red). This suggests there is a linear relationship between the parameters as seen on the normal probability plot.

Table.VI.5 Regression coefficients and model of Average Particle Size (APS). Adj SS = Adjust Sum of Squares, Adj MS = Adjusted Mean Squares.

Source	DF	Adj SS	Adj MS	F-Value	P-Value
Model	13	2199905	169223	5.01	0
Linear	4	1099371	274843	8.13	0
CI	1	515171	515171	15.25	0.001
CT	1	78794	78794	2.33	0.139
F	1	557151	557151	16.49	0.001
S	1	1024	1024	0.03	0.863
Square	3	450469	150156	4.44	0.012
CI*CI	1	3360	3360	0.1	0.755
CT*CT	1	39123	39123	1.16	0.292
F*F	1	411257	411257	12.17	0.002
2-Way	6	486641	81107	2.4	0.056
CI*CT	1	454343	454343	13.45	0.001
CI*F	1	14799	14799	0.44	0.514
CI*S	1	390	390	0.01	0.915
CT*F	1	11	11	0	0.986
CT*S	1	14500	14500	0.43	0.518
F*S	1	2604	2604	0.08	0.784
Error	26	878585	33792		
Lack-of-Fit	16	771223	48201	4.49	0.01
Pure Error	10	107361	10736		
Total	39	3078490			

Following the Table.VI.5, flow rate (F), concentration of $Fe(BF_4)_2 \cdot 6H_2O$ (CI), concentration $C_2H_3N_3$ (CT) have low P-value and shows that they have a significant impact on APS of PiC. On the other hand, the size of reactor S has a high P-value which shows a low impact. However, the coupling of CI*CT, CI*F, CT*F, CT*S and F*S shows high P-values which shows a reduction of their impact on APS. This is particularly the case for CI*S and CT*F with the highest of the P-values, changing those parameters for targeting a particle size should be taken into consideration, changing them together would give unwanted results. With those results the APS targeting equation can be obtained following the method from Chapter V and is given below (equation 60).

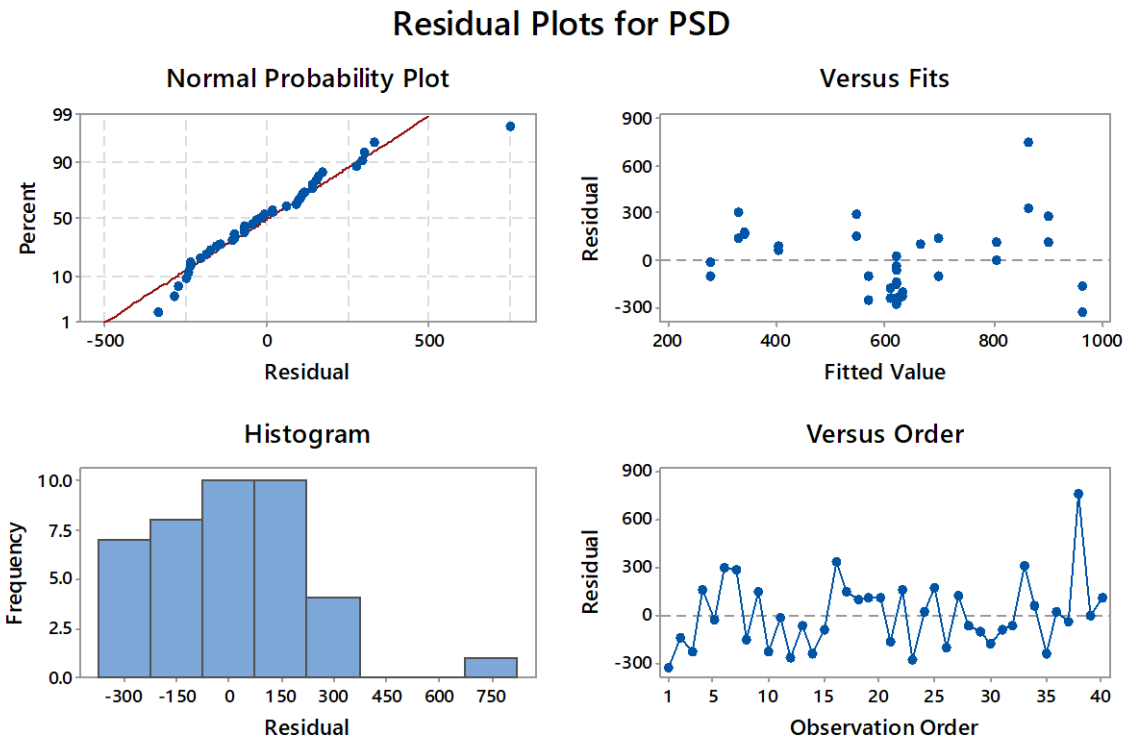

Figure.VI.12 Residual normal probability plots for APS of PiC produced during the DOE in the static mixer reactor.

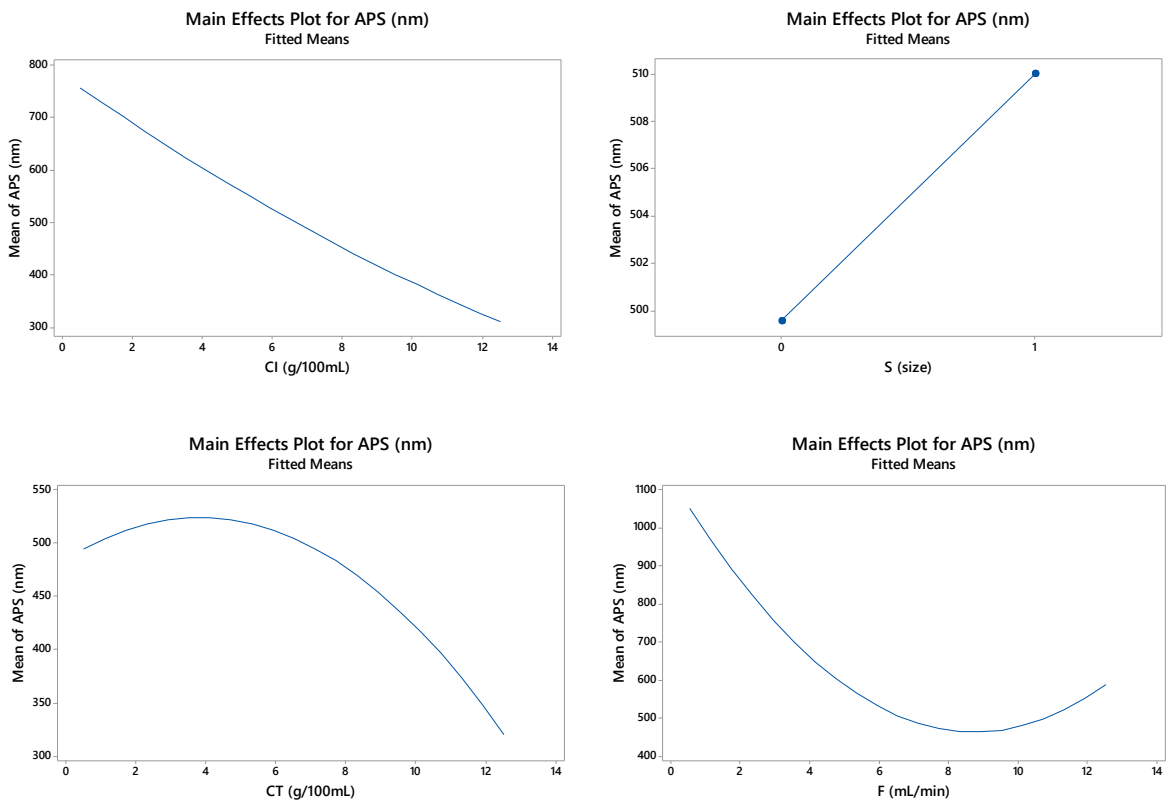

Figure.VI.13 Mean effect of CI, S, CT and F on APS of $[Fe(Htrz)_2(trz)](BF_4)$ in the static mixer reactors.

As can be seen from Figure.VI.13 the size of the reactor has a small impact on the mean particle size (going from 500 to 510 nm). Lowering the concentration of either reagent tends to give 500-800 nm particles and higher concentration smaller particles of 300-400 nm. Flow rate has the same impact as concentration but more significant, the ΔMean is 800 nm for the flow rate and 400 nm for CI. The flow rate controlling the residence time will dictate the time the particle can grow inside the reactor and the mixing intensity.

Compared to the OBR main effect plots here a more consistent trend can be seen, higher concentrations (< 7 g/mL) of both CI and CT result in smaller particle sizes such as those observed for DOEV 3,4,11,18,25 (Table.VI.3). Lower concentrations (> 4 g/mL) result in a higher average particle size like DOEV 1,9,21,39,40 (Table.VI.3). The flow rate also shows an overall effect on the particle growth, fast flow rates results in a smaller residence time reducing the growth of particle inside the reactor like DOEV 10,11,31, a low flow rate such as DOEV 16,38 results in an increase of the average particle size due to the reagents having more time to react and particles to grow. The size of the reactor affects the particle size due to the space in which the particles can grow, the increase in tubing diameter has an increasing effect on the average particle size.

The models calculated for predicting the particle size within the two sizes of static mixer reactors are given below.

S=0

$$APSD = 949 + 9.8CI + 95.8CT - 162.4F + 0.79CI * CI - 2.69CT * CT + 8.74F * F - 10.53CI * CT + 1.90CI * F - 0.05CT * F \quad (60)$$

S=1

$$APSD = 1084 + 7.9CI + 83.8CT - 167.5F + 0.79CI * CI - 2.69CT * CT + 8.74F * F * F - 10.53CI * CT + 1.90CI * F - 0.05CT * F \quad (61)$$

With these two equations it is possible to target and to form a contour plot of the average particle size.

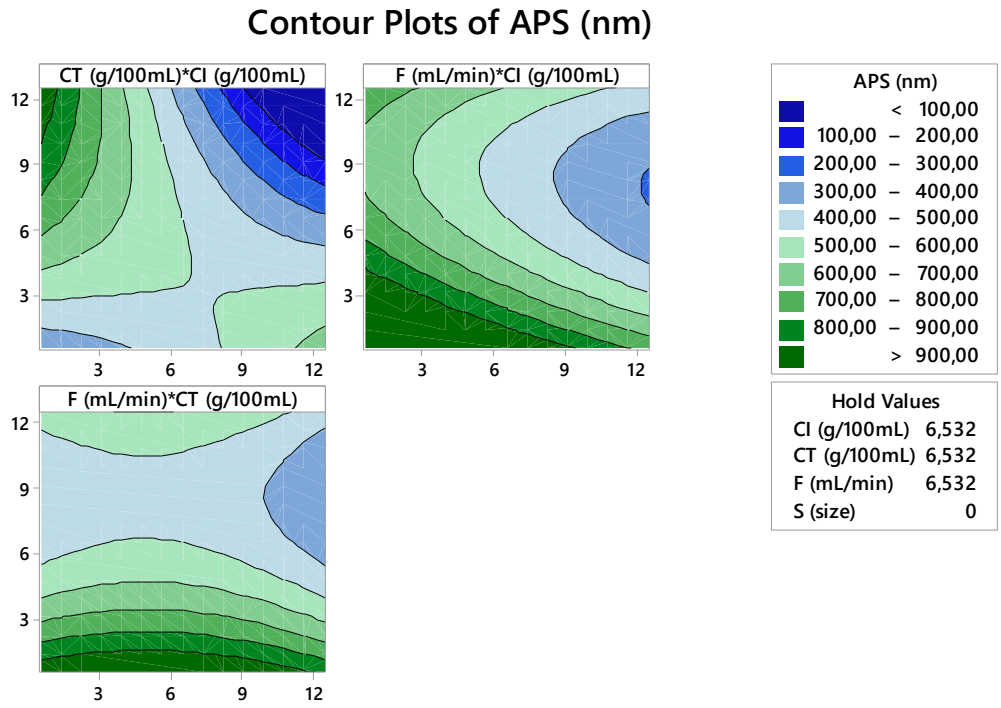

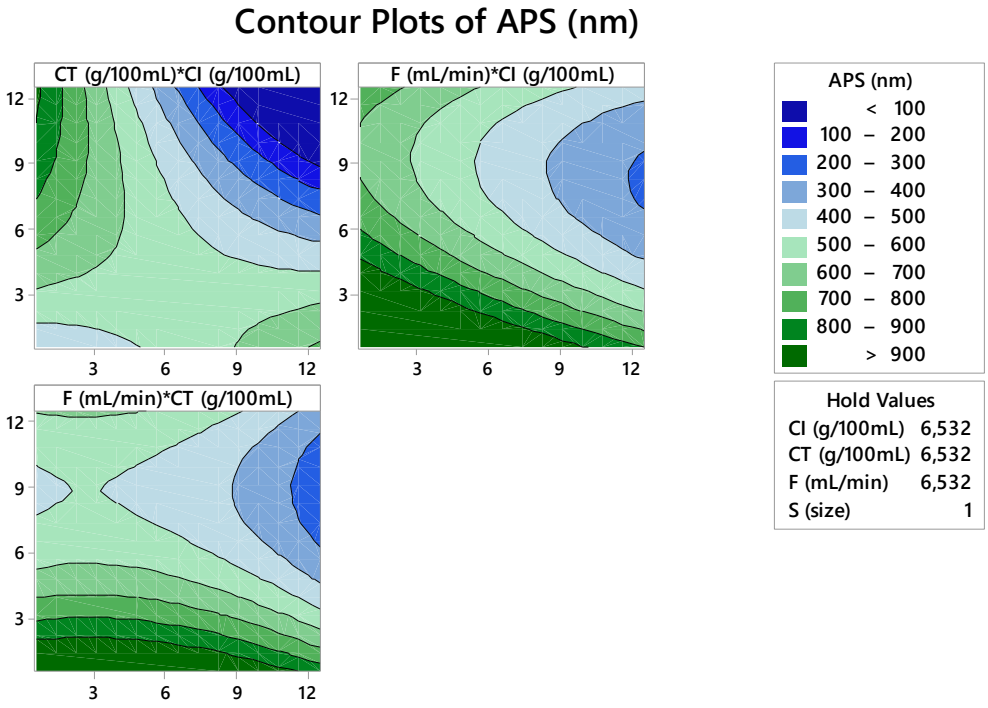

Figure.VI.14 Contour plot of the Average particle size of PiC in the static mixer reactors.

Figure.VI.14 displays the contour plots of the average particle size of PiC, with these graphs it is possible to predict a particle size precisely by inputting parameters into the equation previously presented. The variance of the model is 71.23 %, a higher accuracy value than that obtained for the OBR. Using this model, target values of 100 nm, 500 nm and 1000 nm were set for both sizes of reactor, those values were chosen to represent a low, mid and high range particle size targeting.

Table.VI.6 Particle targeting DLS results for both static mixer reactors of 3.2 mm and 5.6 mm bore tubing.

Target	APS (nm) for 3.2 mm bore tubing residence time		
	RT 1 (nm)	**RT 2 (nm)**	**RT 3 (nm)**
Vta(100 nm)	85.1	95.1	105.8
Vta(500 nm)	575.1	442.0	536.5
Vta(1000 nm)	1238.4	1019.2	955.4

Target	Residence time for 5.6 mm bore tubing		
	RT 1 (nm)	**RT 2 (nm)**	**RT 3 (nm)**
Vta(100 nm)	350.8	346.9	334.0
Vta(500 nm)	668.1	661.3	458.7

Vta(1000 nm) 1106.2 1230.3 1281.5

Table.VI.7 Parameters for targeting particle size in the static mixer reactor.

	S	F	CI	CT
Vta(100 nm)	0	12.5	11.8	11.5
	1	11.4	10.9	12.5
Vta(500 nm)	0	6.5	6.5	6.5
	1	0.7	0.5	5.2
Vta(1000 nm)	0	0.6	12.5	12.5
	1	0.5	0.5	0.8

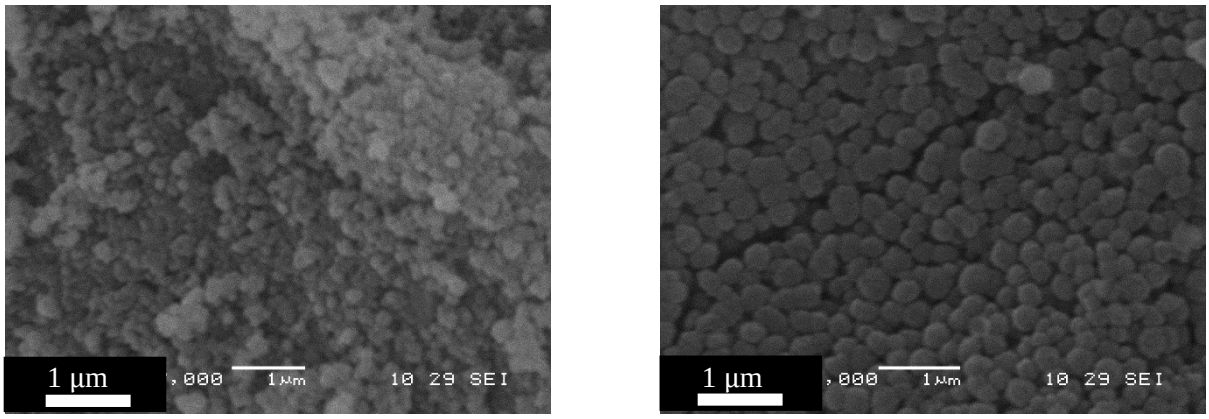

Figure.VI.15 SEM picture of 100 nm target on small 3.2 mm bore tubing (left) and larger 5.6 mm bore tubing (right).

As can be seen from Table.VI.6 the model is able to target the particle size of the compound with better accuracy than the previous OBR targeting in Chapter V, with closer values of the average particle size as determined by DLS. It is also seen on Figure.VI.15 that for 100 nm targeted runs, the SEM shows spherical particles ranging from 80 nm to 150 nm from the small reactor, but a 330 to 360 nm range for the bigger bore tubing reactor; this is confirmed through DLS analysis (Figure.VI.16). Thus better targeting is observed in the small bore reactor. The model also reflects the findings previously stated (from DOE results), that the concentration required to obtain small particles is high for both reactors, as shown in the parameters in Table.VI.7.

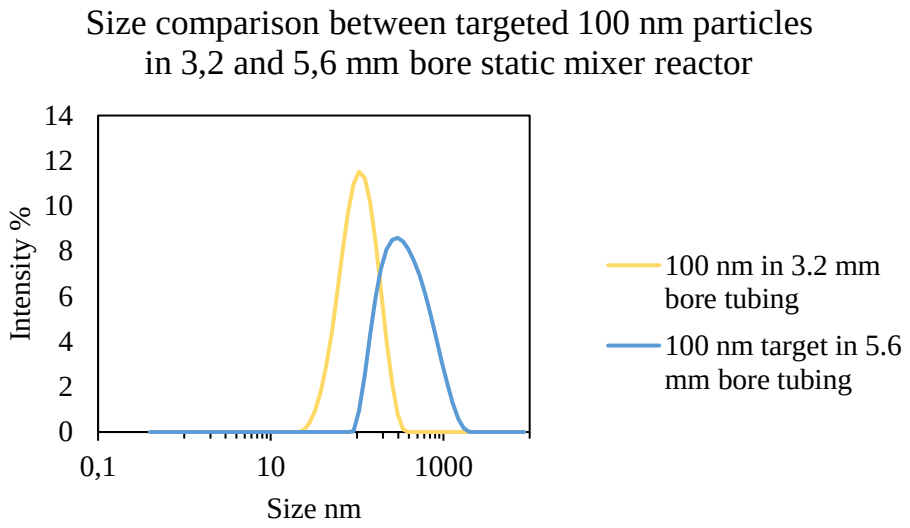

Figure.VI.16 DLS showing PSD observed (in RT3) for 100 nm target particle size for both reactors.

It is noted that, as for PiC synthesis in the KRAIC or the OBR, the spherical particles are again obtained for high concentration run in a flow environment. From the DLS and SEM results, it can be seen that using the larger bore reactor for targeting smaller particle sizes is not ideal. On Figure.VI.15 the SEM shows that, for the 5.6 mm bore reactor, 330 to 360 nm spherical particles are obtained whereas in the 3.2 mm reactor particles from 80 to 150 nm have been achieved. For other particle size trends, the larger reactor produces particles about 100 to 150 nm larger than the smaller reactor. Compared to the OBR the small 3.6 mm static mixers reactor is more capable to target smaller particle size. The model does not allow the region of the 0 to 50 nm to be reached due to negative variables appearing in the model. As for intuitive estimation of the parameters required to get small particles, it would be expected that the parameters required would be impracticably high. The parameters required for the lowest target (100 nm) are already very high, as seen on Table.VI.7, notably high concentration and high flow rate. The latter is almost representative of large scale-up considering the 145 mL and 65 mL volume of the reactors. On Figure.VI.16 the DLS graph shows the precise PSD on each target which lead to the conclusion that the static mixer reactor is operating with an acceptable particle range and accuracy to target particle size, particularly for small bore reactor.

VI.2.4 Synthesis of $[Fe(Htrz)_3](BF_4)_2.H_2O$ (PiCM) in MeOH

This section discusses another compound which can be formed from the reaction of $FeBF_4.H_2O$ with 1,2,4-H triazole; $[Fe(Htrz)_3](BF_4)_2.H_2O$ (PiCM), but instead of using water as the synthesis solvent, here methanol (MeOH) is used. KRAIC, OBR and batch syntheses of this compound have previously been discussed in Chapters III and V. The same concentrations as experiments PiCKM1 to 3 carried out in the KRAIC reported in Chapter III are employed here, parameters are displayed in Table.VI.8. As expected, the reaction was faster than $[Fe(Htrz)_2(trz)](BF_4)$ (PiC) production, the compound started to appear after 30 seconds of flow in the reactor.

Table.VI.8 Parameters for synthesis of PiCM in 1 mm bore tubing.

No.	Concentration $Fe(BF_4)_2$ (g/mL)	Concentration HTrz (g/mL)	Galden Flow Rate (mL/min)	Air Flow Rate (mL/min)	Trz and Iron Flow rate (mL/min)
VM1	0.1	0.1	3	2	2
VM2	0.15	0.15	3	2	2
VM3	0.2	0.2	3	2	2

The compound started to get viscous inside the coils (seen after disconnecting the tubes due to blockages) and the experiment was stopped after 30 min because of a blockage inside the pipes due to accumulation of the viscous compound on the tubing connection at the T-pieces. SEM was then performed on the compound obtained (Figure.VI.17).

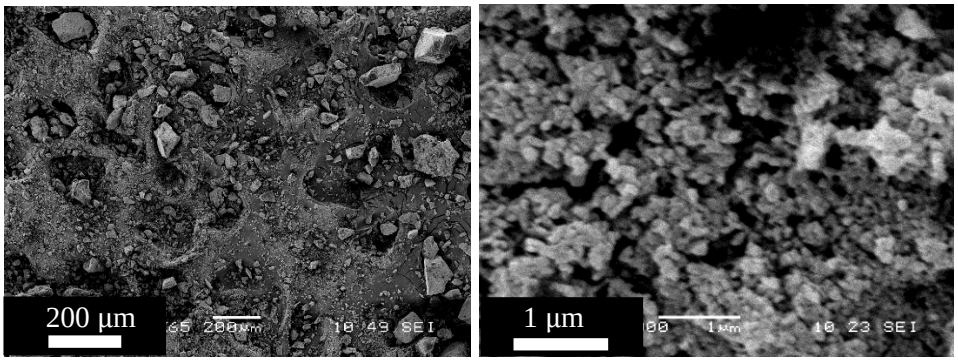

Figure.VI.17 SEM picture of PiCM synthesised in the 1 mm bore tubing reactor for experiments VM2 (left) and VM3(right).

In the 1 mm ID tubing, particles of PiCM present the same morphology as found in the OBR runs POM1 to 4 and the KRAIC PiCKM1 to 3 experiments. The same increase in viscosity behaviour has also been observed during the experiments. Just as seen in the KRAIC and OBR experiments, it was not possible to obtain a full gel in the flow experiments despite using a concentration proven to produce gels in batch.[27] The mixing induced in flow reactors (dean vortices in the open bore reactor, oscillation in the OBR or bolus flow in the KRAIC) seems to disrupt the gel formation for PiCM, although it has been shown in Chapter III that it is possible to produce gels in flow. PXRD confirms the presence of PiCM through comparison to batch PiCM and simulated PiC data (Figure.VI.18).

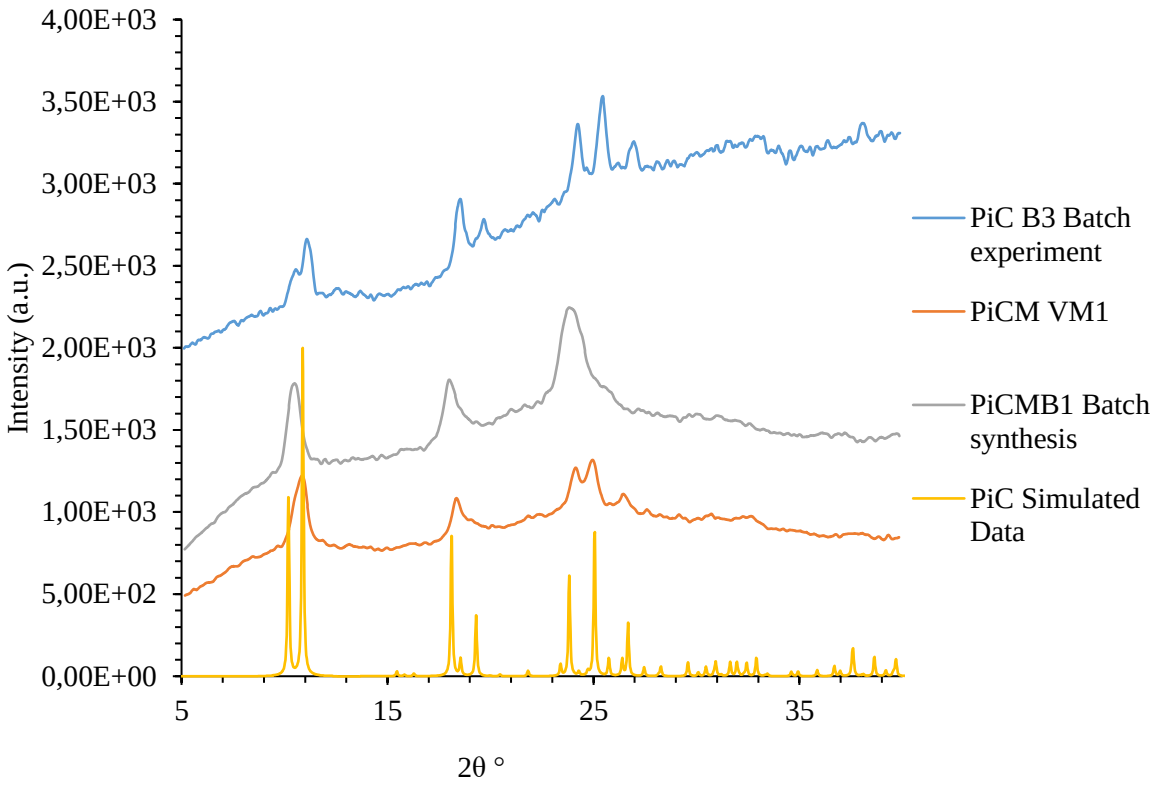

Figure.VI.18 PXRD of VM2 and Vb1 with comparison to batch experiment and simulated data from.[39]

The compound has proven to be easy to produce inside the 1 mm bore tubing reactor from Vapourtec with increase in yield compared to the OBR for the same concentrations. The challenges faced in PiCM synthesis in this reactor and the blockages that occurred are due to fast sedimentation of the particles inside the T-piece. This type of sedimentation was also seen in the OBR during the experiment into the bottom of the baffle in Chapter V, this behaviour will be investigated in Chapter VII with sedimentation study of PiC.

VI.2.5 CFD simulation of the static mixer phase mixing

In this section, to have a better understanding of the mixing inside the static mixer reactor, a CFD study has been carried out to simulate the flow behaviour inside the reactor. Following the mixture model previously presented on Ansys Fluent for the OBR in Chapter V, two water phases were input into the flow reactor and mixed through a 10 cm section of the reactor. Another version of the simulation has also been performed using a simple bore tubing with the same dimensions to compare the mixing behaviour in both situations. In Figure.VI.19 is displayed the mesh model of the Kenics mixer in Ansys Fluent, in total 265441 meshing elements were used for this simulation. Compared to the OBR tracer experiment in Chapter V where the tracer was injected only for 0.1 s, this time the two phases are continuously flowed inside the reactor portion at different flow rates to see the impact of the static

mixers. The two phases are set to be water based, as for the $[Fe(Htrz)_2(trz)](BF_4)$ synthesis reagent used previously. Three different flow rates are compared in Figure.VI.20. The Kenics® type design is also an important part of the study; a CFD simulation is needed to assess the mixer geometry, and several different geometries have been previously studied in literature with each having their advantages. Here with the Kenics mixers the radial mixing is enhanced, with successive elements that can be applied to laminar mixing reactors to improve the heat transfer across the section of the tubing.[58,236,237]

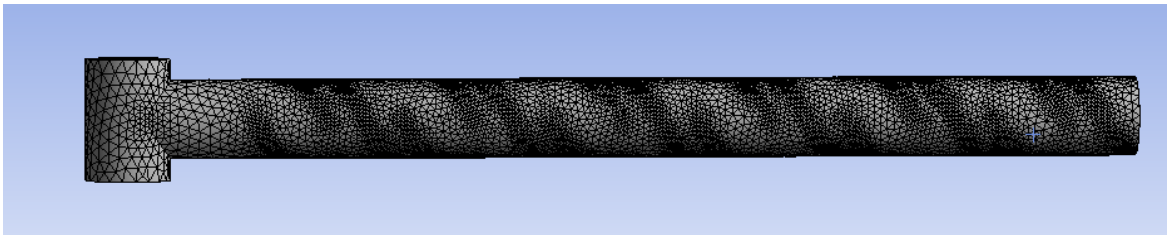

Figure.VI.19 Static mixer mesh model for the 5.6 mm bore tubing reactor.

Table.VI.9 Flow rate parameters from DOE experiments for the static mixer reactor.

Flow rate in mL/min	Flow rate in m^3/s	Flow rate for 5.6 mm bore tubing in m/s
5	8.33E-07	0.033833959
1	1.67E-07	0.006766792
3	0.0000005	0.020300375
6.266	1.04E-06	0.042400717
0.266	4.43E-08	0.001799967

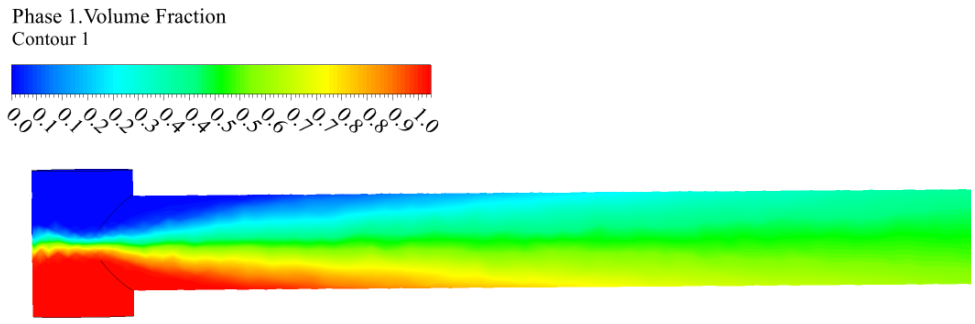

(a)

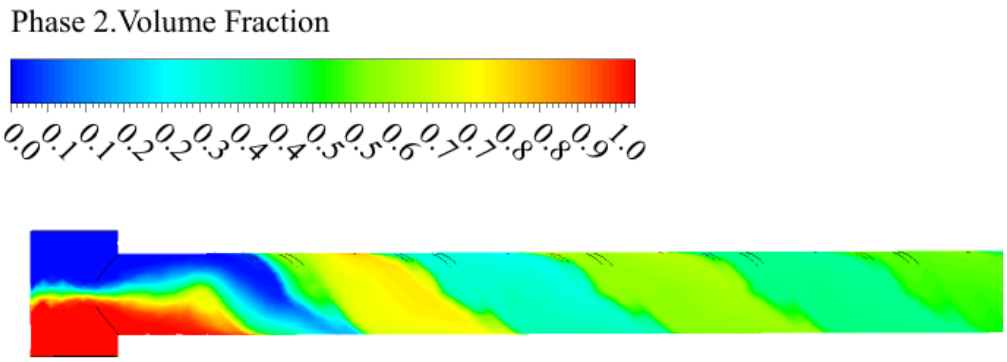

(b)

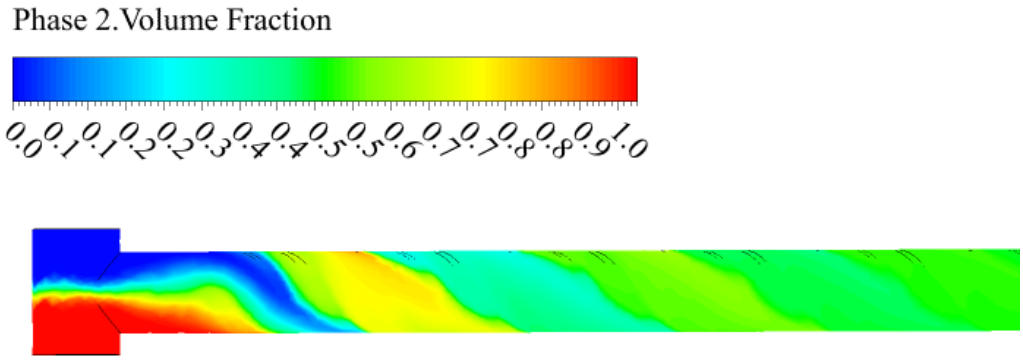

(c)

Figure.VI.20 Comparison of flow rate effect between Static Mixer and plane bore tubing reactor section with different flow rate: (a) no mixers 0.266 (b) 0.266 mL/min and (c) 6.266 mL/min for each inlet.

As can be seen in Figure.VI.20 the static mixer improves drastically the mixing of the two phases where the change in colour gradient is faster in (b) and (c) than in (a). To have a more accurate representation of the phase mixing a phase mass fraction graph is shown in Figure.VI.21. As soon as liquids entering comes into contact with the static mixer structure they are mixed completely within a small length of the reactor. Even at low flow rate the mixing is better than without the structure.

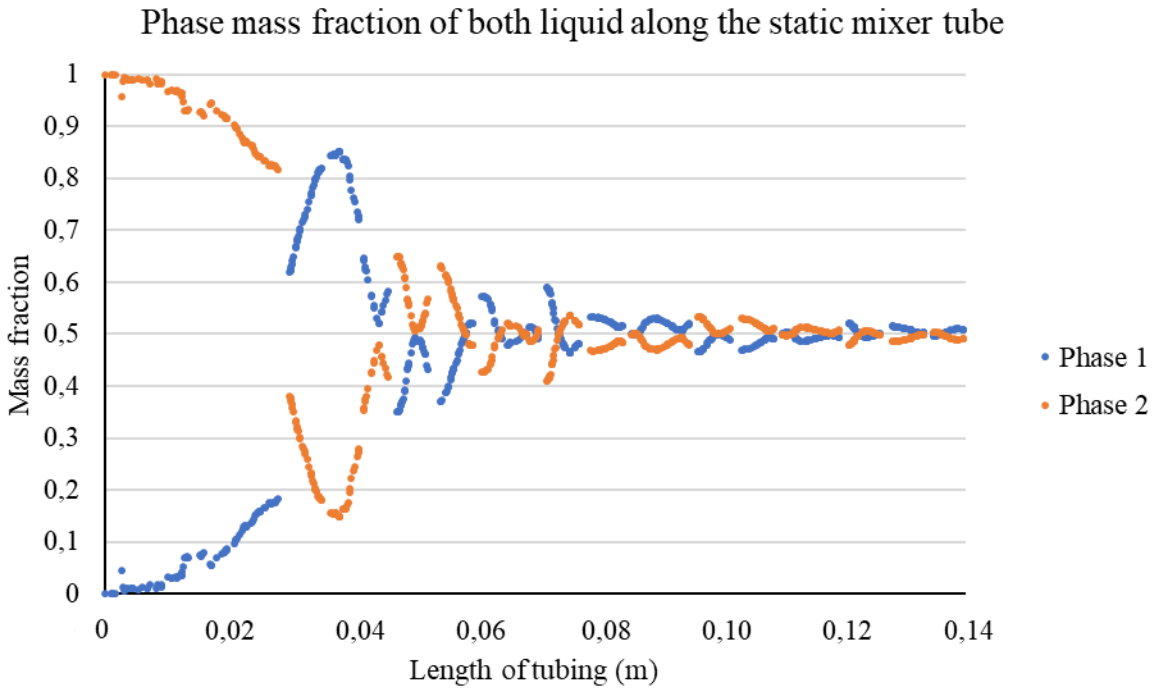

Figure.VI.21 Mass fraction of the two phases along the tubing length showing the mixing effect induced by the static mixers.

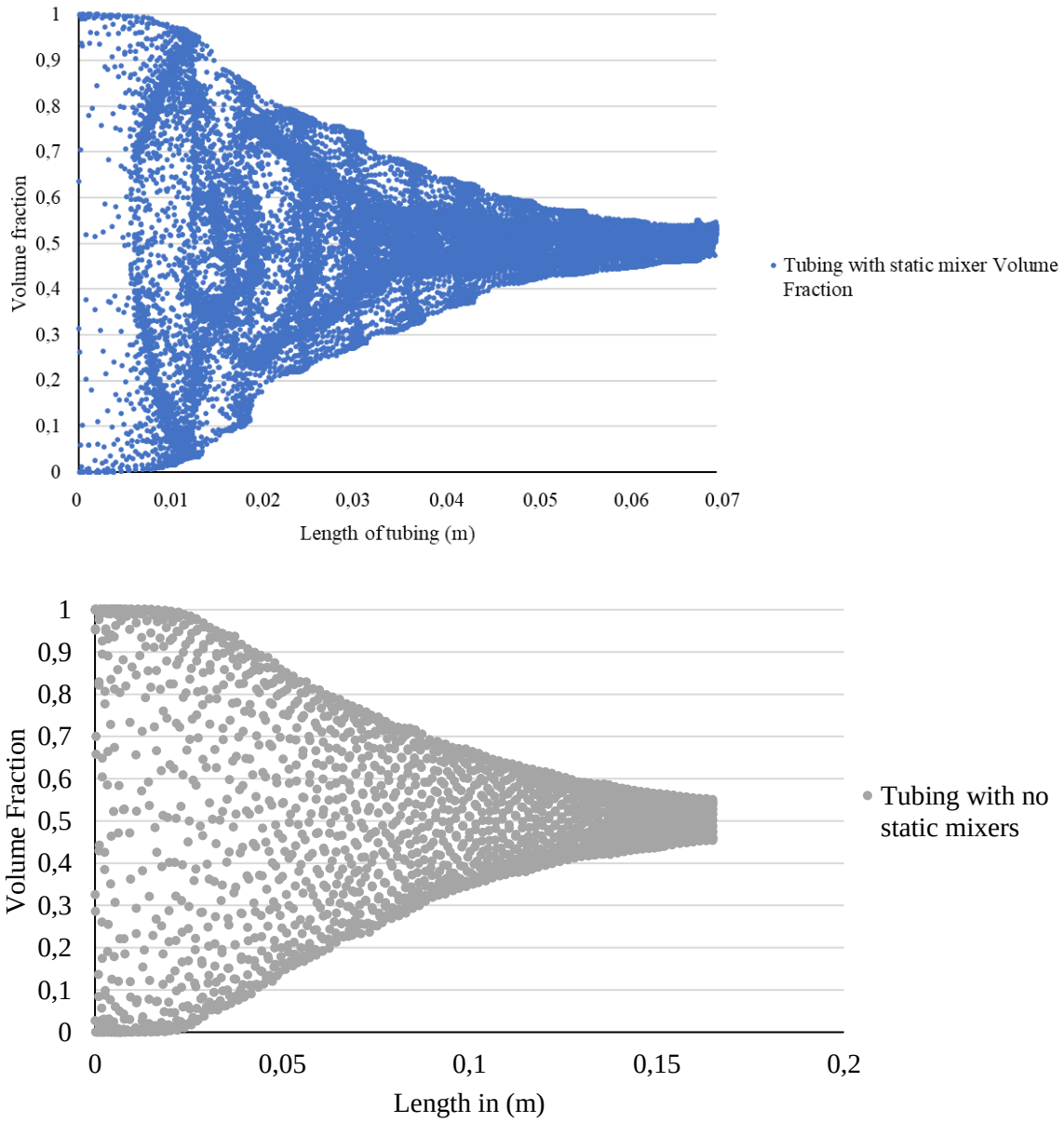

Figure.VI.22 Graph of phase composition along the X axis of the reactor looking at the total conversion for 5 mL/min with and without static mixer for the same tubing bore.

Figure.VI.22 describes the phase fraction evolution alongside the tubing. Each point represents a phase volume fraction of the phases along the section of the tubing; full mixing is indicated when both volume fractions arrive at 0.5. For instance, the length needed to obtain a 50/50 mix of phase volume fraction inside the static mixer reactor (Figure.VI.22, top) is 7 cm, with a higher concentration of cloud points (0.5 volume fraction) present. When no static mixing structure is present (Figure.VI.22, bottom) the phases are not as well mixed at 7 cm and need to reach 14 cm to achieve the same mixing point for a 50/50 conversion. This would mean for a reaction a reduction in volume needed for a reactor of about 50 % and a more homogenous mixing. This shows the importance of using the static mixers in this case

to reduce residence time and increase the mixing compared to the same size tubing with the same parameters.

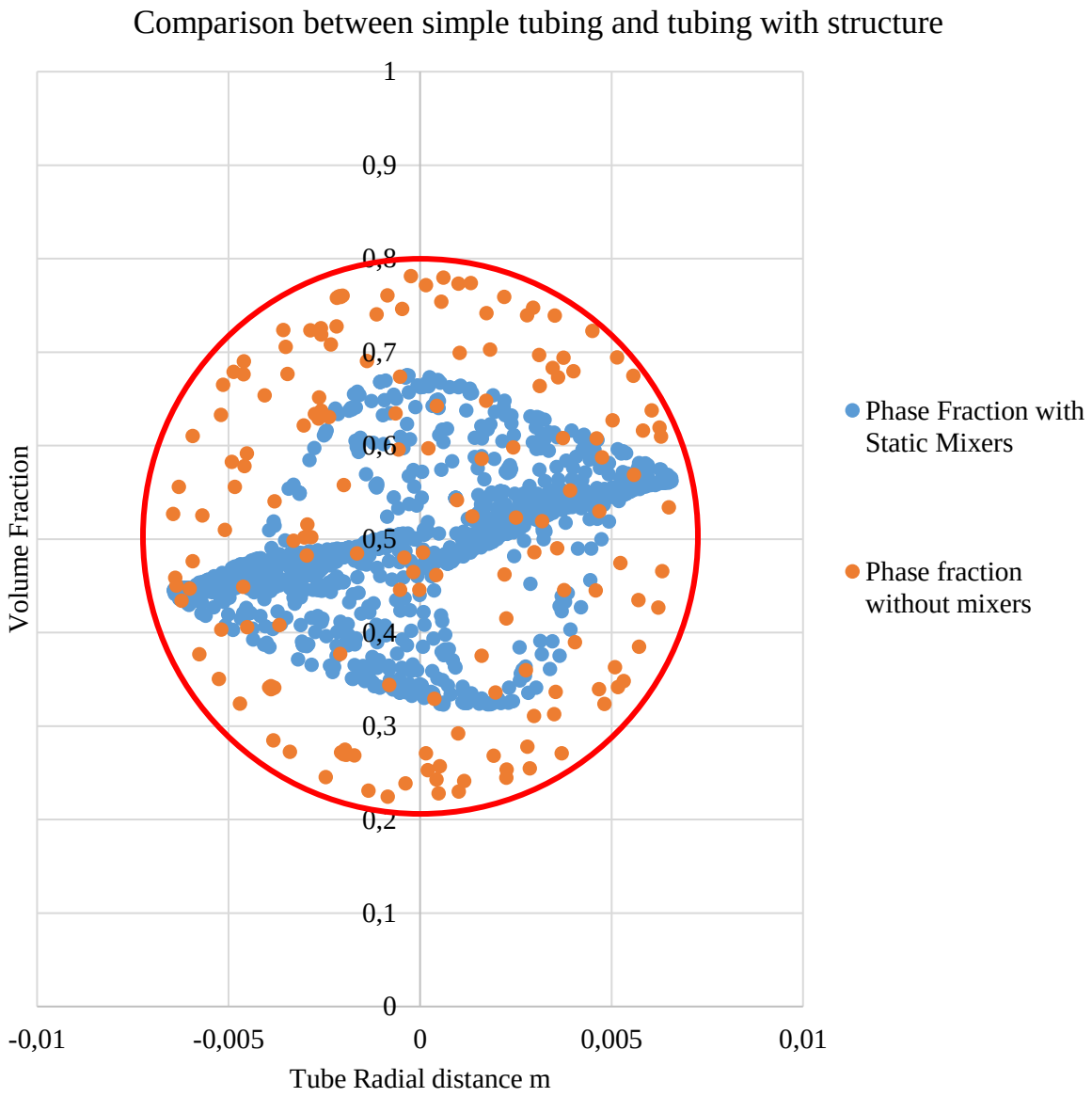

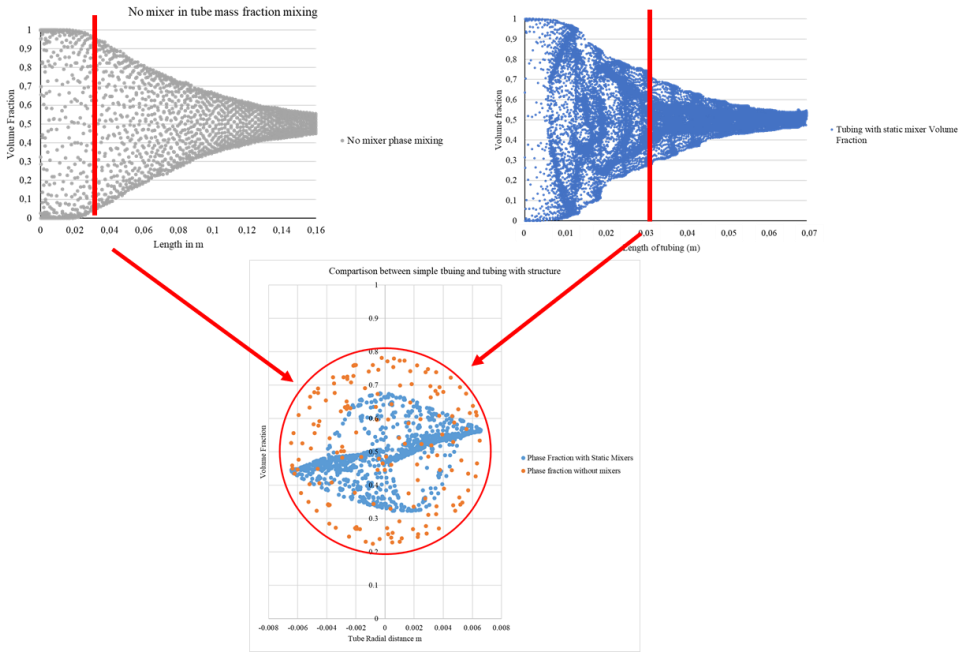

Figure.VI.23 Graph of the volume fraction on the tubing section after 4 cm of flow with (blue) and without (orange) the static mixers for 5 mL/min.

Figure.VI.23 shows the mixing profile on the section of the tubing at 4 cm length. This graph shows the importance of the static mixers, in orange (without mixer) the volume fraction is spread on the radial of the tubing meaning that some part of the tubing is still not mixed. On the other hand, for the same length the tubing with the structure shows a value closer to 0.5 volume fraction which means the mixing is faster and better controlled. In the results presented the mixing of the two fluids is enhanced by the static mixer, without the problem of a dead zone where none of the fluids encounter.

VI.2.6 Conclusion

The Vapourtec flow kit has shown its capability to produce different sizes of $[Fe(Htrz)_2(trz)](BF_4)$ (PiC) crystalline particles continuously. For the synthesis the concentration of reagent has again been shown to be important in the shape and size of the crystals of the compound. For high concentration of both 1H-1,2,4 triazole and $Fe(BF_4)_2$ spherical particles ranging from 50 nm to 150 nm are present on the SEM images, the DLS also confirms the PSD around these values. At lower concentration rod like particles are obtained with size near 1000 nm and for mid-range concentration star shaped particles were present. The targeting model of the static mixer DOE showed better prediction compared to that calculated for the OBR (presented in Chapter V). A difference between the particle size production of the 3.2 and 5.6 mm bore reactors was also presented with larger particles produced for the 5.6 mm than the 3.2 mm for the same target.

CFD simulation of the static mixer reactors has shown the advantage of using structure inside the tubing. The radial mixing simulated showed a concentration of the mixing towards the centre which could enhance the interaction between both phase and reduce reaction. The mixing of different phases is also enhanced with a faster obtention of the fully converted mixture compared to simple bore tubing.

The next sections will introduce the use of a different flow technique (anti-solvent) to produce smart materials.

VI.3. Synthesis of $[FeL_2][BF_4]_2$ [L = 2,6-di(pyrazol-1-yl)pyridine] with progressive mixer reactor

In this section the production of $[FeL_2][BF_4]_2$ [L = 2,6-di(pyrazol-1-yl)pyridine] (YeC) will be studied. This is a spin cross-over compound having an change in spin state at 259 K. The compound is produced in batch in two steps: first, the 2,6-di(pyrazol-1-yl)pyridine is complexed to the Fe^{II} in acetone giving a yellow solution; [20] secondly, the crystalline SCO complex is then obtained by anti-solvent precipitation, pouring diethyl ether into the yellow complex solution. 2,6-di(pyrazol-1-yl)pyridine (2,6-bpp) was provided by Dr Laurence Kershaw-Cook from the Metastable Materials group.

In this section a new way of producing YeC is investigated, using anti-solvent flow precipitation. To pursue this goal the Vapourtec Flow Kit was used with different variations of tubing and compositions.

This work was carried out with Masters Project Student Kathryn Bell. Chapter VII will discuss the effect on the switching behaviour of the material depending on the manner of production.

VI.3.1 First Investigation of YeC synthesis

The first investigations to produce YeC were performed in batch following Cook *et al.*[238] and varying the concentration of both reagents and the drowning out ratio of solution to anti-solvent, diethyl ether (DEE). The two reagents are prepared in two 5 mL vials until the reagents are fully dissolved. The solutions are then added together in a 10 mL vial and a yellow hue or precipitate should appear depending on the concentration. Depending of the concentration used, DEE was then added to make the precipitate appear. The reaction parameters used in the experiments run are displayed in Table.VI.10.

This initial investigation showed that using a high enough concentration of both solutions was sufficient to precipitate out the SCO compound without addition of anti-solvent (DEE) – experiments BY1 and BY2. At lower concentration, such as in BY3 and 4, low levels of precipitation occurred. The problem translating to flow is that using high concentration might cause blockages. The use of an anti-solvent appears to increase the yield for lower concentrations of the reagent used (compare BY1 and BY5). Comparing experiment BY8 with a 2:1 ratio of reagent the yield approaches 52.9 % while the yield is improved for a 1:1 ratio at lower concentration for BY5 and 6. Those first batch investigations led to trials of the same combinations in flow.

DEE and the solution of $[FeL_2][BF_4]_2$ [L = 2,6-di(pyrazol-1-yl)pyridine] are pumped towards a T-piece of 2 mm inside diameter whereupon the compound precipitates inside a 1 mm bore tubing of 2 mL volume, the residence within which allows for full mixing of the two flows, maximising the possible yield.

Table.VI.10 Concentration and anti-solvent diethyl ether (DEE) ratio used in batch

Experiment	Ratio 2,6-bpp:Fe(II) wt/wt	Concentration Fe(II) (mg/mL)	Concentration 3-bpp (mg/mL)	Ratio Solution:DEE	Yield % from $Fe(BF_4)_2$
BY1	1:1	40	40	1:0	50.7
BY2	1:1	10	10	1:0	42.3
BY3	1:1	8	8	1:0	23.1
BY4	1:1	1	1	1:1	19.6
BY5	1:1	0.5	0.5	1:1	63.2
BY6	1:1	0.3	0.3	1:2	61.3
BY7	2:1	1	2	1:1	55.1
BY8	2:1	2	1	1:1	52.9
BY9	2:1	0.6	0.3	1:2	56.4
BY10	2:1	1.6	0.8	1:1.5	53.1

Table.VI.11 Parameters used in the Vapourtec Flow Kit with open bore (1 mm, ID) tubing.

Experiment	Ratio (2,6-bpp): $Fe(BF_4)_2$ $6H_2O$)	Concentration $Fe(BF_4)_2$ $6H_2O$ (mg/mL)	Concentration (3-bpp) (mg/mL)	Flow rate DEE (mL/min)	Flow rate Solution (mL/min)	Yield from $Fe(BF_4)_2$ (%)
FY1	1:1	40	40	n/a	1	62.3
FY2	1:1	10	10	n/a	1	52.1
FY3	1:1	8	8	n/a	1	54.2
FY4	1:1	1	1	1	1	45.6
FY5	1:1	0.5	0.5	1	1	48.7
FY6	1:1	0.3	0.3	2	1	75.4
FY7	2:1	1	2	1	1	62.3
FY8	1:2	2	1	1	1	65.8
FY9	2:1	0.6	0.3	2	1	78.2
FY10	2:1	1.6	0.8	1	1.5	79.9

The flow rate parameters were set to have the same DEE/solution ratio used in batch experiments to see how comparable the flow experiments were to the batch ones and if the reactor was handling the precipitation well. It appears from Table.VI.11 that the flow set-up has increased the yield of the compound produced even for the conditions under which in batch the yield was low. The reduction of yield from BY5 and FY5 could be due to the low concentration of reagent and having the same flow rate of DEE and the solution; at lower concentration FY6 showed improved yield but with a 2 mL/min flow rate for the DEE. In addition to this, from experiment FY4 to FY10 the yield has been improved in flow compared with similar conditions in batch. In particular for experiments 6, 9 and 10 the yield was improved by an average of 20% which shows the importance of the initial DEE drowning-out ratio. As expected, the high concentration runs FY1 and FY2 did block the T-piece, and blocking was found inside the 2 mL volume coil during FY3, indicating that high concentration is to be avoided for that compound in 1 mm bore tubing. The first residence time was recovered before the blockage for FY1 and is displayed in Table.VI.11. Using a bigger T-piece at 3 mm bore did not improve the blocking problem. The particle size of the compound was determined using SEM and shows this to be reduced in flow compared to batch as can be seen in Figure.VI.24. There is also a change in habit; in batch there is parallelopiped type shape while in flow the pentagonal shape is more prominent.

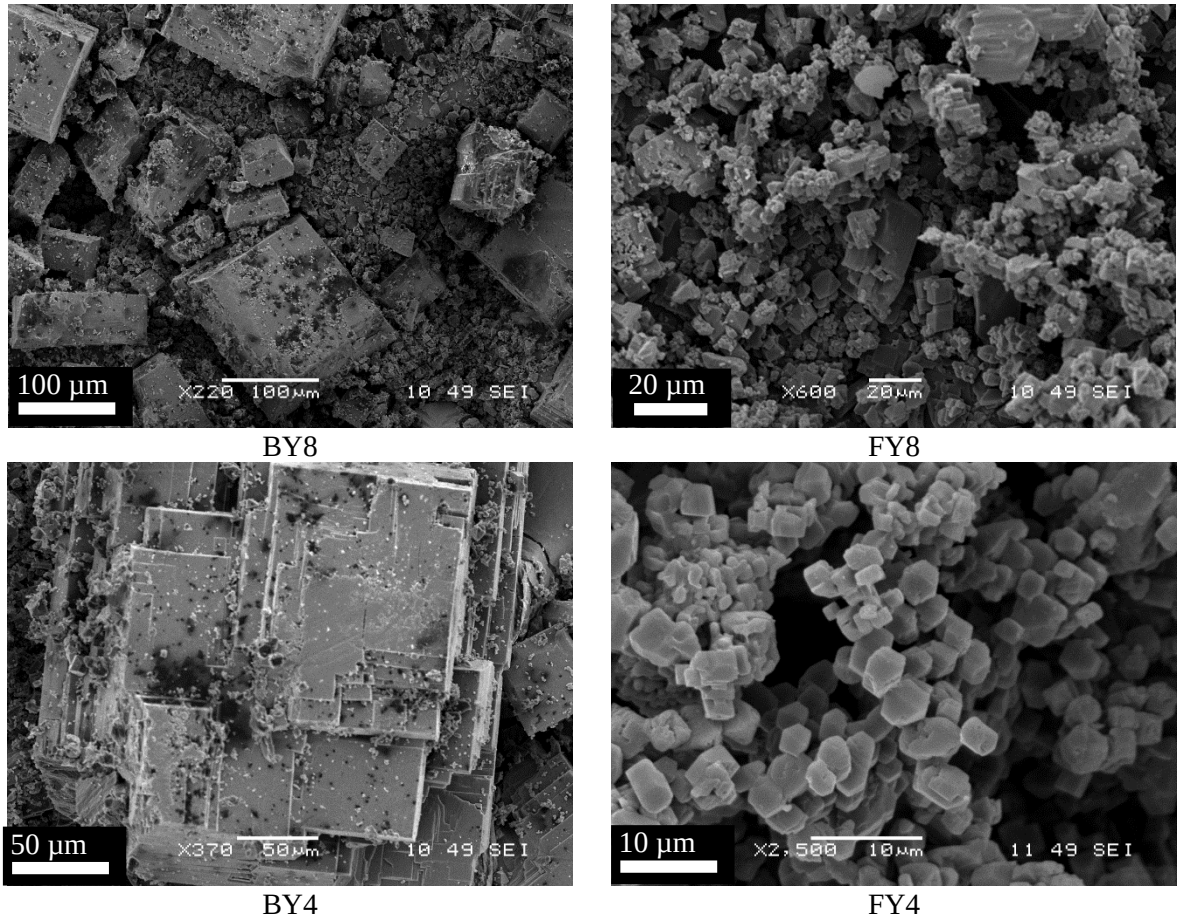

Figure.VI.24 SEM picture of product from batch and using the flow T-piece, showing experiment BY4 and 8 and FY4 and 8.

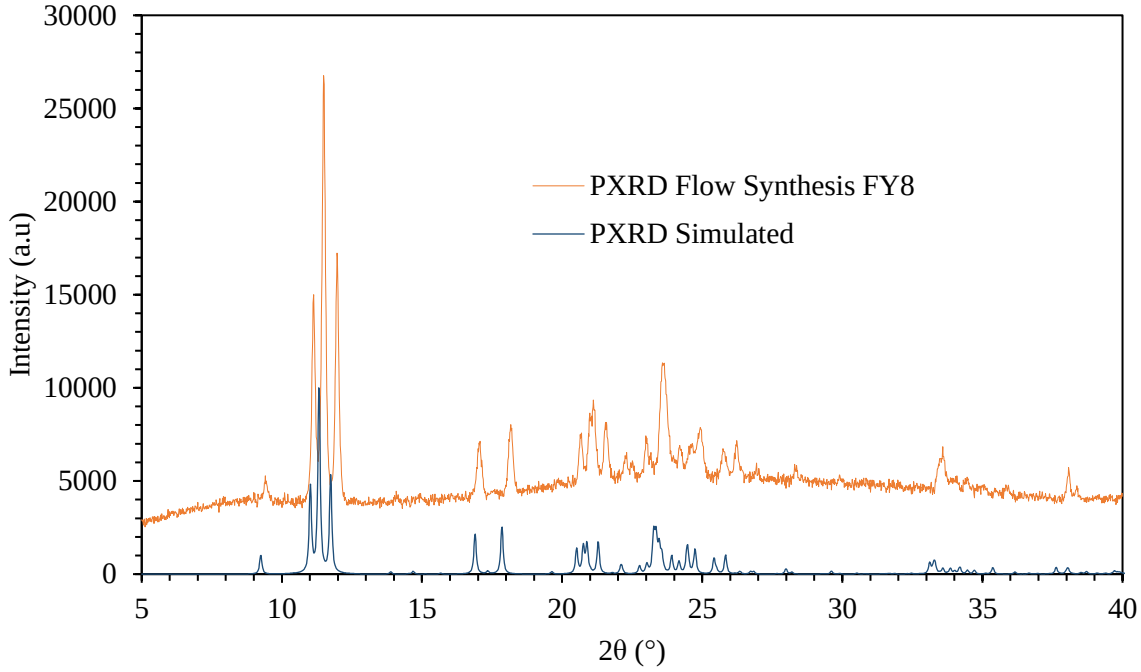

Figure.VI.25 PXRD comparison of $[FeL_2][BF_4]_2$ obtained in flow FY8 and simulated[238].

From these experiments it is concluded that at high concentration of reagents it is possible to crystallise YeC without the addition of DEE but this high concentration induced blockages inside the tubing. To avoid the blockages, it is better to use a lower concentration and a higher drowning-out ratio as in experiments FY 6, 9 and 10. The use of DEE as anti-solvent induced smaller particle size in flow (FY4-10). Following those trials further investigation was made with a progressive mixer reactor which can add an increasing amount of anti-solvent over a length scale to ensure maximum yield and crystallisation control.

VI.3.2 Tube-in-Tube progressive mixer reactor for YeC synthesis

As previously presented in section VI.1 the tube-in-tube reactor consists of a progressive mixing environment provided by two tubes, one inserted into the other, with 50 µm bore holes perforated along the entirety of the length of the inner tube. The purpose of having the small pore between the two tubes is to seek to create smaller particles in the reactor than in batch or the previous flow experiment. This phenomenon occurs due to the very high mixing intensity achieved through using the progressive mixer where a high density of fine streams of anti-solvent are injected into the solution flow, minimising the area of localised concentration of reagents.

The first set-up was as follows. The complexation of 2,6-di(pyrazol-1-yl)pyridine with $Fe(BF_4)_2$ was first prepared in batch with a 10 min complexation time giving a yellow solution. The DEE was connected to the outer tube and the solution feed connected to the inner tube. Here, Vapourtec advised use of a 2:1 volume/flow rate ratio for the drowning out ratio to avoid blockages of the small holes.

The first experiments were done using a concentration of 1 g/100 mL of 2,6-bpp and 0.8 g/100 mL of $Fe(BF_4)_2 \cdot 6H_2O$ (a 1:0.8 ratio, w/w). To drown out the material in the outer tubing a ratio in flow rate of 1:2 for DEE was used, respectively 0.75 mL/min for the solution and 1.5 mL/min for the DEE but no compound was recovered at the end of the reactor and no yellow solution appeared.

The second experiment used a higher concentration, 3.33 g/100 mL of 3-bpp and 2 g/100 mL of Fe(II). In this case a blockage occurred which led to perforation of the inner tubing. Prior to this blockage, crystals were observed within the tubing but were not able to be recovered.

To avoid this problem Vapourtec again modified the reactor and added a new procedure and another fail safe with a 14 bar relief valve to the reactor at the entrance as shown on Figure.VI.26

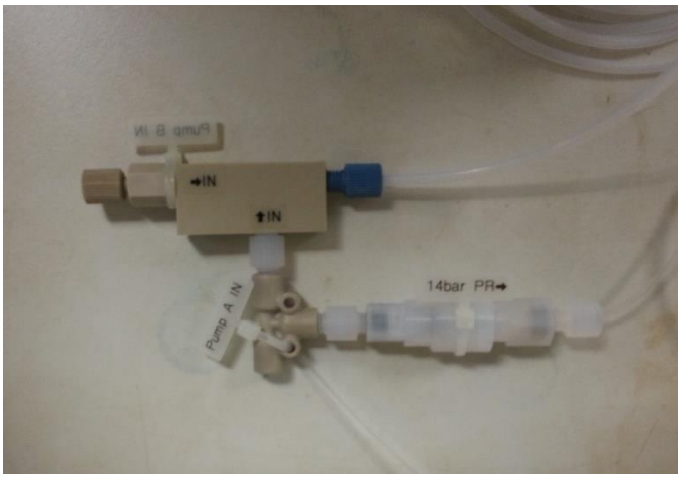

Figure.VI.26 Relief valve for the progressive mixer reactor to avoid pressure build-up.

From those developments it was decided to avoid high concentrations used in the previous experiment and go from low concentration and increasing from there so that the production of the compound did not increase the pressure inside the reactor, while still creating good yield.

The parameters for each experiment are displayed in Table.VI.12.

Table.VI.12 Parameters for the progressive mixer flow reactor and the concentration of the reagent.

	Flow rate solution (mL/min)	**Flow rate DEE (mL/min)**	**Concentration 2,6-bpp (g/100 mL)**	**Concentration $Fe(BF_4)_2$ $6H_2O$ (g/100mL)**	**Yield % from $Fe(BF_4)_2.6H_2O$**
FTY1	1	1.5	1	0.6	19.3
FTY2	1	1.5	1.5	0.75	68.4
FTY3	0.5	1	0.6	0.2	79.6
FTY4	0.5	1	0.6	0.45	82.5

The results from FTY1 showed low yield and so the concentrations were increased for FTY 2 and showed an improvement in yield to 68.4 %. However, the pressure increases from 0.1 to 2 bar inside the

reactor which suggests particles obstructing the reactor at some points. Concentrations were thus decreased for experiment FTY3 and then $Fe(BF_4)_2$ $6H_2O$ concentration was increased for FTY4. The yield was improved to 79.6% and 82.5 % for FTY 3 and 4, respectively; the system worked for over an hour without any problem. The compound was analysed with PXRD (Figure.VI.27). Thermal studies of the switching of the compound synthesised will be discussed in Chapter VII.

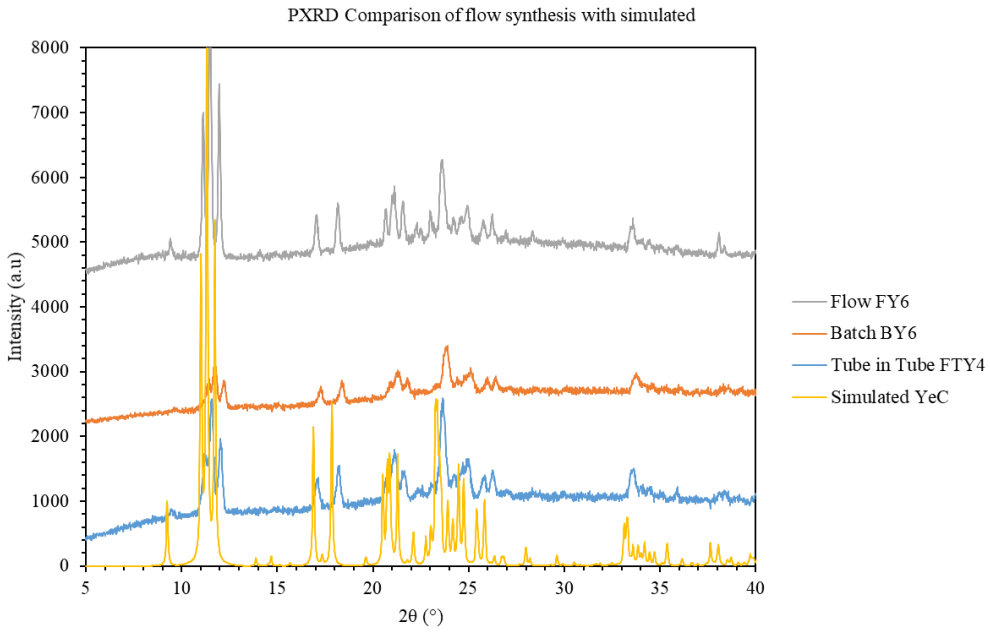

Figure.VI.27 PXRD of YeC produced in Flow FY6, Batch BYA6, with the tube in tube reactor, and the simulated data.

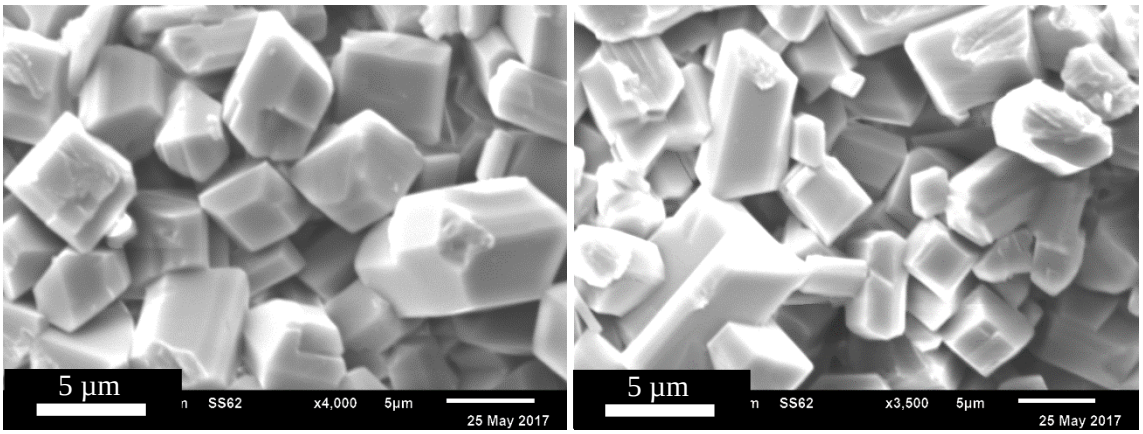

Figure.VI.28 SEM of experiment FTY3(left) and FTY4(right).

As can be seen in Figure.VI.28 the reactor gave smaller particles than previously obtained in batch, around 1 to 5 µm in size. Here the precipitation size is controlled due to the small pore of the progressive mixer reactor creating small injection points where the solution to be precipitated comes out in small

quantities which then crystallise when in contact with DEE. This was a way to get smaller particles and thus be able to incorporate easily the compound into future devices. Increasing the length of the reactor would not significantly increase the amount of the compound obtained, as the yield obtained with the flow reactor was already reaching around 80-90 %, but scaling out with reactors in parallel could be possible to increase the production of target compound, using anti-solvent to precipitate out the product. Using a progressive mixer reactor has been shown to improve the particle size of the material while also avoiding aggregates as seen for FY4 and FY8; more individual crystals are present in FTY3 and FTY4. A size study with DLS will be presented in Chapter VII while studying the switching of the material. It will be seen that using DLS was difficult for these compounds even when using different solvents for the suspension in the DLS cuvette.

VI.4. Thermochromic materials synthesis *via* flow anti-solvent techniques

In this section, the anti-solvent flow preparation of another type of switchable materials, molecular thermochromic complexes, is presented. The complexes and their thermochromic behaviour have been described in Jones *et al*. [15] Thermochromism can be described as an induced change of colour of a material by controlling its temperature. Examples of thermochromics have been studied in literature [21,44,239,240]. Thermochromism can be a result of a change in structure, leading to a change of electronic intermolecular interactions between the components which leads to different coloured crystals; proton transfer on complex formation can also be important in the effect. (I.3). In this section the compounds studied for the purpose of scale-up production using flow crystallisation are the family of iodoanilines co-crystallised with dinitrobenzoic acids. Some of these compounds display thermochromic transition upon increasing temperature to 77-84 °C (Figure.VI.29).

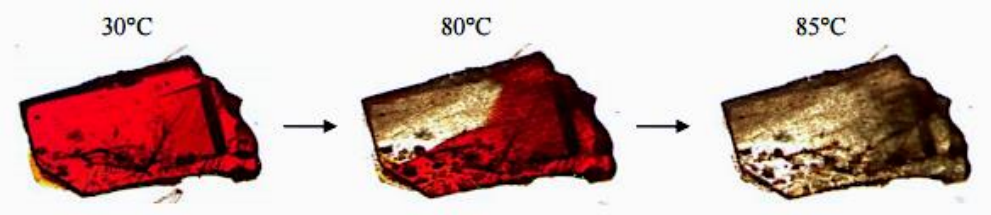

Figure.VI.29 Thermochromism of the 4-iodo-2-methuylaniline:3,5-dinitrobenzoic acid co-crystal.[15]

The reproduction of these complexes has been found to be difficult in batch, for this reason anti-solvent flow crystallisation was investigated to produce the compounds 1 to 6 described in Table.VI.13.

VI.4.2 First trials for the synthesis of proton transfer compounds

This work was been carried out in part with Masters Project Student Alex Mildon.

For the initial investigation evaporative crystallisation had been used to see if it was possible to produce the different polymorph with a different solvent that could be used effectively in flow and also other solvent that could be potential candidates for anti-solvent crystallisation in Table.VI.13. The compounds

formed in Jones *et al*[15] displayed in the table are: (Ch1 and 2) 4-iodoaniline 3,5-dinitrobenzoic acid (4-IA 3,5 DNBA), (Ch3 and 4) 4-iodoaniline 3,5-dinitrosalicylic acid (4-IA 3,5 DNSA) and 4-iodo-2-methylaniline 3,5-dinitrobenzoic acid (4-I2MA 3,5 DNBA) (Ch5). This was carried out in vials with each of the compound dissolved in a series of solvents. The technique used the same molar ratio as in the literature, 1:1 or 2:1 (mol/mol) of the haloaniline to 3,5-dinitrobenzoic acid respectively, 0.2 g and 0.4 g, in 5 mL vials.[15] The vial caps were then perforated and put on hot-plates at different temperatures (30, 40 and 50 °C) to allow evaporation.

Table.VI.13 Compounds names and formulae studied for organic-based thermochromics.

Compounds	**Ch1**	**Ch2**	**Ch3**	**Ch4**	**Ch5**	**Ch6**
Name	4-IA :3,5DNBA	4-IA :3,5DNBA :MeOH	4-IA :3,5-DNSA	4-IA :3,5-DNSA	4-I2MA :3,5-DNBA	4-I2MA :3,5-DNBA
Formula	$(C_6NIH_7)+$ $(C_7N_2O_6H_3)-$	$2(C_6NIH_6)$ $2(C_7N_2O_6H_4)$ (CH_3OH)	$(C_6NIH_7)+$ $(C_7N_2O_7H_3)-$	(C_6NIH_6) $2(C_6NIH_7)+$ $2(C_7N_2O_7H_3)-$	$(C_7NIH_9)+$ $(C_7N_2O_6H_3)-$	(C_7NIH_8) $(C_7N_2O_6H_4)$

This study established that compound Ch1,2 and 5 could be obtained readily from anti-solvent crystallisation techniques, Table.VI.14 gives a list of solvents, their combinations and temperatures studied; methanol, ethanol, acetonitrile isopropanol and acetone produced the desired polymorph. Acetone produced a mixture of black oil and the compound (Ch5). Both hexane and water were good anti-solvents. In batch only Ch1 to Ch5 were succesfuly obtained. Unfortunately, it was not possible to produce the thermochromic complex 6 in the antisolvent set-up in batch. Of the five crystallised in batch only complexes Ch1,2 and 5 were used for flow, since complexes Ch3 and Ch4 took several weeks to crystallise under anti-solvent condition on the bench and some were precipitating out in agregates that could lead to blockages in flow; they were thus not pursued further.

For Ch1, a yellow solution is formed upon mixing the two colourless pre-cursor solutions which is a good indicator of production of a new material. The slow evaporation of the compound with acetonitrile gave block-like colourless crystals. Although most of the trials were inconsistent with respect to the obtention of the compounds, it has been seen that the complex can be obtained in all cases and at all temperatures explored. It was decided to pursue the anti-solvent approach using water as the anti-solvent for flow crystallisation as it uses less reagent than non-anti solvent techniques.

In the published procedure only the slow evaporation of an equimolar solution 4-IA and 3,5 DNBA in methanol yielded in Ch2. Again, using water as anti-solvent was found to produce favourable results.

Ch5 was obtained from a range of conditions and solvents. Mixing 4-I-2MA and 3,5-DNBA solutions, purple and colourless respectivly, a red solution is obtained. Evaporative crystallisation in ethanol gave the most consistent results. The use of water as an anti-solvent again proved successful in both acetonitrile and ethanol in producing Ch5. The previous experiments provided a number of different routes that can be input into flow conditions.

Table.VI.14 Temperature and solvent used for the production of compounds 1,2 and 5 successful trials in Batch and Flow (carried out by Project Student Alex Mildon)

	Temperature °C				
	ThA1	**ThI1**	**ThI2**	**ThI3**	**ThIWe**
Solvent	**Acetonitrile**	**Isopropanol**	**Isopropanol**	**Isopropanol**	**Isopropanol + Water**
4-iodoanilinium 3,5-dinitrobenzoate (Ch1)	20	20	4	0	20
	ThM1	**ThM2**	**ThM3**	**ThMW4**	
Solvent	**Methanol**	**Methanol**	**Methanol**	**Methanol + Water**	
4-iodoaniline 3,5-dinitrobenzoic acid solvate (Ch2)	20	30	40	20	
	ThE1	**ThE2**	**ThAW**	**ThEW**	
Solvent	**Ethanol**	**Ethanol**	**Acetonitrile+ Water**	**Ethanol+ Water**	
4-iodo-2-methylanilinium 3,5-dinitrobenzoate (Ch5)	40	4	20	20	

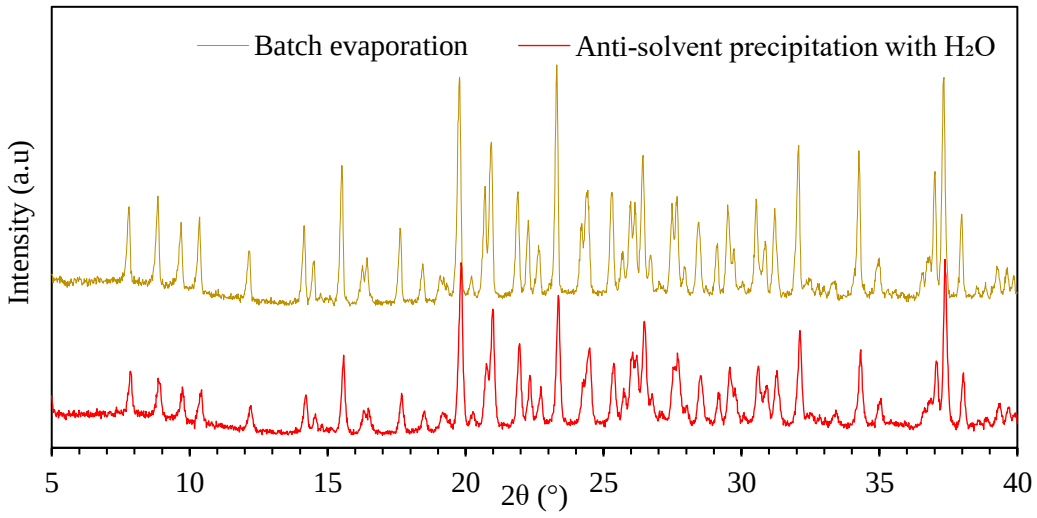

Figure.VI.30 PXRD comparison of Ch1 produced in batch with batch evaporation and anti-solvent precipitation.

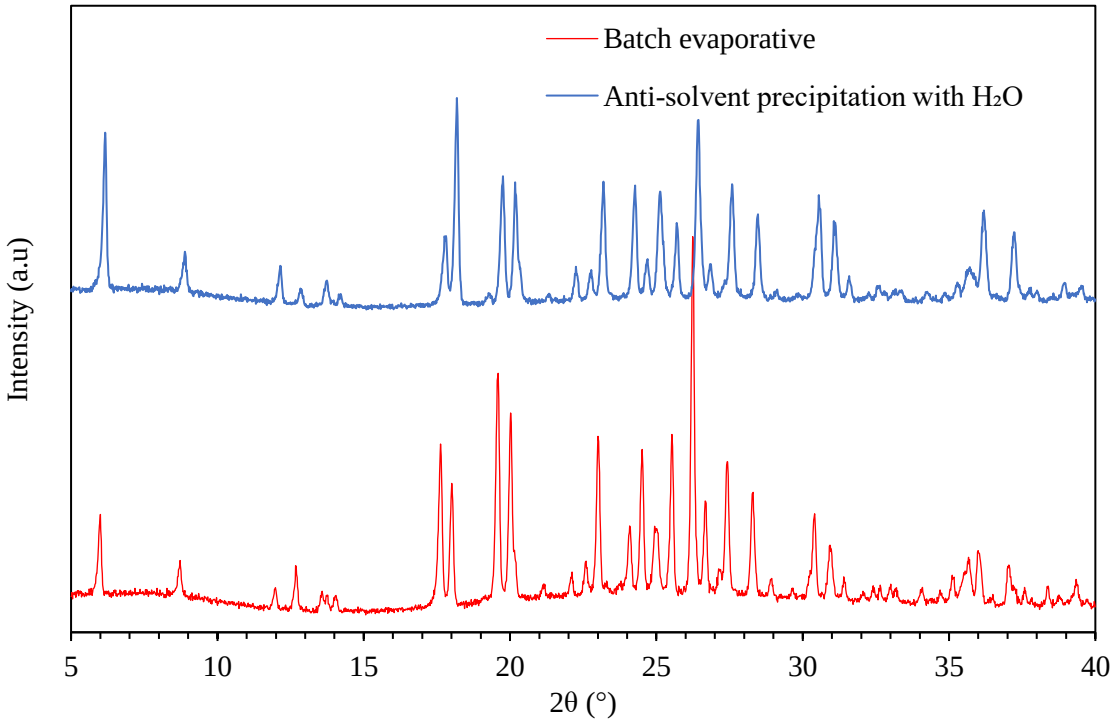

Figure.VI.31 PXRD comparison of co-crystal Ch2 produced in batch with batch evaporation and anti-solvent precipitation.

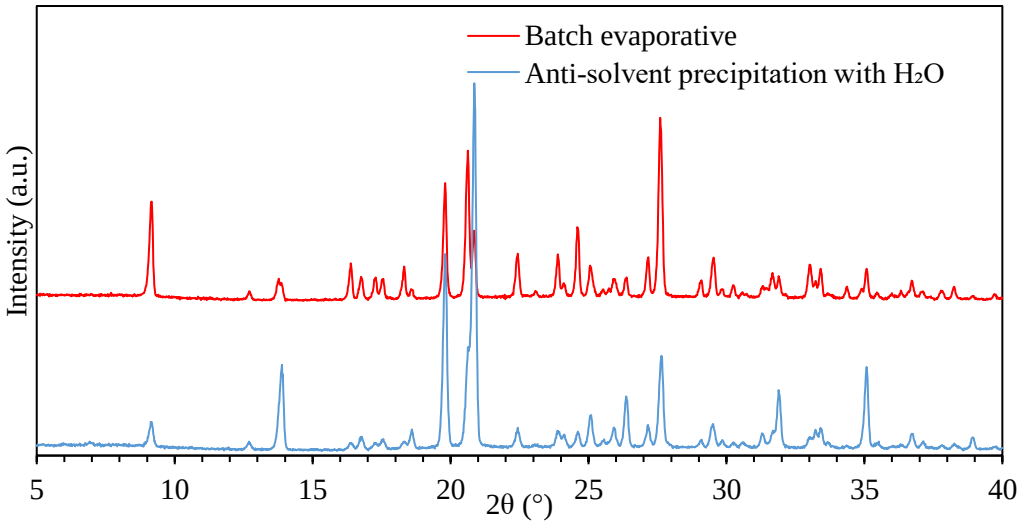

Figure.VI.32 PXRD comparison of Ch5 produced in batch with batch evaporation and anti-solvent precipitation.

As can be seen on Figure.VI.30, Figure.VI.31 and Figure.VI.32 the PXRD analysis of the compound confirm that the expected co-crystal has been obtained in all the cases with water as anti-solvent. This first analysis gave good information to moves towards flow.

VI.4.2.ii Flow synthesis of complexes Ch1, Ch2 and Ch5

The crystallisation of compounds Ch1, Ch2 and Ch5 has been carried out in flow using the Vapourtec flow kit under anti-solvent crystallisation conditions. In these experiments 4 g of 4-IA and 4.3 g of 3,5DNBA were dissolved separately in isopropanol, 20 mL and 20 mL respectively, to get a molar 1:1 ratio in these experiments. The tube-in-tube reactor was not used here, due to the large crystal sizes obtained which could lead to blocking. Experiments were performed in isopropanol as a solvent and using water as an anti-solvent. Experiments using acetonitrile were also attempted but no compound was obtained despite successful crystallisation in comparable batch anti-solvent crystallisation.

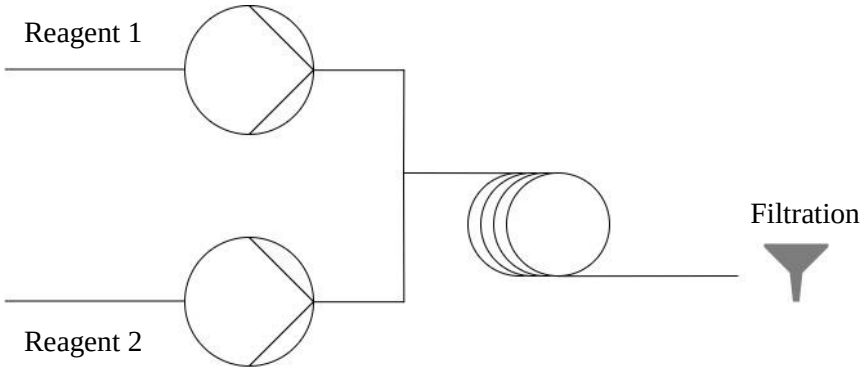

Figure.VI.33 Representation of the flow set-up used for the first trial for compound 1, 2 and 5 (SetF1).

The first set-up, SetF1, described in Figure.VI.33, used the two reagents only without anti-solvent. This set-up without anti-solvent was tried to see if the flow environment could induce nucleation where in batch this was not the case. Each pump was set to 0.3 mL/min flow rate before encountering at a T-piece and entering a 5 m coil (ID 2 mm) at room temperature to induce the crystallisation with a residence time, RT, of 11 minutes.

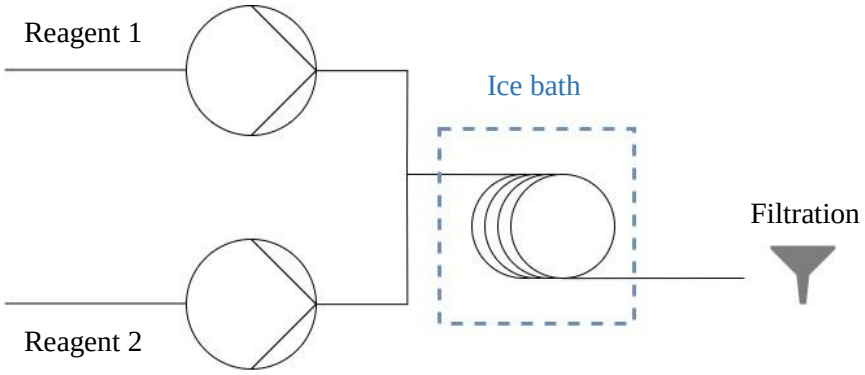

Figure.VI.34 Representation of the second flow set-up for compound Ch1, Ch2 and Ch5 (SetF2).

A second experiment, SetF2, was conducted with a similar set-up to that employed above except that the 5 m coil was submerged into an ice bath at 9-10 °C as seen in Figure.VI.34. The same flow rates as used above were used here. Here a grey powder was obtained in small yield from this experiment and the desired product was not obtained.

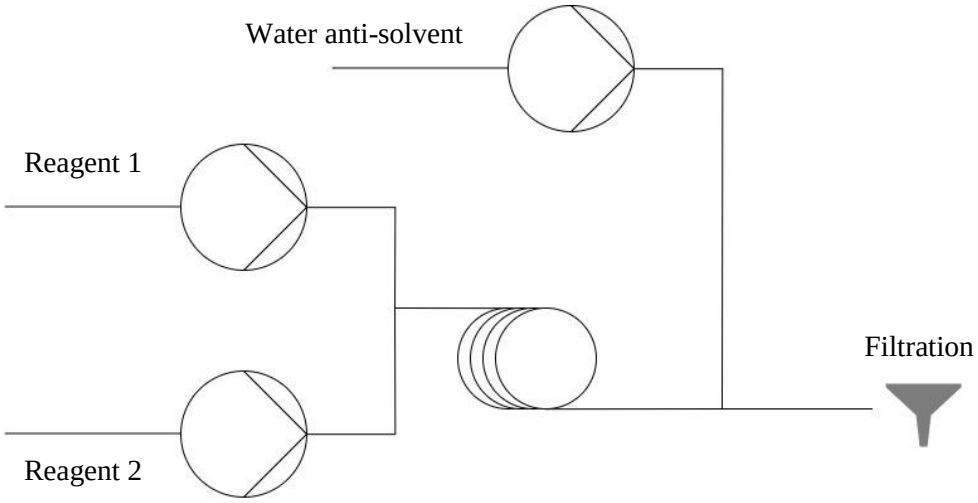

Figure.VI.35 Representation of the third flow set-up for the synthesis of compound Ch1, 2 and 5 (SetF3).

The third set-up (SetF3) consisted of a similar configuration as SetF1 except that after the coil the product outlet goes into a 2 mm ID T piece with a steady flow of anti-solvent, here water, as described on Figure.VI.35.

Table.VI.15 details the yields obtained from all the experiments performed in flow to obtain compounds Ch1, 2 and 5

.

Table.VI.15 Yield (%) obtained from experiments achieved in SetF1 to 3 in flow.

Set-up	**SetFI1**	**SetFI2**	**SetFI3**
Solvent	**Isopropanol**	**Isopropanol**	**Isopropanol**
4-iodoanilinium 3,5-dinitrobenzoate (Ch1) yield % from 3,5-dinitrobenzoate	5	3	40
Set-up	**SetFM1**	**SetFM3**	**SetFM3**
Solvent	**Methanol**	**Methanol**	**Methanol**
4-iodoaniline 3,5-dinitrobenzoic acid solvate(Ch2) yield % from 3,5-dinitrobenzoate	2	20	25
Set-up	**SetFE1**	**SetFE3**	**SetFA3**
Solvent	**Ethanol**	**Ethanol**	**Acetonitrile**
4-iodo-2-methylanilinium 3,5-dinitrobenzoate(Ch5) yield % from 3,5-dinitrobenzoate	<1	35	40

In section VI.4.2 it was highlighted that by using water as anti-solvent it was possible to precipitate out the desired compound from isopropanol. It appeared that it was a fast method for co-crystal production. Compound Ch1 showed to have poor yield for SetFI1 and 2 but when using the anti-solvent set-up SetFI3 the yield increased from 3-5 % to 40 %. The PXRD (Figure.VI.36) of the compound Ch1 showed that the flow synthesis SetFI1 and SetFI2 had showed several unexpected peaks (at 11.5°, 18°) thus showing the potential presence of impurities or unreacted materials.

For compound Ch2, the two set-ups (SetF1 and 3) previously described in Figure.VI.34 and Figure.VI.35 were used. Using the SetFM1 without anti-solvent and using methanol as solvent, the pale purple and colourless solutions on mixing formed an orange-red solution as in batch. This set-up did not yield a good amount of material even at high concentration. It is important to note that the 4IA compound is expensive and using high concentration would be a difficult option for flow synthesis in high volume. Other attempts at the same experiments were carried out, but without improvement in yield. Using SetFM3 with water as anti-solvent proved to increase the yield from 2% to 25%.The PXRD (Figure.VI.36) shows the same behaviour as the compound Ch1, with some new peaks appearing which could be due to impurities (at 14.3°, 20°).

The same set-ups, SetF1 and SetF3, discussed above for the production of compound Ch2 were also used for Ch5. SetFE1 gave the lowest yield (1-2%), but use of the anti-solvent technique SetFE3 increased the yield to 35% with ethanol solvent and 40% using acetonitrile solvent. In Figure.VI.36, the PXRD shows a good correspondence between products from the different production methods.

In those different set-ups it was seen that the anti-solvent technique of SetF3 gave a better yield than that from SetF1 and 2. On the other hand, the PXRD for Ch1 and 2 indicated the potential presence of impurities. To assess the presence of impurities a thermal analysis was carried out; samples from flow experiments were analysed with DSC with a temperature ramp of 10 K/min from 293.15 K to 473.15 K, as shown in Figure.VI.37, Figure.VI.38 and Figure.VI.39.

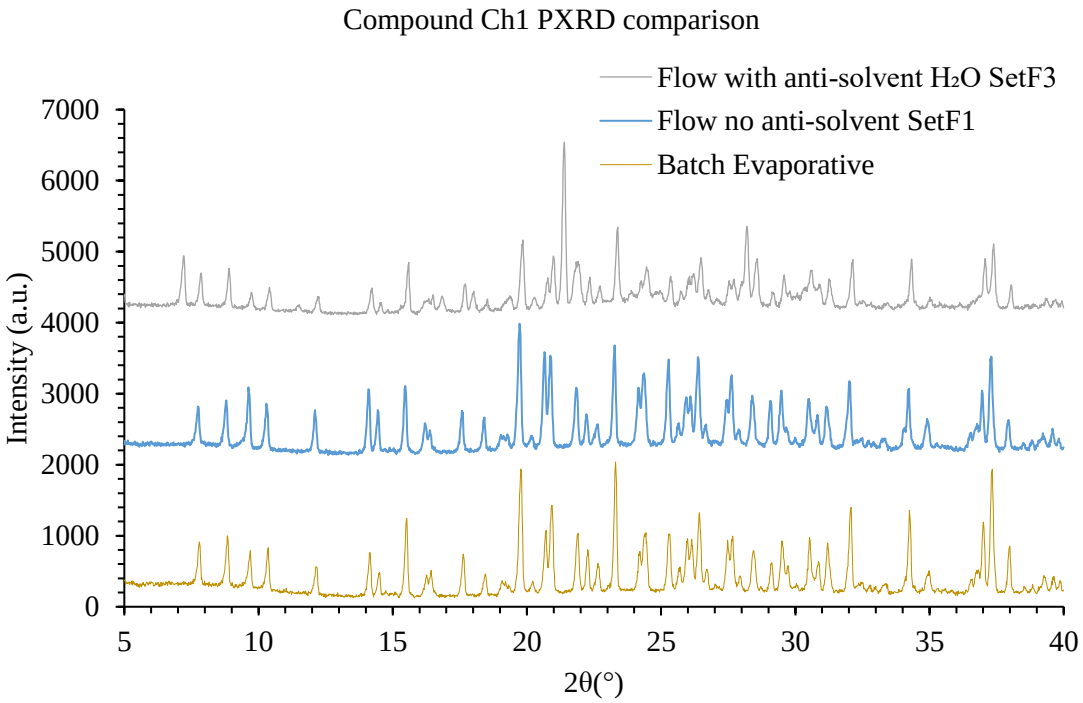
Compound Ch1 PXRD comparison
Flow with anti-solvent H2O SetF3
Flow no anti-solvent SetF1
Batch Evaporative
Intensity (a.u.)
7000
6000
5000
4000
3000
2000
1000
0
5
10
15
20
25
30
35
40
2θ(°)

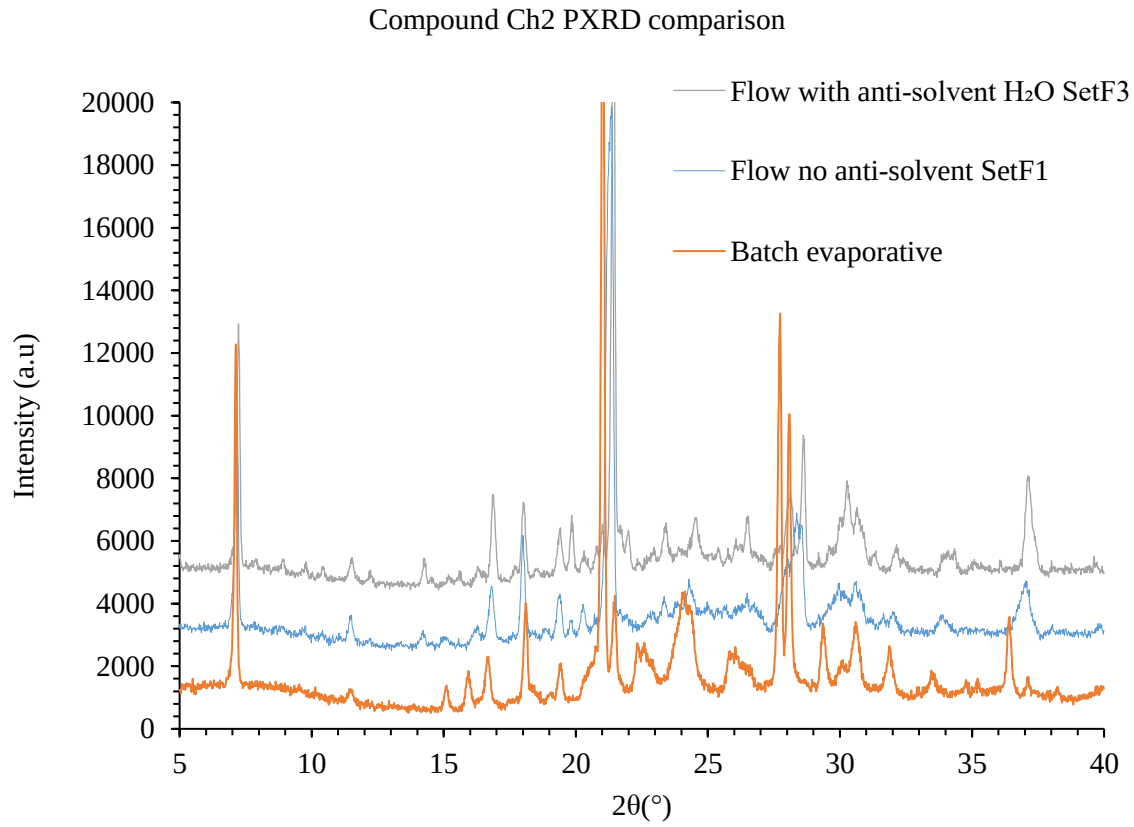
Compound Ch2 PXRD comparison
Flow with anti-solvent H2O SetF3
Flow no anti-solvent SetF1
Batch evaporative
Intensity (a.u)
20000
18000
16000
14000
12000
10000
8000
6000
4000
2000
0
5
10
15
20
25
30
35
40
2θ(°)

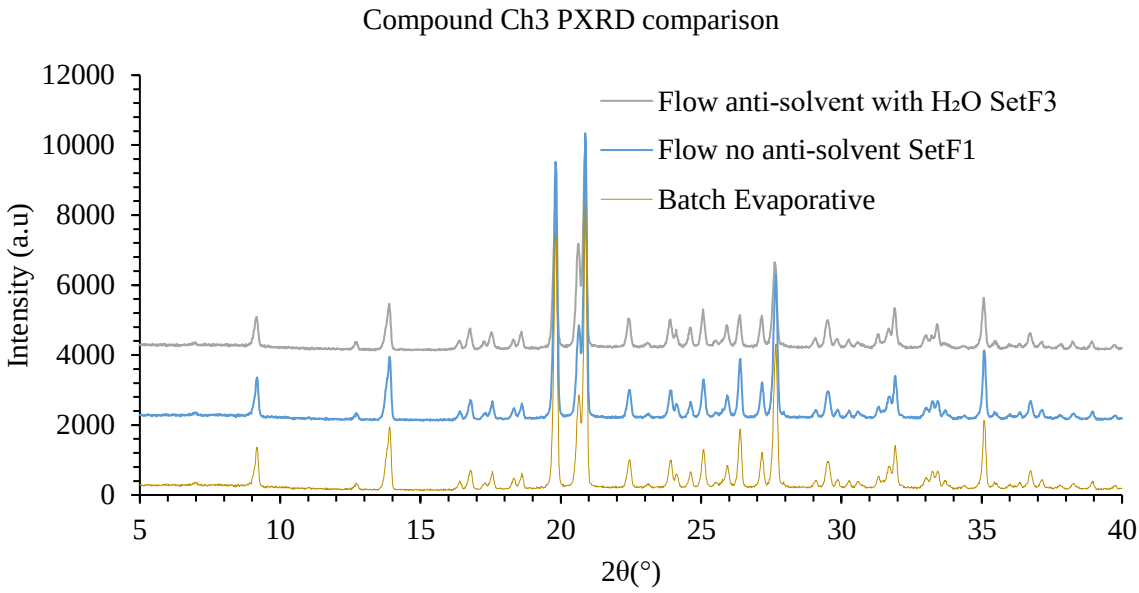

Figure.VI.36 Comparison of PXRD analysis of compounds Ch1,2 and 5 produced in batch and flow.

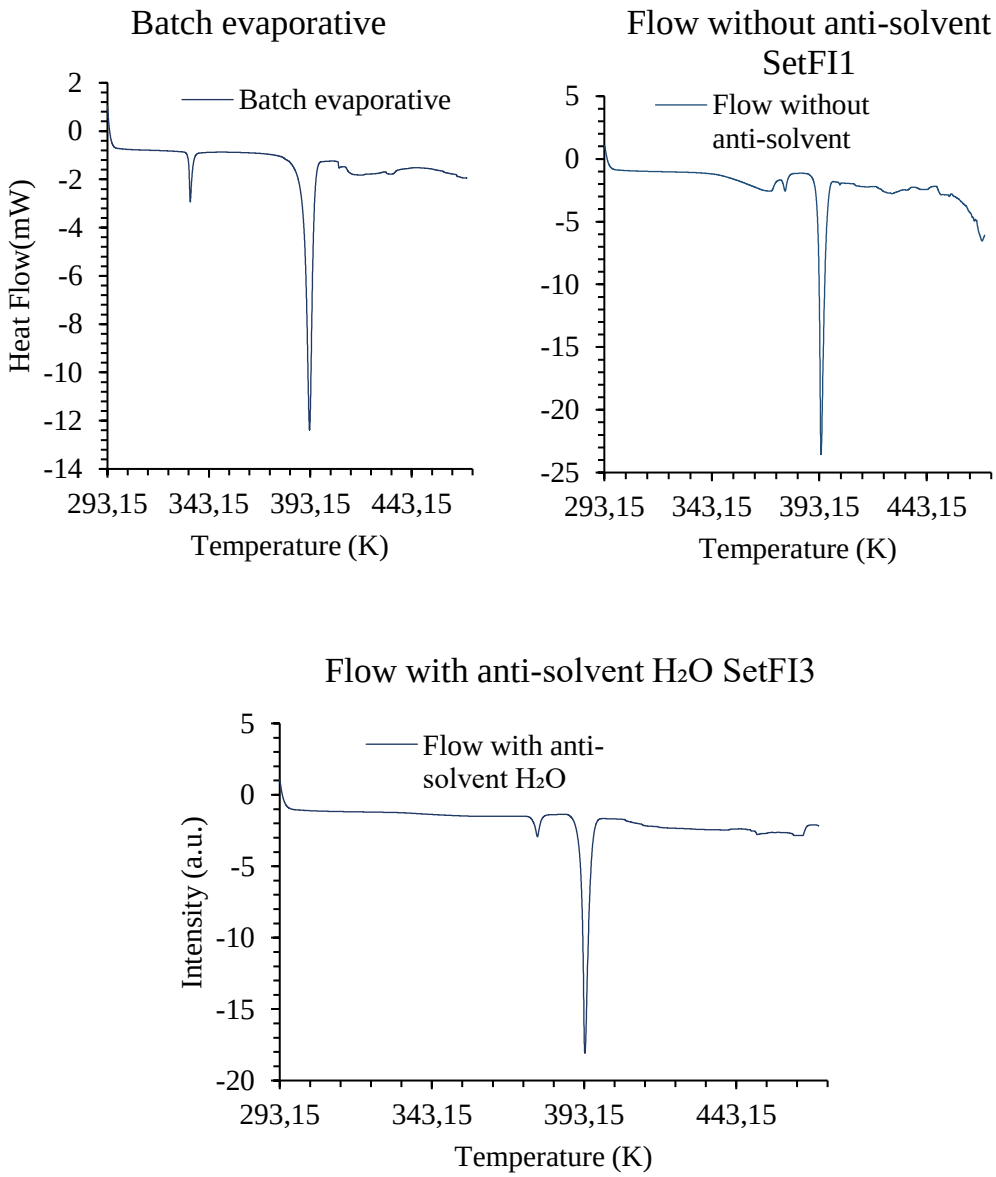

Figure.VI.37 Thermal analysis of compound Ch1 for Batch (e) and Flow SetFI1 and SetFI3.

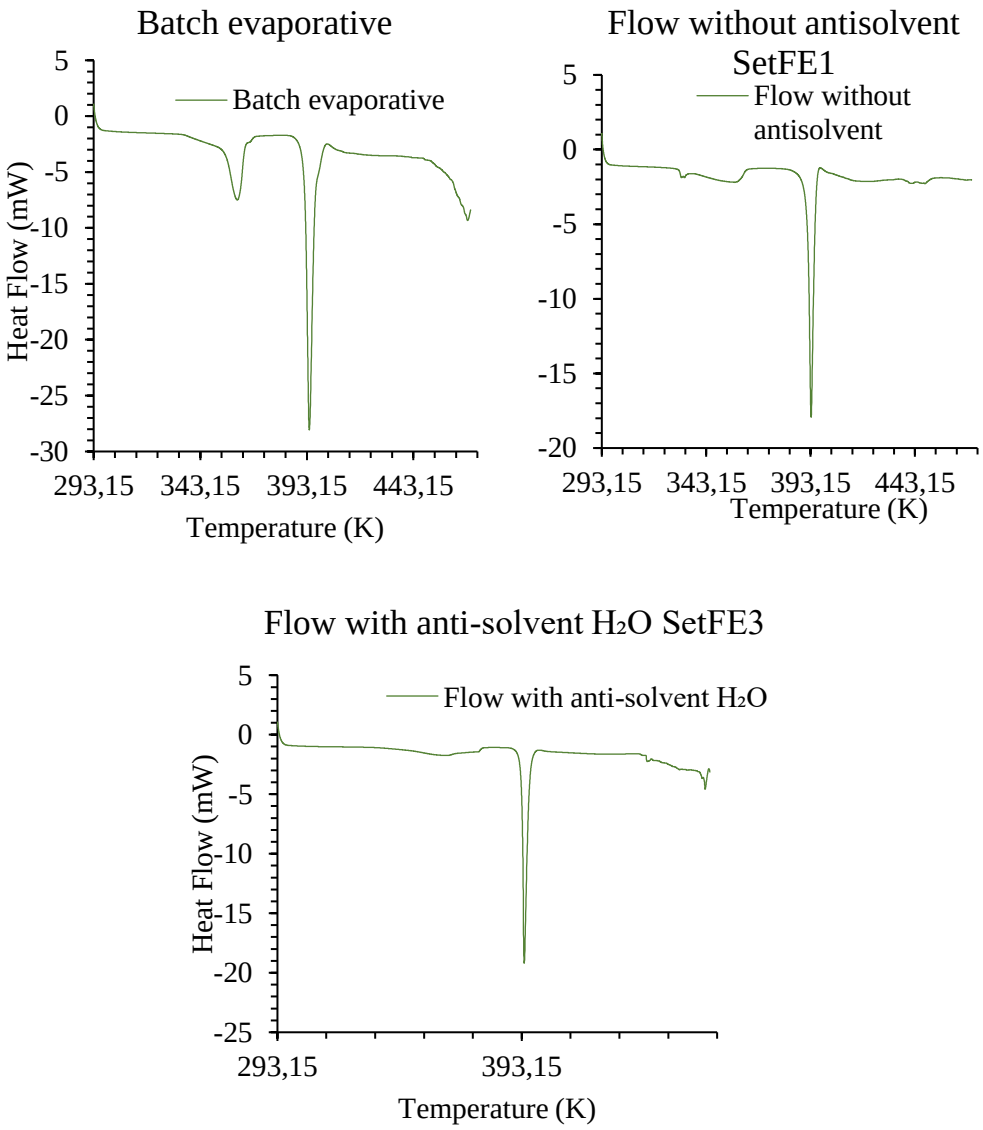

Figure.VI.38 Thermal analysis of compound Ch2 for Batch (i) and Flow SetFE1 and SetFE3.

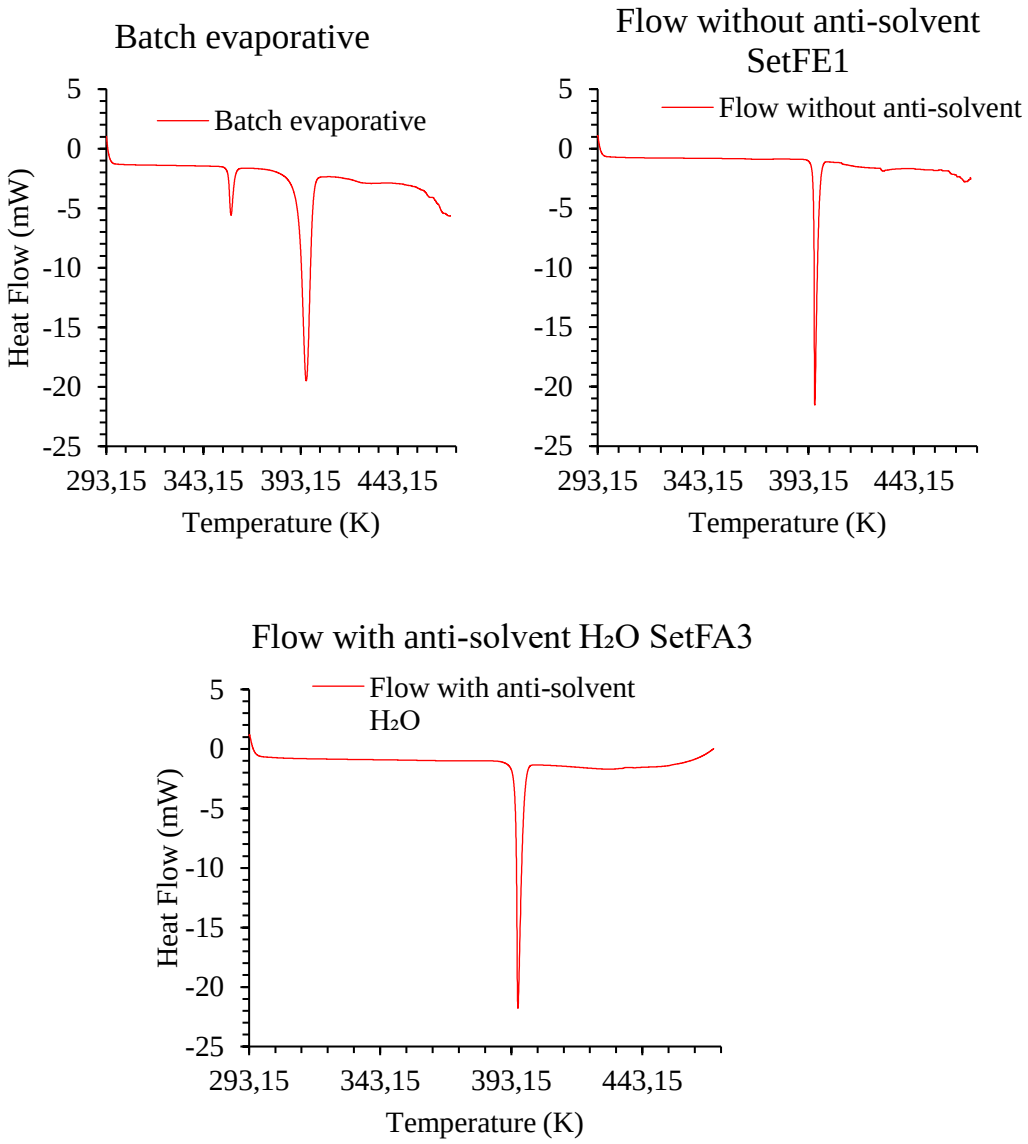

Figure.VI.39 Thermal analysis of compound Ch5 for Batch (m) and Flow SetFE1 and SetFA3.

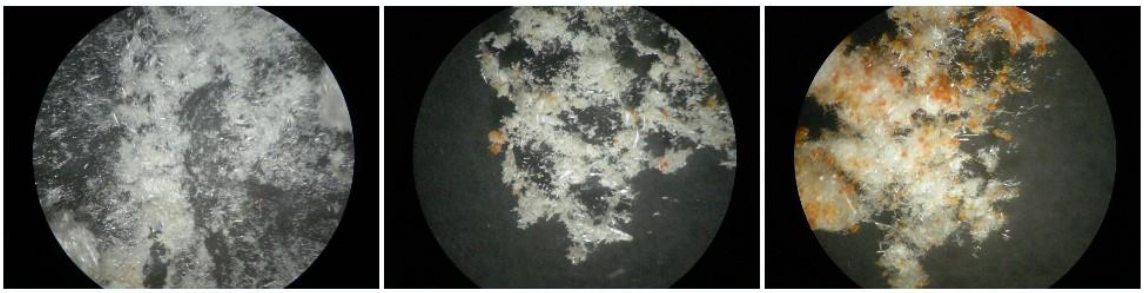

(Ch1)

(Ch2)

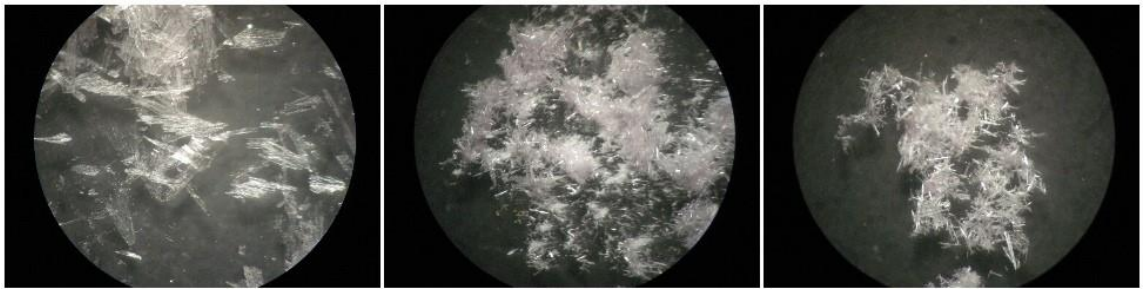

(Ch5)

Figure.VI.40 Crystals of compounds Ch1, Ch2 and Ch5 from the anti-solvent syntheses viewed under the microscope. From left to right are displayed the batch synthesis (ThIW, ThMW, ThEW), the flow set-up SetF1, and the flow set-up SetF3 with anti-solvent.

Figure.VI.40 shows microscope images of the experiments carried out for each compound going from batch to flow (left to right).

It is seen that for Ch1 some orange crystal contaminants are present in both SetFI1 and SetFI3. In Figure.VI.37, the thermograms of Ch1 show the same pattern with an endothermic peak at 119.7 °C, 121.3 °C, 120.7 °C and 120.2 °C that correspond between flow and batch. For some runs some peaks appear below 104 °C which correspond to the crystalline impurities in the product obtained especially from the batch evaporative technique (ThIW, ThMW, and ThEW), which have been detected *via* DSC. The impurity peaks were typically found from samples in which the yield was high, such as Ch1 flow synthesis with SetFI3, indicating low conversion. As for the low yield flow run of compound Ch1 SetFI3, the thermogram of Ch5 shows a 122.8 °C peak but with another at 84.1 °C which corresponds to the recrystallized 4-I-2-MA reagent with a melting point at 86-89 °C. In Jones *et al.*[15,26] the endothermic peaks are close to 123.2 °C which correspond to the one observed in Figure.VI.37, however the 84.1 °C endotherm from starting reagent was not observed.

Ch2 microscope images show a decrease in crystal size from batch to flow. In the SetFM3 product there is a white crystalline impurity present. Compound Ch2 thermal analysis, Figure.VI.38, shows only small changes compared to batch with peaks at 120.38 °C, 120.24 °C and 121.03°C. In Jones *et al.*[15,26] the endothermic peak for Ch2 was observed at 116.7 °C which is close to that observed here. For the run where no anti-solvent was employed, an endothermic peak at 87.9 °C is observed. This can lead to the conclusion that there are still some starting materials present (4-IA has an endothermic peak at 86-89 °C. This peak was also observed by Jones *et al.* at 85.24 °C and was suggested to be a loss of solvent upon heating. An endothermic peak is also seen above 200 °C which corresponds to the melting point of 3,5-DNBA reagent.

Ch5 produced in the different techniques showed a very consistent product in both flow cases SetFE3 and SetFA3 with no impurities or contaminants apparent. This is in contrast with Ch1 and Ch2 which both showed impurities. PXRD (Figure.VI.36) also showed a good correspondence between the products from batch and flow synthesis without any additional peaks. The DSC Figure.VI.39 shows the same single endothermic peak at 122.9 °C and 122.5 °C. In the evaporative batch DSC there is however a peak at 84.1 °C which is suggested to be the 4-I2-MA melting (86-89 °C). Compared to the compound obtained in Jones *et al.*[15,26] the DSC correlates with these results with the endothermic peak of Ch5 being at 122-124 °C in batch evaporative, however in that work the melting of 4-I2-MA was not observed.

Despite the high purity and yields achieved using SetF3, there were blocking issues in the T-piece used for anti-solvent addition during the crystallisation runs. The next section will investigate alternative methods of anti-solvent crystallisation in flow to mitigate this issue.

VI.4.2.iii Conclusions on the crystallisation of Ch1, 2 and 5 in flow

This work on the production of Ch 1, 2 and 5 materials in flow was performed as preliminary investigations to prepare for the production of other switchable materials (section V.3 below). The synthesis of those compounds showed the advantages of using anti-solvent crystallisation SetF3 compare to the batch evaporative and flow synthesis SetF1 and 2. The yield of the reaction for Ch1, 2 and 5 was increased and the crystal size reduced. However, the flow synthesis for Ch1 and Ch2 showed the presence of some crystalline impurities which have been detected with PXRD and DSC, but also some thermal events that could be due to solvent trapped in the crystals for Ch2. Ch5 synthesis displayed good results overall with few to no impurities and good yield. For these compounds the results were in correlation with the Jones *et al*[15,26] investigation. While the production of the thermochromic member of the series investigated here, compound Ch6, was unsuccessful, it has been shown that it was possible to produce Ch1, 2 and 5 using flow crystallisation methods.

The anti-solvent addition methods investigated here could be optimised. For example, the T-piece tended to fill with produced material, creating a blockage; the T-piece used was too small despite its dimension (1 mm ID then 2 mm ID) for the crystallite size being produced. The SetF3 produced smaller crystals and was the most suitable set-up for producing the compounds. Increasing the length of the crystallisation tubing after the T-piece may also help the synthesis in forming more crystals. Using a larger tubing bore for the anti-solvent with an impinging jet to induce the crystallisation will be discussed in the next section.

VI.4.3 Disordered Thermochromic compounds

The previous section gave the set-up for the experiments carried out for anti-solvent synthesis of different candidate thermochromic compounds. This section focuses on the synthesis in flow of the molecular complexes produced from different 2-haloanilines and 3,4-dinitrobenzoic acid. The batch synthesis and thermochromic behaviour of those material has been fully described in [26]. The dissolution of each 2-haloaniline and 3,4-DNBA gives a yellow solution, the crystallisation of that solution gives red crystals of the molecular complexes, and the origin of this colour therefore lies in the solid-state. Each of the crystals exhibit a significant colour changing behaviour upon heating. The objective of this section is to see if the flow production of these complexes has an impact on those properties.

The first complex, 2BA 3,4DNBA, is produced from 2-bromoaniline and 3,4-dinitrobenzoic acid in ethanol at room temperature, the second, 2CLA 3,4DNBA, is obtained with 2-chloroanilinium and 3,4-dinitrobenzoic acid in ethanol and the third, 2IA 3,4DNBA, is produced from 2-iodoaniline and 3,4-dinitrobznoic acid in ethanol at room temperature. As previously shown, using water as anti-solvent has proven to be a successful method to precipitate out and increase the yield of such complexes. The challenge here is to maintain the switching (thermochromic) properties of the resultant product. The same set-ups described in Figure.VI.33 were used with the different reagent configurations. The form I (room temperature polymorphic form) of each of these complexes are red crystals which switch to the colourless polymorphic form by disorder-order phase transformation when increasing the temperature.

Table.VI.16 First trial using T-piece and coil for the production of 2BA 3,4DNBA and 2 CLA 3,4DNBA.

	Solution flow rate mL/min	**Anti-solvent chamber flow rate mL/min**	**Molar ratio 2XA and 3,4 DNBA in 14 mL vial**
2BA-TP(2BA 3,4DNBA)	1	2	1:2 ratio blockage after 8 min
	1	3	1:2 blockage after 18 min
2CA-TP(2 CA 3,4DNBA)	1	3	1:2 blockage after 10 min

In Table.VI.16 are the results from preliminary flow experiments using the first set-up (SetF3) described previously (Figure.VI.35) with anti-solvent technique. For the coil a 2 mm and a 1 mm bore tubing of 2 m were used but both rapidly showed blockages. For all trials a 1:2 mol ratio was used between 2XA and 3,4DNBA (0.2 mol of 2XA, 0.4 mol of 3,4DNBA) in ethanol. For the synthesis of 2BA 3,4DNBA blockages appeared after 8 min inside both 1 mm and 2 mm bore tubing; increasing the flow rate to 3 mL/min showed an improvement with the blockage appearing at 18 min. For 2CA 3,4DNBA synthesis the blockages occurred after 10 min. In all cases Form I of each material was obtained as shown in Figure.VI.45. Blocking issues were found to be highly detrimental, future work therefore focussed on mitigating this.

To overcome this issue a similar set-up was used for the flow synthesis except that this time after the coil a T-piece impinging jet was set-up with a 0.7 mm ID jet and with an 18 mm ID outlet. The set-up principle of the impinging jet is displayed in Figure.VI.41. Parameters used for the crystallisation experiments are displayed in Table.VI.17.

Table.VI.17 Impinging jet parameters for synthesis of 2BA 3,4DNBA, 2CA 3,4DNBA and 2IA 3,4DNBA

	Peristaltic flow rate impinging jet mL/min	**Molar Ratio 2XA/ 3,4 DNBA**
2BA-IJ(2BA 3,4DNBA)	6	1:2
	10	1:2
	10	1:2
2CA-IJ(2CA 3,4DNBA)	6	1:2
	6	1:2
	6	1:2
	10	1:2
2IA-IJ(2IA 3,4DNBA)	3	1:2
	3	1:2
	3	1:2

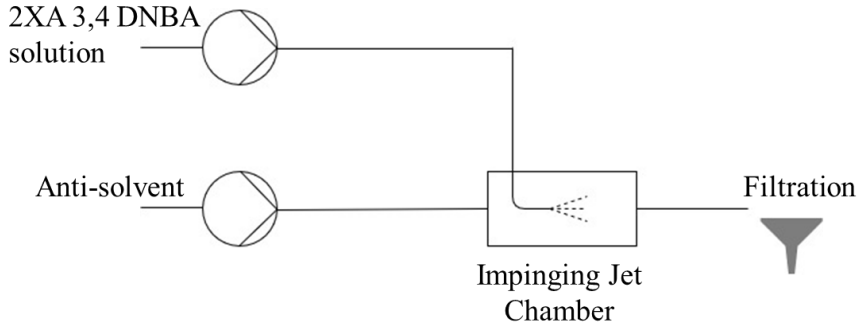

Figure.VI.41 Impinging jet flow set-up.

The jet itself is connected to the coil and the jet chamber is connected to a peristaltic pump flowing into a water trough. This type of technique creates a spray and is favourable to form small droplets leading to smaller particle size obtention and a better interaction between the anti-solvent and the solution which would avoid blockages in flow and instantly precipitate the co-crystal due to the high drowning out ratio. At first the configuration was not giving good results but after some different flow rate optimisation, it was established that high flow rates for the anti-solvent were the key to

producing the material in good quantities. The issues with this set-up are: the chamber having crystals and blocking in the jetting chamber; sometimes the experiments need to be stopped and the apparatus cleaned out before starting again. The longest run was 15 min until complete blockage in the chamber.

To understand the behaviour of the impinging jet chamber, free jet trials have been designed, this consists of a pump flowing the solution through a jet with the same 0.7 mm ID into a large bath filled with water as seen in Figure.VI.42.

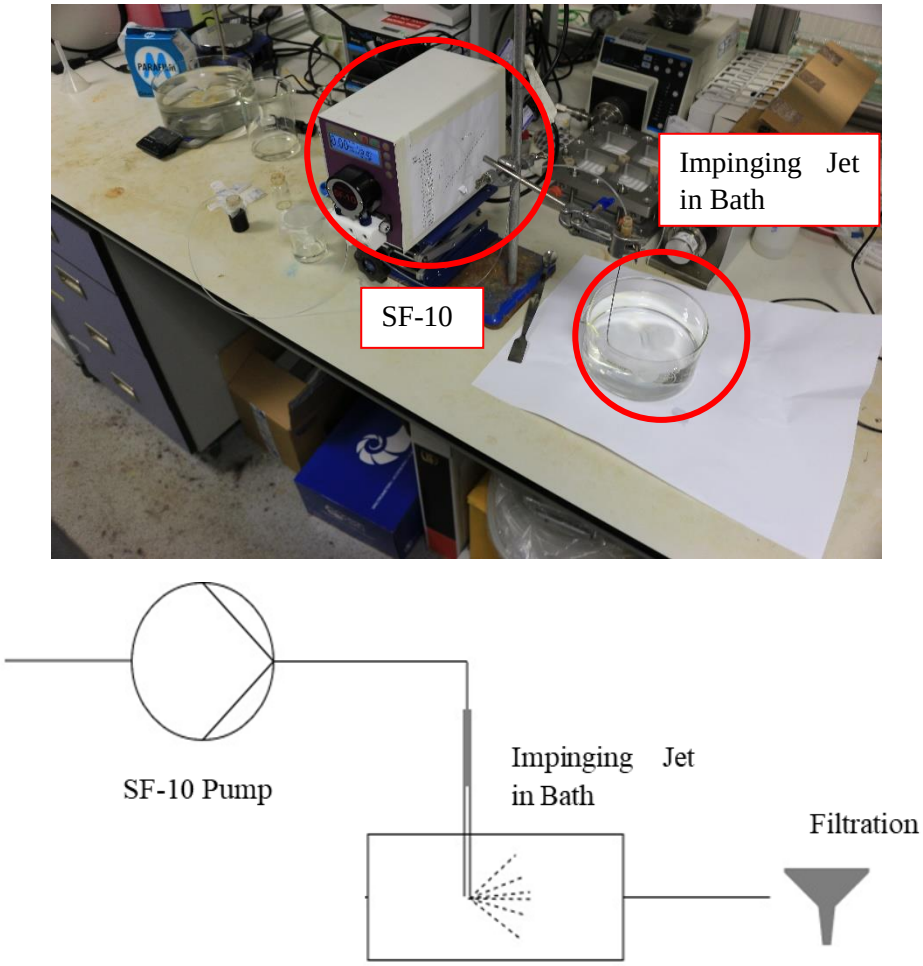

Figure.VI.42 Free jet set-up, the SF-10 peristaltic pump is used to pump the solution through the jet into the bath where the complexes can be crystallised

Before the co-crystallisation trials, different flow rates were investigated from 3 mL/min to 9 mL/min with a coloured solution of water with $KMnO_4$ to investigate the dispersion after the jet inside the bath. As can be seen on Figure.VI.43 different parameters give changes in the dispersion pattern. The dispersion is best for the 9 mL/min flow rate which gives a more homogeneous liquid-liquid interaction between the two solutions.

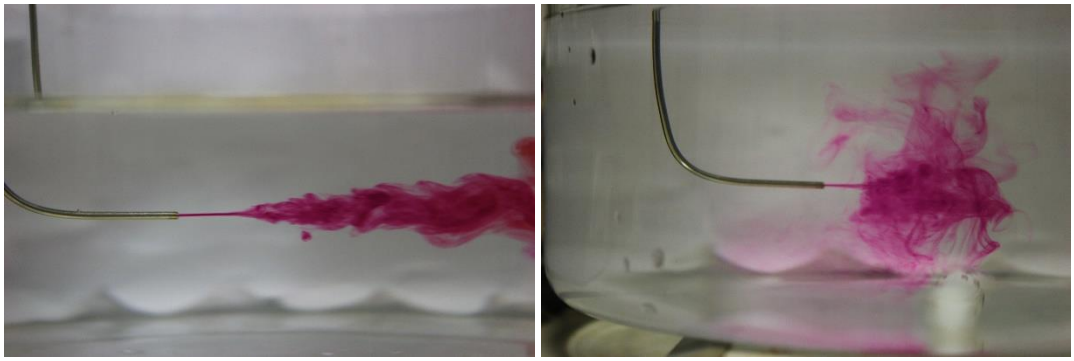

Figure.VI.43 Study of different flow rates used with the free jet; (left) 3 mL/min, (right) 9 ml/min (video of all flow rates is given in supplementary information (**CDCh6-3**)).

The parameter of 9 mL/min was therefore used to pursue a free jet experiment with a solution of 2-IA-3,4DNBA complex (0.2 mol 2IA and 0.4 mol 3,4 DNBA in 14mL), to crystallise in water. As can be seen in Figure.VI.44 the yellow solution starts to turn orange suggesting the formation of product but there was no further change after 5 min. It was subsequently observed that a brown oil settled at the surface of the water in the batch, no crystals appeared and no analysis was able to be made.

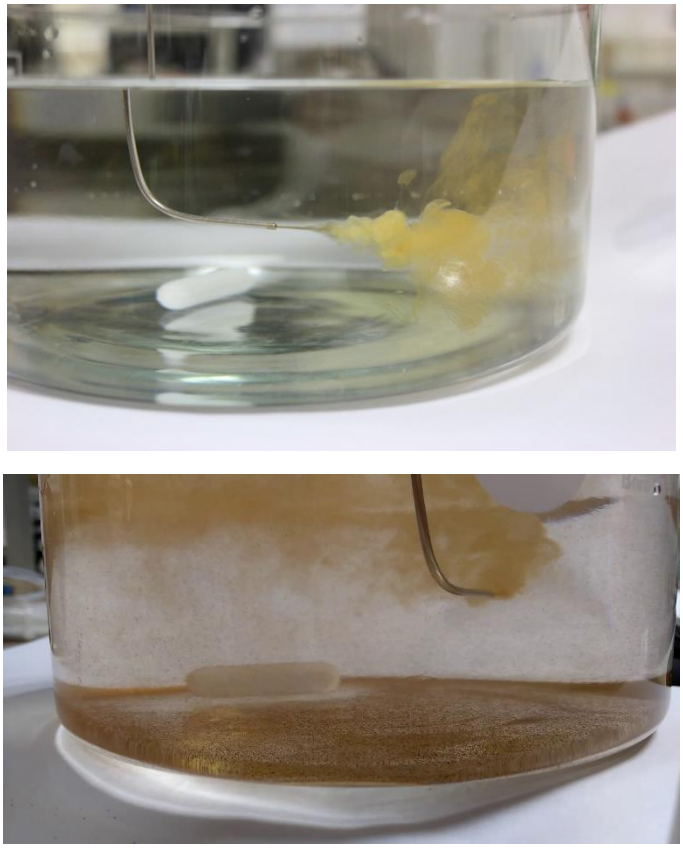

Figure.VI.44 Crystallisation of the solution inside the bath for 2-IA-3,4DNBA after 10 sec flow (above) and after 1 min flow (below).

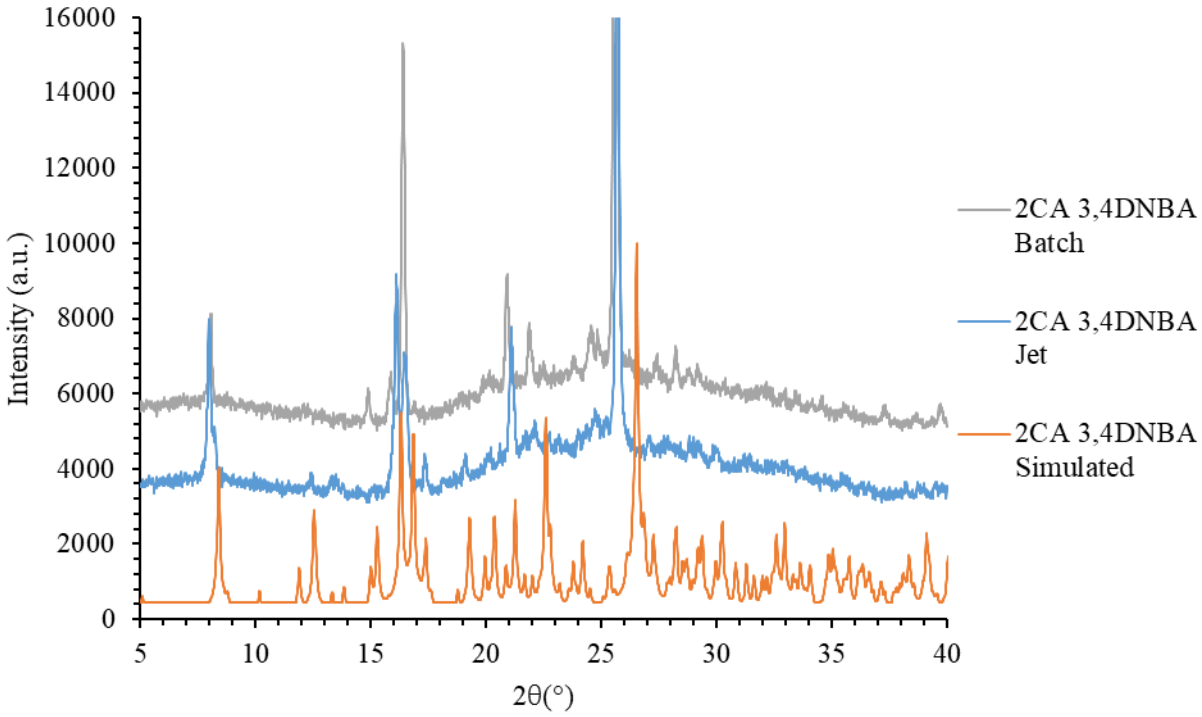
16000
14000
12000
10000
8000
6000
4000
2000
0
Intensity (a.u.)
5
10
15
20
25
30
35
40
2θ(°)
2CA 3,4DNBA Batch
2CA 3,4DNBA Jet
2CA 3,4DNBA Simulated

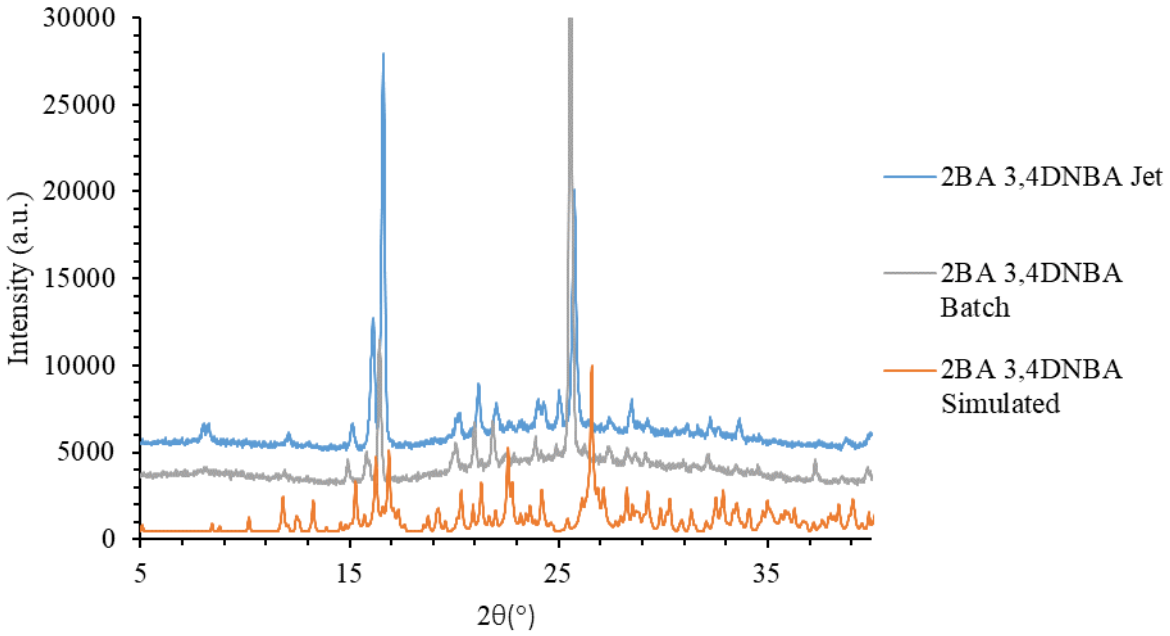
30000
25000
20000
15000
10000
5000
0
Intensity (a.u.)
5
15
25
35
2θ(°)
2BA 3,4DNBA Jet
2BA 3,4DNBA Batch
2BA 3,4DNBA Simulated

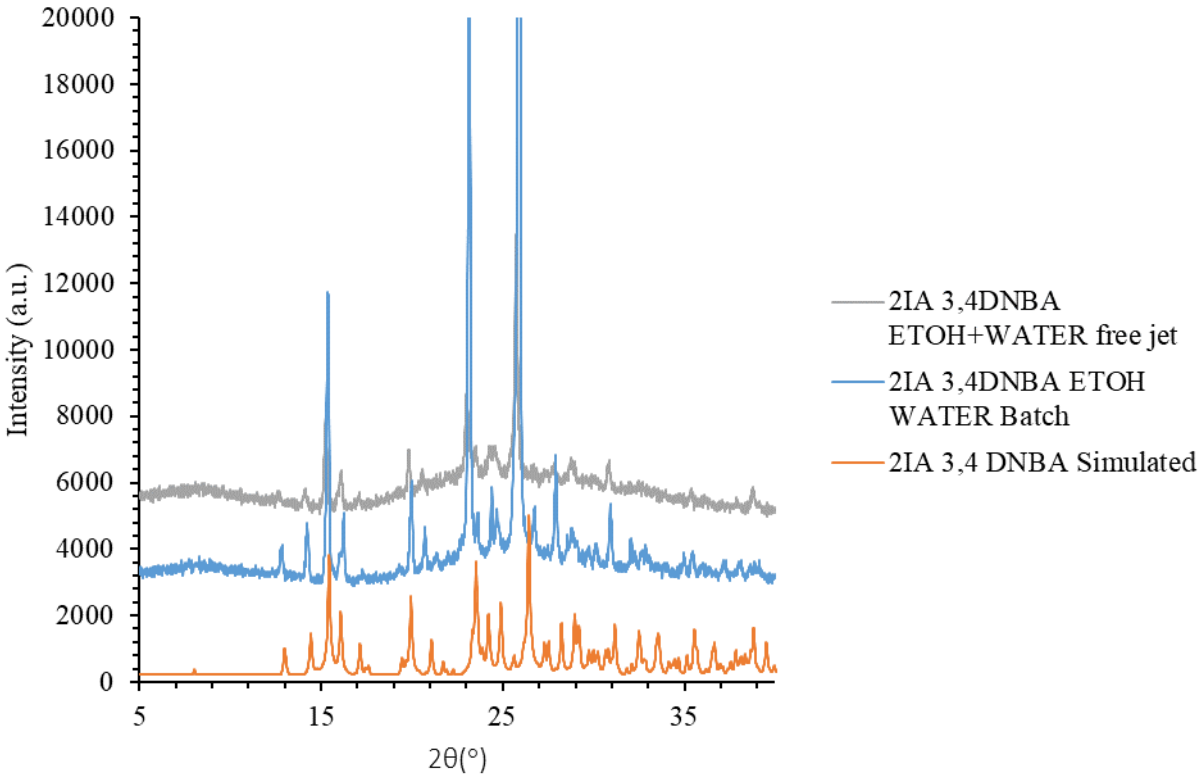

Figure.VI.45 PXRD of 2IA 3,4DNBA, 2CA 3,4DNBA and 2BA 3,4DNBA produce with free jet obtained, batch and simulated patterns from Charlotte Jones' thesis data[26]

As it gave the best result in terms of feasibility and consistency in the jet trials, the complex 2IA 3,4 DNBA was chosen for these trials. PXRD patterns (Figure.VI.45) of 2CA and 2BA with 3,4 DNBA showed to be similar from that obtained in batch and the simulated pattern. It was observed during the synthesis that during filtration some of the orange/red crystals were turning white. In the free jet trials a low amount of crystal was recovered but enough to do analysis. It was therefore decided to use segmented flow in the KRAIC in order to crystallise the complexes.

For segmented flow a similar set-up was used as for the PiC production with the KRAIC (Chapter III). The mixer piece was a combination of a cross PEEK piece with a 1 mm ID to combine the solution, Galden and Air. This cross piece was then connected to a polypropylene Y-piece of 3 mm ID before being connected to the KRAIC where the anti-solvent crystallisation would take place. At the end of the 15 m of the KRAIC tubing (3.2 mm ID) a second anti-solvent point was added with the same set-up as with the neutral solvent used in Chapter III for cooling crystallisation.

The combined set-up used for the crystallisation in the KRAIC is shown in Figure.VI.46.

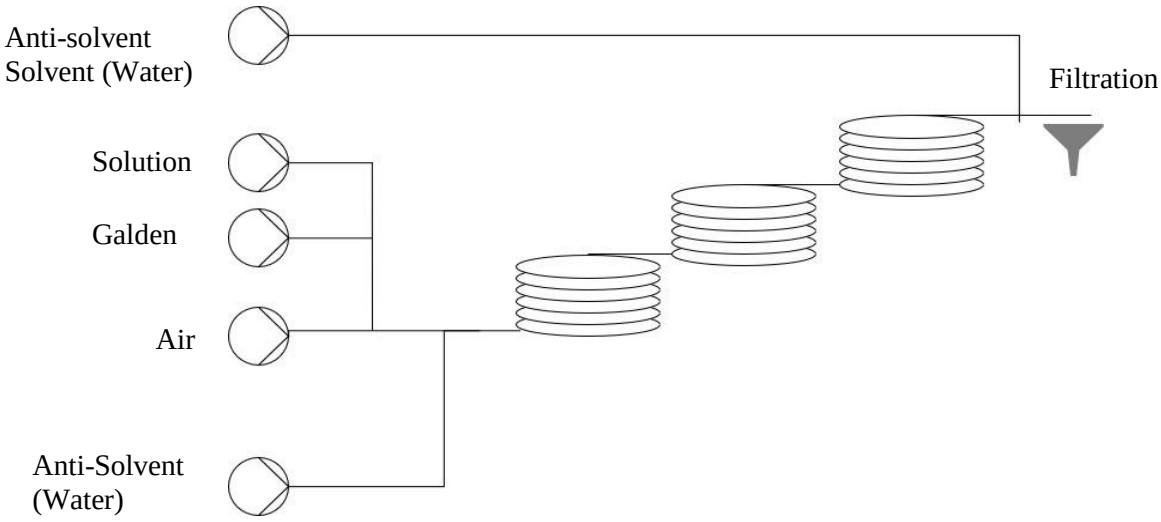

Figure.VI.46 KRAIC Set-up for 2-IA 3,4DNBA crystallisation

The parameters of each experiment are displayed in Table.VI.18.

Table.VI.18 Parameter used for the Vapourtec and the KRAIC pumps for the crystallisation of 2-IA-3,4DNBA

	Galden Increment Flow rate (mL/min)	Air Flow rate (mL/min)	Solution in Ethanol (mL/min)	Water Flow rate at inlet (mL/min)	Molar Ratio 2IA/3,4DNBA
2IA-Be-5m (2IA 3,4DNBA bench flow 5 m tubing)	2.1	2.1	2.1	2.1	1:2
2IA-K-st (2IA 3,4DNBA (KRAIC))	2.1	2.1	2.1	4.2	1:2

The same yellow precipitate appeared after the mixer piece of the KRAIC, with some brown oil appearing in coil 1. No crystallisation appeared along the 15 m of tubing. Anti-solvent was then added at the end of the crystalliser to induce the crystallisation, with 4.2 mL/min flow rate. Here the crystals appeared instantly with an improved yield of 66.25 % and a 22 min 55 s residence time; this was thus a successful run to produce Form I of the complex 2-IA-3,4DNBA. During the crystallisation runs where a second anti-solvent addition point was used, the first anti-solvent addition appeared to produce an emulsion which was then crystallised by interaction with the second addition of anti-solvent.

Table.VI.19 Flow experiment yield for the synthesis of difference thermochromics complexes inside the KRAIC carried out with Dr Anuradha Pallipurath and PhD student Dan Scott.

Experiment	Tubing length (m)	Drowning out ratio Ethanol Water (ml/min)	Temperature (°C)	Yield	Residence time (min)	Form
2IA-IJ(2IA34DNBA Impinging Jet)	2	1:2	40	< 2%	12.56	FI
		1:2	20	< 3%	12.56	FI
2IA-YT(2IA34DNBA y-tubing)	2	1:2	40	< 1%	12.56	FI
2BA34DNBA 2BA-IJ(impinging jet)	2	1:2	20	< 2%	12.56	FI
2CA-IJ(2CA34DNBA impinging jet)	2	1:2	20	< 4%	12.56	FI
		Flow rate Solution:Anti-solvent(Water):Galden (ml/min)				
2IA-SFK-EtOH(2IA34DNBA KRAIC segmented flow)	15	1:2:2	20	66.25 %	22 min 55 s	FI
	0.1	1:2:2	20	39%	10s	FI
	0.1	1:0:4	20	3.2%	10s	FI
	1.82	1:4:2	20	30.2% *	1 min 35 s	FI
	1.82	1:2:2	20	47.5%	1min 52 s	FI
Free Jet 2IA-FJ-EtOH (2IA34DNBA)	N/A	1.5 L water bath	20	< 1%	N/A	
	N/A	750 ml water bath	20	< 2%	N/A	
	N/A	750 ml water bath	10	< 1%	N/A	
2BA-FJ-EtOH (2BA34DNBA)	N/A	750ml water bath	20	< 3%	N/A	
2CA-FJ-EtOH (2CA34DNBA)	N/A	750 ml water bath	20	< 1%	N/A	

*when stopped due to blockage

In Table.VI.19 is a summary of the experiments carried in flow with the impinging jet, the free jet and the KRAIC. From this table it is clear that using the KRAIC with segmented flow increased the yield of the complex drastically. Different set-ups were used with shorter tubing length and drowning out ratio, it appeared that the tubing length has no effect on the apparition of crystals. Instead, the initial drowning out ratio was increased to 1:4 from 1:2 but this created blockages inside the reactor due to an increased amount of crystal precipitating. With a 10 cm of tubing the yield was 39% and the residence time was 10 s with the segmented flow technique with a flow rate of 1 mL/min for the solution, 2 mL/min for the anti-solvent and 2 mL/min for the Galden. Using a 1.82 m tubing length with a 1:2:2 flow rate ratio of solution: anti-solvent: second addition point gives a 47.5 % yield for a residence time of 1 min 52 s. This shows that using two injection points of anti-solvent with the KRAIC produced an excellent yield compared to other techniques. Form I of 2IA - 3,4DNBA has been produced as confirmed by PXRD (Figure.VI.48). The crystals forming inside the KRAIC are displayed in Figure.VI.47.

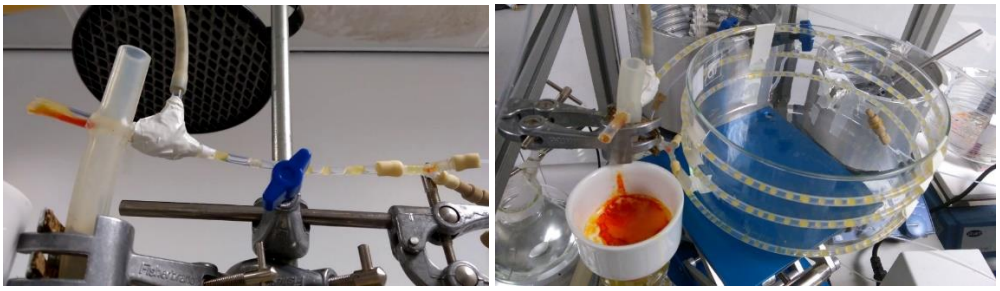

Figure.VI.47 2IA 3,4DNBA(**2IA-SFK-EtOH**) production in 10 cm tubing (left) and 1,82 m (right)

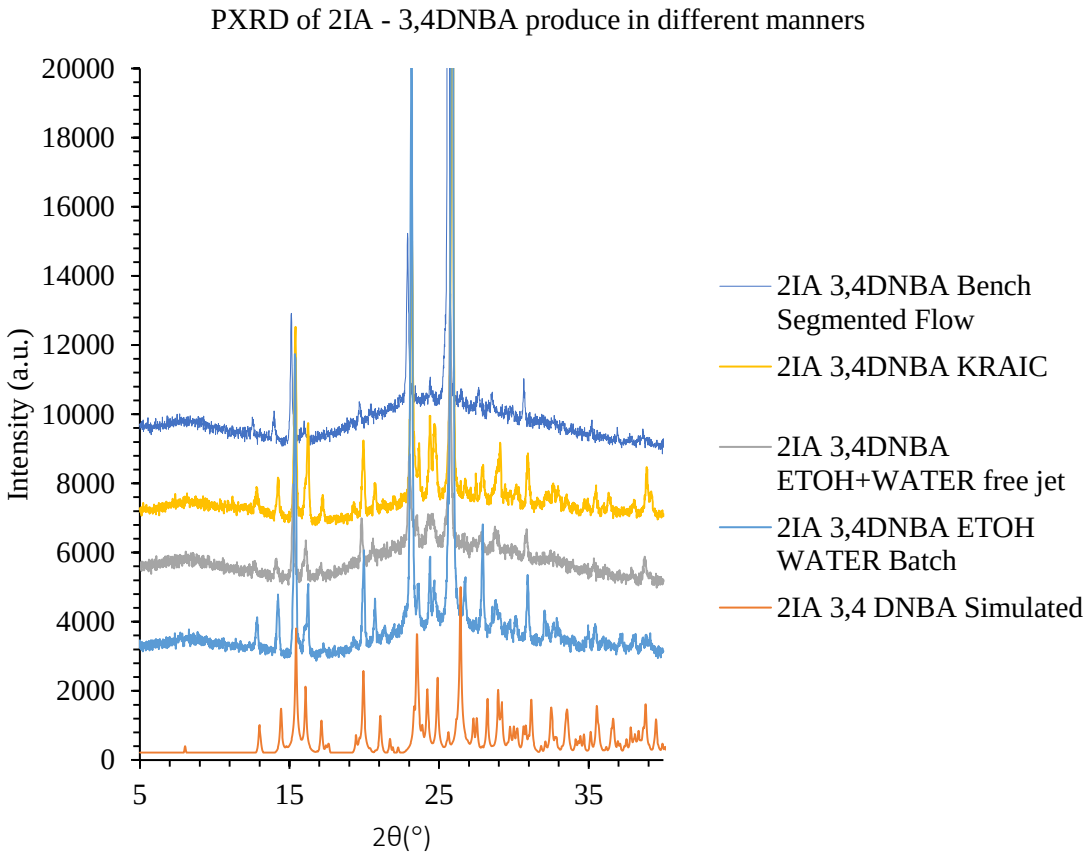

Figure.VI.48 PXRD of Form I of 2IA3,4DNBA obtained from different methodologies.

The increase in yield was one part of the target of those experiments, but it appeared that using flow crystallisation also gave much more possibilities in obtaining smaller particle sizes of the crystal complex while keeping the thermochromic properties. Figure.VI.49 shows the SEM pictures of the crystals produced with different techniques. As can be seen the different techniques used give different particle size and shape which might induce different properties. The impinging jet appears to give the interesting morphology of hollow crystals, as seen in Figure.VI.49.

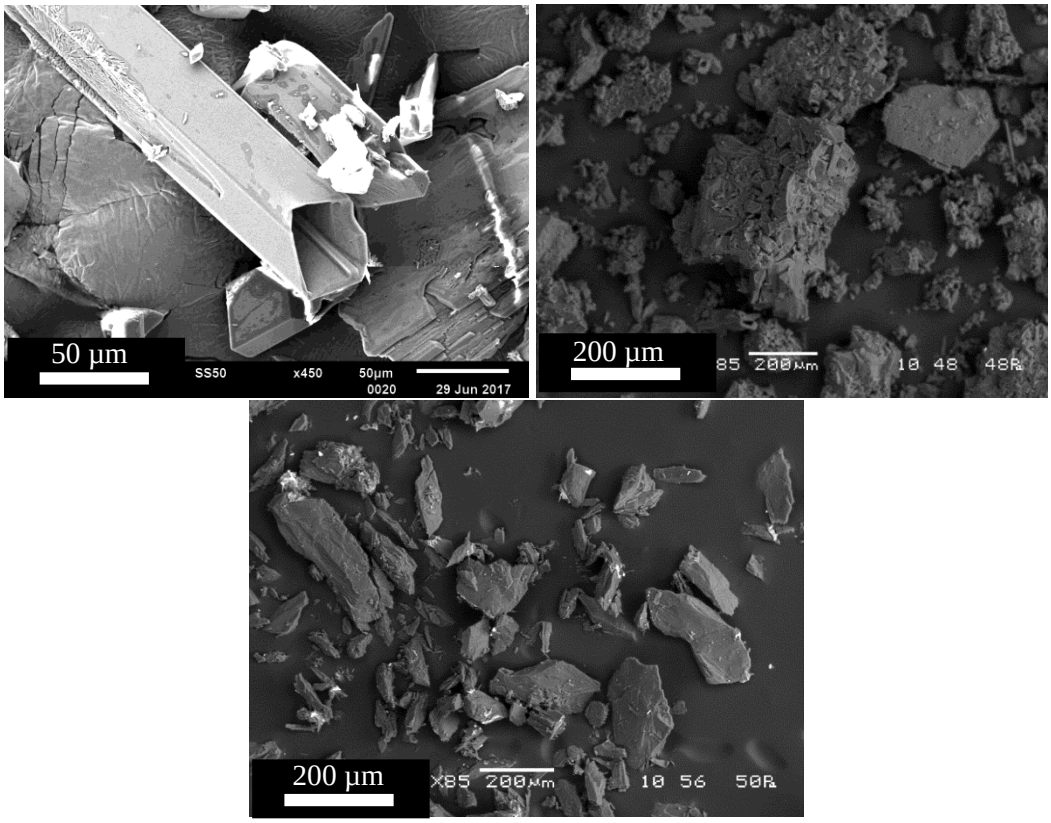

Figure.VI.49 2IA34DNBA produce with impinging jet (top left), 2IA34DNBA produced in segmented flow KRAIC (top right) and 2IA34DNBA produced in evaporative batch

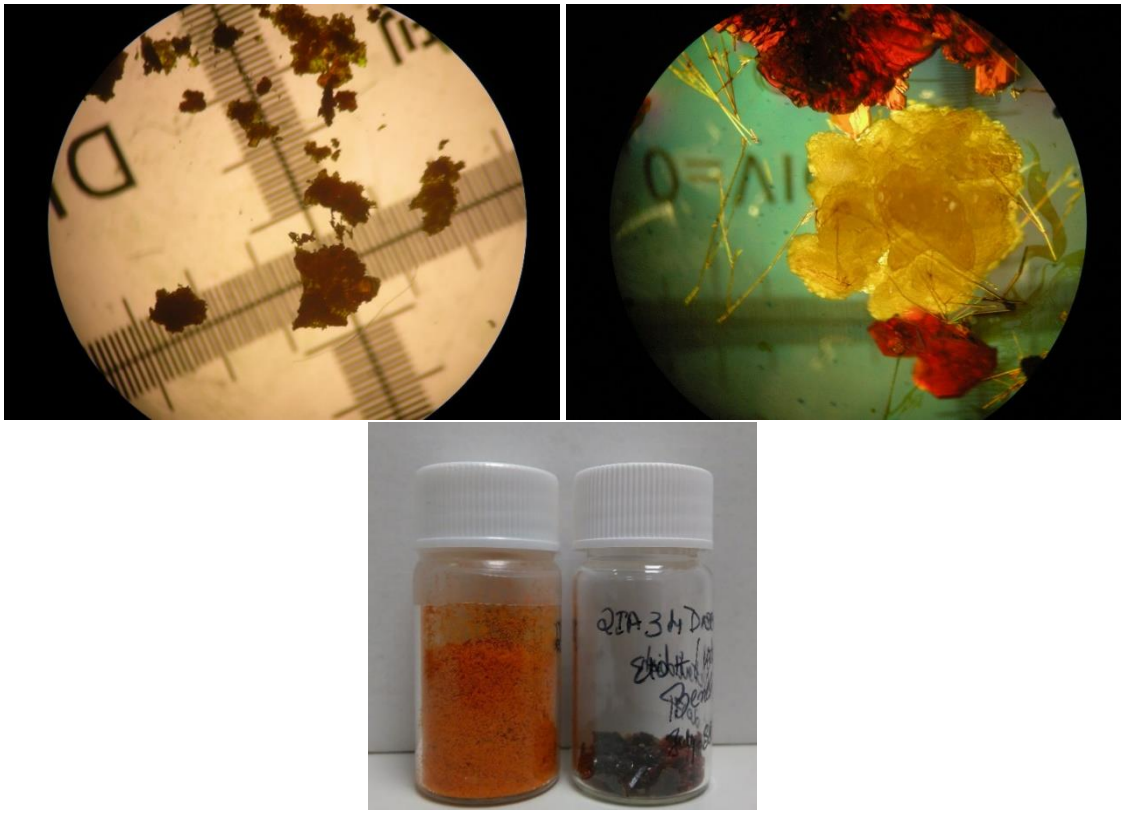

Figure.VI.50 Comparison of 2IA - 3,4DNBA crystals between segmented flow (2IA-SFK-EtOH) synthesis (left) and grown in evaporative batch (right)

There is thus seen to be an overall improvement using flow compared to batch synthesis. The size of the particles in particular has been reduced and could potentially lead to new properties of the material. Longer runs would be needed to ensure the steady state of the reaction and being able to reproduce the particle size repeatability with the different parameters. The hollow crystal morphology is not yet understood and could be responsible for the reversibility of the thermochromic behaviour observed in this material. The study of the thermochromic behaviour of the produced materials will be presented in Chapter VII.

VI.5. Conclusion

The Vapourtec Flow Kit with its different compatible reactors has proven capable to produce a range of different materials. The production of $[Fe(Htrz)_2(trz)](BF_4)$ has been successful inside the Kenics mixer reactor with a better capability to target the particle size of the compound with different parameters; the only drawback was the relatively large size of the reactors employed here which make the use of expensive material difficult necessitating a launch into larger scale study of the production of the compound earlier than desired in the development process. The synthesis of smaller particles down to 80 nm was also possible, but the rod shape that was expected was not present, instead spherical particles such as those reported in Chapters IV and V were seen. Compared to the OBR model, particle size was closely targeted by the static mixer reactor, except for the 5.6 mm bore reactor which gave a particle size 200 nm above the target; this was to be expected due to the bigger bore.

The CFD simulation of the static mixers was successfully used as a tool to confirm the importance of using the static mixer reactor for those reactions. More model optimisation needs to be achieved in order to determine the effect of the geometry if, for instance, the two fluids have different properties (density, viscosity) during an anti-solvent reaction. The helical shape of these structures improved the radial mixing significantly and would reduce the size of reactor needed to achieve the same reaction.

Use of the progressive mixer reactor showed that the anti-solvent technique to produce $[FeL_2][BF_4]_2$ [L = 2,6-di(pyrazol-1-yl)pyridine] could reduce and have a better control over particle size and increase in yield. The anti-solvent flow technique with an impinging jet and T-piece was also investigated showing improved results from batch. The next step would be to have a larger reactor capable of bigger volume and concentration without having to worry about blockages. The particles obtained went from *ca.*100 µm in batch to 5-10µm in flow which is really important if the materials are to be incorporated into devices.

The next step of anti-solvent crystallisation in flow has been investigated for thermochromic complexes. The production scale of those materials has been widely expanded from mg scale to gram scale using flow especially in the KRAIC trials. The compounds Ch1 (4-IA 3,5 DNBA), Ch2 (4-IA 3,5 DNBA MeOH) and Ch5 (4-I2MA 3,5 DNBA) first investigated were successfully crystallised in flow using an anti-solvent technique but blocking of the mixer piece for anti-solvent addition occurred. This investigation led to use of anti-solvent flow crystallisation techniques *via* jets for disordered co-crystals 2IA 3,4DNBA, 2CA 3,4DNBA and 2BA 3,4DNBA with success. The particle size of the compound has been reduced and a new morphology of the crystal was observed with hollow shape. This behaviour is not yet understood but could be the precursor element to the reversible colour switching.

The experiments from the previous experiment Chapters give new ways to produce complex materials and are an introduction to Chapter VII where the switching properties of the material produced are investigated.

Chapter VII Switching properties study of materials produced

VII.1. Introduction

In the previous chapters different compounds with switching properties have been produced. The first family of compounds are spin crossover (SCO) compounds which undergo changes in spin state, the second are organic thermochromic compounds which change colour due to proton transfer and a change in molecular packing. The synthesis of SCO compounds $[Fe(Htrz)_2(trz)](BF_4)\cdot H_2O$ (PiC) described in Krober *et al.*[4] and $FeL_2[BF_4]_2$ [L = 2,6-di(pyrazol-1-yl)pyridine] (YeC) described in Holland *et al.*[20] was successfully carried out in different reactors, as reported in other Chapters. For $[Fe(Htrz)_2(trz)](BF_4)\cdot H_2O$ the KRAIC (Kinetically Automated Input Crystalliser), OBR (Oscillatory Baffled Reactor) and Vapourtec helical Kenics® mixer reactors have shown that different particle sizes and morphologies can be obtained by changing the flow and reaction parameters. $FeL_2[BF_4]_2$ has been produced with anti-solvent techniques in a tube-in-tube reactor. For both of these compounds particle size has been of particular interest, as it is reported that, for SCO compounds, particle size has an effect on the switching properties such as event temperature, magnetic properties and energy level with the change of spin state described in Chapter I.[4,13,218,238,241]

The spin transition (ST) of SCO compounds during LS (Low Spin) to HS (High Spin) cycling has been widely studied using SQUID (Superconducting QUantum Interference Device) analysis, Differential Scanning Calorimetry (DSC), Mossbauer Spectra and Differential Thermal Analysis/Gravimetry (DTA/DTG).[3,4,11,13] Described in this chapter is the study of the switching properties of the different SCO particles produced in different environments using DSC, TGA, SQUID and Raman to assess the effect of particle size and shape on the LS-HS state change. Solid form properties of those materials are also described in this chapter – particle sedimentation rate and DSC light scattering properties.[218,242]

The last section focuses on the thermochromic properties of 2-iodoaniline 3,4-dinitrobenzoic (2-IA 3,4DNBA) 2-bromoaniline 3,4-dinitrobenzoic acid (2BA 3,4DNBA) and 2-chloroaniline 3,4-dinitrobenzoic (2-CLA 3,4DNBA) complexes. Those materials have been shown to possess particular crystal morphology that may contribute to the reversibility of the switching effect. The material produced in batch does not show a switching back when cooling back from 80 °C to room temperature but using flow crystallisation reversible switching properties have been achieved.

VII.2. Analysis of $[Fe(Htrz)_2(trz)](BF_4).H_2O$ (PiC) spin cross over behaviour.

$[Fe(Htrz)_2(trz)](BF_4).H_2O$ (PiC) undergoes a change in spin state from low spin (LS) to high spin (HS) when increasing the temperature above 90 °C, changing the colour from pink to white. PiC also displays an enthalpy variation associated with the temperature increase. When cooling back to room temperature the compound typically goes back to white after 70 °C. [4,5] This reversible transition from LS to HS occurs due to a rearrangement of the valence electrons on the metal ions giving rise to the change in material properties (colour, magnetism).[35] The colour change that arises from this transition is of particular interest for potential use in display devices. Alternatively, the change in magnetic properties could be used for data storage. This change can be characterised by

different techniques that are discussed here, including electron diffraction (EDF), Superconducting Quantum Interference Device (SQUID) analysis, Differential Scanning Calorimetry (DSC) and Thermogravimetry (TGA). [218,242]

VII.2.1 Switching difference between processes of $[Fe(Htrz)_2(trz)](BF_4)\cdot H_2O$

In the previous synthesis of PiC using various reactors (Chapters III, IV, V and VI) it was discovered that depending on reaction parameters such as flow rate, concentration of reagent and mixing intensity (frequency and amplitude in the OBR), different particle sizes and shapes of PiC were obtained. Described in this section is the study of the different shapes obtained; these are named as rods, star shaped and sphere as displayed inTable.VII.1.

Table.VII.1 Different particle shapes obtained from PiC synthesis

Shape Type	SEM Image	Reactor Used
Rods	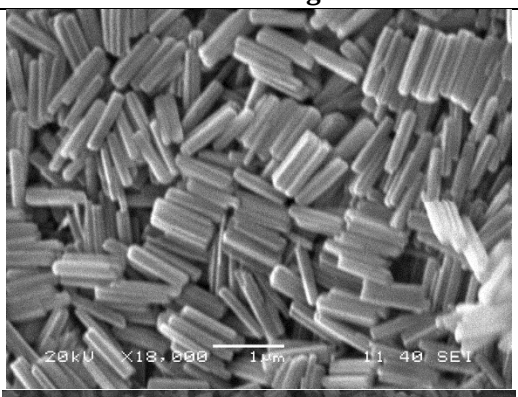	**Vapourtec Static Mixer**
Stars	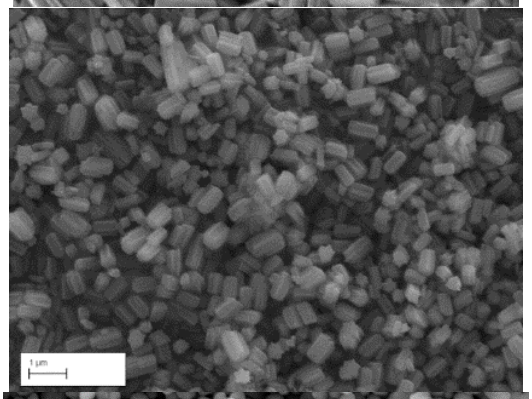	**OBR**
Spheres	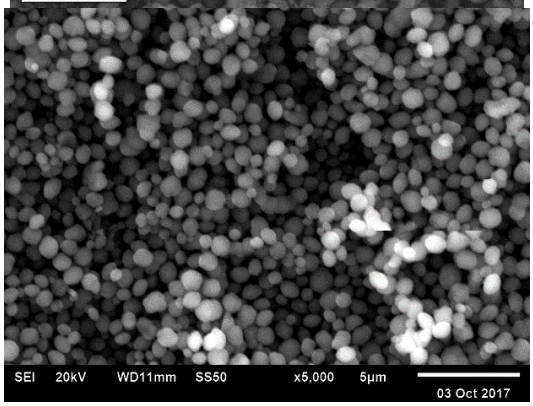	**KRAIC**

Study of the switching behaviour of PiC has been carried out *via* DSC to see the effect of particle size on the temperature range of the change of spin state. Figure.VII.1 shows the DSC comparison between PiC synthesis in batch, the KRAIC, [3] the OBR and the Vapourtec Static Mixer reactor. For all analyses, a heating rate of 2.5 °C/min was used from 20 °C to 140 °C as used by Krober *et al.*[4] It was found that there was a shift in ST temperature when different parameters have been used to produce that compound in different reactors with different flow conditions. It can be seen that a smaller particle size is a factor in faster and earlier switching of the material due to the relatively larger surface area for better heat transfer.[160,243]

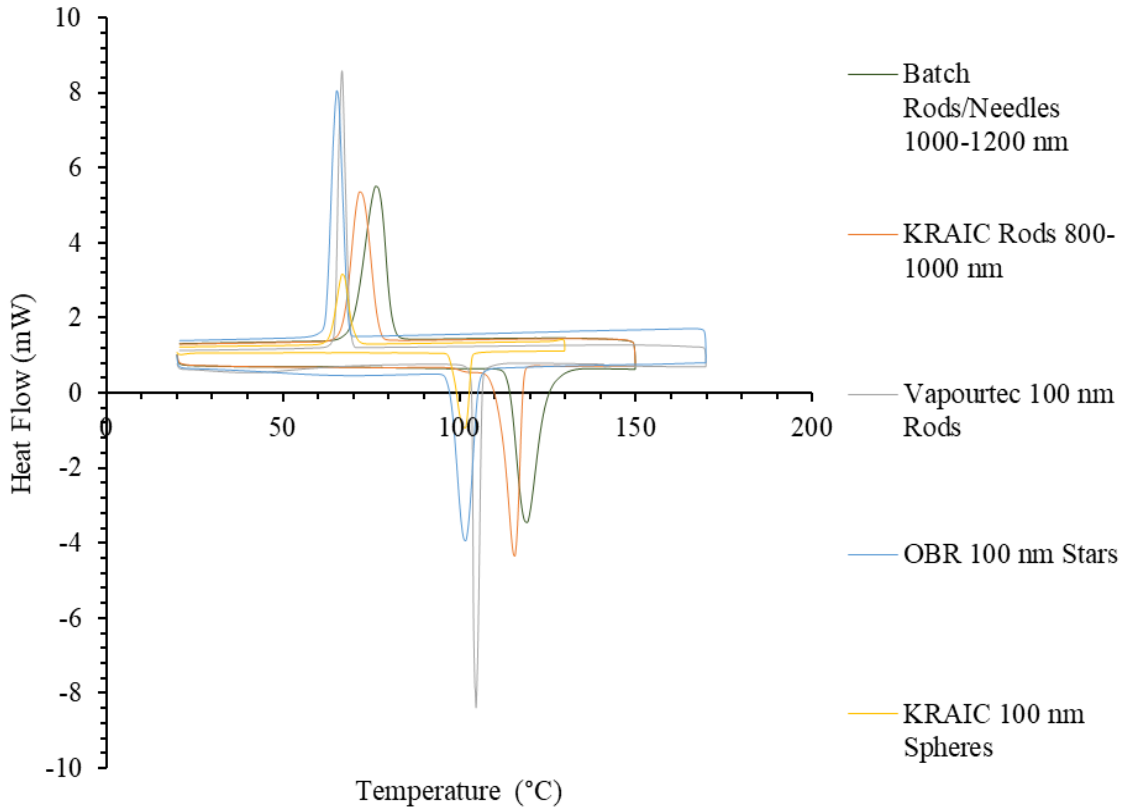

Figure.VII.1 DSC curves of PiC of different particle sizes synthesised in various reactors. Rate of heating/cooling at 2.5 °C/min between 20 °C and 149.85 °C.

On Figure.VII.1 the DSC traces from batch (B2), the KRAIC rod shaped particles (800-1000 nm, K1), the OBR stars (particles of 100 nm), the KRAIC spherical particles (100 nm, PiCKD 7) and the 100 nm rods produced in the 3.2 mm bore static mixer reactor (target 100 nm) are compared. It is seen that the ST loop changes depending on the producing reactor and particle size; for smaller particle size the switching occurs at lower temperatures than is seen for the larger particles. 100 nm particles produced in the OBR show a change from the LS to HS state with an abrupt endothermic peak at 97.5 °C and the change from HS to LS is at 75 °C, lower for the OBR than the other reactors: 114.37 °C; 82.6 °C for the KRAIC rods and 118.15 °C; 87.05 °C for the batch rods needles.

The exo/endothermic peaks are also narrower in the 100 nm rod particles obtained with the Vapourtec Static Mixer (100S), this is interesting for further application of the material, the switching could be faster and more accurate due to the narrow temperature range of the transition. The control over switching properties could be useful for future compounds studied in the Metastable M4 Group. The KRAIC spherical particles have a similar switching behaviour to the OBR stars with a ST at 97.35 °C upon heating and at 73.15 °C upon cooling.

The transition temperatures between the PiC samples produced in the OBR at 100 nm and the 60-165 nm samples evaluated in Moulet *et al.*[218] *via* reverse micelle technique are close to each other. In the OBR sample the LS to HS state has an abrupt endothermic peak at 99.3 °C and the change from HS to LS is at 72.4 °C which is in the range of the literature values. In Moulet *et al.* the sample of 60-165 nm particle size has a LS to HS ST at 95 °C and a HS to LS ST at 76 °C.

In Moulet *et al.* different particle sizes were also obtained. For instance it was reported that smaller particle size had a narrower ST, as discussed in the previous paragraph, in both heating and cooling modes compared to bigger particles (particle sizes 40 to 1200 nm).[218] In the batch sample described

in Figure.VII.1 where particles are bigger and needle-shaped, the LS to HS ST is at 110.3 °C and the LS to HS at 81.3 °C; for Moulet *et al.* these temperatures are at 106 °C and 86 °C for the same range of particle size.

In the literature, the ST transition varies between 92 to 118 °C for LS to HS and 66 to 86°C for HS to LS depending on the particle size. Bigger particles tend to have a LS to HS ST at higher temperature and a HS to LS ST at lower temperature while smaller particles tend to have a lower temperature for LS-HS and a higher one for HS-LS ST.[4,32,35,40,203,244]

For the smallest particle sizes examined, Moulet *et al*[218] describes ST temperatures of 77.85°C (heating) and 98.85 °C (cooling) with particles of 50 nm. The technique in that work used the reverse micelle method which only gives rod-shaped materials, but adds a surfactant coating the rods which could affect the spin state changes. In this thesis work no surfactants were used which could lead to new findings at lower particle size for the PiC compound.

If the switching happens earlier, it requires less heat in order to change the colour or magnetic properties. This has been shown by Letard *et al.* 2004 where a display device is heated up with a certain pattern, pre-printed letters are put behind a screen composed of PiC and upon heating the letters the compounds change from pink to white forming the desired letters.[5]

In some reported cases the DSC analysis (Figure.VII.1) can be affected by different particle sizes present in the same sample. [245] In this experiment (DOE 14), dynamic light scattering (DLS; Figure.VII.3) shows a particle size distribution (PSD) from 91 nm to 615 nm, whereas on the scanning electron microscopy (SEM) image (Figure.VII.3), particles ranging from 450 nm to 550 nm are present. As SEM and DLS only represent a snap shot of a sample, the possibility of having different population among the sample is plausible, which could explain this change in the exo/endothermic peaks on the DSC.

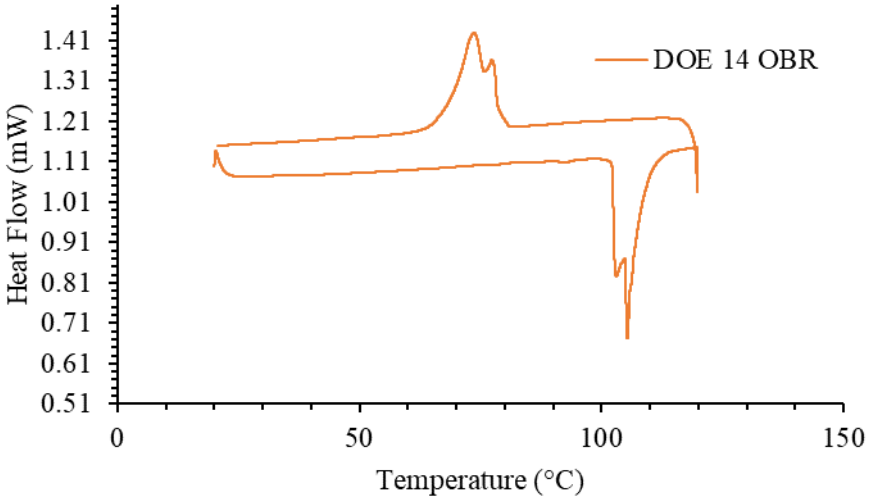

Figure.VII.2 DSC of DOE 14 experiment carried out in the OBR for 2.25 Hz Frequency, 3 mm amplitude, 14 min residence time (RT).

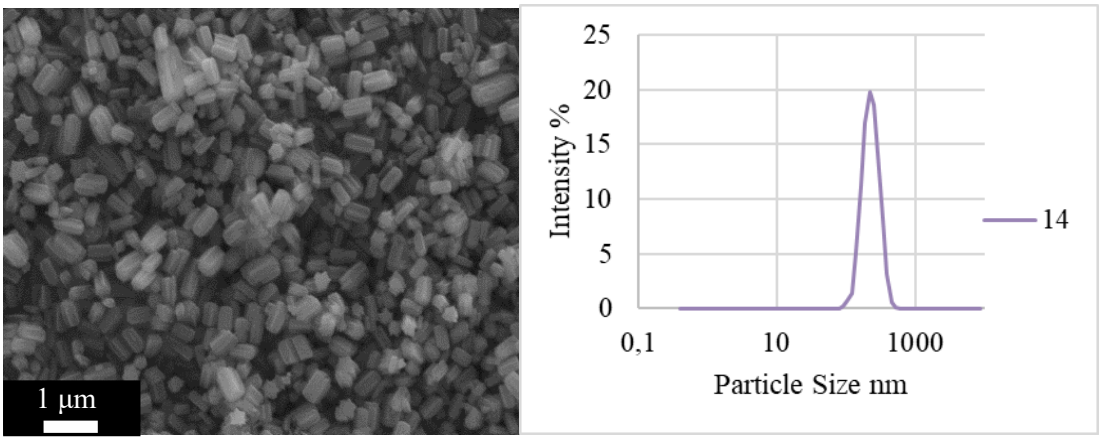

Figure.VII.3 DLS and SEM of DOE 14 corresponding to the DSC in Figure.II.1.2.

Previously the use of stabilizer has been described in Chapter V and showed different particle morphology depending on the stabilizer used. Because the use of stabilizer could have an effect on the switching properties, samples produced with and without polyethylene glycol (PEG) were compared. The use of stabilizer could have a retarding effect on the cooperativity between particles reducing the heat transfer among the sample. In Figure.VII.4 are two graphs of the same PiC produced in the OBR with and without PEG. The stabilizer seems to have an impact on the ST loop, broadening the first endothermic peak and the sample without stabilizer has a HS-LS ST at a lower temperature than with the stabilizer sample (82.3 °C with PEG and 71.5 °C without PEG). During the heating several additional events are present in the sample with PEG at 44.85, 66.85 and 120.85 °C. In Letard *et al.*[218] no change was reported using Tergitol NP9 for the synthesis of PiC on the switching properties. In the case presented here the PEG may be interacting with the PiC product and altered the switching properties or have led to a range of particle sizes or agglomerates (due to capillary action from the surfactant coating) being present. The LS-HS ST peak is at a similar temperature for the samples with or without stabilizer at 113.3 °C with PEG and 115.5 °C without. The Tergitol used in previous studies was not used in this study due to the scale of the reactor and this surfactant being highly corrosive.

Switching longevity of a sample without stabiliser has been tested by DSC analysis at eight months of time interval for PiC produced in the OBR (DOE 14). The change from LS to HS still occurs at close temperature of 118.95 and 118.65 °C for LS to HS and 72.65 and 73.75 °C for HS to LS. The colour change is also still present visually which would be important for future devices. The next step to investigate this would be to design a device capable of repeatedly heating and cooling the compound for a period of time extending the initial month long trials reported by Krober *et al.*

Table.VII.2 details the enthalpy of transition determined from each graph previously introduced in Figure.VII.1, Figure.VII.2, Figure.VII.3, Figure.VII.4 and Figure.VII.5 produced in different platforms (Batch, OBR and KRAIC). Krober *et al.*[4] describe an enthalpy varying between 24 and 27 kJ/mol for the PiC compound produced in small vials of 10 mL. It is seen that the transition enthalpy in the experiments reported here diminishes with particle size depending on which reactor is used and which parameters are employed in the KRAIC, OBR and Vapourtec Static Mixers reactor. Using stabilizers like in Letard *et al.*[218] seems to have the same effect of reducing particle size for the same reactor parameters. If targeting particle sizes with the OBR or the static mixer reactor from Vapourtec is possible then targeting the ST change could be possible also. In experiments conducted to ascertain the longevity of the sample, the switching events still occur at the same temp as it did for the same sample eight months previous but the enthalpy of the event is greater. In all those cases the enthalpy variation is surely related to the particle size effect during the heating process.

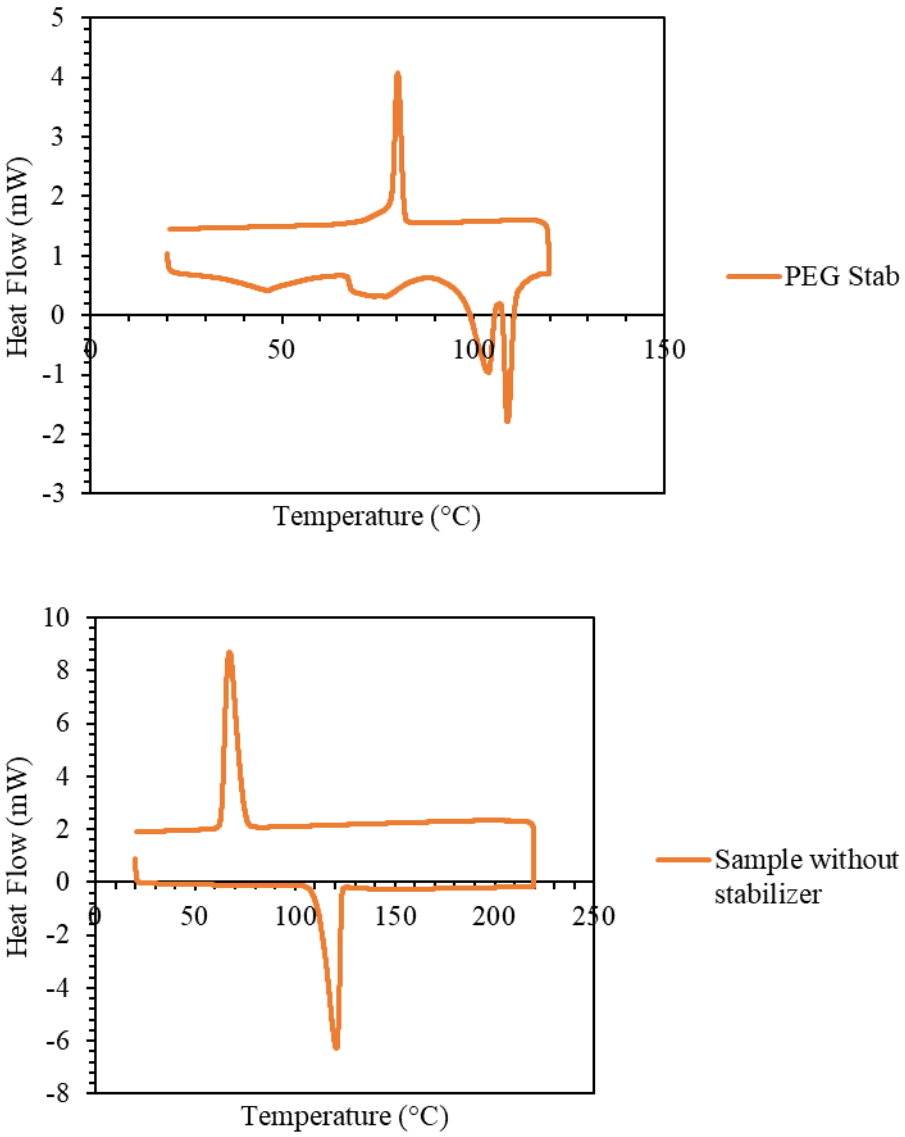

Figure.VII.4 Impact of stabilizer on the change of spin state of PiC using PEG compared to a sample produced in the same conditions without PEG (5.IV.2.(c))

For the Vapourtec samples DSC was obtained on samples presenting rod shaped particles. Samples have been produced using the 3.2 mm and 5.6 mm bore tubing static mixer reactor presented in Chapter VI. In Figure.VII.6, the DSC traces of the two targeted syntheses (using the DOE presented in Chapter VI) for 100 nm particles are displayed showing the change in state temperature. From the graph it can be seen that the 100 nm (±20 nm) particles produced in the 3.2 mm bore reactor switch earlier than the 200-300 nm particles (targeted at 100 nm) produced in the 5.6 mm bore tubing reactor. This shows the same trend as the PiC compound produced in the OBR for 100 nm target; smaller particles display a narrower endothermic peak and an earlier switch: LS to HS, 105 °C for the 3.2 mm bore tubing reactor 100 nm PiC target (100S) and 109.25 °C for the 5.6 mm bore tubing 100 nm PiC target (100B): HS to LS, 73.1 °C for 100B and 70.47 °C for 100S.

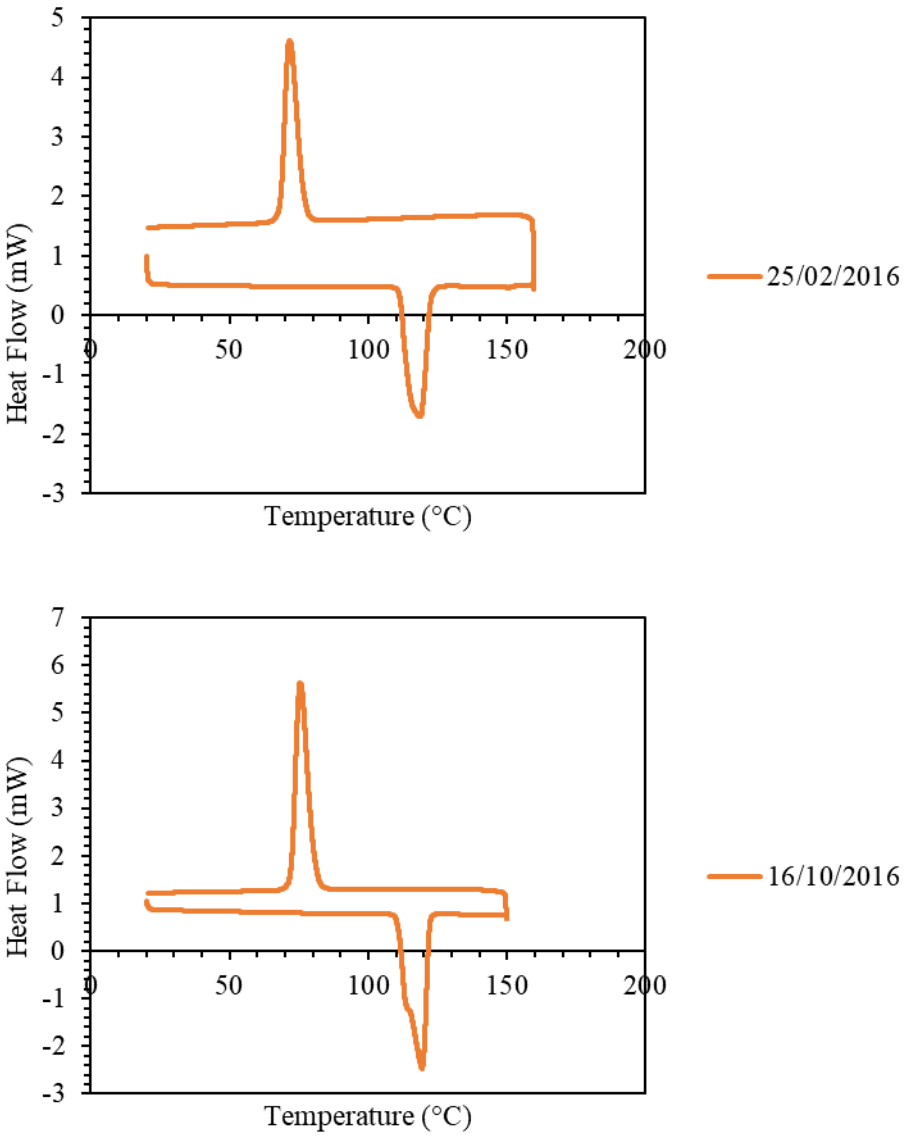

Figure.VII.5 Comparison of the switching behaviour of PiC produced in the OBR (DOE 14) after an interval of time of 8 months.

Table.VII.2 Enthalpy and temperature of spin transition (ST) of PiC obtained from DSC

			1nd ST Heating Temp °C Heating	Heating Enthalpy kJ/mol	2nd ST Cooling Temp °C Cooling	Cooling Enthalpy kJ/mol
Figure. VII.1	**Batch**		76.3	31.51	119.2	30.81
	KRAIC		71.75	26.81	115.67	26.92
	OBR		65.3	25.96	101.79	27.82
Figure. VII.2	**DOE 14 Velocity Ratio**		73.68	13.51	105.37	13.34
Figure. VII.4	**PEG Stabilizer**	**With PEG**	80.27	27.31	108.98	10.72
		Without PEG	74.17	14.28	125.81	14.95
Figure. VII.5	**Longevity of switching**	**1st analysis**	71.52	26.91	71.52	26.41
		8 months after	119.99	29.54	75.44	28.05

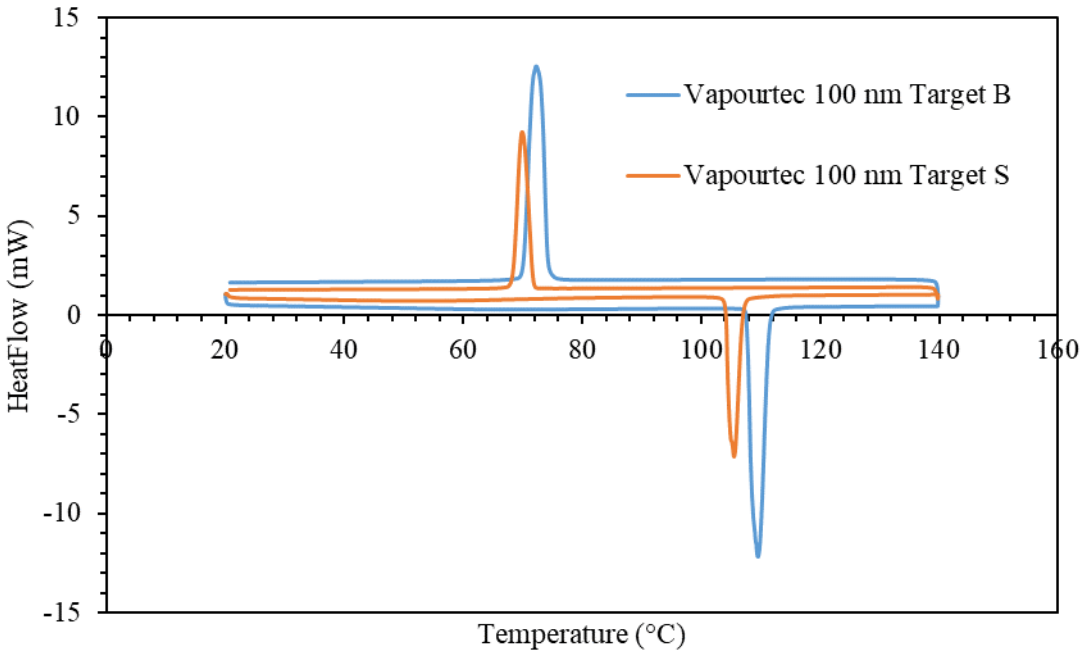

Figure.VII.6 DSC of 100 nm target synthesis of PiC in both static mixer reactor sizes. 100S is from the 3.2 mm bore tubing reactor and 100B from the 5.6 mm bore tubing.

VII.2.2 Magnetic analysis of PiC

To augment the DSC results obtained for the different morphologies, superconducting quantum interference device (SQUID) data were obtained from the University of Kent with Dr Helena Shepherd. SQUID measures the magnetic susceptibility as a function of temperature which can be used to characterize SCO complexes. As SQUID is expensive and intensive for a sample (24 to 48 h measurement for one sample) only the samples with a selected morphology representation of the

rods, stars and sphere were selected from each reactor and analysed (Figure.VII.7, Figure.VII.8 and Figure.VII.9).

The results displayed In Figure.VII.7, Figure.VII.8 and Figure.VII.9 for the different morphologies of PiC particles obtained in the different reactors show the spin transition, as observed through a change in magnetic susceptibility, occurring when increasing and decreasing the temperature. For the OBR star shaped material, the ST starts at 102.85 °C (376 K) and is complete at 110.96 °C (384 K) and during cooling mode at 68.85 °C (342 K) completed at 56.85 °C (330 K). It is observed that the magnetic susceptibility and calorimetry experiments have different results for the rods and the spheres as can be seen inTable.VII.3. For the 100 nm stars the DSC and SQUID results are in close agreement, but the ST observed for the rods and sphere through DSC are at higher temperatures than those observed through SQUID.

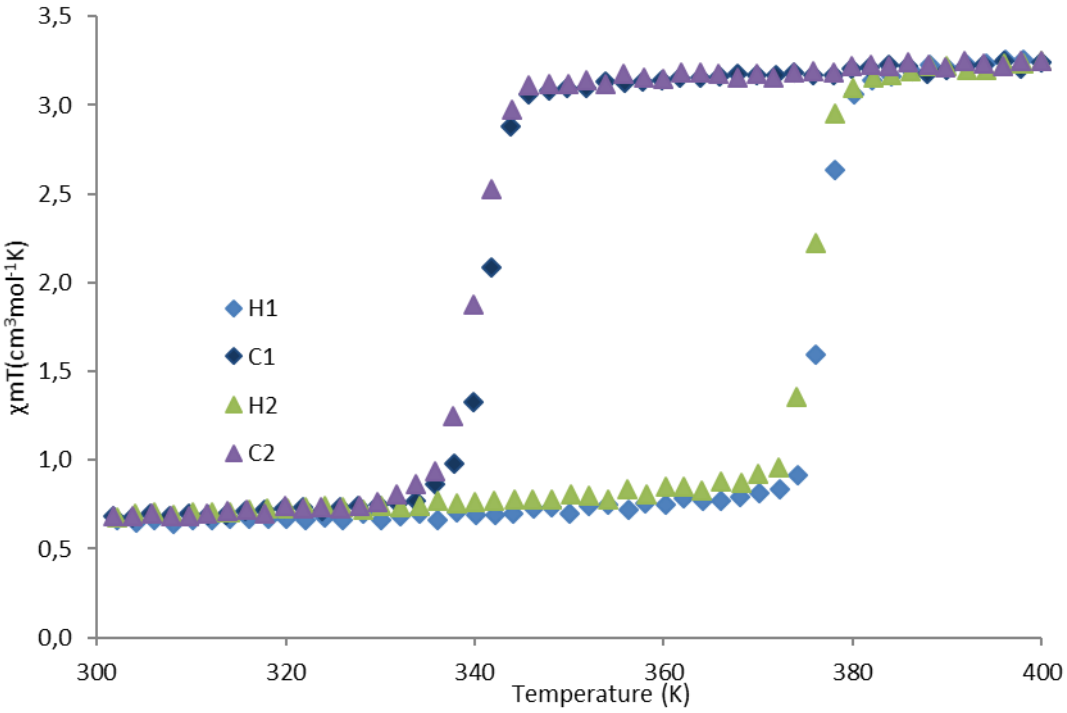

Figure.VII.7 SQUID Data for star shaped 100 nm target particles produced in the OBR: Cycle 1 - LS/HS↑ = 376 K (102.85 °C), HS/LS↓ = 342 K (68.85 °C) -- (Smoothness = Heat – 4 K, Cool – 5 K) – Hysteresis = 34 K;
Cycle 2 - LS/HS↑ = 376 K (102.85 °C), HS/LS↓ = 340 K (66.85 °C) -- (Smoothness = Heat – 3 K, Cool – 5 K) – Hysteresis = 36 K

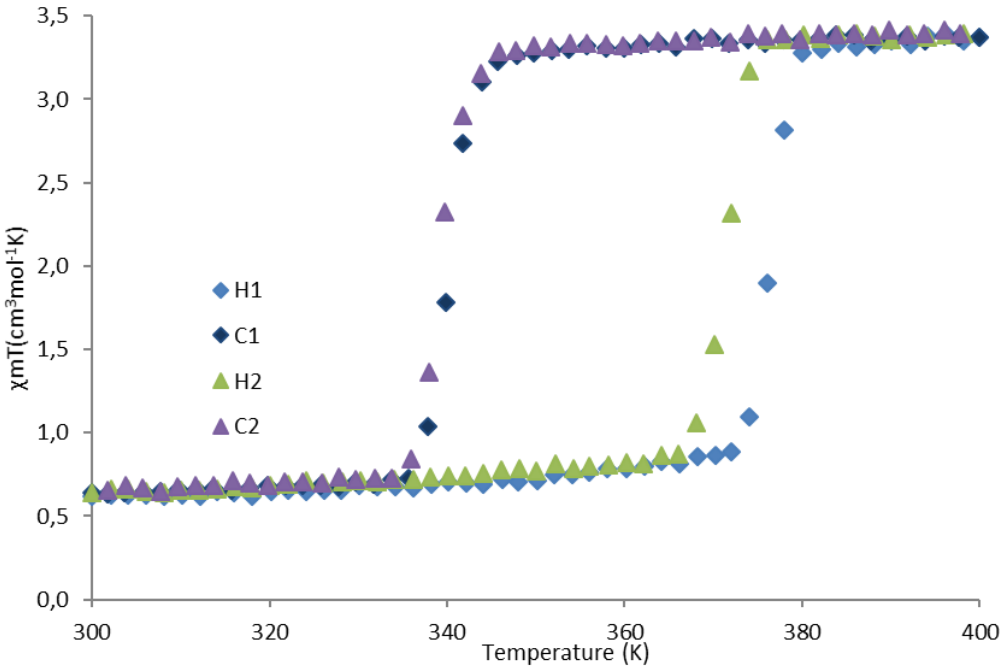

Figure.VII.8 SQUID Data for 100 nm Sphere particles obtained in the KRAIC during beam time experiment 7: Cycle 1 - LS/HS↑ = 377 K (103.85 °C), HS/LS↓ = 340 K (66.85 °C) -- (Smoothness = Heat – 4 K, Cool – 3 K) – Hysteresis = 37 K;
Cycle 2 - LS/HS↑ = 371 K (97.85 °C), HS/LS↓ = 340 K (66.85 °C) -- (Smoothness = Heat – 4 K, Cool – 3 K) – Hysteresis = 31 K

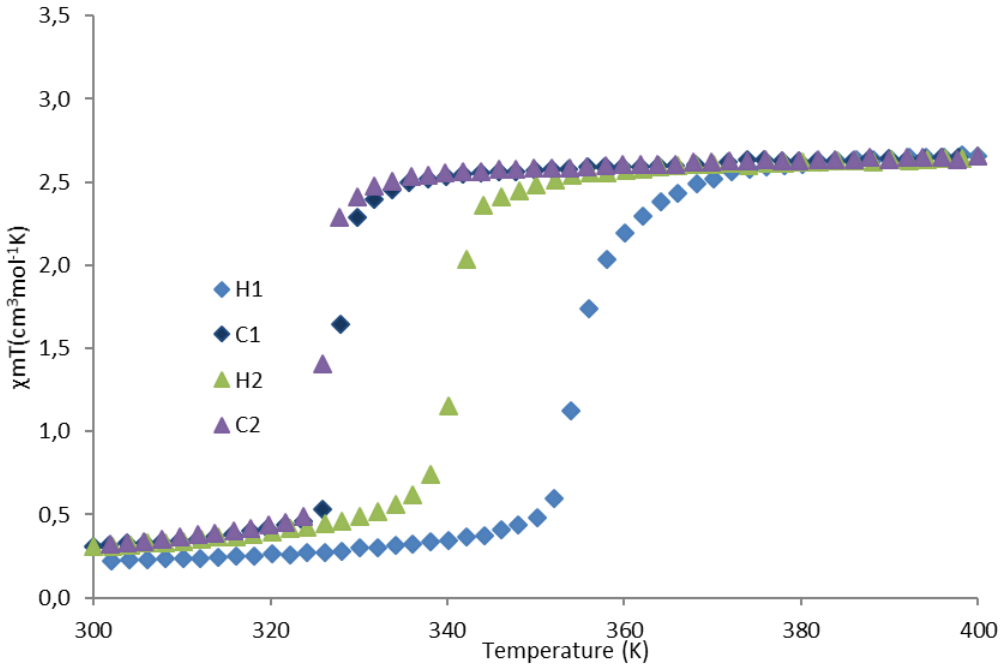

Figure.VII.9 SQUID data of 100 nm rods produce in the small 3.2mm bore tubing static mixer reactor: Cycle 1 - LS/HS↑ = 355 K (81.85 °C), HS/LS↓ = 328 K (54.85 °C) -- (Smoothness = Heat – 8 K (8 °C), Cool – 2 K) – Hysteresis = 27 K:
Cycle 2 - LS/HS↑ = 341 K (67.85 °C), HS/LS↓ = 326 K (52.85 °C) -- (Smoothness = Heat – 5 K, Cool – 3 K) – Hysteresis = 15 K

Table.VII.3 Comparison between DSC and SQUID temperature data for different size and morphologies of PiC obtained.

	Temperature of changes in ºC					
	100 nm Sphere		100 nm Stars		100 nm Rods	
	DSC	SQUID	DSC	SQUID	DSC	SQUID
LS/HS	115.6	102.85	101.3	103.85	104.3	81.85
HS/LS	73.03	68.85	65.83	66.85	66.94	54.85
Hysteresis	31	34	34	37	29	27

The SQUID data show a similar behaviour for the spherical particles obtained with the KRAIC (Figure.VII.1) as the star shaped compound produced in the OBR. For the KRAIC data, the ST upon heating starts at 103.85°C (377 K) and finishes at 108.85 °C (382 K) and during the cooling mode at 68.85 °C (340 K) and 58.85 °C (332 K) which is close to that obtained for the OBR star shape compound.

A 100 nm sample of rod shaped particles produced in the 3.2 mm bore tubing static mixer reactor was analysed by SQUID (Figure.VII.9). Compared to the KRAIC spherical 100 nm particles and the OBR star shaped 100 nm particles of PiC, there is a large difference in magnetic behaviour. The trend in magnetic susceptibility as a function of temperature is more similar to that expressed by $[Fe(Htrz)_3](BF_4)_2 \cdot H_2O$ (PiCM), the other phase produced from synthesis in methanol, as described in Krober *et al.* [4]. Here the magnetism changes from LS to HS at 81.85 °C (355 K) and undergoes the reverse transition at 54.85 °C (328 K), which is 20°C lower than the ST temperatures of the samples produced in the OBR or KRAIC reported above. It is also noted that the second cycle carried out on the rod sample Figure.VII.9 showed a lower LS to HS ST at 66.35° (339.5 K) but the same HS to LS ST temperature. This behaviour also deviates from the DSC analysis discussed previously, which showed comparable behaviour to the star shaped particles from the OBR (DOE 14). The rods sample (100S) was analysed by PXRD three times to check for a phase change through aging after two months between PXRD and SQUID analysis. The patterns displayed in Figure.VII.10 confirm that PiC was produced during the synthesis inside the static mixer reactor.

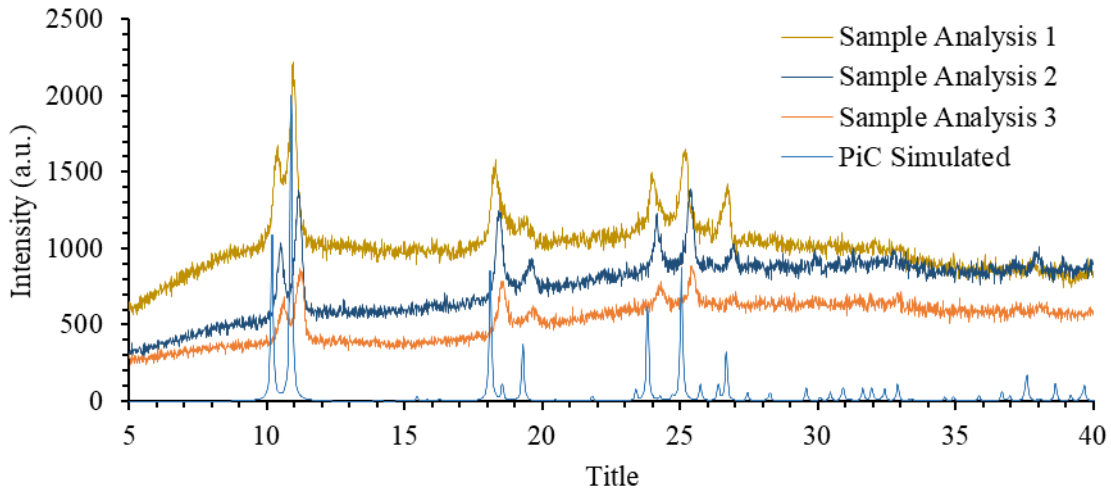

Figure.VII.10 PXRD of 100S sample used for SQUID analysis compared to simulated data of PiC.

The differences observed between the SQUID analysis and the DSC would need a full study of each sample produced in the Static Mixer reactor from Vapourtec to allow any trends to be determined. In these samples (OBR, Vapourtec, KRAIC) the ST is likely to be affected by the particle size. Due to the size of the crystallites, a crystal structure analysis would be difficult to achieve to study the ST of the different morphologies. If bigger crystals presenting the same morphologies as discussed above could be grown and analysed it would be useful to understand this behaviour. The bond strength between the aromatic N of the triazole and Fe may be affected with the nature of the PiC particles. With the structure of PiC from Grosjean *et al.*[39] it is possible to determine the distance of the metal-ligand bond Fe-Trz in the matrix; this distance is 2.192 Å. In the case of an increase of length of this bond the ligand field distance Δ will vary and affect the temperature needed to achieve the ST. In section VII.2.3 below a slow crystallisation technique will be proposed, along with a crystal structure for PiC.

VII.2.2.ii Conclusion on ST behaviour of PiC

For the samples presented here it is clear that the size of the particle has an impact on the switching properties of the Fe^{II} spin states of $[Fe(Htrz)_2(trz)](BF_4)\cdot H_2O$. It showed that with smaller particle sizes for this compound the switching happens at a lower temperature than for bigger particles presumably due to the high surface contact of those at a nanoscale. On the other hand, the morphology of the particles does not seem to have a significant effect of the spin transition. DSC is bulk analysis technique, on several mg of the powder, and further analysis *via* Synchrotron X-ray diffraction and Electron Diffraction (EDF) will be presented to gain further information on the change of spin states at the microscopic scale, in the next sections.

VII.2.3 Slow crystallisation of $[Fe(Htrz)_2(trz)](BF_4)$ H_2O to obtain bigger crystals

It is difficult to obtain a single-crystal structure from PiC from flow or standard batch production due to the nano-sized particles which result. A structure was obtained in literature from powder X-ray diffraction for the LS and HS state of the material but not from a single crystal. [14]

In this section slow, diffusion crystallisation was implemented in 10 cm FEP tubing and standard nuclear magnetic resonance (NMR) tubes with different concentrations to obtain bigger crystals of PiC. Parameters of those experiments are displayed in Table.VII.4. In both methodologies (FEP / NMR tube) the two reagents are separated by a buffer of pure solvent (water) through which the solute ions diffuse (Figure.VII.11). Both reagents enter in contact in the middle of the tube inducing slow crystallisation.

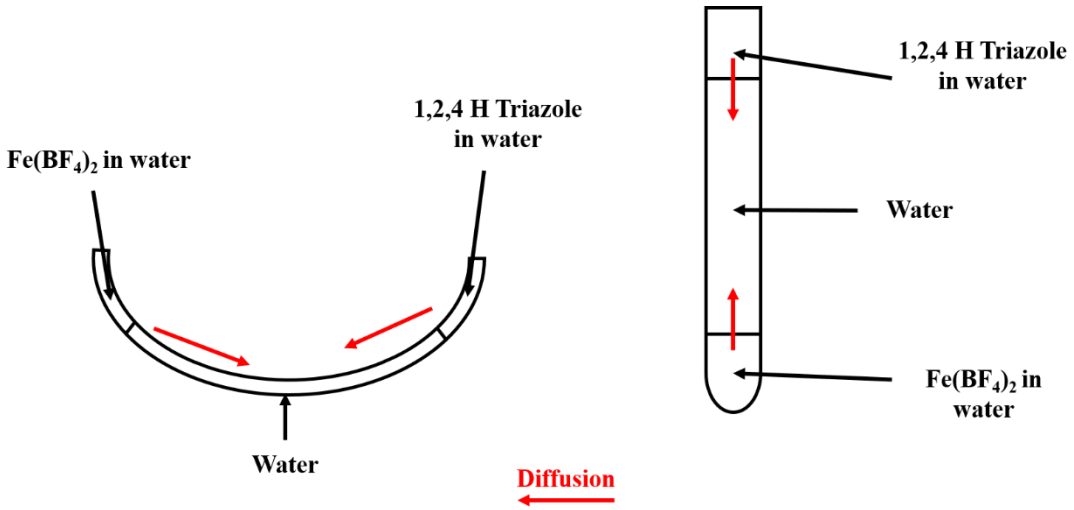

Figure.VII.11 Scheme of diffusion crystallisation in the FEP tubing (left) and the NMR tube (right).

Table.VII.4 Parameters of concentration used for PiC synthesis in FEP tubing and NMR tubes

2,5 mm bore tubing	1,2,4 H triazole concentration (g/mL)	Iron (II) Tetrafluoroborate Hexahydrate concentration(g/mL)
BT 1	0,1071	0.1079
BT 2	0,1078	0,057
BT 3	0.0634	0,1079

1 mm bore tubing	1,2,4 H triazole concentration (g/mL)	Iron (II) Tetrafluoroborate Hexahydrate concentration (g/mL)
LT 1	0,1071	0.1079
LT 2	0,1078	0,057
LT 3	0.0634	0,1079

NMR Tube (3 mm bore)	1,2,4 H triazole concentration (g/mL)	Iron (II) Tetrafluoroborate Hexahydrate concentration (g/mL)
NMRT 1	0,012	0,137
NMRT 2	0,041	0,036
NMRT 3	0,023	0,07

From those experiments small needle crystals of dimension greater than 2 µm were obtained and these were analysed by Dr Harriott Nowell, Diamond Light Source Beam Line I19. For the sample from NMR tube 3 (NMRT3) experiment a partial crystal structure was obtained and helped give a better understanding of the material.

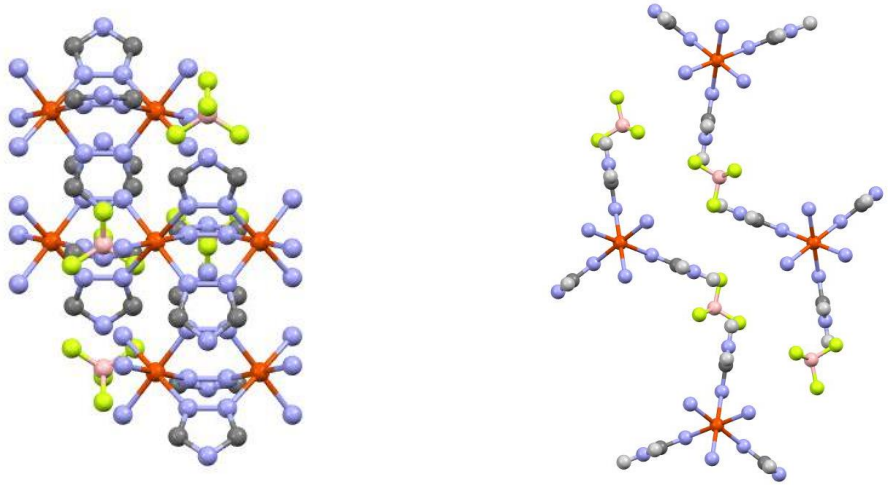

(a) (b)

Figure.VII.12 Partial Crystal Structure obtained at Diamond Light Source Beam Line I19, viewed down (a) direction [100], (b) direction [010].

Table.VII.5 Crystal parameters comparison from obtained PiC structure and literature.

Crystal Parameters	PiC Structure from slow crystallisation	PiC Structure from Grosjean *et. al*[39]
a	17.3474(16) Å	17.2853(15) Å
b	7.3247(6) Å	7.2975(6) Å
c	9.1907(9) Å	9.1261(10) Å
α	90°	90°
β	90°	90°
γ	90°	90°

The single crystal structure obtained here has very similar crystal parameters to that reported by Grosjean *et al.*[14], derived from powder XRD. In this case a rod shape like material was obtained with the diffusion technique. This structure confirms the potential use of slow diffusion crystallisation techniques to obtain bigger crystals of $[Fe(Htrz)_2(trz)](BF_4)$. The CIF file of this structure is given as a supplement to this thesis in **CDCh7-3.**

VII.2.4 Thermogravimetric analysis(TGA) of $[Fe(Htrz)_2(trz)](BF_4).H_2O$

As reported in Manrique-Juárez *et al.*[13], during the change of spin state monitored by Atomic Force Microscopy (AFM) the size of the PiC particles increases in size in the nanoscale realm during the spin transition. Differential thermogravimetry (dTG) was carried out on three different samples obtained in different reactors (OBR, KRAIC and Vapourtec Kenics mixers). The OBR sample DOE 14 is the one studied in Figure.VII.13 for the star shaped particles, the rod shaped particle obtained in the static mixer reactor from Vapourtec (ST-100nm) in Figure.VII.14 and the KRAIC PiCKD-7 is the sphere type particles analysed in Figure.VII.8. Samples were heated up to 180 °C with a 2.5 °C/min rate to concord with heating ramp of the DSC analysis of the same samples. The 180 °C maximum temperature was chosen to be able to see any change during the spin state change of the samples. The dTG and DSC data are displayed in Figure.VII.13, Figure.VII.14 and Figure.VII.15.

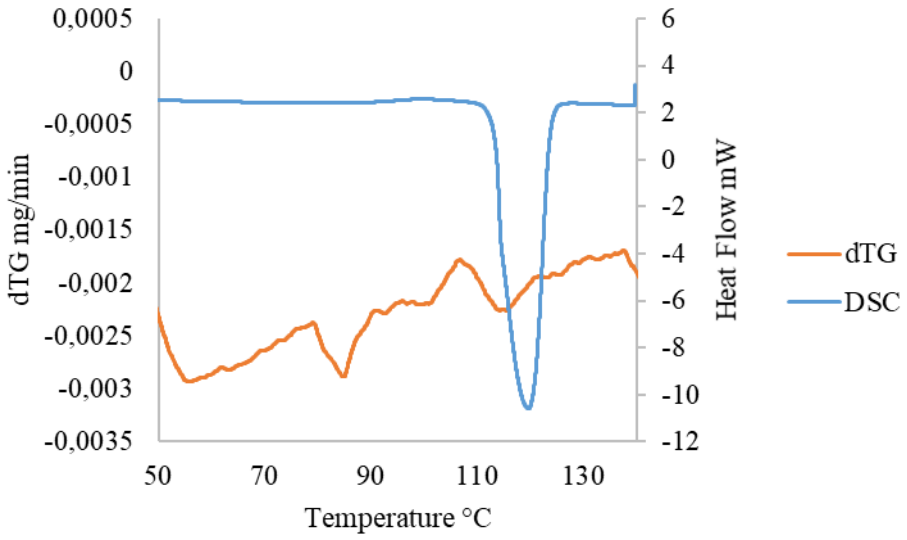

Figure.VII.13 dTG and DSC at 2.5°C/min for DOE 14 Star Shaped PiC materials (parameters: 2.25 Hz Frequency, 3 mm Amplitude, 14 min residence time).

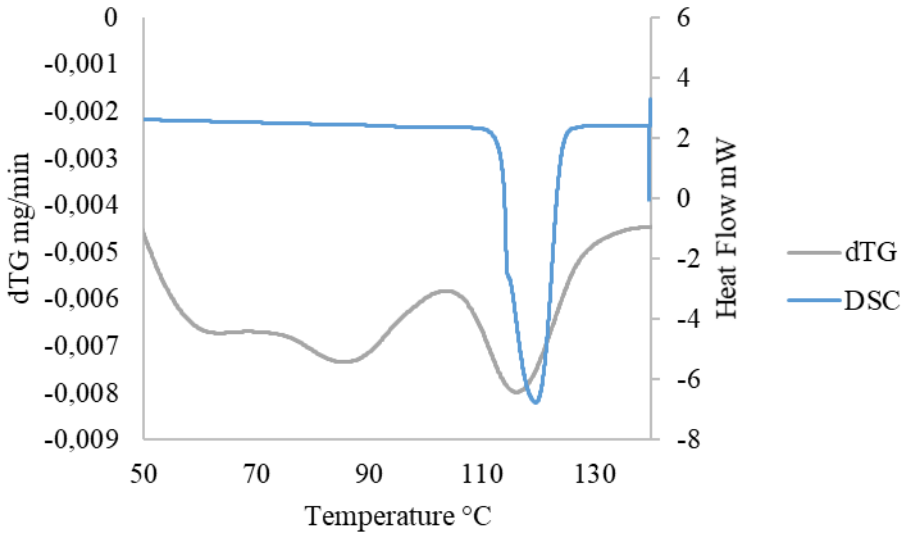

Figure.VII.14 dTG and DSC at 2.5°C/min for Vapourtec Kenics, 100 nm target, 100 S mixers, rod shaped PiC particles obtained in the 3.6 mm bore tubing, 12.56 mL/min flow rate.

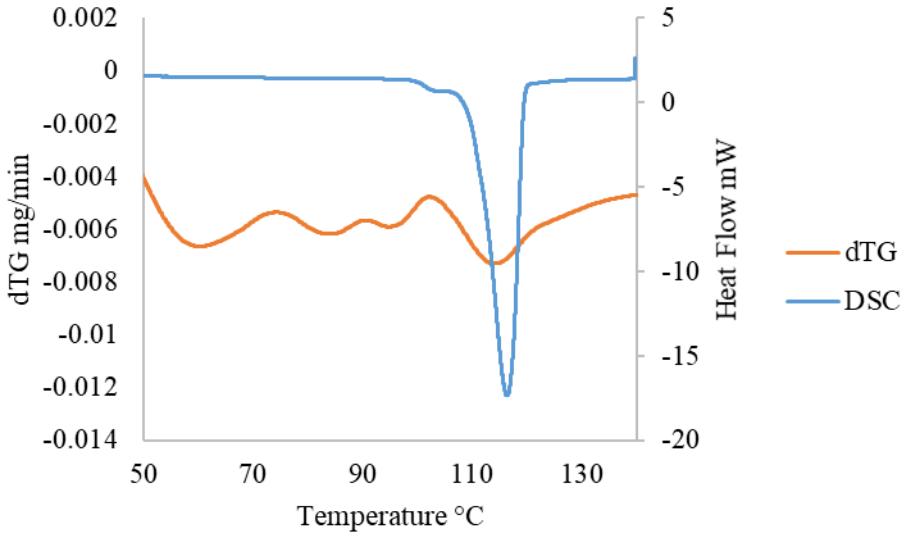

Figure.VII.15 Figure.II.4.2 dTG and DSC at 2.5°C/min for KRAIC-D PiCKD 7 sphere shaped particles of PiC.

As can be seen from the TGA graphs obtained, a discrete event is seen when the spin state change for the KRAIC and Vapourtec samples. For the OBR sample, the event in the dTG cannot be clearly distinguished. During the whole heating process each sample was losing mass over time. Figure.VII.16 shows the loss of mass during TGA of each sample. The graph shows the same event happening for the KRAIC (101-126°C), OBR (91-111 °C) and Vapourtec (97-121°C) samples. As reported in Manrique-Juarez *et al.*[13] during AFM analysis the size of the nano rods increases when changing spin states. The difference of placement of this event could be due to the particle size difference of each samples, the KRAIC being in the range of 100 nm (PiCKD 7), the OBR of 450 nm and the Vapourtec of 100 nm; this could be why the KRAIC and Vapourtec sample have similar event ranges. Comparing to the DSC and SQUID, the TGA data are closer to the DSC results for the LS to HS ST, which is to be expected for similar techniques with event happening at 111.2 °C for the sphere, 109.3 °C for the rods and 105.6°C for stars.

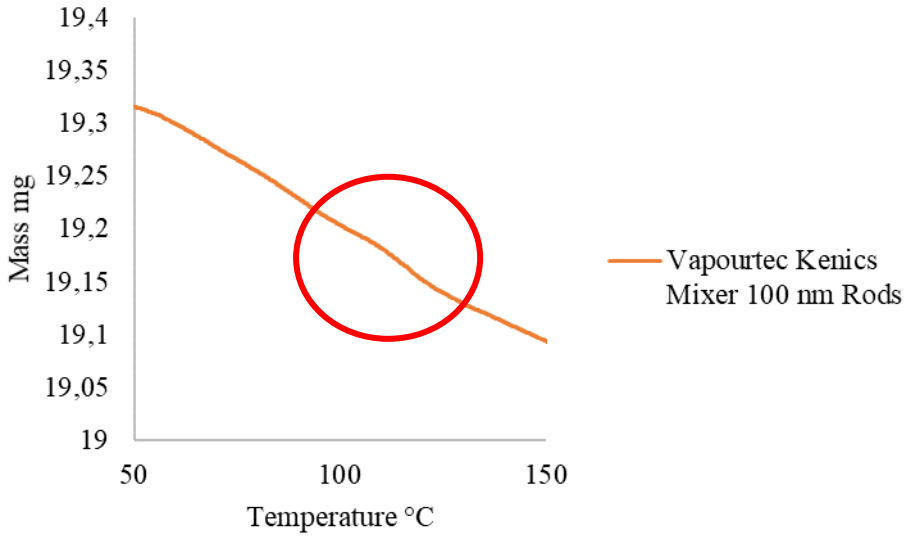

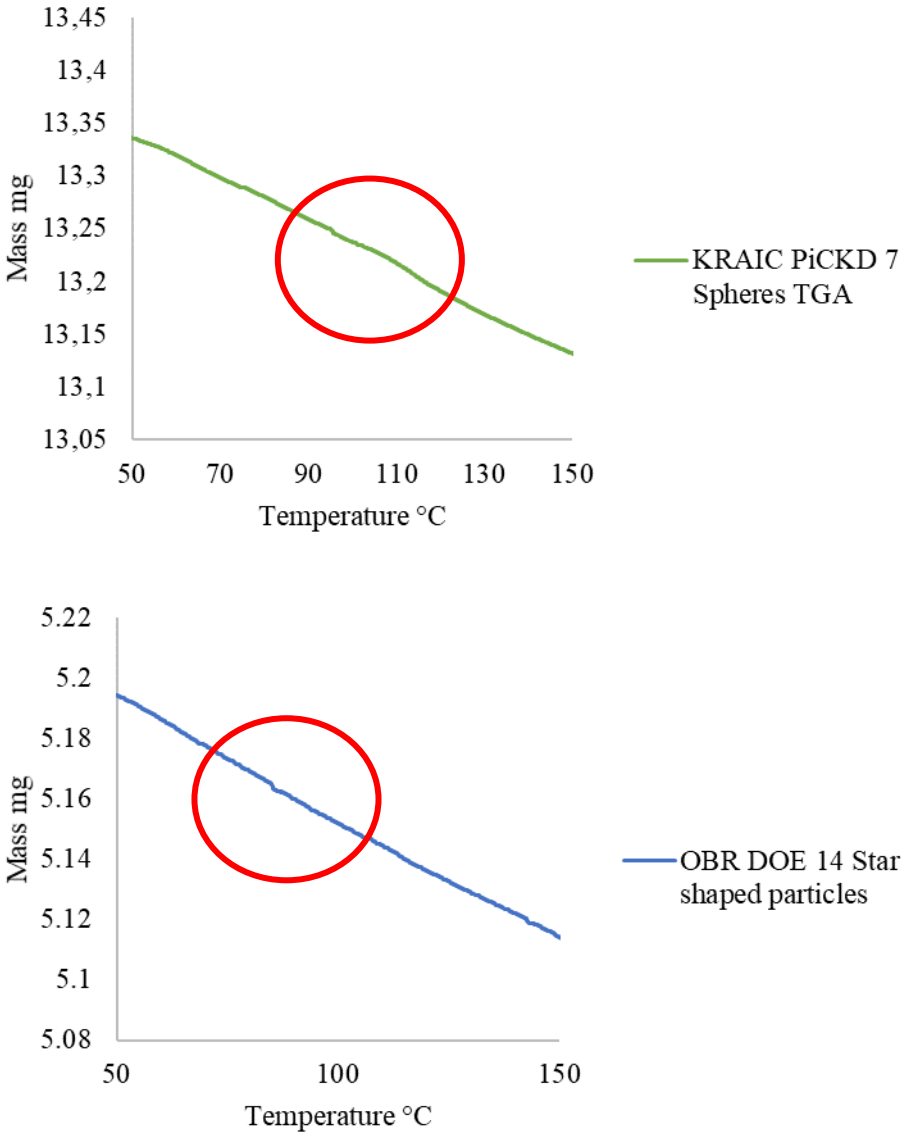

Figure.VII.16 TGA Analysis of PiC samples produced in the different reactors, Vapourtec Kenics Mixer Rods (top), KRAIC spheres (middle), and OBR stars (bottom).

VII.3. Raman powder analysis of $[Fe(Htrz)_2(trz)](BF_4)\cdot H_2O$

In this section Raman spectroscopic analysis of PiC is presented which will complete the study carried out in Chapter IV with the *in situ* Raman analysis in the KRAIC. It is reported in Urakawa *et al.* and Guillaume *et al.* that $[Fe(Htrz)_2(trz)](BF_4).H_2O$ in powder form shows changes in Raman spectra upon changing between HS and LS states due to the bonding properties as described in Chapter IV. [35,36] To study the effect of the spin change during the increase of temperature the set-up depicted in Figure.VII.17 was created.

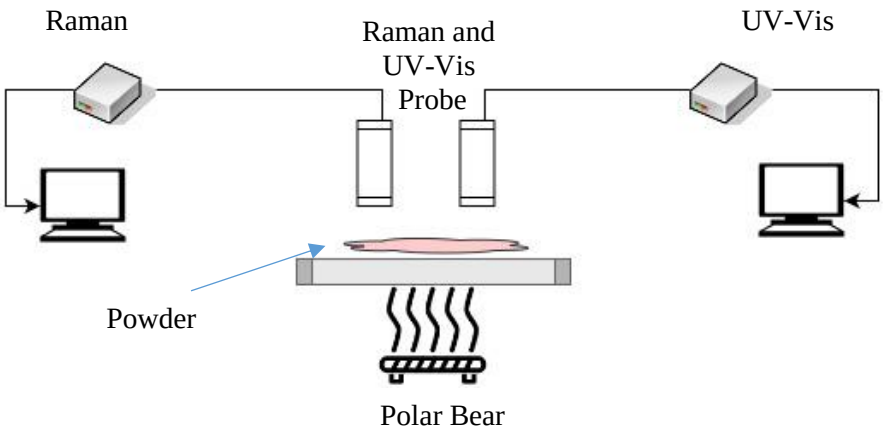

Figure.VII.17 Set-up scheme for investigating the spin state changes of PiC with changing temperature.

Table.VII.6 Parameters from the synthesis of PiC samples in batch and in flow, analysed under Raman

	Concentration $Fe(BF_4)_2 \cdot 6H_2O$ (g/100mL)	**Concentration 1,2,4-HTrz (g/100mL)**	**Frequency (Hz)**	**Amplitude (mm)**	**Residence time (min)**
Flow OBR DOE 14 (FOD14)	5.847	10.793	2.25	3	14 min
Batch DOE 14 (BOD14)	5.847	10.793	/	/	14 min

The set-up consists of using a Cambridge Reactor Design Polar Bear Plus to control the temperature of the $[Fe(Htrz)_2(trz)](BF_4) \cdot H_2O$ powder (the temperature rate was set 2.5 °C/min) and a RamanRXN1® spectrometer from Kaiser Optical Systems to inspect the Raman spectra of the compound during the change of switching. The change between LS and HS was monitored simultaneously by an Ocean Optics Maya2000Pro UV-Vis spectrometer. Two different powder samples were analysed. One was produced in batch (BOD14) with stirring with a concentration of 5.847g/100 mL of iron (II) tetrafluoroborate hexahydrate and 10.793 g/100 mL of 1,2,4 triazole. With the same concentrations the flow sample was produced with the OBR with the DOE 14 parameters (FOD14).

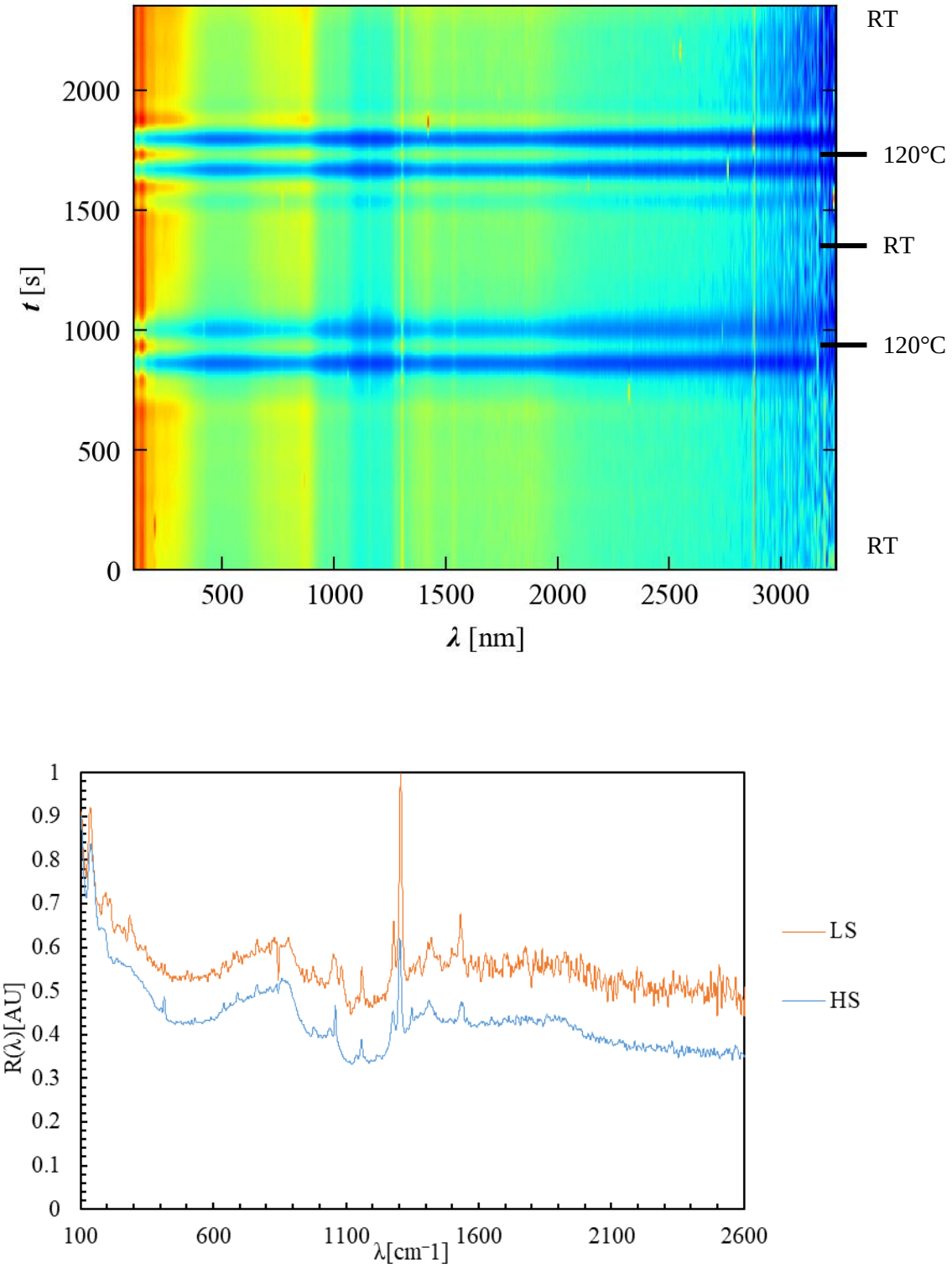

Figure.VII.18 Raman spectra from BOD14 sample of PiC produced with 5.847 g/100mL of iron (II) tetrafluoroborate hexahydrate and 10.793g /100mL of 1,2,4 triazole: (top) temperature cycling Raman spectra; (bottom) individual Raman spectra for LS and HS states.

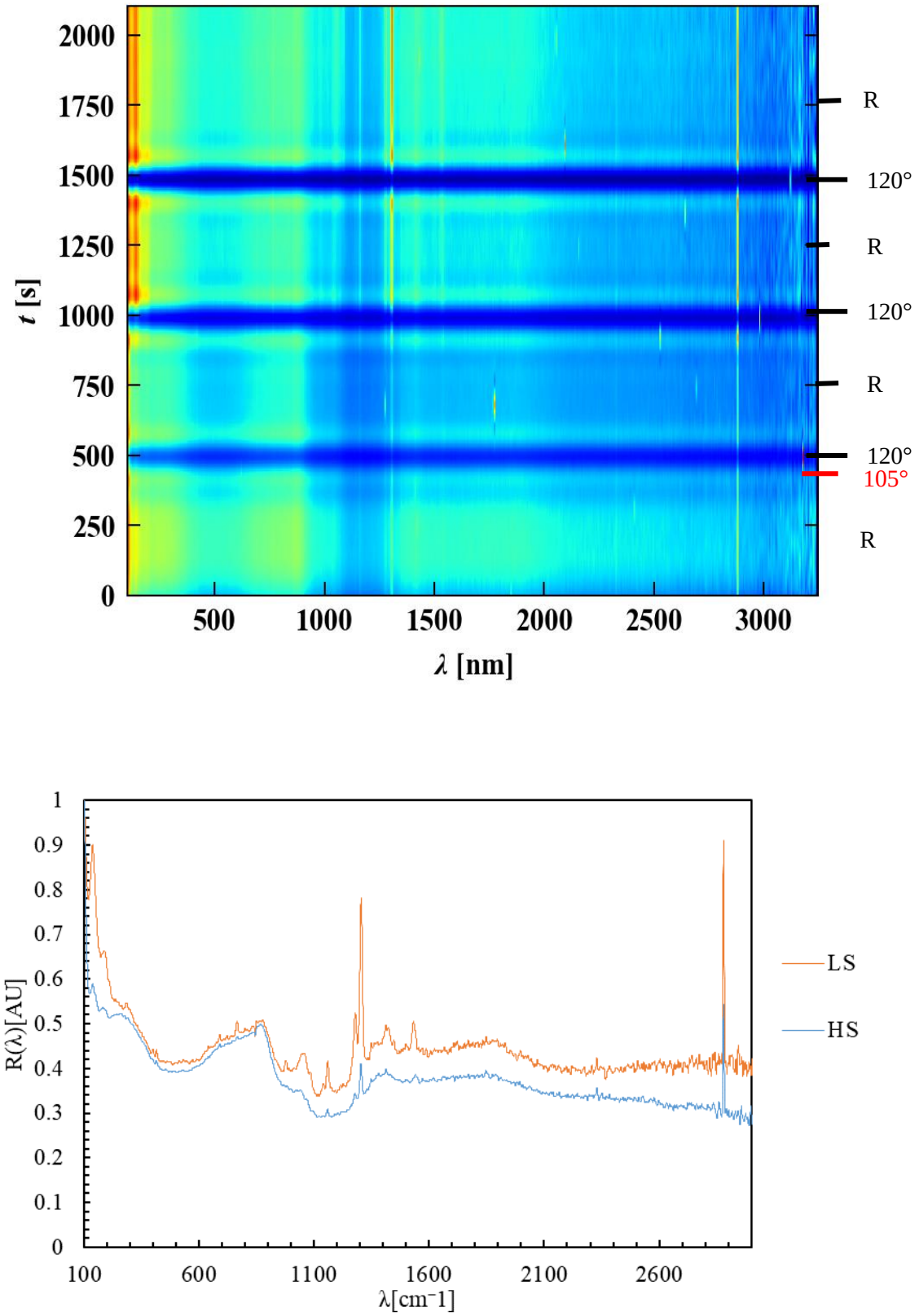

Figure.VII.19 Raman spectra from FOD14 sample of PiC (parameters: 2.25Hz Frequency, 3 mm amplitude, 14 min RT, 5.847g/mL $Fe(BF_4)_2$ $.6H_2O$ and 10.793 g/mL 1,2,4 H Triazole): (top) Raman spectra under heating for 3 cycles; (bottom) individual Raman spectra for LS and HS states.

As can be seen on Figure.VII.18 and Figure.VII.19 the Raman spectra show that at 105 °C the intensity of the spectra diminishes upon transition into the HS state as expected for this compound. Several cycles for both batch and flow synthesis experiment in the OBR show the change in spin states during the heating up process and shows a fast change in that switching. In the graph several peaks disappear from LS to HS ST from samples produced in batch and flow as can be seen in Table.VII.7.

Table.VII.7 Raman peaks that disappear on the transition from LS to HS for PiC during heating process.

Peak (cm^{-1})	
Batch	**Flow**
1052	1221
1087	1179
886	982
650	

Compared to the Chapter IV *in situ* Raman study, some values appear to be similar to the initial white phase or 1,2,4 H triazole, like the 1087 cm^{-1} and 1179 cm^{-1}, peak which could correspond to a CH bending mode and a ring breathing mode. The 982 cm^{-1} and 650 cm^{-1} peaks may correspond to a ring bending mode and a ring torsion respectively in the LS state and are distinctive from the HS state. The bond lengthening could potentially increase the size of the particle as described in Manrique-Juárez *et. al* during AFM.[13]

Throughout the experiment the colour and temperature of the compound was corresponded to the Raman spectrum and in both samples analysed the compound turned white (transition to high spin state) during the heating up process at 105 °C.

A DOE 14 sample was also analysed *via* UV-Vis to check the changing from LS to HS (Figure.VII.20). This experiment was done prior to the Raman analysis previously done on the same sample.

The ST change was detected successfully with the colour absorbance changing after 1500 seconds of heating at 92.2 °C (from Polar Bear probe) which corresponds closely to the transition temperature from DSC previously effected on the same sample at 91.3 °C (Figure.VII.2).

In Chapter IV a Raman probe installed at two positions in the KRAIC was used to analyse the reaction step of the synthesis of $[Fe(Htrz)_2(trz)](BF_4)\cdot H_2O$. It has been seen that different spectra were obtained at the different positions of the light box in the KRAIC. Here is described the same procedure but instead of flow synthesis $[Fe(Htrz)_2(trz)](BF_4)\cdot H_2O$ synthesis was done in a petri dish by pouring each reagent on the far sides of it and allowing them to diffuse slowly together. The reaction was monitored by UV-Vis Reflectance and Raman as for the temperature cycling studies in the above section. The set-up is described in Figure.VII.21 and results are displayed in Figure.VII.23, Figure.VII.22 and Figure.VII.24.

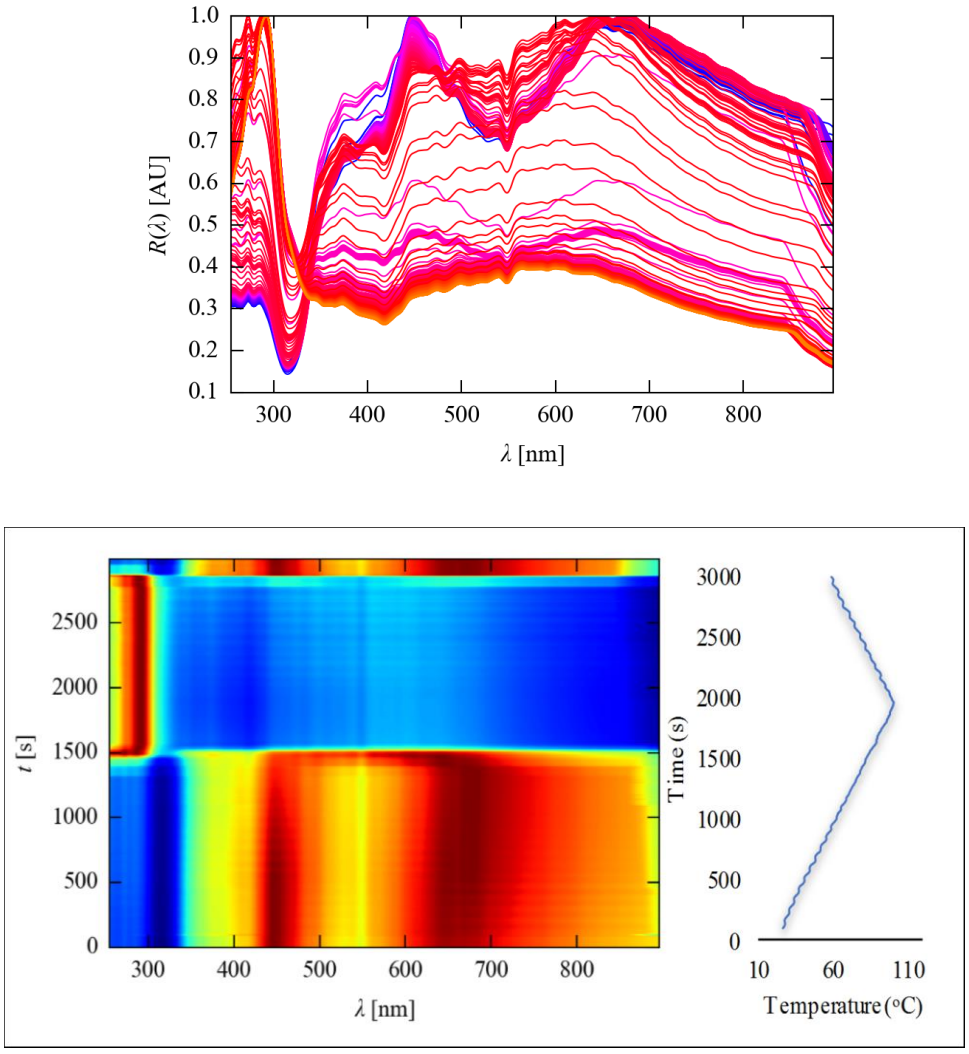

Figure.VII.20 UV-Vis analysis for one cycle LS to HS of $[Fe(Htrz)_2(trz)](BF_4)\cdot H_2O$ produced in DOE14 sample (2.25Hz Frequency, 3 mm amplitude, 14 min RT). (top) UV-Vis graph obtained over time, (bottom) the combination of these graphs *versus* time.

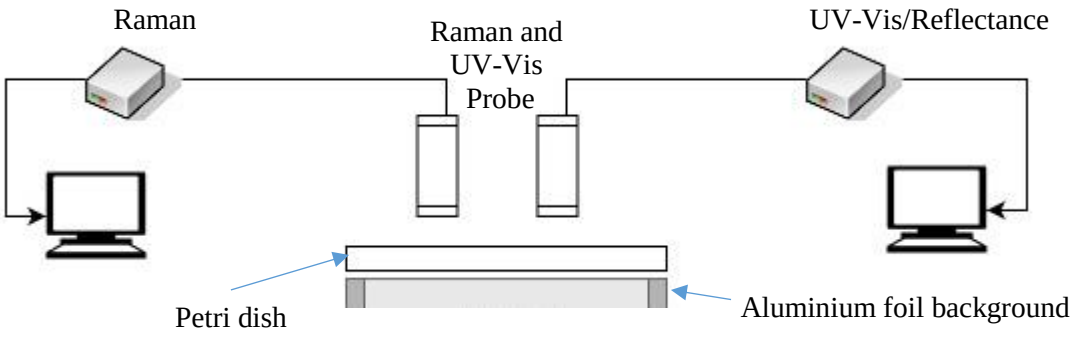

Figure.VII.21 Scheme of the petri dish experiment (PDE) for PiC synthesis.

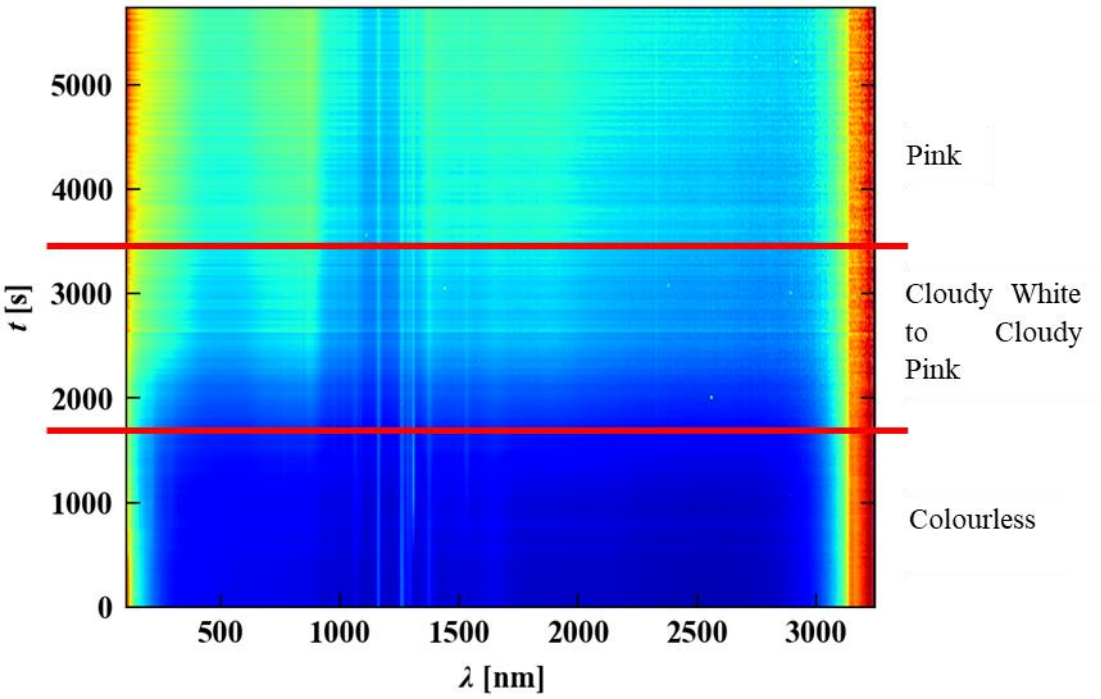

Figure.VII.22 Combined Raman Spectra showing the difference between the different stages of the reaction.

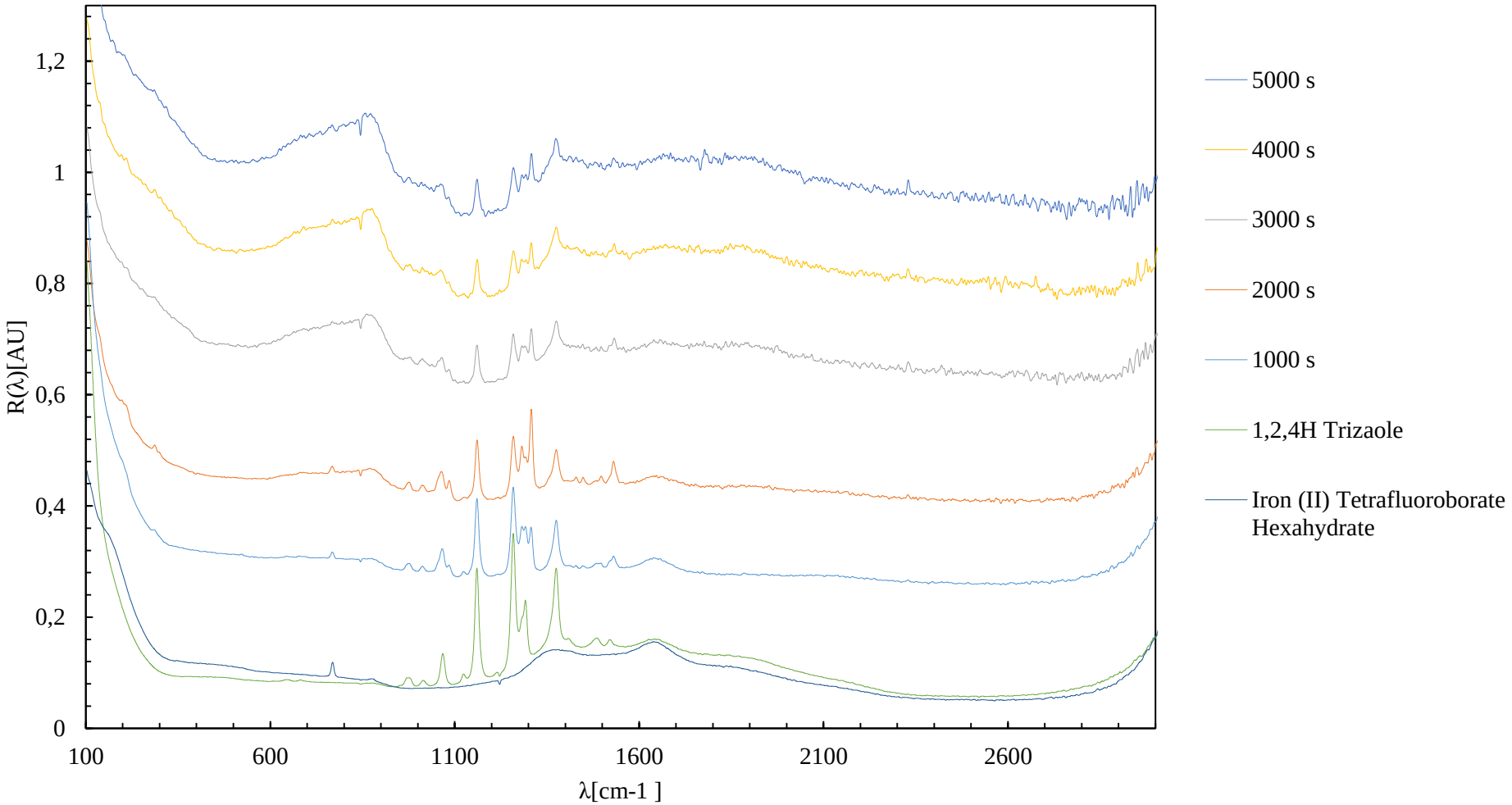

Figure.VII.23 Raman spectra of PDE with single Raman spectrum taken at different time step and comparison with reagent spectra.

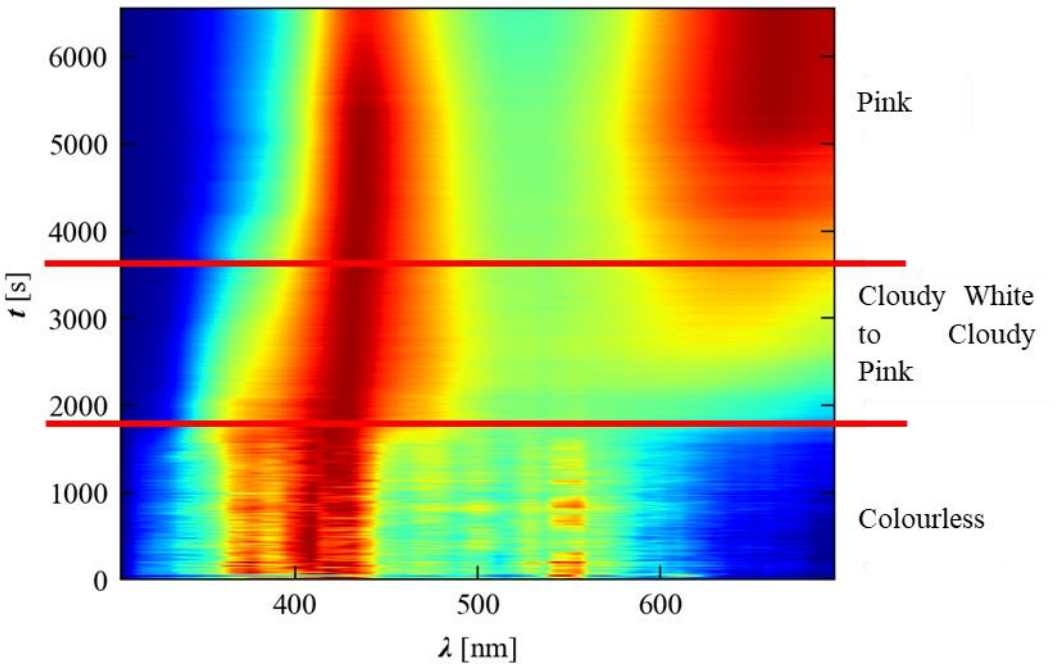

Figure.VII.24 UV-Vis of solution of PDE PiC synthesis showing the different steps of the reaction.

The Raman and UV-Vis spectra showed the change from colourless solution to cloudy white and then on to pink, like observed in the different reactors studied. From the graph the first apparent phenomenon is the increase of fluorescence of the solution which was also reported inside the KRAIC. The B-F bond lengthening at 769-771 cm^{-1} is still present in all graphs during the synthesis which was the case in the KRAIC. The 1375 cm^{-1} and 1545 cm^{-1} for C=C and C=N vibrations are also present with a shift from the 1,2,4 triazole reagent. New peaks appear compared to the KRAIC experiment like the 1258 cm^{-1} and 1303 cm^{-1} that start to appear at 1000 s and are present during the full synthesis, this could be potentially the FEP tubing hiding some peaks during the KRAIC analysis especially in the 200-400 cm^{-1}, 600-800 cm^{-1} and 1200-1400 cm^{-1} regions (Figure.IV.24, Chapter IV). The CH bending mode at 1085 cm^{-1} is also present at 1000 s and in the rest of the reaction. The shift of the 1138-1161 cm^{-1} peak is also present from the 1,2,4 triazole to the final compound. Other peaks present are the same as in the KRAIC but with more visibility.

VII.3.2 Conclusion

From these studies on the powder and the complexation reaction it is clear that compound properties change during the LS to HS transition but also during the synthesis. It is still difficult to tell if the white solution that appears during the reaction is the HS state but the Raman tends to agree with this being a reaction intermediate during the synthesis of the material. The PDE gave more information on the synthesis than the experiments carried out in the KRAIC but the colour of the solution can be assessed more easily using the KRAIC and the position of the black box can be changed accordingly.

VII.3.3 Particle properties of $[Fe(Htrz)_2(trz)](BF_4)\cdot H_2O$

VII.3.3.i Sedimentation rate of nanoparticles

During flow experiments it has been seen that the particles tend to sediment, e.g. in the OBR due to dead zones in Chapter V, as confirmed with CFD, and in the KRAIC particles were settling at the back of the slugs during the experiments in Chapter IV. Sedimentation studies are typically done for nanoparticles of proteins, [130,133] here AUC (analytical ultra-centrifugation) and density measurements were carried out with a density meter on three different morphologies of the particles of $[Fe(Htrz)_2(trz)](BF_4)\cdot H_2O$, rods, stars and spheres (Table.VII.1). The rods were produced in the Vapourtec Kenics Mixers target 100 nm 100S (Table.VII.1,), the stars 400 nm size in the OBR DOE 14 (Table.VII.1) and the spheres 100 nm in the KRAIC-D PiCKD 7 (Table.VII.1) previously studied in VII.2.1. Each of those samples were first dispersed in water with specific concentration with values displayed in Table.VII.8. First the density was measured with a Density Meter DMA™ 5000 M, those measurements were then used by the AUC to determine the sedimentation coefficient. The measurement of density consists of making several analyses, here seven at different concentrations, in a transparent capillary which measures the density as a function of the concentration by the Pulsed Excitation Methods. This consists of a U-Tube where at the inlet and outlet an ultrasonic signal is sent which can be measured back and converted to a time measurement. The flow velocity and the volume of flow are then calculated from the tube diameter.[246,247] The density curves for Rods, Stars and Spheres are displayed in Figure.VII.25. This work has been carried out at Harwell Research Complex with the help of Dr Gemma Harris.

Table.VII.8 Density measurement for each PiC sample performed in water/glycerol mixture (20 %)

	Rods		**Stars**		**Spheres**	
	Concentration (g/mL)	**Density (g/L)**	**Concentration (g/mL)**	**Density (kg/L)**	**Concentration (g/mL)**	**Density (kg/L)**
1	0.01957	1.0454	0.01049	1.0415	0.00108	1.0626
2	0.00979	1.0431	0.00525	1.0389	0.00054	1.0485
3	0.00489	1.0417	0.00262	1.0350	0.00027	1.0416
4	0.00245	1.0404	0.00131	1.0329	0.00014	1.0288
5	0.00122	1.0392	0.00066	1.0322	0.00007	1.0206
6	0.00061	1.0384	0.00033	1.0320	0.00003	1.0175
7	0.00031	1.0380	0.00016	1.0318	0.00002	1.0156

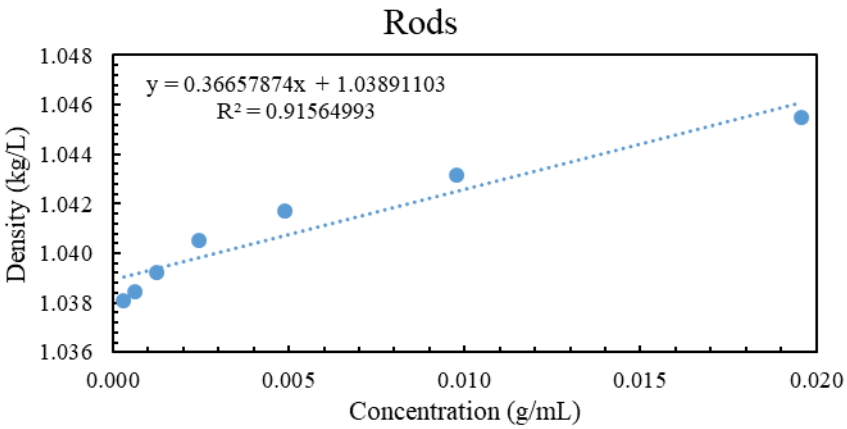

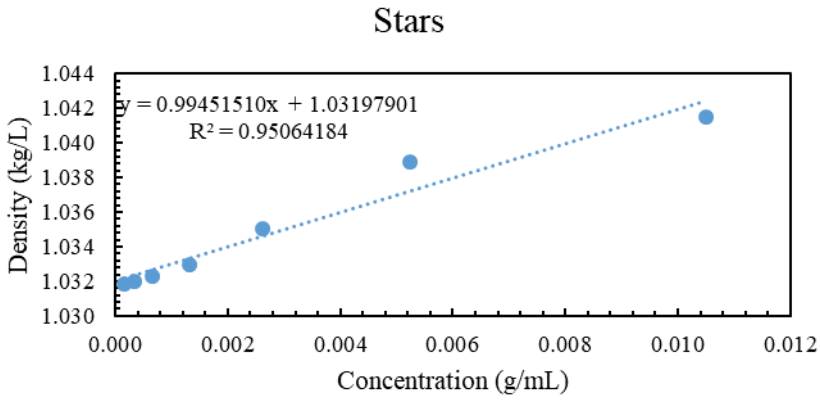

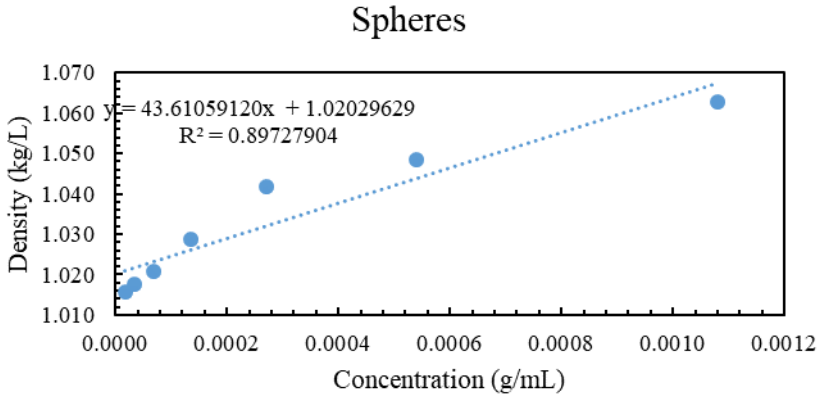

	NP1	NP2	NP3
Density Calculated	1.0389	1.0319	1.0202

Figure.VII.25 Density curves for Rods, Stars and Spheres of PiC.

With those results the density for each nanoparticle can be determined and used for the sedimentation measurement with AUC. The software of the AUC can then process the data to obtain the sedimentation curve (Chapter II.9). The AUC measurement consists of rotating a cuvette where the nanoparticles are dispersed with the same water/glycerol mixture (20 %) at high speed. The application of the centrifugal force causes the depletion of nanoparticles at the meniscus and a laser measures the concentration boundary that moves towards the bottom of the centrifugation and

therefore the cuvette during the rotation. On Figure.VII.26 is displayed for each nanoparticle the results of the AUC. On the left in grey is the image of the cuvette cumulated snapshot over time, above this, in colour, is the sedimentation velocity (SV) over time. On the right is represented the sedimentation coefficient curve obtained after processing the AUC data.

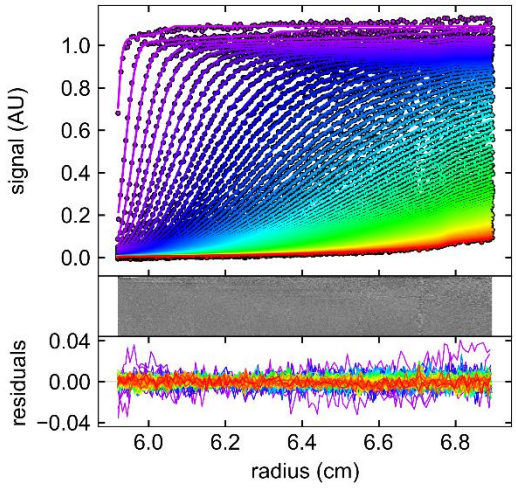

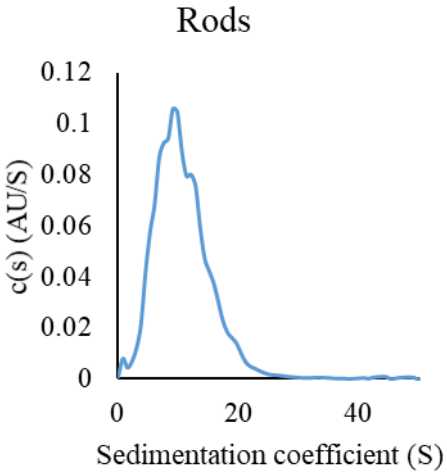

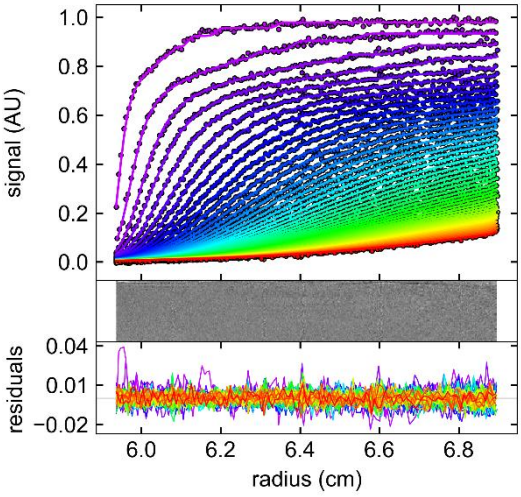

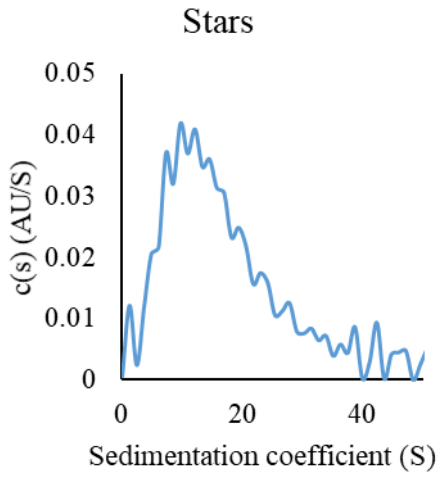

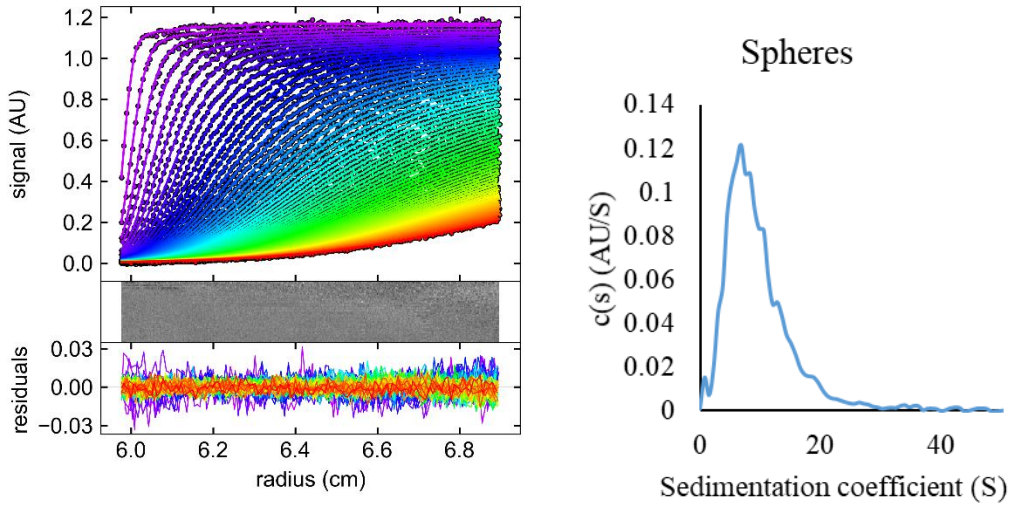

Figure.VII.26 Sedimentation Velocity (SV) curve (left) and sedimentation coefficient curve (right) for Rods (top), Stars (middle) and Spheres (bottom) of PiC.

It has been seen in previous chapters that sedimentation was in certain cases a problem inside the OBR and the Vapourtec (Chapter V and VI). Also, in the KRAIC-D inertia of the slugs gave an interesting behaviour where the PiC particles were pushed on one side of the slugs during the beam time run (Chapter IV). These AUC measurements showed that the sedimentation coefficient of nanoparticles with the different size and morphologies was between 6-7 Svedberg (S) (with the largest concentration). These values show that with 6-7 S particles should travel at around 6-7 micrometres per second in a cuvette. Bigger particles tend to sediment faster and then have a higher S value,[133] which in this case confirms the presence of light small particles. For comparison, gold nanoparticles are between 6.8-30 S for 5 to 12 nm size.[248,249] During the consistency experiment of the 16 RT in the OBR presented in Chapter V it was seen that sedimentation was occurring after several residence times. In this case star shaped material was obtained and Figure.VII.26 shows a broader sedimentation 0 to 40 S coefficient with some particles having a faster travel time in the cuvette which could explain the phenomenon. The PSD for this sample is also wide between 300 to 650 nm which might show the presence of different particle weights inside the sample studied resulting in wider sedimentation coefficient. The spheres and rods have a low sedimentation rate but it was observed for the spherical particles in Chapter V for the OBR production of H1 to H8 that sedimentation occurred, this may however have been explained by the dead zones indicated by CFD for the OBR geometry. The sedimentation ratio of the spherical particles obtained in the KRAIC-D, PiCKD 7, on the other hand shows that the particles are so light that the inertia could succeed into pushing the particles to one side of the slugs creating different colouration of the slugs. On another hand it is difficult to compare the sedimentation velocities inside the reactor under 1*g* and those under centrifugation at very high *g* with AUC.A possibility would be to us DLS technique to measure the number of particle passing through different point of the cuvette at different time under 1*g*.

VII.3.3.ii Dynamic Light Scattering (DLS) confirmation by differential centrifugal sedimentation (DCS)

To check the effectiveness of the DLS, another light scattering technique was used. Differential centrifugal sedimentation (DCS) is a technique employed for high resolution determination of size distributions of micro or nano particles. Like AUC, DCS analyses particles settling according to Stokes' Law. A monochromatic beam (400 to 500 nm) is fired though a cuvette where the signal is

reduced due to absorption by the particles before reaching the detector at the bottom of the cuvette. The reduction of intensity is proportional to the particle concentration. An integral distribution is then obtained from the signal obtained which is then transposed into a Diameter Micron graph. The measurements were done at University College London with Dr. Hendrik Du Toit. Results for two PiC samples (stars and spheres) are displayed in Figure.VII.27.

The DCS results obtained showed similarities with the same sample analysed on DLS by the Zetasizer. In Chapter IV and V it was stated that DLS showed completely different results than SEM pictures, but with DCS being a similar technique it is normal to obtain close results. For DOE 14 the DLS and DCS shows sizes of 0.19 and 0.22 µm and for the KRAIC-D Runs 0.23 and 0.27 µm. Those close results of population confirm the use of both DLS and DCS have the same issue, depending a lot on the sample particle type, in particular for size analysis for non-spherical particles. It is therefore preferable to use SEM as presented in Chapter III to VI to confirm morphology and size of the PiC particles obtained. Again, in those samples not the whole batch of sample is represented and more samples would need to be analysed but the cost of DCS analysis is high and relevance to a full scale-up study would be needed to justify undertaking comprehensive analysis of this type.

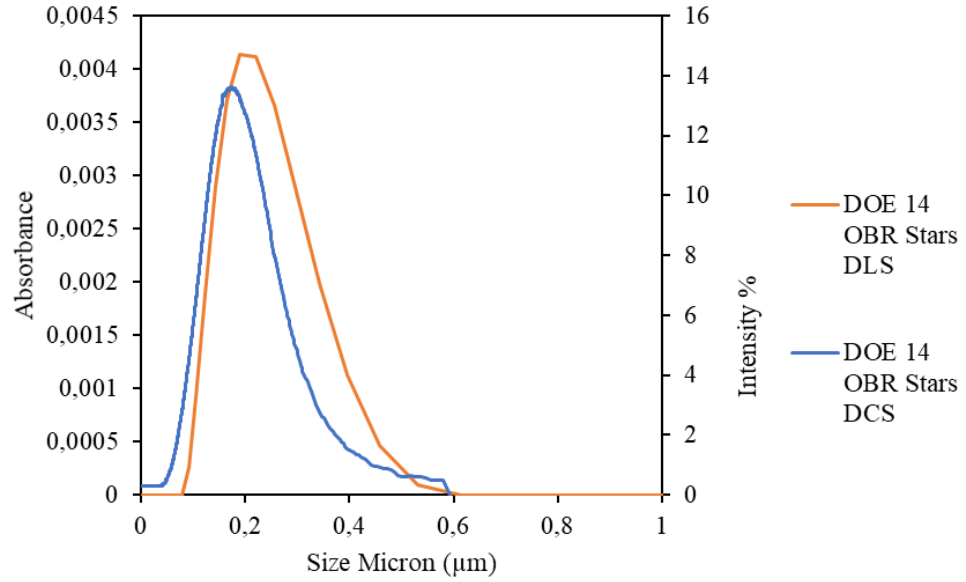

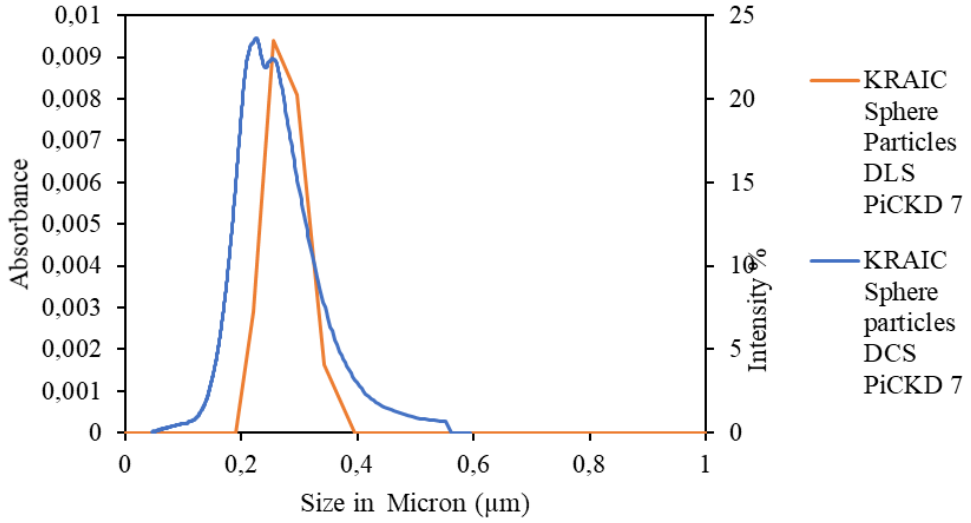

Figure.VII.27 DLS and DCS comparison for PiC DOE 14 experiment (stars) and KRAIC-D PiCKD-7 spherical particles.

VII.3.4 Insertion of PiC SCO Compound in thin Polyacrylonitrile (PAN) film

Electrospray and spinning are two techniques which involve high voltage and slow flow rate. Electrospray uses electricity to form droplets. In electrospray, a liquid is passed through a nozzle with range of bore sizes up to 1 mm. The droplets are formed by electrically charging the liquid emerging from the syringe tip to a very high voltage, Figure.VII.28.[250,251]

These droplets are less than 10 µm in diameter when they emerge from the tip and shrink as solvent molecules evaporate from them. Since the charge does not diminish, this forces the droplets further apart producing a fine spray which will coat the surface of an oppositely charged substrate. On the industrial scale, electrospray is used in the application of paints and coatings to metal surfaces. The fine spray results in very smooth even films, with the paint ionically bonded to the metal, so the paint material is used more efficiently and the resultant coating is hard wearing.

Electrospinning is used for electrostatic fibre formation which utilizes electrical forces to produce polymer fibres with diameters ranging from 2 nm to several micrometres using polymer solutions. This method has seen a rapid increase in research and commercial attention over the past decade for the creation of thin films for the pharmaceuticals industry, organic diodes or tissue reconstruction.[250,252,253] This process offers unique capabilities for producing novel natural nanofibers and fabrics with controllable pore structure.

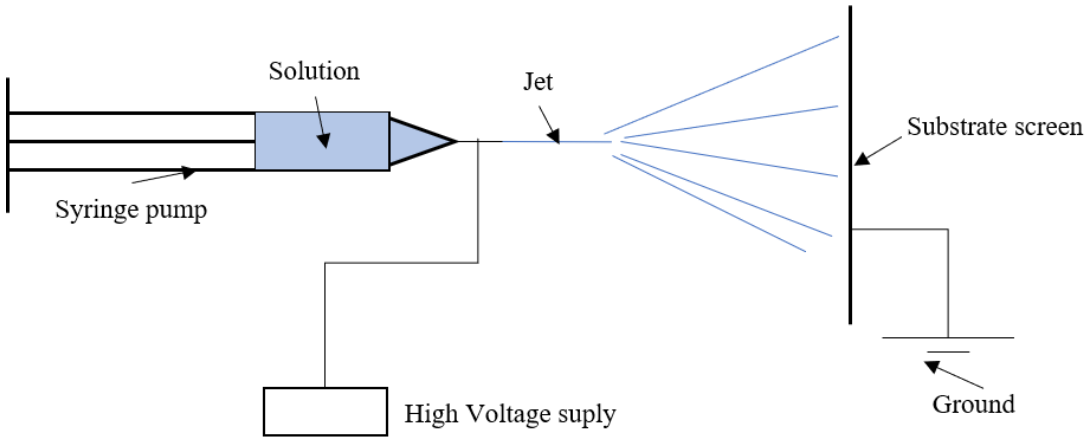

Figure.VII.28 Electrospray principle scheme.

Electrospinning could be an alternative solution for incorporation into thin films for compounds produced in the M^4 group. This section will only focus on electrospinning. This work has been carried out with the help of Dr Sunyhik Ahn and Prof Frank Marken.

Following Yördem *et al.* 2008, PAN (polyacrylonitrile) was dissolved into 10 mL of dimethyl sulfoxide (DMSO) with a 4 wt% ratio for PAN. The solution was stirred overnight before the experiment.[140] After the PAN was completely dissolved, the star shaped particles of the spin crossover compound $Fe(Htrz)_2(trz)](BF_4)\cdot H_2O$ obtained in the OBR DOE 14 were introduced into the solution (0.052 g). The electrospinning device was prepared with a 0.8 mm ID needle in order to create the so-called Taylor cone needed. The prepared solution was placed in a 10 ml plastic syringe, connected to a stainless-steel nozzle (0.8 mm inner diameter) fixed by an earthed copper wire to the collection plate. The feed rate of the solution was maintained with a Binari engineering syringe programmable pump. The voltage supplied to the needle from a Biomedical Vision

apparatus from Binari Engineering power supply was then adjusted until a stable spinning jet was established, as observed by a closed-circuit camera. This voltage was first varied between 15-20 kV depending largely on the concentration and additives in the solution, then it was set at 15 kV which appeared to be the most stable voltage. The needle was at 30 cm distance from the substrate. Samples were air dried after obtention of the white film on the aluminium foil. The thickness of the sample was not uniform as the device did not allow a fully controlled environment that would be needed to have a proper thickness sizing.

Table.VII.9 Parameters used for the electrospray of PiC with PAN.

Experiment	Volume (mL)	PAN (wt%)	PiC mass in solution (g)	Syringe pump flow rate (mL/min)	Charge (kV)	Syringe ID (mm)
ETS1	2	5	0.052	0.06	15	1
ETS2	2	5	0.032	0.06	15	1
ETS3	2	5	0.052	0.08	15	1
ETS4	2	5	0.064	0.08	15	1
ETS5	2	5	0.12	0.1	20	1
ETS6	2	5	0.14	0.1	20	1

After a 1 hour run the film was recovered by pulling it gently from the substrate for each experiment. The obtained film was light pink/white which confirmed the presence of PiC in the fibres as shown in Figure.VII.29. The stream of solution did not spin or was unstable for experiments ETS5 and ETS6 even when increasing the voltage to 20 kV.

Figure.VII.29 Polymer film with embedded PiC obtained by electrospray for ETS1.

SEM pictures were made in order to confirm the presence and bonding of the crystal inside the fibres matrices. Figure.VII.30 shows that the compound $[Fe(Htrz)_2(trz)](BF_4)\cdot H_2O$ produced in the OBR with star shaped particles are found among the polymer PAN fibres, confirming their presence.

As can be seen, the crystals are distributed evenly around the film, but more interestingly the crystals are showing a bonding with the fibres, confirmed by higher resolution microscopy imaging (Figure.VII.31). At this higher magnification the bonding between the fibres and the compound can be seen. The film produced was light and thin and handling it was difficult because of its fragility. It is also seen that increasing the concentration of PiC in the solution increases the extent of bonding between the particles and the fibres.

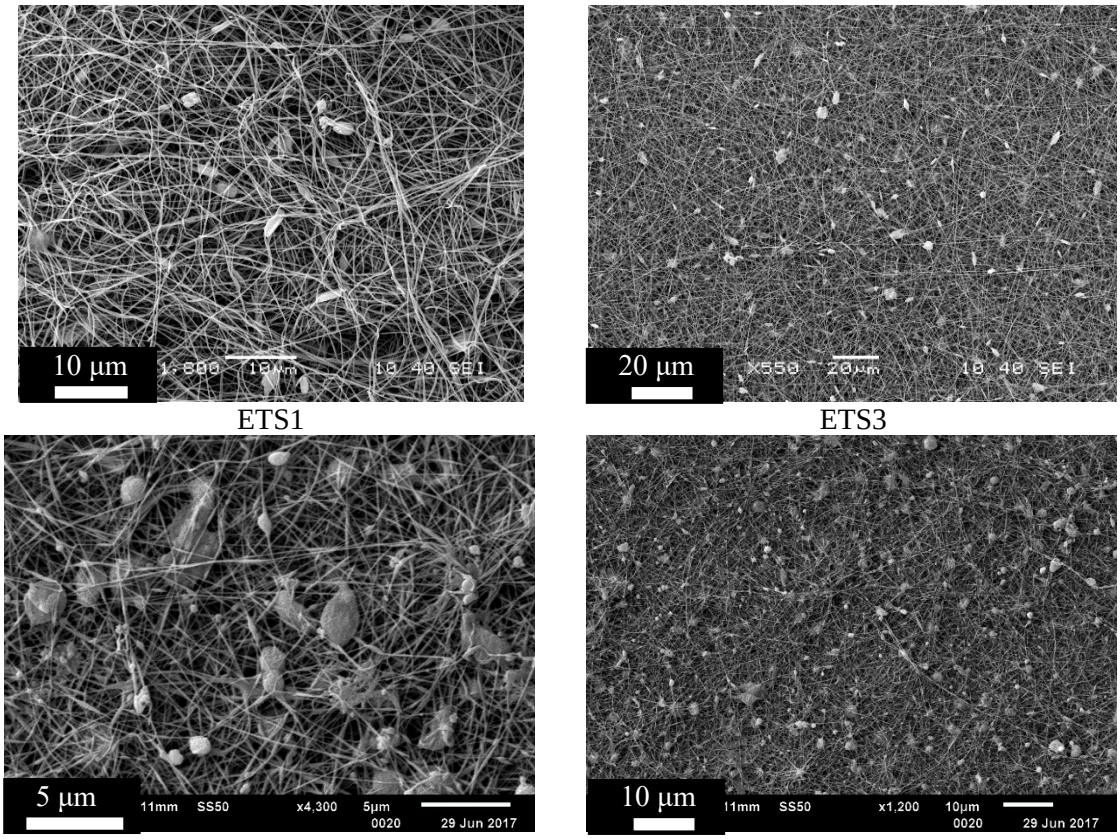

ETS1 ETS3

ETS3 EST4

Figure.VII.30 SEM picture showing the crystals of PiC among the fibres in the film for experiment ETS1 (top left), ETS3 (top right) ETS3 (bottom left) and ETS4 (bottom right).

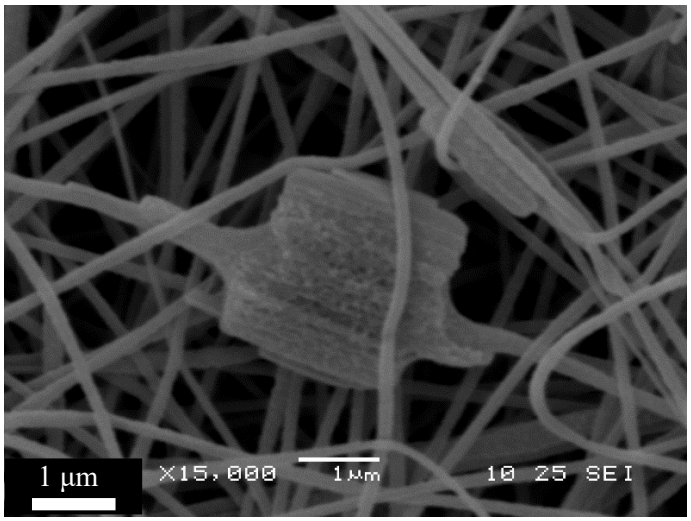

Figure.VII.31 Crystal bonding of PiC with PAN fibres (experiment ETS1).

ETS1 was studied in more depth due to good visibility of each crystal inside the matrices of fibres, as can be seen on Figure.VII.31 where the star shaped crystal is “attached” to the fibres. This film has been analysed by DSC and Reflectance UV-Vis spectroscopy to confirm the presence of spin state change during heating.

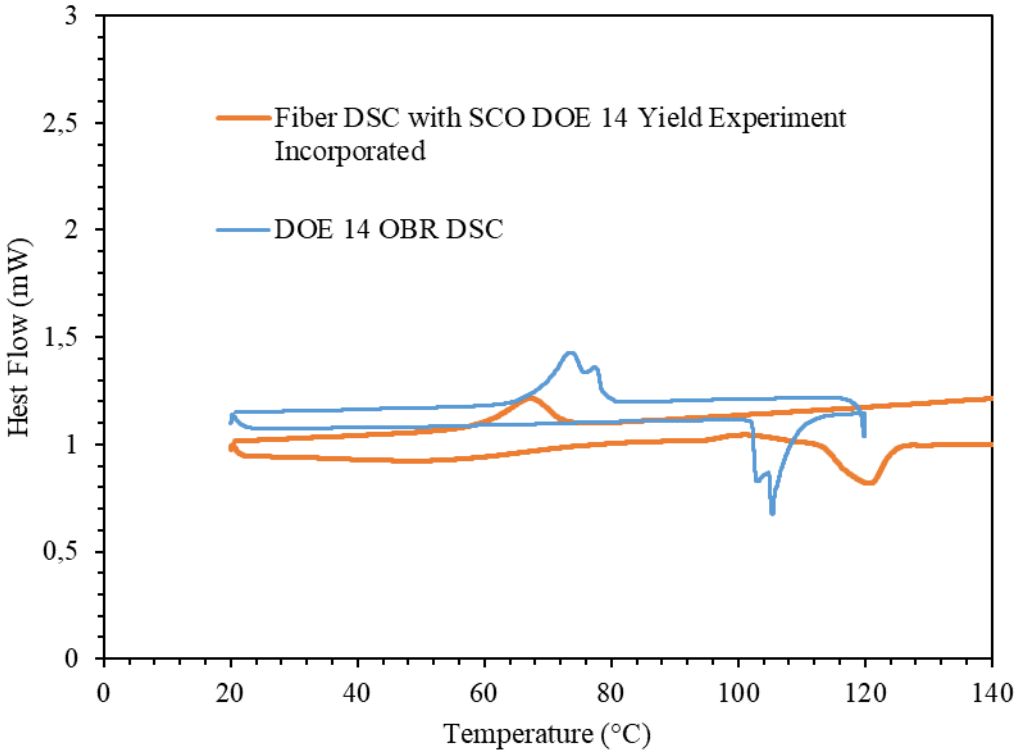

Figure.VII.32 DSC of thin PiC/PAN film obtained with electrospray (ETS1).

Figure.VII.32 shows the DSC analysis of ETS1 where the LS/HS ST can be seen to show some changes compared to the bulk material. This particularity could be due to the PAN present during the analysis as for the surfactant additives previously described. It can be seen that, for the PiC particles embedded in the PAN fibres, the switching happens at higher temperature for the LS to HS ST at 112 °C compared to the 106.4 °C of the DOE 14 OBR sample. The hysteresis in the two STs is larger for the fibre sample (HS/LS transition at 81.2 °C for powder and 72.3 °C for the fibres). This could be due to the small amount of PiC inside the film, the fibres might also reduce heat transfer and cooperativity between the particles of PiC which needs them to be at higher temperature to switch and buffers the reverse switch, reducing its temperature.

UV-Vis reflectance results are displayed in Figure.VII.33, those results were obtained with the same Polar Bear set-up used previously in VII.3; a slight change in absorbance is detected at 112 °C and is shown by the red line on Figure.VII.33. The colour change is so subtle due to the light pink, almost white, colour of the film.

From the DSC and UV-Vis analyses, during the heating process a change in spin state appears but has a lower enthalpy than its bulk powder counterpart, 9.5 J/g for the film and 40.7 J/g for the powder during heating process and 6.1 J/g for the film and 42.81 J/g during cooling. This would be due to the low concentration used for those experiments and also the fact that the compound is dispersed on the PAN film as seen on the SEM pictures. Even if the switching from LS and HS is weak the possibility to use electrospinning as a way to create thin PiC film has been successfully achieved. This technique could be used not only for switching devices but also to incorporate other types of compound with different polymers.[250,251,254]

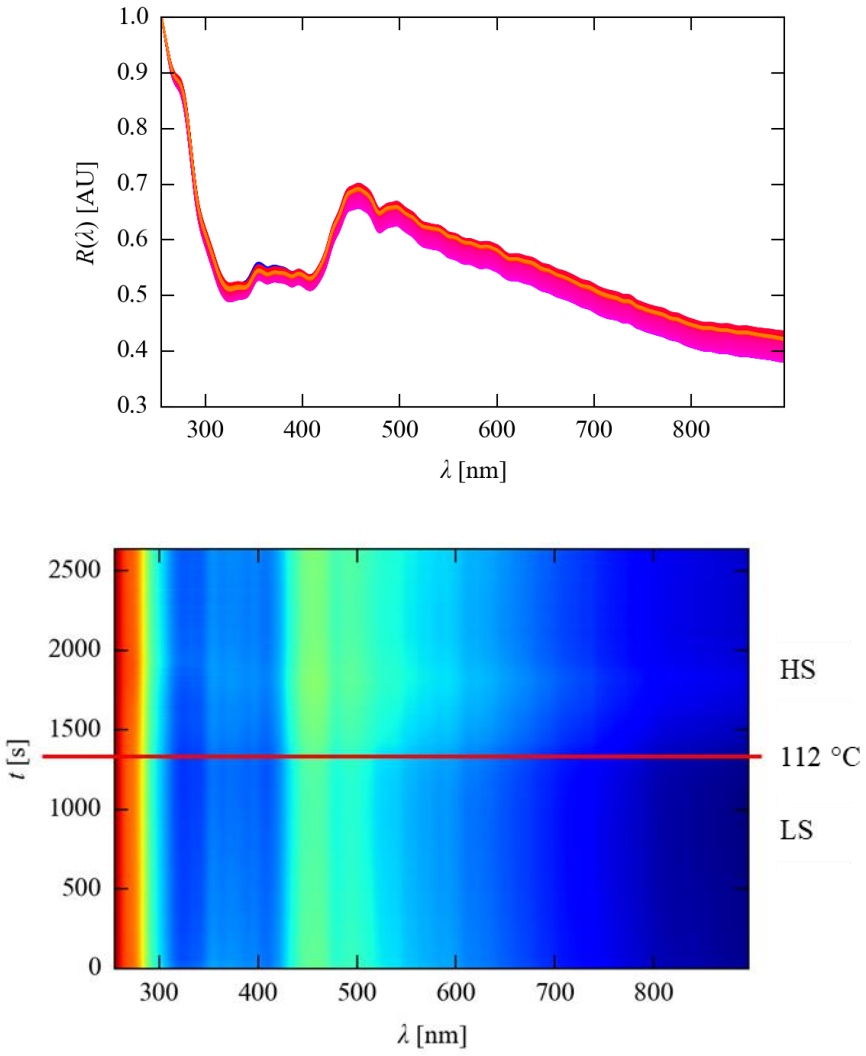

Figure.VII.33 UV-Vis of thin film produce during experiment 1. (top) reflectance graph measured during experiment, (bottom) the combined graph *versus* time.

VII.3.5 Electron diffraction of $[Fe(Htrz)_2(trz)](BF_4)\cdot H_2O$

Different morphologies of PiC have been studied (Table.VII.1) with SQUID, AUC, DCS, PXRD and SEM. Each analysis method highlighted different properties for the ST upon heating and cooling. To take this further, samples of rods, stars and spheres were sent to the University of Manchester to be analysed by Dr Alexander Eggeman using Electron Diffraction (EDF) to see the differences between each particle.

The samples of rod, star and sphere-shaped PiC particles are the same as those used for SQUID analysis (DOE 14, PiCKD 7 and ST-100nm, respectively). During EDF rod samples showed the best crystallinity. With EDF the long axis was determined to be the [010] plane which is parallel to the direction of the 1D coordination chains.

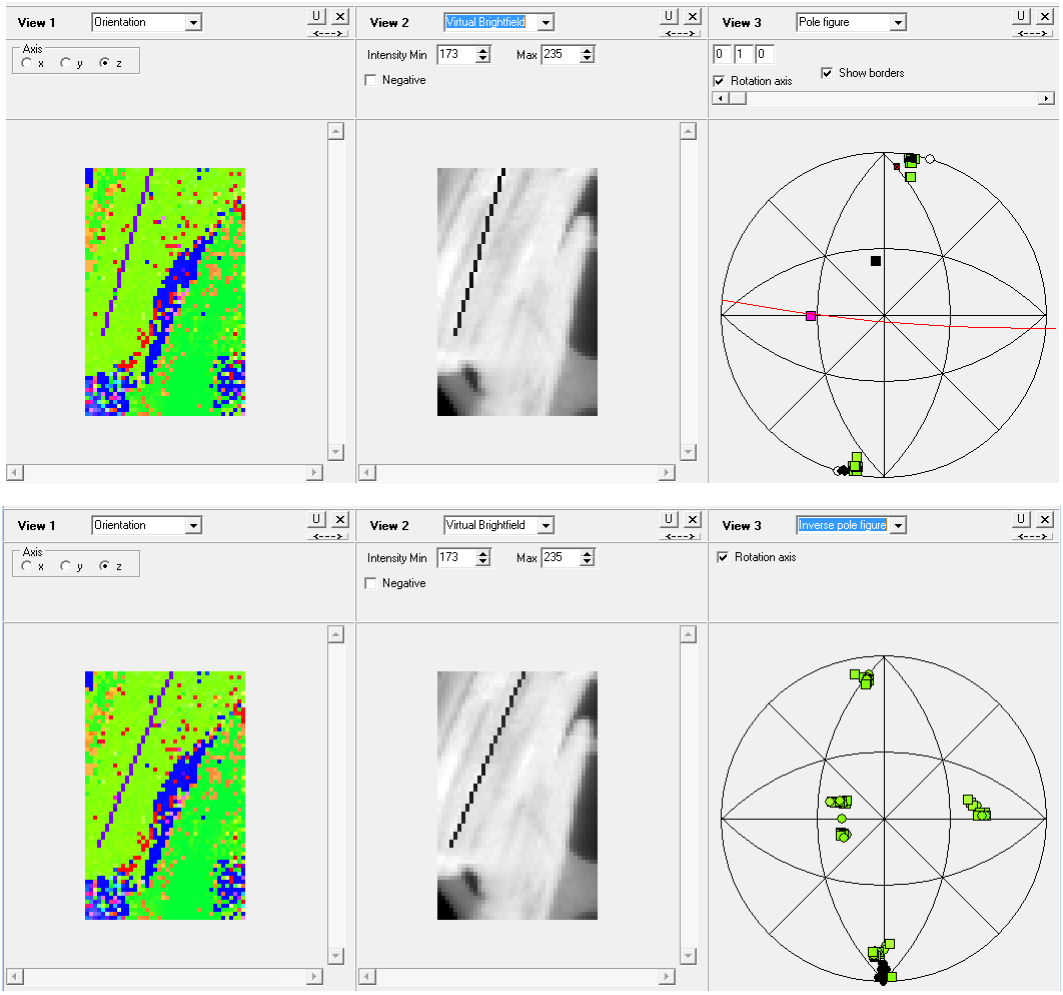

Figure.VII.34 Pole figures for [010] for rods sample of PiC aligned with the rod axis.

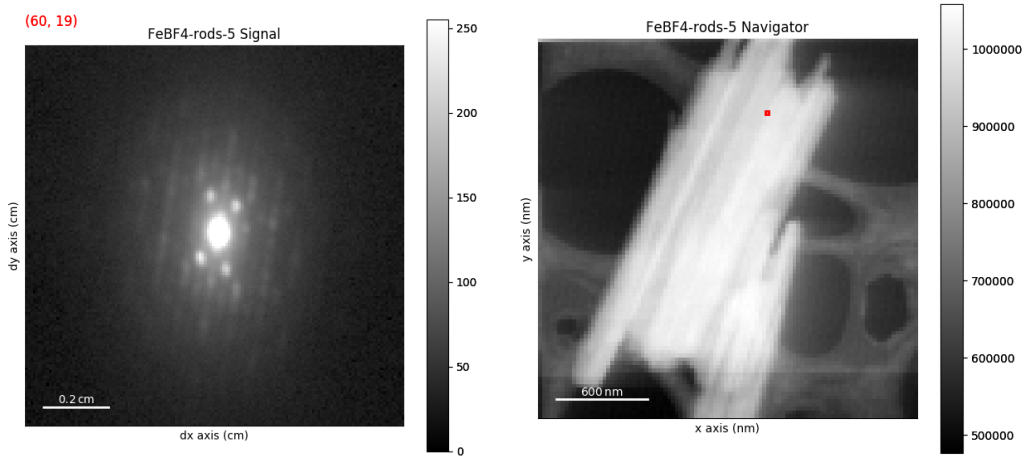

Figure.VII.35 Diffraction pattern of the rods of PiC (red point is where the diffraction pattern is taken).

It was possible to compare these diffraction patterns with the single crystal structure presented in section VII.2.3 above using CrystalMaker® (Figure.VII.15). This showed the good correspondence between the pattern obtained and the one simulated from literature in Grosjean *et al.*. [14]

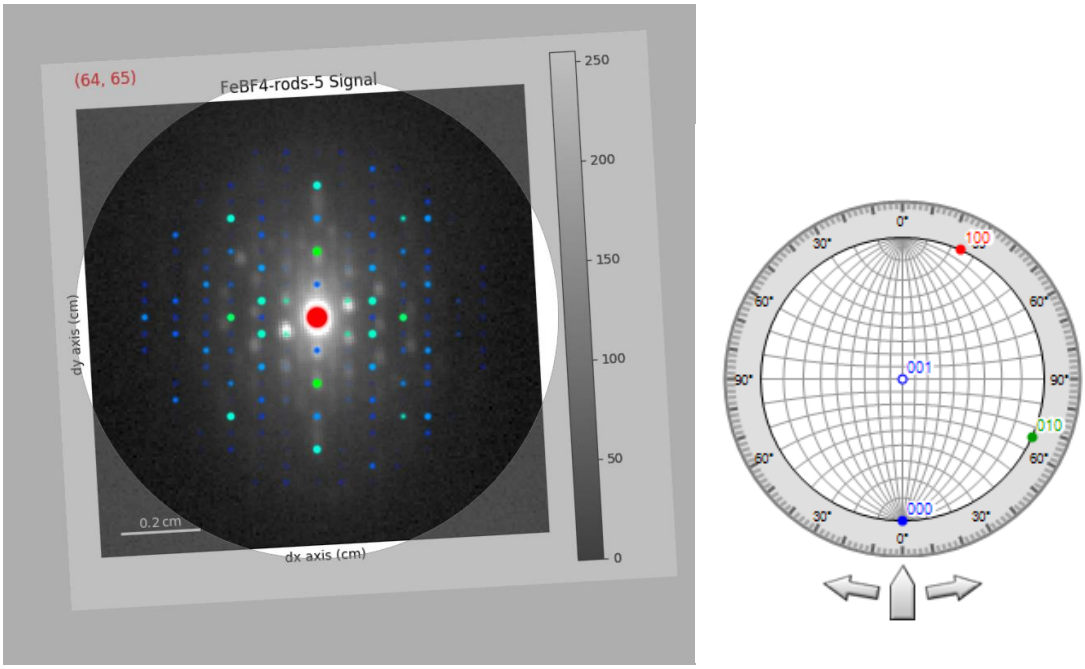

Figure.VII.36 Simulated EDF diffraction pattern obtained from the rods sample analysed.

The rods facets detected were the [100] and [001] or [101] and [10-1] planes suggesting that the rods are approximately rectangular, which was confirmed by SEM. For instance, the crystals displayed on Figure.VII.34 are oriented along [101]. During the analysis of the samples through EDF, all samples presented the HS state. This is most likely due to the heat generated by the beam of the electron gun. In the rods sample, the LS state was detected in some part of the sample as shown on Figure.VII.37. These changes were however difficult to assess due to the small difference in the lattice.

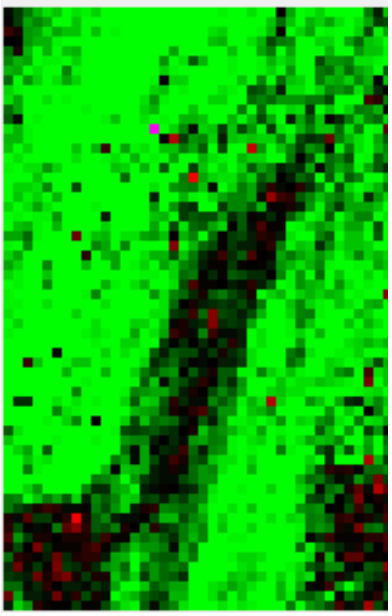

Figure.VII.37 Rod sample under EDF: (green) HS state of the rod; (red) LS.

The sphere sample (Figure.VII.38) appears to be a uniform structure but with a less defined crystallinity. The orientation of the sphere was difficult to determine but, in some cases, the same [010] plane was observed. Some particles were also non-spherical but closer to the star shaped

materials but with a diffraction pattern which did not match either the HS or LS state of PiC. It was supposed that those particles were iron compounds (oxides) that could appear in the system.

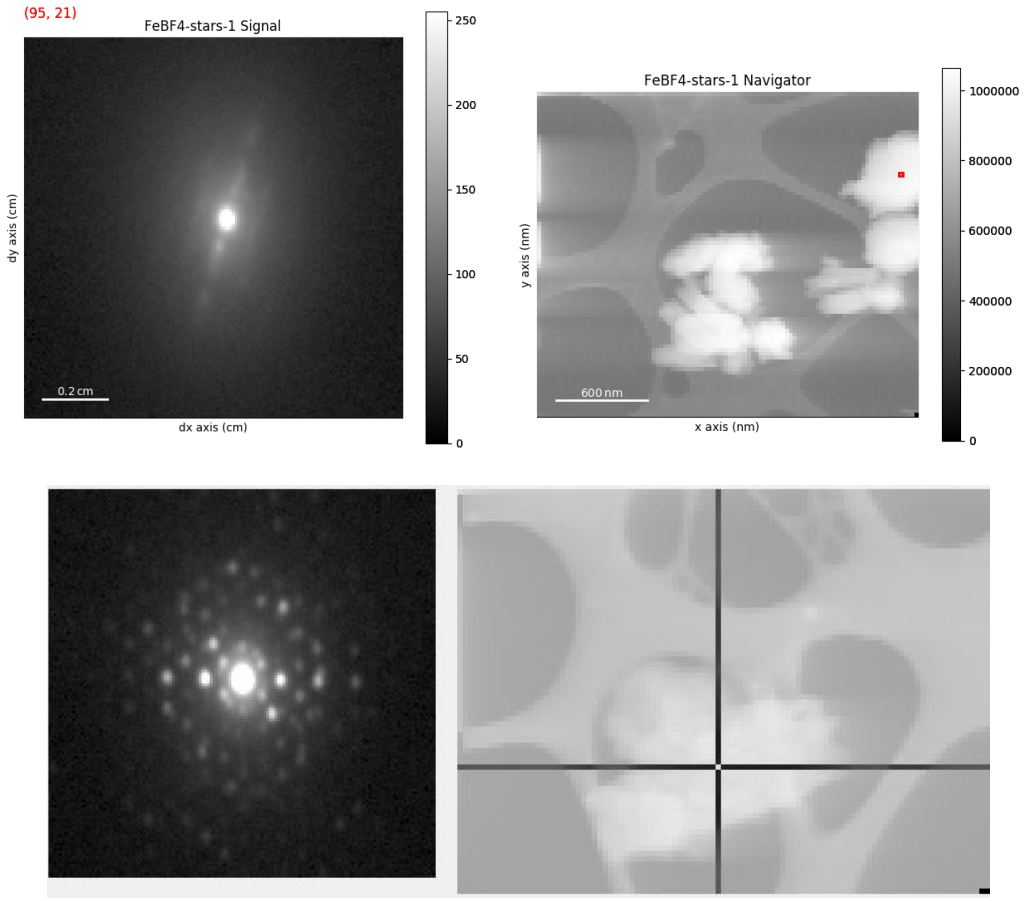

Figure.VII.38 Sphere morphology of PiC present in the star sample (top) and unusual shaped crystal (bottom).

The stars sample appears to be an intermediate between rods and sphere. There are some spherical particles within the stars but there are also lots of small rod-like samples. The major axis shows a [010] growth direction as observed for the rods sample (Figure.VII.39). That the star shaped crystal is a mixture between the rods and the spheres suggests some intermediate growth mechanism between the rods and the spheres.

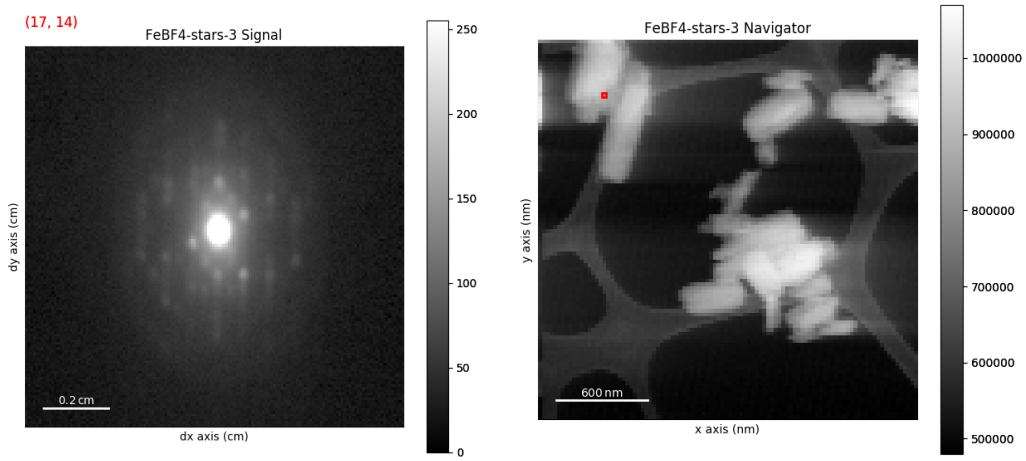

Figure.VII.39 Stars sample of PiC analyzed *via* EDF.

The three different morphologies suggest 1D coordination chains that grow together. This difference of shape can give us more information on the assembly mechanism present during the synthesis of PiC depending of the synthesis conditions. Diffraction files are given in supplementary information **CDCh7-2**.

VII.3.6 Spin state behaviour of $FeL_2[BF_4]_2$ (YeC)

This work has been carried out with Master Student Kathryn Bell Project and is a follow up of section III in Chapter VI.

The SCO compound $FeL_2[BF_4]_2$ [L = 2,6-di(pyrazol-1-yl)pyridine] (YeC) produced in Chapter VI have been analysed using DSC to see the ST change of the compound. Those analyses were done to see if the production method of YeC has an effect on the change of spin state as observed for PiC production. In literature the change in colour is observed at 263 K from yellow to brown.[20,241] This behaviour has been observed during the in-line filtration of the compound and a video is given in supplementary information **CDCh6-1** to have an appreciation of the material switching. This switching was induced by the DEE evaporating at the end of the reactor and creating a cold environment for the compound. To verify any change in behaviour of the compound DLS was used in order to check the particle size from each experiment.

Table.VII.10 DLS analysis of flow and batch experiments of YeC

	Batch			Flow		
	Percentage Intensity / %	**Particle Size / nm**	**Mean Particle Size / nm**	**Percentage Intensity / %**	**Particle Size / nm**	**Mean Particle Size / nm**
B/FY1	100	106 – 295	169	65 35	122 – 396 5 – 8	137
B/FY2	62 33 5	298 – 459 142 10 – 18	272	53 26 21	12 – 44 164 – 712 2 – 4	111
B/FY4	73 23	68 – 91 106 – 142	88	100	190 – 295	241
B/FY5	67 31 2	68 – 91 190 – 255 5 – 7	125	67 33	91 – 106 142 – 220	125
B/FY6	100	142 – 255	188	64 33 3	142 – 255 68 – 78 3 – 4	143
B/FY7	98 2	44 – 91 1	66	100	142 – 396	244
B/FY8	100	142 – 164	152	67 33	51 – 59 164 – 190	94
B/FY9	84 16	164 – 295 12 – 28	183	95 5	142 – 255 12 – 18	178
B/FY10	84 16	255 – 396 24 – 33	276	67 27 6	51 – 91 122 – 190 21 – 24	90

The DLS results displayed in Table.VII.10 show particle size ranging from 30 nm to 300 nm. In Chapter VI the SEM shows particles between 2-5 µm which could explain the difficulties of the DLS to detect a proper particle size. There is still a general decrease in APS using flow compared to batch but in some cases like FY4 and FY7 the particle size is increased. A proper DOE study would be needed to assess the variation in these results and to build a proper model.

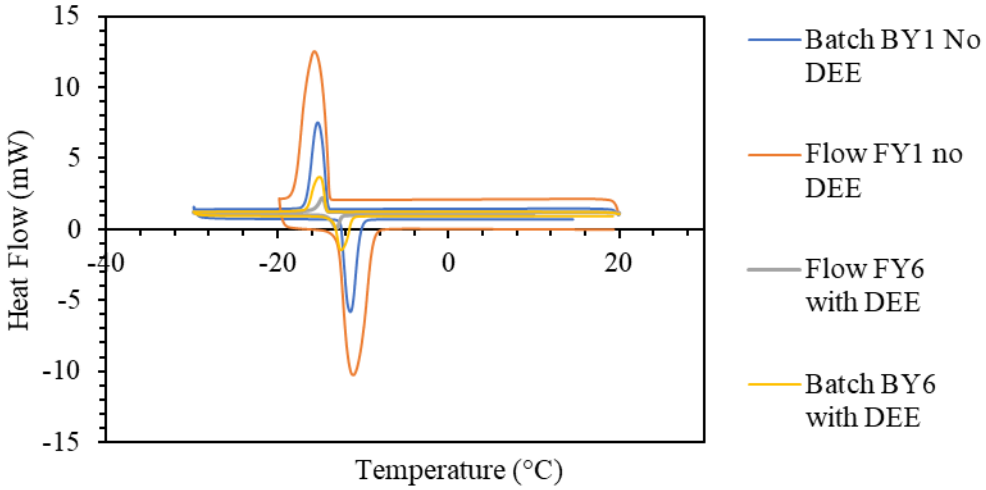

Figure.VII.40 DSC comparison of continuous and batch production of YeC with and without using DEE as an anti-solvent.

As can be seen on Figure.VII.40 there is a difference between YeC compounds produced in batch and in flow with 1 mm bore tubing. In flow with DEE the peak is narrower and has a shorter ST than the flow trials without using DEE. The batch processed samples do not seem to have any difference compared to the flow processed samples with and without using DEE. Using DEE seems to reduce the switching time from batch and flow, and the flow with DEE shows a shorter switching time than the batch experiment. There was also less sample used in some experiments due to low yield.

Figure.VII.41 shows the difference in DSC for each compound from batch and flow. No clear trend can be seen compared to $Fe(Htrz)_2(trz)](BF_4)\cdot H_2O$ where a bigger difference between flow and batch production could be discerned and even between reaction parameters. The transition enthalpies are displayed in Table.VII.11.

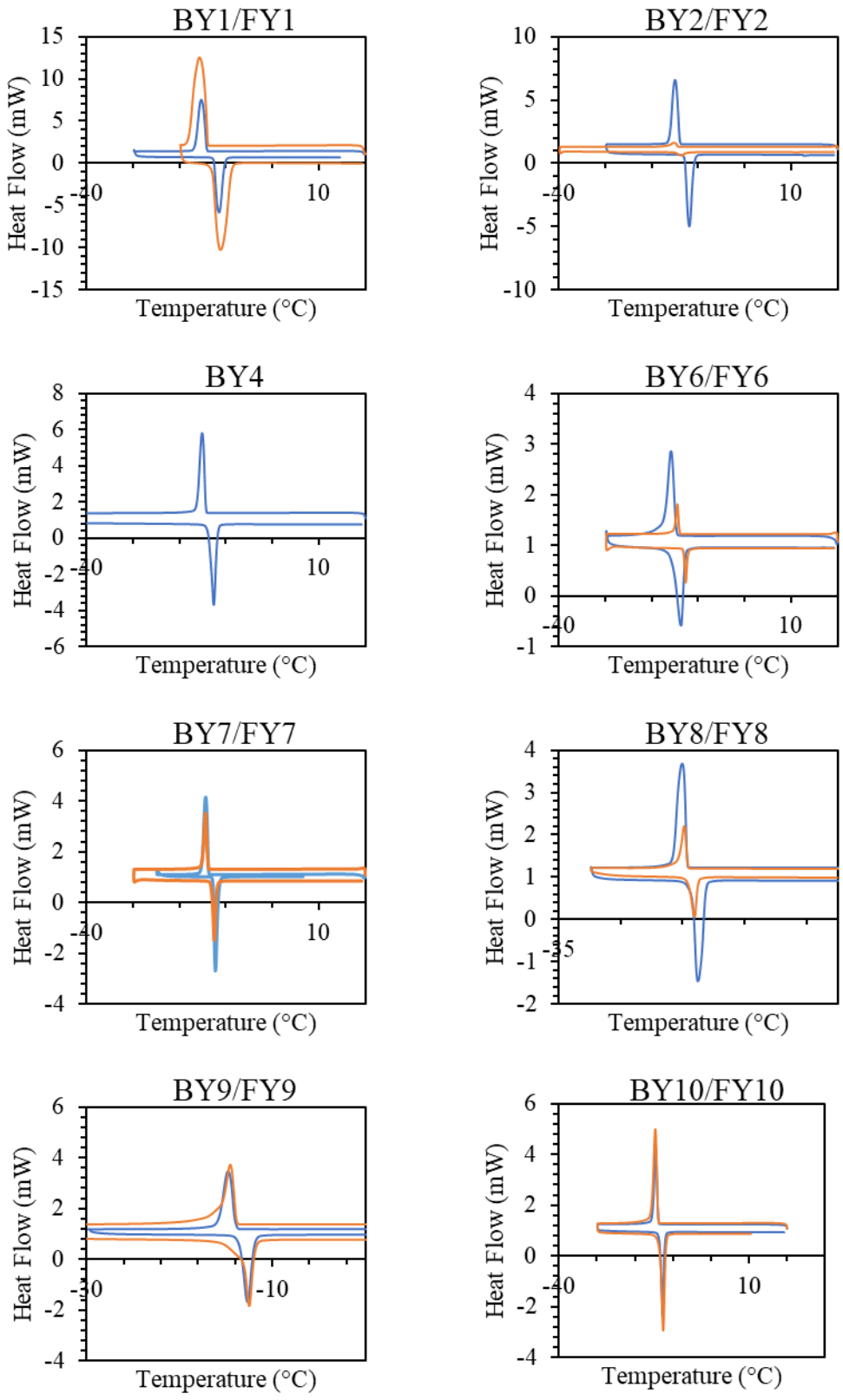

Figure.VII.41 DLS comparison of YeC produced in batch (blue) and flow (orange).

Table.VII.11 Enthalpy variation of the ST of YeC samples.

Experiment	Batch Enthalpy (kJ/mol)	Flow Enthalpie (kJ/mol)
B/FY1	-11.3, 10.1	-16.3, 17.9
B/FY2	-9.1, 7.8	-0.6, 0.4
B/FY4	-	-7.3, 5.7
B/FY5	-0.6, 0.8	-
B/FY6	-2.9, 3.4	-0.5, 0.5
B/FY7	3.7, 3.0	-2.7, 2.7
B/FY8	-3.4, 3.9	-1.1, 1.7
B/FY9	-4.2, 4.4	-3.3, 3.7
B/FY10	-4.8, 5.1	-3.1, 3.5

Using the progressive mixer reactor showed a narrower ST (with a 1-2 µm particle size) but the same 2-3 °C ST hysteresis is present centred on -12.15 °C (Figure.VII.42).

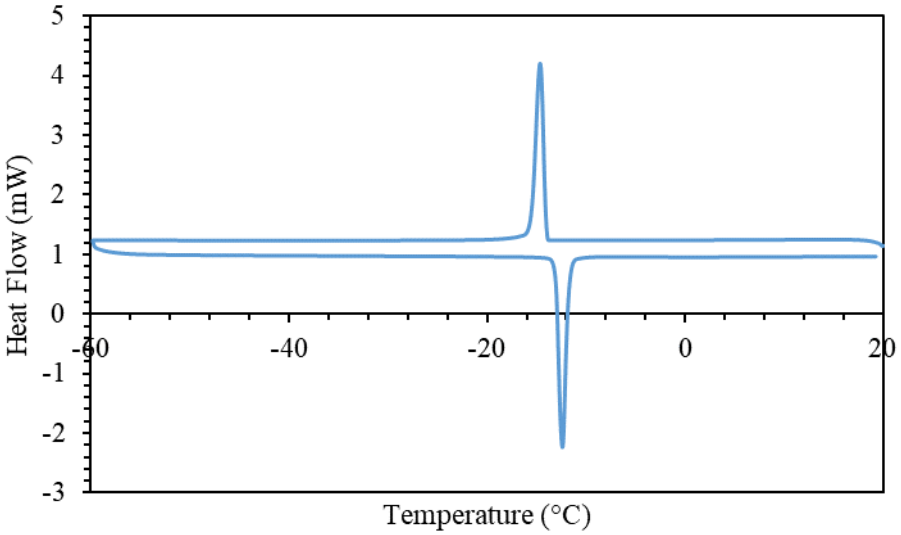

Figure.VII.42 DSC of $[FeL_2][BF_4]_2$ produced in progressive mixer reactor.

Compared to $Fe(Htrz)_2(trz)](BF_4)\cdot H_2O$ previously studied with the Kenics mixer, $[FeL_2][BF_4]_2$ [L = 2,6-di(pyrazol-1-yl)pyridine] does not seems to have a change in enthalpy with different particle size of crystals (Figure.VII.42). A full DOE study has not been made for this as it would need large quantities of 2,6-bis(N-pyrazolyl) pyridine to be synthesised (and is difficult to obtain at larger scale). The switching on the other hand has not been affected by the type of production used even with the tube-in-tube progressive mixing reactor. The results obtained are still in close relation with those from Holland *et al.*.[20] The first ST is observed and centred around -13.15 °C. For flow and batch samples the ST width is between 3-5 °C with a hysteresis of 2-3 °C which corresponds to the literature. There is no significant improvement using batch or flow techniques as can be seen from Figure.VII.41.

Due to its micro scale size crystals YeC might not have significant changes in the ST loop but if a technique could produce below 1 µm particles it may be that the ST could be shifted to higher

temperatures. Here, with 2 µm particles produced in the progressive mixer reactor, the 1 °C shift to a higher temperature could be a lead in that direction. The most particular characteristic that has been successfully displayed is the particle size improvement using flow environment, producing smaller particles for $[FeL_2][BF_4]_2$ [L = 2,6-di(pyrazol-1-yl)pyridine].

Going further into the anti-solvent crystallisation/precipitation a study of thermochromic compound has been made and is described in the next section.

VII.4. Thermochromism of molecular complexes produced in flow

In Chapter VI several complexes were discussed that have successfully been produced in a flow environment with the Vapourtec and the KRAIC *via* anti-solvent techniques. Using the Vapourtec flow kit 4-iodoanilinium 3,5-dinitrobenzoate, 4-iodoaniline 3,5-dinitrobenzoic acid solvate and 4-iodo-2-methylanilinium 3,5-dinitrobenzoate have been successfully produced using anti-solvent technique using flow. Those compounds corresponded to co-crystal 1, 2 and 5 from Jones *et al.*, 2014. Unfortunately, none of those co-crystals had switching properties but led towards the production of thermochromic complexes. Here 2-iodoaniline 3,4-dinitrobenzoic (2-IA 3,4DNBA) will be studied as it was the most stable of all complexes recovered; other complexes changed from an orange/red colour to a white colour during filtration or drying due to loss of the aniline component. Here is described the analysis work on 2-IA 3,4DNBA switching properties.

VII.4.1 Colour switching of 2-IA 3,4DNBA

In Charlotte Jones' Thesis[26] it was reported that 2-IA 3,4DNBA Form I was obtained using evaporative crystallisation gave dark-red block crystals. This red crystal shown to change colour upon heating at 90 °C which was potentially polymorphic change behaviour. Due to the difficulties in reproducibility of this compound *via* evaporative crystallisation flow synthesis was investigated.

In Chapter VI different techniques were used to synthesise in flow 2-IA 3,4DNBA. Synthesis from ethanol and methanol, with water as an anti-solvent showed that form I of the compound was obtained *via* the different anti-solvent techniques. In this section is shown that Form II of this compound was obtained by heating the sample to 55 °C on a hot stage microscope (Mettler Toledo FP82) and Form III of this complex was obtained by heating the crystal to 90 °C, while undergoing a colour change from red to orange.

Hot-stage microscopy was carried out on the products from the different synthetic routes; anti-solvent flow crystallisation from ethanol (impinging jet) and methanol (T-piece and impinging jet), with results shown in Table.VII.12.

Table.VII.12 Picture before (left) and after heating (right) of 2IA 34DNBA produced in flow at 40 °C in different configurations with water as antisolvent.

Synthesis	Before heating	After heating to 90 °C then cooling
2IA-MeOH-IJ (Flow 2IA 3,4DNBA Impinging Jet)	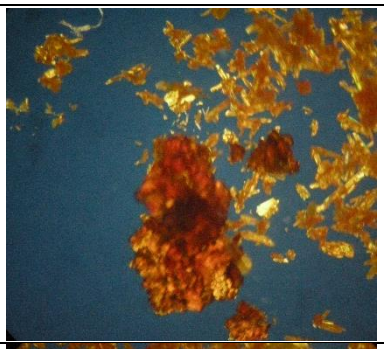	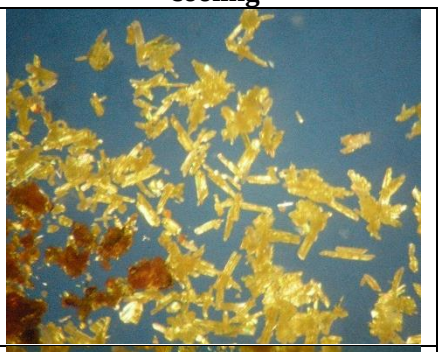
2IA-MeOH-T(2IA-3,4DNBA bench flow 5 m tubing with MeOH)	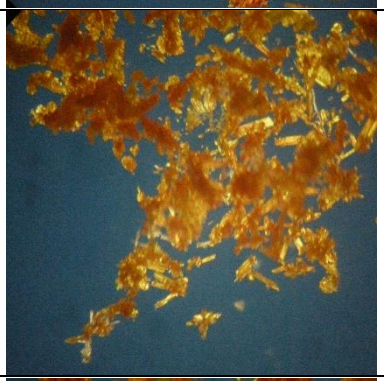	
2IA-EtOH-IJ (2IA34DNBA Impinging Jet with EtOH)	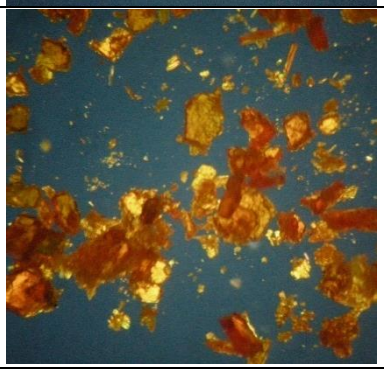	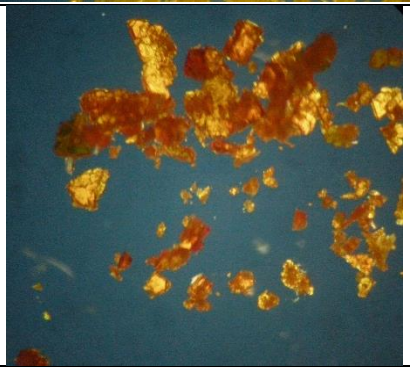

As can be seen from the images above, the crystals go from orange to yellow and do not transition back to orange except for the EtOH synthesis which goes back to its orange colour. DSC analysis of the EtOH sample was carried out and shows the thermal events as shown in Figure.VII.43. The first event at 53 °C (327.9 K) corresponds to the change from Form I to Form II followed by the Form II to Form III change at 85°C (358.3 K). A third event occurs at 76.25 °C (349.4 K) upon cooling which corresponds to the switch of colour back from yellow to red Form I+II. A second heating ramp did not result in another thermal transition from Forms I and II to III. The recovery of lower temperature polymorphs upon cooling was not reported in Jones *et al.*[255] for 2-IA 3,4DNBA produced in vials through evaporation or any batch produced sample reported in this thesis. It is therefore possible that reversibility has been induced with the change in material properties due to its production in flow.

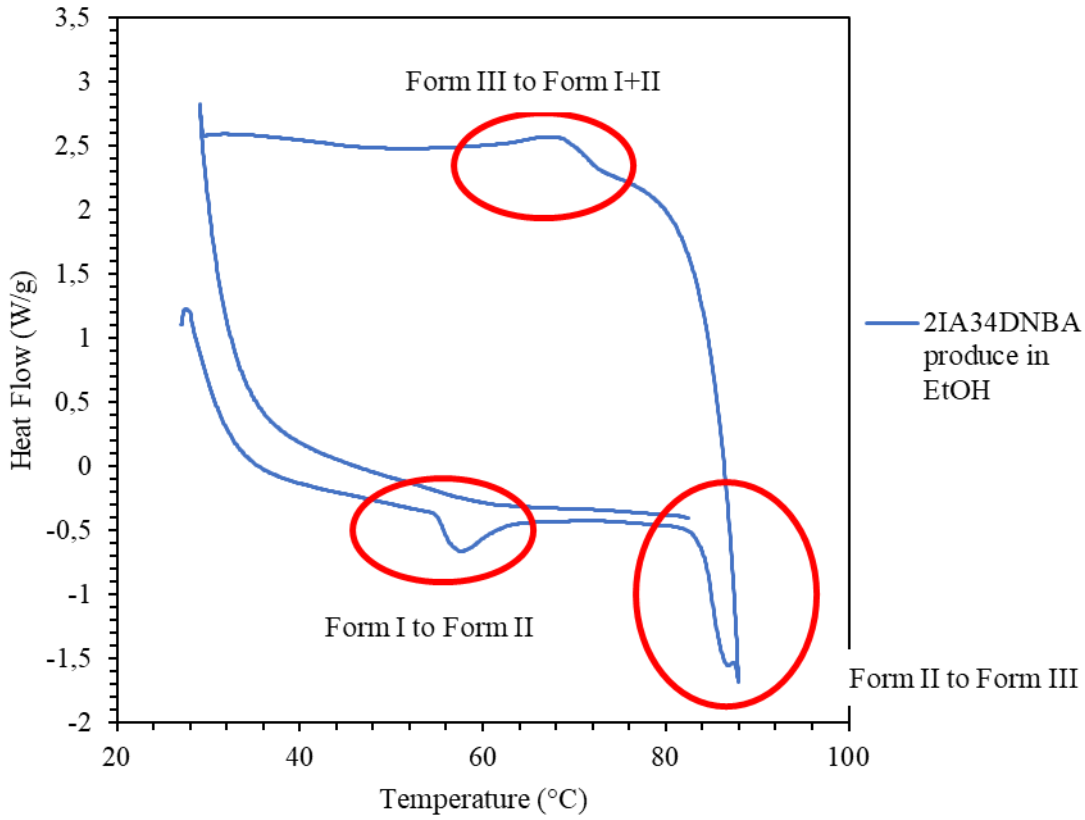

Figure.VII.43 DSC graph of 2-IA 3,4DNBA produced in flow crystallisation in EtOH.

In order to confirm the DSC analysis, larger crystals of 2-IA 3,4DNBA from EtOH were produced in a petri dish *via* anti-solvent crystallisation for clear optical analysis *via* hot-stage microscopy. Figure.VII.44 below shows the hot-stage microscopy of this material during the thermal cycle.

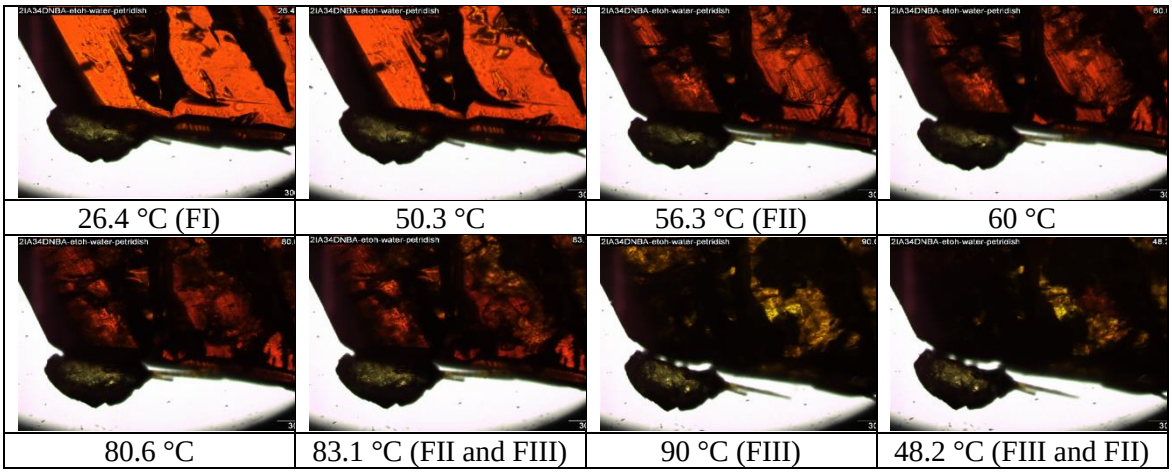

Figure.VII.44 Hot-stage microscopy images of 2IA 34DNBA produced in Petri dish in EtOH-water antisolvent technique showing the reversibility of the polymorphic transitions.

In Figure.VII.44 it can be seen that Form III starts to appear after 83.1 °C and at 90 °C Form III is present throughout the whole crystal. When cooling to room temperature the colour goes from orange/yellow to red and orange at 48.2 °C. In the DSC (Figure.VII.43) similar events are observed,

at 57.4 °C a transition from FI to FII is observed and at 84.1 °C the transition to FIII begins which is completed at 88.1 °C. When cooling, the DSC also shows the thermal event which could potentially be the change from FIII to FI with FII, at 62.3 °C. Analysing the sample *via* PXRD with a temperature variation could potentially confirm the presumed transition during those events on the DSC. In the next paragraph offline PXRD and Raman will investigate this further.

To assess this change in polymorph during the heating and cooling of the sample, concurrent Raman and reflectance UV-Vis spectroscopy was carried out with the same set-up as for PiC in section VII.3 of Chapter VII. The set-up is displayedFigure.VII.45.

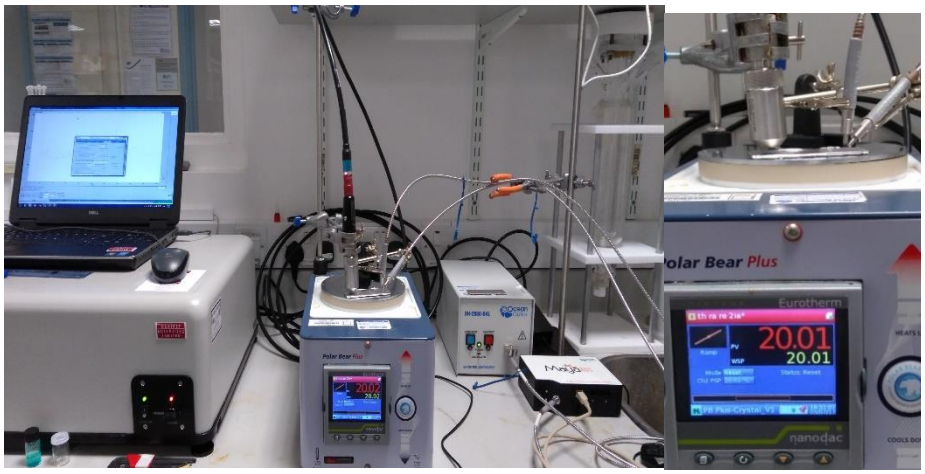

Figure.VII.45 Raman and Reflectance analysis set-up above the Polar Bear.

On Figure.VII.46 and Figure.VII.47 is displayed the UV-Vis and Raman analysis of 2-IA 3,4DNBA showing the change in signal from Form I to Form II of the crystal at 52 °C which corresponds to the previous DSC analysis. The Form II to Form III transition occurs also close to the DSC results at 79 °C. The reverse transition is also seen on cooling after 85 °C from Form III to Form I then Form II after 45 °C. The difference in polymorphic form can be seen in the Raman spectra between 50 and 300 cm^{-1}. In Jones *et al.*[255]only 2BA 3,4DNBA and 2-CLA 3,4DNBA showed a change in polymorphism upon heating but no reversibility in the produced compounds in evaporative crystallisation. The change in coloration of 2-IA 3,4DNBA is due to the polymorphic change from Form I to Form III occurring upon heating.

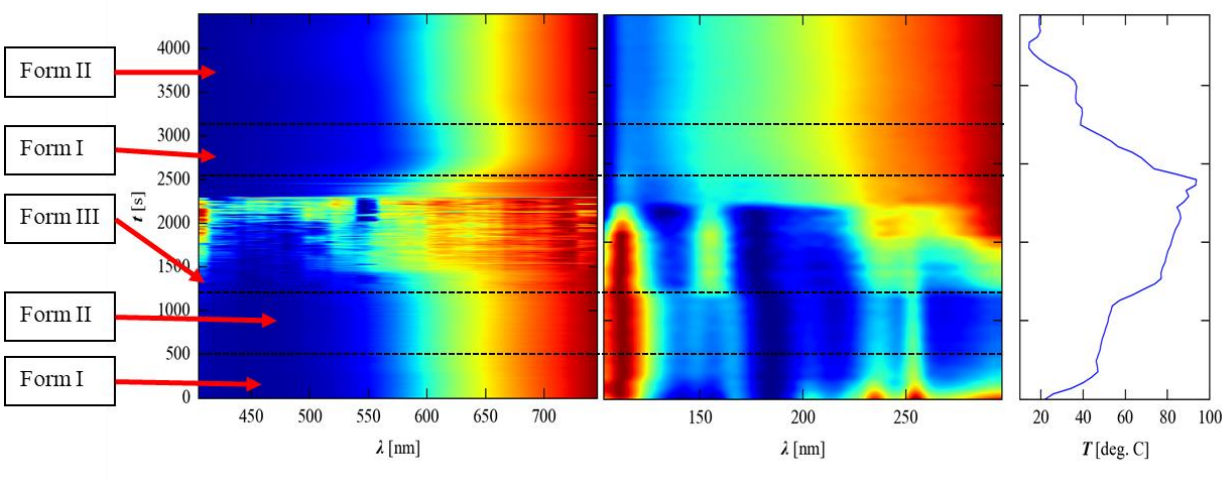

Figure.VII.46 Reflectance (left) and UV-VisRaman (right) spectroscopy of 2IA2DNBA during temperature cycling.

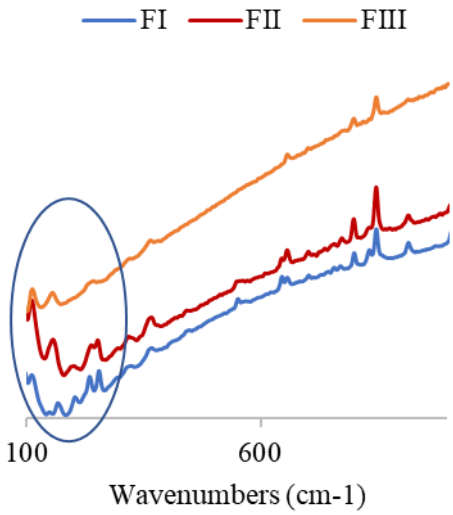

Figure.VII.47 Reflectance patterns of 2-IA 3,4DNBA during temperature cycling.

The reversibility seems to be due to the solvent trapped inside the crystals, as can be seen on Figure.VII.48 which shows the solvent escaping *via* evaporation during heating of the sample The sample was put into Fomblin® oil due to suspicion of solvent escaping upon heating up the material. This sample was produced in the KRAIC experiment 2IA34DNBA KRAIC segmented flow (SG-2IA-EtOH) from Chapter VI.

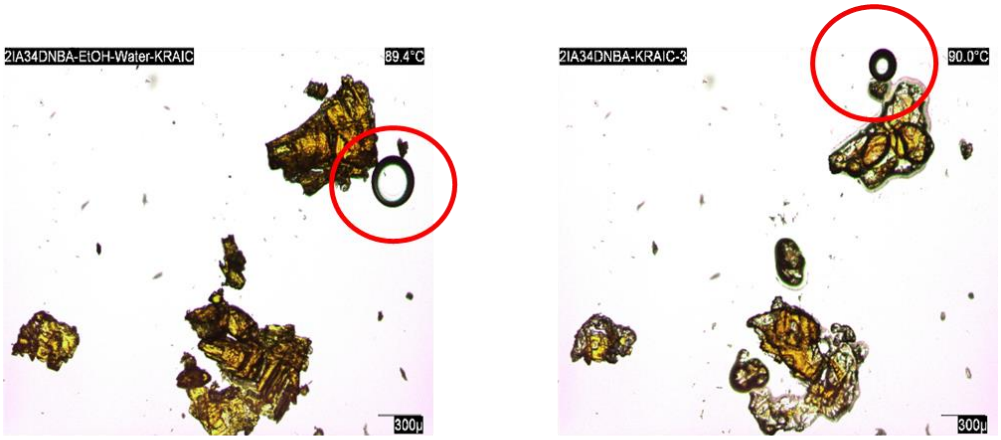

Figure.VII.48 Hot-stage microscopy of 2IA 34DNBA produce in experiment 2IA34DNBA KRAIC segmented This sample is submerged in oil to see any bubbles coming out of the compound (highlighted) (2IA-SFK-EtOH Chapter VI).

Figure.VII.48 displayed this experiment showing bubbles of solvent escaping from the crystals at 89.4 °C and 90 °C, each picture has been taken on the same sample over two heating/cooling cycle. This showed that some solvent was still trapped inside the crystal and this solvent might have facilitated the switching. SEM was then carried out to look at the crystals at a different scale. The first crystals analysed were those produced with the Vapourtec Jet in EtOH 2IA-EtOH-IJ which show the reversible phase transitions. Figure.VII.49 shows those SEM images, illustrating that the crystals show both hollow crystals and plate-like structures.

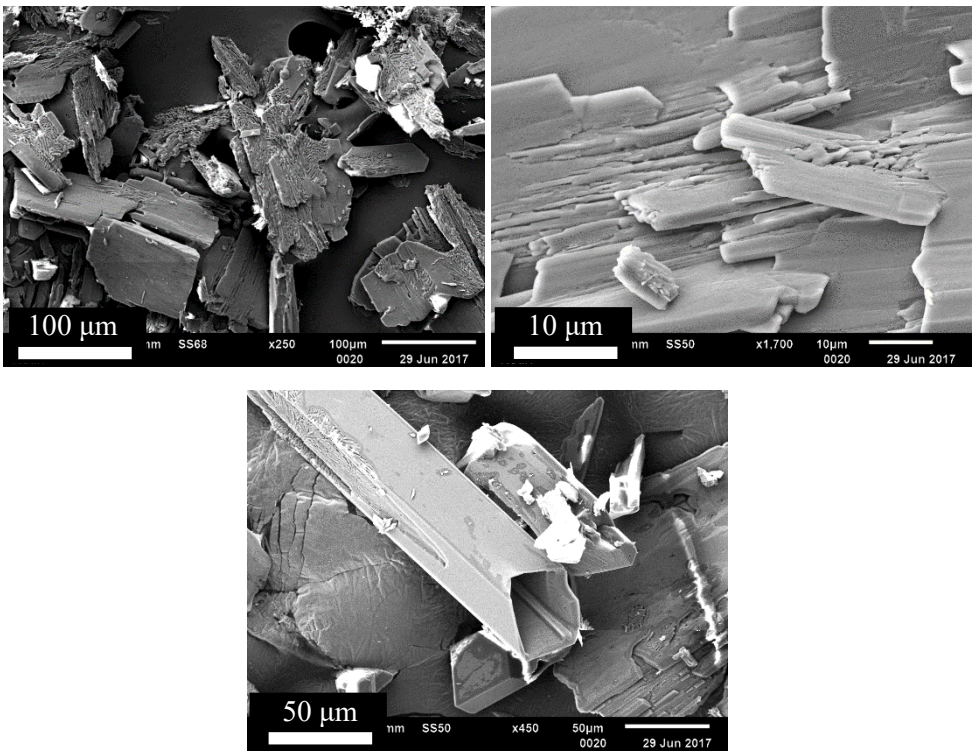

Figure.VII.49 SEM of 2IA 34DNBA produced in flow in EtOH-water 2IA34DNBA Impinging Jet showing plates and hollow crystals (2IA-IJ Chapter VI).

The sample produced in the KRAIC segmented flow experiment SG-2IA-MeOH showed a porous morphology, as can be seen on Figure.VII.50, which could trap even more solvent.

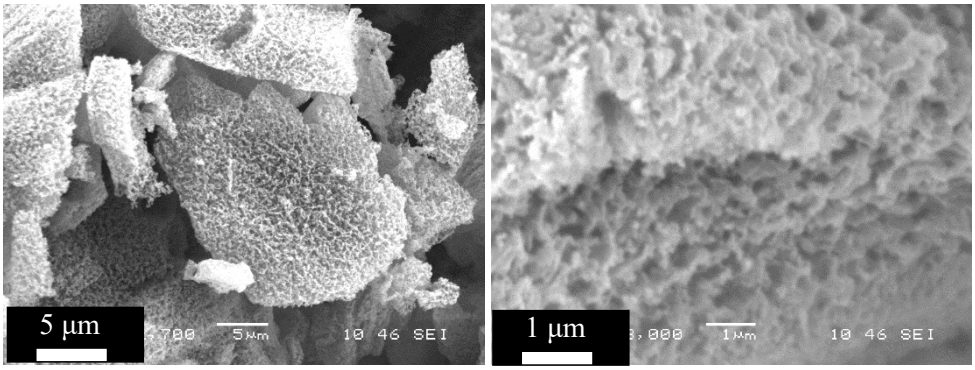

Figure.VII.50 SEM of 2IA 34DNBA produce in the KRAIC showing porosity of the crystals (2IA-SFK-EtOH Chapter VI).

This porous structure is still under investigation and needs further understanding of the switching properties of the complexes between each Form. As the sample is unstable under ambient conditions, resulting in loss of the aniline component, further investigation has proved difficult.

VII.5. Conclusion

In this chapter the different switching properties of samples produced in flow have been assessed. The size and morphology of $[Fe(Htrz)_2(trz)](BF_4)\cdot H_2O$ (PiC) has shown to be an important factor in the spin transition, whether it was sphere, rods or stars. The size of particles was also an important factor displaying a reduction in the temperature needed to achieve the ST of PiC with smaller particle size. The comparison from 1000 nm range particle to 100 nm was made, with a temperature reduction for ST of 20 K. In Moulet *et al.*[218], this change of ST due to size reduction was also assessed using SQUID analysis for different samples displaying rods at different sizes, the bigger particle (>1 µm) giving a ST upon heating at 370 K and the smallest (< 40 nm) a ST at 345 K.

The SQUID and EDF data presented here showed that the morphology type could affect spin transition temperature and dictate the growth direction of the crystals produced. In particular the rods sample showed a ST earlier than its sphere and star counterpart. The EDF sample analysis displayed the presence of both LS and HS in the rods but only HS states in the spheres and stars, this can be explained by heating of the sample by the electron beam and the fact that the rods samples were larger than the other morphologies (for better energy diffusion). The AUC analysis gave information on the PiC sedimentation rate for different particle morphologies, it was not confirmed that the sedimentation rate was fast enough to induce sedimentation as observed in Chapter V for the OBR. On the other hand, the KRAIC inertia phenomenon described in Chapter IV could be explained by the fluidic dynamics and the density of the PiC particles synthesised. The DCS graphs gave confirmation over previous measurements and interpretations for DLS and sedimentation for the Vapourtec, KRAIC and OBR produced PiC samples. Analysing rods shaped particles with DLS is still difficult as the DLS software might measure the transversal length of the particle or the section depending on the particle orientation in the cuvettes.

Electrospinning was successfully performed to create thin switchable films of PiC incorporated in PAN. The presence of the ST during the change of temperature of the film was observed. This could lead to incorporation of the switchable material into thin polymers film to create devices.[250,252]

However during the electrospinning process the ability to detect a colour change and switching properties has been reduced significantly compared to the raw material.

The SCO compound YeC $FeL_2[BF_4]_2$ did not show a significant difference of switching *via* DSC over samples depending on the size of the particle.

Flow synthesis of the organic thermochromic complex, 2-IA 3,4DNBA has been shown to be a candidate to produce larger quantity of the material, but also different morphologies that could lead to potential new discoveries in that field. The polymorphic forms I, II and III are accessed upon heating and the reversibility of the polymorphic change was only possible in flow synthesised samples. The hollow and porous crystal shapes discovered for that compound synthesised in this manner are assumed to trap the solvent used for the synthesis of the complex which may facilitate the reversibility of the polymorphism.

Conclusion

The aim of the present work was to investigate the use of flow chemistry and crystallisation platforms in order to control properties and scale-up production of switchable smart materials developed in the Metastable Materials M^4 group at the University of Bath, such as thermochromics and spin-crossover compounds. The properties control focus of the materials investigated has been crystal structure, particle size and switching temperature. In this thesis, production in larger scale was investigated for several switching materials, optimisation of the platforms used leading to new discoveries for the switching properties on those materials and particle size control during the process. The ability to control particle size has been of main interest, particularly in the Oscillatory Baffled Reactor (OBR) from the Makatsoris group at Cranfield University and the static mixer reactor from Vapourtec and it was assessed that more DOE data would be necessary to obtain a proper model.

The Kinetically Regulated Automated Input Crystalliser (KRAIC) was first improved by trying different configurations for cooling crystallisation of succinic acid (SA) and urea barbituric acid (UBA). The investigation of SA production led to improvement of the KRAIC design including the use of tri-segmented flow with carrier fluid, air and the solution to improve slug formation inside the reactor and an end piece with recovery system for the carrier fluid. Crystallisation of SA in the tri-segmented flow displayed the presence of an unexpected polymorph from solution crystallisation, α-SA, in addition to the expected β-polymorph, which may be indicative of a polymorphic influence from the liquid-segmented environment in the crystallisation process at some point inside the reactor. With UBA crystallisation, the KRAIC design was more advanced and experiments could be run for longer time with the new recovery systems and improved formation of slugs. As for SA, UBA showed the presence of different polymorphs in the crystallised product, in particular Form I and Form III were present with a predominance of Form I. The KRAIC was also used for the production of molecular gels with 4-[[3,5-bis[(4-carboxyphenyl)carbamoyl]benzozoyl]amino]benzoate sodium (BTA) which was successful and could potentially lead to encapsulation of different type of crystals from pharmaceuticals to switchable materials inside gel slugs. Crystallisation within the forming gels was attempted but the results have thus far been inconclusive. To further investigate the possibility to encapsulate a crystal into a gel, a pH solubility curve of Vanillin and the BTA would be necessary to be able to control at which Vanillin concentration and pH the gel and the crystallisation will occur. The Galden recovering system could be improved using a PTFE membrane instead of perforated holes in the FEP tubing, this would improve the recycling system to prevent loss of carrier fluid overtime for long runs.

For $[Fe(Htrz)_2(trz)](BF_4)$, a spin crossover compound with temperature activated colour and magnetic switching, production was investigated using the KRAIC. During this process several observations were made. The first was the reaction colour changing from colourless, to cloudy white and then turning to a pink colour at the end of the KRAIC, this was also observed in batch synthesis. In terms of particle size, the analysis *via* scanning electron microscopy (SEM) and dynamic light scattering (DLS) confirmed the presence of rod shaped materials ranging from 800 nm to 1200 nm depending on the concentration used. A variant of this compound, $[Fe(Htrz)_3](BF_4)_2{\cdot}H_2O$, was also produced in methanol. This was of particular interest for production in the KRAIC due to some reports of gelation at high concentration. Unfortunately, only an increased viscosity of solution was obtained inside the KRAIC without the formation of gel slugs previously obtained with BTA.

From the understanding of the use of the KRAIC in crystallization and material production, those studies led to the design of the KRAIC-D for *in situ* X-ray diffraction inside each of the slugs. At first UBA crystallisation was analysed in the reactor and confirmed the presence of the different

polymorphs during the crystallization and also that different polymorphs were dominant at different points of the crystallisation process, Form I and III were present at the beginning of the crystallisation with Form III being predominant, overtime Form I is then becoming prominent at the end of the process. These results were obtained at the synchrotron at Diamond Light Source which showed that using segmented flow for *in situ* X-ray diffraction was possible and helpful to determine and study polymorph formation for pharmaceutical compounds. It was then decided to try to identify the initial white phase that was reported during the reaction of $[Fe(Htrz)_2(trz)](BF_4)$ using the KRAIC-D, but unfortunately the signal strength was not good enough to detect any diffraction during the cloudy white phase and only the final the pink phase of the material was detected. This was then taken to a next step of *in situ* analysis for this compound by using Raman spectroscopy to detect the differences between the phases. This gave successful results by showing a change in bond length of B-F, C-N and C=N bonds due to the interaction between 1,2,4-H triazole and iron (II) tetrafluoroborate, the two-reagents used to produce $[Fe(Htrz)_2(trz)](BF_4)$. This proved that during the synthesis of that compound some intermediate system is present which differs from either spin state of the final form. With the KRAIC-D configuration it was seen during the UBA experiments, blockages were occurring in the Kapton® windows stopping the experiment due to the beam damaging the Aquapel® coating. Further SEM and EDX studies could help finding the damaging rate of the beam on the coating and help chose another type of coating with a low interference with the beam. Multi-phase flow with the Volume of Fluid (VOF) model has been also successfully used in order to simulate the KRAIC segmented flow behaviour for different flow rates and the simulations were able to show the mixing bolus flow phenomenon inside the slugs formed by a Y-piece. These VOF simulations showed the importance of the inlet flow rate on the bolus flow intensity inside each slug formed, with a high flow rate slugs are long but mixing can be intense, on the other hand slow flow rates give low mixing and small slugs. Having too fast flow rates can disrupt the slugs and give unwanted results such as annular flow, this is why a good mid-range parameter needs to be chosen to have mixing homogeneity and constant slug size.

In Chapter V, $[Fe(Htrz)_2(trz)](BF_4)$ production was successfully achieved in the Oscillatory Baffled Reactor (OBR), the purpose of this work was to study the possibility to target and control particle size of the nano rods like those obtained in the KRAIC. The initial experiment showed a range of particle sizes ranging from 600 nm to 1300 nm depending on the parameters used. Here a 'design of experiments' (DOE) study gave the possibility to target the particle size *via* an equation based on a campaign of experimental results from differing reaction and flow parameters. Different frequency, amplitude, flow rate and concentration of reagent were used to target from 100 nm to 1000 nm. The targeting of the particles was successful for particles targeted at 200, 500 and 600 nm and gave more information on the particle dependency on some parameters. For instance, to target small particles the concentration was high (8 g/mL to 12 g/mL) and gave spherical particles around 100-300 nm. For 400 to 700 nm, with concentration of 4 g/mL to 7 g/mL, the particles were star shaped rod crystals and for 800 nm to 1000 nm needle like crystals (concentration of 1 g/mL to 3 g/mL). This behaviour of concentration dependence was also reported for the KRAIC; when high concentration of reagent was used spherical particles were obtained and at lower concentration the rods/needle likes particle were obtained and for mid-range concentration (4 g/mL – 7 g/mL) star shaped particles were present. The targeting model for the OBR required further optimisation with a 62.5 % variance and so it was not capable in some cases to target the desired particle size. This is where residence time distribution (RTD) studies were carried out to obtain plug flow behaviour inside the OBR. The RTD curves were optimized and successful experiments were done with better targeting of the particle sizes. The only problem was the high flow rate needed for those experiments and hence the volume of material needed. Several experiments were repeated and monitored with SEM and DLS analysis showing consistency in particle size and morphology. The use of the OBR showed that control of the nano particle size and shape of $[Fe(Htrz)_2(trz)](BF_4)$ was possible but that the

optimization of the reactor needed to be addressed for future experiments. The DOE for the OBR showed inconsistent result as steady state was not achieve after three residence time, the DOE also as a lot of factor which could affect the precision of this one, making more experiment studies on the impact of each parameter on the size of PiC could reduce the number of factor at least to 3 to make a 64 experiment 3 factor DOE which could be more precise than the one presented in Chapter V.

In Chapters III, IV, V and VI $[Fe(Htrz)_2(trz)](BF_4)$ was produced in various reactors and different particle sizes and shapes were reported. Here also the same particle shape behaviour was observed as in the OBR and the KRAIC with spherical, star shaped and rods particles produced for high concentration runs. Decreasing the concentration of $Fe(BF_4)_2 \cdot 6H_2O$ lead to rod shaped/needle particles of PiC while increasing it tends to create start shape to spherical particle with concentration above 4 g/mL, increasing the mixing intensity in all reactors in combination with higher (< 7 g/mL) or low (> 3 g/mL) concentration tends to produce spherical particles for the PiC synthesis. The use of static mixers improved the PSD of $[Fe(Htrz)_2(trz)](BF_4)$ but the relatively high volume and throughput of the reactors are restrictive for some experiments (65 and 142 mL). The Vapourtec R-Series was also used with a progressive mixer tube-in-tube reactor to study the synthesis of another SCO compound, $[FeL_2][BF_4]_2$ [L = 2,6-di(pyrazol-1-yl)pyridine] (YeC), *via* anti-solvent crystallisation. Here the reactor proved useful for the reduction of particle size from *ca.*100 µm to 2-5 µm due to the small holes inside the reactor giving homogenous formation of the crystals compared to batch anti-solvent crystallisation. Due to these successful experiments other syntheses could be tried using that reactor but the small size of the holes readily led to blocking of the reactor. That anti-solvent crystallisation study led to the use of different tubing configurations to produce thermochromic compounds through optimised anti-solvent crystallisation methodologies. At first the production of co-crystals 2-bromoaniline 3,4-dinitrobenzoic (2BA 3,4DNBA), 2-chloroanilinium 3,4-dinitrobenzoic (2CA 3,4 DNBA) and 2-iodoaniline3,4-dinitrobznoic (2IA 3,4 DNBA) acid in ethanol at room temperature was investigated using simple open bore tubing and anti-solvent addition *via* a T-piece but blockages were present during the synthesis with different parameters and configuration of tubing and pumps. Impinging and free jets were then investigated to mimic the environment in the progressive mixer used for YeC with lower reagent volumes needed. These however also showed blockages due to build-up of the crystallised material around the jet. It is only by using segmented flow with two anti-solvent addition points (both T-pieces) that the blockage was not present and yield was increased to 66.25% compared to the poor 5% yield obtained in simple T-piece anti-solvent crystallisation without segmentation. This showed the advantages to use segmented flow in certain cases to transport solids through the full system.

From the many experiments to synthesise switchable materials on the different platforms an evaluation of the crystallisation parameters on the resultant properties has been undertaken. For PiC, $[Fe(Htrz)_2(trz)](BF_4)$, the thermal behaviour has previously been suggested to change depending on particle size as described in Chapter VII. The differential scanning calorimetry (DSC) analysis of the powder obtained from the different reactors and experimental parameters showed that the reduction of the particle size gave an earlier onset of the LS-HS transition. For PiC it was noted that different particle shapes are present depending on the concentration used in the synthesis (< 3 g/mL rods/needles, 3-7 gm/L stars, < 7 g/mL sphere). The spherical particles that were around 100 nm displayed an earlier switch than the star (456 nm APS) and rod shaped particles (100 nm APS) that gave switching properties close to the ones reported in the literature. Stars and rods were reported but not widely studied for the switching area and it was hard to define any correlation. The magnetic properties of PiC particles of 100 nm were also analysed using SQUID. The rods displayed a spin transition at lower temperature than the sphere and stars which has not been reported with particles of these dimensions. Electron diffraction of the different shapes showed that PiC was present in all morphologies and that the growth direction observed implied that the central core of all three shapes was the [010] plane which corresponds to the direction of growth for the coordination polymer chain.

The spheres grew in all directions from this central plane, the rods grew along the [010] plane and the long axis of the stars was [010], out from which the addition of further chains produced the star-shaped cross-section. During the synthesis of the PiC compound the different phase, white intermediate phase and final pink phase, were seen using the different reactor,Raman analysis for both the powder and the *in-situ* flow experiments of PiC from Chapter IV and VII showed some similarities in the shift in the B-F bonds during the change of the initial white phase to the final pink phase between 769 – 800 cm^{-1} wavelength. Additionally, during the heating of the powder the bond lengthening was confirmed by the reduction of signal that was evident with the cycling in temperature during the analysis. The detection of the two distinct phases during the synthesis confirm the presence of an intermediate with confirmation using UV-Vis on the petri dish. It is not yet clear is this white phase could potentially be the HS state of PiC that might appear but more investigation would be needed to analyse this intermediate.

For YeC ($FeL_2[BF_4]_2$ [L = 2,6-di(pyrazol-1-yl)pyridine]), the DSC analysis showed no evidence of a shift in switching temperature shift or hysteresis for the spin transition (ST)due to the reduction in particle size, but the reduction of size could be useful for the incorporation of the compound in a device.

With the collaboration of Dr Alex Eggeman from Manchester University, the understanding of spin state behaviour of PiC in the different morphologies (using electron diffraction) could be improved, and crystal structure of the compound could be obtained with this technique. This work will be carried out in the future between Leeds (Dr Anuradha Pallipurath), Bath (Prof Chick Wilson), Kent (Dr Helena Shepherd) and Nottingham (Dr Karen Robertson). Further SQUID analysis could be investigated for the magnetism of those different particles to see the impact on the LS to HS change and determine their Gibbs energy that could lead to the better understanding of change in the 10Dq distance with the lengthening of the bonds during the ST.

The production of the organic thermochromic materials 2BA 3,4DNBA, 2CA 3,4 DNBA and 2IA 3,4 DNBA in flow showed an improvement of the colour-change properties. In batch it is difficult to obtain crystals which display a reversible change of colour when returning to room temperature, but crystals reported here which were produced in flow do display this ability. The crystal morphology of those synthesised in flow changed from solid block-shaped crystals to hollow-crystals. This morphology effect is suspected to encapsulate solvent left from the synthesis and upon heating some of the solvent is retained which is suspected to facilitate the reversibility. This change of morphology is not yet understood and would need more analysis and production of the materials.

Choosing a specific reactor for producing switchable materials can be dictated depending on the different outputs desired. It was seen while using the reactors that the different particle size obtained, in particular for the $[Fe(Htrz)_2(trz)](BF_4)$ SCO compound, had an impact on the switching properties. Being able to target a certain particle size could be useful for the design or switchable devices. For the PiC compound a certain size and shape was obtained depending on the reaction parameters or reactor employed and different switching temperature were obtained and studied using DSC and SQUID. If a reactor is capable of targeting a specific switching temperature of PiC, a preferable switchable device could be selected. The KRAIC for instance was capable to produce large PiC particles above 1 µm with rods shape and small particles below 200 nm with spherical shape showing different behaviour The OBR produced the different particles in the range of 400 to 600 nm size with a star shape and the Vapourtec static mixer reactor was able to target a wide range of particles with spherical, star shaped and rods ranging from 80 nm to 1200 nm. For the production of PiC, choosing the suitable reactor for a certain size and shape would be the ideal, but the production configuration is also important such as mixing type, steady state, reactor volume and scaling up possibilities.

The OBR in particular showed inconsistent results over the production of PiC with some configurations and results were inconclusive on its capability to produce the same particle size continuously over long run time. The DOE showed low reproducibility of particle targeting. Optimising the reactor design for long run would be necessary, especially the baffle geometry which could be improved, as reported in Ejim *et al.*,[256] to avoid sedimentation of small particles in dead zones. This is where the optimisation of plug flow behaviour with CFD *via* RTD curve studies should be done prior to production experiment of PiC with CFD studies of different baffle geometry. For the OBR in Chapter V the method of simulating the motion of the fluid with the oscillating inlet has been incorporated in the analysis to simulate the eddies inside each interbaffle spacing. A study of the mixing and particle tracking showed that the geometry used for this reactor was not perfect and some improvement could be made in order to avoid dead zones. The RTD studies of the reactor confirmed that the use of more optimal parameters could lead to better mixing conditions and therefore a faster and more homogenous reaction inside the reactor. Some models, such as the OBR CFD, also need to be changed to be closer to reality, the use of more accurate models for the oscillation generation could be beneficial to the CFD and adding an inlet to simulate the pump and the injection of tracer would lead to improvements on the RTD curve obtained. These results will be used in the future to optimize the reactor. So far, scale-up production of PiC using the OBR would not be advised due to the optimisation needed for the reactor. In the OBR, future experiments by doing a full DOE set-up with better velocity ratios could be pursued with 64 experiments to give better precision of the data and variables to obtain a variance at least greater than 90% with a full control on particle size. If successful those models could be used to inform models for other nanoparticle compounds.

The static mixer reactor from Vapourtec showed better steady state and consistent results for the targeting of small and large particles of PiC. Applying the same DOE principle as used in the OBR, another response surface model was produced to target particle size. By using this reactor, the variance here increased to 73.5% which gave a more accurate model than that calculated for the OBR. This was confirmed with the targeting of 100, 500 and 1000 nm particles with the reactors and the particle size obtained was close to the target. Those experiments were repeated and checked over three residence times (RT) to assure consistency. In terms of scaling up PiC production and control over the synthesis, the Vapourtec reactors seem to be more appropriate but their volume needs to be reduced in order to make more optimisation without using too much material. Having a coil which is properly horizontal would also be necessary to avoid any change in mixing intensity along the tubing. In the static mixer reactor model, the advantages of mixing structure inside a tubing have been assessed in Chapter VI by comparing to open bore tubing of the same size. CFD simulations have been very useful to understand and improve the flow reactors used for this thesis but the use of supercomputer methods could allow the evaluation of more complex models such as three phase flows which are intensive in terms of calculation. This reactor would be used in the case of fast reaction time a low residence time which could lead to smaller particles. From the thesis studies of the different reactor for the PiC synthesis it is seen that the Vapourtec has been able to produce different size of the compound while being able to be consistent in the targeting results, the KRAIC on another hand was able to give more information using *in*-situ analytical techniques of the PiC synthesis and give the opportunity to compare them with off-line analysis. However the OBR reactor showed inconsistent results in the production of PiC during the DOE and the targeting, while each reactors needs to have some optimization and more result analysis (SEM, DLS, DOE, RTD, CFD) the OBR is the one where change in design and more study needs to be carried out to be able to produce PiC in consistence manner.

The KRAIC and KRAIC-D reactors, compared to the Vapourtec and OBR reactors, were more suitable for *in-situ* analytical techniques and anti-solvent crystallisation. The *in-situ* X-Ray diffraction carried out at Diamond Light Source I11 and *in-situ* Raman with the KRAIC-D showed good results in identifying different polymorphs (UBA) or different phases (PiC). For UBA the X-

Ray diffraction data analysis showed the presence of the different polymorph Form I, II and III during the crystallisation with some more predominant than other at different stage of the crystallisation which could be useful to have a better understanding of polymorphism. *In-situ* Raman of the PiC synthesis gave more information on the suspected intermediate white phase which appeared in each reactor where the synthesis of PiC was carried out, further investigation needs to be done in order to explain this change of color and reaction intermediate. The inlet piece modulation could be improved by using mixer pieces with quick connectors to produce the slugs which would give more opportunities for different designs of inlet for other synthesis. The carrier fluid recovery system needs to be changed, the use of PTFE membrane with laser drilled holes could be helpful due to the wetting described in Chapter III. The KRAIC-D challenges are the windows, as previously displayed in Chapter IV the Kapton tubing used to allow *in situ* diffraction induced blockages due to unwanted nucleation at some point in the reactor. To solve these problems, new windows need to be designed to avoid a slight change in the wetting surfaces between the PTFE and the Window. This could be solved by studying alternative fluorinated coating solutions for the Kapton that could lead to better wetting. The production of co-crystal thermochromics set-up and reaction needs to be assessed, the anti-solvent synthesis in the KRAIC will be investigated by PhD student Dan Scott. This could lead to new discoveries in anti-solvent crystallisation of smart materials that could be used for devices such as thermic sensors. At Diamond Light Source compounds other than UBA and PiC could be studied with the KRAIC-D to have better understanding of crystallisation of pharmaceuticals and switchable compounds. This work will be carried out by PhD students Lois Wayment and Mark Levenstein as part of their PhD projects between University of Bath, Future Manufacturing Hub in Continuous Manufacturing and Advanced Crystallisation (CMAC), University of Leeds and Diamond Light Source.

With all platforms assessed in this work, is was shown that the KRAIC was more suitable for reaction or crystallisation monitoring due to the small "batch reactor" that the slugs were forming inside the tubing, which could be taken separately for *in-situ* analysis. It was also seen that the KRAIC was suitable for solid handling and scale up due the absence of solid liquid interface between the tubing and the solution. The control of the mixing inside each slug needs better understanding through CFD, but this needs to be made in correlation with experimental results. The OBR did not show good consistency in results and should have more optimisation in order to scale up products at least for solid handling e.g. PiC. Like for the KRAIC, a better control over mixing using experimental data and CFD would be needed. Between the reactors it is the Vapourtec static mixers that shows the best understood a best potential to scale up the production of PiC and also YeC with the progressive mixer reactor, however for the progressive mixer reactor blockages were occurring if large particles (<50 µm) were present, concentration studies need to be carried out before using this reactor to avoid this issue. More studies would be needed on the SCO compounds such as DSC and SQUID data to make a correlation between size and switching temperature, linking them together it would be possible to design specific devices for different purposes.

References

1. Hatcher, L. E., Bigos, E. J., Bryant, M. J., MacCready, E. M., Robinson, T. P., Saunders, L. K., Thomas, L. H., Beavers, C. M., Teat, S. J., Christensen, J. & Raithby, P. R. *CrystEngComm* **16,** 8263–8271 (2014).

2. Shepherd, H., Tonge, G., Hatcher, L., Bryant, M., Knichal, J., Raithby, P., Halcrow, M., Kulmaczewski, R., Gagnon, K. & Teat, S. *Magnetochemistry* **2,** 9 (2016).

3. Robertson, K., Flandrin, P. B., Shepherd, H. J. & Wilson, C. C. *Chim. Oggi/Chemistry Today* **35,** 19–22 (2017).

4. Krober, J., Audiere, J. P., Claude, R., Codjovi, E., Kahn, O., Haasnoot, J. G., Groliere, F., Jay, C., Bousseksou, A., Linares, J., Varret, F. & Gonthiervassal, A. *Chem. Mater.* **6,** 1404–1412 (1994).

5. Letard, J. F., Guionneau, P. & Goux-Capes, L. *Spin Crossover Transit. Met. Compd. Iii* **235,** 221–249 (2004).

6. Adleman, L. *Science (80-.).* **266,** 1021–1024 (1994).

7. de Rosnay, J. *Thin Solid Films* **210–211,** 1–3 (1992).

8. Gütlich, P., Gaspar, A. B., Garcia, Y. & Ksenofontov, V. *Comptes Rendus Chimie* **10,** 21–36 (2007).

9. Baker, W. A. & Bobonich, H. M. *Inorg. Chem.* **2,** 1071–1072 (1963).

10. Bonhommeau, S., Molnár, G., Galet, A., Zwick, A., Real, J. A., McGarvey, J. J. & Bousseksou, A. *Angew. Chemie - Int. Ed.* **44,** 4069–4073 (2005).

11. Moulet, L., Daro, N., Etrillard, C., Letard, J. F., Grosjean, A. & Guionneau, P. *Magnetochemistry* **2,** (2016).

12. Kahn, O. *Science (80-.).* **279,** 44–48 (1998).

13. Manrique-Juárez, M. D., Suleimanov, I., Hernández, E. M., Salmon, L., Molnár, G. & Bousseksou, A. *Materials (Basel).* **9,** (2016).

14. Grosjean, A., Négrier, P., Bordet, P., Etrillard, C., Mondieig, D., Pechev, S., Lebraud, E., Létard, J.-F. & Guionneau, P. *Eur. J. Inorg. Chem.* **2013,** 796–802 (2013).

15. Jones, C. L., Wilson, C. C. & Thomas, L. H. *CrystEngComm* **16,** 5849–5858 (2014).

16. Robertson, K., Flandrin, P. B., Klapwijk, A. R. & Wilson, C. C. *Cryst. Growth Des.* **16,** 4759–4764 (2016).

17. MAKATSORIS; Charalampos et al. *EP2747884 - A MODULAR FLOW REACTOR*. (2014).

18. Matsumoto, T., Newton, G. N., Shiga, T., Hayami, S., Matsui, Y., Okamoto, H., Kumai, R., Murakami, Y. & Oshio, H. *Nat. Commun.* **5,** (2014).

19. Cantin, C., Kliava, J., Servant, Y., Sommier, L. & Kahn, O. *Appl. Magn. Reson.* **12,** 81–86 (1997).

20. Holland, J. M., Kilner, C. A., Thornton-Pett, M., Halcrow, M. A., McAllister, J. A., Lu, Z., Davies, J. E. & Halcrow, M. A. *Chem. Commun.* **35,** 577–578 (2001).

21. Yan, D., Lu, J., Ma, J., Wei, M., Evans, D. G. & Duan, X. *Angew. Chemie - Int. Ed.* **50,** 720–723 (2011).

22. Gershenfeld, N. & Chuang, I. L. *Sci. Am.* **278,** 66–71 (1998).

23. Overvelde, J. T. B., De Jong, T. A., Shevchenko, Y., Becerra, S. A., Whitesides, G. M., Weaver, J. C., Hoberman, C. & Bertoldi, K. *Nat. Commun.* **7,** (2016).

24. Ueberschlag, P. *Sensor Review* **21,** 118–125 (2001).

25. Dhar, P., Katiyar, A. & Maganti, L. S. *J. Appl. Phys.* **120,** (2016).

26. Charlotte Louise Jones. *Multi-component Crystallisation Routes to Tuneable Optical Properties*. (University of Bath, 2015).

27. Mahfoud, T., Bousseksou, A. & Bousseksou, A. (2012).

28. Cambi, L. & Cagnasso, A. *Atti della Accad. Naz. dei Lincei, Cl. di Sci. Fis. Mat. e Nat. Rend.* **13,** 809–813 (1931).

29. Hauser, A. *Top. Curr. Chem.* **233,** 49–58 (2004).

30. Decurtins, S., Gütlich, P., Köhler, C. P., Spiering, H. & Hauser, A. *Chem. Phys. Lett.* **105,** 1–4 (1984).

31. Boldog, I., Gaspar, A. B., Martínez, V., Pardo-Ibañez, P., Ksenofontov, V., Bhattacharjee, A., Gütlich, P. & Real, J. A. *Angew. Chemie - Int. Ed.* **47,** 6433–6437 (2008).

32. Zhao, T., Cuignet, L., Dirtu, M. M., Wolff, M., Spasojevic, V., Boldog, I., Rotaru, A., Garcia, Y. & Janiak, C. *J. Mater. Chem. C* **3,** 7802–7812 (2015).

33. Tobon, Y. A., Etrillard, C., Nguyen, O., Létard, J.-F., Faramarzi, V., Dayen, J.-F., Doudin, B., Bassani, D. M. & Guillaume, F. *Eur. J. Inorg. Chem.* **2012,** 5837–5842 (2012).

34. Sorai, M. & Seki, S. *J. Phys. Chem. Solids* **35,** 555–570 (1974).

35. Guillaume, F., Tobon, Y. A., Bonhommeau, S., Létard, J.-F., Moulet, L. & Freysz, E. *Chem. Phys. Lett.* **604,** 105–109 (2014).

36. Urakawa, A., Van Beek, W., Monrabal-Capilla, M., Galan-Mascaros, J. R., Palin, L. & Milanesio, M. *J. Phys. Chem. C* **115,** 1323–1329 (2011).

37. König, E., Ritter, G., Waigel, J. & Goodwin, H. A. *J. Chem. Phys.* **83,** 3055–3061 (1985).

38. N N Greenwood; T C Gibb. *Kniha* **766,** 669 (1971).

39. Grosjean, A., Négrier, P., Bordet, P., Etrillard, C., Mondieig, D., Pechev, S., Lebraud, E., Létard, J. F. & Guionneau, P. *Eur. J. Inorg. Chem.* 796–802 (2013).

40. Faulmann, C., Chahine, J., Malfant, I., de Caro, D., Cormary, B. & Valade, L. *Dalt. Trans.* **40,** 2480 (2011).

41. Létard, J.-F., Guionneau, P. & Goux-Capes, L. in *Top. Curr. Chem.* **235,** 221–249 (2004).

42. Coronado, E., Galán-Mascarós, J. R., Monrabal-Capilla, M., García-Martínez, J. & Pardo-Ibáñez, P. *Adv. Mater.* **19,** 1359–1361 (2007).

43. Catrin, G., Rainer, H., Josef, R., Bogdan, T. & Jakob, W. *Helv. Chim. Acta* **92,** 1909–1922 (2009).

44. Carletta, A., Buol, X., Leyssens, T., Champagne, B. & Wouters, J. *J. Phys. Chem. C* **120,** 10001–10008 (2016).

45. Scaccia, R. L., Coughlin, D. & Ball, D. W. *J. Chem. Educ.* **75,** 769 (1998).

46. Volpatti, L. R. & Yetisen, A. K. *Trends in Biotechnology* **32,** 347–350 (2014).

47. Abgrall, P. & Gué, A. M. *Journal of Micromechanics and Microengineering* **17,** (2007).

48. Bannock, J. H., Krishnadasan, S. H., Heeney, M. & de Mello, J. C. *Mater. Horizons* **1,** 373 (2014).

49. Suranani, S., Maralla, Y., Gaikwad, S. M. & Sonawane, S. H. *Chem. Eng. Process. Process Intensif.* **126,** 62–73 (2018).

50. Irfan, M., Glasnov, T. N. & Kappe, C. O. *ChemSusChem* **4,** 300–316 (2011).

51. Mercadante, M. A., Kelly, C. B., Lee, C. & Leadbeater, N. E. *Org. Process Res. Dev.* **16,** 1064–1068 (2012).

52. Hornung, C. H., Postma, A., Saubern, S. & Chiefari, J. *Polymer (Guildf).* **55,** 1427–1435 (2014).

53. Lobry, E., Lasuye, T., Gourdon, C. & Xuereb, C. *Chem. Eng. J.* **259,** 505–518 (2015).

54. Witt, P. M., Somasi, S., Khan, I., Blaylock, D. W., Newby, J. A. & Ley, S. V. *Chem. Eng. J.* **278,** 353–362 (2015).

55. Jähnisch, K., Hessel, V., Löwe, H. & Baerns, M. *Angewandte Chemie - International Edition* **43,** 406–446 (2004).

56. Schubert, K., Brandner, J., Fichtner, M., Linder, G., Schygulla, U. & Wenka, A. *Microscale Thermophys. Eng.* **5,** 17–39 (2001).

57. Ehrfeld, W., Dechema. & Institut für Mikrotechnik Mainz GmbH. *Microsystem technology for chemical and biological microreactors : papers of the Workshop on Microsystem Technology, Mainz, 20-21 February, 1995 : organized by DECHEMA and IMM*. (DECHEMA, 1996).

58. Zidouni, F., Krepper, E., Rzehak, R., Rabha, S., Schubert, M. & Hampel, U. *Chem. Eng. Sci.* **137,** 476–486 (2015).

59. Ramesh, S., Cherkupally, P., De La Torre, B. G., Govender, T., Kruger, H. G. & Albericio, F. *Amino Acids* **46,** 2091–2104 (2014).

60. Elvira, K. S., Casadevall i Solvas, X., Wootton, R. C. R. & de Mello, A. J. *Nat. Chem.* **5,** 905–15 (2013).

61. Koos, P., Gross, U., Polyzos, A., O'Brien, M., Baxendale, I. & Ley, S. V. *Org. Biomol. Chem.* **9,** 6903 (2011).

62. Chan, K. L. A. & Kazarian, S. G. *Anal. Chem.* **84,** 4052–4056 (2012).

63. Fabry, D. C., Sugiono, E. & Rueping, M. *React. Chem. Eng.* **1,** 129–133 (2016).

64. Carter, C. F., Lange, H., Ley, S. V., Baxendale, I. R., Wittkamp, B., Goode, J. G. & Gaunt, N. L. *Org. Process Res. Dev.* **14,** 393–404 (2010).

65. Hartman, R. L. & Jensen, K. F. *Lab on a Chip* **9,** 2495–2507 (2009).

66. Mascia, S., Heider, P. L., Zhang, H., Lakerveld, R., Benyahia, B., Barton, P. I., Braatz, R. D., Cooney, C. L., Evans, J. M. B., Jamison, T. F., Jensen, K. F., Myerson, A. S. & Trout, B. L. *Angew. Chemie - Int. Ed.* **52,** 12359–12363 (2013).

67. Farkas, L., Lewin, M. & Bloch, R. *J. Am. Chem. Soc.* **71,** 1988–1991 (1949).

68. *9th Symposium on Continuous Flow Reactor Technology for Industrial Applications*.

69. Porta, R., Benaglia, M. & Puglisi, A. *Organic Process Research and Development* **20,** 2–25 (2016).

70. Schaber, S. D., Gerogiorgis, D. I., Ramachandran, R., Evans, J. M. B., Barton, P. I. & Trout, B. L. *Ind. Eng. Chem. Res.* **50,** 10083–10092 (2011).

71. Davey, R. & Garside, J. From Mol. to Cryst. in *From molecules to crystallizers* 1–52 (2000).

72. Plooster, M. N. *Nature* **217,** 1246–1247 (1968).

73. Myerson, A. S. & Ginde, R. *Handbook of Industrial Crystallization (Crystals, Crystal Growth, and Nucleation). Handbook of Industrial Crystallization* (2002).

74. Price, C. J. & Ottoboni, S. *Addressing the challenges of continuous filtration, washing and drying*. (2017).

75. Su, Q., Nagy, Z. K. & Rielly, C. D. *Chem. Eng. Process. Process Intensif.* **89,** 41–53 (2015).

76. Agnew, L. R., McGlone, T., Wheatcroft, H. P., Robertson, A., Parsons, A. R. & Wilson, C. C. *Cryst. Growth Des.* **17,** 2418–2427 (2017).

77. Hussain, K., Thorsen, G. & Malthe-Sørenssen, D. *Chem. Eng. Sci.* **56,** 2295–2304 (2001).

78. Ambrus, R., Radacsi, N., Szunyogh, T., van der Heijden, A. E. D. M., ter Horst, J. H. & Szabo-Revesz, P. *J. Pharm. Biomed. Anal.* **76,** 1–7 (2013).

79. Woo, X. Y., Tan, R. B. H., Chow, P. S. & Braatz, R. D. *Cryst. Growth Des.* **6,** 1291–1303 (2006).

80. Thun, J., Seyfarth, L., Butterhof, C., Senker, J., Dinnebier, R. E. & Breu, J. *Cryst. Growth Des.* **9,** 2435–2441 (2009).

81. Bauer, J., Spanton, S., Henry, R., Quick, J., Dziki, W., Porter, W. & Morris, J. *Pharm. Res.* **18,** 859–866 (2001).

82. Miller, J. M., Collman, B. M., Greene, L. R., Grant, D. J. W. & Blackburn, A. C. *Pharm. Dev. Technol.* **10,** 291–297 (2005).

83. Lohani, S. & Grant, D. J. W. in *Polymorphism: in the Pharmaceutical Industry* 21–42 (2006).

84. González-Contreras, P., Weijma, J. & Buisman, C. J. N. *Water Res.* **46,** 5883–5892 (2012).

85. Yu, Q., Dang, L., Black, S. & Wei, H. *J. Cryst. Growth* **340,** 209–215 (2012).

86. Powell, K. A., Bartolini, G., Wittering, K. E., Saleemi, A. N., Wilson, C. C., Rielly, C. D. & Nagy, Z. K. *Cryst. Growth Des.* **15,** 4821–4836 (2015).

87. Leubner, I. H. *J. Dispers. Sci. Technol.* **22,** 373–380 (2001).

88. Ekato. *Chemical - Ekato https://www.ekato.com/en-us/industries/chemical/*. (2017).

89. Powell, K. A., Saleemi, A. N., Rielly, C. D. & Nagy, Z. K. *Chem. Eng. Process. Process Intensif.* **97,** 195–212 (2015).

90. Alvarez, A. J., Singh, A. & Myerson, A. S. *Cryst. Growth Des.* **11,** 4392–4400 (2011).

91. Wong, S. Y., Tatusko, A. P., Trout, B. L. & Myerson, A. S. *Cryst. Growth Des.* **12,** 5701–5707 (2012).

92. Lawton, S., Steele, G., Shering, P., Zhao, L., Laird, I. & Ni, X. W. *Org. Process Res. Dev.* **13,** 1357–1363 (2009).

93. Manninen, M., Gorshkova, E., Immonen, K. & Ni, X. W. *J. Chem. Technol. Biotechnol.* **88,** 553–562 (2013).

94. McLachlan, H. & Ni, X.-W. *J. Cryst. Growth* **442,** 81–88 (2016).

95. Siddique, H., Brown, C. J., Houson, I. & Florence, A. J. *Org. Process Res. Dev.* **19,** 1871–1881 (2015).

96. Harvey, A. P., Mackley, M. R. & Stonestreet, P. in *Industrial and Engineering Chemistry Research* **40,** 5371–5377 (2001).

97. Phan, A. N. & Harvey, A. *Chem. Eng. J.* **159,** 212–219 (2010).

98. Levenspiel, O. *Ind. Eng. Chem. Res.* **38,** 4140–4143 (1999).

99. Mo, Y. & Jensen, K. F. *React. Chem. Eng.* **1,** 501–507 (2016).

100. Miracca, I. & Capone, G. *Chem. Eng. J.* **82,** 259–266 (2001).

101. Jiang, M., Zhu, Z., Jimenez, E., Papageorgiou, C. D., Waetzig, J., Hardy, A., Langston, M. & Braatz, R. D. *Cryst. Growth Des.* **14,** 851–860 (2014).

102. Davis, S. F. *SIAM J. Sci. Stat. Comput.* **9,** 445–473 (1988).

103. MacCormack, R. W. *AIAA Pap.* **69–354,** (1969).

104. Glowinski, R., Pironneau, O., Angrand, F., Periaux, J., Perrier, P. & Poirier, G. *PROC. 3RD INT. CONF. FINITE Elem. FLOW Probl. , D.H. NORRIE* **1, Calgar,** (1980).

105. Form, N., Equations, N., Element, F., Fluid, M., Equations, C., Variables, V., Element, F., Fluid, M., Euler, T., Element, F., Fluid, M., Zienkiewicz, O. C., R.L. Taylor, N. ., Taylor, R. L., Nithiarasu, P., Deville, M. O., Gatski, T. B., Zienkiewicz, O. C., Taylor, R. L., Nithiarasu, P., Petrov-galerkin, T., Finite, T., Method, E., Finite, T. & O.C. Zienkiewicz, R.L. Taylor, and P. N. Finite Elem. Method Fluid Dyn. *Finite Elem. Method Fluid Dyn.* **3,** 163–194 (2014).

106. *Fluid Mechanics of Mixing*. **10,** (Springer Netherlands, 1992).

107. Ducoste, J. J., Clark, M. M. & Weetman, R. J. *AIChE J.* **43,** 328–338 (1997).

108. Tabor, G., Gosman, R. I. & Issa. in *Institution of Chemical Engineers Symposium Series* 25–34 (1996).

109. Qian, D. & Lawal, A. *Chem. Eng. Sci.* **61,** 7609–7625 (2006).

110. Kimuli, E. N., Onyemelukwe, I. I., Benyahia, B. & Rielly, C. D. in *Computer Aided Chemical Engineering* **40,** 223–228 (2017).

111. Höhne, W. H. G., Hemminger, W. H. & Flammersheim, H. J. *Differential scanning calorimetry*. *Differential Scanning Calorimetry* (2004).

112. Calorimetry ASTM D3418 - 03. *Test* **08,** 1–7 (2004).

113. Faulmann, C., Chahine, J., Malfant, I., de Caro, D., Cormary, B. & Valade, L. *Dalt. Trans.* **40,** 2480–2485 (2011).

114. ICDD. *The International Centre for Diffraction Data, www.icdd.com*. (2012).

115. Douglas A. Skoog, F. James Holler, S. R. C. *Principle of Instrumental Analysis*. *Principles of Instrumental Analysis* **53,** (2007).

116. Ooi, L. in *Principles of x-ray crystallography* 112–113 (2010).

117. Kartzow, M. B. & Moxnes, H. *Relig. Theol.* **17,** 184–204 (2010).

118. Goldstein, J. I., Newbury, D. E., Echlin, P., Joy, D. C., Lyman, C. E., Lifshin, E., Sawyer, L. & Michael, J. R. *Scanning Electron Microscopy and X-ray Microanalysis*. *Scanning Electron Microscopy and X-Ray Microanalysis* (2003).

119. Scanning Electron Microscopy, I. & Sangster, A. G. *Scanning electron microscopy. Scanning Microscopy* **4,** (1978).

120. Jeol Ltd. *Basic Knowledge For Using The SEM https://www.jeol.co.jp/en/applications/pdf/sm/sem_atoz_all.pdf. Jeol Ltd* 1–32 (2009).

121. Lemmens, H., Butcher, A. & Botha, P. *Petrophysics-SPWLA-Journal …* 1–12 (2011).

122. Horovitz, O., Cioica, N., Jumate, N., Pojar-Feneşan, M., Balea, A., Liteanu, V., Mocanu, A. & Tomoaia-Cotişel, M. *Stud. Univ. Babes-Bolyai Chem.* 211–219 (2011).

123. Cowley, J. M. *Adv. Electron. Electron Phys.* **46,** 1–53 (1978).

124. DIFPACK. *DIFPACK Module | Gatan, Inc. http://www.gatan.com/products/tem-imaging-spectroscopy/difpack-module*.

125. Xie, C., Chen, D. & Li, Y. *Opt. Lett.* **30,** 1800 (2005).

126. Minsky, M. *Scanning* **10,** 128–138 (1988).

127. Perkampus, H.-H. *UV-VIS Spectrosc. its Appl. UV-VIS spectroscopy and its application* **12,** (1992).

128. Saleemi, A. N., Rielly, C. D. & Nagy, Z. K. *Chem. Eng. Sci.* **77,** 122–129 (2012).

129. Liu, T. & Xiao, Z. W. *Macromol. Chem. Phys.* **213,** 1697–1705 (2012).

130. Stetefeld, J., McKenna, S. A. & Patel, T. R. *Biophysical Reviews* **8,** 409–427 (2016).

131. Nemati, M., Presura, C. N., Urbach, H. P. & Bhattacharya, N. *Biomed. Opt. Express* **5,** 2145–2156 (2014).

132. Sales, R. S. & Support, A. *ATA Sci.* (2014).

133. Lebowitz, J., Lewis, M. S. & Schuck, P. *Protein Sci.* **11,** 2067–2079 (2009).

134. Langevin, D., Lozano, O., Salvati, A., Kestens, V., Monopoli, M., Raspaud, E., Mariot, S., Salonen, A., Thomas, S., Driessen, M., Haase, A., Nelissen, I., Smisdom, N., Pompa, P. P., Maiorano, G., Puntes, V., Puchowicz, D., Stępnik, M., Suárez, G., Riediker, M., Benetti, F., Mičetić, I., Venturini, M., Kreyling, W. G., van der Zande, M., Bouwmeester, H., Milani, S., Rädler, J. O., Mülhopt, S., Lynch, I. & Dawson, K. *NanoImpact* **10,** 97–107 (2018).

135. Cascio, C., Gilliland, D., Rossi, F., Calzolai, L. & Contado, C. *Anal. Chem.* **86,** 12143–12151 (2014).

136. Monopoli, M. P., Walczyk, D., Campbell, A., Elia, G., Lynch, I., Baldelli Bombelli, F. & Dawson, K. A. *J. Am. Chem. Soc.* **133,** 2525–2534 (2011).

137. CPS Instruments Europe. in *Analytical Ultracentrifugation* 270–290 (2018).

138. Draper, N. R. in 267–269 (Springer, New York, NY, 1992).

139. Roche, A. *Local Optimization of Black-Box Function with High or Infinite-Dimensional Inputs*. (2015).

140. Yördem, O. S., Papila, M. & Menceloğlu, Y. Z. *Mater. Des.* **29,** 34–44 (2008).

141. Bösiger, P., Richard, I. M. T., Le Gat, L., Michen, B., Schubert, M., Rossi, R. M. & Fortunato, G. *Carbohydr. Polym.* **186,** 122–131 (2018).

142. Carley, K. M., Kamneva, N. Y. & Reminga, J. *Response Surface Methodology: CASOS Technical Report School of Computer Science*. (2004).

143. Lapkin, A. A., Loponov, K., Tomaiuolo, G. & Guido, S. in *Sustainable Flow Chemistry: Methods and Applications* 277–308 (2017).

144. Yang, H., Yu, X., Raval, V., Makkawi, Y. & Florence, A. *Cryst. Growth Des.* **16,** 875–886 (2016).

145. McGlone, T., Briggs, N. E. B., Clark, C. A., Brown, C. J., Sefcik, J. & Florence, A. J. *Organic Process Research and Development* **19,** 1186–1202 (2015).

146. Van Erdeghem, P. M. M., Logist, F., Dittrich, C. & Van Impe, J. F. in *IFAC Proceedings Volumes (IFAC-PapersOnline)* **18,** 477–482 (2011).

147. Soman, S. S. & Madhuranthakam, C. M. R. *Chem. Eng. Process. Process Intensif.* **122,** 31–43 (2017).

148. Kumar, V., Shirke, V. & Nigam, K. D. P. *Chem. Eng. J.* **139,** 284–295 (2008).

149. Kreutzer, M. T., Kapteijn, F., Moulijn, J. A. & Heiszwolf, J. J. *Chem. Eng. Sci.* **60,** 5895–5916 (2005).

150. Guillemet-Fritsch, S., Aoun-Habbache, M., Sarrias, J., Rousset, A., Jongen, N., Donnet, M., Bowen, P. & Lemaître, J. *Solid State Ionics* **171,** 135–140 (2004).

151. Mallia, C. J., Walter, G. C. & Baxendale, I. R. *Beilstein J. Org. Chem.* **12,** 1503–1511 (2016).

152. Alonso, N., Juan de, M. M., Egle, B., Vrijdag, J. L., De Borggraeve, W. M., de la Hoz, A., Díaz-Ortiz, A. & Alcázar, J. *J. Flow Chem.* **4,** 105–109 (2014).

153. Muzychka, Y. S., Walsh, E. J. & Walsh, P. *J. Heat Transfer* **133,** 041902 (2011).

154. Solvay®. *Solvay® Galden https://www.solvay.com/en/markets-and-products/featured-products/Galden.html*. (2013).

155. Handique, K. & Burns, M. A. *J. Micromechanics Microengineering* **11,** 548–554 (2001).

156. Takeishi, N. & Imai, Y. *Sci. Rep.* **7,** (2017).

157. Song, H., Tice, J. D. & Ismagilov, R. F. *Angew. Chemie - Int. Ed.* **42,** 768–772 (2003).

158. Prothero, J. & Burton, A. C. *Biophys. J.* **1,** 565–579 (1961).

159. Johnson, P. C. & Wayland, H. *Am J Physiol* **212,** 1405–1415 (1967).

160. Robertson, K., Flandrin, P. B., Shepherd, H. J. & Wilson, C. C. *Chim. Oggi-Chemistry Today* **35,** 19–22 (2017).

161. Shah, J. C., Chen, J. R. & Chow, D. *Drug Dev. Ind. Pharm.* **25,** 63–67 (1999).

162. Yu, L. *Acc. Chem. Res.* **43,** 1257–1266 (2010).

163. Zhang, J., Wu, Y., Liu, A., Li, W. & Han, Y. *RSC Adv.* **4,** 21599–21607 (2014).

164. Thakker, C., Martínez, I., San, K.-Y. & Bennett, G. N. *Biotechnol. J.* **7,** 213–224 (2012).

165. Rutesh, D. H. *Drug Topics* **152,** (2008).

166. Matano, C., Meiswinkel, T. M. & Wendisch, V. F. in *Wheat and Rice in Disease Prevention and Health* 493–505 (Elsevier, 2014).

167. Schultheiss, N. & Newman, A. *Crystal Growth and Design* **9,** 2950–2967 (2009).

168. Klapwijk, A. R. *Disorder and additive control of solid form and morphology in continuous crystallisation*. (2016).

169. Balaconis, M. K. & Clark, H. A. in *Journal of Diabetes Science and Technology* **7,** 53–61 (2013).

170. Vidinha, P., Augusto, V., Almeida, M., Fonseca, I., Fidalgo, A., Ilharco, L., Joaquim, J. M. & Barreiros, S. *J. Biotechnol.* **121,** 23–33 (2006).

171. Du, Y., Wang, H., Du, S., Wang, Y., Huang, C., Qin, Y. & Gong, J. *Fluid Phase Equilib.* **409,** 84–91 (2016).

172. Omari, A., Chauveteau, G. & Tabary, R. *Colloids Surfaces A Physicochem. Eng. Asp.* **225,** 37–48 (2003).

173. Yokoyama, F., Achife, E. C., Matsuoka, M., Shimamura, K., Yamashita, Y. & Monobe, K. *Polymer (Guildf).* **32,** 2911–2916 (1991).

174. Perazzo, A., Nunes, J. K., Guido, S. & Stone, H. A. *Proc. Natl. Acad. Sci.* 201710927 (2017).

175. Chang, Y. W., He, P., Marquez, S. M. & Cheng, Z. *Biomicrofluidics* (2012).

176. Gupta, R., Fletcher, D. F. & Haynes, B. S. *Chem. Eng. Sci.* **65,** 2094–2107 (2010).

177. van Baten, J. M. & Krishna, R. *Chem. Eng. Sci.* **59,** 2535–2545 (2004).

178. Araújo, J. D. P., Miranda, J. M. & Campos, J. B. L. M. *J. Pet. Sci. Eng.* **111,** 1–14 (2013).

179. Azargoshasb, H., Mousavi, S. M., Amani, T., Jafari, A. & Nosrati, M. *J. Ind. Eng. Chem.* **27,** 207–217 (2015).

180. Ansys. *Ansys fluent 12.0 Theory Guide*. *ANSYS Inc.* (2009).

181. Temple, G. & Gillis, J. *Phys. Today* **12,** 36–38 (1959).

182. Hirt, C. W. & Nichols, B. D. *J. Comput. Phys.* **39,** 201–225 (1981).

183. Fetter, C. W. *Appl. Hydrogeol. Applied Hydrogeology* (2001).

184. Brackbill, J. U., Kothe, D. B. & Zemach, C. *J. Comput. Phys.* **100,** 335–354 (1992).

185. Dang, M., Yue, J. & Chen, G. *Chem. Eng. J.* **262,** 616–627 (2015).

186. Kaushik, V. V. R., Ghosh, S., Das, G. & Das, P. K. *J. Pet. Sci. Eng.* **86–87,** 153–164 (2012).

187. Cueto Díaz, S., Ruiz Encinar, J. & García Alonso, J. I. *Anal. Chim. Acta* **844,** 48–53 (2014).

188. Foley, D. A., Bez, E., Codina, A., Colson, K. L., Fey, M., Krull, R., Piroli, D., Zell, M. T. & Marquez, B. L. *Anal. Chem.* **86,** 12008–12013 (2014).

189. Welch, C. J., Gong, X., Cuff, J., Dolman, S., Nyrop, J., Lin, F. & Rogers, H. *Org. Process Res. Dev.* **13,** 1022–1025 (2009).

190. Gao, Z., Rohani, S., Gong, J. & Wang, J. *Engineering* (2017).

191. Birch, M., Fussell, S. J., Higginson, P. D., McDowall, N. & Marziano, I. *Org. Process Res. Dev.* (2005).

192. Xiang, Y., Lucas, J., VanAlsten, J., Li, B., Preston, B., Lovdahl, M. & Hayward, C. M. *Am. Pharm. Rev.* **15,** (2012).

193. Baxendale, I. R., Hayward, J. J., Ley, S. V. & Tranmer, G. K. *ChemMedChem* **2,** 768–788 (2007).

194. Codling, K. *J. Synchrotron Radiat.* **4,** 316–333 (1997).

195. Willmott, P. *An Introduction to Synchrotron Radiation*. *An Introduction to Synchrotron*

Radiation: Techniques and Applications (John Wiley & Sons, Ltd, 2011).

196. Diamond Light Source. *About Diamond, How Diamond Works http://www.diamond.ac.uk/Home/About/How-Diamond-Works.html*. *About Diamond, How Diamond Works* (2016).

197. Shian, S. & Sandhage, K. H. *Rev. Sci. Instrum.* **80,** (2009).

198. Dootz, R., Evans, H., Köster, S. & Pfohl, T. *Small* **3,** 96–100 (2007).

199. Otten, A., Köster, S., Struth, B., Snigirev, A. & Pfohl, T. in *Journal of Synchrotron Radiation* **12,** 745–750 (2005).

200. Akamatsu, Y., Makita, K., Inaba, H. & Minami, T. *Thin Solid Films* (2001).

201. Hendon, C. H., Wittering, K. E., Chen, T. H., Kaveevivitchai, W., Popov, I., Butler, K. T., Wilson, C. C., Cruickshank, D. L., Miljanić, O. S. & Walsh, A. *Nano Lett.* **15,** 2149–2154 (2015).

202. Etrillard, C., Faramarzi, V., Dayen, J. F., Letard, J. F. & Doudin, B. *Chem. Commun.* **47,** 9663–9665 (2011).

203. Durand, P., Pillet, S., Bendeif, E.-E., Carteret, C., Bouazaoui, M., El Hamzaoui, H., Capoen, B., Salmon, L., Hébert, S., Ghanbaja, J., Aranda, L. & Schaniel, D. *J. Mater. Chem. C* **1,** 1933 (2013).

204. Baxendale, I. R. *Journal of Chemical Technology and Biotechnology* **88,** 519–552 (2013).

205. Ni, X., Mackley, M. R., Harvey, A. P., Stonestreet, P., Baird, M. H. I. & Rama Rao, N. V. *Chem. Eng. Res. Des.* **81,** 373–383 (2003).

206. Stonestreet, P. & Van Der Veeken, P. M. J. *Chem. Eng. Res. Des.* **77,** 671–684 (1999).

207. Reis, N., Harvey, A. P., Mackley, M. R., Vicente, A. . & Teixeira, J. . *Chem. Eng. Res. Des.* **83(A4),** 357–371 (2005).

208. Reis, N., Vicente, A. A. & Teixeira, J. A. *Chem. Eng. Process. Process Intensif.* **49,** 793–803 (2010).

209. Rajavathsavai, D., Khapre, A. & Munshi, B. *Brazilian J. Chem. Eng.* **31,** 119–129 (2014).

210. Roco, M. C., Mirkin, C. A. & Hersam, M. C. *WTEC-World Technol. Eval. Cent.* 476–477 (2010).

211. Makatsoris, C., Paramonov, L. & Alsharif, R. *Modular flow reactor US20150010445*. (2015).

212. MAKATSORIS, Charalampos; ALSHARIF, R. M. S. *A Modular Flow Reactor WO 2013/050764 Al*. (2013).

213. Makatsoris, C., Paramonov, L. & Alsharif, R. *MODULAR FLOW REACTOR United States Patent Application 20150010445*. (2015).

214. Charalampos MAKATSORIS, L. P. A. *A modular flow reactor EP2747884A1*. (2012).

215. Ni, X. & Gough, P. *Chem. Eng. Sci.* **52,** 3209–3212 (1997).

216. Ni, X.-W. *Innov. Pharm. Technol.* 8–12 (2006).

217. Zhao, T., Cuignet, L., Dîrtu, M. M., Wolff, M., Spasojevic, V., Boldog, I., Rotaru, A., Garcia, Y. & Janiak, C. *J. Mater. Chem. C* **3,** 7802–7812 (2015).

218. Moulet, L., Daro, N., Etrillard, C., Létard, J.-F., Grosjean, A. & Guionneau, P.

Magnetochemistry **2,** 10 (2016).

219. Lopez-Miranda, A., Lopez-Valdivieso, A. & Viramontes-Gamboa, G. *J. Nanoparticle Res.* **14,** (2012).

220. Fleming, R., Pardini, L. C., Alves, N., Garcia, E. & Brito, C. *Polim. E Tecnol.* **24,** 259–268 (2014).

221. Royal Society of Chemistry & Nuffield Foundation. *Adv. Chem. Sci.* 228–231

222. González-Juárez, D., Solano, J. P., Herrero-Martín, R. & Harvey, A. P. *Chem. Eng. Res. Des.* **118,** 259–269 (2017).

223. González-Juárez, D., Solano, J. P., Herrero-Martín, R. & Harvey, A. P. *Chem. Eng. Res. Des.* **118,** 259–269 (2017).

224. Kolmogorov, A. N. *Proc. R. Soc. A Math. Phys. Eng. Sci.* **434,** 9–13 (1991).

225. Ansys Inc. *Knowl. Creat. Diffus. Util.* **15317,** 724–746 (2013).

226. Arastoopour, H., Gidaspow, D. & Abbasi, E. *Computational Transport Phenomena of Fluid-Particle Systems*. (2017).

227. You, D. & Moin, P. *Phys. Fluids* **19,** (2007).

228. Kolmogorov, A. N. *Proc. R. Soc. A Math. Phys. Eng. Sci.* **434,** 9–13 (1991).

229. Langhans, W., Schmidli, J. & Schär, C. *Mon. Weather Rev.* **140,** 226–244 (2012).

230. Arendt, W., Warma, M. & Philippe Bénilan, D. *Math. Subj. Classif.* **3,** 47–54 (2003).

231. Stephens, G. G. & Mackley, M. R. *Exp. Therm. Fluid Sci.* **25,** 583–594 (2002).

232. Barlow, K. J., Bernabeu, V., Hao, X., Hughes, T. C., Hutt, O. E., Polyzos, A., Turner, K. A. & Moad, G. *React. Funct. Polym.* **96,** 89–96 (2015).

233. Plutschack, M. B., McQuade, D. T., Valenti, G. & Seeberger, P. H. *Beilstein J. Org. Chem.* **9,** 2022–2027 (2013).

234. Zhou, M., Bai, D., Zong, Y., Zhao, L. & Thornock, J. N. *Chem. Eng. Process. Process Intensif.* **122,** 190–203 (2017).

235. Saubern, S., Nguyen, X., Nguyen, V., Gardiner, J., Tsanaktsidis, J. & Chiefari, J. *Macromol. React. Eng.* **11,** (2017).

236. Jones, S. C., Sotiropoulos, F. & Amirtharajah, A. *J. Environ. Eng.* **128,** 431–440 (2002).

237. Bakker, A., Laroche, R. D. & Marshall, E. M. *Online CFM B.* 1–11 (2000).

238. Cook, L. & Halcrow, M. *Magnetochemistry* **1,** 3–16 (2015).

239. Hutchins, K. M., Dutta, S., Loren, B. P. & Macgillivray, L. R. *Chem. Mater.* **26,** 3042–3044 (2014).

240. Carletta, A., Spinelli, F., d'Agostino, S., Ventura, B., Chierotti, M. R., Gobetto, R., Wouters, J. & Grepioni, F. *Chem. - A Eur. J.* **23,** 5317–5329 (2017).

241. Jameson, D. L. & Goledsby, K. A. *J. Org. Chem.* **55,** 4992–4994 (1990).

242. Cantin, C., Kliava, J., Servant, Y., Sommier, L. & Kahn, O. *Appl. Magn. Reson.* **12,** 87–93 (1997).

243. Lefter, C., Tan, R., Dugay, J., Tricard, S., Molnar, G., Salmon, L., Carrey, J., Rotaru, A. & Bousseksou, A. *Phys. Chem. Chem. Phys.* **17,** 5151–5154 (2015).

244. Bartual-Murgui, C., Natividad, E. & Roubeau, O. *J. Mater. Chem. C* **3,** 7916–7924 (2015).

245. Peng, H. *Synthesis of spin crossover micro-and nano-particles and study of the effect of their sizes and morphologies on their bistability properties*. (2015).

246. Kazys, R., Sliteris, R., Rekuviene, R., Zukauskas, E. & Mazeika, L. *Sensors (Switzerland)* (2015).

247. Bircher, B. A., Krenger, R. & Braun, T. *Sensors Actuators, B Chem.* (2016).

248. Alexander, C. M., Dabrowiak, J. C. & Goodisman, J. *J. Colloid Interface Sci.* (2013).

249. Carney, R. P., Kim, J. Y., Qian, H., Jin, R., Mehenni, H., Stellacci, F. & Bakr, O. M. *Nat. Commun.* (2011).

250. Morota, K., Matsumoto, H., Mizukoshi, T., Konosu, Y., Minagawa, M., Tanioka, A., Yamagata, Y. & Inoue, K. *J. Colloid Interface Sci.* **279,** 484–492 (2004).

251. Kurban, Z., Lovell, A., Jenkins, D., Bennington, S., Loader, I., Schober, A. & Skipper, N. *Eur. Polym. J.* **46,** 1194–1202 (2010).

252. Hwang, W., Xin, G., Cho, M., Cho, S. M. & Chae, H. *Nanoscale Res. Lett.* **7,** (2012).

253. Lv, J., Chen, L., Zhu, Y., Hou, L. & Liu, Y. *ACS Appl. Mater. Interfaces* **6,** 4954–4964 (2014).

254. Yang, F., Murugan, R., Wang, S. & Ramakrishna, S. *Biomaterials* **26,** 2603–2610 (2005).

255. Jones, C. L., Skelton, J. M., Murray, C. A., Parker, S. C., Paul, R., Walsh, A., Wilson, C. C. & Thomas, L. H. *Designing the Flexibility to Switch – Molecular Disorder Facilitated Thermochromism (unpublished)*.

256. Ejim, L. N., Yerdelen, S., McGlone, T., Onyemelukwe, I., Johnston, B., Florence, A. J. & Reis, N. M. *Chem. Eng. J.* **308,** 669–682 (2017).

Appendix

Appendix Chapter III (A3)

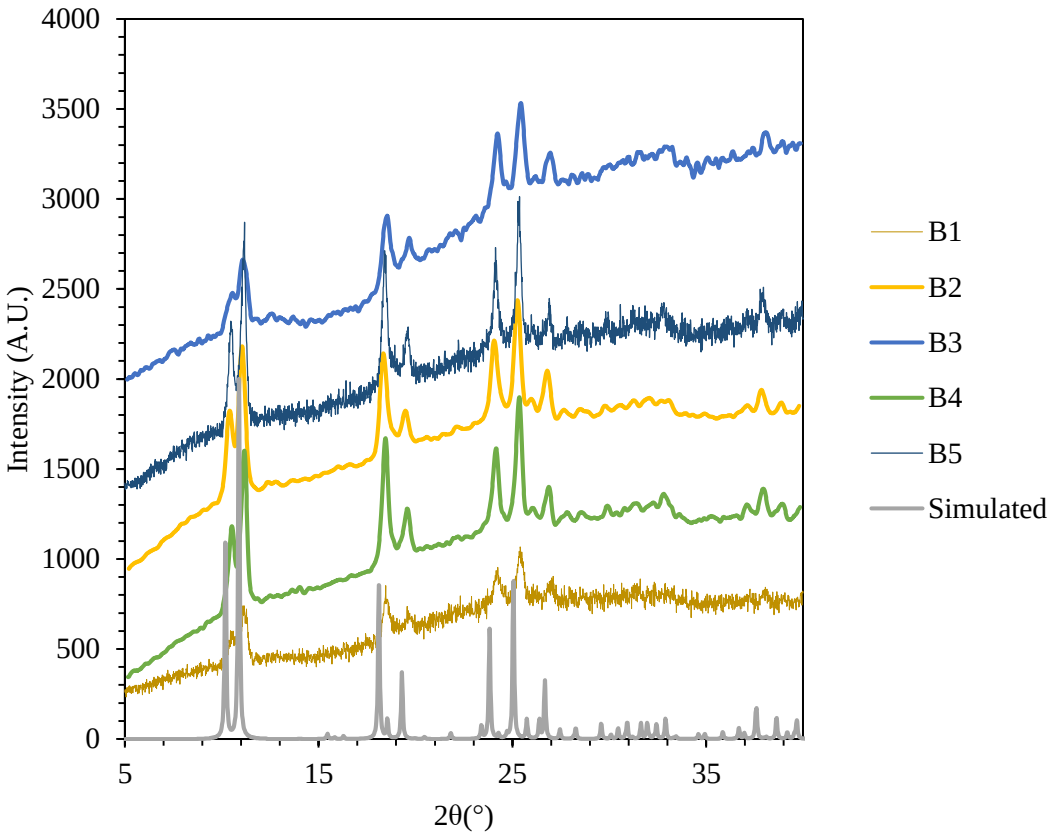

Figure A3.1 PXRD of PiC experiment carried out in Batch for B1 to B5 compared to simulated data from Grosjean *et al.*[14]

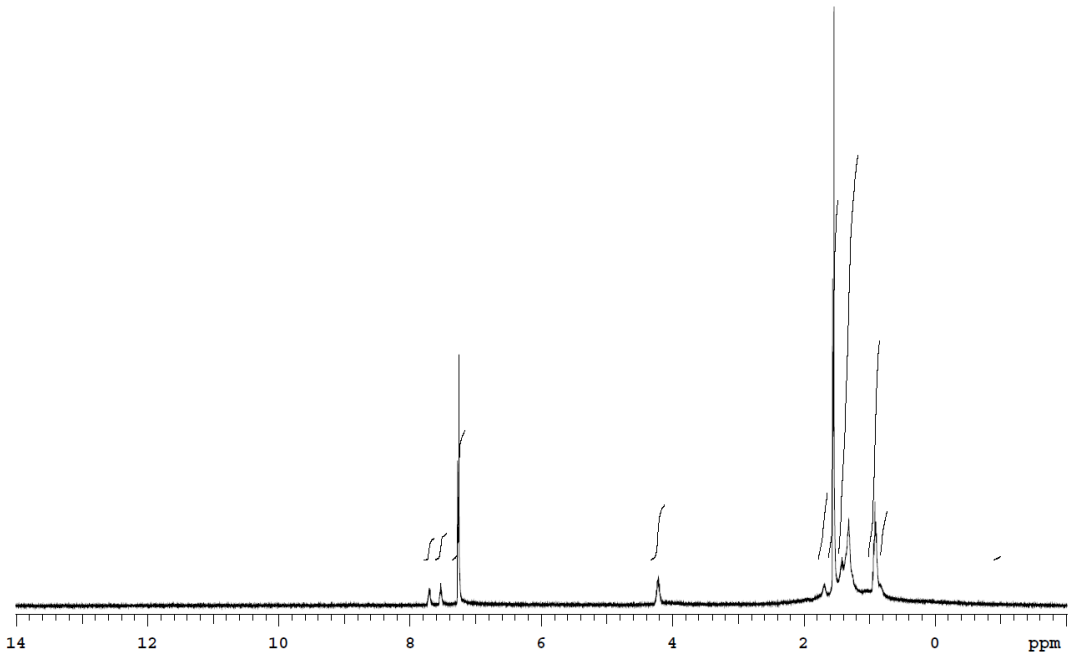

Figure A3.2 NMR of solution recovered from digestion after BTA gelation with incorporated vanillin produced in batch

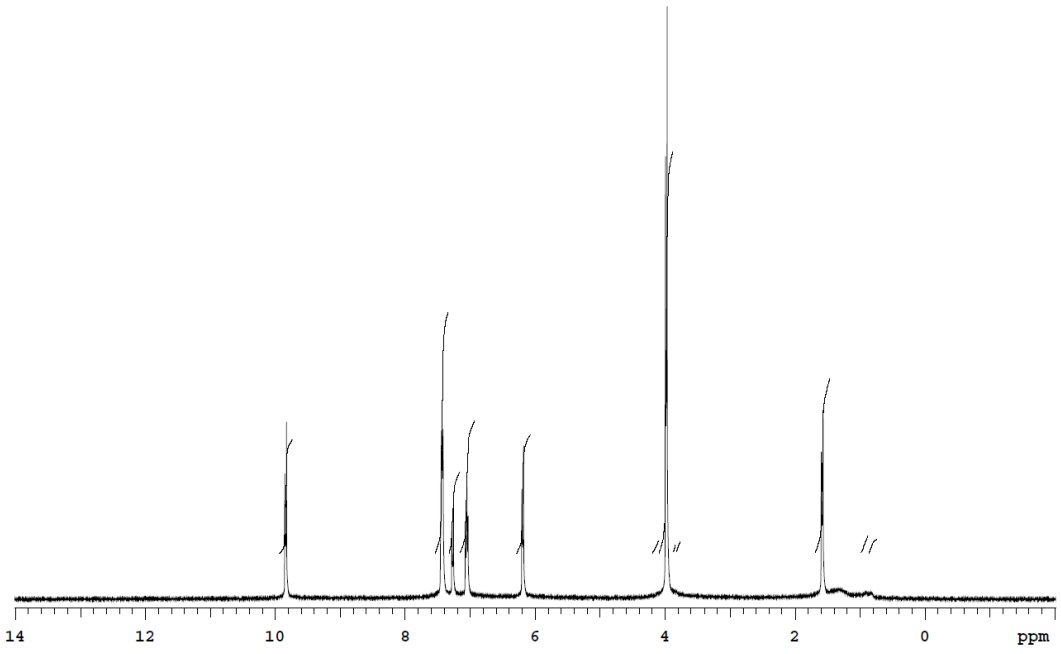

Figure A3.3 Vanillin alone NMR analysis

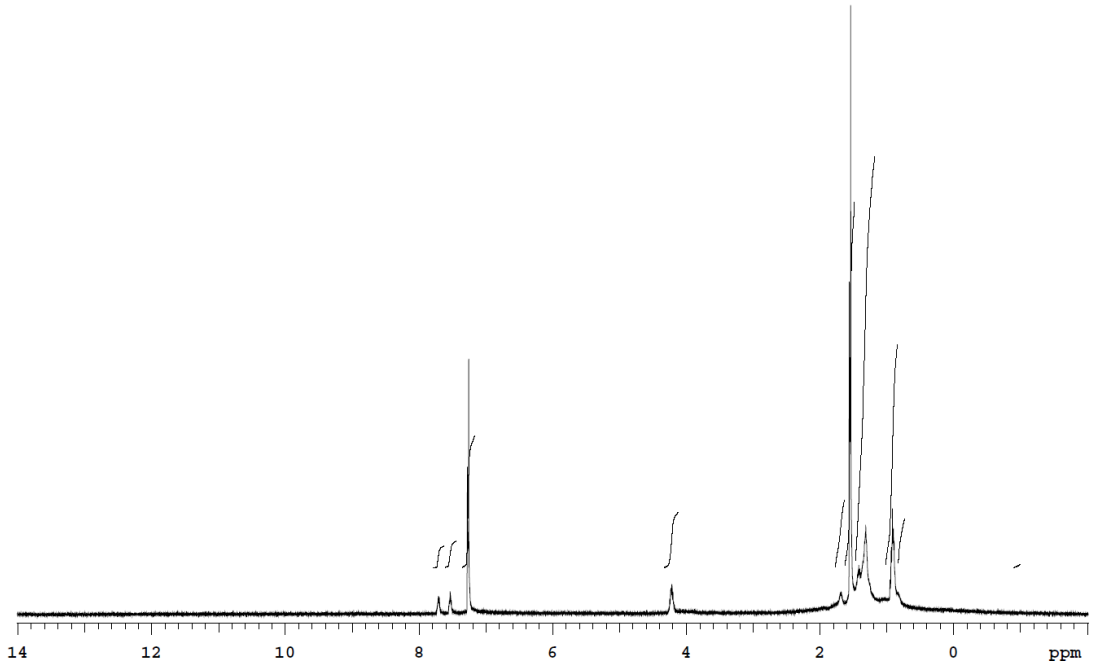

Figure A3.4 Digested BTA gel with no vanillin NMR analysis

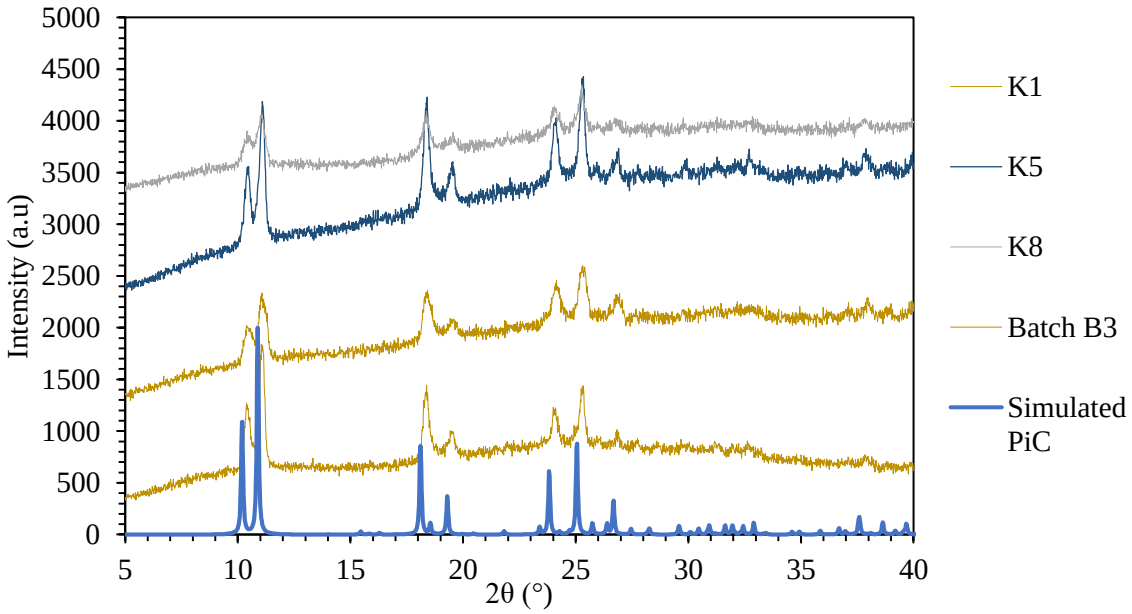

Figure A3.5 PXRD of $[Fe(Htrz)_2(trz)](BF_4)$ obtained in the KRAIC *vs* batch and simulated

Appendix Chapter V(A5)

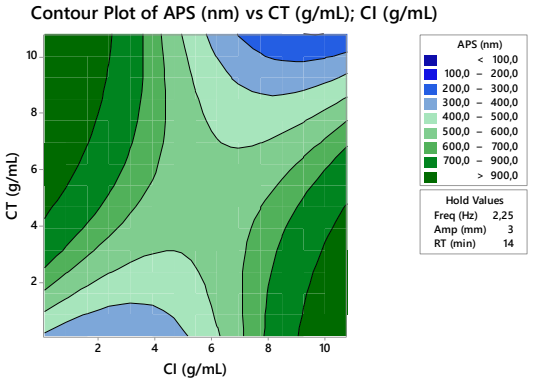

(a)

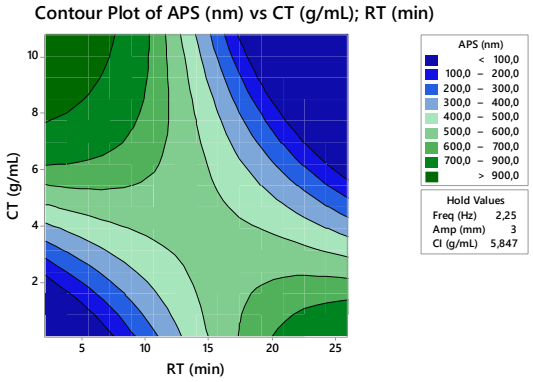

(b)

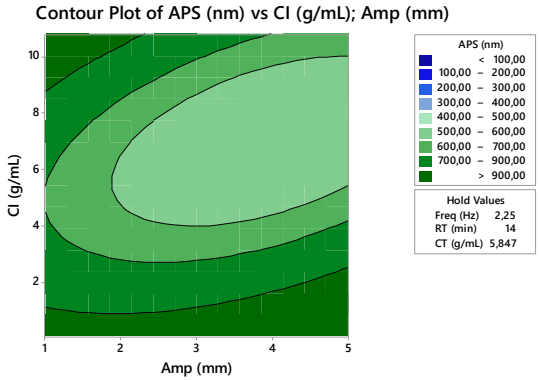

(c)

Figure A5.1 Control plot of APS for CT vs CI (a), CT vs RT (b) and CI vs Amp (c)

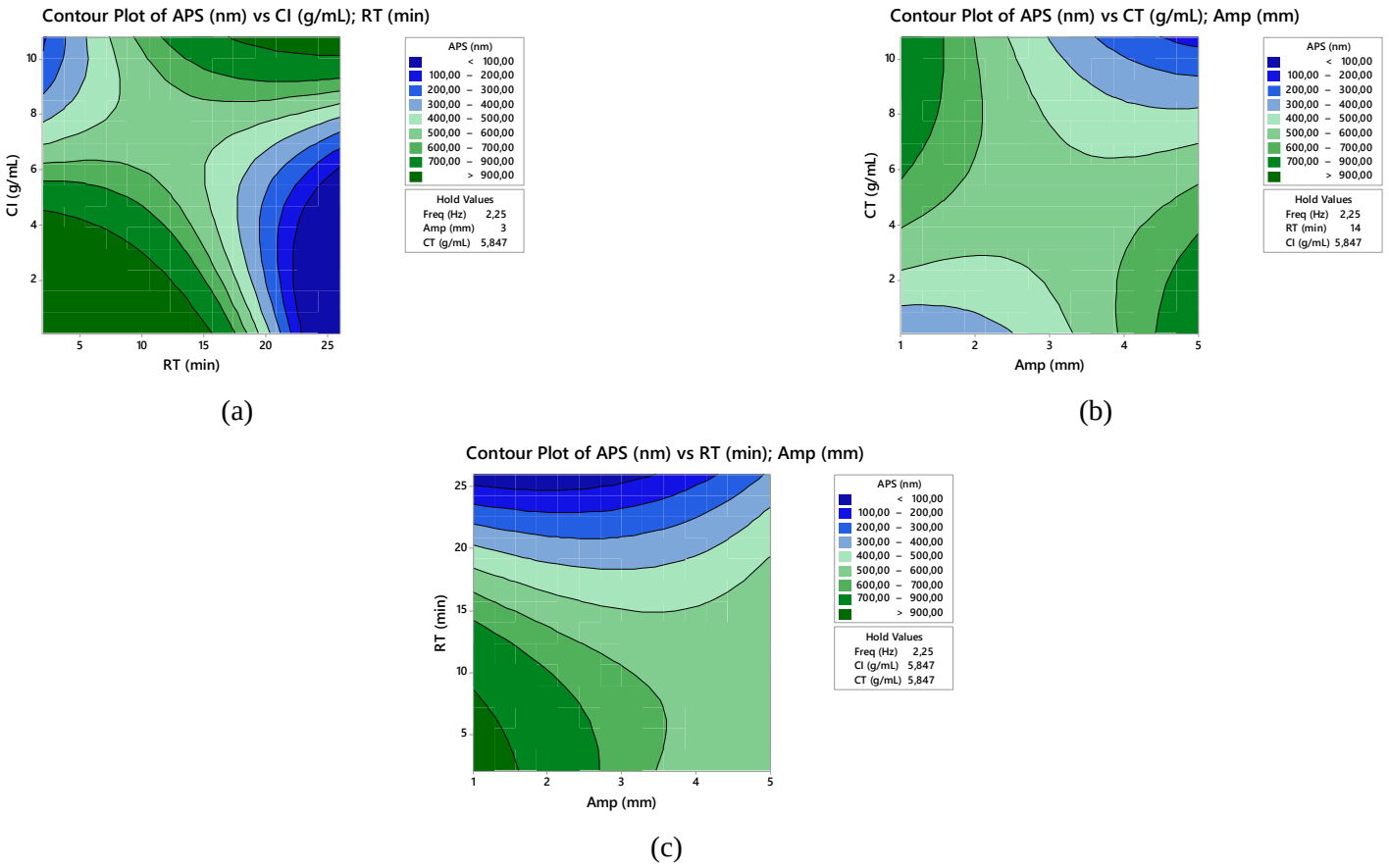

Figure A5.2 Control plot of APS for CI vs RT (a), CT vs Amp (b) and RT vs Amp (c)

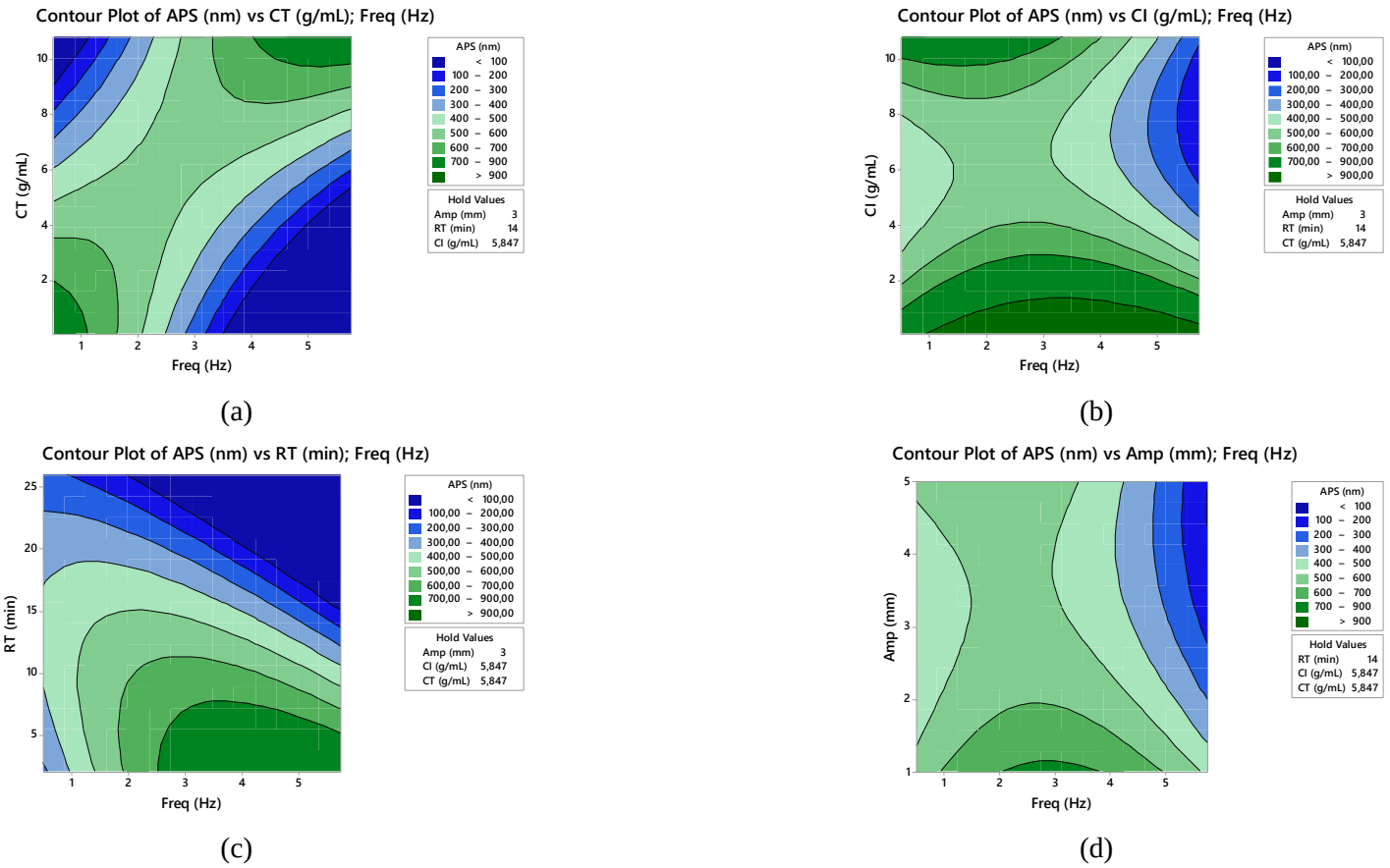

Figure A5.3 Control plot of APS for CT vs Freq (a), CI vs Freq (b) and RT vs Freq (c) and Amp vs Freq (d)

Table A5.1 SEM and DLS Graph for targeting parameters from 100 nm to 1000 nm

SEM Picture	Target and parameters (Target, Frequency, Amplitude , RT and concentrations)	DLS Graph
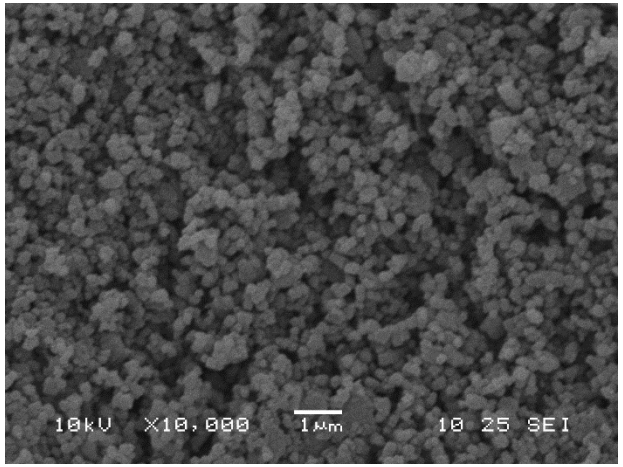	100 nm 3.5 Hz 2 mm 25.2 min CI 10.793 CT 10.71	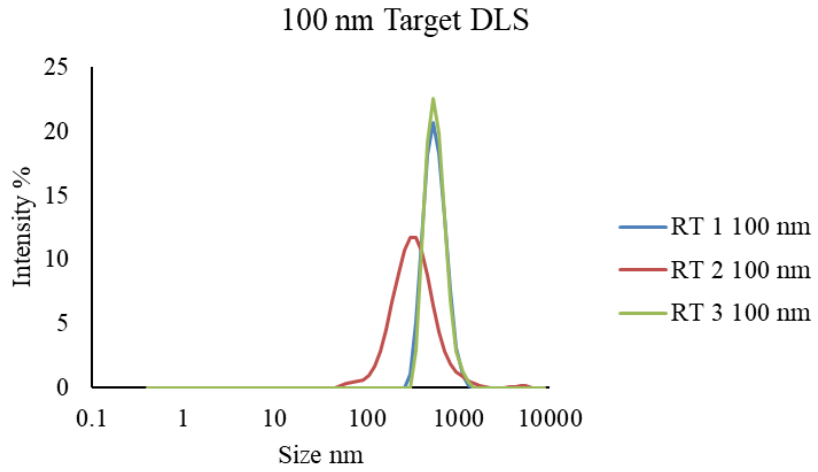

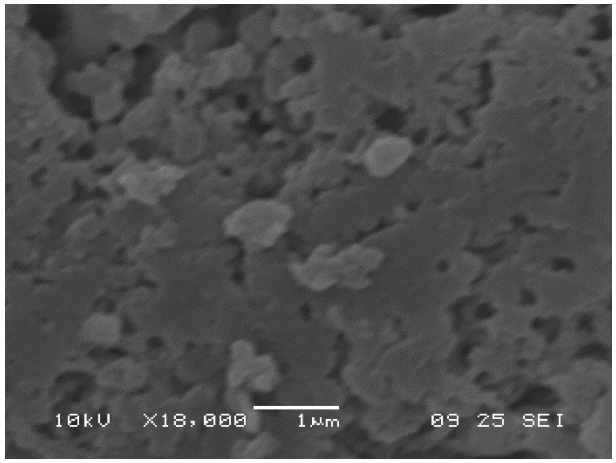	200 nm 1 Hz 5 mm 4 min CI 10.793 CT 0.901	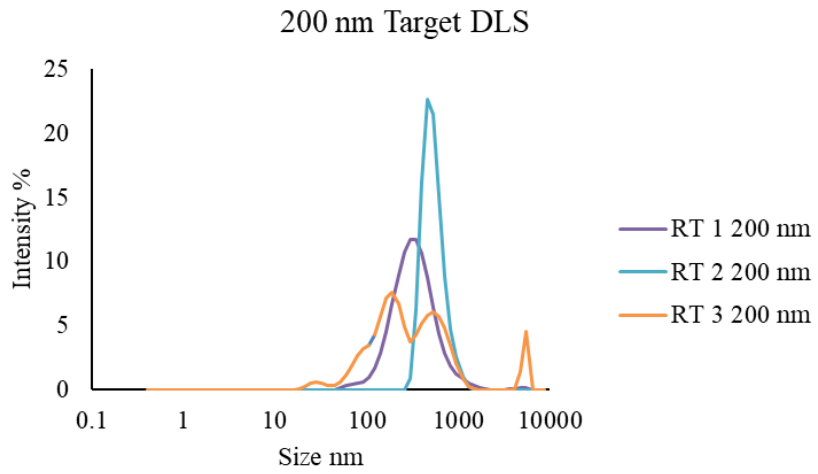
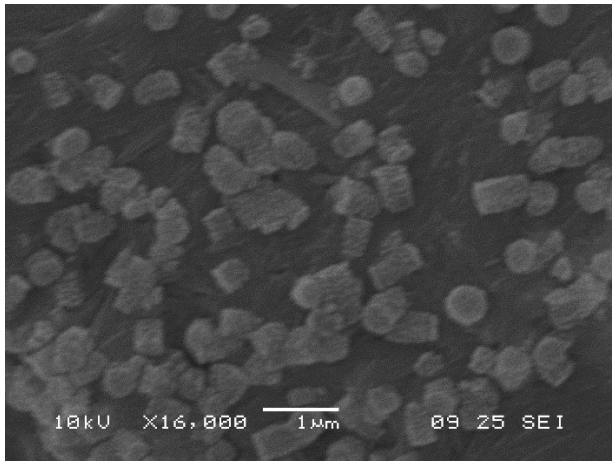	300 nm 5.0544 Hz 2 mm 7.5 min CI 10.793 CT 3.1792	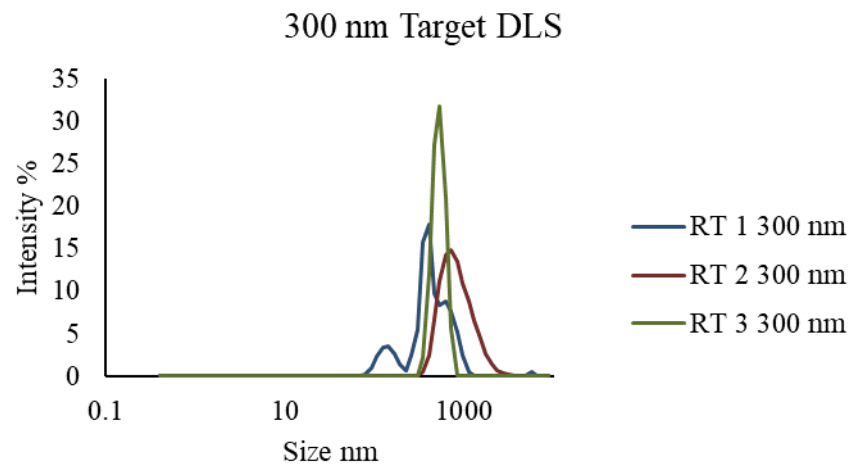

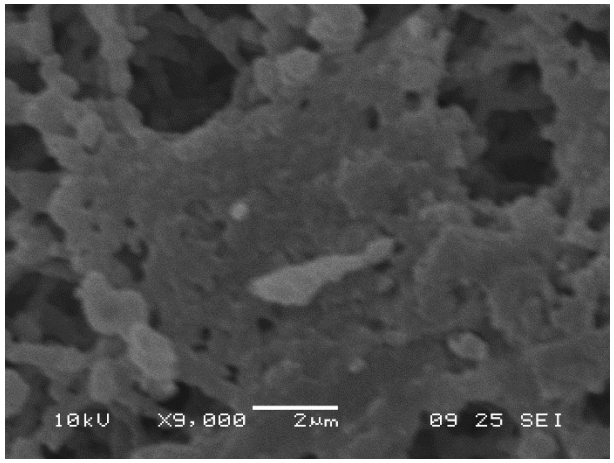	400 nm 5.6884 Hz 3.5 mm 26 min CI 10.793 CT 0.901	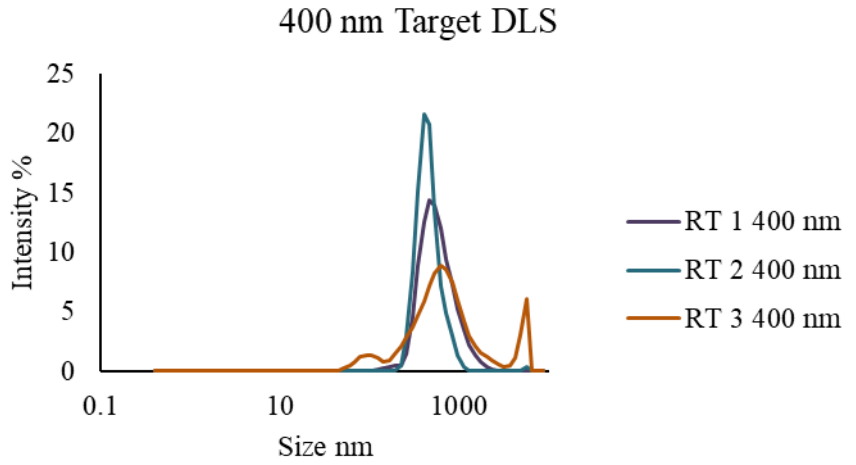
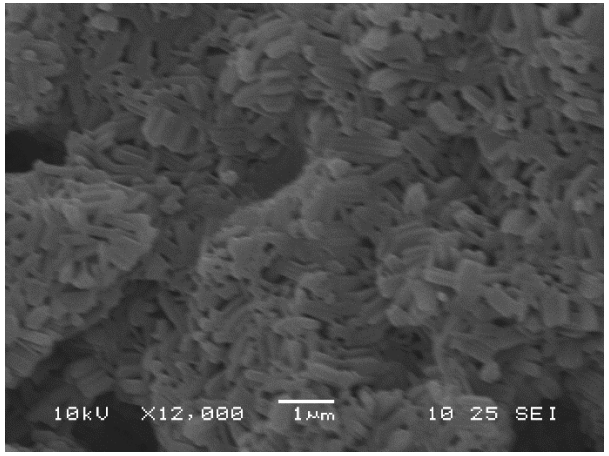	500 nm 3 Hz 5 mm 2 min CI 2.5709 CT 0.901	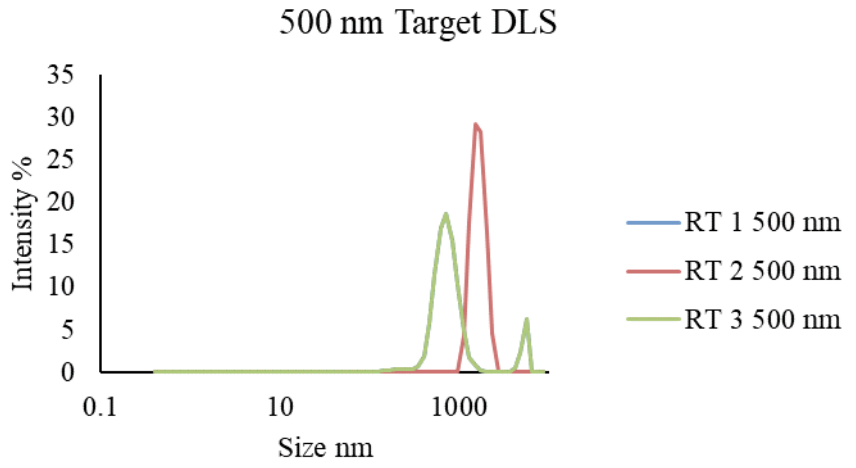

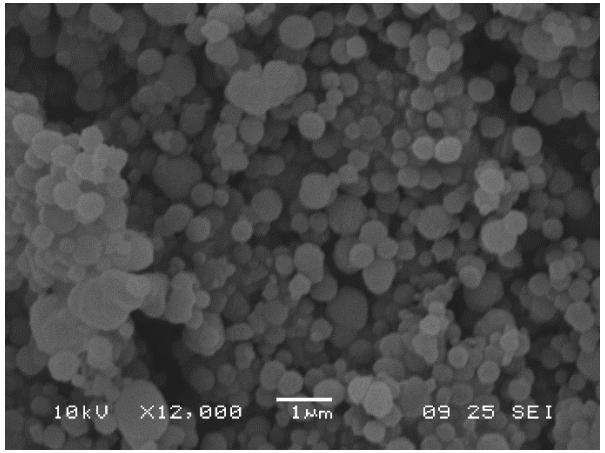	600 nm 3.125 Hz 3 mm 14 min CI 5.7032 CT 10.793	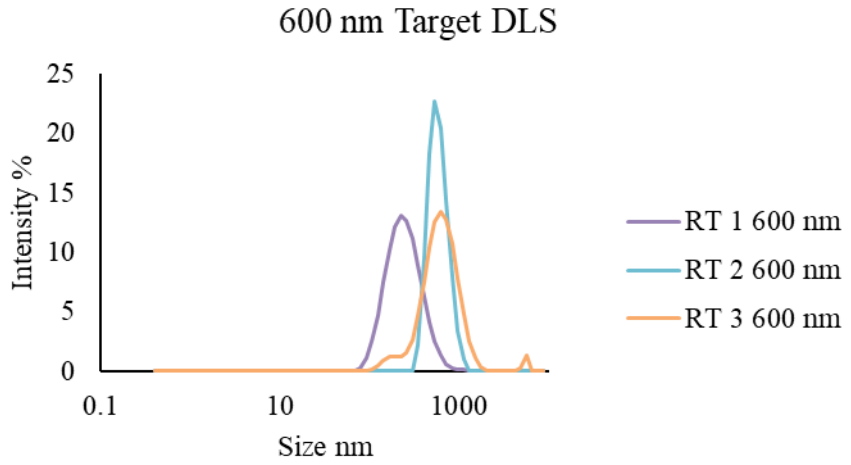
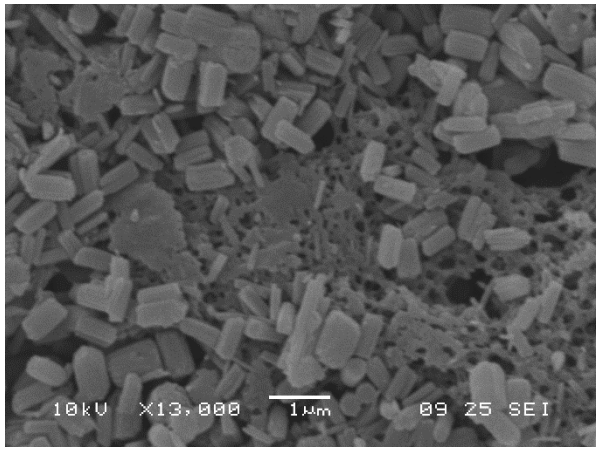	700 nm 5 Hz 2 mm 2.1382 min CI 0.901 CT 1.7268	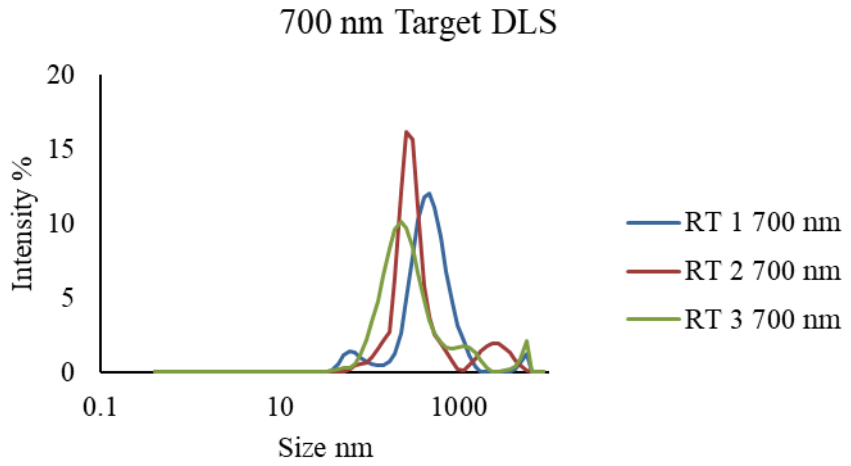

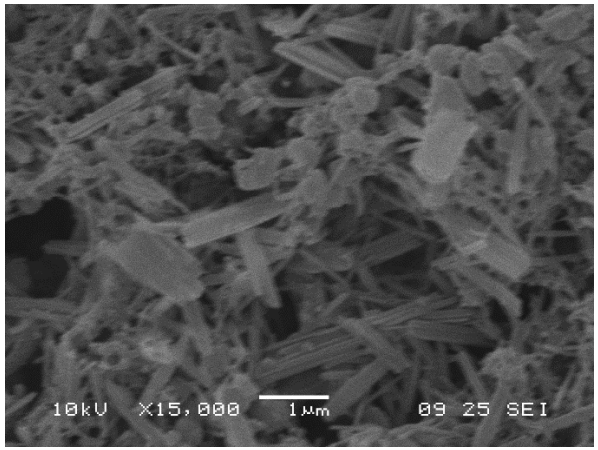	800 nm 5 Hz 2 mm 2.2026 min CI 0.901 CT 1.9611	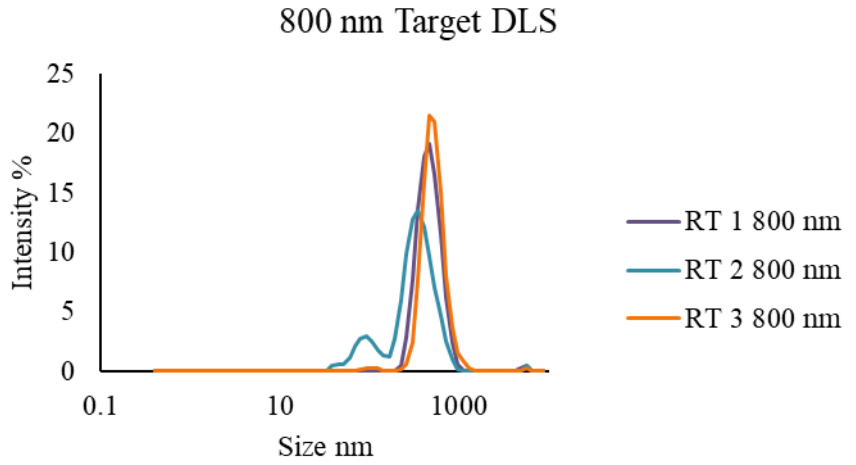
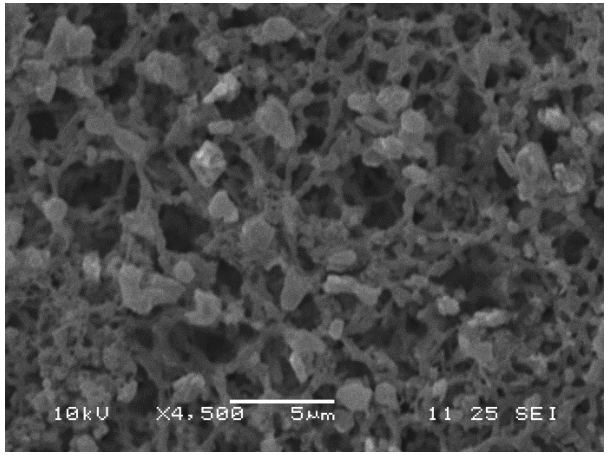	900 nm 3 Hz 2 mm 2.2669 min CI 0.901 CT 2.4	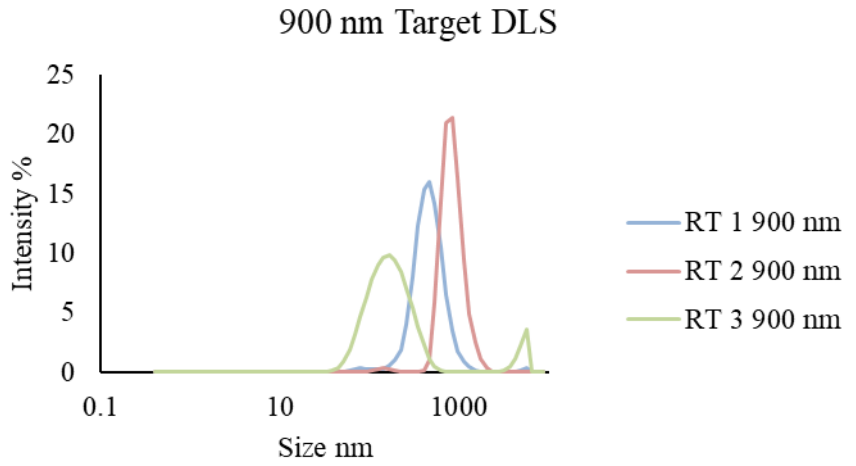

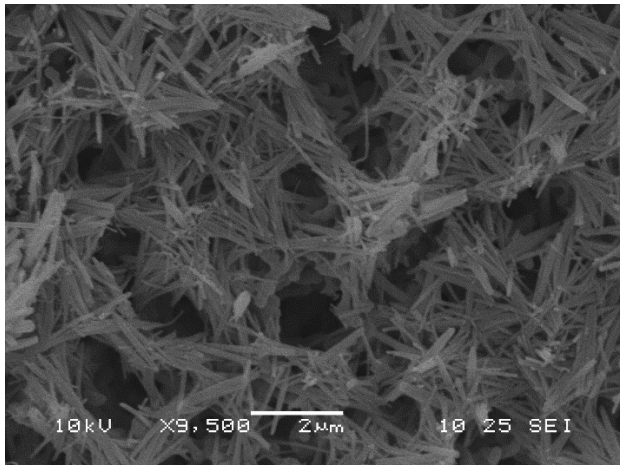	1000 nm 4 Hz 2 mm 2.3312 min CI 0.901 CT 2.4275	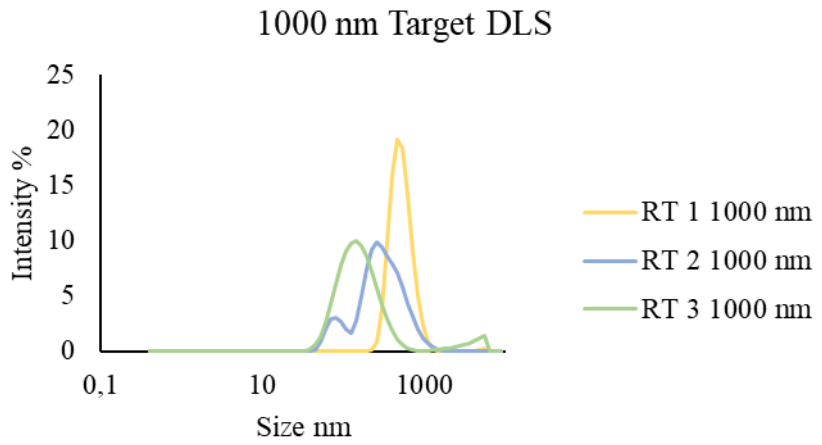

Table A5.2 DOE Experiment with corresponding SEM and DLS

Exp	SEM	Parameters ~(Frequency , Amplitude RT and concentrations)	DLS
1	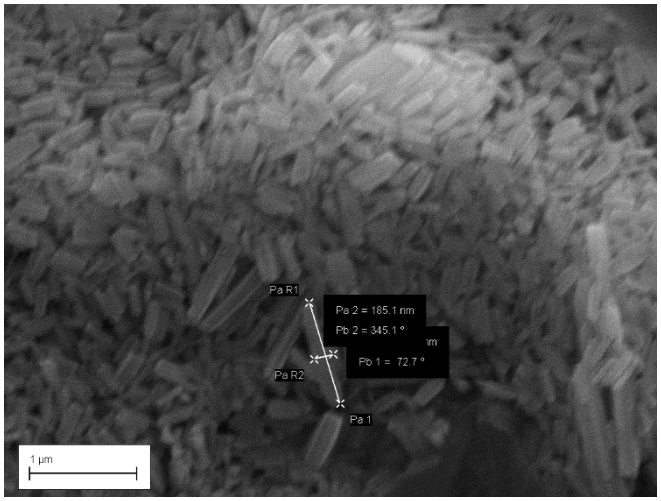	2.25 Hz 3 mm 14 min CI 5.847 CT 5.847	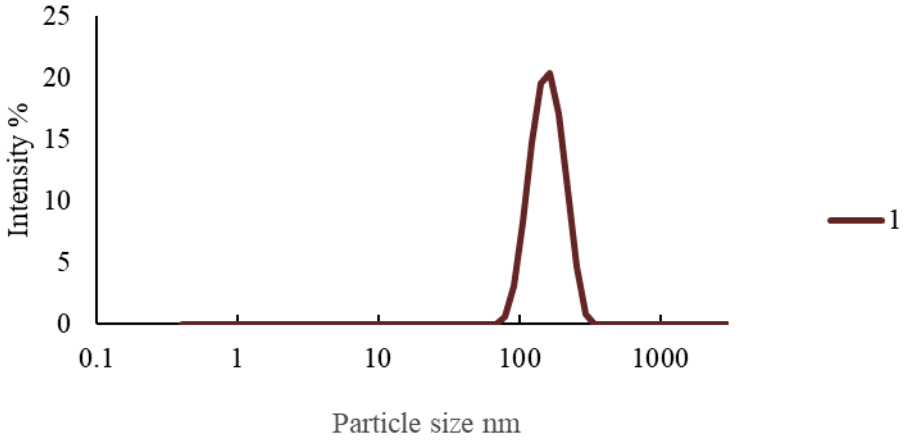

2	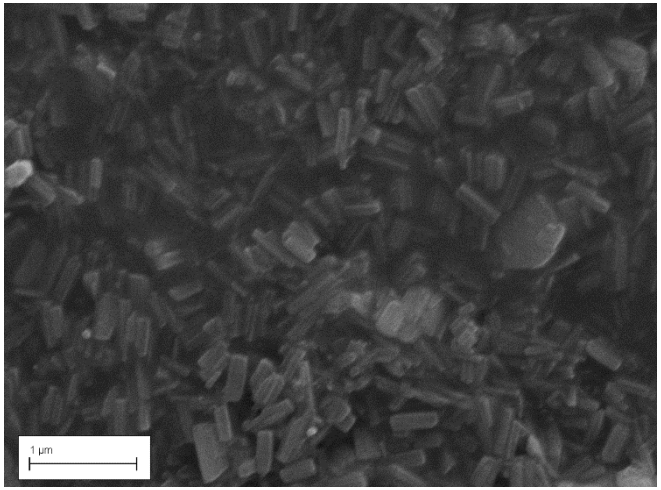	2.25 Hz 5 mm 14 min CI 5.847 CT 5.847	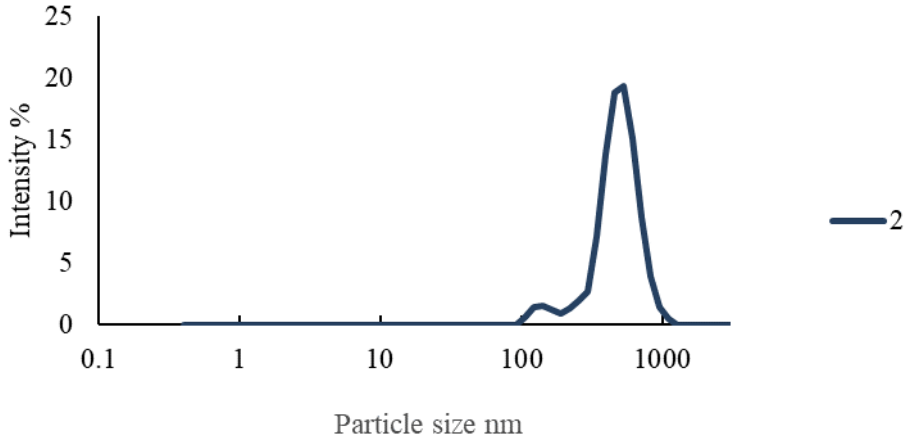
3	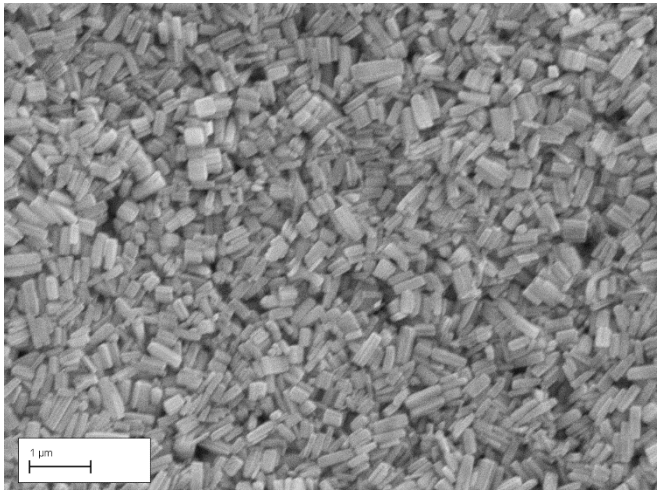	2.25 Hz 2 mm 14 min CI 5.847 CT 5.847	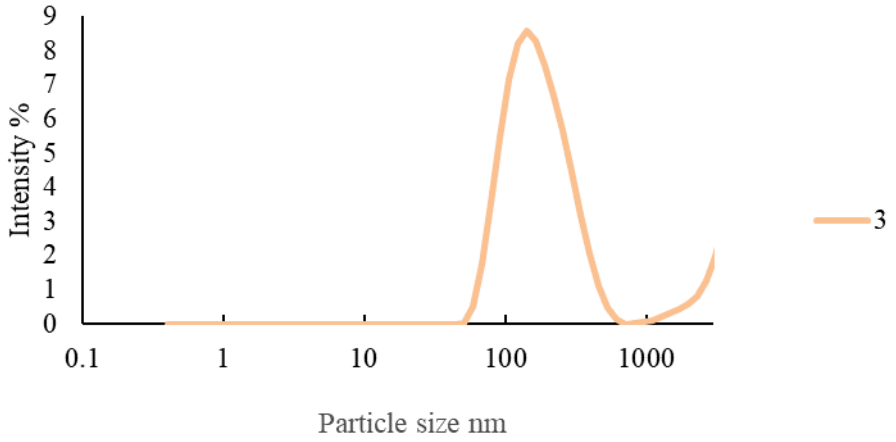

4	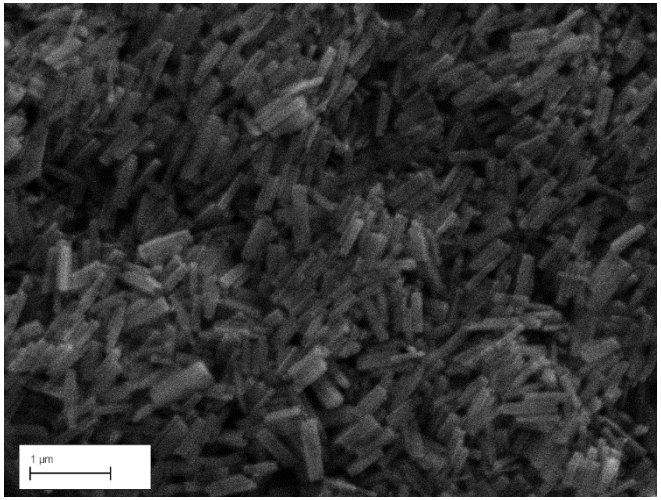	2.25 Hz 3 mm 26 min CI 5.847 CT 5.847	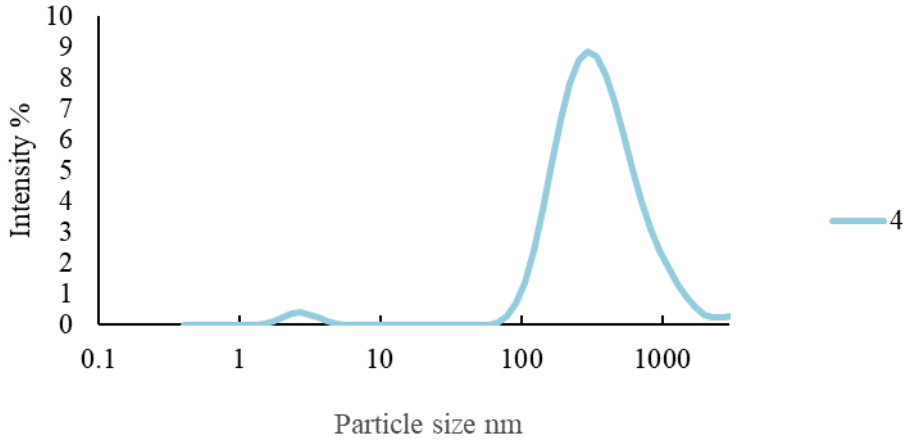
5	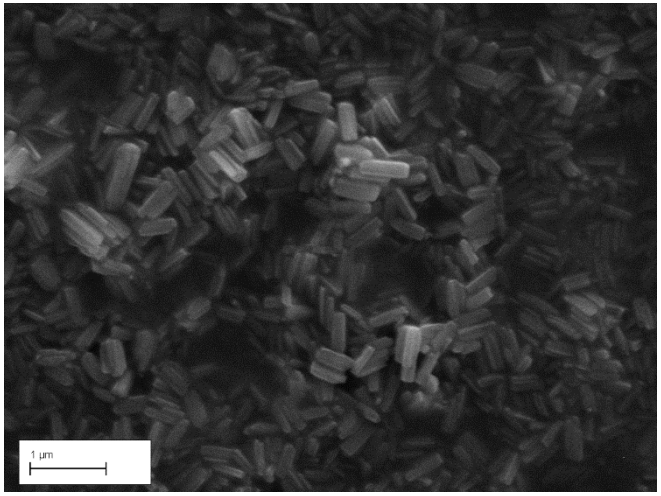	2.25 Hz 3 mm 14 min CI 5.847 CT 5.847	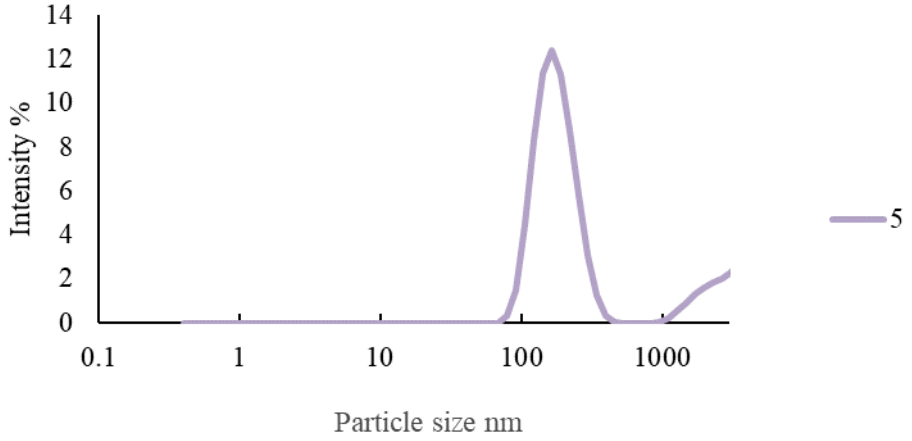

6	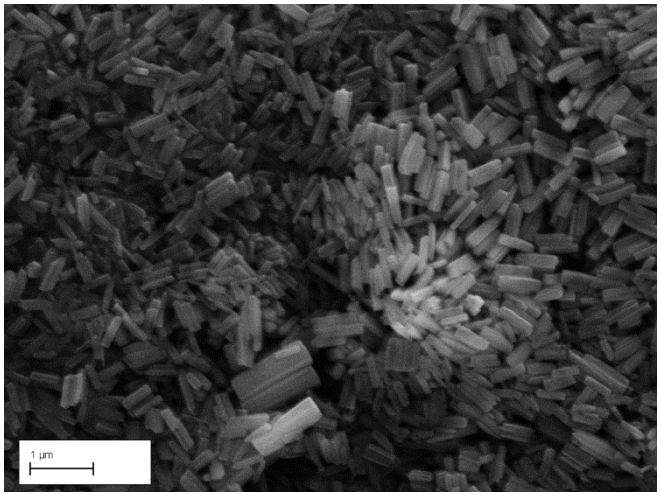	2.25 Hz 3 mm 14 min CI 5.847 CT 5.847	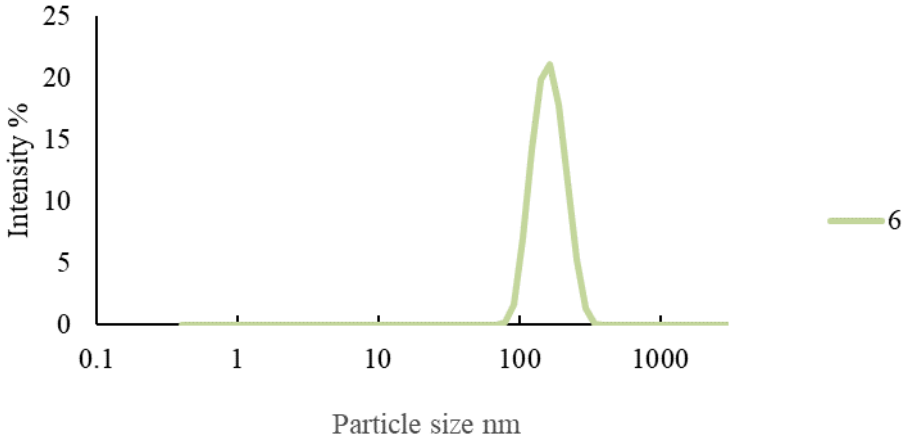
7	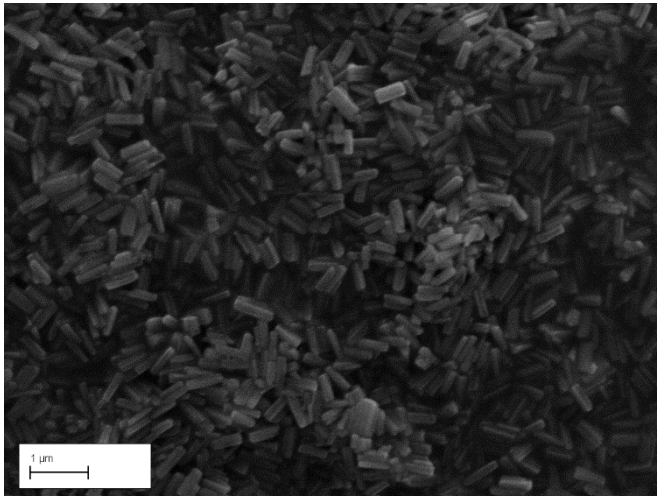	1.25 Hz 3 mm 14 min CI 5.847 CT 5.847	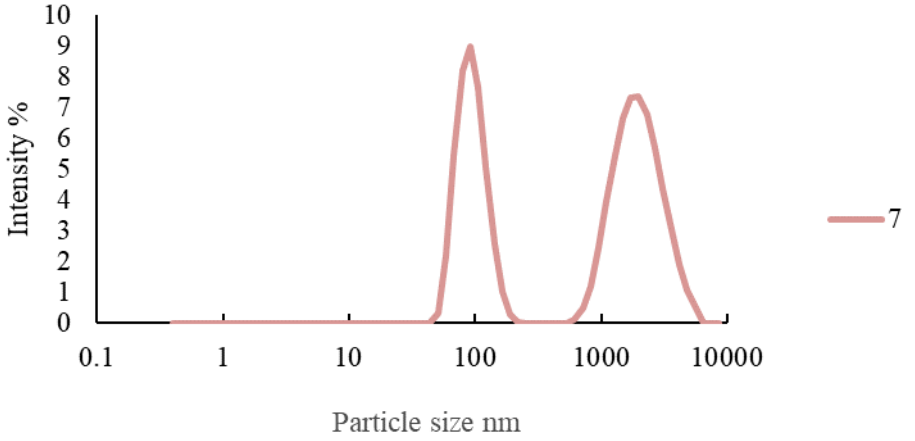

8	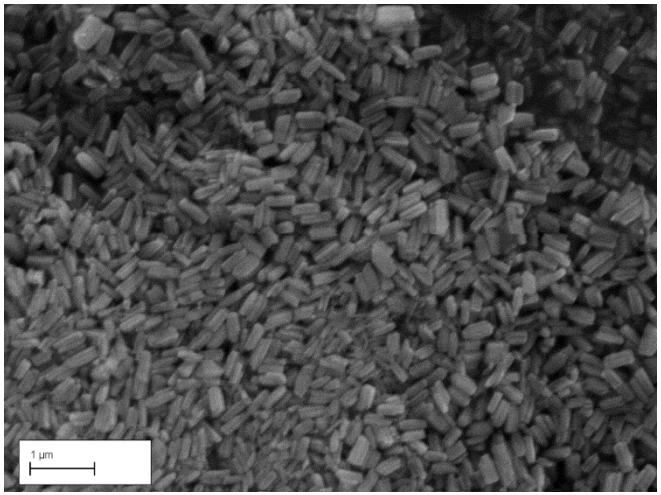	2.25 Hz 3 mm 14 min CI 5.847 CT 5.847	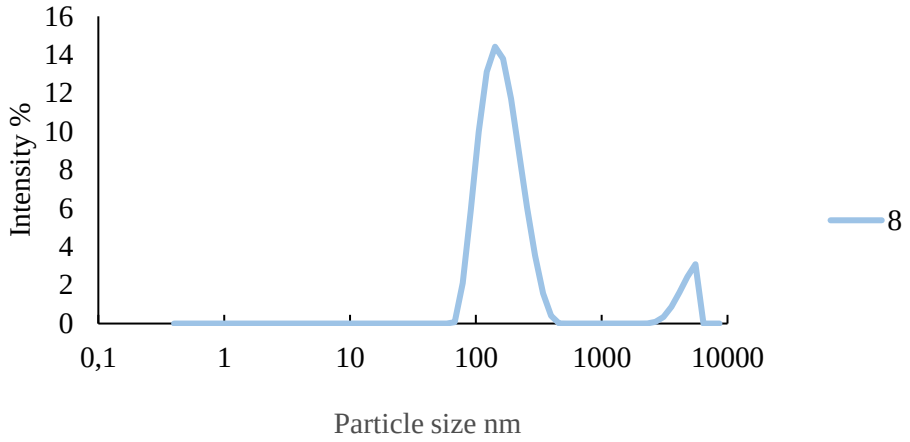
9	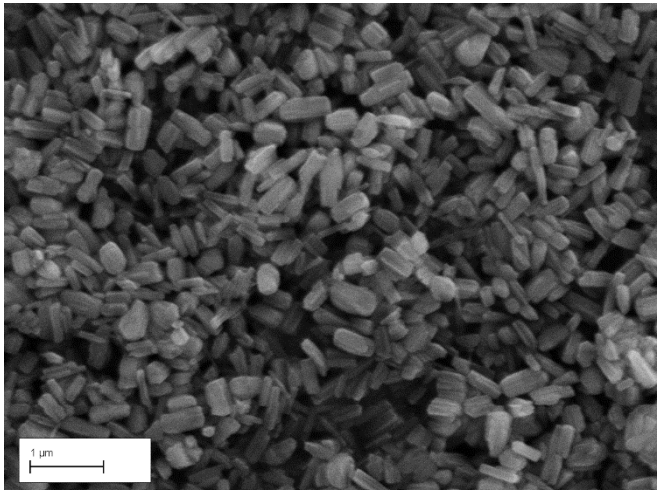	2.25 Hz 3 mm 14 min CI 5.847 CT 5.847	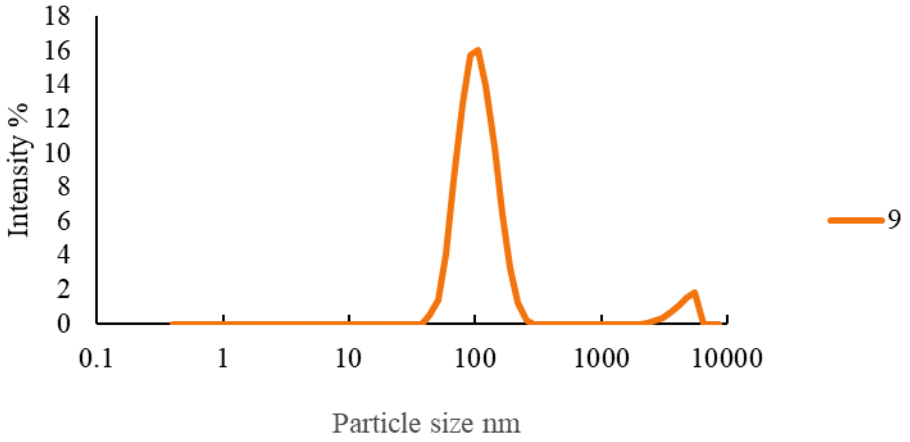

10	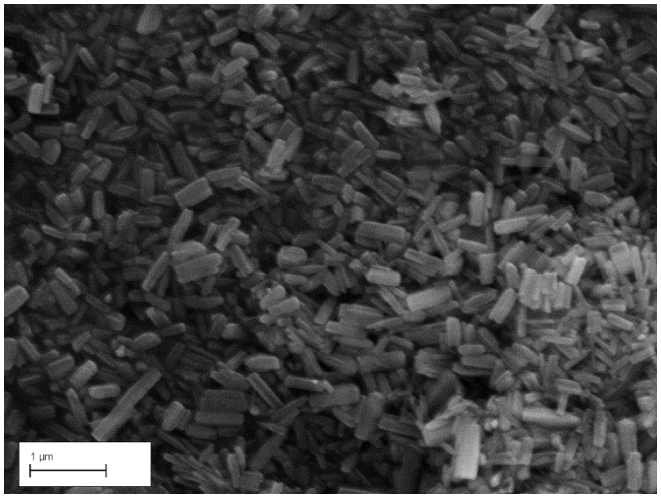	2.25 Hz 3 mm 14 min CI 5.847 CT 5.847	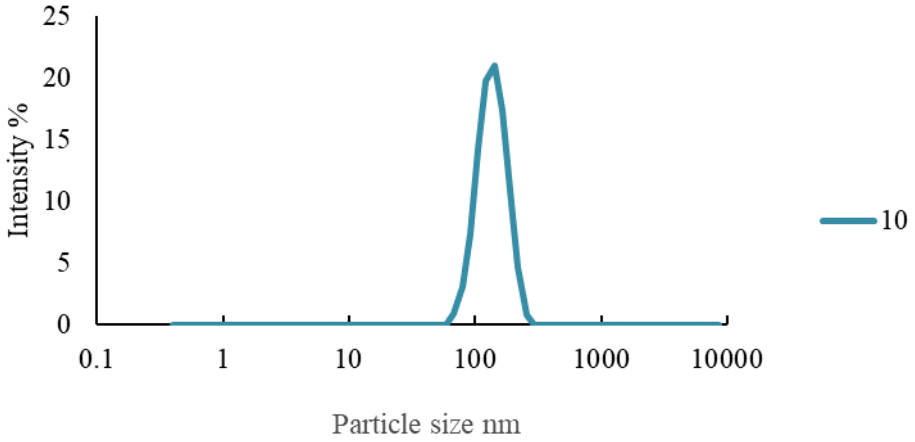
11	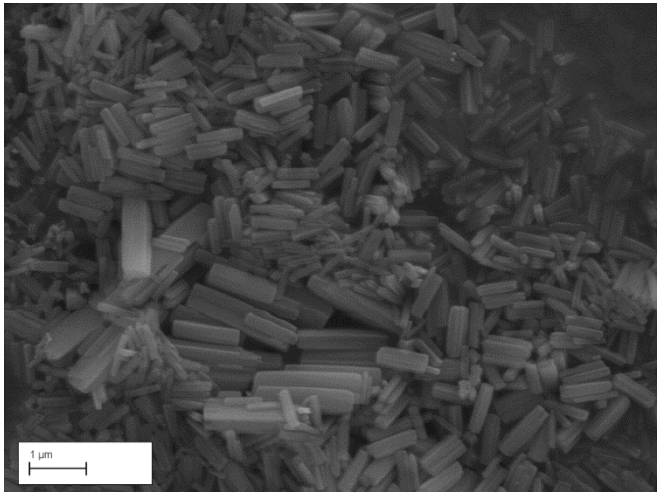	2.25 Hz 3 mm 14 min CI 5.847 CT 5.847	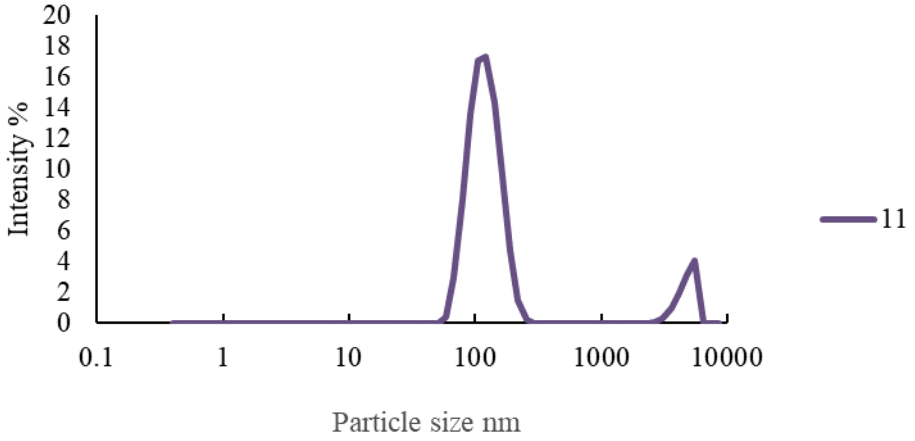

12	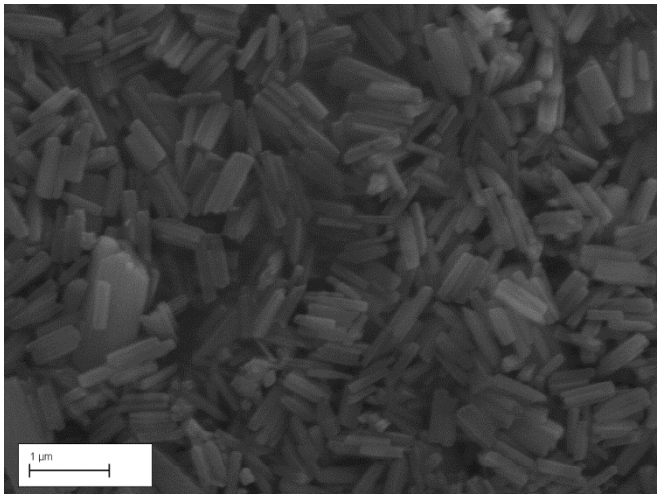	2.25 Hz 3 mm 2 min CI 5.847 CT 5.847	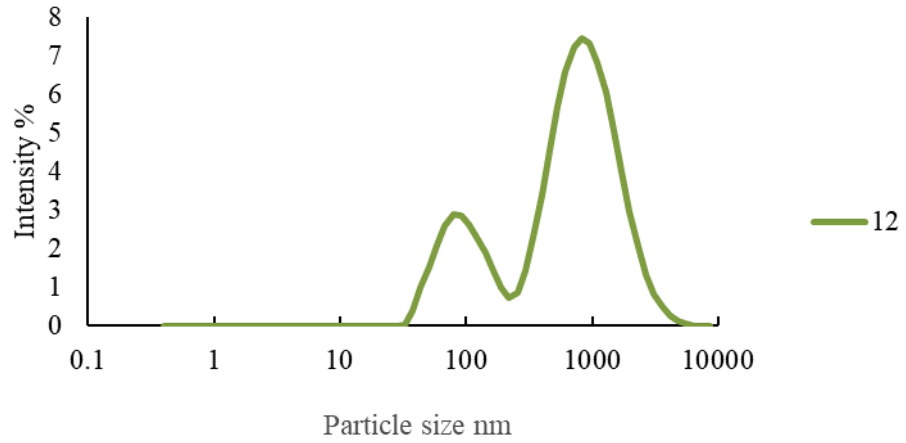
13	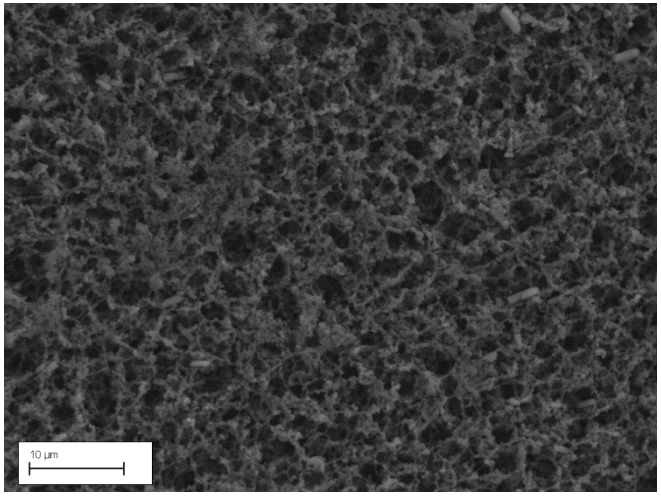	2.25 Hz 3 mm 14 min CI 5.847 CT 0.901	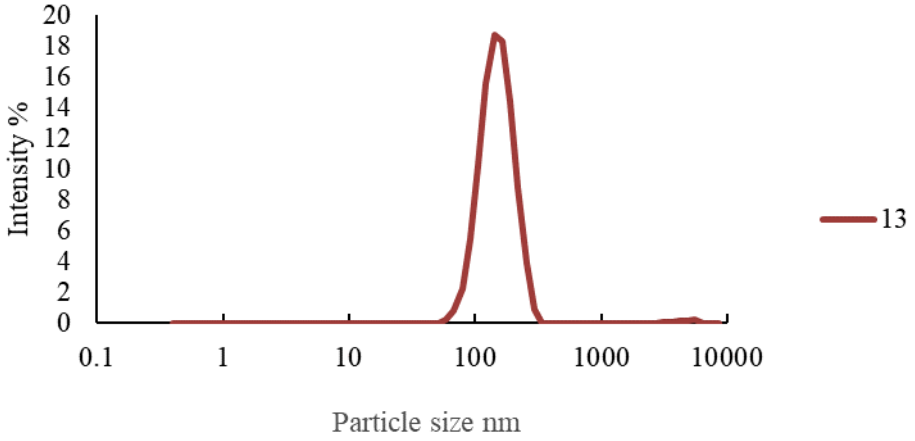

14	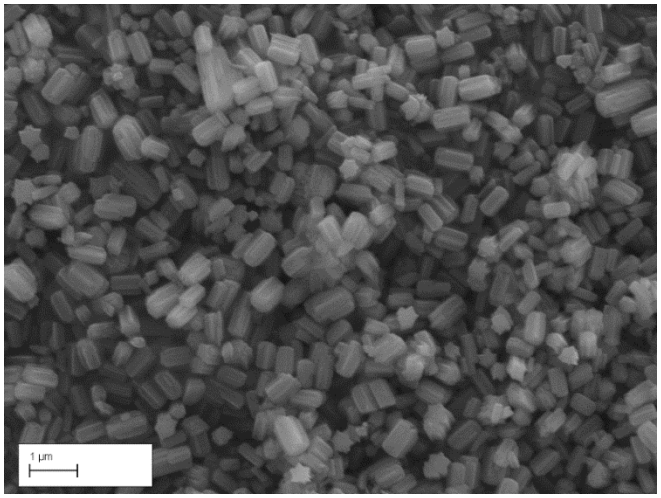	2.25 Hz 3 mm 14 min CI 5.847 CT 10.793	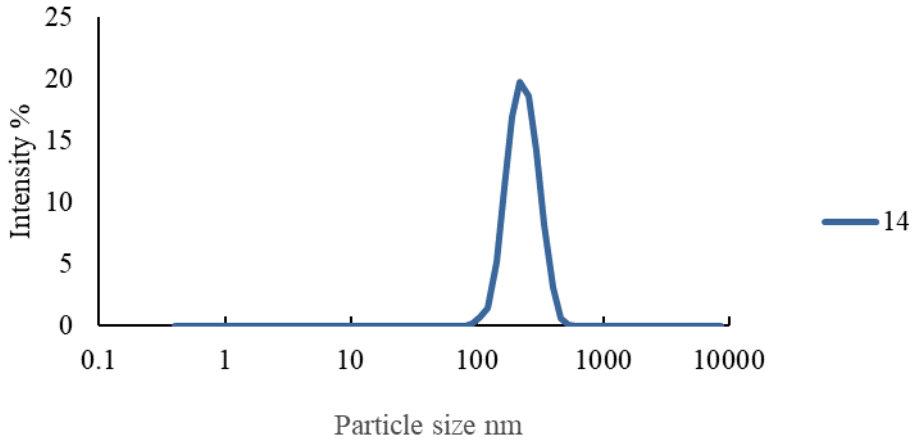
15	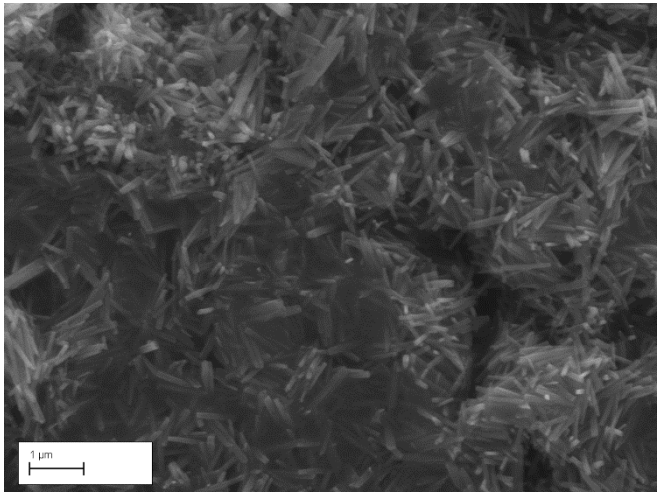	2.25 Hz 3 mm 14 min CI 0.901 CT 5.847	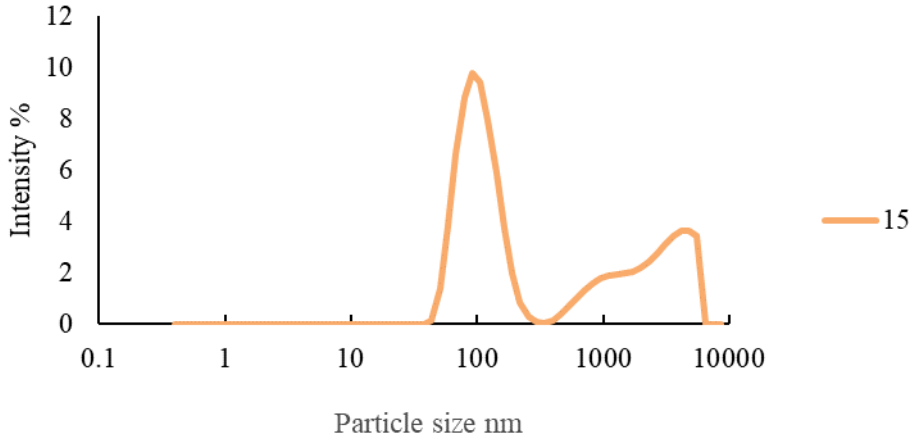

16	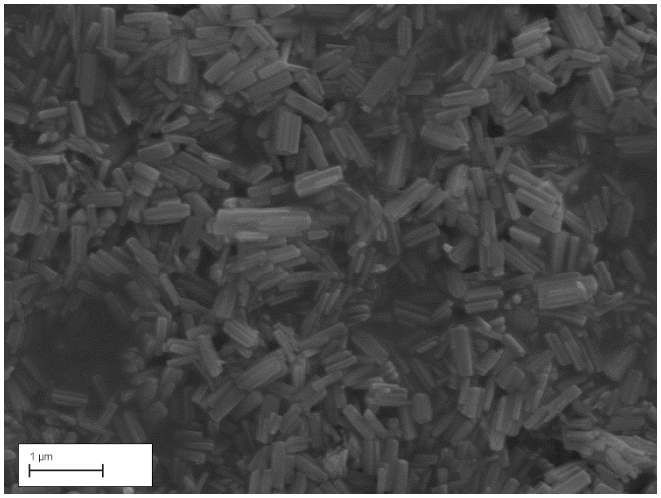	2.25 Hz 3 mm 14 min CI 10.793 CT 5.847	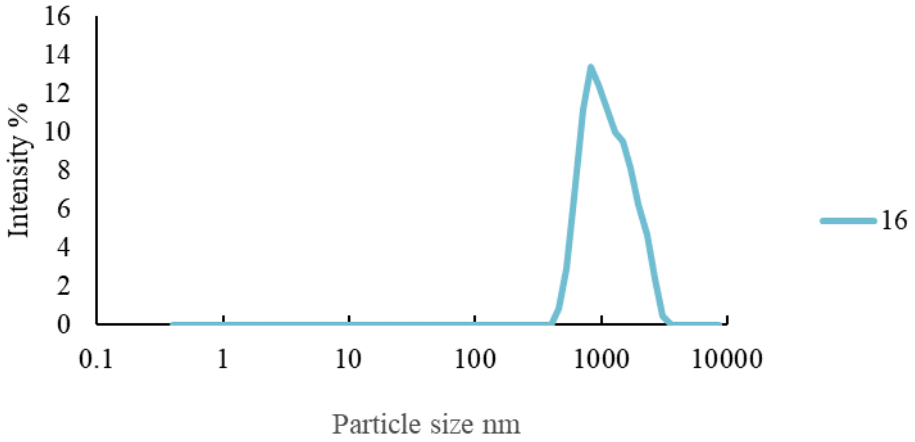
17	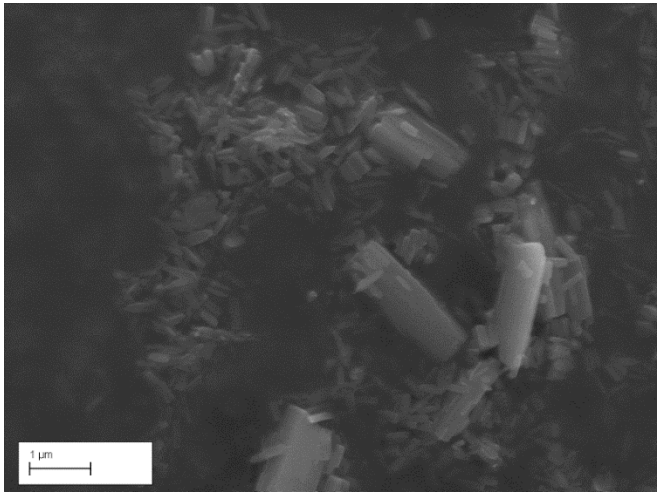	4 Hz 2 mm 20 min CI 8.32 CT 3.374	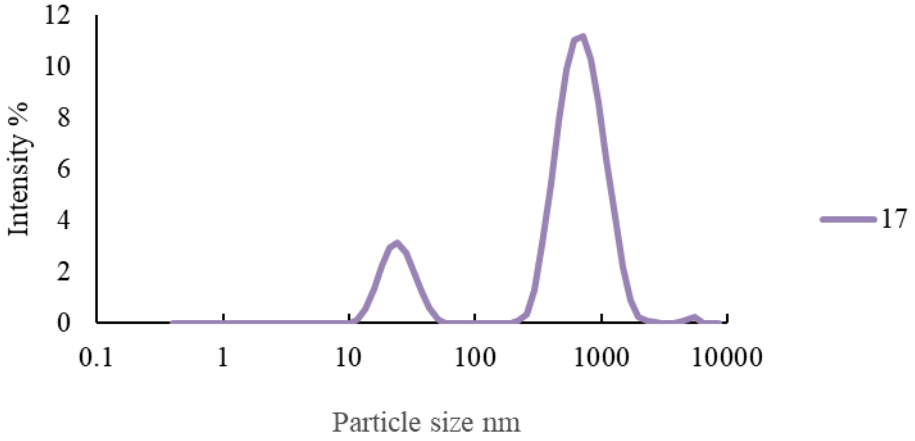

18	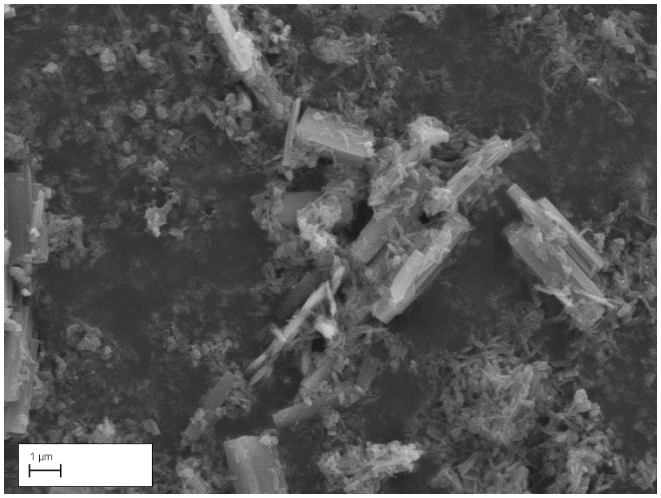	4 Hz 4 mm 14 min CI 5.847 CT 3.374	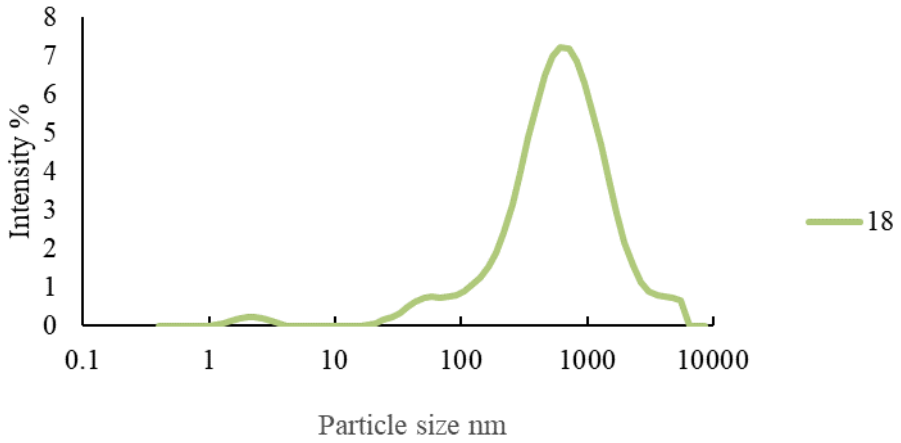
19	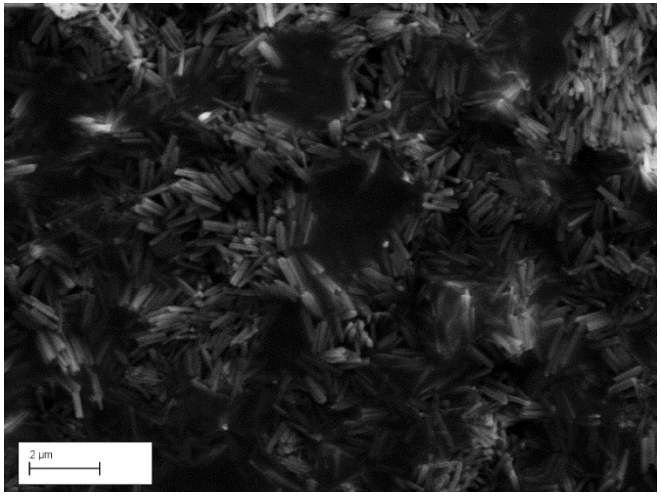	0.5 Hz 4 mm 20 min CI 8.32 CT 3.374	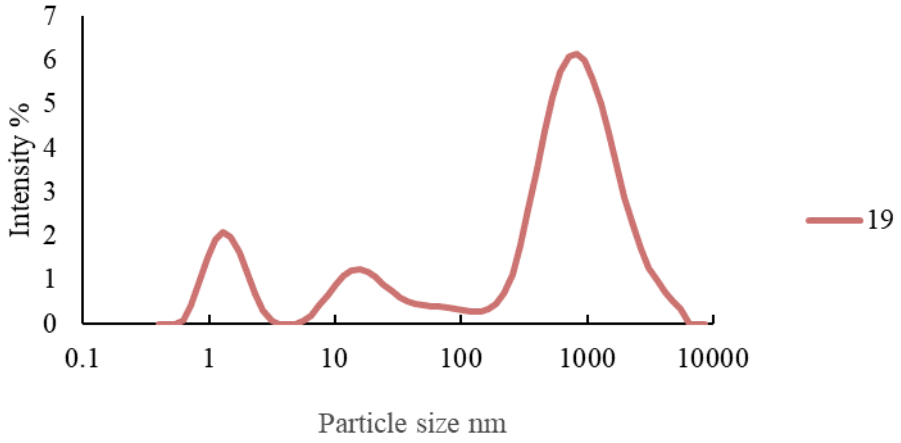

20	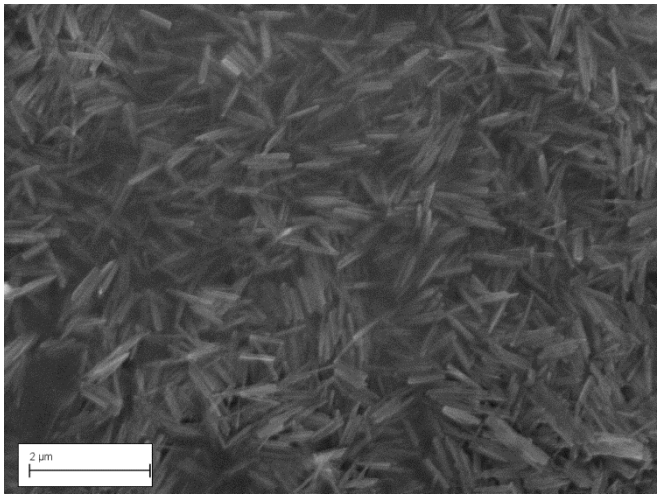	0.5 Hz 2 mm 8 min CI 8.32 CT 3.374	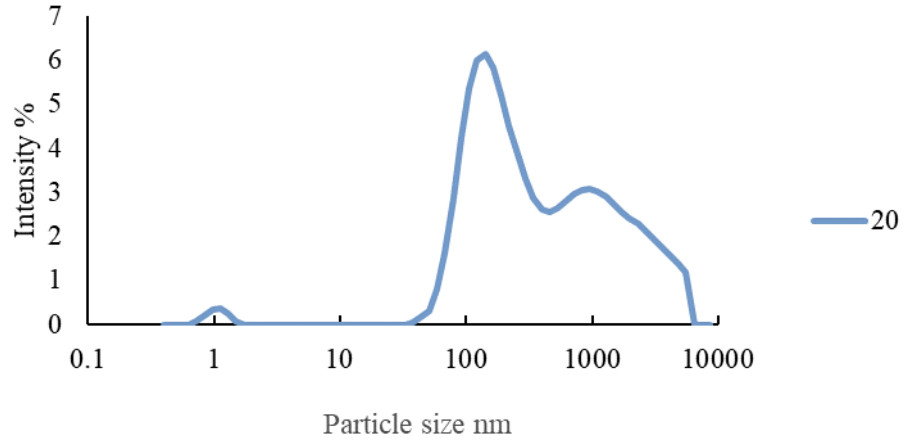
21	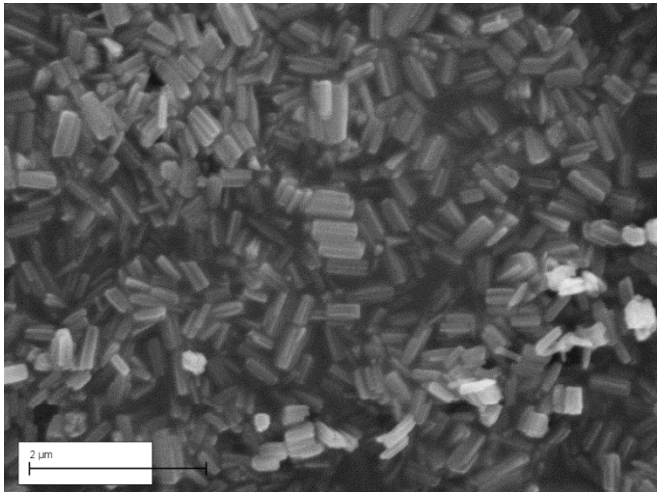	0.5 Hz 4 mm 8 min CI 8.32 CT 8.32	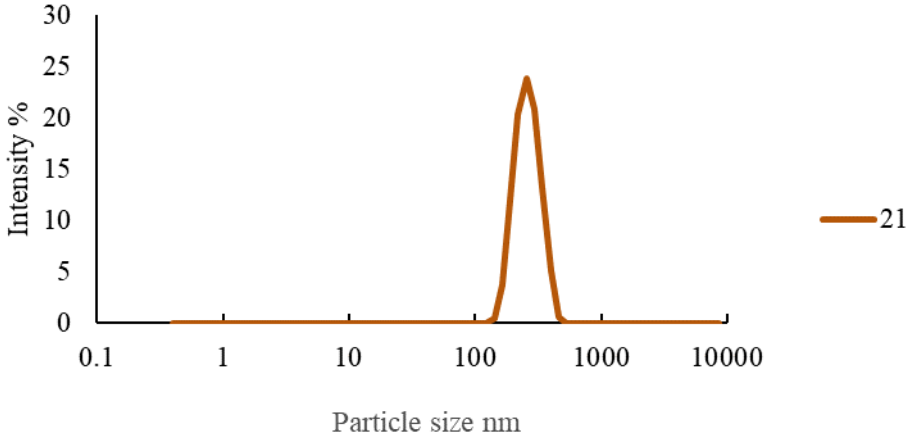

22	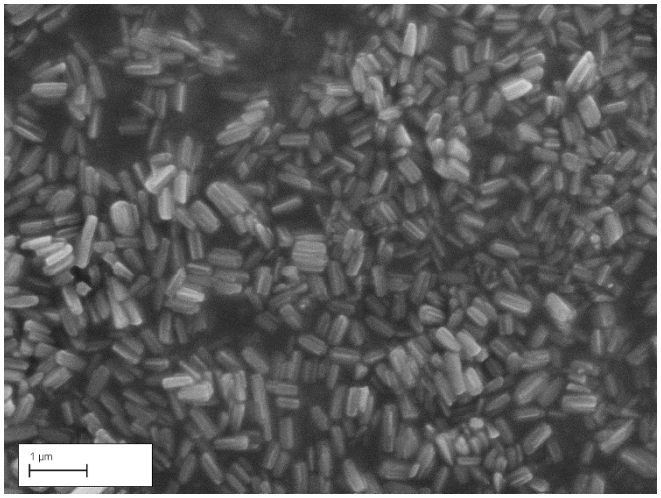	0.5 Hz 2 mm 20 min CI 8.32 CT 8.32	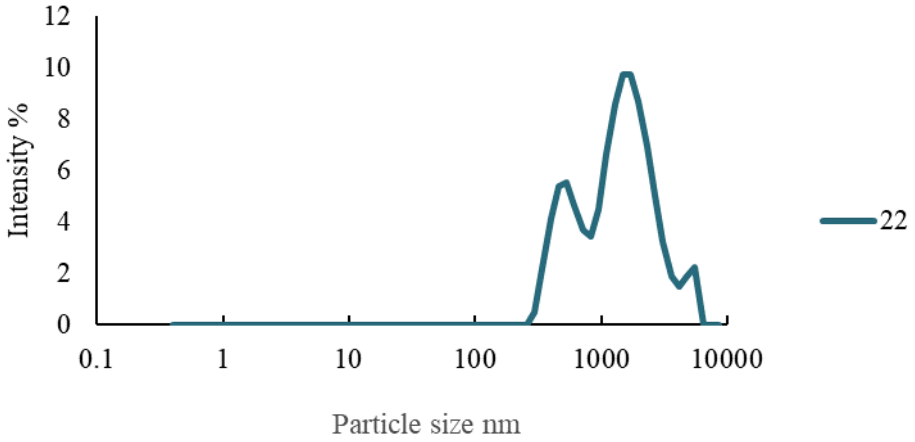
23	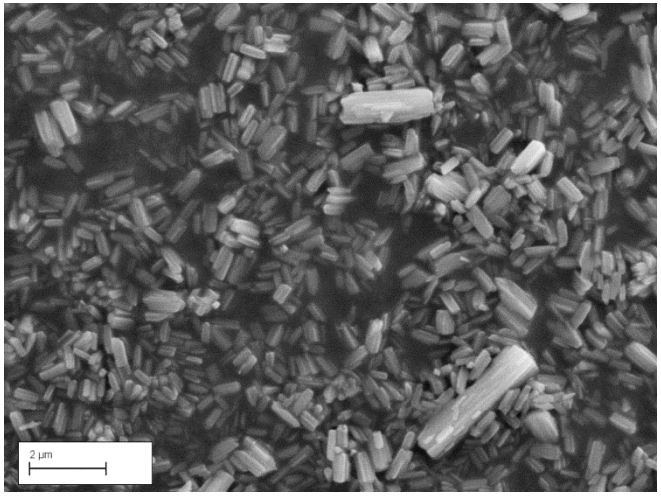	4 Hz 4 mm 20 min CI 8.32 CT 8.32	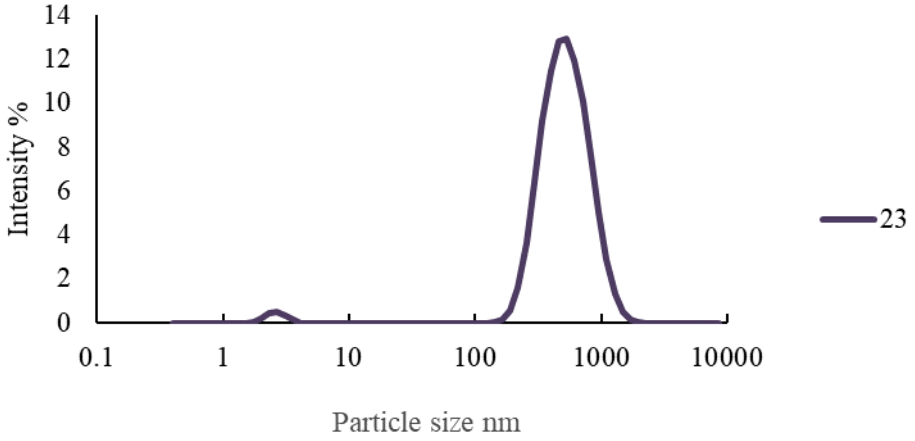

24	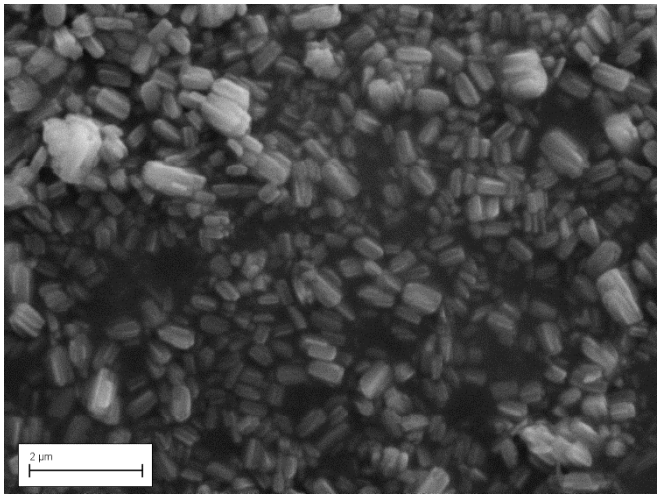	4 Hz 2 mm 8 min CI 8.32 CT 8.32	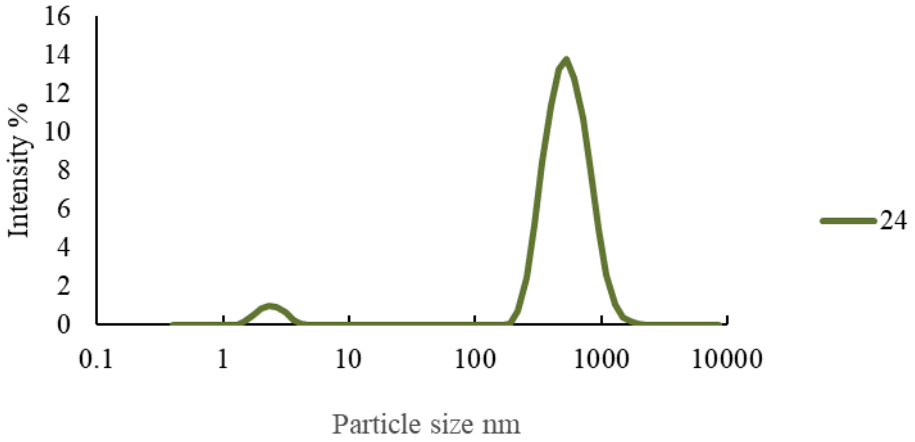
25	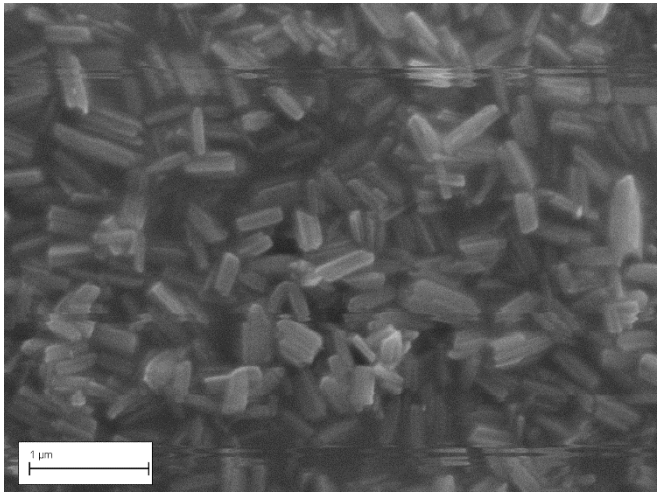	4 Hz 2 mm 20 min CI 3.374 CT 8.32	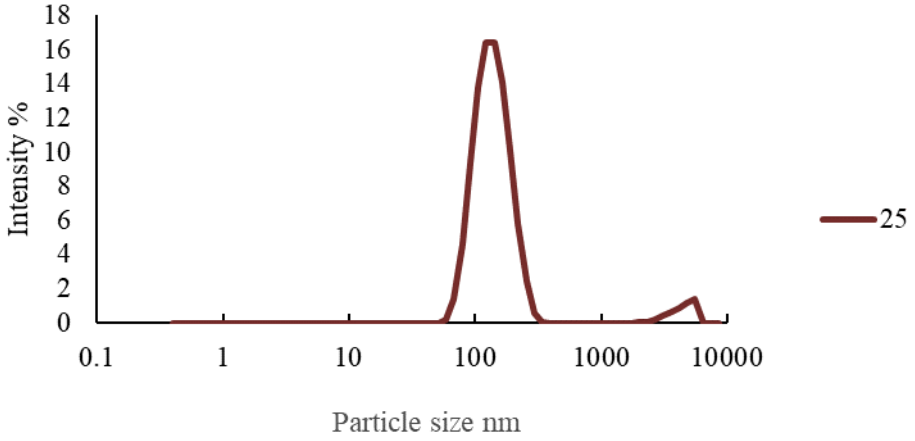

26	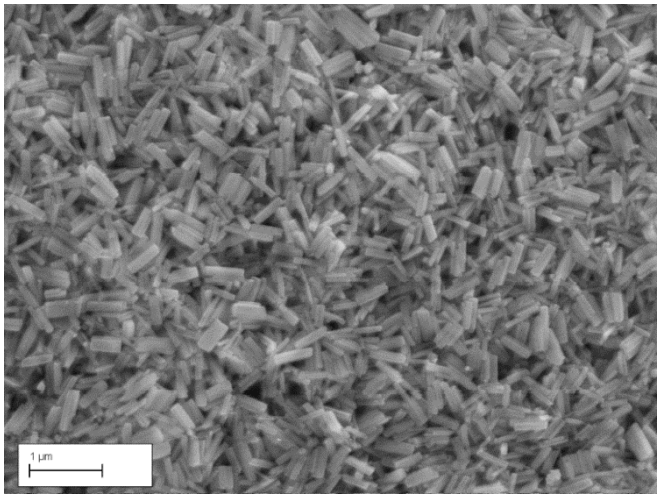	4 Hz 4 mm 8 min CI 3.374 CT 8.32	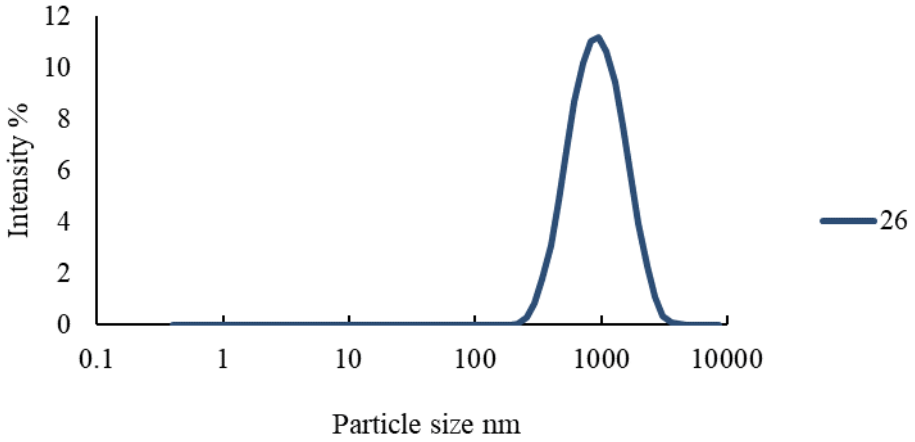
27	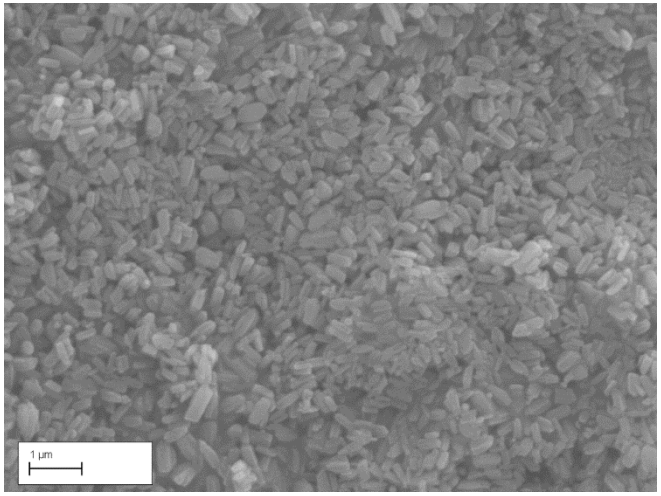	0.5 Hz 4 mm 20 min CI 3.374 CT 8.32	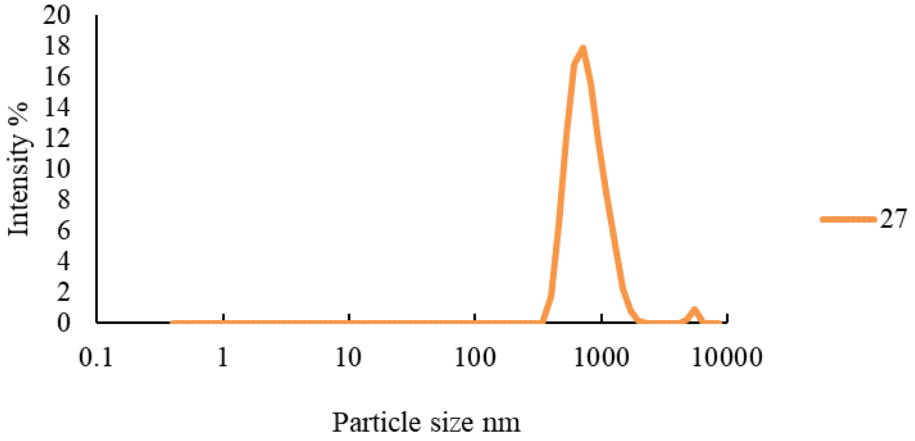

28	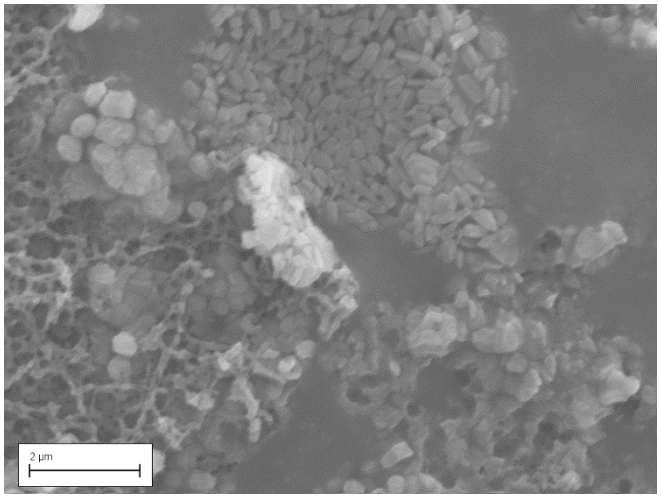	0.5 Hz 2 mm 8 min CI 3.374 CT 8.32	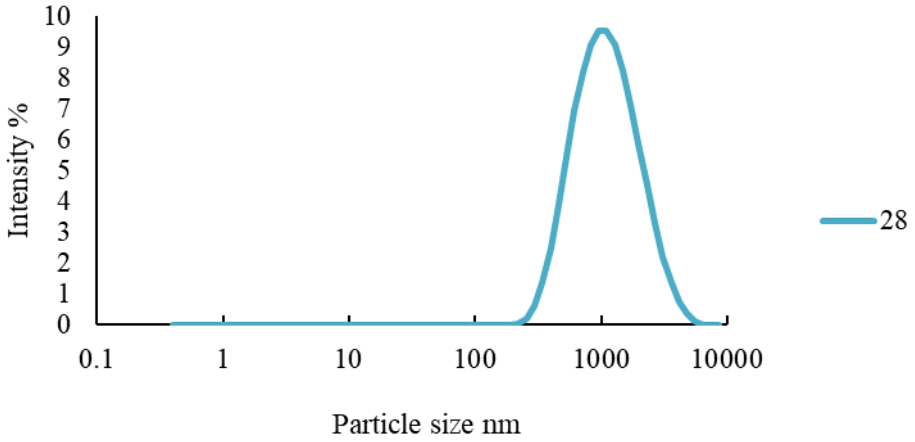
29	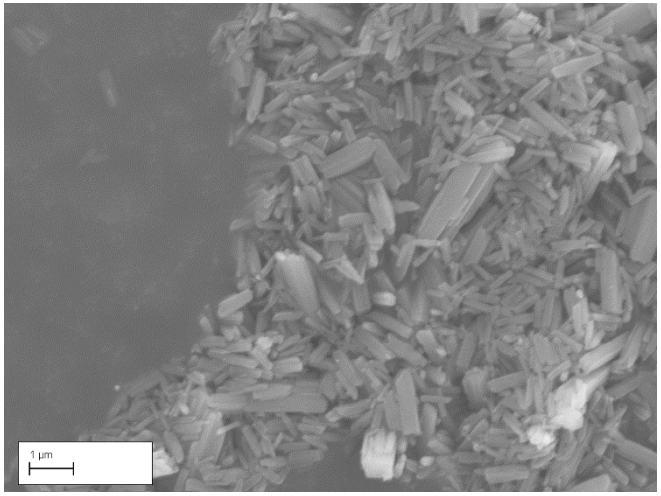	0.5 Hz 2 mm 20 min CI 3.374 CT 3.374	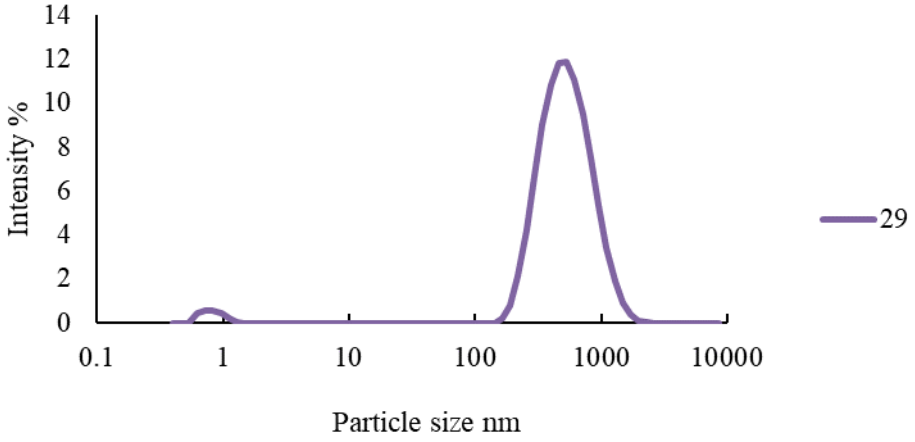

30	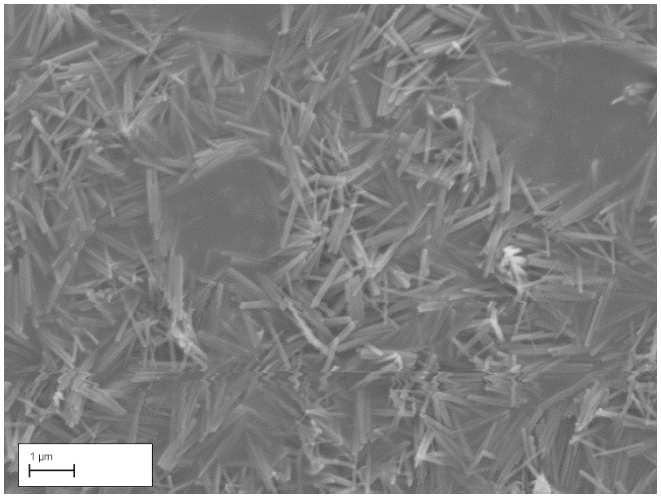	0.5 Hz 4 mm 8 min CI 3.374 CT 3.374	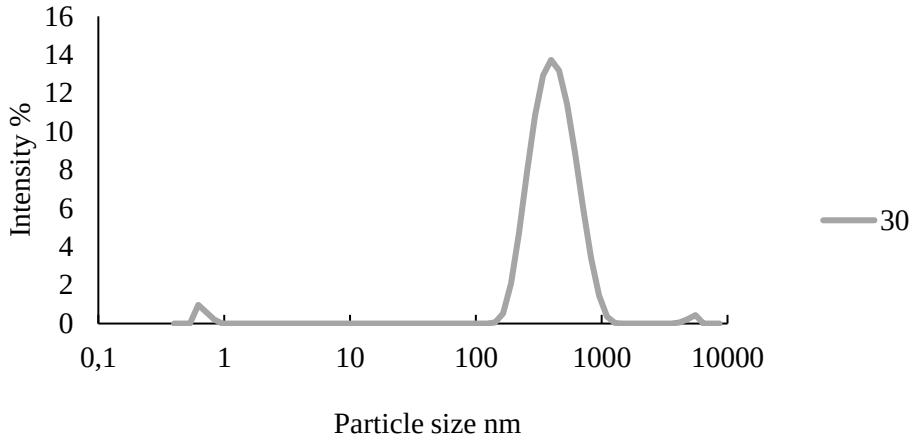
31	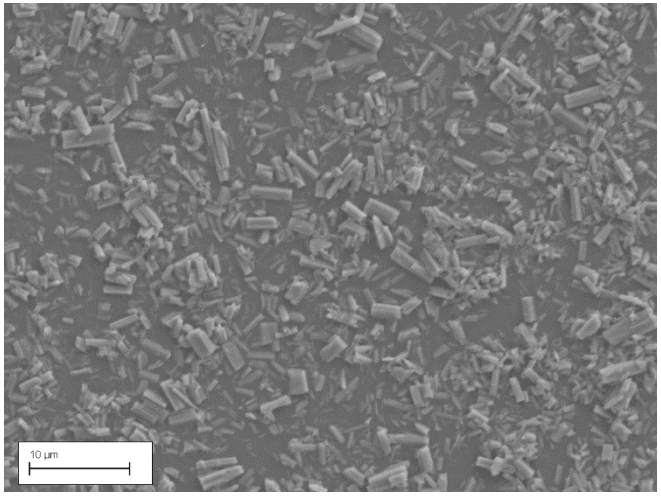	4 Hz 4 mm 20 min CI 3.374 CT 3.374	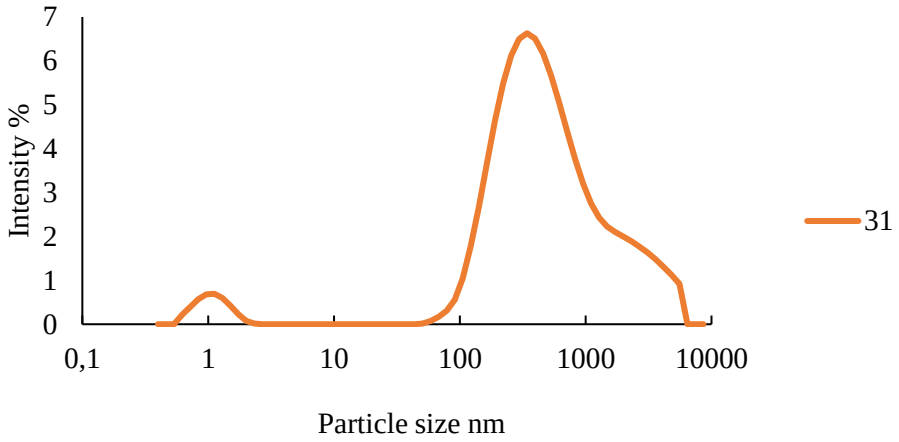

32	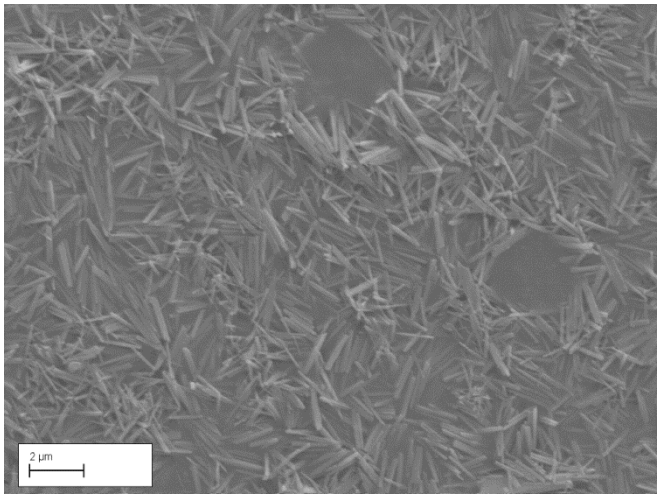	4 Hz 2 mm 8 min CI 3.374 CT 3.374	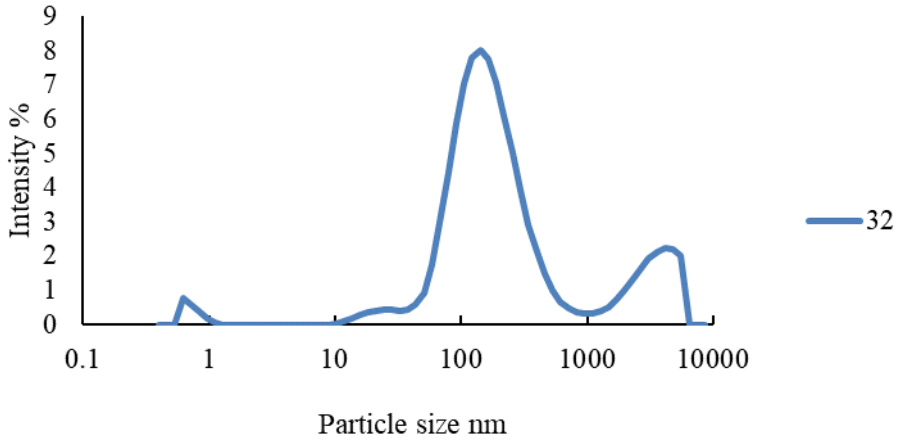

$$A\,PS = 225 + 187\,Freq - 28\,Amp + 19\,RT - 183\,CI + 273\,CT - 29.5\,Freq * Freq + 31.8\,Amp * Amp - 1.56\,RT * RT + 14.9\,CI * CI - 2.5\,CT * CT - 17.3\,Freq * Amp - 12.8\,Freq * RT - 13.0\,Freq * CI + 44.4\,Freq * CT + 8.5\,Amp * RT - 19.2\,Amp * CI - 28.1\,Amp * CT + 12.98\,RT * CI - 12.03\,RT * CT - 17.2\,CI * CT$$

$$APS = 225 + a(187 - 29.5a - 17.3b - 13c - 12.8e + 44.4d) + b(31.8b - 28 + 8.5e - 19.2c - 28.1d) + c(14.9c - 183) + d(273 - 2.5d - 17.c) + e(19 - 1.56e + 12.98c - 12.03d)$$

Equation A5.1 Response Surface Equation for targeting experiment non-factorised and factorised with A= Freq b= Amp c= CI d = CT e=RT

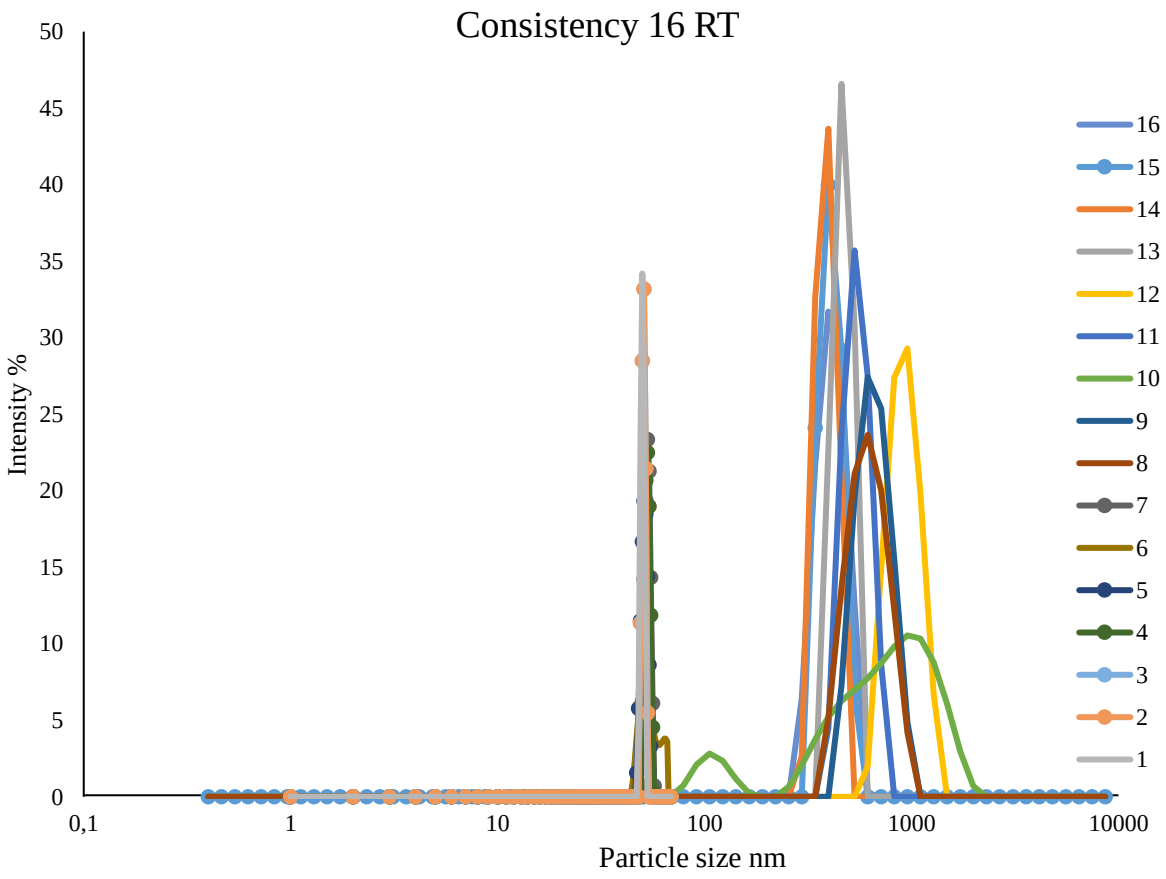

Figure A5.4 Consistency 16 RT full DLS set carried out in the OBR for PiC synthesis

Table A5.3 CFD Vectors Simulations for the OBR

Experiment number	CFD Vectors Simulations
	Velocity Contour [m.s-1] 0 0.034 0.088 0.122
DOE 1,5,8,9,10,11,13,14,15,16	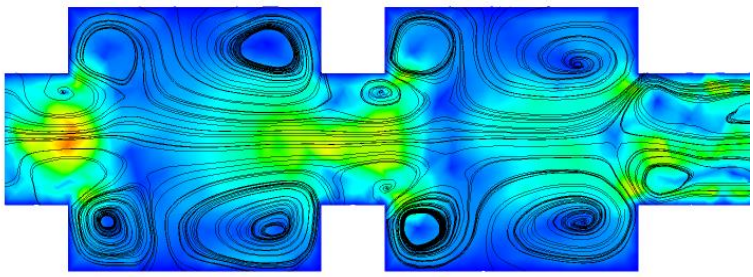
DOE 3	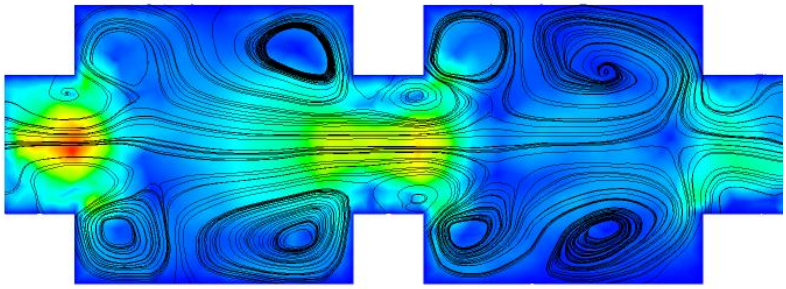
DOE 4	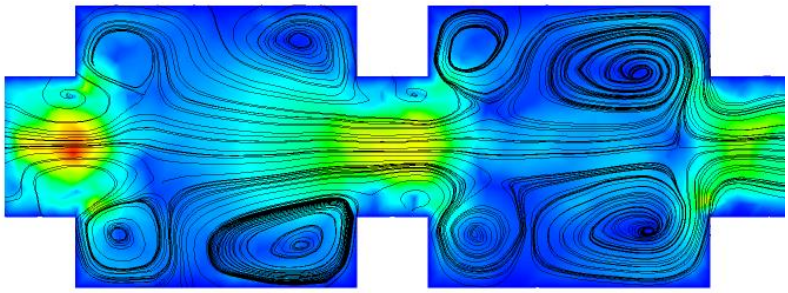
DOE 7	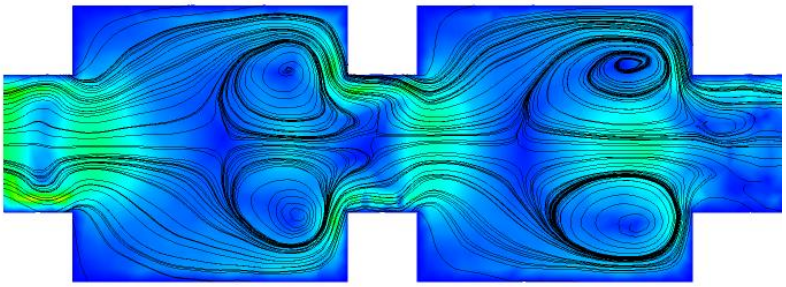

DOE 12	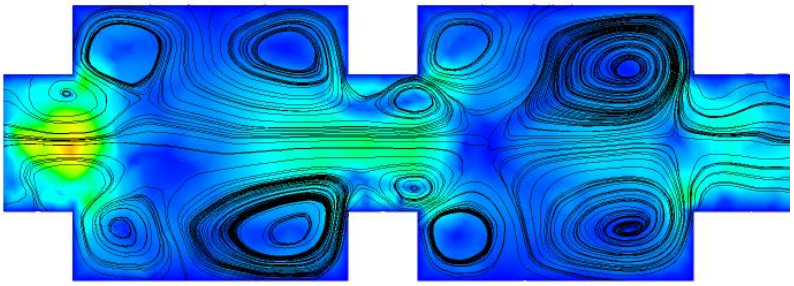
DOE 17,25	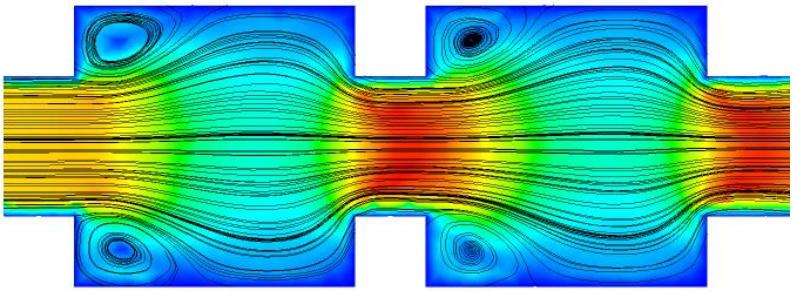
DOE 18,26	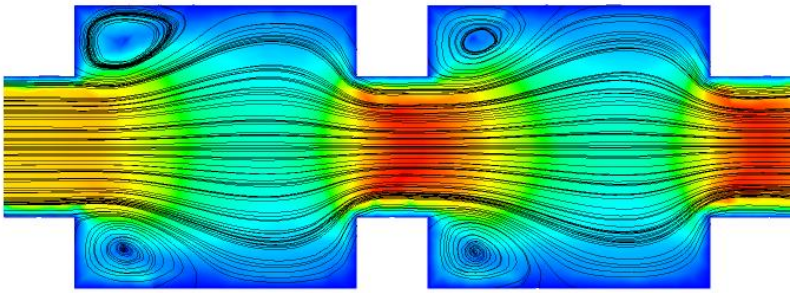
DOE 19,27	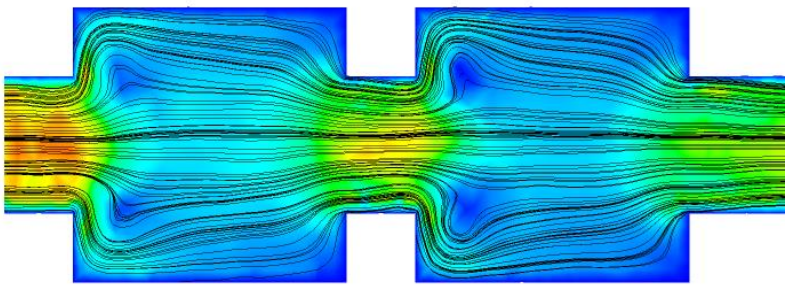
DOE 20,28	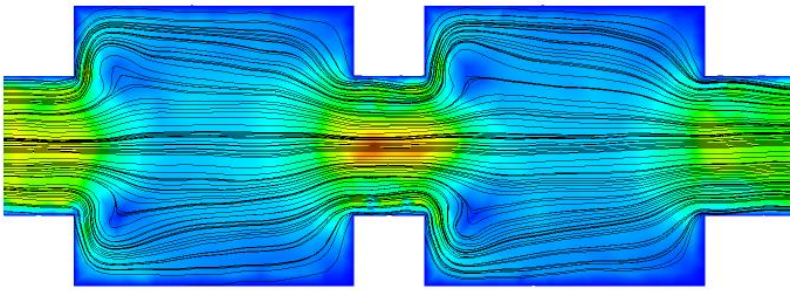

DOE 21	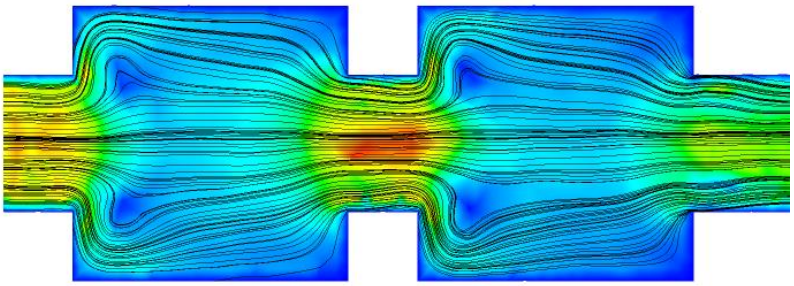
DOE 22,29	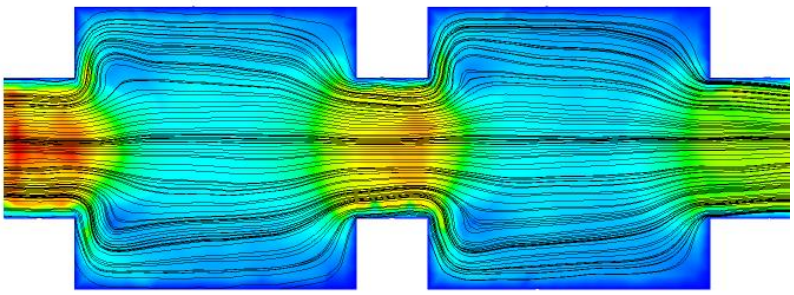
DOE 23	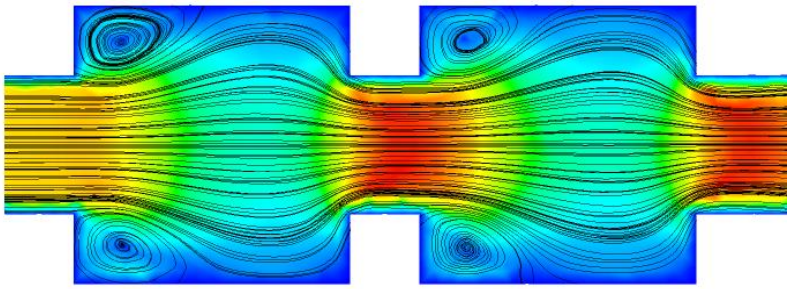
DOE 24,32	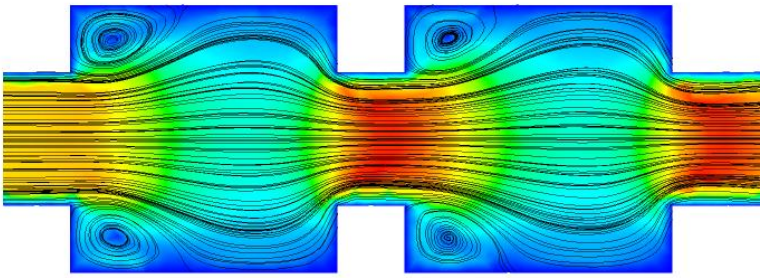

H1 to H5	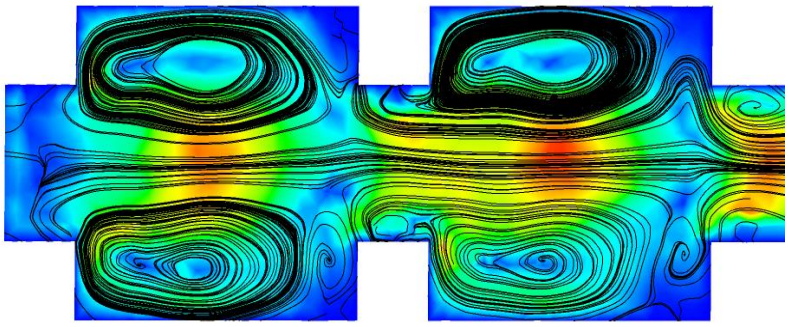
H6 to H8	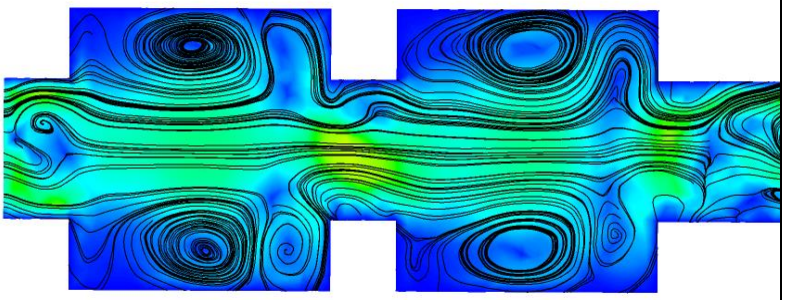

Appendix Chapter VI Vapourtec (A6)

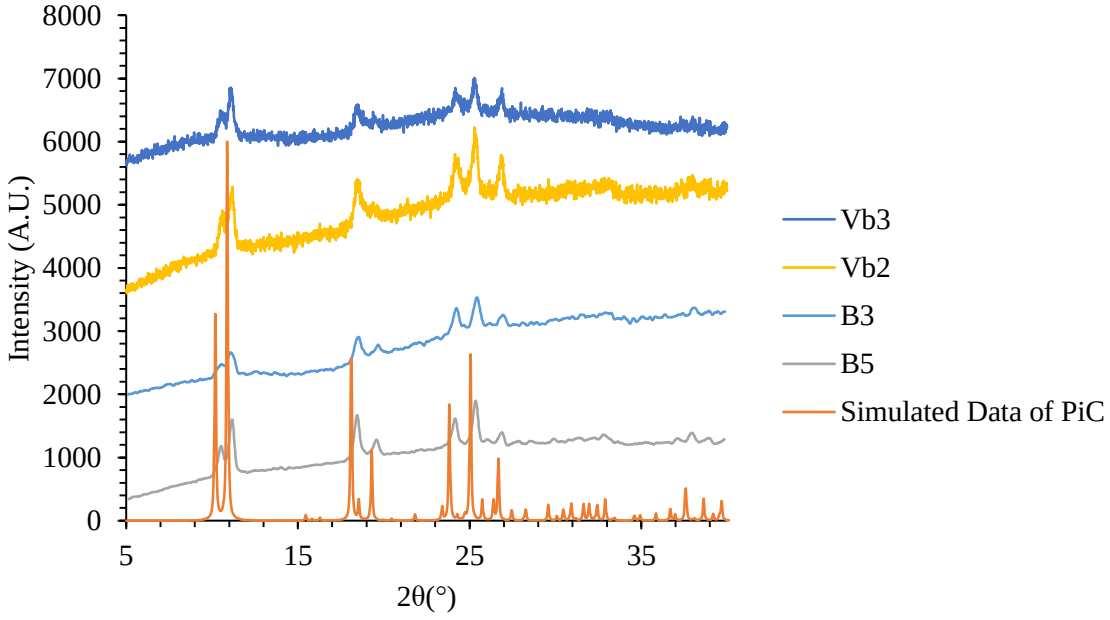

Figure A6.1 PXRD of produced PiC in Vapourtec 1 mm bore tubing compared to batch PXRD and simulated data from Grosjean *et al.*[14]

Supplementary Information CD

CD/Chapter III-IV KRAIC

CDCh3-1: CD\Chapter 3-4 KRAIC\CFD Video for 0.020 m per s flow rate

CDCh3-2: CD\Chapter 3-4 KRAIC\KRAIC-D

CDCh3-3: CD\Chapter 3-4 KRAIC\KRAIC-D\SEM

CD/Chapter V OBR

CDCh5-1: CD\Chapter 5 OBR

CDCh5-2: CD\Chapter 5 OBR\Batch SEM for Concentration for 100 nm to 1000 nm target

CDCh5-3: CD\Chapter 5 OBR\CFD

CDCh5-4: CD\Chapter 5 OBR\Consistency 16 Residence Time in a row SEM and DLS

CDCh5-5: CD\Chapter 5 OBR\DLS Repeat of H1 to H8 with SEM

CDCh5-6: CD\Chapter 5 OBR\DOE Data DLS + SEM

CDCh5-7: CD\Chapter 5 OBR\Velocity Ratio and RTD analysis

CDCh5-8: CD\Chapter 5 OBR\Yield Optimization

CD/Chapter VI Vapourtec

CDCh6-1: CD\Chapter 6 Vapourtec

CDCh6-2: CD\Chapter 6 Vapourtec\DOE Static Mixers

CDCh6-3: CD\Chapter 6 Vapourtec\Jet Stirring

CD/Chapter VII Switching

CDCh7-1: CD\Chapter 7 Switching\Color Switching SCO

CDCh7-2: CD\Chapter 7 Switching\EDF

CDCh7-3: CD\Chapter 7 Switching\PiC Crystal Structure